8-7-2018

Young Stars, Young Planets, and Habitable Zones

Justin Cantrell

YOUNG STARS, YOUNG PLANETS, AND HABITABLE ZONES

by

JUSTIN CANTRELL

Under the Direction of Russel White, PhD

ABSTRACT

We present the results of a high precision infrared radial velocity (RV) search for hot-Jupiters around young stars in nearby young clusters and Moving Groups. Utilizing high resolution infrared spectroscopy with Gemini South Phoenix and VLT CRIRES, we targeted a sample of 28 young stars. Our second survey was of 38 young stars observed with Keck NIRSPEC. Our technique for determining RVs for young stars utilizes telluric features as an absolute wavelength reference. With this technique, we have been able to achieve RV precisions of 22-31 m/s with Gemini Phoenix, 32-63 m/s with VLT CRIRES, and 41-182 m/s with Keck NIRSPEC on single field stars.

With Gemini Phoenix and VLT CRIRES, we identified TWA 13A and ScoPMS 13 as candidate RV variables. We identified two spectroscopic binaries (RXJ1204.7-7731 and 1RXS J195602.8320720). We show initial orbital fits for RXJ1204.7-7731, that show a ∼5.5 day period with and eccentricity of ∼0.1, and a mass ratio of K_A/K_B= 0.37. Initial orbital fits for 1RXS J195602.832072019 show a nearly equal mass system, with a mass ratio of K_A/K_B=0.97, with a ∼19 day period and an eccentricity of ∼0.2.

In our Keck NIRSPEC sample, we report a young (∼ 10 Myr) candidate hot Jupiter in Upper-Scorpius around RXJ 1540.9-3024, and present an initial orbit for planet RXJ 1540.9-3024b as having a 10.7 day period with an eccentricity of 0.28 and an $M\sin i$ of 5.4 M_J. We also report the discovery of two spectroscopic binaries, RXJ 1548.9-3045 and V1096 Tau, but our temporal sampling was insufficient to obtain orbital solutions.

We use the sample of known stars and brown dwarfs within 5 pc of the Sun, and AFGK stars within 10 pc, to determine which stellar spectral types provide the most empirical habitable zone, or EHZ. M stars provide more EHZ real estate than other spectral types, possessing 36.5% of the habitable real estate *en masse*. K stars are second with 21.5%, while A, F, and G stars offer 18.5%, 6.9% and 16.6%, respectively. If Earth-like planets are as common around low mass stars as Kepler results suggest, M stars are the most likely place to find Earth-like planets in habitable zones.

INDEX WORDS: stars: young stars – exoplanets stars: binaries stars: habitable zones – solar neighborhood

YOUNG STARS, YOUNG PLANETS, AND HABITABLE ZONES

by

JUSTIN CANTRELL

A Dissertation Submitted in Partial Fulfillment of the Requirements for the Degree of

Doctor of Philosophy

in the College of Arts and Sciences

Georgia State University

2018

YOUNG STARS, YOUNG PLANETS, AND HABITABLE ZONES

by

JUSTIN CANTRELL

Committee Chair:	Russel White
Committee:	Doug Gies
	Sebastien Lépine
	Alexander Kozhanov

Electronic Version Approved:

Office of Graduate Studies

College of Arts and Sciences

Georgia State University

August 2018

DEDICATION

I'd like to dedicate this to Brenda Cantrell, my wife of 20 years, and two my kids Alala and Logan. I love you all.

ACKNOWLEDGMENTS

Growing up in the Silicon Forest (Portland, OR), if you were relatively good at math and science, you were steered towards an engineering track. In my last year of high school, I took an engineering prep class that was cross listed with my high school and the nearby community college. It was on the job shadow portion of that class that I decided I did not want to be an engineer. The work seemed dreadfully boring with less big ideas and more tedious tinkering.

After I graduated high school, I joined the Marine Corps. After boot camp and my Military Occupational Specialty (MOS) school for ground radio and electronics repair, I was given my first duty station at 11th Marine Regiment, 1st Marine Division in Camp Pendleton California. I spent a couple years at Headquarters (HQ) Battalion before I transfered to HQ Battery 5th Battalion 11th Marine Regiment. There I worked with some very good people who I am still friends with today. I worked as a section head in charge of the Communications Electronics Maintenance (CEM) shop. I can't say it was fun all the time, but I have many great memories of good times with good people.

When I left the Marine Corps in 2002, I started my journey through higher education not knowing if I could finish. My wife had just given birth to my daughter two months before I was discharged from the Marine Corps, and we needed to make ends meet. After applying for several jobs, I decided the best route for us was for me to get an undergraduate degree and finish as soon as possible. I was allowed 36 months to finish my undergraduate degree by

the Montgomery GI Bill. By using community college in California, I had planned transfer to a the University of California San Diego once I had enough credits. After two years at Palomar Community College, my wife was promoted, and we moved to Atlanta Georgia in January of 2004. I started at Georgia State University the following semester.

I was looking into physics or astronomy as a career field, and having learned my lesson about engineering, I decided to try it out first. Todd Henry was kind enough to pick me as an undergraduate assistant soon after I started in the physics undergraduate program at Georgia State University. It was with Todd that I started my work on habitable zones around nearby stars that is presented in this dissertation. The lessons I learned from him and other RECONS members were invaluable in my undergraduate and graduate career.

After my second year qualifying exams, I changed course to work with Russel White on search for young planets around young stars using high resolution infrared radial velocity techniques. His patience and insight have helped me considerably through my long journey to finishing my dissertation.

Along the way I was helped by so many individuals. Thank you to all who gave me guidance, opportunity, and support throughout the years.

TABLE OF CONTENTS

LIST OF TABLES

LIST OF FIGURES

CHAPTER 1

Introduction and Motivation

While I was writing this introduction, I took a break and came across a replay of the movie version of The Hitchhiker's Guide to the Galaxy. Not only did it remind me how terrible that movie was, but it got me thinking about"The Question". In the book (and terrible movie) a supercomputer named Deep Thought is constructed to answer the "Ultimate Question of Life, The Universe, and Everything", which turns out to be 42. Unfortunately nobody bothered to ask what "The Question" was, so the Earth was built as a supercomputer to determine The Question, but, unfortunately, the Earth is destroyed before it can finish running the program. This is all rather hilarious, but The Question is a real one. Although I do not purport to know The Question or the answer (although I suspect it is not 42), three equally profound questions do come to mind. Why are we here? Where did we come from? and Are we alone?

The first question, "Why are we here?", is best left to philosophers and theologians. The second question, "Where did we come from?", is starting to become tangible with advances in scientific knowledge since the early 20^{th} century. From the introduction of the Big Bang Theory and advances in particle physics, to the discovery of DNA, we have begun to discover some of the basic building blocks of the life and the Universe.

The third question, "Are we alone?", is one that astronomical techniques and measurements have begun to investigate.

Early astronomers looked to the sky and saw the Moon as a habitable world covered

in vast oceans, Venus as a swampy marshland enshrouded in clouds, and Mars with grand canals (Lowell 1895). Not one of these worlds has maintained its promise of abundant life. Instead, the Solar System, once thought to be teeming with life, may be barren, although hope remains for environments under the icy crust of Europa (Marion et al. 2003; Greenberg 2010, Schmidt et al. 2011), in the tiger stripes of Enceladus (Parkinson et al. 2007), in water under the Martian surface (Malin & Edgett 2000), or perhaps lurking somewhere as yet unidentified. Planets around stars other than the Sun provide new hope for finding life on another planet.

Over the past two and a half decades, the exoplanet community has produced a wealth of planet discoveries spanning almost every imaginable configuration. There have been planets found around A type to M type stars, pulsars, and even giant stars, in sizes ranging from Earth size to gas giants near the brown dwarf boundary, in single planet systems to multi-planet systems, in orbital configurations from very close in to circumbinary. In addition, results from NASA's Kepler mission have added valuable coverage to the gaps in our understanding of exoplanet systems. These data have allowed for the first statistical studies of the frequency of planets of different types in our galaxy showing that planets are quite common. For example, Fressin et al. (2013) found that 16.5% of FGK stars have at least one planet between 0.8 and 1.25 $R_\oplus$. Dressing & Charbonneau (2013), find that the planet occurrence rate for 0.5-4 $R_\oplus$ planets around stars cooler than 4000K is 0.9 planets per star and that one in five solar type stars have Earth-like planets in the habitable zone. These frequencies are important, as they provide an important step towards determining the number of earth size

planets where we might search for life.

In 1961, Frank Drake proposed an equation which he hoped would quantify the number of civilizations in our galaxy with which communication might be possible. This has become known as the Drake Equation:

$$N = R_* \cdot f_\mathrm{p} \cdot n_\mathrm{e} \cdot f_\mathrm{l} \cdot f_\mathrm{i} \cdot f_\mathrm{c} \cdot L \tag{1.1}$$

where:

N = the number of civilizations in the Milky Way from which we might detect communication

R = the average star formation rate in the Milky Way

f_p = the fraction of stars that have planets

n_e = the fraction of those stars with habitable planets

f_l = the fraction of habitable planets on which life emerges

f_i = the fraction of planets with life which sufficiently evolves to become intelligent life

f_c = the fraction of intelligent civilizations that broadcast detectable signals

L = the length of time for which such civilizations are producing those detectable signals

While f_p is becoming clearer with more statistical certainty, and we are beginning to find planets within the habitable zone of their parent stars, n_e remains an elusive quantity. Understanding the process by which planets form and evolve will help astronomers better understand how planets come to reside in the orbital configurations we find them.

1.1 Searching for Young Planets

It was assumed as far back as Kant (1755) that planets in the solar system formed in a circumstellar disk. Shortly before the first exoplanets around main sequence stars were discovered, Lissauer (1993), in a review article on planet formation, discussed planet formation with respect to the solar system. They concluded, with an admittedly limited sample (e.g., the Sun and our solar system), that formation models should account for planets with fairly circular, coplanar orbits consistent with formation within a circumstellar disk. As such, an interesting, and at first unexpected, exoplanet configuration is that of the giant planets found in short orbital periods, or in retrograde orbits (Winn et al. 2009), or with highly eccentric orbits and high obliquity orbits (e.g., Albrecht et al. 2012. The discovery of 51 Peg b by Mayor & Queloz (1995) was the first planet discovered around a Sun-like star, being a short period Jupiter mass planet, it forced sweeping changes in theories of how planets form and dynamically evolve (e.g., Santos et al. 2005). These planets, called "hot Jupiters" for their large mass and proximity to their parent star, are defined in Wright et al. (2012) as an exoplanet having a period of < 10 days and an $M\sin i > 0.1$ M_{Jup}. Additionally, Wright et al. (2012) give a rate of $1.2\pm0.38\%$ of FGK dwarfs that host hot Jupiter planets.

Although studies suggest that planets as large as Neptune could form at small separations (Hansen & Murray 2012; Boley et al. 2016), it is still believed that most gas giant planets form beyond the frost line. Consequently, there must be a mechanism responsible for their migration inwards (Winn & Fabrycky 2015). Two competing migration scenarios, planet-disk and planet-planet interactions, have emerged to explain the presence of hot Jupiters.

Although migration through a disk is considered to be the most efficient migration mechanism (e.g., Goldreich & Tremaine 1980; Lin et al. 1996; Cossou et al. 2013), this process typically circularized orbits. Thus some additional dynamical interactions must take place in order to produce the broad range of eccentricities observed for extrasolar planets (e.g., Adams & Laughlin 2003; Chatterjee et al. 2008; Ford & Rasio 2008; Nagasawa et al. 2008; Smith & Lissauer 2009; Guillochon et al. 2011; Beaugé & Nesvorný 2012).

If we hope to better understand the planet formation and migration process, we must search for planets around young stars (O'Connor & Hansen 2018). However, searching for planets orbiting young stars presents very difficult challenges. Chromospheric activity, such as spots and flares, manifests as a distortion in the spectral line profiles, which appears in the spectrum as a shift in radial velocity as the spot or flare rotates across the visible disk of the star. These radial velocity perturbations are known as stellar jitter. In two case studies of two very young ($\lesssim$5 Myr) stars, Hubble I 4 (Mahmud et al. 2011) and PTFO 8-8695 (Ciardi et al. 2015), the authors show how spots on the surface of a star can mimic the RV signature of a planet, and, furthermore, Bailey et al. (2012) describe the correlation of large amplitude ($\leq$ 2 km/s) RV variability due to stellar activity with age and vsini.

Although flares are short lived, on young late type stars, spots can be long lived and cover a significant portion of the stellar surface. Bradshaw & Hartigan (2014) discuss earlier type T Tauri stars (F,G,K) and show observed spot lifetimes from 31 days for the F9 star CoRoT 2 to >20 years for K4 star V410 Tau in Taurus-Auriga. In order to use the Doppler RV method to search for planets orbiting young stars, we must look at methods to mitigate

the effects of stellar jitter to ascertain if RV variations are caused by a companion or by stellar jitter.

One such method, used in this work, is to observe stars at infrared wavelengths. On the stellar surface, magnetic spots that inhibit convection appear cooler (ΔT_{eff} ≈2000 K in the Sun) than the surrounding photosphere. Since the surface radiates according to Planck's law, the contrast between the spot and the photosphere can be reduced by observing at longer wavelengths, where this RV distortion is decreased compared to visible light. Marchwinski et al. (2015), in a study of the Sun using the Solar Irradiance Monitor (SIM) on the SOURCE spacecraft, determined that for solar type stars, the jitter can be reduced by a factor of 4 by observing in near infrared wavelengths versus observations taken in the optical. Although this does not completely resolve the underlining jitter associated with photospheric activity, it can be a first step to identifying RV variability caused by companions.

As the distortion in the spectral line caused by spots is dependent on the difference in the temperature of the spot and the photosphere, the RV amplitude should be different at different wavelengths. As such, a multi-wavelength campaign would be ideal for determining if a periodic RV signal is due to jitter or a companion. Unfortunately, telescope time is limited, and getting sufficient telescope time for high resolution spectroscopic surveys at multiple wavelengths with large (8 m class) telescopes is challenging at best. To address this issue, several groups have developed techniques to cope with stellar jitter by analyzing the spectral profile to determine if RV shifts are caused by spots or an orbiting companion. As a spot rotates across the visible disk of the star, it distorts the line profile by blocking

out a portion of the star light on the blue or red (approaching or receding) side of the absorption line. This causes a change in the shape of the absorption line profile, resulting in an apparent shift, whereas an orbiting companion causes a systematic shift in wavelength of the absorption line profile. There are different techniques being developed to identify and/or remove this effect. These techniques rely on determining the shape of the absorption line profiles and how they correlate to shifts in RV (e.g., line bisector analysis; Queloz et al. 2001; Clearing Activity Signals In Line-profiles (ClearASIL); Moulds et al. 2013).

Recently, an international effort has been directed towards finding young planets using some of these techniques. Based on data obtained with the revised Kepler mission (K2), a transiting short-period planet was identified orbiting a young star in the Upper Scorpius region (Mann et al. 2016; David et al. 2016). At 5-10 Myr this is one of the youngest planets known. Nevertheless, without RV confirmation, its limiting mass ($m\sin i$) and eccentricity remain unknown. Equally tantalizing, 2 planets have recently been announced in the 2 Myr Taurus association (Johns-Krull et al. 2016; Donati et al. 2016) based on RV variations, and equally intriguing, the discovery of a planet around the weak-line T Tauri Star TAP 26 (Yu et al. 2017). The properties of these planets are likewise poorly determined because they orbit an accreting star (CI Tau) and a very heavily spotted star (V830 Tau), and a very active star (TAP 26). Nevertheless, the work collectively demonstrates that short period planets can be found while young, with dedicated precision measurements.

We conducted a survey of nearby young clusters and Moving Groups to search for hot Jupiters with the intent on increasing the number of known young planets. With more

examples of these young systems, we can begin to distinguish between proposed formation and migration scenarios. Understanding how hot Jupiters form may elucidate how and why gas giant planets come to be in the peculiar orbital configurations we find them. Gas giant planets can be important to habitability, as they clear the inner solar system of leftover debris and planetesimals by dynamical effects (Rasio & Ford 1996). Without this large gravitational body, over time, large impactors may sterilize a planet with too much frequency for complex life to gain a foothold (Georgakarakos et al. 2018).

1.2 Habitable Zones

The ongoing search for planets has provided us with important statistics on the fraction of stars with planets, f_p. While we know that one in five solar type stars have Earth-like planets in the habitable zone (Dressing & Charbonneau 2013), that does not imply that these planets are habitable. Habitability is more complicated than a location around a star. We only need to look to our Solar System, where Venus, Earth, and Mars are in the traditional habitable zone of the Sun, yet only Earth is currently able to harbor intelligent life. Several factors are involved in making and keeping a planet habitable. These are, but may not be not limited to, liquid water (Kasting et al. 1993; Kasting 1996; Tarter et al. 2007; Selsis et al. 2007), a magnetic field (See et al. 2014), plate tectonics (Doyle et al. 1998), and possibly the presence of a distant gas giant planet in the same system (Georgakarakos et al. 2018).

Although the fraction of stars with habitable planets, n_e, remains elusive, in order to begin to answer the question "Are we alone?" we first need to better understand how much

habitable area, a term we call habitable "real estate", main sequence stars provide. To do this, we determined habitable zones for each star for a nearby population of stars whose stellar properties are well known. This is used to estimate the total habitable real estate for each spectral type in the solar neighborhood.

1.3 Dissertation Layout

In Chapter 2 and Chapter 3, we present our search for hot Jupiters around young (2-45 Myr) stars, using high dispersion infrared spectra from the Phoenix instrument on the Gemini South Telescope, the CRIRES instrument on the Very Large Telescope (VLT), and the NIRSPEC instrument on the W.M. Keck telescope. We will introduce our technique for determining high precision radial velocities (RVs) for these young stars, as well as present our results. We identify four double-lined spectroscopic binaries (SB2s) and one young star with a candidate planet. Additionally, in Appendix A, we show figures plotting the epoch RV for each observing day for all stars in Chapter 2 and Chapter 3.

In Chapter 4, we present a detailed investigation of the challenges of finding young planets in the presence of spots. Additionally, we present our companion detection limits for the samples discussed in Chapter 2 and Chapter 3. We discuss stars with large amplitude RV variability, some of which have disks or suspected companions.

In Chapter 5, we use the complete sample of all stars currently known to be within 5 pc of the Sun from Henry (2012), and an extended 10 pc sample of AFGK stars as well as binary properties, photometric and astrometric data to determine habitable zones for each star. We

present our derived T_{eff} and $R_\star$ for each star in the sample and discuss the methods used to derive each star's empirical habitable zone (EHZ). For multiple star systems, we assess dynamical stability to eliminate stellar systems unsuitable for long-term planetary orbits. Our main goal is to determine, as a function of spectral type, the cumulative available EHZ in the solar neighborhood.

In Chapter 6, we provide a summary of this body of work.

CHAPTER 2

A precision Infrared Radial Velocity Survey of Southern Young Stars

2.1 Infrared Spectra with Gemini Phoenix

This RV survey of young southern stars was initiated with a 5 night observing run using the high resolution near infrared (NIR) spectrograph Phoenix on the Gemini South Telescope.

2.1.1 Sample & Selection Criterion

A sample of young southern hemisphere stars was selected that spanned a range in right ascension, allowing for many to be observed over the course of one night. Specific selection criteria include spectral type cooler than mid-K (which have strong CO R-branch lines at 2.3 μm), K_s magnitude brighter than 9.5 mag, no known spatially resolved companions, a low projected rotational velocity ($v\sin i < 12$ km/s), and no evidence for active accretion (e.g., only weak-lined T Tauri stars). The observed sample includes 15 stars from nearby Moving Groups (e.g., Zuckerman & Song 2004), including 5 from β Pictoris (β Pic), 1 from Tucana-Horologium (Tuc-Hor), 3 from η Chamaeleontis (η Cham), and 8 from the TW Hydrae (TWA). It also includes 11 stars in nearby star forming regions, including 3 from Chamaeleon (Cham; Covino et al. 1997), 6 from Upper Scorpius (Upper Sco; Köhler et al. 2000), 2 from Lupus (Lup; Hughes et al. 1994), and 1 from Corona Australis (CrA; Neuhäuser et al. 2000). Ages for these nearby Moving Groups and star forming regions are listed in Table 2.1 with references. It is worth noting that the ages given for Cham (4.5±1.6), Lupus (9.1±2.1), and CrA (9±4) given by James et al. (2006) are slightly older than others

(e.g., Lupus 3±2 Myr; Alcalá et al. 2014) possibly due to their selection of weak-lined (non-accreting) T Tauri stars. As our stars were selected to be non-accreting, we use James et al. (2006) ages.

Table 2.1: Ages of Nearby Moving Groups & Star Forming Regions

Group	Age (Myr)	Reference
β Pic	24±3	Bell et al. (2015)
η Cha	11±3	Bell et al. (2015)
Cham	4.5±1.6	James et al. (2006)
TWA	10±3	Bell et al. (2015)
Upper Scorpius	10 Myr	Feiden (2016)
Lup	9.1±2.1	James et al. (2006)
CrA	9±4	James et al. (2006)
Tuc-Hor	45±4	Bell et al. (2015)

In total, a sample of 25 young stars was observed with Gemini South Phoenix and these are listed in Table 2.2, along with 2MASS coordinates, cluster associations, 2MASS K_s magnitudes, spectral types, projected rotational velocities, and rotational periods. Multiplicity is noted for stars with known close companions based on high-spatial resolution imaging, if available. We do not designate stars with wide companions as "multiples" (e.g., HD 155555C - 8.0″, TWA 8B - 13.2″, TWA 9A/B - 5.9″, TWA 13A/B - 5.1″; Hartkopf et al. 2013) as their companions are sufficiently separated as not to contaminate the spectra. The references are included in the table and footnotes.

These stars range from K4-M5 in spectral type, have 2MASS K magnitudes from 6.244-

9.265, range in $v\sin i$ from 5-16 km/s. We note that since this sample was first assembled (2005), several studies now provide more accurate assessments of these stellar properties; we use these modern references in these cases. Rotation periods range from 0.2-20 days, with a average value of $\sim$6 days. We note that this does not represent the typical rotation period for young stars (1-3 days; Saylor et al. 2018, Marilli et al. 2007). Our sample is biased to slow rotation periods, as it was selected for slow rotators.

Table 2.2: Young Southern Stars Sample

Literature Values

	RA	Dec		K_{2MASS}			$v\sin i$		P_{rot}		
Name	(2000)	(2000)	Cluster	(mag)	SpT	Ref	(km/s)	Ref	($days$)	Ref	Multiplicity
Young Stars - Gemini South Phoenix											
HIP 23309	05 00 47.1	−57 15 26	βPic	6.244 ± 0.024	M0	MW12	5.8	M10	8.60 ± 0.07	M10	single (B13)
HIP 29964	06 18 28.2	−72 02 42	βPic	6.814 ± 0.029	K4	MW12	16.4 ± 1.2	T06	2.67 ± 0.01	M10	single (B13)
HD 155555C	17 17 31.3	−66 57 06	βPic	7.629 ± 0.018	M3	MW12	···	···	···	···	···
Recx 4	08 42 23.7	−79 04 03	η Cha	8.615 ± 0.019	K7	J06	6.0	J06	7.1 ± 0.4	M11	···
Recx 10	08 44 31.9	−78 46 31	η Cha	8.732 ± 0.021	K7	J06	< 5.0	J06	20.0 ± 3.0	M11	···
Recx 12	08 47 56.8	−78 54 53	η Cha	8.410 ± 0.031	M2	J06	6.4 ± 2.5	M14	1.26 ± 0.05	M11	···
RXJ 1005.3-7749	10 05 20.1	−77 48 42	Cham	8.892 ± 0.019	M1	C97	11 ± 3	C97	8.08	K12	···
RXJ 1204.6-7731	12 04 36.2	−77 31 35	Cham	8.881 ± 0.019	M2	C97	6 ± 4	C97	···	···	Single (B17)
RXJ 1219.7-7403	12 19 43.7	−74 03 57	Cham	8.858 ± 0.023	M0	C97	7 ± 3	C97	···	···	Single (B17)
TWA 7	10 42 30.1	−33 40 16	TWA	6.899 ± 0.027	M1	J06	< 5.0	J06	5.00 ± 0.03	M10	single (B13)
TWA 13A	11 21 17.2	−34 46 46	TWA	7.491 ± 0.038	M1	J06	10.5	J06	5.56 ± 0.03	M10	single (B13)
TWA 13B	11 21 17.4	−34 46 50	TWA	7.460 ± 0.027	M2	J06	10.3	J06	5.35 ± 0.03	M10	single (B13)
TWA 8B	11 32 41.1	−26 52 09	TWA	9.012 ± 0.025	M5	R14	11.2	J06	0.78	M10	single (B13)
TWA 9A	11 48 24.2	−37 28 49	TWA	7.848 ± 0.036	K5	J06	11.3	J06	5.01 ± 0.01	M10	···
TWA 9B	11 48 23.7	−37 28 49	TWA	9.151 ± 0.024	M1	J06	8.4	J06	3.980	M10	···
TWA 10	12 35 04.3	−41 36 39	TWA	8.186 ± 0.029	M2.5	J06	6.3	J06	8.4 ± 0.01	M10	···
RXJ 1534.3-3300	15 34 23.1	−33 00 09	Upper-Sco	9.130 ± 0.021	M0	K00	···	···	5.37	K12	single (K00)
RXJ 1552.5-2633	15 52 31.2	−26 33 53	Upper-Sco	8.976 ± 0.023	M0	K00	···	···	3.3	A18	single (K00)
ScoPMS 13	15 56 29.4	−23 48 20	Upper-Sco	8.745 ± 0.019	M1.5	C06	···	···	7.98	A18	double (L14)
RXJ 1557.8-2305	15 57 50.0	−23 05 09	Upper-Sco	9.265 ± 0.021	M0	K00	···	···	···	···	single (K00)
ScoPMS 42A	16 10 28.6	−19 04 47	Upper-Sco	8.714 ± 0.019	M3	W94	···	···	6.67	A18	···
SZ 78	15 53 41.2	−39 00 37	Lupus	7.767 ± 0.016	···	···	···	···	···	···	single (M03)
SZ 96	16 08 12.6	−39 08 33	Lupus	8.957 ± 0.019	M1.5	W99	10.5	···	···	···	single (M03)
V721 CrA	19 09 45.9	−37 04 26	CrA	8.311 ± 0.024	K6	T06	···	···	···	···	single (K08)

Table 2.2: Young Southern Stars Sample

Literature Values

	RA	Dec		K_{2MASS}			$v\sin i$		P_{rot}		
Name	(2000)	(2000)	Cluster	(mag)	SpT	Ref	(km/s)	Ref	($days$)	Ref	Multiplicity
HIP 107345	21 44 30.1	−60 58 39	Tuc-Hor	7.874 ± 0.026	M0	T06	8.2	M10	4.50 ± 0.02	M10	single (B13)
Young Stars - VLT CRIRES											
TWA 13A	11 21 17.2	−34 46 46	TWA	7.491 ± 0.038	M1	J06	10.5	J06	5.56 ± 0.03	M10	single (B13)
V721 CrA	19 09 45.9	−37 04 26	CrA	8.311 ± 0.024	K6.0	T06	···	···	···	···	single (K08)
TYC 7443-1102-1	19 56 04.3713	−32 07 37.659	βPic	7.846 ± 0.021	K9IV	···	···	···	···	···	quadruple (this work)
1RXS J195602.8320720	19 56 02.938	−32 07 18.73	βPic	8.114 ± 0.027	M4	···	···	···	···	···	quadruple (this work)
Radial Velocity - Standards Gemini South Phoenix and VLT CRIRES											
GJ 628	16 30 18.1	−12 39 43	Field	5.075 ± 0.024	M3.5	J09	<1.1	D98	···	···	···
GJ 752A	19 16 55.3	+05 10 08	Field	4.673 ± 0.020	M3.5	J09	<2.8	D98	···	···	···

A18 Ansdell et al. (2018)
B13 Biller et al. (2013)
B17 Briceño & Tokovinin (2017)
C06 Carpenter et al. (2006)
C97 Covino et al. (1997)
D98 Delfosse et al. (1998)
J06 Jayawardhana et al. (2006)
J09 Jenkins et al. (2009)
K12 Kiraga (2012)
K00 Köhler et al. (2000)
K08 Köhler et al. (2008)
L14 Lafrenière et al. (2014)
LS04 Luhman & Steeghs (2004)
M14 Malo et al. (2014)
M03 Melo (2003)
M10 Messina et al. (2010)
M11 Messina et al. (2011)
MW12 McCarthy & White (2012)
R14 Riedel et al. (2014)
T06 Torres et al. (2006)
W10 Weise et al. (2010)
W94 Walter et al. (1994)
W99 Wichmann et al. (1999)

2.1.2 Phoenix Observations, Reductions and Extractions

Using the single order Phoenix spectrograph (Hinkle et al. 2000) on Gemini South, high dispersion infrared spectra were obtained over 5 nights (2005 Apr 29 - 2005 May 2) with only 4 nights providing useful observations as 1 night was completely cloudy. Discretionary time was awarded on 2 additional nights (2005 June 17 and 2005 June 23) to obtain follow-up observations for RXJ 1204.6-7731, identified during the initial run as being a spectroscopic binary (SB). In addition to these young star targets, our observing strategy each night included observations of the two slowly rotating field stars GJ 628 and GJ 752A; their properties are also listed in Table 2.2. Since GJ 628 and GJ 752A have RVs constant to $\leq$100 m/s (Nidever et al. 2002), they were observed to empirically determine our RV precision. In addition, two spectral type A stars, HR 4796A (A0V) & HR 7329A (A0V), were observed each night to assist in identifying telluric absorption features; A type stars are essentially featureless at 2.3 μm. Telluric absorption features are used as a wavelength reference and as a measure of the instrumental profile.

A 4 pixel (0.35″) slit and the K4308 blocking filter were used, giving us a wavelength range of 2.296 μm - 2.308 μm (120 Å) at a resolving power of R$\sim$50,000. For modest separation spatially resolved binaries (e.g., HD 155555C, TWA 8AB, TWA 9AB & TWA 13AB), the slit was oriented on the sky in a way to avoid the companion star from illuminating the slit. Integration times were chosen to achieve a S/N of $>$ 50 for both young stars and RV standard stars; a S/N of $>$100 was chosen for telluric calibrator stars (e.g., spectral type A stars). All stars were observed in nod pairs, separated by $\sim$130 pixels (11″) along the slit,

for pair subtraction during image reduction. Finally, for each night, dark and flat frames were obtained for image reduction purposes. A layout of the Phoenix instrument is shown in Figure 2.1

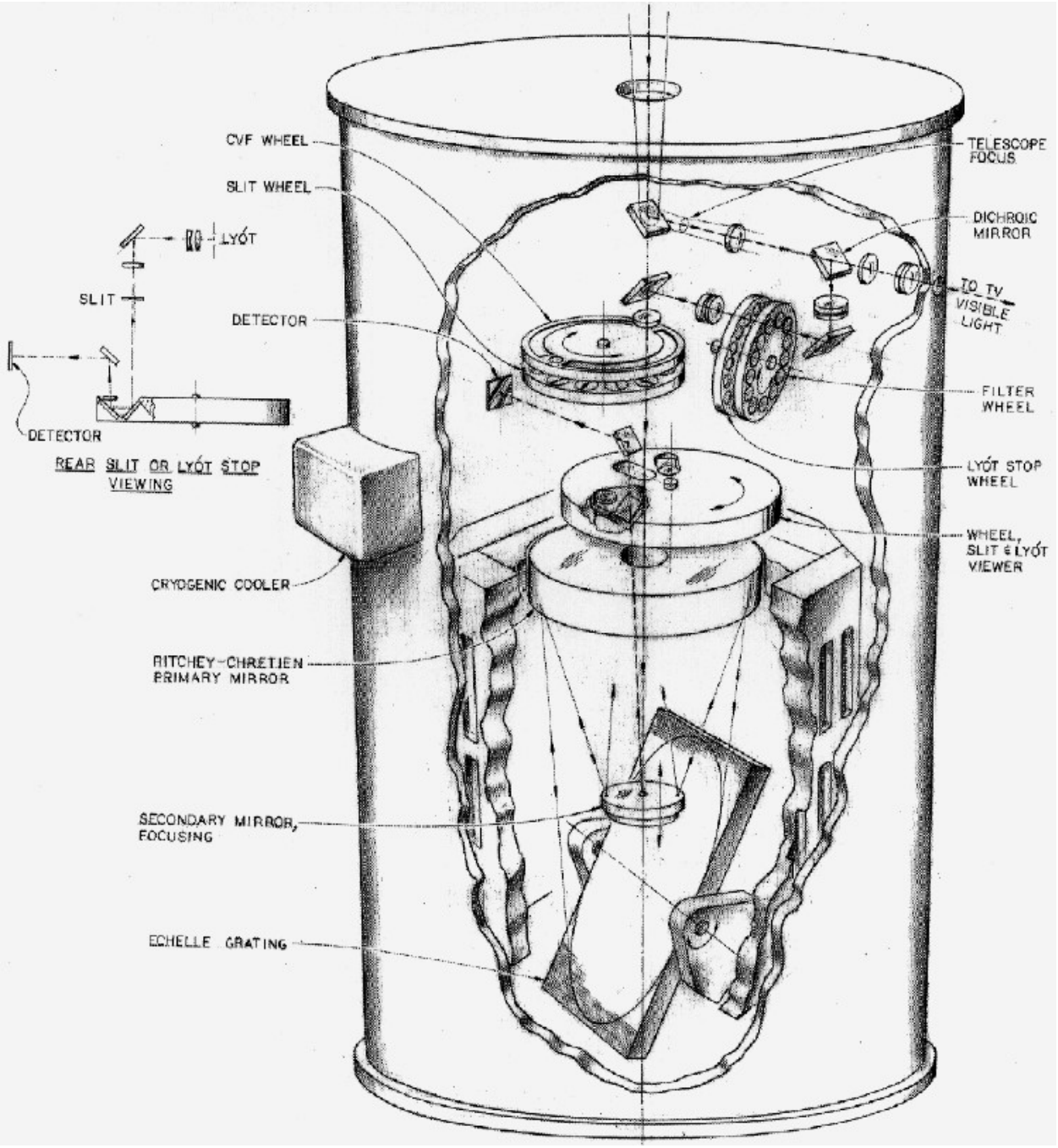

Figure 2.1 The Gemini Phoenix instrument design from Hinkle et al. (1998).

The dark images from each night were median combined and subtracted from each flat

field image. These flats were then normalized, using the central 10% of the chip as the normalization region, and median combined to produce a master flat for each night. All images for a given night were then divided by this master flat and then nod pair subtracted to remove the sky emission, as well as detector bias and dark current. Spectra were then extracted using the 'optimal extraction' method described in Horne (1986) and as implemented in Bailey et al. (2012) for pair subtracted infrared spectra. This extraction technique assumes that the light profile in the spatial direction changes slowly. Using this profile, the spectrum can be constructed by using the average weighted by the profile signal. This can help reduce contribution from noise, as it weights the pixels which lie further from the center of the profile less. Using the same assumption that the profile will vary slowly in the spatial direction, this technique can also be useful in removing cosmic ray hits if the contaminating counts are significantly higher than the local signal.

2.1.3 Phoenix Radial and Rotational Velocity Measurements

Our prescription for determining precise radial and rotational velocities was first developed by Bailey et al. (2012), and is summarized here. We utilize a technique for determining precise RV measurements that relies on the use of telluric features at 2.3 μm as an absolute wavelength reference. The ^{12}CO bandhead in the K-band of the stellar spectrum, which is strong in late-K and M stars, is used to determine the star's RV. We use a model telluric spectrum from KPNO/FTS (Livingston & Wallace 1991) and model stellar spectra generated using NexGen (Hauschildt et al. 1999). These spectral models of our RV standards (GJ 628 and GJ 752A) have a log$g$=4.8 dex, which is consistent with values measured for field dwarfs

(e.g., see the compilation in Hillenbrand & White 2004). We use and updated version of the IDL routine *barycentric_vel.pro* to make the barycentric correction for all stars in our sample. The remaining stars in our sample are young ($\sim$ 2-45 Myr), therefore a log$g$=4.2 dex is assumed, consistent with surface gravity measurements of young stars (Mentuch et al. 2008).

Our fitting routine attempts to reconstruct an observed spectrum by using 18 free parameters to characterize the product of a telluric and synthetic model spectrum as seen in Figure 2.3. These parameters characterize the properties of the instrument, the spectral properties of the star, and the telluric absorption. For the instrumental properties, we model the wavelength solution as a quadratic polynomial. In the original Bailey et al. (2012), prescription, a single Gaussian model was used to determine the instrumental profile (IP). In our updated version, we determined the IP by using a 9 Gaussian model described in Valenti et al. (1995). An example fit for the IP is shown in Figure 2.2. We note that the IP was different over several nights. The spectral and telluric properties modeled by the routine are as follows - depth of telluric features, the depth of stellar features, the projected rotational velocity ($v$sin$i$), a linear (2 parameter) continuum normalization offset, and the star's RV. A limb darkening coefficient is used to calculate rotationally broadened profiles, but is held constant at 0.3 (Claret et al. 2012), consistent with NIR values.

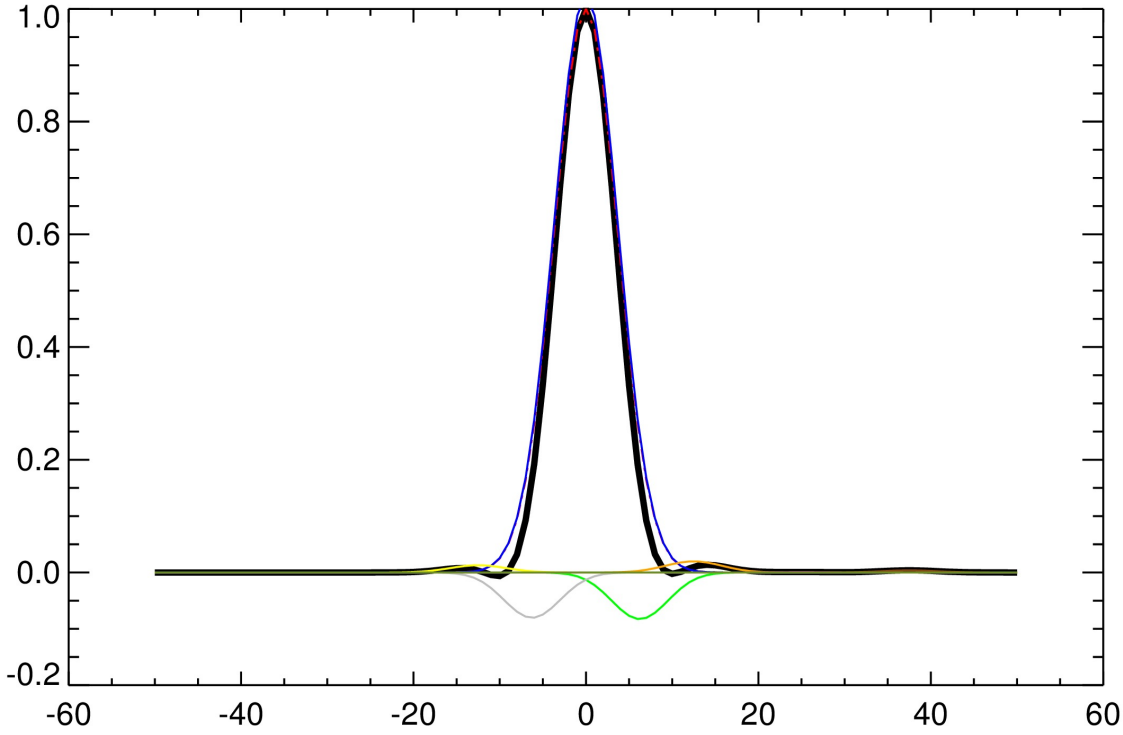

Figure 2.2 An example of the IP for Gemini South Phoenix. 9 Gaussian profiles (colored lines) were combined to create the total IP (black line).

Our fitting procedure is done by following an iterative process utilizing a modified double precision version of AMOEBA for IDL to determine the best fit parameters. The final RV is determined after a 4 stage fitting process with each stage using the best fit results from the previous stage as initial starting parameters. In the first stage, the wavelength solution and instrumental profile are determined by fitting the A spectral type star spectra to a telluric template. In the second stage the results of the A type star modeling are used as inputs for the wavelength solution of the target stars. In this stage, the RV, wavelength solution,

normalization parameters, telluric depths, and stellar depths are allowed to vary, while the $v\sin i$ and IP are held fixed. The $v\sin i$ initial guess is set by literature values where available; otherwise it is set to 10 km/s. The third stage allows the $v\sin i$, RV, normalization parameters, telluric, and stellar depths to vary, while holding the wavelength and IP parameters fixed. For the final stage, the mean of the $v\sin i$ values, for all spectra of a star, from the previous iteration is used, and all parameters, with the exception of the limb darkening coefficient, are allowed to vary.

Several portions of the spectrum were tested to determine the wavelength region that yielded the best RV precision based on minimizing the RV dispersion of the RV standards. In the end, we chose a central fitting region 700 pixels wide ($\sim$85 Å) that removed noise at the edges of the chip and which maximized the number of telluric and stellar features.

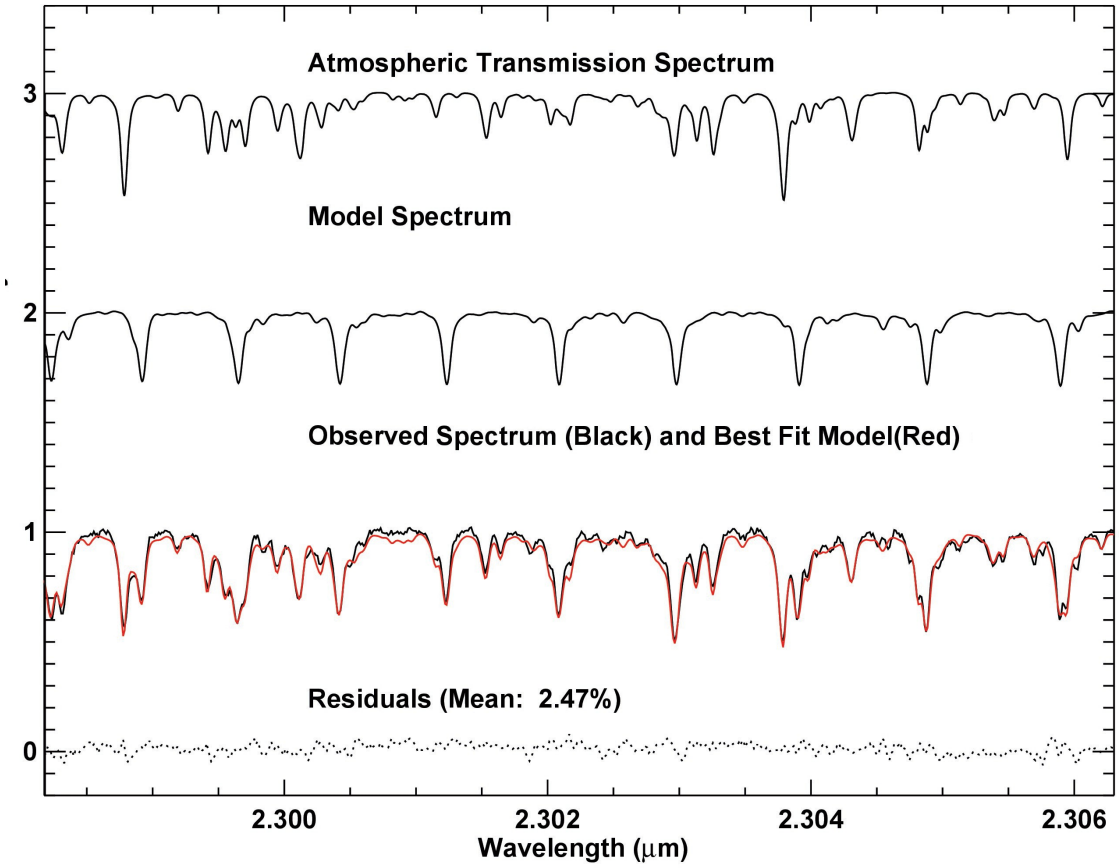

Figure 2.3 An example of our fitting procedure on the RV standard GJ 628. The top solid line show the model telluric spectrum. The second solid line shows the model fit using NexGen spectral models with the best fit parameters. The set of lines shows the observed spectrum (black) and the product of the telluric model and the NexGen Model (red). The bottom dotted line shows the residuals.

2.1.4 Spectroscopic Results with Phoenix

The RV of each individual nod observation determined from the prescription in Section 2.1.3 is listed in Table 2.3. Included are the star identifier, Modified Julian Date (MJD), RV, RV uncertainty (σ_{Obs_A} or σ_{Obs_B} calculated below), and the signal to noise ratio (SNR) of each observation. In this work, an epoch is defined as an A and B pair of spectra. For this work, we will refer to an *epoch RV* as the unweighted average RV of the A and B pair. For high S/N ($\geq$65) spectra, we expect the observed standard deviation of epoch RVs for a slowly rotating inactive star with constant RV to give an empirical estimate of the precision of our technique. We used GJ 628 and GJ 752A for this purpose. The standard deviation of the epoch RVs is 22 m/s (N_{epochs}=5) for GJ 628 and 31 m/s (N_{epochs}=4) for GJ 752A. We note that it has been suggested that telluric lines are estimated to be stable to better than $\sim$20 m/s in our wavelength region on CRIRES (Bean et al. 2010).

Table 2.3: Gemini South Phoenix Individual Radial Velocity Measurements

Star	MJD	RV	σ_{Obs}	SNR
		(m/s)	(m/s)	
Young Stars - Gemini/Phoenix				
HIP 23309	53490.0	20228.0	288.1	79.4

Table 2.3: Gemini South Phoenix Individual Radial Velocity Measurements

Star	MJD	RV	σ_{Obs}	SNR
		(m/s)	(m/s)	
HIP 23309	53490.0	20162.8	350.2	72.0
HIP 23309	53491.0	20034.0	221.0	90.7
HIP 23309	53491.0	20190.0	305.9	77.1
HIP 23309	53492.0	20074.4	140.2	113.8
HIP 23309	53492.0	20170.5	170.0	103.4
HIP 29964	53490.0	17718.1	227.1	89.4
HIP 29964	53490.0	17356.8	249.4	85.3
HIP 29964	53491.0	17619.1	202.4	94.7
HIP 29964	53491.0	17705.1	224.0	90.0
HIP 29964	53492.0	17437.9	168.5	103.8
HIP 29964	53492.0	17719.8	195.1	96.5
HD 155555C	53489.4	4603.0	431.2	64.9
HD 155555C	53489.4	4088.8	709.9	50.6
HD 155555C	53490.4	4283.0	298.1	78.1
HD 155555C	53490.4	4353.0	319.3	75.4
HD 155555C	53491.4	4389.7	375.4	69.6
HD 155555C	53491.4	4332.6	448.0	63.7
HD 155555C	53492.4	4312.8	222.3	90.4
HD 155555C	53492.4	4151.1	289.3	79.2
RecX 4	53490.0	18607.3	297.8	78.1
RecX 4	53490.0	18585.0	338.0	73.3
RecX 4	53491.0	18424.1	299.7	77.9

Table 2.3: Gemini South Phoenix Individual Radial Velocity Measurements

Star	MJD	RV	σ_{Obs}	SNR
		(m/s)	(m/s)	
RecX 4	53491.0	18493.9	320.4	75.3
RecX 4	53492.0	18529.1	276.9	81.0
RecX 4	53492.0	18519.0	288.1	79.4
RecX 10	53490.0	18727.4	303.3	77.4
RecX 10	53490.0	18591.2	396.7	67.7
RecX 10	53491.0	18917.1	315.7	75.8
RecX 10	53491.0	18584.3	372.3	69.8
RecX 10	53492.0	18575.4	304.8	77.2
RecX 10	53492.0	18479.0	364.6	70.6
RecX 12	53490.0	22270.9	306.2	77.0
RecX 12	53490.0	22194.8	463.1	62.6
RecX 12	53491.1	22374.8	274.6	81.3
RecX 12	53491.1	21978.7	334.2	73.7
RJX 1005.3-7749	53489.1	17417.2	470.9	62.1
RJX 1005.3-7749	53489.1	17797.3	738.9	49.6
RJX 1005.3-7749	53490.1	17477.9	416.9	66.0
RJX 1005.3-7749	53490.1	17540.5	533.9	58.3
RJX 1005.3-7749	53491.1	17674.2	308.3	76.8
RJX 1005.3-7749	53491.1	17409.1	341.3	72.9
RJX 1005.3-7749	53492.1	17522.2	362.3	70.8
RJX 1005.3-7749	53492.1	17778.4	382.5	68.9
RJX 1204.6-7731	53489.2	18346.5	537.3	58.1

Table 2.3: Gemini South Phoenix Individual Radial Velocity Measurements

Star	MJD	RV	σ_{Obs}	SNR
		(m/s)	(m/s)	
RJX 1204.6-7731	53489.2	18318.9	676.5	51.8
RJX 1204.6-7731	53490.1	26270.8	286.3	79.7
RJX 1204.6-7731	53490.1	26378.4	398.4	67.5
RJX 1204.6-7731	53491.1	17726.6	335.7	73.6
RJX 1204.6-7731	53491.1	17532.4	319.5	75.4
RJX 1204.6-7731	53492.0	7329.9	434.2	64.7
RJX 1204.6-7731	53492.0	7115.3	428.4	65.1
RJX 1204.6-7731	53492.3	4782.2	252.5	84.8
RJX 1204.6-7731	53492.3	4683.7	293.6	78.6
RJX 1219.7-7403	53489.2	15044.0	468.8	62.2
RJX 1219.7-7403	53489.2	14551.9	542.7	57.9
RJX 1219.7-7403	53492.1	14789.2	340.1	73.0
RJX 1219.7-7403	53492.1	14792.3	304.1	77.3
TWA 7	53489.1	12586.9	184.3	99.3
TWA 7	53489.1	12606.4	242.3	86.6
TWA 7	53490.1	12519.2	167.4	104.2
TWA 7	53490.1	12468.6	190.4	97.7
TWA 7	53491.1	12453.4	281.5	80.3
TWA 7	53491.1	12417.2	321.2	75.2
TWA 7	53492.1	12685.8	253.9	84.6
TWA 7	53492.1	12481.4	289.1	79.3
TWA 13A	53489.1	11862.6	231.4	88.6

Table 2.3: Gemini South Phoenix Individual Radial Velocity Measurements

Star	MJD	RV	σ_{Obs}	SNR
		(m/s)	(m/s)	
TWA 13A	53489.1	11829.5	183.5	99.5
TWA 13A	53490.1	12174.4	260.2	83.5
TWA 13A	53490.1	12367.0	297.5	78.1
TWA 13A	53491.2	11806.7	245.2	86.1
TWA 13A	53491.2	11819.2	317.6	75.6
TWA 13A	53492.1	11953.9	206.1	93.9
TWA 13A	53492.1	11905.3	245.6	86.0
TWA 13B	53489.1	12397.1	173.9	102.2
TWA 13B	53489.1	12628.5	195.5	96.4
TWA 13B	53490.2	12395.4	234.0	88.1
TWA 13B	53490.2	12404.5	241.9	86.7
TWA 13B	53491.2	12186.0	229.9	88.9
TWA 13B	53491.2	12456.2	280.2	80.5
TWA 13B	53492.1	12720.3	408.4	66.7
TWA 13B	53492.1	12202.9	711.1	50.5
TWA 8B	53491.2	8727.5	516.8	59.3
TWA 8B	53491.2	8986.5	546.9	57.6
TWA 9A	53492.1	11763.2	382.4	68.9
TWA 9A	53492.1	11464.5	461.6	62.7
TWA 9B	53492.1	13194.6	447.4	63.7
TWA 9B	53492.1	12822.5	430.3	65.0
TWA 10	53489.1	7572.8	303.2	77.4

Table 2.3: Gemini South Phoenix Individual Radial Velocity Measurements

Star	MJD	RV	σ_{Obs}	SNR
		(m/s)	(m/s)	
TWA 10	53489.1	7419.6	278.3	80.8
TWA 10	53490.2	7677.8	282.0	80.3
TWA 10	53490.2	7743.5	296.4	78.3
TWA 10	53491.2	7779.0	410.9	66.5
TWA 10	53491.2	7551.2	472.4	62.0
TWA 10	53492.2	7566.8	638.7	53.3
TWA 10	53492.2	7619.2	686.3	51.4
RJX 1534.3-3300	53489.4	2725.2	493.9	60.6
RJX 1534.3-3300	53489.4	2240.6	466.2	62.4
RJX 1534.3-3300	53491.3	2568.9	298.3	78.0
RJX 1534.3-3300	53491.3	2415.0	316.7	75.7
RJX 1534.3-3300	53492.3	2464.3	301.3	77.7
RJX 1534.3-3300	53492.3	2294.9	318.1	75.6
RJX 1552.5-2633	53490.3	-1929.0	282.7	80.2
RJX 1552.5-2633	53490.3	-2575.9	278.9	80.7
ScoPMS 13	53490.3	-2270.0	243.8	86.3
ScoPMS 13	53490.3	-2491.2	229.1	89.0
ScoPMS 13	53491.3	-2875.4	321.9	75.1
ScoPMS 13	53491.3	-3275.9	306.3	77.0
ScoPMS 13	53492.4	-2670.3	184.5	99.2
ScoPMS 13	53492.4	-2993.4	203.6	94.5
RJX 1557.8-2305	53490.3	-4251.8	599.6	55.0

Table 2.3: Gemini South Phoenix Individual Radial Velocity Measurements

Star	MJD	RV	σ_{Obs}	SNR
		(m/s)	(m/s)	
RJX 1557.8-2305	53490.3	-4781.2	476.4	61.7
RJX 1557.8-2305	53491.3	-4294.2	422.2	65.6
RJX 1557.8-2305	53491.3	-5378.8	395.7	67.8
RJX 1557.8-2305	53492.3	-4098.6	318.1	75.6
RJX 1557.8-2305	53492.3	-4834.0	420.9	65.7
ScoPMS 42A	53490.3	-6487.6	248.7	85.5
ScoPMS 42A	53490.3	-6586.3	257.6	84.0
SZ 78	53489.2	-5025.1	218.2	91.2
SZ 78	53489.2	-5038.8	406.3	66.9
SZ 78	53490.2	-5099.9	184.4	99.2
SZ 78	53490.2	-5193.9	238.0	87.4
SZ 78	53491.2	-5134.4	186.8	98.6
SZ 78	53491.2	-5211.8	224.4	90.0
SZ 78	53492.2	-5016.1	209.8	93.1
SZ 78	53492.2	-5118.0	217.7	91.3
SZ 96	53489.3	-1963.9	566.0	56.6
SZ 96	53489.3	-2311.9	534.1	58.3
SZ 96	53490.2	-1665.9	458.9	62.9
SZ 96	53490.2	-2090.7	533.8	58.3
SZ 96	53491.2	-2428.8	571.6	56.4
SZ 96	53491.2	-1624.7	590.4	55.5
SZ 96	53492.3	-2742.5	476.6	61.7

Table 2.3: Gemini South Phoenix Individual Radial Velocity Measurements

Star	MJD	RV	σ_{Obs}	SNR
		(m/s)	(m/s)	
SZ 96	53492.3	-2656.8	660.0	52.5
V721 CrA	53490.4	-466.4	279.4	80.6
V721 CrA	53490.4	-999.3	363.1	70.7
V721 CrA	53491.4	-301.1	310.6	76.5
V721 CrA	53491.4	-996.6	269.2	82.1
V721 CrA	53492.4	-774.2	271.9	81.7
V721 CrA	53492.4	-450.6	275.8	81.2
HIP 107345	53489.4	2696.2	254.6	84.5
HIP 107345	53489.4	2852.0	272.3	81.7
HIP 107345	53490.4	2804.1	246.1	85.9
HIP 107345	53490.4	2773.0	318.4	75.5
HIP 107345	53491.4	2873.1	147.7	110.9
HIP 107345	53491.4	2858.6	166.4	104.5
HIP 107345	53492.4	2811.5	227.4	89.4
HIP 107345	53492.4	2888.5	225.2	89.8
Radial Velocity Standards				
GJ 628	53489.2	-20935.5	146.9	111.2
GJ 628	53489.2	-21123.2	138.4	114.6
GJ 628	53489.2	-20952.4	134.7	116.6
GJ 628	53489.2	-21030.1	131.3	117.6

Table 2.3: Gemini South Phoenix Individual Radial Velocity Measurements

Star	MJD	RV (m/s)	σ_{Obs} (m/s)	SNR
GJ 628	53490.2	-21117.5	79.5	151.1
GJ 628	53490.2	-20936.1	94.9	138.3
GJ 628	53491.3	-21009.9	97.2	136.7
GJ 628	53491.3	-21092.6	95.5	137.9
GJ 628	53492.3	-21039.0	61.0	172.5
GJ 628	53492.3	-20986.3	63.5	169.2
GJ 752A	53489.4	35851.0	331.6	74.0
GJ 752A	53489.4	36244.4	427.1	65.2
GJ 752A	53490.4	36076.0	95.6	137.8
GJ 752A	53490.4	35986.7	106.6	130.5
GJ 752A	53491.4	36039.4	174.4	102.1
GJ 752A	53491.4	36141.0	292.1	78.9
GJ 752A	53492.3	36004.1	124.4	120.8
GJ 752A	53492.3	36033.4	158.1	107.2

While the standard deviation of the RVs can be used to get an empirical precision for slowly rotating field stars, it is not sufficient for determining the *effective* RV precision for young, and possibly more active, stars. We, therefore, use the ensemble set of observations of young stars to assess the error sources associated with the internal RV error for this technique, $\sigma_{Internal}$, and the error caused by stellar jitter, $\sigma_{Stellar}$, once the photon limited error, σ_{Photon},

is removed. σ_{Photon} for each nod observation is calculated using the prescription in Butler et al. (1996), which essentially accounts for the number of lines, widths and strengths of the lines, and SNR . In determining these errors, we consider the difference between the fitted RV values for the A and B nodded observations. We define a total error for a nod observation as σ_{Obs_A} (or σ_{Obs_B}), given by Equation 2.1.

$$\sigma^2_{Obs_A} = \sigma^2_{Photon} + \sigma^2_{Internal} + \sigma^2_{Stellar} \tag{2.1}$$

In calculating σ_{Obs_A}, we assume the contribution from stellar variability to be zero since the time between nod observations (minutes) is typically less than the stellar surface changes (e.g., star spots) that cause stellar jitter, and thus we set $\sigma_{Stellar}$=0. We note that when compared to the median value of σ_{Photon} (90 m/s), the difference in RV between individual A and B nods can be quite large. Figure 2.4 illustrates the difference in the RV for A/B pairs versus the average SNR of the epoch. The median A/B pair difference was 154 m/s, but 11% of these differences are as large as 500$\sim$1100 m/s. We attempted to account for possible systematic differences between A and B nods by making adjustments to our code, but were unable to ascertain the cause of the large discrepancy. For example, stars with large pair differences were not preferentially stars with large $v\sin i$ values (see Figure 2.4) We, therefore, accounted for this dominant error term, the internal error ($\sigma_{Internal}$), as follows. Assuming the RV measurements from the A and B positions have similar uncertainties (σ_{Obs_A}=σ_{Obs_B}), their differences should have a 1σ distribution around zero of $\sqrt{2}\sigma_{Obs_A}$ or $\sqrt{2}\sigma_{Obs_B}$. Since the distribution appears to depend on SNR, we fit the RV difference in the A and B nods

to a polynomial function (Δ_{RVFit}) in the form of $\Delta_{RV} = P_0/SNR^2$, where Δ_{RV} was taken to be the RV difference between A nod and B nod and the SNR is the signal-to-noise ratio of the epoch. The internal uncertainty for each nod observation could then be calculated under the assumption that the $\sigma_{Stellar}$ is zero. From the best fit Δ_{RVFit}, we can calculate the σ_{Obs_A} or σ_{Obs_B} values using Equation 2.2. We then subtracted off in quadrature σ_{photon} to determine $\sigma_{Iternal}$ as a function of SNR (See Figure 2.4), and we see that it is, indeed, the dominant error in our RV.

$$\sigma_{Obs_A} = \frac{P_0/SNR^2}{\sqrt{2}} \tag{2.2}$$

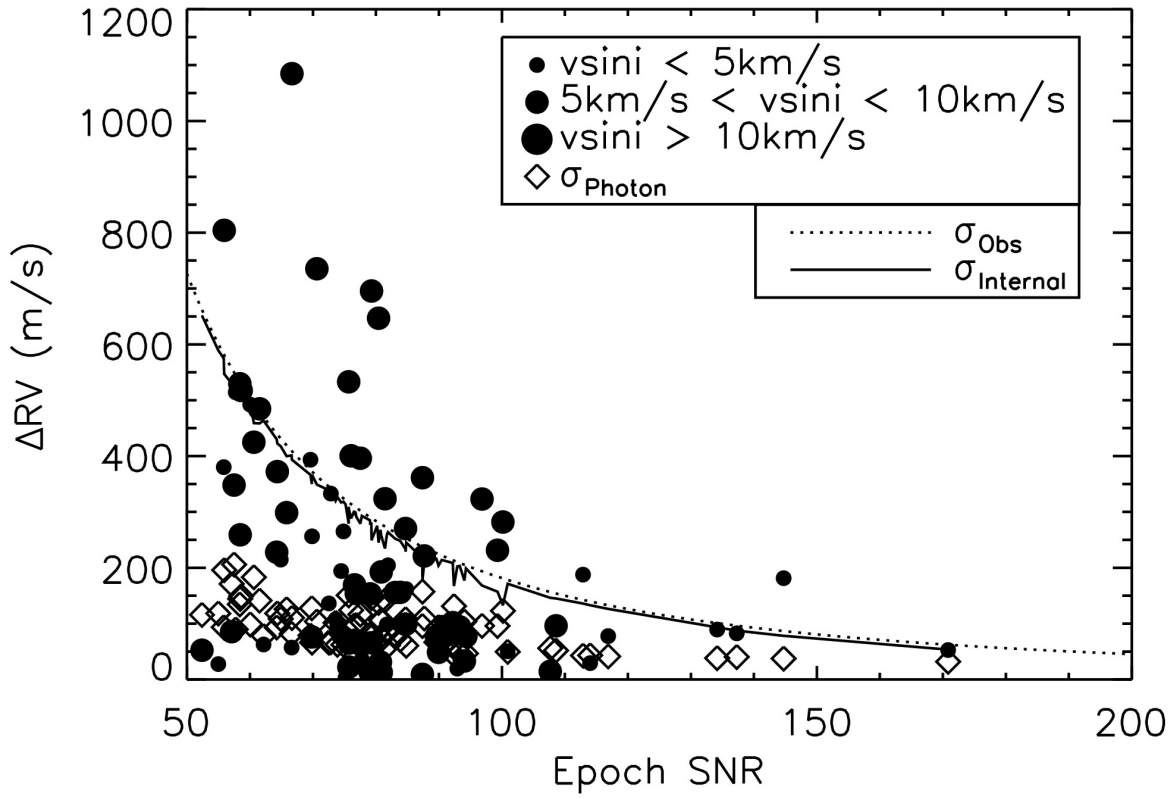

Figure 2.4 The difference in RV measurements between nod A and nod B positions in a single epoch are plotted as a function of epoch SNR for the Phoenix observations. Small filled circles are objects with $v\sin i$ less than 5 km/s, medium filled circles are objects with $v\sin i$ 5-10 km/s, and large filled circles are objects with $v\sin i$ larger than 10 km/s. We fit a polynomial to the SNR in the form of $\Delta_{RV} = P_0/SNR^2$ (dotted line) to determine the total error. The internal error, $\sigma_{Internal}$, (solid line) was then calculated by subtracting the photon limited error, σ_{Photon}, (open diamonds) from the total error, σ_{Obs_A} or σ_{Obs_B}, in quadrature.

This prescription appears to work well for the Gemini Phoenix data. This assessment is based on the fact that the observed RV dispersions of the standard stars are roughly consistent with their errors. However, it proved less successful for the higher SNR Keck NIRSPEC data presented in Chapter 3. In this case, the observed RV dispersions were much greater than the assigned uncertainties, making the standard stars look like RV variables. We believe this stems from the higher SNR Keck NIRSPEC data being greater than where the 'knee' of the polynomial is, and thus it is unable to model the data properly. In order to use data spanning a broader range of SNR, and to be consistent in our method for all young stars in this dissertation, we thought it prudent to devise a uniform method for determining errors. In doing so, we used the ensemble of observations from Chapter 2 and Chapter 3 to fit Δ_{RVFit} in Figure 2.5. This is the fit that will be used to determine the errors in Chapter 2 and Chapter 3. Using this method, our RV standards GJ 628 and GJ 752A had errors (33 m/s and 76 m/s, respectively) consistent with their RV dispersions (22 m/s and 31 m/s, respectively).

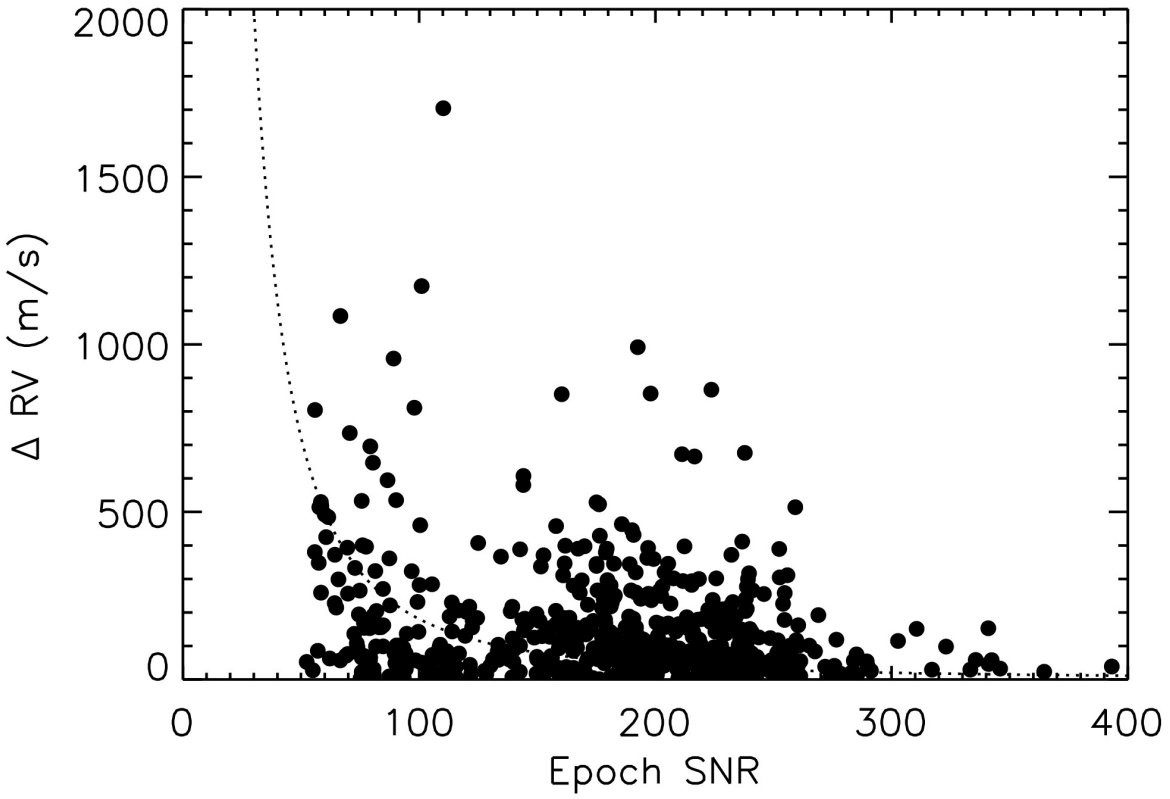

Figure 2.5 The difference in RV measurements between nod A and nod B positions in a single epoch are plotted as a function of epoch SNR for observations presented in Chapter 2 and Chapter 3. We fit a polynomial to the SNR in the form of $\Delta_{RV} = P_0/SNR^2$ (dotted line) to determine the total error. The internal error, $\sigma_{Internal}$, (solid line) was then calculated by subtracting the photon limited error, σ_{Photon}, (open diamonds) from the total error, σ_{Obs_A} or σ_{Obs_B}, in quadrature.

For each star we also calculate an absolute RV from an unweighted average of all epoch RVs for each star. Each epoch RV is determined by the average of the A and B nod pair from Table 2.3, and the average error for each epoch RV (σ_{Epoch}) is given by Equation 2.3. The exception is for binaries in Sections 2.1.5.2 and 2.2.5.1. For these systems, we use the average values for the systemic velocity (γ) for both components. Additionally, with the exception of binaries, we find that RVs for stars in each group or cluster agree to within 2 σ of kinematic studies (Tuc-Hor; Kraus et al. 2014, η Cham; Lopez Martí et al. 2013, Cham; Dubath et al. 1996, TWA; Ducourant et al. 2014,Upper Sco; Pecaut et al. 2012, Lup; Dubath et al. 1996, and CrA; Neuhäuser et al. 2000).

$$\sigma_{Epoch} = \frac{< \sigma_{Obs_A}, \sigma_{Obs_B} >}{\sqrt{2}} \tag{2.3}$$

The total error in the absolute RV for each star over the observing period ($\sigma_{\bigstar}$) is calculated in Equation 2.4. For six stars (TWA 8B, TWA 9B, TWA 9A, TWA 16, RXJ 1552.5, and ScoPMS 42A) only a single epoch was obtained , therefore, the absolute RV uncertainty is set to σ_{Epoch}. Based on comparisons with absolute RVs presented in Section 2.2.3 measured with a different telescope and instrument, these absolute RVs may have systematic errors of a few 100 m/s.

$$\sigma_{\bigstar} = \frac{< \sigma_{Epoch_1}, \sigma_{Epoch_2}, ...\sigma_{Epoch_N} >}{\sqrt{N}} \text{ ;Where N is the number of epochs.} \tag{2.4}$$

A best fit value for $v\sin i$ is obtained by our fitting code for each observation. We then

calculate a mean $v\sin i$ value for each star, as well as the standard deviation. These $v\sin i$ values range from 0.30 km/s to 15 km/s. We note that with a velocity resolution of $\sim$6 km/s, $v\sin i$ values below $<$3 km/s should be considered upper limits. The reported values here indicate the best fit of the model. With the exception of two stars (RXJ 1005.3-7749 and RXJ 1204.6-7731), our $v\sin i$ agree to within 18% of published values. Although our $v\sin i$ value of 2 km/s for RXJ 1005.3-7749 is inconsistent with the published value of 11 km/s (Covino et al. 1997), we believe our value is consistent with the rotation period of 8.08 days from Kiraga (2012). If we assume a radius for 0.5 R$\odot$ for an M1V spectral type and an edge on inclination, we can calculate the maximum rotational velocity for an 8.08 day period. This calculation yields a maximum rotational velocity of 3.16 km/s, which is consistent with our $v\sin i$ value of 2 km/s. For RXJ 1204.6-7731 our $v\sin i$ value of 4 km/s is marginally inconsistent with the published $v\sin i$ value of 6 km/s. However, as we will discuss in Section 2.1.5 RXJ 1204.6-7731 is identified as a double-lined spectroscopic binary (SB2), and our code is only designed to fit single-lined spectra. Our results for each young star and RV standard are summarized in Table 2.4. Within this table, we report the effective temperature and surface gravity (logg) values associated with the model spectra used, along with the $v\sin i$ with the uncertainty set by the standard deviation of multiple epochs, and the absolute RV with the uncertainty in the absolute RV ($\sigma_{\bigstar}$). RV curves are shown in Appendix A for all stars in Chapters 2 and 3 with multiple observations.

Table 2.4: Gemini South Phoenix Rotational and Absolute Radial Velocities

Star Name	Model T_{eff}, log$g$	vsini (km/s)	<RV> (m/s)
Single-Epoch Young Stars			
HIP 23309	3800, 4.2	5.08±0.46	20143±100
HIP 29964	4000, 4.2	15.03±0.43	17593± 86
HD 155555C	3400, 4.2	3.35±0.48	4314±137
RecX 4	3800, 4.2	5.14±0.39	18526±124
RecX 10	3800, 4.2	2.43±0.10	18646±140
RecX 12	3400, 4.2	6.29±1.07	22205±172
RXJ 1005.3-7749	3800, 4.2	1.72±0.53	17577±157
RXJ 1204.6-7731	3600, 4.2	4.16±3.71	5795 *
RXJ 1219.7-7403	3800, 4.2	4.95±0.43	14794±207
TWA 7	3600, 4.2	0.30±0.09	12527± 85
TWA 13A	3800, 4.2	11.54±0.47	11965± 88
TWA 13B	3800, 4.2	11.23±0.44	12424±109
TWA 10	3600, 4.2	5.19±0.38	7616±149
RXJ 1534.3-3300	3800, 4.2	8.81±0.24	2451±149
ScoPMS 13	3600, 4.2	11.89±0.37	−2763±101
RXJ 1557.8-2305	3800, 4.2	8.93±1.05	−4606±179
SZ 78	3800, 4.2	5.04±0.23	−5105± 83
SZ 96	3600, 4.2	8.75±1.02	−2186±194
V721CrA	4000, 4.2	11.86±0.70	−665±120
HIP 107345	3800, 4.2	5.68±0.25	2820± 82
Field Stars			
GJ 628	3400, 4.8	0.95± 0.12	-21022± 33
GJ 752A	3400, 4.8	0.56± 0.06	36047± 76
Single-Epoch Young Stars			
TWA 8B	3400, 4.2	11.45±0.14	8857±376
TWA 9B	3800, 4.2	10.40±0.82	11614±298
TWA 9A	4000, 4.2	9.65±0.23	13009±310
RXJ 1552.5-2633	3800, 4.2	12.30±0.06	-2252±199
ScoPMS 42A	3800, 4.2	11.30±0.56	-6537±179

* The average value of the A and B component systemic velocities (γ) from our orbital fits.

2.1.5 Identifying Candidate Variables with Phoenix

Stellar jitter is well known to increase with stellar rotation. As well as having faster rotation than older stars of similar spectral type, young stars show significant stellar jitter due to increased chromospheric activity (Campbell et al. 1991; Bailey et al. 2012). By comparing the standard deviation of the epoch RV for each star with the measured $v\sin i$ values, we can produce an empirical estimate of the expected activity induced variability. We note that there is no standard prescription for identifying companion-induced RV variation for young stars. As such, we investigate the average standard deviation versus $v\sin i$, and the statistical P-χ^2 test to identify RV variables. Objects that show a higher than average standard deviation for a given $v\sin i$ may have an additional component to their variability, such as the reflex motion from a companion. In Figure 2.6 we show the standard deviation in the epoch RVs for young stars in the Phoenix sample. There are four young stars in our sample with modest $v\sin i$ values (4 - 12 km/s) that have RV standard deviations above 200 km/s (TWA 13A - 209 m/s; ScoPMS 13 - 353 m/s; RXJ 1557.8-2305 - 201 m/s; SZ 96 - 359 m/s). However, the majority of young stars (15) show similar RV dispersion ($\lesssim$100 m/s) independent of $v\sin i$ over a range of $v\sin i$ values (0.3 - 15 km/s). Of the latter group, the average standard deviation for young stars is 63 m/s with a standard deviation of that average of 25 m/s. In Figure 2.6, we see four stars that lie 5σ above the average standard deviation. These include TWA 13A, SZ96, RXJ 1557.8-2305, and ScoPMS 13. TWA 13A which had been previously identified as a candidate RV variable (Bailey et al. 2012) and was targeted for additional follow-up in our CRIRES observations (see Section 2.2). The average

SNR for young stars in this sample is 82, and in the case of SZ 96 and RXJ 1557.8-2305, lower SNR spectra (SNR_{SZ96}=52-63; $SNR_{RXJ1557.8-2305}$=55-76) is the likely explanation as to their elevation above the average standard deviation. ScoPMS 13, with a higher than average SNR (SNR=75-99), needs further investigation into the cause of the its higher than average RV standard deviation. In addition to these four stars, RXJ1204.6-7731 has a standard deviation more than 2 orders of magnitude above the average standard deviation (σ=8,825 m/s), and we identify this as a spectroscopic binary and discuss it further in Section 2.1.5.2.

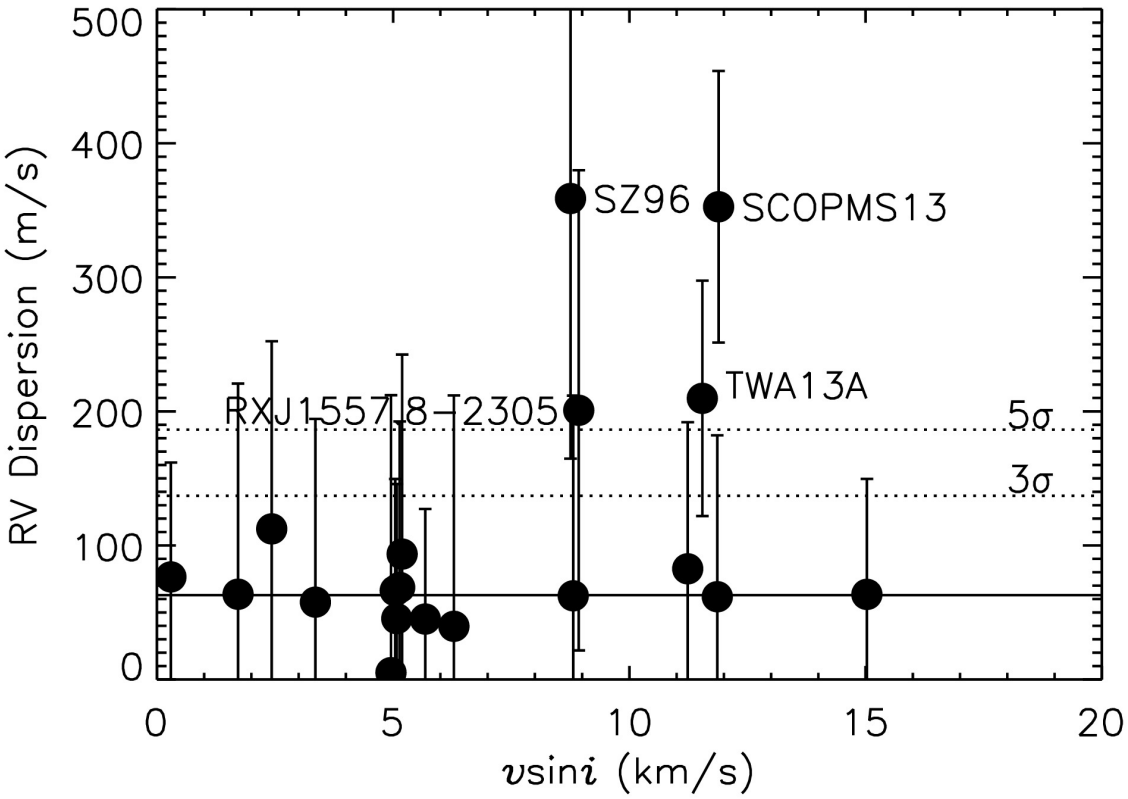

Figure 2.6 Here we plot the standard deviation of the epoch RVs (m/s) versus $v\sin i$ for each star with multiple epoch observations. The error bars are the average σ_{Obs_A} and σ_{Obs_B} values for each star. Excluding the stars with average standard deviations greater than 200 m/s, we calculated the average of the standard deviations for young stars in the sample (solid line) to be 63 m/s with standard deviation in the average of 25 m/s. This gives a empirical estimate for the stellar jitter for these young stars. We plot 3σ and 5σ (dotted lines) lines above the average standard deviation for a given $v\sin i$. 4 stars (SZ 96, ScoPMS 13, RXJ 1557.8-2305, and TWA 13A) show significant RV variability ($>5\sigma$), but only ScoPMS 13 has errors that do not cross below the 5σ line.

Although identifying stars with a higher than average standard deviation is a good first order indication of variability, high standard deviations can also be caused by low signal-to-noise particularly with a small number of observations. To quantitatively assess RV variability, given the short temporal baseline, we used a P-χ^2 test to independently identify RV variability. A P-χ^2 test shows how significant a set of observations deviates from a χ^2 distribution (Carney et al. 2003). In calculating the p-values from the P-χ^2 test, we use the epoch RV and the associated σ_{AB}. A p-value of .01 would indicate a 99% confidence that a star has significant RV variability over the observational run. Our histogram of p-values from our P-χ^2 test is plotted in Figure 2.7 for the stars observed with more than 1 epoch of data from Gemini South Phoenix. The distribution shows a strong cluster near 1. As we expect the distribution of p-values to be uniform, this suggests our uncertainties in the RV error are being overestimated. By reducing our errors by 50%, we were able to achieve a flat P-χ^2 distribution. This gives a good estimate as to how overestimated our RV errors are. Nevertheless, we adopt the more conservative values. Despite this, two stars showed significant p-values: the spectroscopic binary RXJ1204.6-7731 with a p-value $<$0.0001 and ScoPMS 13 with a p-value of 0.024. None of the remaining candidate variables (SZ 96, TWA 13A, and RXJ 1557.8-2305) were identified by the P-χ^2 test. P-values are listed in Table 2.5. The following subsections discuss the candidate variable ScoPMS 13 and the new spectroscopic binary RXJ1204.6-7731.

Table 2.5: Gemini South Phoenix P-χ^2 Values

Star	P-χ^2 Value
GJ 628	0.688535
GJ 752A	0.987186
HD155555C	0.986277
HIP107345	0.970670
HIP23309	0.907517
HIP29964	0.773007
V721Cra	0.882744
RecX 10	0.736741
RecX 12	0.811978
RecX 4	0.864611
RXJ 1005.3-7749	0.987853
RXJ 1204.6-7731	0.000000
RXJ 1219.7-7403	0.979684
RXJ 1534.3-3300	0.920422
RXJ 1557.8-2305	0.551008
ScoPMS 13	0.003198
SZ 78	0.917578
SZ 96	0.434182
TWA 10	0.956949
TWA 13A	0.206557
TWA 13B	0.928382
TWA 7	0.886298

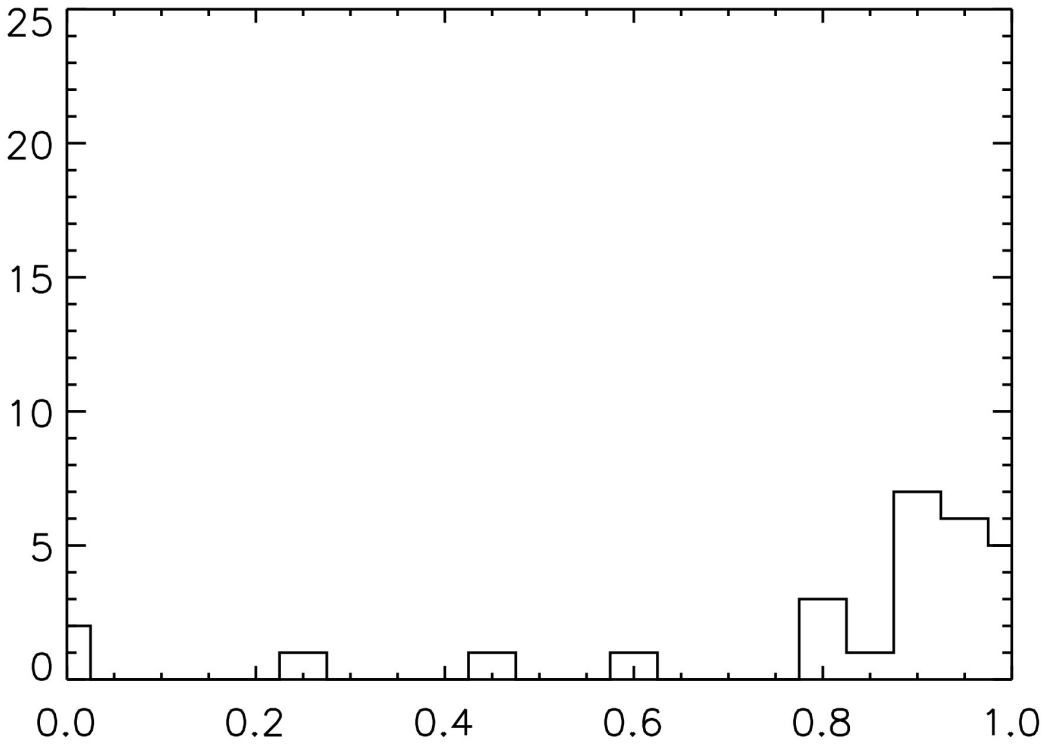

Figure 2.7 A histogram of the p-values from our P-χ^2 test on the Phoenix sample are shown. The two objects with p-values <0.1 show significant deviation from the χ^2 distribution and indicates RV variability. The large cluster of objects with p-values near 1 show that our errors are slightly overestimated.

2.1.5.1 ScoPMS 13

ScoPMS 13 is a young M1.5 spectral type star in the Scorpius-Centaurus region (Köhler et al. 2000). After our program began, a companion with a separation of 0.146″ and likely with

a comparable brightness (ΔK=0.10) was identified using adaptive optics (AO) observations (Lafrenière et al. 2014). At a distance of $\sim$145 pc for Sco-Cen (de Zeeuw et al. 1999), this would correspond to a projected separation of $\sim$21 AU.

We show the RV curve for ScoPMS 13 in Figure 2.8. Our results show $\sim$+380 m/s and ~ -310 m/s deviation from the mean RV over the observation time frame (3 days). Given the 21 AU separation of the known companion, we would not expect to see a RV variation of this amplitude caused by th companion. We, therefore, classify ScoPMS 13 as a candidate RV variable, that requires more observations to determine if the variations are caused by stellar jitter, a close companion, or possible contamination of the spectrum by its spatially unresolved companion. We caution that while ScoPMS 13 is identified as a candidate variable, we note that this is based on only 3 epochs. Additionally, ScoPMS 13 was observed in the Kepler 2 EPIC dataset and was not flagged as an object of interest.

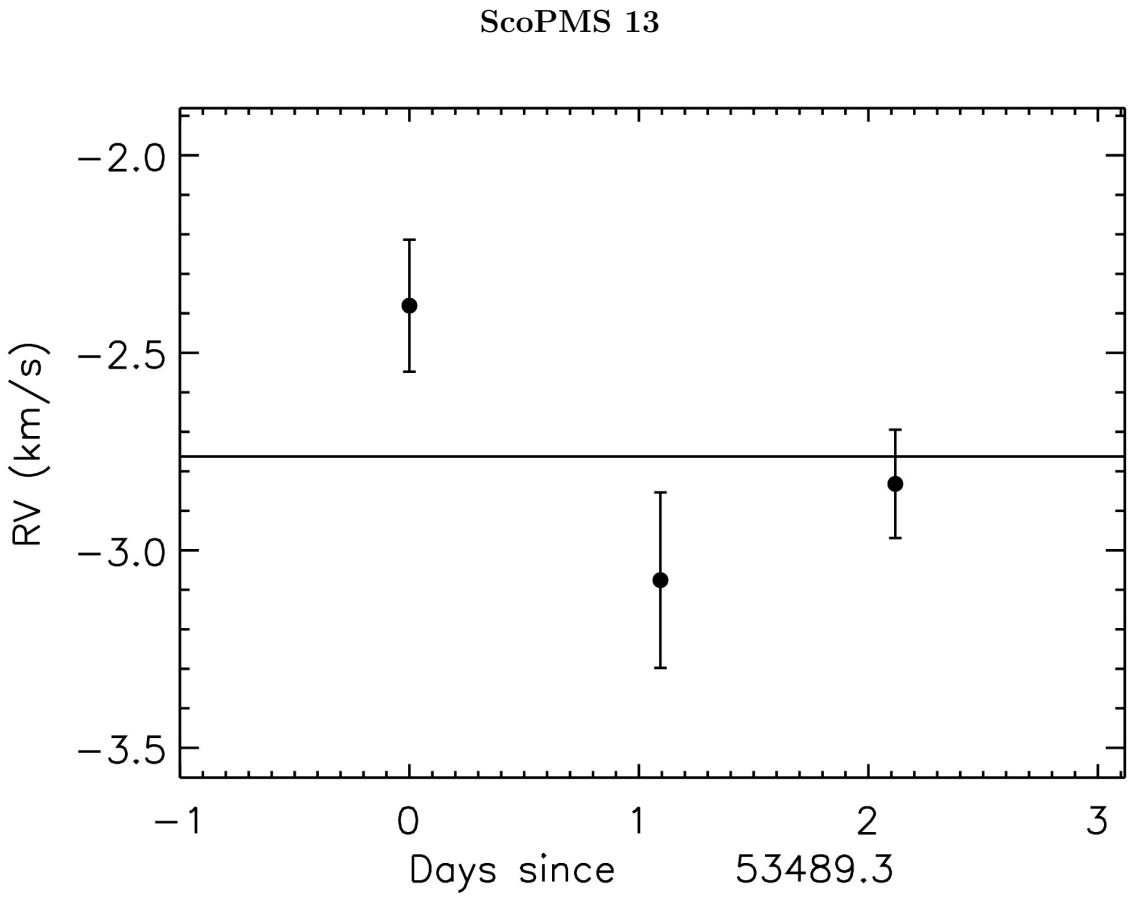

Figure 2.8 The RV curve for candidate variable ScoPMS 13 is plotted with epoch errors for each observing day.

2.1.5.2 RXJ 1204.6-7731

RXJ1204.6-7731 is a M2 spectral type young star in the Chamaeleon star forming region (Covino et al. 1997). It was observed by an AO-aided speckle companion search by Briceño & Tokovinin (2017) and found to be single within their spatial detection limits of 0.04″ and maximum detectable magnitude difference of Δm(0.15″)=2.3 and Δm(1″)=4.5. RXJ

1204.6-7731 was identified as a SB2 during the initial observing run, so two spectra were obtained on the last night separated by ∼7 hours. As noted in Section 2.1.2, two additional observations were obtained 46 days later, providing a total of 7 RV values.

Our RV code identified it as having large (∼20 km/s) amplitude RV change over a short time period, and the appearance of a companion spectrum in residuals of our fits, indicate that RXJ1204.6-7731 is an SB2. Since our code is not designed to model a composite spectrum, we used an IDL adaptation of TODCOR[1] originally described by Zucker & Mazeh (1994), a two-dimensional correlation algorithm, to determine the RVs of both components. TODCOR determines the RV of both components of a SB2 by correlating two template spectra with an observed spectrum by Doppler shifting the template spectra. As our code was able to fit the telluric features of this star, we used the output wavelength calibrated spectrum fitted with our code to input into TODCOR. We then subtracted the telluric lines from our spectra using the same telluric template used in our fitting. These telluric-removed composite spectra were then fit with TODCOR using a template spectra with T_{eff} and log$g$ from Table 2.4. Using the same T_{eff} and log$g$ for both components, the template spectral intensities for the secondary were scaled to be 50% of the primary to obtain this fit. This choice of 50% was a "χ-by-eye" selection. The individual RVs are listed in Table 2.6, and the first 5 epochs are shown in Figure 2.9. As there is no standard method for determining the error in the RVs obtained from TODCOR, we adopt the average difference in the RVs between the A and B nod for each component (346 m/s for RXJ 1204.6-7731A and 43 m/s for RXJ 1204.6-7731B with a standard deviation of 589 m/s and 106 m/s, respectively).

[1]https://doi.org/10.5281/zenodo.557089

With the resulting RV's from TODCOR, we fit Keplerian orbits to each component separately utilizing a Markov Chain Monte Carlo (MCMC) algorithm described in Quinn et al. (2015). We use the component RVs from TODCOR, the estimated error, and the estimated stellar jitter (see Chapter 4) to fit for orbital period (P), time of periastron passage (T_0), radial velocity semi-amplitude (K), center-of-mass velocity (γ), eccentricity (e) and the argument of periastron (ω). Quinn et al. (2015) describe this method as assigning best-fit parameters from the mode of each distribution which they identify from the peak of the probability density function (PDF). The errors are assigned from the region that encloses 1σ of the PDF. The best fit for each component is listed in Table 2.7, and the orbital fits are shown in Figure 2.10. Although we do not fit components simultaneously, we note the agreement in period and T_0 shows self-consistent results. While the best orbital fit is preliminary, we report the system to be a 5.6 day SB2 component RV amplitudes of RXJ 1204.6-7731A (10.8 km/s) and RXJ 1204.6-7731B (29.6 km/s) corresponding to a mass ratio of $K_A/K_B = 0.37$.

Table 2.6: RXJ1204.6-7731 Individual Radial Velocities

MJD	$RV_{Component1}$ (m/s)	$RV_{Component2}$ (m/s)
53489.2	7087.6	−5174.5
53490.1	14842.1	−23314.1
53491.1	7473.4	−3256.0
53492.0	−3153.9	24318.5
53492.3	−5244.3	30159.3

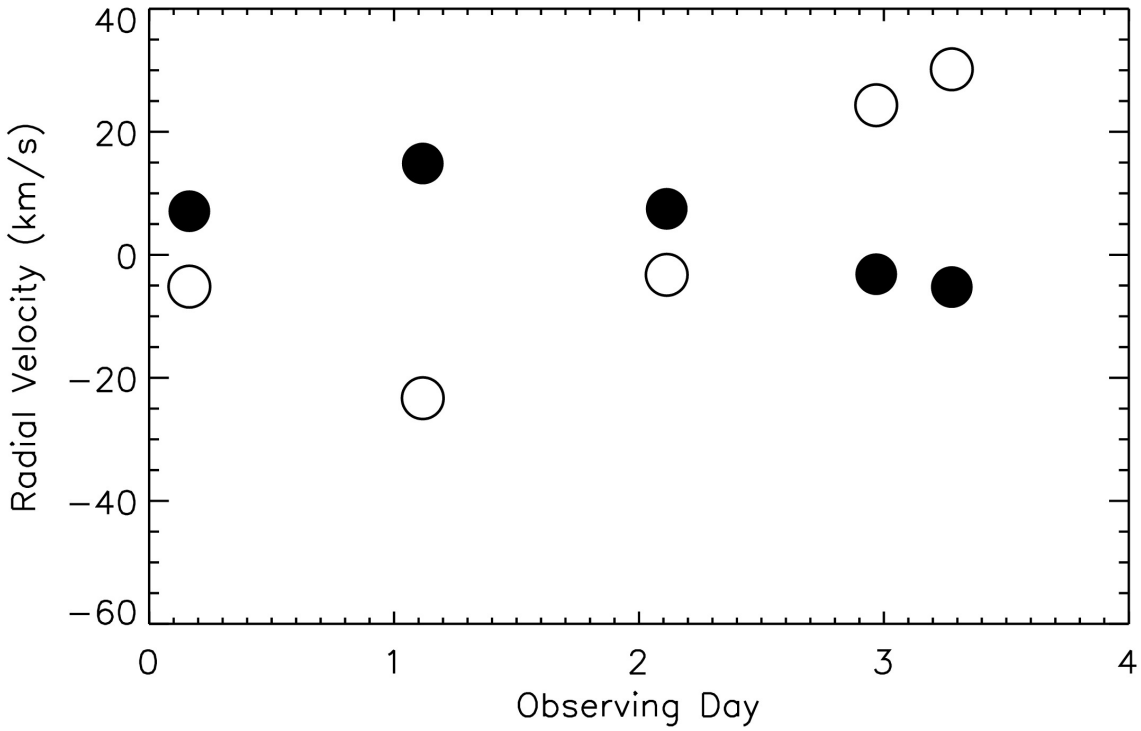

Figure 2.9 RV's of RXJ1204.6-7731A (filled circles) and RXJ1204.6-7731B (open circles) in km/s over the initial 5 observations with Gemini Phoenix.

Table 2.6: RXJ1204.6-7731 Individual Radial Velocities

MJD	$RV_{Component1}$ (m/s)	$RV_{Component2}$ (m/s)
53538.2	3009.2	34718.3
53544.1	7945.5	35769.7

The error in the RV is estimated to be 346 m/s for RXJ 1204.6-7731A and 43 m/s for RXJ 1204.6-7731B. See the discussion in Section 2.1.5.2

Table 2.7: Orbital Parameters of RXJ 1204.6-7731

Parameter	RXJ 1204.6-7731A	RXJ 1204.6-7731B
P	5.48±0.001 days	5.69±0.002 days
T_0	53491.40±0.01	53491.43±0.003
K	10793.1±74.9 m/s	−29550.2±70.7 m/s
γ	3222.6±65.1 m/s	8366.4±57.8 m/s
e	0.1001±0.008	0.078±0.002
ω	29.51±3.31	18.01±2.10

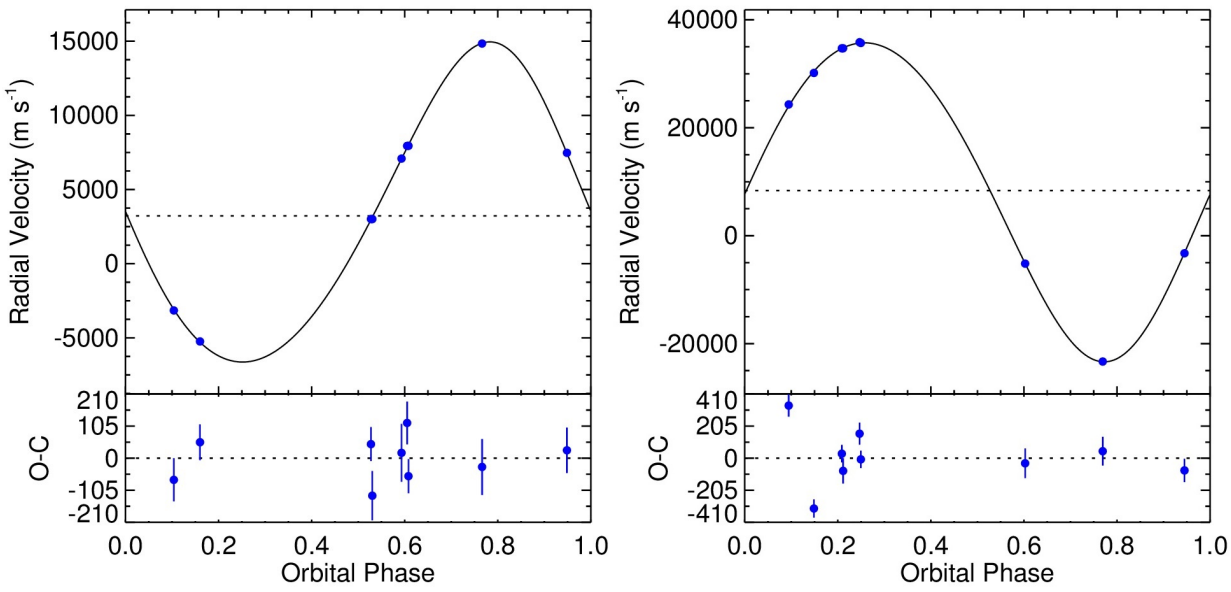

Figure 2.10 Best fit orbit for RXJ1204.6-7731A (left) and RXJ1204.6-7731B (right).

2.2 Follow-up Spectroscopic Observations with CRIRES

2.2.1 CRIRES Observations, Reductions and Extractions

TWA 13A was identified by Bailey et al. (2012) as a candidate RV variable, and we collected 4 spectroscopic observations over 5 nights using Phoenix for this star. A P-χ^2 test (see Section 2.1.5) on the Phoenix observations resulted in a p-value of 0.21, not high enough to show significant RV variation over the 4 epochs, but Phoenix results did show large amplitude (> 350 m/s) RV variability and the errors are likely slightly overestimated. Therefore additional follow-up observations of TWA 13A were conducted to investigate the cause of its tentative RV variability.

We requested follow-up observations on VLT CRIRES[2] (Kaeufl et al. 2004), and were

[2]In Jan 2011, the Phoenix spectrograph was removed from Gemini South, leaving the VLT CRIRES

granted service observing for 2 targets (TWA 13A and V721 CrA). V721 CrA was chosen to ascertain our empirical precision on a young star with similar spectral type and $v\sin i$ (11.54±0.47 km/s - TWA 13A; 11.86±0.70 km/s - V721 CrA; 2.1.4), and we obtained 8 epochs for TWA 13A and 10 epochs for V721 CrA. The observations were carried out from 2011 April 15 - 2011 July 23. Due to queue scheduling constraints, we modified our observing strategy to obtain one star for telluric calibration (HR 7507; B8III) for each observation block. In addition, 5 epochs of the RV standard GJ 628 were obtained to determine the empirical RV precision of the technique. Due to a technical time slot cancellation on the VLT UT1 telescope, we were granted additional service observing on CRIRES. However, the alloted time was from 2012 August 12 - 2012 October 1, when TWA 13A was not observable. We used this time to observe a common proper motion pair of stars, TYC 7443-1102-1 (K=7.846, K9IV) and 1RXS J195602.8–320720 (K=8.114, M4) identified as members of the young Beta Pictoris Moving group by Lépine & Simon (2009). We obtained 19 epochs of TYC 7443-1102-1 and 18 epochs of 1RXS J195602.8–320720. As before, 6 epochs of the RV standard GJ 752A were obtained to determine the empirical RV precision of the technique.

The settings used on both CRIRES runs were chosen to give nearly the same wavelength range and resolution as the previous Phoenix data. Similar to the Phoenix data, a S/N of >50 for targets and >100 for calibrators was chosen to maximize precision. An image of the optical design of the CRIRES instrument is shown in Figure 2.11. Adaptive optics (AO) was not used. Nod pairs of each star were taken in succession for nod subtraction during the reduction process. Grating encoder 120870 utilizing order number 25 to give a wavelength

instrument the only high resolution infrared spectrograph in the southern hemisphere.

range of 2.297 μm - 2.307 μm (100 Å) on detector 3. A 0.4″ slit was used resulting in a resolving power of R$\sim$50,000. All observations were taken in nod pairs separated by $\sim$125 pixels (12″) along the slit. FowlerNsampGRstWin readout mode was utilized to readout detectors #2 and #3 only, as the wavelength range used to fit the CO band is on detector #3 in this configuration. As this was service (queue) observing, dark and flat frames were taken nightly by the observer.

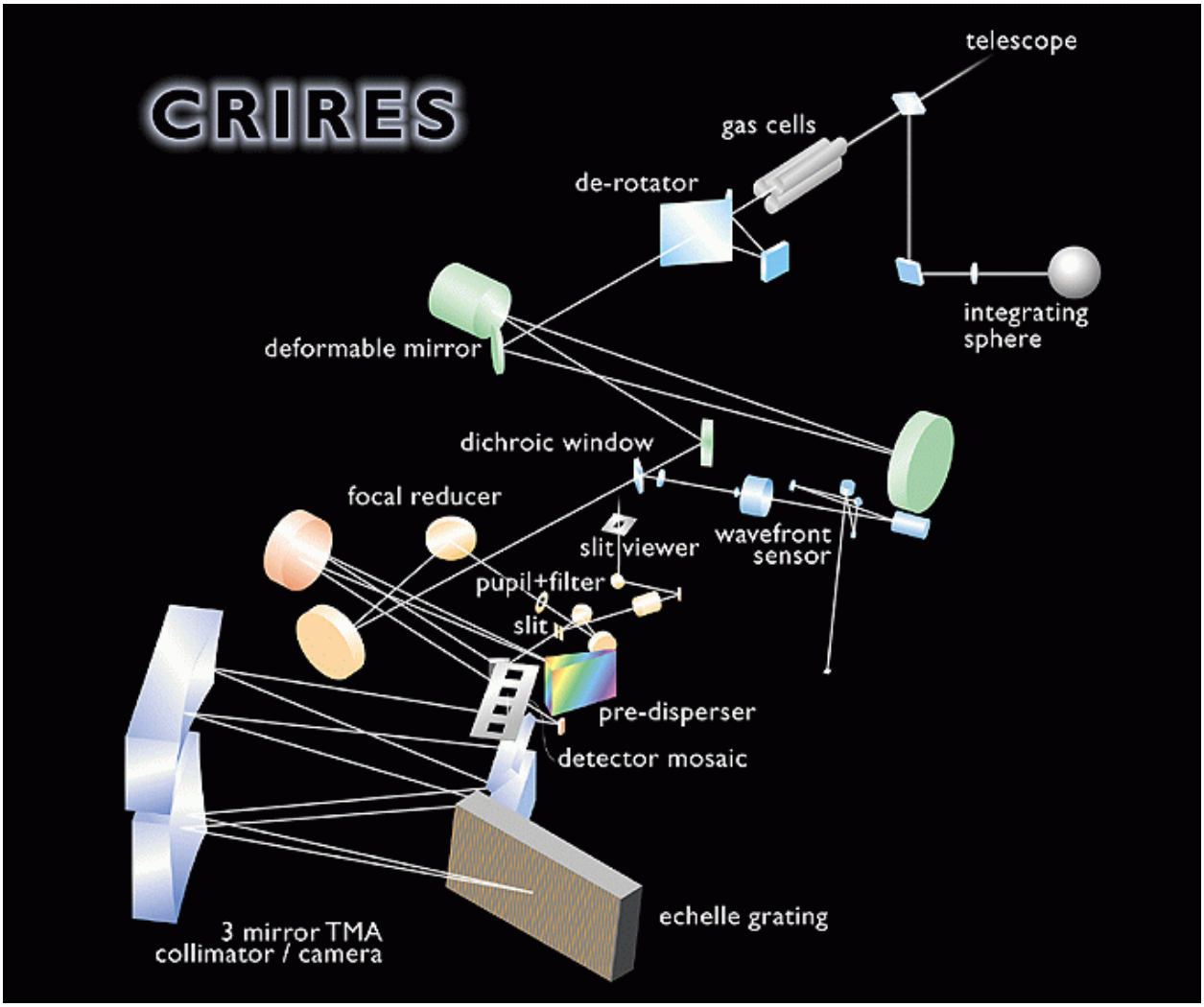

Figure 2.11 The VLT CIRES optical design from the CIRES User Manual:`http://www.eso.org/sci/facilities/paranal/instruments/crires/doc/VLT-MAN-ESO-14500-3486_v87.pdf`

CRIRES data come in a multi-extension FITS (MEF) file, with all four detectors in one file. In our readout mode, detectors #1 & #4 have zero values in their frames. As we are only using the spectrum from detector #3, we use IRAF to separate those data from the

MEF. This is done for all calibration frames as well.

Prior to the standard reductions, proper analysis of CRIRES data requires correcting for the non-linearity and an 'odd-even' effect that must be corrected for (see: CRIRES User Manual [3]). The effects have been carefully modeled and cannot be corrected for using only a flat-field. The European Southern Observatory (ESO) provides a static calibration file in MEF format to correct for this using a quadratic with coefficients in a 3-D data cube for every pixel on each chip. We utilized the static calibration file available for data obtained April 2011 and later available on the ESO website [4]. As our CIRES observations were taken using the FowlerNsampGRstWin readout mode using 256 pixels in the Y direction of the 512 Y pixels available on the chip, we had to find correct "stripe" used to correct for non-linearity. This was determined by finding corresponding bad pixels of the chip and employing an offset and pixel crop in the static calibration frames. The flats and science frames were corrected using the Equation 5.1. In this equation, A, B, and C coefficients are the values of each slice in the data cube. I_{orig} and $I_{corrected}$ are the original and corrected intensities respectively.

$$I_{corrected} = \frac{-B^2 + B^2 * \sqrt{\frac{1-4*C*(A-I_{orig})}{B^2}}}{(2 * C)} \tag{2.5}$$

After each flat and science frame was corrected for these effects, the science data were flat fielded and pair subtracted following the same prescription used to reduce Phoenix data.

[3] http://www.eso.org/sci/facilities/paranal/instruments/crires/doc/VLT-MAN-ESO-14500-3486_v87.pdf
[4] http://www.eso.org/observing/dfo/quality/CRIRES/pipeline/pipe_calib.html

2.2.2 CRIRES Radial and Rotational Velocity Measurements

Our technique determining RV's for CRIRES was identical to the spectral modeling prescription used for Phoenix and described in depth in Section 2.1.3 and paraphrased as follows.

We use telluric features at 2.3 μm as an absolute wavelength reference and the ^{12}CO bandhead in the K-band of the stellar spectrum to determine the radial velocity of our target stars. This is achieved by combining a model telluric spectrum from KPNO/FTS and model stellar spectra generated using NexGen (Hauschildt et al. 1999) and fitting it to our observed spectra using an 18 parameter fit. We chose $\sim$70 Å in the same wavelength region as Phoenix and 700 pixels to fit over, as it gave us a uniform fitting region for both Phoenix and CRIRES. An example fit for the IP is shown in Figure 2.12. We note that the IP was different over several nights.

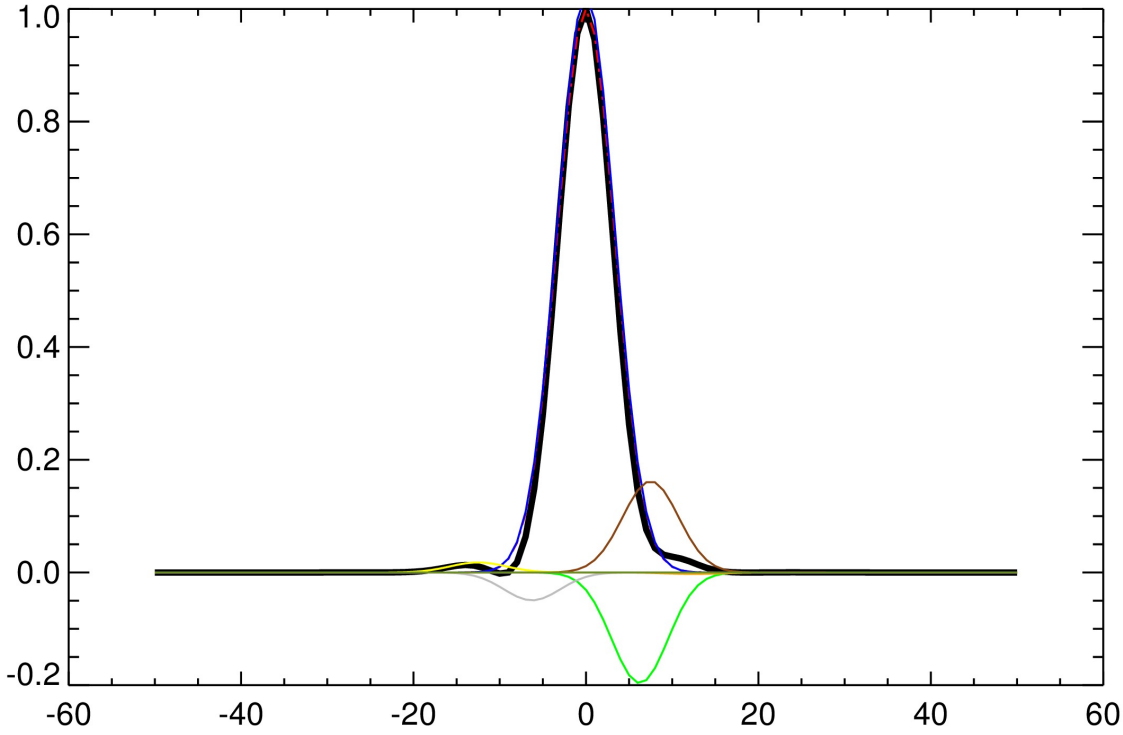

Figure 2.12 An example of the IP for VLT CRIRES. 9 Gaussian profiles (colored lines) were combined to create the total IP (black line).

2.2.3 Results with CRIRES

As discussed in Section 2.2, our observations were taken in nod pairs. These individual nod observations are shown in Table 2.8, where we list the star identifier, MJD, RV, σ_{Obs_A} or σ_{Obs_B}, and SNR. The σ_{Obs_A} and σ_{Obs_B} are the observational uncertainty in each nod and were calculated using identical error analysis as described in Section 2.1.4. We remind the reader that data from all observations from Chapter 2 and Chapter 3 are used to determine

the internal error (see Figure 2.5). The total error, $\sigma_{\star}$, for the RV standards GJ 628 (23 m/s) and GJ 752A (23 m/s) using this method are consistent with the RV dispersions for these stars (32 m/s and 63 m/s, respectively).

Star	MJD	RV	σ_{Obs}	SNR
		(m/s)	(m/s)	
Young Stars - VLT/CRIRES				
TWA 13A	55667.3	11435.2	207.8	93.5
TWA 13A	55667.3	11577.5	161.9	105.9
TWA 13A	55668.0	11521.2	161.2	106.1
TWA 13A	55668.0	11578.7	131.6	117.5
TWA 13A	55672.2	11377.9	125.7	120.2
TWA 13A	55672.2	11533.1	116.9	124.6
TWA 13A	55681.2	11915.3	152.6	109.1
TWA 13A	55681.2	11936.4	127.3	119.5
TWA 13A	55682.2	11319.1	231.9	88.5
TWA 13A	55682.2	11603.2	121.2	122.4
TWA 13A	55683.2	11537.7	148.8	110.5
TWA 13A	55683.2	11335.9	108.3	129.5
TWA 13A	55685.3	11735.3	181.7	100.0
TWA 13A	55685.3	11667.4	136.5	115.3
TWA 13A	55755.0	11432.3	154.9	108.3
TWA 13A	55755.0	11459.8	133.7	116.5

Star	MJD	RV	σ_{Obs}	SNR
		(m/s)	(m/s)	
V721 CrA	55668.3	-1319.17	75.0	155.6
V721 CrA	55668.3	-1204.94	67.6	164.0
V721 CrA	55669.4	-1301.65	77.6	153.0
V721 CrA	55669.4	-1308.33	65.2	167.0
V721 CrA	55671.3	-1071.81	64.2	168.3
V721 CrA	55671.3	-1220.87	57.8	177.2
V721 CrA	55678.4	-1073.80	86.5	144.9
V721 CrA	55678.4	-1278.75	62.2	170.9
V721 CrA	55701.4	-1118.45	132.7	117.0
V721 CrA	55701.4	-935.017	104.0	132.1
V721 CrA	55727.4	-1068.75	78.6	152.0
V721 CrA	55727.4	-1232.22	66.4	165.4
V721 CrA	55728.2	-1228.42	70.9	160.1
V721 CrA	55728.2	-1265.66	67.1	164.5
V721 CrA	55736.4	-1300.33	154.1	108.6
V721 CrA	55736.4	-1297.06	119.3	123.4
V721 CrA	55737.4	-1271.10	100.7	134.3
V721 CrA	55737.4	-1264.22	87.0	144.5
V721 CrA	55739.4	-1159.35	92.4	140.2
V721 CrA	55739.4	-1141.72	71.7	159.1
TYC 7443-1102-1	56152.1	-5189.07	179.4	100.6
TYC 7443-1102-1	56152.1	-5131.78	196.0	96.3
TYC 7443-1102-1	56152.1	-5264.83	254.6	84.5
TYC 7443-1102-1	56152.1	-5233.88	167.2	104.2

Star	MJD	RV	σ_{Obs}	SNR
		(m/s)	(m/s)	
TYC 7443-1102-1	56157.1	-5297.76	148.0	110.8
TYC 7443-1102-1	56157.1	-5249.74	144.7	112.0
TYC 7443-1102-1	56168.1	-5309.09	181.5	100.0
TYC 7443-1102-1	56168.1	-5284.05	152.9	109.0
TYC 7443-1102-1	56169.1	-5275.83	106.8	130.4
TYC 7443-1102-1	56169.2	-5359.90	98.1	136.1
TYC 7443-1102-1	56170.1	-5317.27	92.3	140.3
TYC 7443-1102-1	56170.1	-5303.67	90.2	141.9
TYC 7443-1102-1	56172.2	-5309.93	152.2	109.2
TYC 7443-1102-1	56172.2	-5261.85	177.2	101.3
TYC 7443-1102-1	56178.1	-5291.45	106.6	130.5
TYC 7443-1102-1	56178.1	-5306.81	113.9	126.3
TYC 7443-1102-1	56180.1	-5299.06	166.7	104.4
TYC 7443-1102-1	56180.1	-5195.22	141.2	113.4
TYC 7443-1102-1	56181.1	-5245.88	96.0	137.5
TYC 7443-1102-1	56181.1	-5269.00	83.3	147.7
TYC 7443-1102-1	56187.1	-5159.62	411.6	66.4
TYC 7443-1102-1	56187.1	-5218.54	214.9	91.9
TYC 7443-1102-1	56188.1	-5140.75	234.5	88.0
TYC 7443-1102-1	56188.1	-5147.70	185.6	98.9
TYC 7443-1102-1	56188.1	-5226.67	162.3	105.8
TYC 7443-1102-1	56188.1	-5153.45	163.2	105.5
TYC 7443-1102-1	56189.1	-5217.44	122.1	122.0
TYC 7443-1102-1	56189.1	-5173.78	124.0	121.0

Star	MJD	RV	σ_{Obs}	SNR
		(m/s)	(m/s)	
TYC 7443-1102-1	56190.0	-5189.86	101.8	133.6
TYC 7443-1102-1	56190.0	-5250.20	89.6	142.4
TYC 7443-1102-1	56196.2	-5209.03	163.9	105.3
TYC 7443-1102-1	56196.2	-5212.08	136.2	115.5
TYC 7443-1102-1	56196.2	-5195.01	137.3	115.0
TYC 7443-1102-1	56196.2	-5215.62	161.5	106.1
TYC 7443-1102-1	56198.1	-5147.24	176.5	101.4
TYC 7443-1102-1	56198.1	-5103.41	165.6	104.7
TYC 7443-1102-1	56201.1	-5189.31	131.7	117.5
TYC 7443-1102-1	56201.1	-5171.56	113.1	126.7
1RXS-J195602.8-320720	56152.1	-4073.21	196.3	96.2
1RXS-J195602.8-320720	56152.1	-4113.49	150.3	109.9
1RXS-J195602.8-320720	56157.1	28115.9	231.8	88.5
1RXS-J195602.8-320720	56157.1	27655.4	143.8	112.4
1RXS-J195602.8-320720	56157.1	27974.0	136.1	115.5
1RXS-J195602.8-320720	56157.1	27830.6	143.7	112.4
1RXS-J195602.8-320720	56168.1	12640.0	202.0	94.8
1RXS-J195602.8-320720	56168.1	11466.2	157.8	107.3
1RXS-J195602.8-320720	56169.2	430.690	198.1	95.8
1RXS-J195602.8-320720	56169.2	424.086	149.3	110.3
1RXS-J195602.8-320720	56170.2	-5222.50	122.9	121.6
1RXS-J195602.8-320720	56170.2	-5005.08	124.3	120.9
1RXS-J195602.8-320720	56171.2	3145.46	123.3	121.4
1RXS-J195602.8-320720	56171.2	2969.26	118.2	123.9

Star	MJD	RV	σ_{Obs}	SNR	
		(m/s)	(m/s)		
1RXS-J195602.8-320720	56172.2	40856.1	563.9	56.8	
1RXS-J195602.8-320720	56172.2	40927.0	274.9	81.3	
1RXS-J195602.8-320720	56172.2	41285.9	172.7	102.6	
1RXS-J195602.8-320720	56172.2	40475.0	208.2	93.4	
1RXS-J195602.8-320720	56178.1	7408.25	134.6	116.2	
1RXS-J195602.8-320720	56178.1	7277.92	120.4	122.8	
1RXS-J195602.8-320720	56180.1	-4802.37	230.3	88.8	
1RXS-J195602.8-320720	56180.1	-4666.01	179.2	100.7	
1RXS-J195602.8-320720	56181.1	-39842.3	106.4	130.6	
1RXS-J195602.8-320720	56181.1	20862.8	94.3	138.8	
1RXS-J195602.8-320720	56187.1	10934.0	213.2	92.3	
1RXS-J195602.8-320720	56187.1	11469.2	233.6	88.2	
1RXS-J195602.8-320720	56188.1	-2854.39	203.9	94.4	
1RXS-J195602.8-320720	56188.1	-1896.75	257.6	84.0	
1RXS-J195602.8-320720	56188.1	-1929.14	229.6	88.9	
1RXS-J195602.8-320720	56188.2	-2523.75	255.7	84.3	
1RXS-J195602.8-320720	56189.2	-5171.20	149.4	110.3	
1RXS-J195602.8-320720	56189.2	-5085.75	153.0	109.0	
1RXS-J195602.8-320720	56190.1	4788.76	129.8	118.3	
1RXS-J195602.8-320720	56190.1	5196.12	104.8	131.7	
1RXS-J195602.8-320720	56201.1	6653.62	162.2	105.8	
1RXS-J195602.8-320720	56201.1	8358.26	138.3	114.6	[1ex]

Radial Velocity Standards

Star	MJD	RV	σ_{Obs}	SNR
		(m/s)	(m/s)	
GJ 628	55667.3	-21125.1	75.2	155.4
GJ 628	55667.3	-21161.3	70.3	160.8
GJ 628	55682.2	-21211.3	63.5	169.2
GJ 628	55682.2	-21204.6	65.9	166.0
GJ 628	55685.3	-21229.3	62.6	170.3
GJ 628	55685.3	-21208.0	62.8	170.1
GJ 628	55728.2	-21164.9	68.2	163.2
GJ 628	55728.2	-21154.3	64.2	168.2
GJ 628	55765.0	-21132.0	97.4	136.6
GJ 628	55765.0	-21219.4	88.9	143.0
GJ 752A	56152.1	35858.3	113.6	126.5
GJ 752A	56152.1	35899.7	101.3	133.9
GJ 752A	56168.1	35870.7	115.4	125.5
GJ 752A	56168.1	35938.8	80.5	150.2
GJ 752A	56170.1	35984.3	56.7	178.9
GJ 752A	56170.1	35975.0	54.0	183.4
GJ 752A	56172.2	36033.2	67.0	164.6
GJ 752A	56172.2	36030.2	96.3	137.4
GJ 752A	56178.1	36008.5	77.4	153.2
GJ 752A	56178.1	36028.3	65.6	166.5
GJ 752A	56180.1	36001.9	71.8	159.1
GJ 752A	56180.1	35996.8	70.9	160.0

The absolute RVs with errors and the average $v\sin i$ from the model fits are listed in

Table 2.9. As with the Gemini Phoenix data, the mean of the epoch RV is used to calculate the absolute RV for each star, and the $v\sin i$ for each star is calculated from the mean of the epoch $v\sin i$ best fit values as well as the standard deviation. Again, we note that with the same velocity resolution of $\sim$6 km/s as Gemini Phoenix, $v\sin i$ values obtained with VLT CRIRES below $<$3 km/s should be considered upper limits.

As with Gemini Phoenix, we observed GJ 628 and GJ 752A as RV standards to estimate our observational precision based on the observed standard deviation of the RV epochs over the observing run for these RV standards. The RV standard deviation of GJ 625 was 32 m/s over 5 epochs and 63 m/s over 6 epochs for GJ 752A. RV curves are shown in Appendix A for all stars in this dissertation.

Table 2.9: VLT CRIRES Rotational and Absolute Radial Velocities

Star Name	Model T_{eff}, log$g$	vsini (km/s)	<RV> (m/s)
	Young Stars		
TWA 13A	3800, 4.2	11.14± 0.24	11560 ± 38
V721CrA	4000, 4.2	11.58± 0.22	−1203 ± 19
TYC 7443-1102-1	3200, 4.2	0.99± 0.34	−5229 ± 25
1RXS J195602.8320720	3200, 4.2	6.09± 11.03	33784 *
	Field Stars		
GJ 628	3400, 4.8	0.86± 0.22	−21181 ± 23
GJ 752A	3400, 4.8	0.81± 0.14	35969 ± 23

* The average value of the A and B component systemic velocities (γ) from our orbital fits.

For stars observed with both Gemini Phoenix and VLT CRIRES, we note that the $v$sin$i$ values agree to within the errors, but the absolute RV measurements show slight disagreements. The VLT CRIRES measurements all have slightly lower values. For GJ 628, GJ 752A, TWA 13A and V721 CrA, the absolute RV values are lower by 121 m/s, 78 m/s, 405 m/s and 538 m/s respectively. This may indicate that the absolute RV depends on the exact spectral region or spectral profile. As such, our absolute RV values likely have a systematic uncertainty of a few 100 m/s.

2.2.4 Identifying Candidate Variables with CRIRES

Similar to our Phoenix procedure, we make use of known single field stars as RV standards to determine our observational standard deviation. Given the newer and less noisy detector, we had expected to achieve a higher precision with CRIRES as compared to Phoenix,

but our precision was slightly worse than that from the Phoenix results. With CRIRES, the RV standards (GJ 628 and GJ 752A) showed standard deviations (32 m/s and 63 m/s) consistent with those from Gemini Phoenix. Two young stars (V721 CrA; 10 epochs and TYC 7443-1102-1; 19 epochs) showed standard deviations similar to the Phoenix young star measurements (88 m/s and 58 m/s respectively). 8 epochs of TWA 13A were obtained as follow-up from our Phoenix sample, as it showed a standard deviation of 210 m/s, more than 5 standard deviations above the average standard deviation for young stars (<Standard Deviation>=63 m/s). Our CRIRES measurements exhibited a slightly lower standard deviation of 171 m/s, but statistically consistent and still well above the average for young stars. The 18 epochs obtained for 1RXS J195602.8–320720 showed very high standard deviation (15794 m/s) indicative of a stellar companion.

A P-χ^2 test was conducted on the CRIRES follow-up stars. 1RXS J195602.8–320720 and TWA 13A have p-values low enough to indicate RV variability to a high significance (p-value <<0.0001 and 0.004 respectively). V721 CrA and TYC 7443-1102-1 had p-values of 0.06 and 0.99, respectively.

2.2.5 TWA 13A

The M1 spectral type young star in the TW Hydrae (TWA) Association, TWA 13A had been identified by Bailey et al. (2012) as a RV variable. It does show higher than average standard deviation (see Figure 2.6) in our analysis. we revise its classification as a candidate RV variable. Despite the additional measurements (8 epochs over ∼88 days), our sampling is insufficient to determine the underlying cause of this elevated RV standard deviation,

although the p-value is quite low at 0.004. Figure 2.13 shows the RV curve for TWA 13A.

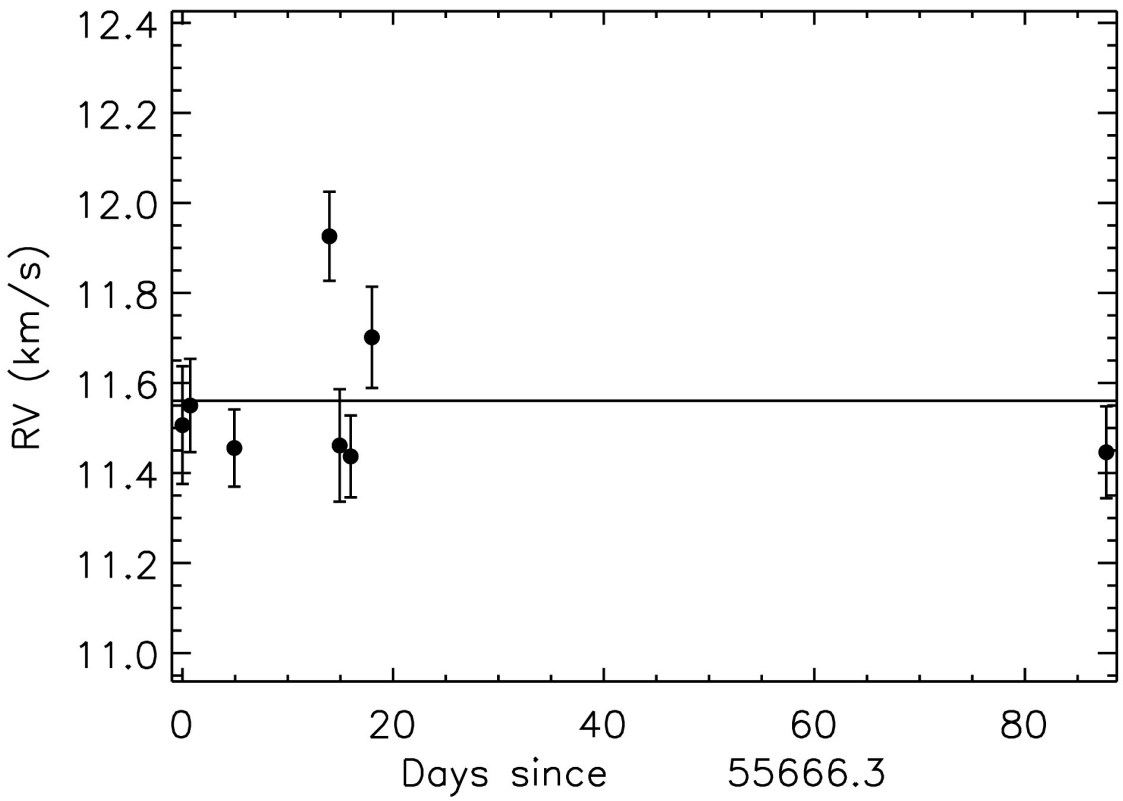

Figure 2.13 RV's curve for TWA 13A observed with VLT/CRIRES over the observing period.

2.2.5.1 TYC 7443-1102-1 & 1RXS J195602.8–320720

Lépine & Simon (2009) identified TYC 7443-1102-1 and 1RXS J195602.8–320720 as a common proper motion pair in the Beta Pic Moving Group with a separation of 26.3″ at a distance of 58 pc (McCarthy & White 2012) giving a projected separation of ∼1525 AU. Similar to TWA 13A & TWA 13B, this pair gives us a unique opportunity to study a young

coeval pair, although they are not of similar spectral type (TYC 7443-1102-1 M0 & 1RXS J195602.8–320720 M4).

We obtained 18 epochs for 1RXS J195602.8–320720, 19 epochs for TYC 7443-1102-1, and 6 epochs for our RV standard GJ 752A. Of this pair, only 1RXS J195602.8–320720 also showed extreme RV variability indicative of a spectroscopic binary. The dispersion of TYC 7443-1102-1 was 58 m/s, while the dispersion for 1RXS J195602.8–320720 was 15.8 km/s. Although Lannier et al. (2016) identified a close binary with a companion at 0.20″ (∼11.6 AU) to 1RXS J195602.8–320720, this would be too large a separation to show up as an RV signal in our observational time constraints. The RV signal we detect is for a stellar companion of similar mass and short period (See Figure 2.14). The companion spectrum is seen in the residuals of our fits, thus we classify this as a SB2.

We followed the prescription using TODCOR described in Section 2.1.5.2, using template spectra with T_{eff} and log$g$ from Table 2.9. The same T_{eff} and log$g$ template spectrum was used to for the secondary in this system, but the intensities were scaled using "χ-by-eye" to 90% of the primary to achieve a fit. Individual RV measurements for each component are listed in Table 2.10. We adopt the average difference in the RVs between the A and B nod for each component (241 m/s for 1RXS J195602.8–320720A and 216 m/s for 1RXS J195602.8–320720 with a standard deviation of 357 m/s and 402 m/s respectively).

TODCOR was unable to fit epochs on the dates MJD 56168.1 and MJD 56201.1. As with RXJ1204.6-7731, we attempted to fit Keplerian orbits to the individual components, but were unable to come up with a solution which had residuals <4 km/s. We also find evidence for a

trend in the average epoch RV of the system in Figure 2.14 (dashed line). Nevertheless, we list the best fit parameters for one possible solution in Table 2.11. We note that the period appears to be ∼19 days with an eccentricity of 0.19, and that there is a quadratic trend in Figure 2.15. However, we fit each component separately, and the quadratic trends are not the same. This best fit orbital solution corresponds to 1RXS J195602.8–320720A and 1RXS J195602.8–320720B having nearly equal masses, with a mass ratio of K_A/K_B=0.97.

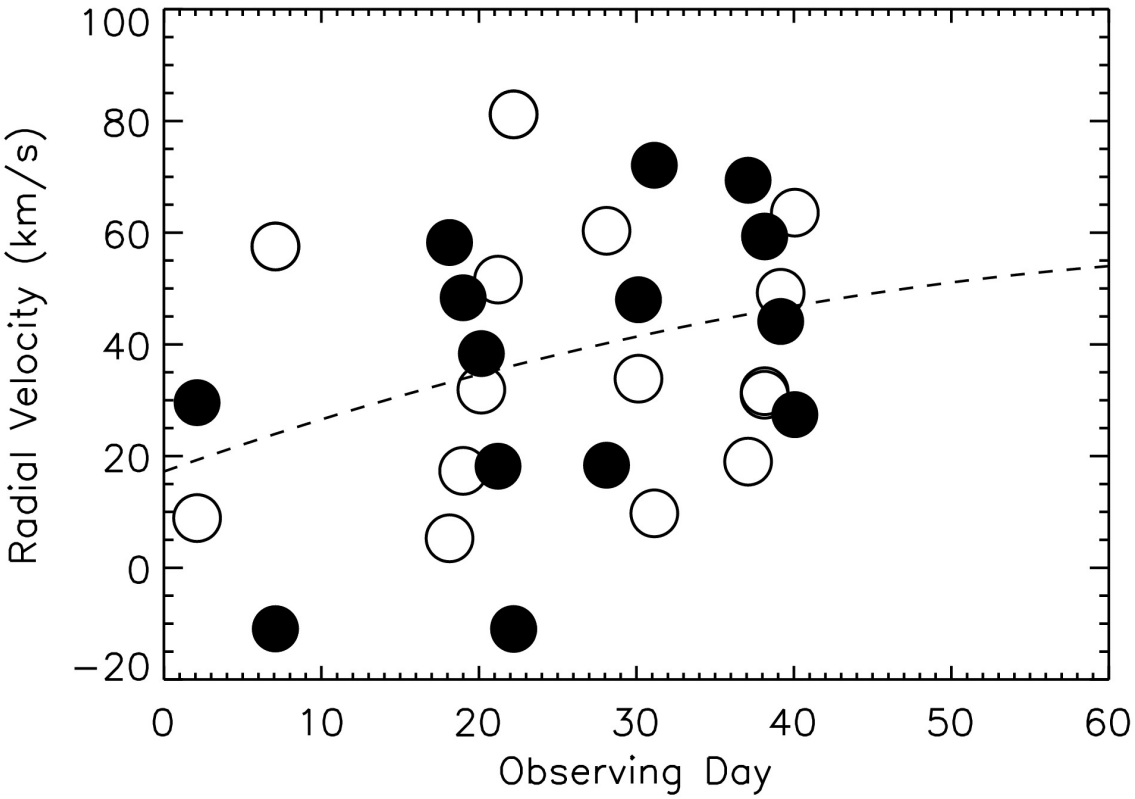

Figure 2.14 RV's of both components of 1RXS J195602.8–320720 in km/s over the 49 day observing period, with a quadratic trend shown (dashed line).

Table 2.10: 1RXS J195602.8320720 Individual Radial Velocity Measurements

MJD	$RV_{Component1}$ (m/s)	$RV_{Component2}$ (m/s)
56152.1	29563.4	8898.4
56157.1	−10937.1	57515.6
56157.1	−10914.7	57538.0
56168.1	···	···
56169.0	48347.7	17350.2
56170.2	31888.1	38345.9
56171.2	18182.2	51593.3
56172.2	−10884.0	81169.2
56172.2	−11026.1	80851.0
56178.1	18357.8	60333.8
56180.1	47988.1	33852.7
56181.1	72066.8	9745.43
56187.1	69377.5	19006.4
56188.1	58748.6	30980.0
56188.1	59244.9	31613.3
56189.2	44098.8	49239.0
56190.1	27417.3	63581.2

The error in the RV is estimated to be 241 m/s for 1RXS J195602.8320720A and 216 m/s for 1RXS J195602.832072. See the discussion in Section 2.2.5.1

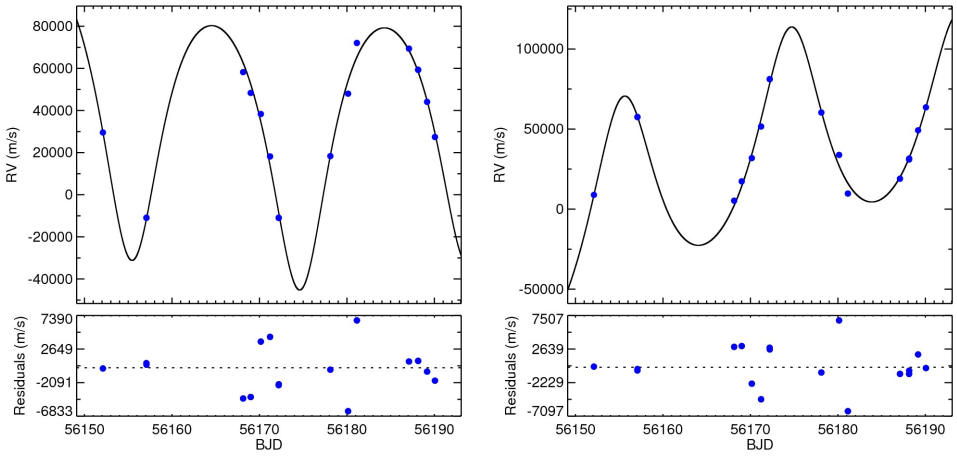

Figure 2.15 Best fit orbit for 1RXS J195602.8–320720A (left) and 1RXS J195602.8–320720B (right) with a quadratic trend.

Table 2.11: Preliminary Orbital Parameters for 1RXS J195602.8320720

Parameter	1RXS J195602.8320720A	1RXS J195602.8320720B
P	19.20±0.01 days	19.23±0.01 days
T_0	56170.57±0.01	56170.75±0.01
K	58827.7±143.3 m/s	60777.5±167.0 m/s
γ	37570.5±52.3 m/s	29998.1±49.0 m/s
e	0.1889±0.0016	0.2265±0.0016
ω	185.18±0.28	183.50±0.25

CHAPTER 3

A Precision Infrared Radial Velocity Survey of Young Stars in Taurus-Auriga and Upper Scorpius

3.1 Young Star Sample and Spectroscopic Observations with Keck/NIRSPEC

This RV survey of young stars in Taurus-Auriga and Upper Scorpius was conducted during 29 nights over a >5 year time period obtaining, in most cases, 7-10 measurements per star using the high resolution near infrared (NIR) spectrograph NIRSPEC on the W.M. Keck telescope.

3.1.1 Sample & Selection Criterion

The sample of young stars for this study was chosen from non-accreting stars in two nearby young clusters: Taurus-Auriga (∼1-2 Myr; Kraus & Hillenbrand (2009)) and Upper Scorpius (∼10 Myr; Feiden (2016)). From these clusters, we selected stars that are slowly rotating ($v\sin i < 15$ km/s), late K spectral type or cooler, all of which have strong CO R-branch lines at 2.3 μm, and with K_s magnitudes < 10.5. This selection criteria was chosen to maximize the number of targets we could obtain using the Keck NIRSPEC instrument, and to allow for the best quality RV measurements using our technique. The observations for this sample were taken in concert and with the same setup and instrument as the young stars surveyed in Bailey et al. (2012), although this sample is younger.

Our sample consists of 38 young stars (24 from Taurus-Auriga; 14 from Upper Sco) and is listed in Table 3.1 along with their 2MASS coordinates, 2MASS K_s magnitudes, spectral types, projected rotational velocities, rotational periods, and multiplicity information based

on high-spatial resolution imaging, if available. The references for this information are included in the table and table footnotes. In addition to these young stars, our observing strategy each night included observations of slowly rotating field stars that included one or more of the following: GJ 628, GJ 289, GJ 382, GJ 725A, and GJ 725B. The field star properties are also listed in Table 3.1. Since these field stars have RVs constant to $\leq$100 m/s (Nidever et al. 2002), they were observed to empirically determine our observational precision. Rotation periods range from 2-10 days for Upper Sco and 3-12 days for Taurus-Auriga. We note that this does not represent the typical rotation period for young stars (1-3 days; Saylor et al. 2018, Marilli et al. 2007). Our sample is biased to slow rotation periods, as it was selected for slow rotators.

Table 3.1: Keck/NIRSPEC Sample - Literature Values

	RA	Dec	K_{2MASS}			$v\sin i$		P_{rot}		
Name	(2000)	(2000)	(mag)	SpT	Ref	(km/s)	Ref	($days$)	Ref	Multiplicity
Young Stars - Taurus-Auriga										
V1306 Tau(RXJ0409.8)	04 09 51.132	+24 46 21.13	9.247±0.017	M1V	D15	5.9	N12	5.56	H11	Single (D15)
V1096 Tau	04 13 27.227	+28 16 24.78	7.460±0.029	M0V	R12	···	···	6.45	X12	
FN Tau	04 14 14.590	+28 27 58.06	8.189±0.018	M5V	R12	···	···	···	···	
CY Tau	04 17 33.726	+28 20 46.85	8.597±0.021	M1.5V	R12	10.6	N12	7.5	B95	
CIDA 3	04 17 49.655	+28 29 36.27	9.081±0.019	M2V	B93	···	···	···	···	
V410 X-ray 7	04 18 42.504	+28 18 49.85	9.257±0.017	M1V	S94	···	···	···	···	
IP Tau	04 24 57.080	+27 11 56.50	8.349±0.018	M0V	H86	12.3	N12	3.25	B95	
KPNO-Tau 13	04 26 57.326	+26 06 28.41	9.580±0.021	M5V	L03	···	···	···	···	
DH Tau	04 29 41.558	+26 32 58.27	8.178±0.026	M1V	H77	10.9	N12	7.2	B95	
IQ Tau	04 29 51.563	+26 06 44.90	7.779±0.023	M0.5V	R12	14.4	N12	6.902	X12	
JH 56	04 31 14.440	+27 10 17.99	8.794±0.017	M1V	X12	···	···	5.919	K12	
J1-665	04 31 58.444	+25 43 29.92	9.559±0.020	M5V		···	···	···	···	
V1321 Tau(RXJ0432.8)	04 32 53.237	+17 35 33.78	9.022±0.018	M2V		11.18	N12	···	···	
DM Tau	04 33 48.718	+18 10 09.99	9.522±0.020	M2V	H77	4.0	N12	43.478	H09	
JH 108	04 34 10.993	+22 51 44.54	9.426±0.018	M1V		···	···	···	···	
DN Tau	04 35 27.375	+24 14 58.93	8.342±0.027	M1V	H77	12.30	N12	6.00	B95	
RXJ0437.4+1851 B	04 37 26.847	+18 51 22.50	9.065±0.029	M0.5		···	···	···	···	
RXJ0437.4+1851 A	04 37 26.872	+18 51 26.69	8.67 ±0.05	K6V		···	···	···	···	
RXJ0438.2+2303	04 38 15.62	+23 02 27.6	9.769±0.021	M1V		4.5	N12	···	···	
CoKu Tau 4	04 41 16.813	+28 40 00.06	8.656±0.019	M1.5V	C80	25.8	N12	···	···	
GM Aur	04 55 10.983	+30 21 59.54	8.283±0.017	K3V	H77	14.8	N12	12	B95	
V1353 Tau(RXJ0457.0)	04 56 56.54	+16 00 24.9	9.843±0.019	M1V		···	···	···	···	
CIDA 8	05 04 41.399	+25 09 54.40	9.597±0.019	M3.5V	B93	···	···	···	···	
CIDA 10	05 06 16.747	+24 46 10.23	9.815±0.022	M3V	B93	···	···	···	···	

Table 3.1: Keck/NIRSPEC Sample - Literature Values

	RA	Dec	K_{2MASS}			$v\sin i$		P_{rot}		
Name	(2000)	(2000)	(mag)	SpT	Ref	(km/s)	Ref	($days$)	Ref	Multiplicity
Young Stars - Upper Scorpius										
RXJ1534.3-3300	15 34 23.140	-33 00 08.762	9.130±0.021	M0V	K00	···	···	5.377	K12	
RXJ1540.9-3024	15 40 56.552	-30 24 24.59	9.762±0.021	M2V	K00	···	···	···	···	
RXJ1546.0-2920	15 46 05.294	-29 20 53.11	9.468±0.021	M0V	K00	···	···	···	···	
RXJ1546.7-3210	15 46 46.646	-32 10 00.63	10.354±0.025	M2V	E07	···	···	···	···	
RXJ1548.9-3045	15 48 57.392	-30 45 04.38	10.311±0.021	M2V	K00	···	···	···	···	
RXJ1551.1-2402	15 51 06.608	-24 02 19.03	9.734±0.025	M2V	K08	···	···	9.929	K12	
RXJ1552.5-2633	15 52 31.227	-26 33 52.94	8.976±0.023	M0V	K00	···	···	3.3	A18	
RXJ1557.8-2305	15 57 50.029	-23 05 09.42	9.265±0.021	M0V	E07	···	···	···	···	
RXJ1558.8-2512	15 58 53.520	-25 12 33.41	9.651±0.021	M1V	E07	···	···	···	···	
RXJ1605.6-2152	16 05 39.364	-21 52 33.83	9.468±0.021	M1V	K08	···	···	···	···	
RXJ1607.0-2043	16 07 03.730	-20 43 07.43	9.534±0.024	M1V	K00	···	···	···	···	
ScoPMS 14	15 56 54.969	-23 29 47.80	10.285±0.023	M3V	S04	···	···	2.2	A98	
ScoPMS 32	16 06 39.901	-20 01 28.16	10.076±0.019	M3V	S04	···	···	···	···	
ScoPMS 42 B	16 10 21.741	-19 04 06.73	9.624±0.023	M1V		···	···	···	···	
Radial Velocity Standards										
GJ 289	07 48 16.386	+20 22 05.252	7.396±0.024	M1.5V	L13	···	···	···	···	
GJ 382	10 12 17.669	-03 44 44.397	5.015±0.020	M2V	K91	2.90	H10	21.56	K12	
GJ 628	16 30 18.1	−12 39 43	5.075 ± 0.024	M3.5	J09	<1.1	D98	···	···	···
GJ 725 A	18 42 46.704	+59 37 49.367	4.741±0.036	M3V	K91	<2.8	D98	···	···	CPM 13.88″
GJ 725 B	18 42 46.896	+59 37 36.783	5.000±0.023	M3.5V	K91	<2.8	D98	···	···	CPM 13.88″
GJ 876	22 53 16.734	-14 15 49.319	5.010±0.021	M3.5V	W83	<2.0	D98	···	···	

(CPM) Denotes a common proper motion binary.

A18 Ansdell et al. (2018)
A98 Adams et al. (1998)
B95 Bouvier et al. (1995)
B93 Briceno et al. (1993)
C80 Cohen (1980)
D15 Daemgen et al. (2015)
D98 Delfosse et al. (1998)
E07 Eisner et al. (2007)
H11 Hartman et al. (2011)
H02 Henry et al. (2002a)
H77 Herbig (1977)
H86 Herbig et al. (1986)
H09 Hoffman et al. (2009)
H10 Houdebine (2010)
J09 Jenkins et al. (2009)
K00 Köhler et al. (2000)
K08 Kraus et al. (2008)
K12 Kiraga (2012)
K91 Kirkpatrick et al. (1991)
L03 Luhman et al. (2003)
L13 Lépine et al. (2013)
N12 Nguyen et al. (2012)
R12 Riviere-Marichalar et al. (2012)
S04 Samus et al. (2004)
W83 Walker (1983)
X12 Xiao et al. (2012)

3.1.2 Keck/NIRSPEC Observations, Reductions and Extractions

Observations were taken over 29 nights (Nov 18 2004 to July 24 2010) on the Keck II Telescope using the NIRSPEC instrument (McLean et al. 1998) to obtain high dispersion infrared spectra. The optical design for the NIRSPEC instrument is shown in Figure 3.1. A 3 pixel (0.432″) slit and N7 blocking filter were used with an approximate grating angle of 35.5 degrees and echelle angle of 62.65 degrees. This gave 7 orders with a wavelength range of 1.99 μm - 2.39 μm (with gaps between the orders) at a resolving power of $\sim$30,000. We used a single order with a wavelength range from $\sim$2.280 - 3.315 μm for our analysis. Integration times were chosen to achieve a S/N of > 50 for both young stars and RV standard stars. All stars were observed in nod pairs, separated by 6″ along the slit, for pair subtraction during image reduction. For each night, dark and flat frames were obtained for image reduction purposes. The dark images from each night were median combined and subtracted from each flat field image. These flats were then normalized, using the central 10% of the chip as the normalization region, and median combined to produce a master flat for each night. All images for a given night were then divided by this master flat and then nod pair subtracted to remove the sky emission, as well as detector bias and dark current. Spectra were then extracted using the 'optimal extraction' method described Section 2.1.2 for pair subtracted infrared spectra.

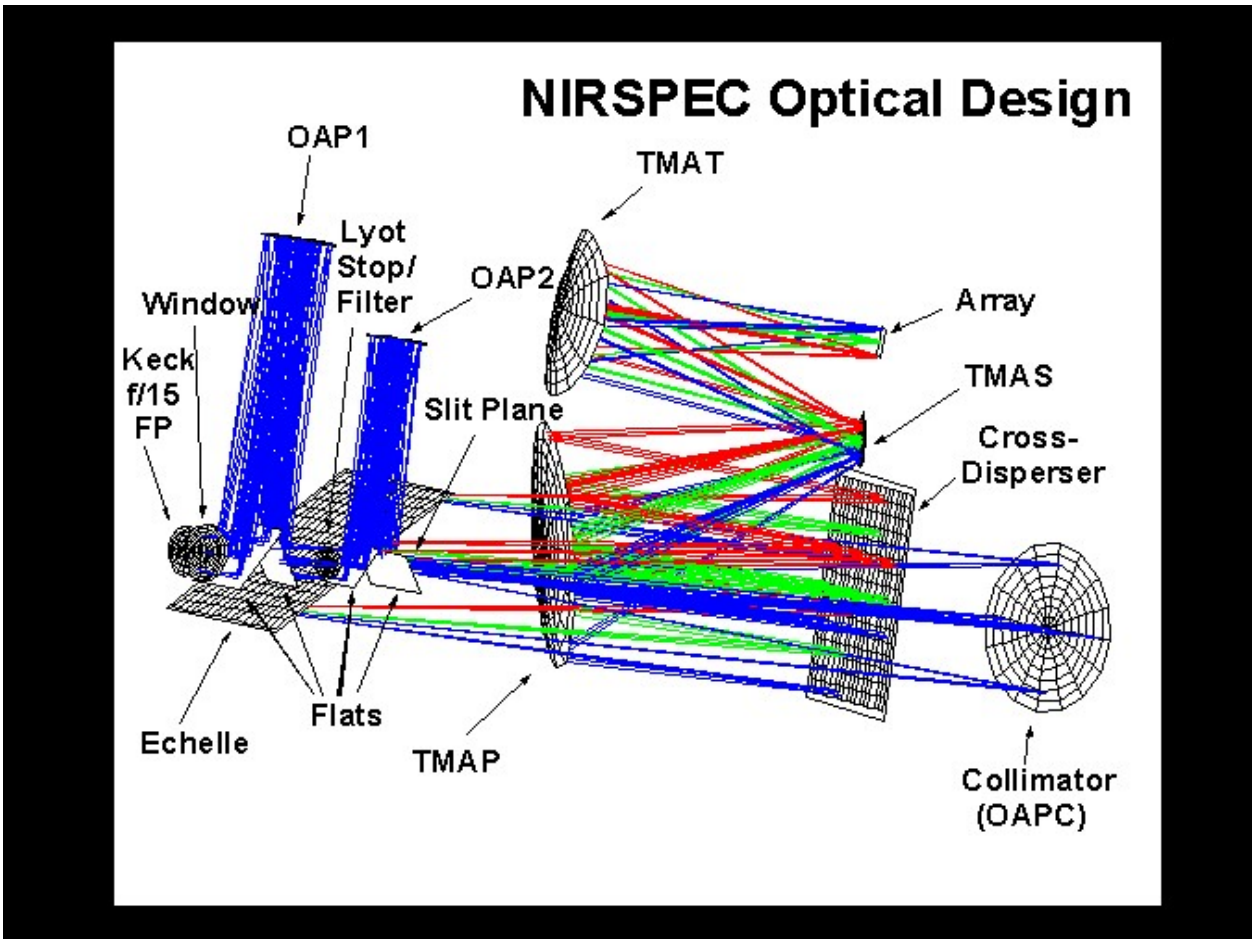

Figure 3.1 The Keck NIRSPEC optical design from `https://www2.keck.hawaii.edu/koa/public/nspec/nirspec_data_description.html`

3.2 Keck/NIRSPEC Radial and Rotational Velocity Measurements

Our prescription for determining precise radial and rotational velocities follows that of Section 2.1.3, and is summarized here. Precise RV's are determined relative to the telluric features at 2.3 μm using the ^{12}CO bandhead. We use a model telluric spectrum from KPNO/FTS and model stellar spectra generated using NexGen (Hauschildt et al. 1999).

These spectral models of our RV standards (GJ 628, GJ 289, GJ 382, GJ 725A, and GJ 725B) have a log$g$=4.8 dex, which is consistent with values measured for field dwarfs (e.g., see the compilation in Hillenbrand & White 2004). The remaining stars in our sample are young ($\sim$ 1-10Myr), therefore a log$g$=4.2 dex is assumed, consistent with previous surface gravity measurements (Johns-Krull et al. 1999; Johns-Krull et al. 2004). We use and updated version of the IDL routine *barycentric_vel.pro* to make the barycentric correction for all stars in our sample.

Our fitting routine attempts to reconstruct an observed spectrum by using 18 free parameters to characterize the product of a telluric and synthetic model spectrum as seen in Figure 2.3. These parameters are determined both by the properties of the instrument as well as the spectral properties of the star. For the instrumental properties, we model the wavelength solution as a quadratic polynomial. The instrumental profile (IP) is determined by using a 9 Gaussian model described in Valenti et al. (1995). An example fit for the IP is shown in Figure 3.2. We note that the IP was different over several nights. The spectral properties modeled by the routine are as follows - depth of telluric, the depth stellar features, $v$sin$i$, a linear (2 parameter) continuum normalization offset, and the target star's RV. The limb darkening coefficient is used to calculate rotationally broadened profiles, but is held constant at 0.3 (Claret et al. 2012).

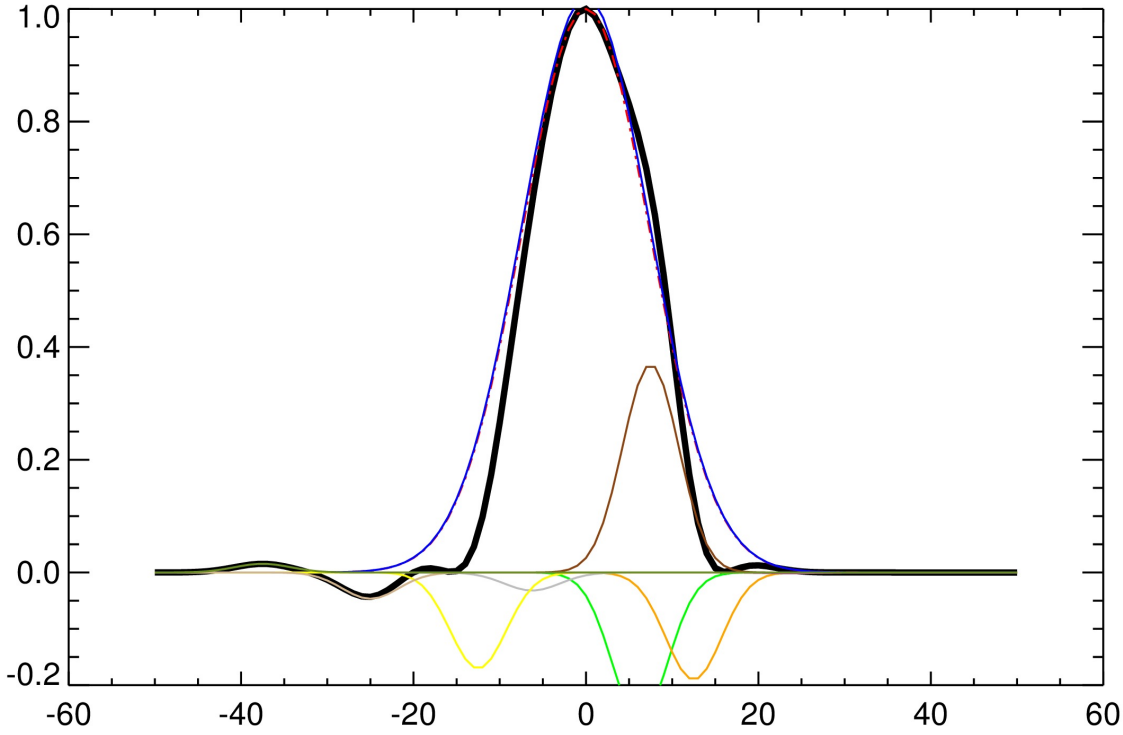

Figure 3.2 An example of the IP for Keck NIRSPEC. 9 Gaussian profiles (colored lines) were combined to create the total IP (black line).

Our fitting procedure is done by following an iterative process utilizing a modified double precision version of AMOEBA for IDL to determine the best fit parameters. The final RV is determined after a 4 stage fitting process with each stage using the best fit results from the previous stage as initial starting parameters. In the first stage, the wavelength solution and instrumental profile are determined by fitting the A spectral type star calibrators to a telluric template. In the second stage, the RV, wavelength solution, normalization parameters, telluric depths, and stellar depths are allowed to vary, while the $v\sin i$ and IP are held fixed.

The $v\sin i$ initial guess is set by literature values where available; otherwise it is set to 10 km/s. The third stage allows the $v\sin i$, RV, normalization parameters, telluric, and stellar depths to vary, while holding the wavelength and IP parameters fixed. The final stage is the same as the second, utilizing the weighted mean of the $v\sin i$ from the previous iteration.

3.2.1 Spectroscopic Results with Keck/NIRSPEC

In analyzing the spectroscopic results with NIRSPEC, we follow the same procedure outlined in Section 2.1.4. We used the ensemble set of observations of young stars to assess the error sources associated with the internal RV error for this technique, $\sigma_{Internal}$, and the error caused by stellar jitter, $\sigma_{Stellar}$, once the photon limited error, σ_{Photon}, is removed. We defined a total error for a single A or B nod observation (σ_{Obs_A} or σ_{Obs_B}) in Equation 3.1.

$$\sigma^2_{Obs_A} = \sigma^2_{Photon} + \sigma^2_{Internal} + \sigma^2_{Stellar} \tag{3.1}$$

The photon limited error term, σ_{Photon}, for each nod observation was calculated using the prescription in Butler et al. (1996).

Table 3.2: Keck NIRSPEC Individual Radial Velocity Measurements

Star	MJD	RV (m/s)	σ_{Obs} (m/s)	SNR

Young Stars - Taurus-Auriga

Table 3.2: Keck NIRSPEC Individual Radial Velocity Measurements

Star	MJD	RV	σ_{Obs}	SNR
		(m/s)	(m/s)	
V1306 Tau	53327.4	12914.9	35.8	225.2
V1306 Tau	53327.4	12790.8	28.5	252.3
V1306 Tau	53328.4	12962.2	58.1	176.8
V1306 Tau	53328.4	13015.5	41.7	208.7
V1306 Tau	53329.5	12762.6	64.8	167.4
V1306 Tau	53329.5	12761.7	53.0	185.0
V1306 Tau	53421.2	12718.2	40.8	211.0
V1306 Tau	53421.2	12718.3	34.7	228.8
V1306 Tau	53422.3	12761.0	32.8	235.3
V1306 Tau	53422.3	12738.3	33.9	231.5
V1306 Tau	53742.3	12832.5	60.6	173.1
V1306 Tau	53742.3	12555.4	19.6	304.4
V1306 Tau	53743.3	12762.0	26.3	262.9
V1306 Tau	53743.3	12620.4	38.0	218.5
V1306 Tau	54100.3	12777.1	33.1	234.2
V1306 Tau	54100.3	12757.1	29.8	246.8
V1306 Tau	54101.3	12933.3	69.9	161.2
V1306 Tau	54101.4	12588.5	50.8	189.0
V1096 Tau	53327.4	5230.2	17.7	320.3
V1096 Tau	53327.4	5132.1	17.1	325.8
V1096 Tau	53328.4	8882.1	35.1	227.6

Table 3.2: Keck NIRSPEC Individual Radial Velocity Measurements

Star	MJD	RV	σ_{Obs}	SNR
		(m/s)	(m/s)	
V1096 Tau	53328.4	8779.7	30.8	243.0
V1096 Tau	53329.5	9637.6	64.9	167.3
V1096 Tau	53329.5	10488.9	77.2	153.4
V1096 Tau	53421.2	692.2	29.5	248.1
V1096 Tau	53421.2	651.8	24.5	272.4
V1096 Tau	53422.3	979.7	27.6	256.7
V1096 Tau	53422.3	1096.9	26.4	262.5
V1096 Tau	53742.3	29089.9	46.6	197.4
V1096 Tau	53742.3	29501.4	23.8	276.1
V1096 Tau	54100.4	17425.0	47.2	196.1
V1096 Tau	54100.4	17065.4	44.4	202.3
V1096 Tau	54101.3	17527.4	60.6	173.2
V1096 Tau	54101.3	17619.2	59.7	174.4
FN Tau	53327.4	15853.6	31.1	241.9
FN Tau	53327.4	15753.0	24.6	272.0
FN Tau	53328.4	16026.8	54.0	183.5
FN Tau	53328.4	16103.9	45.7	199.5
FN Tau	53328.6	15960.2	36.2	223.9
FN Tau	53328.6	15981.2	31.7	239.2
FN Tau	53329.5	16001.7	48.7	193.2
FN Tau	53329.5	15622.5	66.8	164.8
FN Tau	53422.3	15215.8	30.5	244.0
FN Tau	53422.3	15330.0	33.6	232.5

Table 3.2: Keck NIRSPEC Individual Radial Velocity Measurements

Star	MJD	RV	σ_{Obs}	SNR
		(m/s)	(m/s)	
FN Tau	53669.4	15399.7	84.7	146.4
FN Tau	53669.4	15563.8	63.4	169.3
FN Tau	53743.3	15198.2	29.9	246.6
FN Tau	53743.3	15187.1	47.4	195.7
FN Tau	54100.4	15426.4	53.2	184.7
FN Tau	54100.4	15437.2	49.0	192.5
FN Tau	54101.3	15306.2	40.3	212.2
FN Tau	54101.3	15180.8	23.9	275.4
CY Tau	53327.4	17143.1	29.2	249.3
CY Tau	53327.4	16753.7	27.8	255.6
CY Tau	53328.4	17173.4	71.7	159.2
CY Tau	53328.4	17453.6	61.7	171.5
CY Tau	53329.5	17179.8	42.7	206.3
CY Tau	53329.5	16886.0	38.6	216.9
CY Tau	53743.3	16449.2	24.1	274.5
CY Tau	53743.3	16715.4	42.1	207.7
CY Tau	53744.3	16739.4	29.6	247.8
CY Tau	53744.3	16738.2	53.3	184.6
CY Tau	54100.4	16815.2	30.5	244.0
CY Tau	54100.4	16748.0	31.0	242.1
CY Tau	54101.3	17174.1	43.5	204.4
CY Tau	54101.3	16956.5	27.1	258.7
CIDA 3	53327.4	17535.1	35.7	225.5

Table 3.2: Keck NIRSPEC Individual Radial Velocity Measurements

Star	MJD	RV	σ_{Obs}	SNR
		(m/s)	(m/s)	
CIDA 3	53327.4	17473.2	35.7	225.7
CIDA 3	53328.4	17636.0	42.4	207.1
CIDA 3	53328.4	17763.7	36.0	224.6
CIDA 3	53329.5	18536.2	50.7	189.2
CIDA 3	53329.5	18410.4	66.2	165.6
CIDA 3	53421.3	17819.8	54.3	183.0
CIDA 3	53421.3	17766.3	46.1	198.5
CIDA 3	53422.3	16745.9	48.8	192.9
CIDA 3	53422.3	16698.6	41.4	209.5
CIDA 3	54100.4	17745.4	101.1	134.0
CIDA 3	54100.4	17620.5	68.0	163.4
CIDA 3	54101.4	16841.9	82.4	148.5
CIDA 3	54101.4	17180.9	44.6	201.7
V410X-ray 7	53327.4	18862.6	29.4	248.8
V410X-ray 7	53327.4	18604.5	26.7	260.7
V410X-ray 7	53421.3	19022.4	44.9	201.1
V410X-ray 7	53421.3	19003.9	29.1	250.0
V410X-ray 7	53422.3	18454.8	38.5	217.2
V410X-ray 7	53422.3	18531.1	34.5	229.3
V410X-ray 7	53744.3	18144.7	21.0	293.8
V410X-ray 7	53744.3	18219.5	63.7	168.8
V410X-ray 7	54100.4	18128.8	35.2	227.1
V410X-ray 7	54100.4	17940.5	31.2	241.2

Table 3.2: Keck NIRSPEC Individual Radial Velocity Measurements

Star	MJD	RV	σ_{Obs}	SNR
		(m/s)	(m/s)	
V410X-ray 7	54101.4	18152.5	40.1	212.9
V410X-ray 7	54101.4	18243.2	32.2	237.6
IP Tau	53327.4	17362.8	25.7	265.7
IP Tau	53327.4	17244.0	22.0	287.6
IP Tau	53328.5	16869.5	47.2	196.2
IP Tau	53328.5	17133.6	42.3	207.2
IP Tau	53422.3	17557.5	41.7	208.8
IP Tau	53422.3	17635.7	41.7	208.6
IP Tau	54100.4	17097.3	42.7	206.2
IP Tau	54100.4	17140.3	34.6	229.1
IP Tau	54101.4	17339.6	31.3	241.0
IP Tau	54101.4	17359.5	32.8	235.4
KPNO-Tau 13	53327.4	17414.3	35.7	225.5
KPNO-Tau 13	53327.5	17271.7	35.8	225.3
KPNO-Tau 13	53328.5	17377.6	51.5	187.9
KPNO-Tau 13	53328.5	17626.8	38.5	217.2
KPNO-Tau 13	53329.5	17240.5	35.6	225.9
KPNO-Tau 13	53329.5	17191.4	26.7	260.8
KPNO-Tau 13	53421.3	16645.2	30.3	244.7
KPNO-Tau 13	53421.3	16720.8	25.0	269.5
KPNO-Tau 13	53742.4	16620.7	25.9	264.9
KPNO-Tau 13	53742.4	16652.8	47.5	195.5
KPNO-Tau 13	53743.3	16657.7	16.4	332.9

Table 3.2: Keck NIRSPEC Individual Radial Velocity Measurements

Star	MJD	RV	σ_{Obs}	SNR
		(m/s)	(m/s)	
KPNO-Tau 13	53743.3	16674.6	36.2	224.0
KPNO-Tau 13	53744.4	16293.2	26.8	260.5
KPNO-Tau 13	53744.4	16346.8	113.9	126.0
KPNO-Tau 13	54100.4	16527.0	31.3	240.9
KPNO-Tau 13	54100.4	16677.8	31.8	239.1
KPNO-Tau 13	54101.5	16570.1	53.8	183.7
KPNO-Tau 13	54101.5	16820.5	54.8	182.0
DH Tau	53327.5	16147.1	37.4	220.3
DH Tau	53327.5	16189.4	38.1	218.4
DH Tau	53328.5	16401.8	73.6	157.1
DH Tau	53328.5	16406.0	50.3	189.9
DH Tau	53421.3	15976.6	46.8	197.0
DH Tau	53421.3	16155.1	31.8	239.0
DH Tau	53422.3	15916.0	51.5	187.8
DH Tau	53422.3	16347.5	48.4	193.7
DH Tau	53742.4	16136.7	45.7	199.4
DH Tau	53742.4	16092.2	22.9	281.4
DH Tau	53743.3	16012.6	20.2	300.0
DH Tau	53743.3	16094.0	43.8	203.6
DH Tau	54100.4	15786.1	36.7	222.3
DH Tau	54100.4	15578.0	36.7	222.4
DH Tau	54101.5	15792.2	43.3	204.8
DH Tau	54101.5	15911.3	33.7	232.3

Table 3.2: Keck NIRSPEC Individual Radial Velocity Measurements

Star	MJD	RV	σ_{Obs}	SNR
		(m/s)	(m/s)	
IQ Tau	53327.5	16248.2	36.9	221.7
IQ Tau	53327.5	15946.6	34.4	229.8
IQ Tau	53328.5	16651.4	63.2	169.5
IQ Tau	53328.5	16747.4	45.0	200.9
IQ Tau	53329.5	16207.8	71.9	159.0
IQ Tau	53329.5	16056.9	80.9	149.9
IQ Tau	53421.3	16455.2	39.0	215.9
IQ Tau	53421.3	16422.7	27.3	258.2
IQ Tau	53422.3	15562.4	27.5	257.0
IQ Tau	53422.3	15048.3	26.6	261.5
IQ Tau	53743.3	16636.4	26.3	263.0
IQ Tau	53743.3	16862.3	30.2	245.1
IQ Tau	53744.4	17028.6	53.0	185.2
IQ Tau	53744.4	17557.2	66.8	165.0
IQ Tau	54100.4	16394.4	27.8	255.5
IQ Tau	54100.4	16083.1	27.6	256.3
JH 56	53327.5	17401.7	33.2	233.8
JH 56	53327.5	17252.2	31.9	238.7
JH 56	53328.5	17961.9	40.2	212.6
JH 56	53328.5	17934.3	36.2	223.9
JH 56	53329.5	17709.2	71.3	159.7
JH 56	53329.5	17556.2	79.6	151.0
JH 56	53421.3	17632.5	35.9	224.9

Table 3.2: Keck NIRSPEC Individual Radial Velocity Measurements

Star	MJD	RV	σ_{Obs}	SNR
		(m/s)	(m/s)	
JH 56	53421.3	17607.8	33.0	234.7
JH 56	53422.3	17320.5	42.3	207.3
JH 56	53422.3	17153.5	43.8	203.6
JH 56	53742.4	17184.8	27.6	256.4
JH 56	53742.4	17362.5	28.4	253.0
JH 56	53743.4	17441.6	22.1	286.6
JH 56	53743.4	17340.6	30.6	243.8
JH 56	54100.4	17633.1	41.4	209.5
JH 56	54100.4	17571.3	38.4	217.6
JH 56	54103.5	17257.3	37.3	220.6
JH 56	54103.5	17230.3	37.1	221.2
J1-665	53327.5	7871.8	39.6	214.1
J1-665	53327.5	7007.2	33.4	233.3
J1-665	53328.5	7822.3	73.7	157.0
J1-665	53328.5	7476.0	65.8	166.2
J1-665	53421.3	8562.2	54.2	183.1
J1-665	53421.3	8242.7	45.3	200.2
J1-665	53742.4	8520.1	37.0	221.7
J1-665	53742.4	7843.9	28.1	254.1
J1-665	53743.4	8162.3	27.0	259.3
J1-665	53743.4	7907.3	33.6	232.5
J1-665	54100.4	7616.6	41.1	210.1
J1-665	54100.4	7219.3	39.5	214.5

Table 3.2: Keck NIRSPEC Individual Radial Velocity Measurements

Star	MJD	RV	σ_{Obs}	SNR
		(m/s)	(m/s)	
J1-665	54103.5	8154.9	45.7	199.4
J1-665	54103.5	8420.7	56.1	180.0
V1321 Tau	53327.5	19723.6	35.7	225.4
V1321 Tau	53327.5	19586.1	33.0	234.5
V1321 Tau	53328.5	20053.1	54.6	182.3
V1321 Tau	53328.5	19938.1	47.0	196.6
V1321 Tau	53329.6	19756.8	77.2	153.3
V1321 Tau	53329.6	19659.6	43.7	204.0
V1321 Tau	53422.3	19252.5	43.8	203.5
V1321 Tau	53422.3	19258.7	47.1	196.3
V1321 Tau	53742.4	19213.2	48.5	193.4
V1321 Tau	53742.4	19110.1	39.5	214.4
V1321 Tau	53743.4	19368.4	45.2	200.5
V1321 Tau	53743.4	19203.4	37.8	219.3
V1321 Tau	53744.4	18817.6	38.3	217.8
V1321 Tau	53744.4	19005.4	71.0	160.0
V1321 Tau	54100.3	19368.8	38.4	217.6
V1321 Tau	54100.3	19422.6	30.0	246.2
V1321 Tau	54101.4	19361.8	61.8	171.4
V1321 Tau	54101.4	19461.8	49.9	190.8
DM Tau	53327.5	19051.7	49.0	192.5
DM Tau	53327.5	19053.4	47.1	196.4
DM Tau	53328.5	19205.6	68.4	163.0

Table 3.2: Keck NIRSPEC Individual Radial Velocity Measurements

Star	MJD	RV	σ_{Obs}	SNR
		(m/s)	(m/s)	
DM Tau	53328.5	19197.2	57.9	177.1
DM Tau	53328.6	19140.1	47.0	196.6
DM Tau	53328.6	19076.3	39.0	215.8
DM Tau	53329.6	18982.5	70.9	160.0
DM Tau	53329.6	18878.8	158.9	106.0
DM Tau	53744.4	18509.3	38.4	217.4
DM Tau	53744.4	18579.4	75.4	155.2
DM Tau	54100.3	18649.8	44.5	201.9
DM Tau	54100.3	18801.6	35.5	226.2
DM Tau	54101.4	18870.3	59.1	175.4
DM Tau	54101.4	18589.5	52.1	186.7
JH 108	53327.5	17939.3	54.0	183.4
JH 108	53327.5	17475.8	51.3	188.2
JH 108	53328.5	18033.0	56.9	178.6
JH 108	53328.5	18108.9	46.6	197.5
JH 108	53421.3	17478.6	38.8	216.3
JH 108	53421.3	17506.3	33.5	232.9
JH 108	53743.4	17390.2	19.7	304.0
JH 108	53743.4	17707.1	59.1	175.3
JH 108	53744.4	17531.3	22.8	282.1
JH 108	53744.4	17808.7	118.5	123.0
JH 108	54100.5	17519.3	45.3	2.200
JH 108	54100.5	17517.6	45.7	199.4

Table 3.2: Keck NIRSPEC Individual Radial Velocity Measurements

Star	MJD	RV	σ_{Obs}	SNR
		(m/s)	(m/s)	
DN Tau	53327.5	17695.8	55.6	180.8
DN Tau	53327.5	17852.0	48.3	194.0
DN Tau	53328.5	17796.1	34.7	228.8
DN Tau	53328.5	17825.7	30.7	243.2
DN Tau	53329.6	17745.8	122.2	121.0
DN Tau	53329.6	17783.9	152.4	109.0
DN Tau	53329.6	17867.9	88.6	143.1
DN Tau	53329.6	17800.3	74.1	156.6
DN Tau	53421.3	17989.4	29.8	247.1
DN Tau	53421.3	17951.0	27.1	258.7
DN Tau	54100.5	17690.3	36.0	224.5
DN Tau	54100.5	17697.0	32.8	235.4
RXJ0437.4+1851 A	53327.5	16394.9	49.9	190.7
RXJ0437.4+1851 A	53327.5	16380.7	41.0	210.6
RXJ0437.4+1851 A	53328.5	16659.5	60.7	173.0
RXJ0437.4+1851 A	53328.5	16882.5	63.0	169.8
RXJ0437.4+1851 A	53329.6	16729.7	62.3	170.7
RXJ0437.4+1851 A	53329.6	16488.3	52.8	185.5
RXJ0437.4+1851 A	53421.3	16672.1	62.6	170.4
RXJ0437.4+1851 A	53421.3	16702.4	43.9	203.3
RXJ0437.4+1851 A	53422.3	16691.9	41.9	208.1
RXJ0437.4+1851 A	53422.3	16465.4	43.4	204.7
RXJ0437.4+1851 A	53742.5	16806.1	54.3	182.8

Table 3.2: Keck NIRSPEC Individual Radial Velocity Measurements

Star	MJD	RV (m/s)	σ_{Obs} (m/s)	SNR
RXJ0437.4+1851 A	53742.5	16460.7	34.9	228.0
RXJ0437.4+1851 A	53743.5	16720.8	39.8	213.6
RXJ0437.4+1851 A	53743.5	16479.9	26.3	263.0
RXJ0437.4+1851 A	54100.3	16446.2	25.9	264.9
RXJ0437.4+1851 A	54100.3	16440.7	22.7	282.8
RXJ0437.4+1851 A	54101.5	16263.2	52.9	185.3
RXJ0437.4+1851 A	54101.5	16564.9	34.3	230.2
RXJ0437.4+1851 B	53327.5	15086.3	36.8	222.1
RXJ0437.4+1851 B	53327.5	15023.8	34.9	228.1
RXJ0437.4+1851 B	53328.5	15640.3	48.5	193.5
RXJ0437.4+1851 B	53328.5	15477.9	34.8	228.4
RXJ0437.4+1851 B	53329.6	15581.7	57.2	178.1
RXJ0437.4+1851 B	53329.6	15184.2	69.3	161.9
RXJ0437.4+1851 B	53421.3	15270.2	54.1	183.3
RXJ0437.4+1851 B	53421.3	15052.2	56.8	178.9
RXJ0437.4+1851 B	53422.3	15243.4	61.0	172.5
RXJ0437.4+1851 B	53422.3	15159.2	53.0	185.0
RXJ0437.4+1851 B	53742.5	15088.9	34.1	230.9
RXJ0437.4+1851 B	53742.5	15170.6	43.6	204.0
RXJ0437.4+1851 B	53743.5	15435.5	31.1	241.6
RXJ0437.4+1851 B	53743.5	15240.5	40.7	211.3
RXJ0437.4+1851 B	54100.3	15137.6	24.0	275.1
RXJ0437.4+1851 B	54100.3	15099.4	25.2	268.7

Table 3.2: Keck NIRSPEC Individual Radial Velocity Measurements

Star	MJD	RV	σ_{Obs}	SNR
		(m/s)	(m/s)	
RXJ0437.4+1851 B	54101.5	15241.6	58.3	176.5
RXJ0437.4+1851 B	54101.5	15228.2	41.9	208.1
RXJ0438.2+2303	53329.6	16918.7	154.2	108.0
RXJ0438.2+2303	53329.6	16689.0	128.0	119.1
RXJ0438.2+2303	53421.3	16670.6	58.4	176.3
RXJ0438.2+2303	53421.3	16849.3	55.4	181.1
RXJ0438.2+2303	53422.4	16871.7	56.4	179.5
RXJ0438.2+2303	53422.4	16777.7	63.1	169.7
RXJ0438.2+2303	53743.4	16745.0	47.0	196.5
RXJ0438.2+2303	53743.4	16534.2	23.0	280.9
RXJ0438.2+2303	54101.4	16562.2	76.1	154.5
RXJ0438.2+2303	54101.4	16858.7	43.3	204.9
CoKu Tau4	53327.5	15847.1	52.7	185.6
CoKu Tau4	53327.5	15587.4	46.4	197.8
CoKu Tau4	53328.4	15861.9	92.1	140.4
CoKu Tau4	53328.4	16442.1	83.2	147.8
CoKu Tau4	53421.3	16640.0	29.1	249.9
CoKu Tau4	53421.4	16552.7	25.8	265.3
CoKu Tau4	53742.5	16505.7	37.9	219.0
CoKu Tau4	53742.5	16133.8	30.2	245.3
CoKu Tau4	53744.4	16351.3	48.8	193.0
CoKu Tau4	53744.4	15359.7	49.2	192.1
CoKu Tau4	54100.5	16032.5	34.0	231.1

Table 3.2: Keck NIRSPEC Individual Radial Velocity Measurements

Star	MJD	RV	σ_{Obs}	SNR
		(m/s)	(m/s)	
CoKu Tau4	54100.5	16104.8	31.0	242.0
CoKu Tau4	54101.5	16281.2	47.8	194.9
CoKu Tau4	54101.5	17134.4	44.9	201.1
GM Aur	53327.5	15898.3	39.4	214.7
GM Aur	53327.5	15598.5	36.8	222.2
GM Aur	53328.4	16382.1	55.1	181.5
GM Aur	53328.4	16037.9	46.9	196.8
GM Aur	53329.6	15576.2	112.7	126.0
GM Aur	53329.6	15628.5	77.7	152.9
GM Aur	53421.4	15794.5	25.6	266.4
GM Aur	53421.4	15710.8	25.2	268.7
GM Aur	53422.4	16195.3	29.1	249.9
GM Aur	53422.4	16167.1	34.4	229.7
GM Aur	53743.5	16434.7	54.5	182.5
GM Aur	53743.5	16230.4	21.0	293.9
GM Aur	53744.5	15797.5	36.2	224.1
GM Aur	53744.5	15771.1	34.3	230.1
GM Aur	54100.5	15582.0	41.3	209.6
GM Aur	54100.5	15530.3	39.7	213.9
GM Aur	54101.5	15212.9	37.0	221.6
GM Aur	54101.5	15384.1	35.8	225.3
V1353 Tau	53327.5	20247.4	57.5	177.7
V1353 Tau	53327.5	20160.9	58.0	177.0

Table 3.2: Keck NIRSPEC Individual Radial Velocity Measurements

Star	MJD	RV	σ_{Obs}	SNR
		(m/s)	(m/s)	
V1353 Tau	53328.5	20708.4	64.6	167.6
V1353 Tau	53328.5	20533.8	56.2	179.7
V1353 Tau	53421.3	20445.5	61.3	172.1
V1353 Tau	53421.3	20311.5	53.5	184.3
V1353 Tau	53422.3	20441.3	53.9	183.6
V1353 Tau	53422.3	20608.5	59.9	174.1
V1353 Tau	53741.5	19925.3	58.6	176.0
V1353 Tau	53741.5	19976.4	49.0	192.5
V1353 Tau	53742.4	20098.0	34.0	231.3
V1353 Tau	53742.4	20124.9	37.2	221.1
V1353 Tau	54100.3	20260.1	38.7	216.5
V1353 Tau	54100.3	20228.0	33.3	233.7
V1353 Tau	54103.5	19889.7	57.2	178.3
V1353 Tau	54103.5	20103.0	58.3	176.6
CIDA 8	53327.6	18369.4	52.2	186.6
CIDA 8	53327.6	18814.8	48.5	193.6
CIDA 8	53328.6	18747.8	61.7	171.5
CIDA 8	53328.6	19176.8	55.2	181.4
CIDA 8	53421.4	18972.5	37.7	219.4
CIDA 8	53421.4	18955.0	37.2	220.9
CIDA 8	53422.2	19045.8	49.2	192.1
CIDA 8	53422.2	18726.0	39.1	215.7
CIDA 8	53741.5	17535.6	40.7	211.2

Table 3.2: Keck NIRSPEC Individual Radial Velocity Measurements

Star	MJD	RV	σ_{Obs}	SNR
		(m/s)	(m/s)	
CIDA 8	53741.5	17582.8	32.3	237.0
CIDA 8	53743.5	18483.0	33.5	232.9
CIDA 8	53743.5	18782.7	30.1	245.5
CIDA 8	53744.5	18714.4	42.7	206.1
CIDA 8	53744.5	18895.7	59.2	175.2
CIDA 8	54100.5	19721.8	40.5	211.7
CIDA 8	54100.5	19056.4	37.0	221.5
CIDA 10	53327.6	19724.0	50.0	190.7
CIDA 10	53327.6	19615.4	48.8	193.0
CIDA 10	53328.6	19789.9	59.0	175.4
CIDA 10	53328.6	19543.5	50.5	189.6
CIDA 10	53421.4	18668.4	41.2	210.0
CIDA 10	53421.4	19340.7	40.2	212.5
CIDA 10	53422.2	19941.0	58.9	175.7
CIDA 10	53422.2	19675.2	59.1	175.4
CIDA 10	53422.4	19293.4	64.2	168.2
CIDA 10	53422.4	19231.5	59.7	174.4
CIDA 10	53742.5	18610.2	36.9	222.0
CIDA 10	53742.5	18578.3	47.1	196.3
CIDA 10	53743.5	19335.2	35.0	227.8
CIDA 10	53743.5	19515.6	40.6	211.6
CIDA 10	54100.5	19742.8	46.2	198.3
CIDA 10	54100.5	19350.1	47.5	195.5

Table 3.2: Keck NIRSPEC Individual Radial Velocity Measurements

Star	MJD	RV	σ_{Obs}	SNR
		(m/s)	(m/s)	
Young Stars - Upper Scorpius				
RXJ1534.3-3300	53420.6	2790.8	82.1	148.7
RXJ1534.3-3300	53420.6	2729.9	79.5	151.2
RXJ1534.3-3300	53523.3	2316.0	95.9	137.6
RXJ1534.3-3300	53523.3	2316.5	45.1	200.7
RXJ1534.3-3300	53741.7	2370.0	42.1	207.8
RXJ1534.3-3300	53741.7	2465.4	55.6	180.7
RXJ1534.3-3300	53783.6	2337.2	67.3	164.3
RXJ1534.3-3300	53783.6	2472.0	57.9	177.1
RXJ1534.3-3300	53928.3	2557.1	99.8	134.9
RXJ1534.3-3300	53928.3	2488.6	90.6	141.6
RXJ1534.3-3300	53930.2	2698.5	94.5	138.7
RXJ1534.3-3300	53930.2	2650.8	34.2	230.3
RXJ1534.3-3300	53931.2	2568.4	83.2	147.8
RXJ1534.3-3300	53931.2	2475.3	62.5	170.4
RXJ1534.3-3300	54311.2	2599.7	50.5	189.6
RXJ1534.3-3300	54311.2	2679.0	44.0	203.1
RXJ1534.3-3300	54312.2	2683.3	40.7	211.3
RXJ1534.3-3300	54312.2	2763.0	37.8	219.3
RXJ1540.9-3024	53420.6	−7600.5	84.5	146.6

Table 3.2: Keck NIRSPEC Individual Radial Velocity Measurements

Star	MJD	RV	σ_{Obs}	SNR
		(m/s)	(m/s)	
RXJ1540.9-3024	53420.6	−7729.8	73.2	157.5
RXJ1540.9-3024	53523.3	−7986.7	59.3	175.0
RXJ1540.9-3024	53523.3	−7972.5	66.3	165.5
RXJ1540.9-3024	53523.4	−7351.9	70.7	160.3
RXJ1540.9-3024	53523.4	−7440.5	34.1	230.7
RXJ1540.9-3024	53929.3	−7369.0	69.6	161.5
RXJ1540.9-3024	53929.3	−7664.9	58.5	176.1
RXJ1540.9-3024	53930.2	−7238.5	42.1	207.8
RXJ1540.9-3024	53930.2	−6715.8	87.0	144.5
RXJ1540.9-3024	53931.2	−6999.7	46.9	196.7
RXJ1540.9-3024	53931.3	−6866.1	103.2	132.7
RXJ1540.9-3024	54308.2	−8586.1	50.6	189.4
RXJ1540.9-3024	54308.2	−8467.3	45.3	200.3
RXJ1540.9-3024	54309.3	−8267.1	61.9	171.2
RXJ1540.9-3024	54309.3	−8323.5	53.9	183.5
RXJ1540.9-3024	54311.3	−8522.4	69.0	162.3
RXJ1540.9-3024	54311.3	−8263.1	60.2	173.7
RXJ1540.9-3024	54312.3	−7808.3	71.4	159.5
RXJ1540.9-3024	54312.3	−7923.1	72.5	158.3
RXJ1546.0-2920	53420.6	−4047.9	66.9	164.7
RXJ1546.0-2920	53420.6	−4076.3	60.8	172.9
RXJ1546.0-2920	53522.4	−4331.3	43.6	204.1
RXJ1546.0-2920	53522.4	−4094.6	49.0	192.5

Table 3.2: Keck NIRSPEC Individual Radial Velocity Measurements

Star	MJD	RV	σ_{Obs}	SNR
		(m/s)	(m/s)	
RXJ1546.0-2920	53523.3	−4324.5	33.6	232.4
RXJ1546.0-2920	53523.3	−4276.9	32.5	236.6
RXJ1546.0-2920	53742.7	−4311.1	60.0	174.0
RXJ1546.0-2920	53742.7	−4308.6	113.6	126.5
RXJ1546.0-2920	53783.6	−4361.0	57.6	177.5
RXJ1546.0-2920	53783.6	−4343.9	50.5	189.7
RXJ1546.0-2920	53929.3	−4485.8	52.9	185.2
RXJ1546.0-2920	53929.3	−4257.3	57.5	177.8
RXJ1546.0-2920	53930.3	−4383.1	35.9	225.0
RXJ1546.0-2920	53930.3	−4226.6	45.3	200.3
RXJ1546.0-2920	53931.3	−4240.8	71.1	159.8
RXJ1546.0-2920	53931.3	−4410.5	31.3	241.0
RXJ1546.0-2920	54308.3	−4082.0	46.3	198.0
RXJ1546.0-2920	54308.3	−4225.3	37.8	219.3
RXJ1546.7-3210	53421.6	2569.8	101.8	133.6
RXJ1546.7-3210	53421.6	2352.8	86.1	145.3
RXJ1546.7-3210	53522.4	1849.3	90.8	141.4
RXJ1546.7-3210	53522.4	1907.9	115.0	125.7
RXJ1546.7-3210	53523.4	2092.9	67.3	164.3
RXJ1546.7-3210	53523.4	2090.2	66.6	165.1
RXJ1546.7-3210	53783.6	2118.3	82.8	148.2
RXJ1546.7-3210	53783.6	2108.5	73.6	157.1
RXJ1546.7-3210	53931.3	2275.8	89.5	142.5

Table 3.2: Keck NIRSPEC Individual Radial Velocity Measurements

Star	MJD	RV	σ_{Obs}	SNR
		(m/s)	(m/s)	
RXJ1546.7-3210	53931.3	2072.0	99.6	135.1
RXJ1546.7-3210	54308.3	2185.1	75.8	154.8
RXJ1546.7-3210	54308.3	2254.8	73.9	156.8
RXJ1546.7-3210	54309.3	2333.4	79.7	151.0
RXJ1546.7-3210	54309.3	2205.7	71.4	159.5
RXJ1546.7-3210	54311.2	2230.5	76.6	153.9
RXJ1546.7-3210	54311.3	2240.0	65.8	166.1
RXJ1548.9-3045	53421.6	13562.1	93.8	139.1
RXJ1548.9-3045	53421.6	13708.7	81.3	149.5
RXJ1548.9-3045	53522.4	−15664.5	43.9	203.3
RXJ1548.9-3045	53522.4	−15507.7	43.2	205.2
RXJ1548.9-3045	53523.4	13503.2	46.9	196.9
RXJ1548.9-3045	53523.4	13657.5	97.1	136.8
RXJ1548.9-3045	53783.6	38772.4	78.2	152.4
RXJ1548.9-3045	53783.6	38799.1	67.9	163.5
RXJ1548.9-3045	53931.3	−28440.0	164.4	105.1
RXJ1548.9-3045	53931.3	−28839.2	38.0	218.6
RXJ1548.9-3045	54308.3	−19773.9	71.6	159.3
RXJ1548.9-3045	54308.3	−19660.8	60.3	173.5
RXJ1548.9-3045	54309.2	13666.0	84.1	147.0
RXJ1548.9-3045	54309.2	14036.6	72.5	158.3
RXJ1548.9-3045	54311.3	−12276.9	72.1	158.7
RXJ1548.9-3045	54311.3	−12383.3	62.1	171.

Table 3.2: Keck NIRSPEC Individual Radial Velocity Measurements

Star	MJD	RV	σ_{Obs}	SNR
		(m/s)	(m/s)	
RXJ1548.9-3045	54312.2	−3260.3	76.5	154.1
RXJ1548.9-3045	54312.2	−2802.6	69.3	161.9
RXJ1551.1-2402	54312.3	−4766.8	86.0	145.3
RXJ1551.1-2402	54312.3	−4592.3	74.0	156.6
RXJ1551.1-2402	53522.4	−4519.6	30.1	245.5
RXJ1551.1-2402	53522.4	−4348.3	39.4	214.7
RXJ1551.1-2402	53523.4	−4289.8	40.0	213.0
RXJ1551.1-2402	53523.4	−4390.5	30.8	242.7
RXJ1551.1-2402	53929.3	−4451.5	55.2	181.3
RXJ1551.1-2402	53929.3	−4477.6	40.5	211.8
RXJ1551.1-2402	53930.3	−4066.5	68.1	163.3
RXJ1551.1-2402	53930.3	−4307.4	36.1	224.4
RXJ1551.1-2402	53931.3	−4447.3	35.8	225.1
RXJ1551.1-2402	53931.3	−4327.7	67.2	164.4
RXJ1551.1-2402	54308.3	−4232.4	55.8	180.4
RXJ1551.1-2402	54308.3	−4387.9	44.0	203.2
RXJ1551.1-2402	54309.3	−4401.0	45.9	198.8
RXJ1551.1-2402	54309.3	−4362.9	37.1	221.2
RXJ1552.5-2633	54311.3	−4273.6	43.9	203.5
RXJ1552.5-2633	54311.3	−4170.9	41.3	209.6
RXJ1552.5-2633	53522.4	−2287.6	36.2	224.1
RXJ1552.5-2633	53522.4	−2518.6	31.2	241.4
RXJ1552.5-2633	53523.4	−2140.6	39.6	214.2

Table 3.2: Keck NIRSPEC Individual Radial Velocity Measurements

Star	MJD	RV	σ_{Obs}	SNR
		(m/s)	(m/s)	
RXJ1552.5-2633	53523.4	−2056.0	39.3	215.0
RXJ1552.5-2633	53929.3	−2508.4	48.3	193.9
RXJ1552.5-2633	53929.3	−2118.0	91.8	140.7
RXJ1552.5-2633	53930.3	−2487.0	27.4	257.3
RXJ1552.5-2633	53930.3	−2301.4	63.4	169.3
RXJ1552.5-2633	53931.3	−2780.9	73.9	156.7
RXJ1552.5-2633	53931.3	−2435.4	41.9	208.2
RXJ1552.5-2633	54308.3	−2397.7	35.0	227.9
RXJ1552.5-2633	54308.3	−2370.1	26.8	260.4
RXJ1557.8-2305	54309.3	−2277.7	31.9	238.6
RXJ1557.8-2305	54309.3	−2219.4	26.9	260.0
RXJ1557.8-2305	53419.6	−4477.5	68.6	162.8
RXJ1557.8-2305	53419.6	−4338.6	70.8	160.1
RXJ1557.8-2305	53522.5	−4428.6	50.5	189.6
RXJ1557.8-2305	53522.5	−4348.6	42.9	205.8
RXJ1557.8-2305	53783.7	−4406.7	94.7	138.5
RXJ1557.8-2305	53783.7	−4528.9	91.8	140.7
RXJ1557.8-2305	53930.3	−4420.5	67.8	163.7
RXJ1557.8-2305	53930.3	−4360.0	51.7	187.5
RXJ1557.8-2305	53931.3	−4361.8	82.5	148.4
RXJ1557.8-2305	53931.3	−4400.5	69.8	161.4
RXJ1557.8-2305	54308.3	−4359.7	41.6	208.9
RXJ1557.8-2305	54308.3	−4348.0	33.9	231.4

Table 3.2: Keck NIRSPEC Individual Radial Velocity Measurements

Star	MJD	RV	σ_{Obs}	SNR
		(m/s)	(m/s)	
RXJ1558.8-2512	54309.3	−4283.3	55.5	180.9
RXJ1558.8-2512	54309.3	−4397.8	47.0	196.7
RXJ1558.8-2512	53523.5	−2840.0	78.5	152.1
RXJ1558.8-2512	53523.5	−2881.0	74.7	155.9
RXJ1558.8-2512	53929.3	−3083.7	67.2	164.4
RXJ1558.8-2512	53929.3	−3246.0	57.7	177.4
RXJ1558.8-2512	53931.3	−2949.5	109.1	129.0
RXJ1558.8-2512	53931.3	−2854.2	43.4	204.6
RXJ1558.8-2512	54308.3	−3169.6	49.1	192.4
RXJ1558.8-2512	54308.3	−2806.8	45.1	200.8
RXJ1605.6-2152	54309.3	−2881.3	54.0	183.4
RXJ1605.6-2152	54309.3	−2882.6	49.0	192.5
RXJ1605.6-2152	53522.4	−6801.8	70.4	160.7
RXJ1605.6-2152	53522.4	−6738.4	33.3	233.7
RXJ1605.6-2152	53523.5	−6602.8	46.4	197.9
RXJ1605.6-2152	53523.5	−6732.7	43.6	204.1
RXJ1605.6-2152	53929.3	−7030.9	44.8	201.3
RXJ1605.6-2152	53929.3	−6916.0	58.6	176.0
RXJ1605.6-2152	53930.3	−6866.1	42.2	207.4
RXJ1605.6-2152	53930.3	−6825.0	45.4	200.0
RXJ1605.6-2152	53931.3	−6769.2	43.3	204.8
RXJ1605.6-2152	53931.3	−6657.8	51.5	187.9
RXJ1605.6-2152	54308.3	−6586.9	47.9	194.8

Table 3.2: Keck NIRSPEC Individual Radial Velocity Measurements

Star	MJD	RV	σ_{Obs}	SNR
		(m/s)	(m/s)	
RXJ1605.6-2152	54308.3	−6637.4	46.3	198.0
RXJ1605.6-2152	54309.3	−6661.4	37.3	220.5
RXJ1605.6-2152	54309.3	−6452.0	32.5	236.5
RXJ1607.0-2043	54311.3	−6680.7	47.7	195.1
RXJ1607.0-2043	54311.3	−6771.1	43.8	203.6
RXJ1607.0-2043	53419.7	−6268.4	127.2	119.5
RXJ1607.0-2043	53419.7	−6208.0	88.8	143.1
RXJ1607.0-2043	53422.6	−6231.8	53.4	184.5
RXJ1607.0-2043	53422.6	−6094.7	45.7	199.4
RXJ1607.0-2043	53522.5	−6257.9	41.7	208.8
RXJ1607.0-2043	53522.5	−6153.9	35.0	228.0
RXJ1607.0-2043	53523.5	−6135.5	53.8	183.8
RXJ1607.0-2043	53523.5	−6094.2	46.1	198.4
RXJ1607.0-2043	53929.3	−6479.5	46.7	197.3
RXJ1607.0-2043	53929.3	−6412.6	36.7	222.5
RXJ1607.0-2043	53930.3	−6248.5	48.4	193.8
RXJ1607.0-2043	53930.3	−6238.1	46.5	197.7
RXJ1607.0-2043	54309.3	−6128.2	36.3	223.5
RXJ1607.0-2043	54309.3	−6294.1	33.3	233.6
ScoPMS 14	53419.6	−3843.4	120.1	123.0
ScoPMS 14	53419.6	−3817.4	103.4	132.5
ScoPMS 14	53420.6	−3812.4	97.9	136.2
ScoPMS 14	53420.6	−3990.6	79.5	151.2

Table 3.2: Keck NIRSPEC Individual Radial Velocity Measurements

Star	MJD	RV	σ_{Obs}	SNR
		(m/s)	(m/s)	
ScoPMS 14	53420.7	−3833.9	95.7	137.7
ScoPMS 14	53420.7	−3928.4	87.7	143.9
ScoPMS 14	53421.6	−3637.3	73.0	157.7
ScoPMS 14	53421.6	−3948.0	67.4	164.2
ScoPMS 14	53422.6	−3214.0	66.0	165.8
ScoPMS 14	53422.6	−3357.1	67.5	164.1
ScoPMS 14	53480.4	−3795.5	75.3	155.3
ScoPMS 14	53480.4	−3829.5	68.1	163.3
ScoPMS 14	53522.4	−3951.2	51.4	188.0
ScoPMS 14	53522.4	−3940.4	45.3	200.4
ScoPMS 14	53523.3	−4041.7	45.1	200.8
ScoPMS 14	53523.3	−4008.5	109.6	128.7
ScoPMS 14	53931.3	−3906.5	78.7	151.9
ScoPMS 14	53931.3	−3910.4	81.1	149.7
ScoPMS 14	54308.3	−3749.3	58.5	176.3
ScoPMS 14	54308.3	−3829.1	51.8	187.3
ScoPMS 14	54309.3	−3894.6	65.5	166.5
ScoPMS 14	54309.3	−3667.0	50.3	190.0
ScoPMS 14	54311.3	−3806.2	73.6	157.1
ScoPMS 14	54311.3	−3821.4	68.3	163.1
ScoPMS 32	53419.7	−3051.6	89.9	142.1
ScoPMS 32	53419.7	−2856.1	73.4	157.3
ScoPMS 32	53420.6	−2901.1	70.9	160.1

Table 3.2: Keck NIRSPEC Individual Radial Velocity Measurements

Star	MJD	RV	σ_{Obs}	SNR
		(m/s)	(m/s)	
ScoPMS 32	53420.6	−2866.6	62.4	170.6
ScoPMS 32	53420.7	−2636.3	84.9	146.2
ScoPMS 32	53420.7	−2804.7	86.0	145.3
ScoPMS 32	53421.6	−2761.7	73.8	156.9
ScoPMS 32	53421.6	−2578.5	65.7	166.3
ScoPMS 32	53422.6	−2842.3	78.4	152.3
ScoPMS 32	53422.6	−3026.5	59.3	175.0
ScoPMS 32	53480.4	−2922.8	52.1	186.7
ScoPMS 32	53480.4	−3020.3	46.1	198.4
ScoPMS 32	53522.4	−2971.1	55.5	180.9
ScoPMS 32	53522.4	−2900.0	41.5	209.3
ScoPMS 32	53931.4	−2873.2	91.2	141.1
ScoPMS 32	53931.4	−2738.1	66.0	165.9
ScoPMS 32	54308.3	−2701.0	71.1	159.8
ScoPMS 32	54308.3	−2854.9	54.2	183.1
ScoPMS 42B	53419.7	−6447.2	95.3	138.1
ScoPMS 42B	53419.7	−6058.8	83.6	147.4
ScoPMS 42B	53420.6	−6071.6	59.2	175.2
ScoPMS 42B	53420.6	−6119.7	55.0	181.7
ScoPMS 42B	53421.6	−6147.2	53.3	184.5
ScoPMS 42B	53421.6	−6144.3	44.7	201.7
ScoPMS 42B	53421.7	−6080.9	49.6	191.4
ScoPMS 42B	53421.7	−6063.4	41.2	209.9

Table 3.2: Keck NIRSPEC Individual Radial Velocity Measurements

Star	MJD	RV	σ_{Obs}	SNR
		(m/s)	(m/s)	
ScoPMS 42B	53480.4	−6274.9	53.3	184.5
ScoPMS 42B	53480.4	−6327.2	49.6	191.5
ScoPMS 42B	53522.5	−6537.0	48.3	193.9
ScoPMS 42B	53522.5	−6484.4	27.6	256.4
ScoPMS 42B	53523.3	−6521.0	44.9	201.1
ScoPMS 42B	53523.3	−6283.51	29.7	247.4
ScoPMS 42B	53931.4	−6386.9	53.6	184.1
ScoPMS 42B	53931.4	−6093.6	29.8	246.7
ScoPMS 42B	54311.3	−6485.8	49.7	191.2
ScoPMS 42B	54311.3	−6414.3	40.2	212.6
Radial Velocity Standards				
GJ 289	53742.5	53171.0	44.6	201.9
GJ 289	53742.5	53475.7	19.7	303.4
GJ 289	53743.5	53327.7	22.1	286.4
GJ 289	53743.5	53288.1	36.2	224.0
GJ 289	53744.5	53048.0	25.6	266.3
GJ 289	53744.5	53143.7	54.2	183.1
GJ 289	54100.5	53225.5	22.3	285.6
GJ 289	54100.5	53251.5	20.6	296.9
GJ 289	54101.5	53137.9	21.4	291.2

Table 3.2: Keck NIRSPEC Individual Radial Velocity Measurements

Star	MJD	RV	σ_{Obs}	SNR
		(m/s)	(m/s)	
GJ 289	54101.5	53289.0	16.7	329.9
GJ 289	54102.5	53020.2	18.3	315.1
GJ 289	54102.5	53066.6	13.5	367.0
GJ 382	53741.6	7852.8	59.7	174.4
GJ 382	53741.6	7870.7	42.1	207.8
GJ 382	53742.6	8210.7	35.0	227.8
GJ 382	53742.6	8204.6	32.2	237.6
GJ 382	53744.6	8185.7	32.0	238.2
GJ 382	53744.6	8169.0	41.3	209.8
GJ 382	53783.5	8201.9	13.8	362.8
GJ 382	53783.5	8178.8	13.5	366.4
GJ 382	53783.5	8069.9	38.4	217.3
GJ 382	53783.5	8175.7	37.3	220.8
GJ 382	54100.5	8092.6	27.2	258.2
GJ 382	54100.5	8142.8	32.6	236.0
GJ 382	54101.6	7921.5	83.6	147.4
GJ 382	54101.6	8258.7	75.0	155.7
GJ 382	54101.6	8041.9	41.8	208.5
GJ 382	54101.6	8045.6	40.8	210.9
GJ 382	54103.5	8187.4	29.1	249.6
GJ 382	54103.5	8242.15	26.5	261.8
GJ 628	53522.3	−20776.1	244.3	86.2
GJ 628	53522.3	−20691.9	96.5	137.2

Table 3.2: Keck NIRSPEC Individual Radial Velocity Measurements

Star	MJD	RV (m/s)	σ_{Obs} (m/s)	SNR
GJ 628	53522.3	−20877.7	214.0	92.1
GJ 628	53522.3	−20671.5	91.1	141.2
GJ 628	53522.3	−20774.3	122.	122.0
GJ 628	53522.3	−20768.8	20.0	301.4
GJ 628	53522.3	−20669.8	18.5	313.2
GJ 628	53522.3	−20728.1	14.2	358.0
GJ 628	53523.5	−20814.7	30.5	243.9
GJ 628	53523.5	−20938.1	28.3	253.3
GJ 628	53597.2	−20776.2	45.3	200.2
GJ 628	53597.2	−20702.5	30.2	245.4
GJ 628	53929.4	−21183.0	23.5	277.9
GJ 628	53929.4	−20990.8	26.9	260.1
GJ 628	53930.3	−20877.9	80.0	150.7
GJ 628	53930.3	−20776.8	100.2	134.7
GJ 628	53930.3	−21035.5	43.0	205.5
GJ 628	53930.3	−20894.7	35.4	226.6
GJ 628	53931.4	−20984.5	28.9	250.8
GJ 628	53931.4	−20978.7	28.7	251.8
GJ 628	54103.7	−20715.0	22.5	284.0
GJ 628	54103.7	−20735.3	22.8	282.2
GJ 628	54308.4	−21143.2	27.7	256.3
GJ 628	54308.4	−21194.1	28.1	254.2
GJ 628	54309.4	−21127.1	16.3	333.9

Table 3.2: Keck NIRSPEC Individual Radial Velocity Measurements

Star	MJD	RV	σ_{Obs}	SNR
		(m/s)	(m/s)	
GJ 628	54309.4	−21069.3	14.8	350.8
GJ 628	54311.3	−21035.1	27.5	257.1
GJ 628	54311.3	−21024.3	25.8	265.6
GJ 628	54312.3	−20999.2	22.8	282.4
GJ 628	54312.3	−21053.3	20.7	296.5
GJ 725A	53419.7	−688.9	46.5	197.6
GJ 725A	53419.7	−523.4	42.7	206.4
GJ 725A	53420.7	−543.4	32.8	235.2
GJ 725A	53420.7	−472.8	34.8	228.4
GJ 725A	53421.6	−517.4	26.7	260.8
GJ 725A	53421.6	−476.6	21.5	290.7
GJ 725A	53422.6	−450.6	24.7	271.1
GJ 725A	53422.6	−506.5	20.6	296.9
GJ 725A	53522.5	−628.0	40.5	211.7
GJ 725A	53522.5	−473.5	29.7	247.2
GJ 725A	53523.4	−548.0	39.9	213.5
GJ 725A	53523.4	−500.0	28.1	254.2
GJ 725A	53596.4	−682.5	38.5	217.3
GJ 725A	53596.4	−594.5	28.4	252.8
GJ 725A	53597.3	−461.6	20.4	298.4
GJ 725A	53597.3	−576.5	19.3	307.0
GJ 725A	53670.2	−795.4	26.8	260.4
GJ 725A	53670.2	−678.5	30.7	243.3

Table 3.2: Keck NIRSPEC Individual Radial Velocity Measurements

Star	MJD	RV	σ_{Obs}	SNR
		(m/s)	(m/s)	
GJ 725A	53928.5	−582.3	17.2	324.7
GJ 725A	53928.5	−611.7	15.5	341.9
GJ 725A	53929.5	−666.9	18.9	310.4
GJ 725A	53929.5	−637.7	17.3	323.8
GJ 725A	53930.4	−624.7	54.8	182.1
GJ 725A	53930.4	−483.1	56.2	179.8
GJ 725A	53931.5	−611.8	28.1	254.4
GJ 725A	53931.5	−587.0	30.8	243.
GJ 725A	54308.4	−573.5	30.5	244.1
GJ 725A	54308.4	−572.7	31.2	241.5
GJ 725A	54309.4	−515.6	45.6	199.6
GJ 725A	54309.4	−475.1	36.2	223.9
GJ 725A	54311.4	−773.3	40.4	212.
GJ 725A	54311.4	−491.0	38.0	218.7
GJ 725A	54312.3	−626.1	35.5	226.3
GJ 725A	54312.3	−747.0	30.1	245.6
GJ 725A	55401.5	−812.1	46.9	196.8
GJ 725A	55401.5	−556.3	46.6	197.3
GJ 725A	55401.5	−660.3	13.6	365.5
GJ 725A	55401.5	−627.9	17.1	326.4
GJ 725B	53419.7	1286.6	109.4	128.8
GJ 725B	53419.7	920.1	92.1	140.4
GJ 725B	53420.7	1226.6	64.3	168.1

Table 3.2: Keck NIRSPEC Individual Radial Velocity Measurements

Star	MJD	RV	σ_{Obs}	SNR
		(m/s)	(m/s)	
GJ 725B	53420.7	1616.9	49.9	190.7
GJ 725B	53421.6	1465.1	78.7	151.9
GJ 725B	53421.6	1400.3	70.5	160.5
GJ 725B	53421.6	1471.2	46.1	198.5
GJ 725B	53421.6	1520.9	32.8	235.2
GJ 725B	53522.6	1332.0	28.3	253.3
GJ 725B	53522.6	1365.6	36.8	222.1
GJ 725B	53523.4	1394.7	24.9	270.0
GJ 725B	53523.4	1469.6	20.1	300.3
GJ 725B	53523.6	1387.2	18.1	316.6
GJ 725B	53523.6	1401.9	28.1	254.3
GJ 725B	53596.4	1368.8	32.6	236.2
GJ 725B	53596.4	1290.2	30.3	245.0
GJ 725B	53597.3	1451.7	33.8	231.9
GJ 725B	53597.3	1486.2	39.9	213.3
GJ 725B	53670.2	1400.3	62.1	171.1
GJ 725B	53670.2	1268.4	47.7	195.2
GJ 725B	53928.5	1289.6	23.2	279.7
GJ 725B	53928.5	1329.8	20.2	299.9
GJ 725B	53929.5	1118.2	29.8	247.0
GJ 725B	53929.5	1148.7	31.4	240.7
GJ 725B	53930.4	1284.7	37.6	219.8
GJ 725B	53930.4	1337.3	28.1	254.4

Table 3.2: Keck NIRSPEC Individual Radial Velocity Measurements

Star	MJD	RV	σ_{Obs}	SNR
		(m/s)	(m/s)	
GJ 725B	53931.5	1252.5	27.8	255.6
GJ 725B	53931.5	1250.1	29.3	248.8
GJ 725B	54308.4	1330.8	55.1	181.5
GJ 725B	54308.4	1238.1	31.9	238.5
GJ 725B	54309.4	1218.6	51.3	188.1
GJ 725B	54309.4	1250.3	32.8	235.3
GJ 725B	54311.4	1334.9	29.1	249.8
GJ 725B	54311.4	1256.7	28.3	253.3
GJ 725B	54312.3	1307.7	28.5	252.5
GJ 725B	54312.3	1252.9	24.9	270.2
GJ 725B	55401.5	1098.3	17.3	324.4
GJ 725B	55401.5	1251.1	14.2	357.4
GJ 876	53327.2	−1148.7	28.6	252.1
GJ 876	53327.2	−1250.6	25.0	269.6
GJ 876	53329.2	−1215.8	71.1	159.9
GJ 876	53329.2	−1130.6	62.5	170.5
GJ 876	53522.6	−1227.9	28.7	251.4
GJ 876	53522.6	−1237.6	26.2	263.5
GJ 876	53522.6	−1288.0	41.7	208.8
GJ 876	53522.6	−1175.9	25.1	268.8
GJ 876	53522.6	−1348.1	36.6	222.8
GJ 876	53522.6	−1198.1	30.4	244.6
GJ 876	53522.6	−1292.8	27.0	259.3

Table 3.2: Keck NIRSPEC Individual Radial Velocity Measurements

Star	MJD	RV	σ_{Obs}	SNR
		(m/s)	(m/s)	
GJ 876	53522.6	−1196.6	27.5	257.1
GJ 876	53523.6	−1254.5	25.1	269.0
GJ 876	53523.6	−1092.7	28.6	251.9
GJ 876	53597.4	−962.12	30.5	243.9
GJ 876	53597.4	−1031.9	25.9	264.9
GJ 876	53670.3	−1278.5	81.8	149.0
GJ 876	53670.3	−1297.5	29.1	249.8
GJ 876	53743.2	−1449.1	36.6	222.6
GJ 876	53743.2	−1464.3	29.4	248.6
GJ 876	53744.2	−1385.8	46.3	198.1
GJ 876	53744.2	−1469.8	32.8	235.3
GJ 876	54311.4	−1262.3	11.5	398.2
GJ 876	54311.4	−1301.0	12.1	388.2
GJ 876	54312.4	−1198.2	25.9	264.8
GJ 876	54312.4	−1176.0	28.4	252.8

In this work we define an epoch as an A and B nod pair of spectra and an epoch RV as the average RV of the A and B measurements. In comparing the RVs of A and B nods for each star, we noted large and apparently random differences in RVs . A similar effect was noted in the analysis of Gemini Phoenix spectra (see Section 2.1.4). In fact, compared to the median value of σ_{Photon} (26 m/s), the differences in RVs between individual A and B nods

can be quite large. Figure 3.3 illustrates the differences in the RVs for A/B pairs versus the average SNR of the epoch. The median A/B pair difference was 98 m/s, with 12% of these differences ranging from 300-992 m/s. In the majority of cases, these RV changes cannot be associated with real RV variations in the star (i.e., $\sigma_{Stellar}$), as these observations are taken less than 15 mins apart which is typically less than the stellar surface changes (e.g., star spots) that cause stellar jitter. As with the Gemini Phoenix results, we assume the differences are a result of the internal error ($\sigma_{Internal}$), and use the differences to determine this value empirically as a function of SNR. First, we assume the contribution from stellar variability to be zero and thus we set $\sigma_{Stellar}$=0. Thus, the only contributions to the error of the difference in A and B are $\sigma_{Internal}$ and σ_{Photon}. Assuming the RV measurements from the A and B positions have similar uncertainties (σ_{Obs_A} or σ_{Obs_B}), their differences should have a 1σ distribution around zero of $\sqrt{2}\sigma_{Obs_A}$ or $\sqrt{2}\sigma_{Obs_B}$. Since the distribution appears to depend on SNR, we fit the RV difference in the A and B nods to a polynomial function (Δ_{RVFit}) in the form of $\Delta_{RV} = P_0/SNR^2$, where Δ_{RV} was taken to be the RV difference between A nod and B nod and the SNR is the signal-to-noise ratio of the epoch to all star in Chapter 2 and Chapter 3. The internal uncertainty for each nod observation could then be calculated as follows. From the best fit, we calculate σ_{Obs_A} or σ_{Obs_B} in Equation 3.2, and we subtracted off in quadrature σ_{photon} to determine $\sigma_{Iternal}$ as a function of SNR (See Figure 3.3).

$$\sigma_{Obs_A} = \frac{P_0/SNR^2}{\sqrt{2}} \tag{3.2}$$

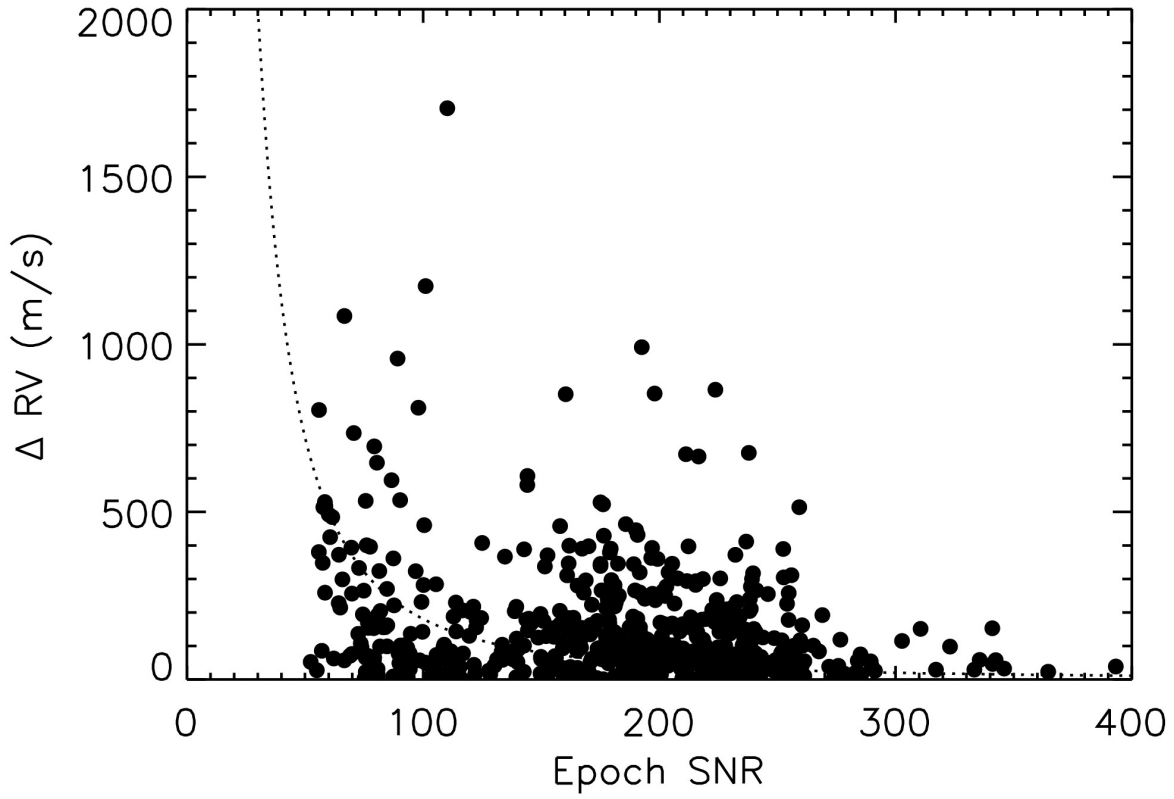

Figure 3.3 The difference in RV measurements between nod A and nod B positions in a single epoch are plotted as a function of epoch SNR for observations presented in Chapter 2 and Chapter 3. We fit a polynomial to the SNR in the form of $\Delta_{RV} = P_0/SNR^2$ (dotted line) to determine the total error. The internal error, $\sigma_{Internal}$, (solid line) was then calculated by subtracting the photon limited error, σ_{Photon}, (open diamonds) from the total error, σ_{Obs_A} or σ_{Obs_B}, in quadrature.

Each epoch RV is determined by the average of the A and B nod pair from Table 3.2. The average error for each observation epoch (σ_{Epoch}) is given by Equation 3.3.

$$\sigma_{Epoch} = \frac{< \sigma_{Obs_A}, \sigma_{Obs_B} >}{\sqrt{2}} \tag{3.3}$$

Finally, for each star, we calculate the absolute RV from the unweighted average of all

the epoch RVs for each star. We then calculate the total average uncertainty in the absolute RV for each star over the observing period ($\sigma_{\bigstar}$) using Equation 3.4. The average uncertainty ($< \sigma_{\bigstar} >$) for the sample of stars observed with Keck NIRSPEC is 12.3 m/s. For each star we also calculate an absolute RV from an unweighted average of the epoch RVs for each star. With the exception of binaries, we find that RVs for stars in Upper Sco and Taurus-Auriga agree agree to within 2 σ of kinematic studies (Upper Sco; Pecaut et al. 2012, Taurus-Auriga Bertout & Genova 2006).

$$\sigma_{\bigstar} = \frac{< \sigma_{Epoch_1}, \sigma_{Epoch_2}, ...\sigma_{Epoch_N} >}{\sqrt{N}} \text{ ; where N is the number of epochs.} \quad (3.4)$$

The $v\sin i$ for each star is calculated using unweighted average of the epoch $v\sin i$ values, and the standard deviation is derived from the epoch $v\sin i$ values as well. For young stars, these $v\sin i$ values range from 4 km/s to 52 km/s. For young stars, our $v\sin i$ values agree to within 30% of published values. Our values are lower than published values for 8 out of 11 young stars by 1.5-30%; the 3 values for which our fits were higher than published values were higher by 3-28%. For all RV standards, our $v\sin i$ values are lower by between 29-58% than the published upper limits. We think this may be a systematic bias, as our code fits both $v\sin i$ and PSF simultaneously in the final step of fitting, and may be overcompensating by inflating the PSF.

Our RV results for each young star and RV standard are summarized in Table 3.3. Within this table, we report the effective temperature and logg values associated with the model spectra used, along with the $v\sin i$ with the uncertainty set by the standard deviation of

multiple epochs, the absolute RV with the uncertainty in the absolute RV ($\sigma_{\bigstar}$), the number of epochs (N_{obs}), and the timespan over which the star was observed (Δ T). The absolute RV for the two SB2s discovered in this sample is calculated differently than single stars. Unlike binaries identified in Chapter 2, we were unable to fit orbital properties for Keck NIRSPEC SB2s (see discussion in Section 3.6). As such, we assign the mean value for the epoch RVs as the absolute RV for each star.

RV curves for all stars from Chapters 2 and 3 are shown in Appendix A.

Table 3.3: Keck NIRSPEC Rotational and Absolute Radial Velocities

Star	Model	vsini	<RV>	N_{obs}	Δ T
Name	T_{eff}, log$g$	(km/s)	(m/s)		Days
Young Stars - Taurus-Auriga					
V1306 Tau(RXJ0409.8)	3800, 4.20	7.59± 0.62	12776± 10	9	774
V1096 Tau	3800, 4.20	3.40± 0.22	112378*	8	774
FN Tau	3200, 4.80	6.53± 1.31	15586± 10	9	774
CY Tau	3600, 4.20	9.57± 0.68	16923± 11	7	774
CIDA 3	3600, 4.20	9.62± 0.98	17555± 14	7	774
V410 X-ray 7	3800, 4.20	14.20± 2.09	18442± 10	6	774
IP Tau	3800, 4.20	9.51± 0.79	17274± 11	5	774
KPNO-Tau 13	3200, 4.80	8.06± 0.44	16852± 9	9	774
DH Tau	3800, 4.20	7.65± 0.39	16059± 10	8	774
IQ Tau	3800, 4.20	13.54± 1.26	16369± 11	8	773
JH 56	3800, 4.20	13.26± 0.41	17475± 9	9	776
J1-665	3400, 4.20	52.42± 0.40	7916± 12	7	776
V1321 Tau(RXJ0432.8)	3600, 4.20	11.01± 0.27	19420± 11	9	774
DM Tau	3600, 4.20	4.16± 1.20	18899± 16	7	774
JH 108	3800, 4.20	12.89± 0.61	17668± 14	6	773
DN Tau	3800, 4.20	9.76± 0.46	17808± 18	6	773
RXJ0437.4+1851 A	4000, 4.20	13.72± 0.36	16569± 11	9	774
RXJ0437.4+1851 B	3400, 4.20	10.55± 0.40	15242± 11	9	774
RXJ0438.2+2303	3800, 4.20	3.95± 0.98	16748± 22	5	772

Table 3.3: Keck NIRSPEC Rotational and Absolute Radial Velocities

Star	Model	vsini	<RV>	N_{obs}	Δ T
Name	T_{eff}, log$g$	(km/s)	(m/s)		Days
CoKu Tau 4	3600, 4.20	26.60± 0.55	16202± 12	7	774
GM Aur	4000, 4.20	13.88± 0.30	15830± 10	9	774
V1353 Tau(RXJ0457.0)	3800, 4.20	7.95± 0.95	20254± 13	8	776
CIDA 8	3400, 4.20	29.55± 1.03	18724± 11	8	773
CIDA 10	3400, 4.20	26.79± 0.81	19372± 12	8	773
Young Stars - Upper Scorpius					
RXJ1534.3-3300	3800, 4.20	9.37± 0.33	2553± 15	9	892
RXJ1540.9-3024	3600, 4.20	17.36± 0.58	−7480± 14	11	892
RXJ1546.0-2920	3800, 4.20	9.91± 0.56	−4266± 12	9	888
RXJ1546.7-3210	3600, 4.20	8.07± 0.97	2180± 21	8	890
RXJ1548.9-3045	3600, 4.20	11.73± 6.23	−413*	10	891
RXJ1551.1-2402	3600, 4.20	7.90± 1.29	−4341± 11	8	789
RXJ1552.5-2633	3800, 4.20	13.03± 0.56	−2350± 12	7	787
RXJ1557.8-2305	3800, 4.20	9.56± 0.42	−4390± 17	7	890
RXJ1558.8-2512	3800, 4.20	7.27± 1.68	−2959± 20	5	786
RXJ1605.6-2152	3800, 4.20	7.95± 0.67	−6733± 11	8	789
RXJ1607.0-2043	3400, 4.20	4.37± 0.86	−6232± 14	7	890
ScoPMS 14	3400, 4.20	8.54± 0.47	−3814± 15	12	892
ScoPMS 32	3400, 4.20	8.19± 0.60	−2850± 16	9	889
ScoPMS 42 B	3800, 4.20	13.56± 0.26	−6275± 12	9	892

Table 3.3: Keck NIRSPEC Rotational and Absolute Radial Velocities

Star	Model	vsini	<RV>	N_{obs}	Δ T
Name	T_{eff}, log$g$	(km/s)	(m/s)		Days
	Radial Velocity Standards				
GJ 289	3600, 4.80	0.75± 0.41	53204± 8	6	360
GJ 382	3600, 4.80	0.51± 1.25	8114± 9	9	362
GJ 628	3800, 4.80	0.71± 1.29	−20900± 9	15	790
GJ 725 A	3400, 4.80	0.67± 0.88	−588± 5	19	1982
GJ 725 B	3400, 4.80	0.41± 1.10	1318± 6	19	1982
GJ 876	3400, 4.80	0.65± 1.15	−1244± 7	13	985

* The absolute RV listed is the average value of the epoch RVs.

3.3 Identifying Candidate Variables with Keck/NIRSPEC

As discussed in Section 2.1.5, stellar jitter is well known to increase with stellar rotation. With very young stars, it can be difficult to distinguish between activity induced RV variability, and RV variability induced by an orbiting companion. In this section, we consider three metrics to assess the magnitude and potential cause of RV variability in these young stars.

The projected rotational velocity, $v\sin i$, provides a useful minimum value for the stellar rotation rate, and is measured uniformly for all stars in our sample. For each star, we compare the $v\sin i$ value with RV dispersion, defined as the standard deviation of the epoch RVs, to determine an empirical estimate of the expected activity induced variability. Objects that show a higher than average standard deviation for a given $v\sin i$ may have an additional component to their variability, such as the reflex motion from a companion. In Figure 3.4, we plot the RV dispersion versus the fitted $v\sin i$ values for the young stars in the sample along with star names for stars with large RV dispersions with the exception of two objects, RXJ1548.9-3045 and V1096 Tau; their dispersions lie far above this plotting region at 20.3 km/s and 9.7 km/s respectively. These two are newly discovered spectroscopic binaries and are discussed in Section 3.6, and will not be included in the following discussion on identifying variability. RV dispersions for all stars are listed in Table 3.4.

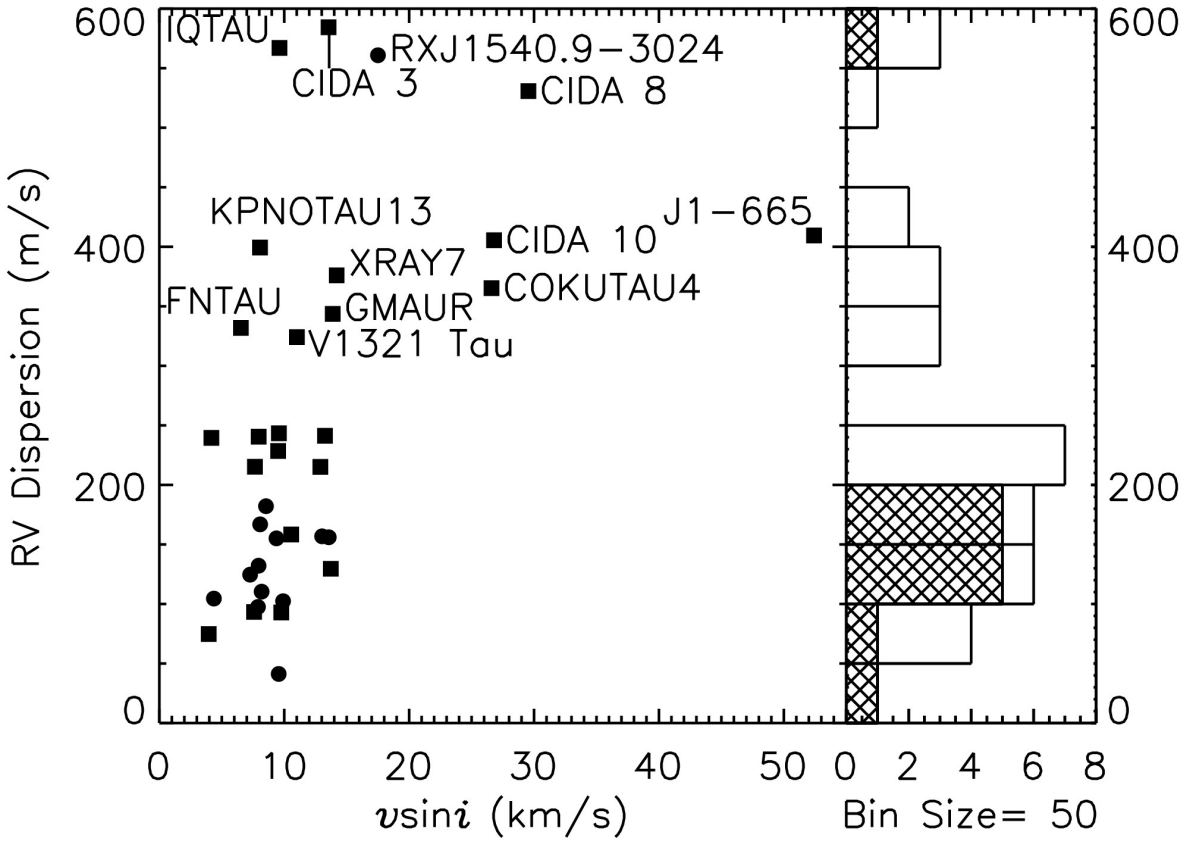

Figure 3.4 Here we plot the RV dispersion, defined as the standard deviation of the epoch RVs (m/s), versus $v\sin i$ for Upper Scorpius (solid circles) and Taurus-Auriga (solid squares). Stars with large dispersions are labeled. A histogram with a bin size of 50 m/s is shown to the right with Taurus-Auriga in open boxes and Upper-Sco in crosshatched boxes.

Figure 3.4 shows a pronounced difference in the RV distributions of dispersions of Upper-Sco stars at ∼10 Myr and Taurus-Auriga stars at ∼1-2 Myr. Consequently, we discuss these samples separately. Taurus-Auriga stars (24, solid squares) have wide range of RV dispersion values between 75-584 m/s with an average of 296 m/s and $v\sin i$ fit values between 4-52 km/s

with an average of 14 km/s. It is worth noting that for the Taurus-Auriga sample that while there is a large range in RV dispersion values for slowly rotating stars ($v\sin i \leq 15$ km/s), all rapidly rotating stars show large ($\geq$360 m/s) RV dispersions. The correlation of rotation and chromospheric induced RV variably appears to exist even at this young age. Overall, because of the large range in RV dispersions of the Taurus-Auriga stars, it is not possible to identify any of the most RV variable stars as having a orbiting companions.

The Upper-Sco stars (13, solid circles) have a range of RV dispersions between 41-561 m/s with an average of 161 m/s and $v\sin i$ fit values that range from 4-18 km/s with an average of 10 km/s. Only RXJ1540.9-3024, a candidate RV variable to be discussed in Section 3.5, stands out as an outlier with an average RV dispersion of 561 m/s. Treating RXJ1540.9-3024 as an outlier, the remaining 12 stars in Upper-Sco have a much smaller range in RV dispersions than Taurus-Auriga with RV dispersions between 41-182 m/s with an average of 127 m/s. Our RV standards have RV dispersions between 75-115 m/s with an average of 114 m/s. This is roughly two times worse empirical precision than that achieved by the same technique on Gemini Phoenix and VLT CRIRES in 2.

To determine how statistically significant the RV dispersions are, we compute a second metric we call Δ, in Equation 3.5, defined as the RV dispersion divided by the average error ($< \sigma_{Epoch} >$) and listed in Table 3.4. In Figure 3.5 we plot Δ vs $v\sin i$ for each object in Taurus-Auriga (solid squares) and Upper-Sco (solid circles). Taurus-Auriga stars show a large spread in Δ values between 1.5-19.3 with an average value of 9.4 and a standard deviation of 4.8. With this metric, we still see no evidence for the RV variability being

caused by an orbiting companion. For Upper-Sco stars, excluding RXJ 1540.9-3024, there is a concentration of Δ values objects between 0.9-5.1 with an average value of 3.2 and a standard deviation of 1.1. RXJ 1540.9-3024 has a Δ value of 12.4, implying that the large RV dispersion for this star is not a consequence of large RV errors. Our RV standards had Δ values between 3.3-6.1 with an average value of 4.4.

$$\Delta = \frac{RV\,Dispersion}{< \sigma_{Epoch_1}, \sigma_{Epoch_2}, ...\sigma_{Epoch_N} >} \tag{3.5}$$

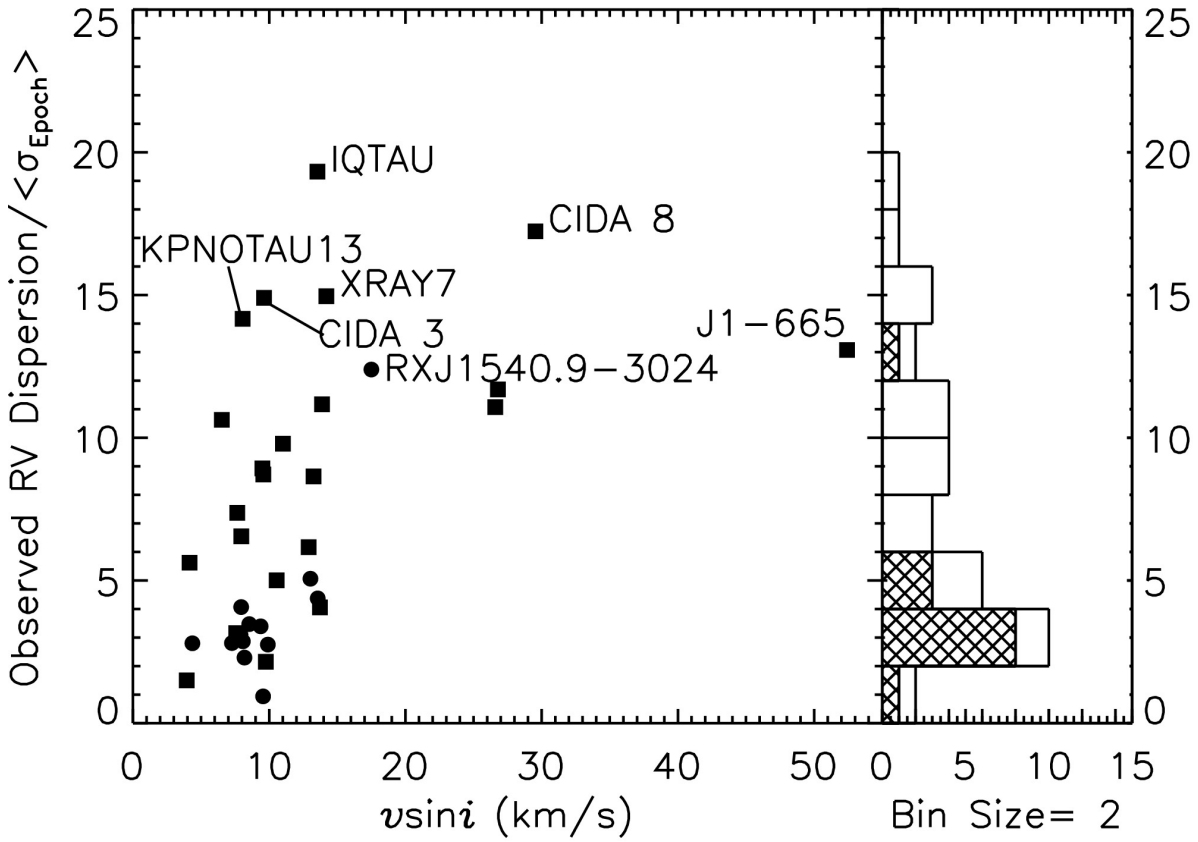

Figure 3.5 Here we plot the standard deviation of the epoch RV's divided by the error versus $v\sin i$ for Upper Scorpius (solid circles) and Taurus-Auriga (solid squares). A histogram with a bin size of 2 is shown to the right. Taurus-Auriga stars are in open boxes and Upper-Sco stars are in crosshatched boxes.

Table 3.4: RV Dispersions - Keck/NIRSPEC

Star	RV Dispersion m/s	Mean Error $< \sigma_{Epoch} >$ m/s	Δ
Young Stars - Taurus-Auriga			
V1306 Tau(RXJ0409.8)	93	30	3.2
V1096 Tau	9724	28	347.6
FN Tau	332	31	10.6
CY Tau	243	28	8.7
CIDA 3	567	38	14.9
V410 X-ray 7	376	25	15.0
IP Tau	229	26	8.9
KPNO-Tau 13	399	28	14.2
DH Tau	215	29	7.4
IQ Tau	584	30	19.3
JH 56	241	28	8.6
J1-665	409	31	13.1
V1321 Tau(RXJ0432.8)	324	33	9.8
DM Tau	240	43	5.6
JH 108	215	35	6.2
DN Tau	93	43	2.2
RXJ0437.4+1851 A	130	32	4.1
RXJ0437.4+1851 B	158	32	5.0
RXJ0438.2+2303	75	50	1.5
CoKu Tau 4	365	33	11.1
GM Aur	344	31	11.2
V1353 Tau(RXJ0457.0)	240	37	6.5

Table 3.4: RV Dispersions - Keck/NIRSPEC

Star	RV Dispersion m/s	Mean Error $< \sigma_{Epoch} >$ m/s	Δ
CIDA 8	531	31	17.2
CIDA 10	405	35	11.7
Young Stars - Upper Scorpius			
RXJ1534.3-3300	155	46	3.4
RXJ1540.9-3024	1055	47	22.5
RXJ1546.0-2920	102	37	2.8
RXJ1546.7-3210	167	58	2.9
RXJ1548.9-3045	20276	52	386.6
RXJ1551.1-2402	97	31	3.1
RXJ1552.5-2633	157	31	5.1
RXJ1557.8-2305	41	44	0.9
RXJ1558.8-2512	125	44	2.8
RXJ1605.6-2152	132	32	4.1
RXJ1607.0-2043	105	37	2.8
ScoPMS 14	182	52	3.5
ScoPMS 32	110	48	2.3
ScoPMS 42 B	156	36	4.4
Radial Velocity Standards			
GJ 289	113	19	6.1

Table 3.4: RV Dispersions - Keck/NIRSPEC

Star	RV Dispersion m/s	Mean Error $< \sigma_{Epoch} >$ m/s	Δ
GJ 382	111	28	4.0
GJ 628	159	37	4.3
GJ 725 A	75	22	3.3
GJ 725 B	109	28	3.9
GJ 876	115	24	4.9

The third metric we consider is the P-χ^2 test. A P-χ^2 test shows how significant a set of observations deviates from an expected χ^2 distribution (Carney et al. 2003). In our implementation, it indicates how significant the epoch RV varies from the average RV given the calculated error and the number of epochs. We use Equation 3.6 in calculating our χ^2 values, where RV_{Epoch} is the epoch RV, $\mathrm{RV}_\star$ is the average RV for all epochs, and σ_{Epoch} is the epoch error as described in Section 3.2.1. A p-value of 0.01 would indicate a 99% confidence that a star has significant RV variability over the observational period.

$$\chi^2 = \sum \frac{(RV_{Epoch} - RV_\star)^2}{\sigma^2_{Epoch}} \tag{3.6}$$

In Figure 3.6 we show histograms for of p-values from our P-χ^2 test are plotted for Taurus-Auriga (open boxes) and Upper-Sco (crosshatched boxes). We can see that these two populations are quite different. The ensemble of Upper-Sco stars exhibit a flat distribution

between zero and one. This is consistent with a population of RV non-variable stars. The two exceptions in Upper-Sco are RXJ1548.9-3045 and RXJ1540.9-3024, with p-values of $<<0.0001$ and 2.2×10^{-25} respectively. Taurus-Auriga stars, on the other hand, show a higher fraction of low p-values with 16 out of 24 stars having a p-values less than 0.01. Our RV standards have values between 0.24-1 with an average value of 0.73.

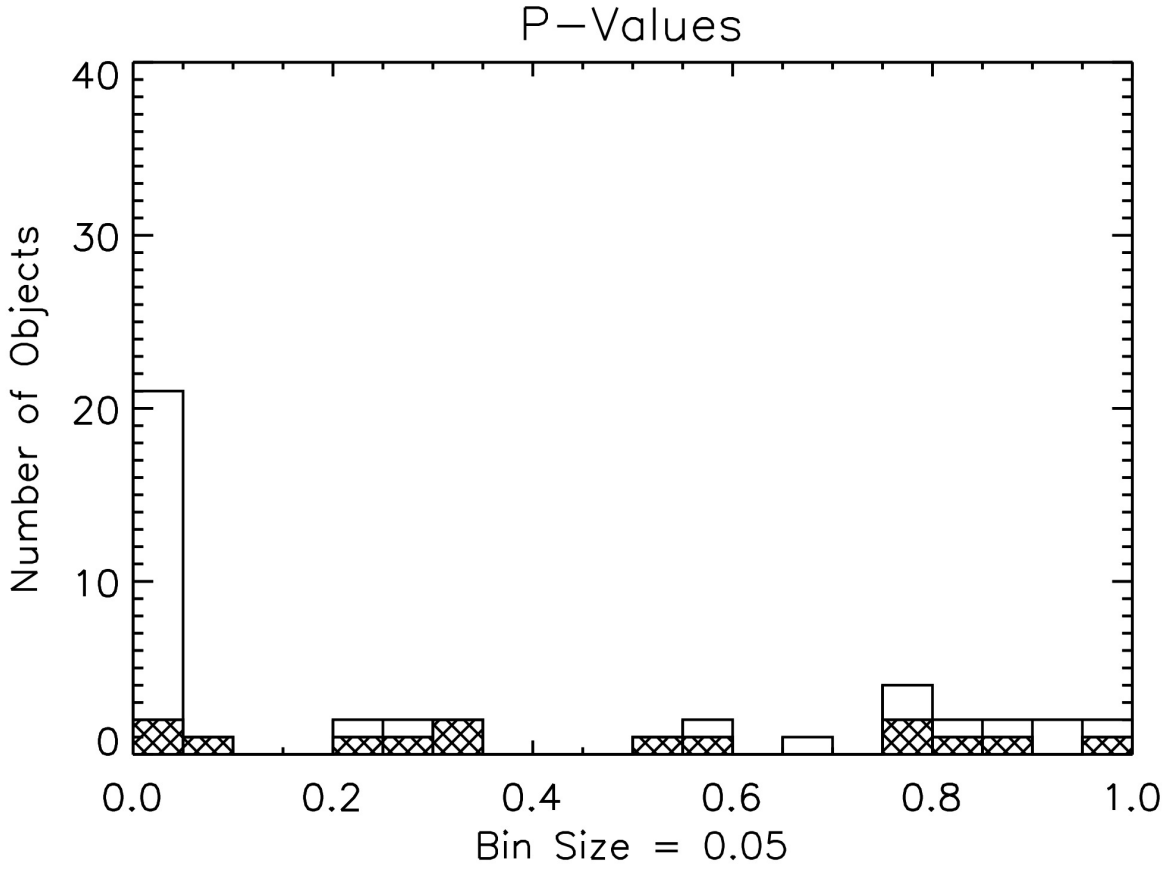

Figure 3.6 A histogram of the p-values from our P-χ^2 test on 24 Taurus-Auriga and 12 Upper-Sco (crosshatch) stars are shown here. Stars with p-values less than 0.01 have statistically significant deviation from the expected χ^2 distribution. This signals that they have significant RV variability.

Using all three metrics, a large fraction of stars in Taurus-Auriga stars exhibit evidence of having statistically significant RV variability. However, since we do not expect the majority of these stars to have hot Jupiter-like companions, we interpret this as indicating that many

Taurus-Auriga stars have large amplitude stellar induced RV variations. Consequently, we do not identify any of these stars as candidate planet hosts, however, in Section 4.0.2 we investigate identifying planets in the presence of spots.

For Upper-Sco stars, all three metrics identify only RXJ1540.9-3024 as an RV variable with an amplitude unlike the remainder of Upper-Sco stars. We classify RXJ1540.9-3045 as a candidate planet host.

3.4 Recovering Known Planets – Testing our Technique

GJ 876 is a nearby (4.66 pc) M-dwarf (M4.0V; V=10.18; K_s=5.01) with a rotation period of 97 days (Rivera et al. 2005) and a $v\sin i$ of <2 km/s (Delfosse et al. 1998). Subsequent studies of this star have found three additional terrestrial mass planets (Marcy et al. (2001); Rivera et al. (2005); Rivera et al. (2010)). Nevertheless, the first planet with a mass of 2 M_J and a period of 61 days (Delfosse et al. 1998) dominates the RV reflex motion. Although long period Jupiter mass planets are not in the maximum efficiency range for our planet searching study, we decided to observe this star and test our ability to detect a known planet using our technique.

A total of 13 observations were obtained from November 2004 to July 2007. The epoch RVs show a modest dispersion of 115 m/s, nearly identical to the average dispersion for RV standards of 114 m/s. Using the same Keplerian obit fitting code described in Section 2.1.5.2, we were able to fit for the orbital properties of GJ 876a (Table 3.5). We adopted the stellar mass from Marcy et al. (1998) of $M_\star$= 0.32 $M_\odot$. Figure 5.5 shows our fit for the orbital

solution. As the velocity semi-amplitude is near our detection limits, we fixed the eccentricity to the Marcy et al. (1998) value of e=0.27 to get a meaningful result. This suggests that finding planets like GJ 876a in our sample would be difficult given our bias toward short period hot Jupiters. Nevertheless, this result is a good test of our fitting procedure and suggests that larger amplitude planets should be detectable using our technique.

Table 3.5: Orbital Parameters of GJ 876b

Parameter	This Work	Delfosse et al. (1998)	Marcy et al. (1998)
P	61.97±0.51 days	60.97±0.19 days	60.85±0.15 days
T_0	53544.36±3.37	2450661.7±1.5 (JD)	2450301.0±1 (JD)
K	193.00±40.01 m/s	248.0±6.6 m/s	239±5 m/s
γ	−12169.12±24.46 m/s	−1902±6 m/s	···
e	0.27 (fixed)	0.336±0.019	0.27±0.03
ω	56.0±49.8 deg	5.2±4.8 deg	24±6 deg
M sin i	1.7±0.4 M_J	2 M_J	2.11±0.01 M_J

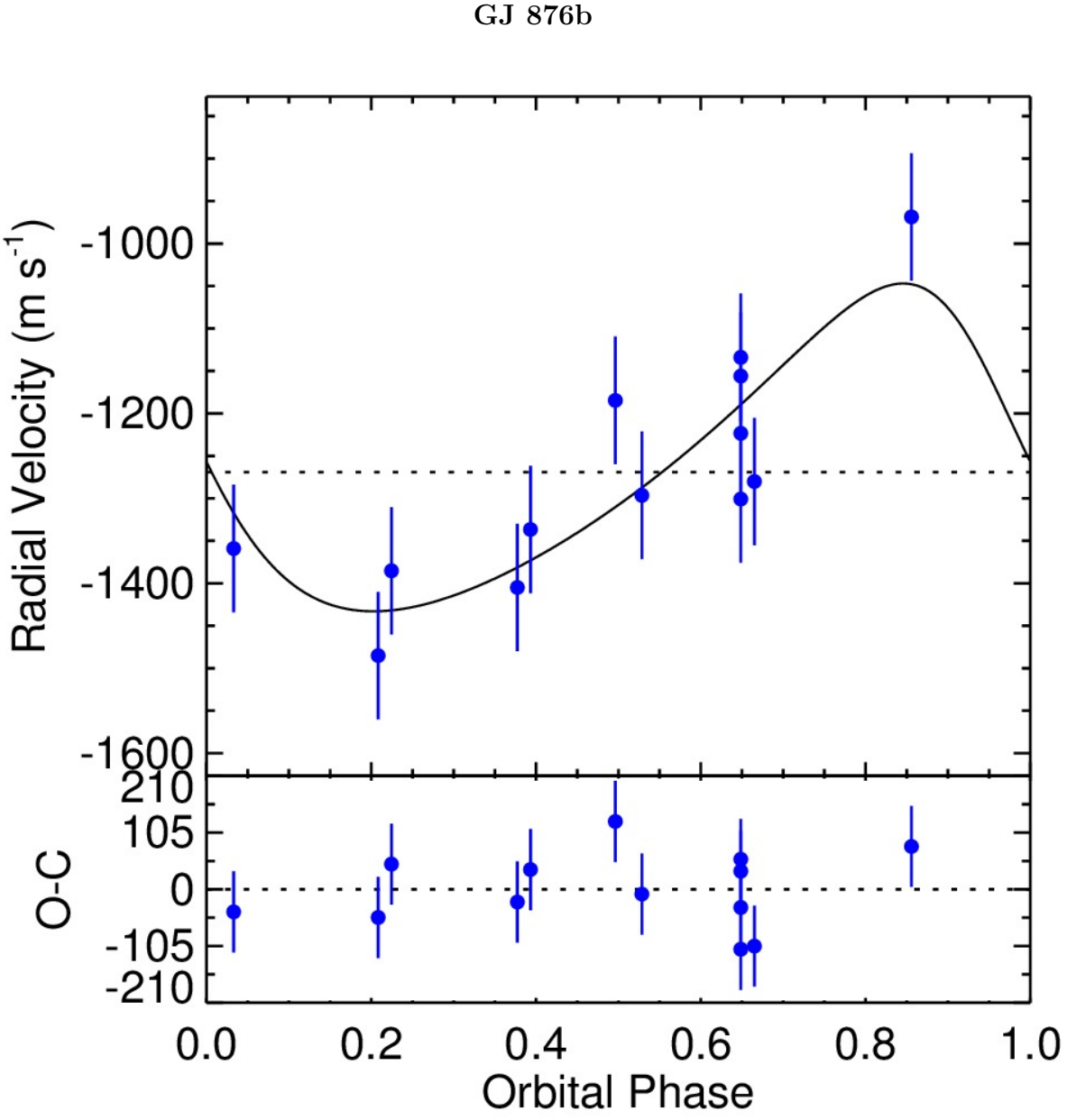

Figure 3.7 Here we show the phased RV plot of GJ 876b with the orbital fit (top panel). Residuals are shown in the bottom panel.

3.5 The Candidate Planet Host RXJ 1540.9-3024

RXJ 1540.9-3024 is a M2 T Tauri star in Upper-Sco (V=14.53 (Brandner et al. 2000); K_S=9.762). Relatively little is known about this star; a SIMBAD search (April 11, 2018) shows only 3 references. Although portions of Upper-Sco were targeted for the Kepler K2 Mission, this star was not in any of the fields observed by Kepler. In Figure 3.8 we show 10 epoch RVs obtained from February 2005 and July 2007. They exhibit a dispersion of 561 m/s and full amplitude variations of 1594 m/s over the time period observed. The data also show evidence of large variations (>100 m/s) on short timescales (<days) indicative of a hot Jupiter-like companion.

RXJ 1540.9-3024

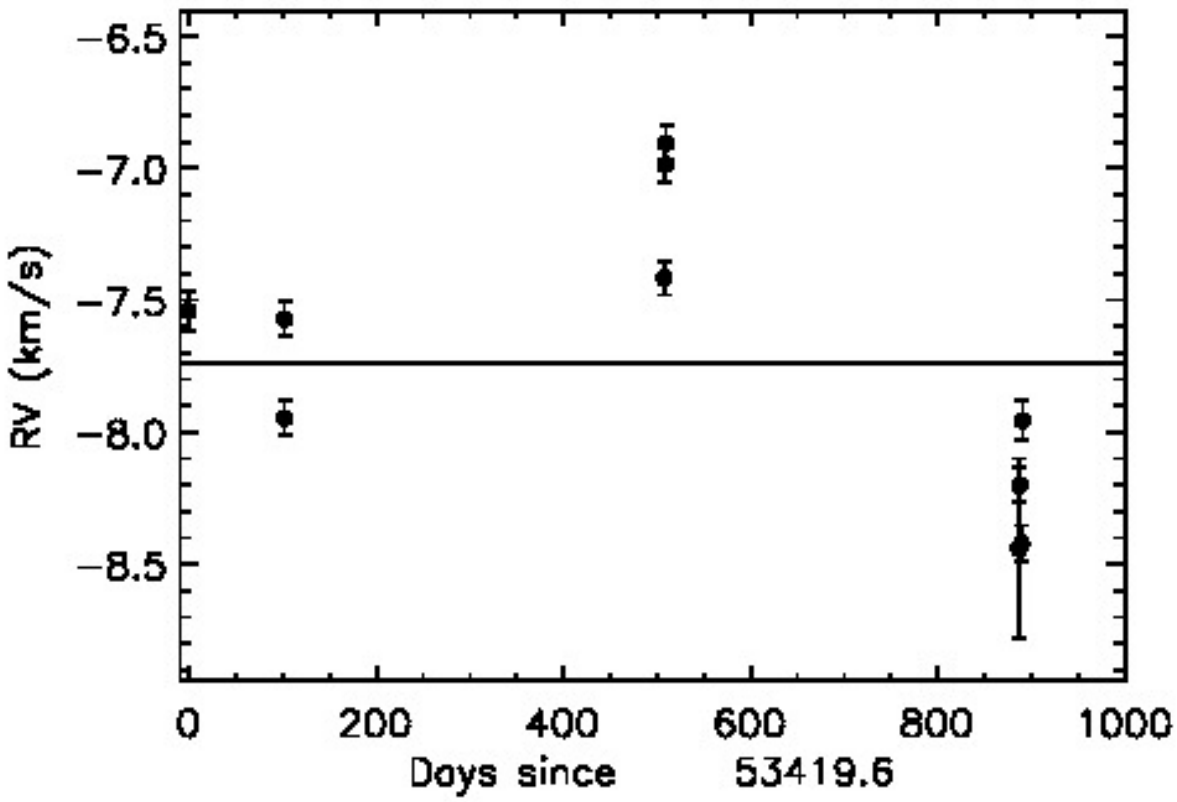

Figure 3.8 The RV curve for candidate planet host RXJ 1540.9-3024 is plotted with epoch errors for each observing day.

Under the assumption that the RV variability is caused by a companion, we fit Keplerian orbits (see Section 2.1.5.2) to the epoch RVs to search for orbital solutions that match the observations. We assume a stellar mass of 0.49 $M_{\odot}$ based on an estimate provided by Kraus & Hillenbrand (2007a). The best fit orbital solution corresponds to an eccentricity of e=0.275, a full amplitude variation of K=821 m/s, and a Jupiter mass ($m\sin i$=5.4 M_J) companion in a 10.7 day period. In Table 3.6, we list the full orbital properties for a possible companion to RXJ 1540.9-3024. The phased RV curve is shown in Figure 3.9 with a RMS value of 197 m/s. This RMS difference is only slightly larger than the average RV dispersions of other Upper-Sco stars (127 m/s).

Given a $v\sin i$ of 7.65 km/s and assuming a stellar radius for RXJ 1540.9-3024 of 0.89 $M_{\odot}$, we calculate an upper limit on the rotation period, assuming an edge on inclination, to be 5.9 days. This rotation period is much faster than the period of the candidate planet. This suggests that the RV variability we detect is not associated to the rotation of the star.

Additional precise observations are needed to confirm the presence of this companion, and most importantly its mass and eccentricity. Mass is important, of course, because it will constrain whether a companion is a planet or brown dwarf. Nevertheless, eccentricity is equally important, as it potentially could constrain how the planet migrated. As noted in the introduction, migration through a disk is assumed to dampen eccentricities, while dynamical interactions can produce a range of eccentricities.

RXJ 1540.9-3024

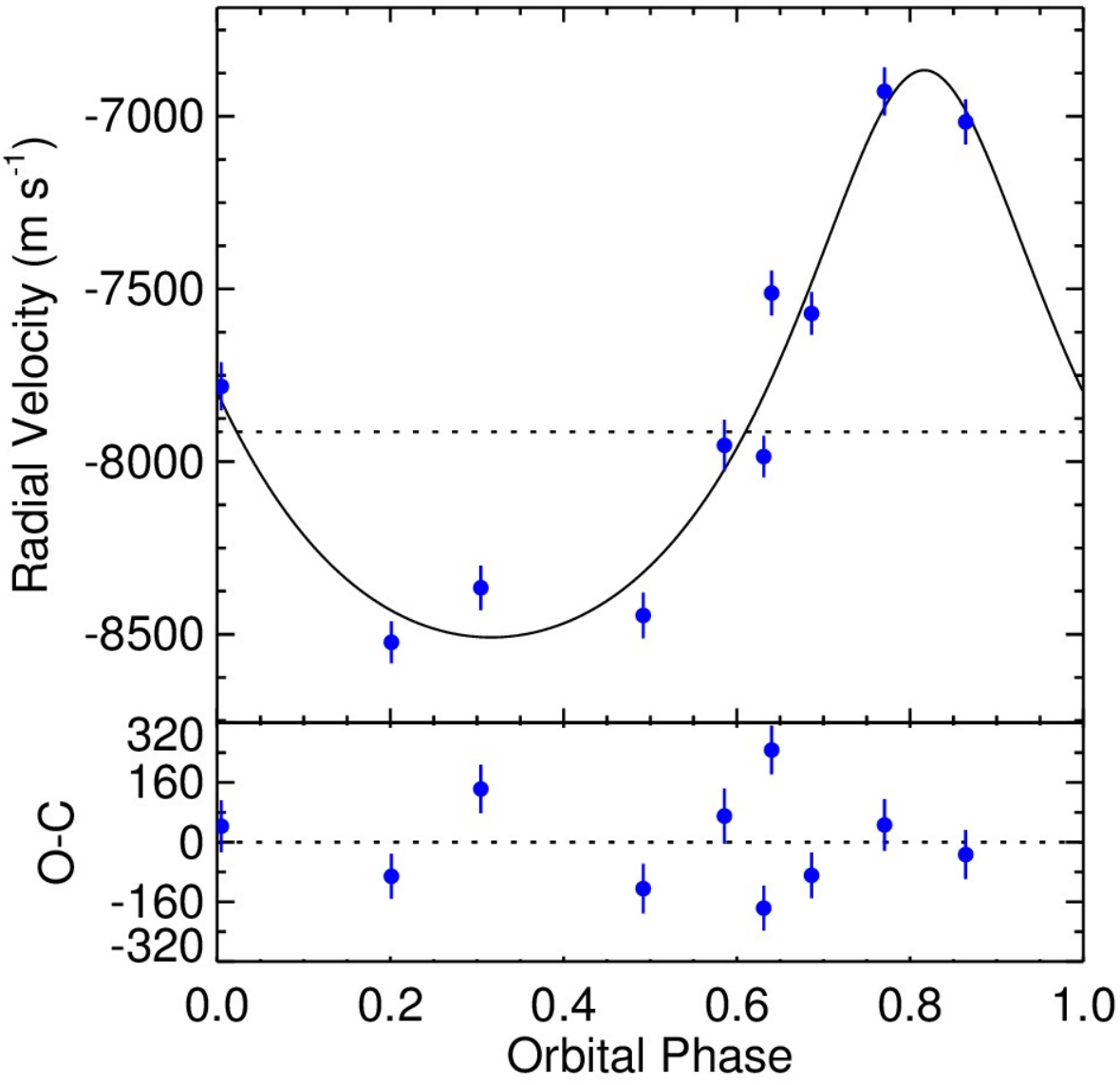

Figure 3.9 The phased RV curve with residuals plotted below.

Table 3.6: Orbital Parameters of RXJ 1540.9-3024b

Parameter	RXJ 1540.9-3024
P	10.67±0.003 days
T_0	53537.91±0.33
K	821.1±91.5 m/s
γ	−7913.5±45.4 m/s
e	0.275±0.076
ω	0.00±12.83
M_P	5.35±0.74 M_J

3.6 Newly discovered Spectroscopic Binaries

Two stars exhibit large amplitude (>20 km/s) RV variations and double-lined spectra, indicating that they are spectroscopic binaries. Neither has been identified as such previously.

RXJ 1548.9-3045 is a M2 T Tauri star in Upper-Sco (Köhler et al. 2000) with a previously unknown rotation period. We obtained 10 epochs from February 2005 to July 2007. This star shows significant RV variation (σ_{disp}= 20.3 km/s) over this time frame. The RV curve is shown in Figure 3.11 and illustrates the large amplitude RV variations indicative of a stellar companion. Additionally, we detect a second spectrum in the residuals of some fits. This is shown in Figure 3.10, where we plot the model telluric spectrum (top solid line), the model fit using NexGen spectral models with the best fit parameters (second solid line), the observed spectrum (third solid line) and the product of the telluric model and the

NexGen Model (dotted line), and the residuals (bottom dotted line). We, therefore, classify this as a double lined spectroscopic binary (SB2). We used and IDL version of TODCOR (Zucker & Mazeh 1994) to attempt to separate the two RV components from the combined spectrum. TODCOR achieves this by utilizing a two dimensional cross correlation technique of two model spectra and obtain individual radial velocities. Unfortunately, the large $v\sin i$ (14 km/s) of RXJ 1548.9-3045A causes stellar features to have a width that blends with the second spectrum too much to get reliable RV measurements for each component. Although we assume our fitting routine described in Section 3.2 is able to recover the RV of the primary, unfortunately, given the sparseness of the observations (10 epochs over 29 months) we were unable to derive any orbital properties for this binary.

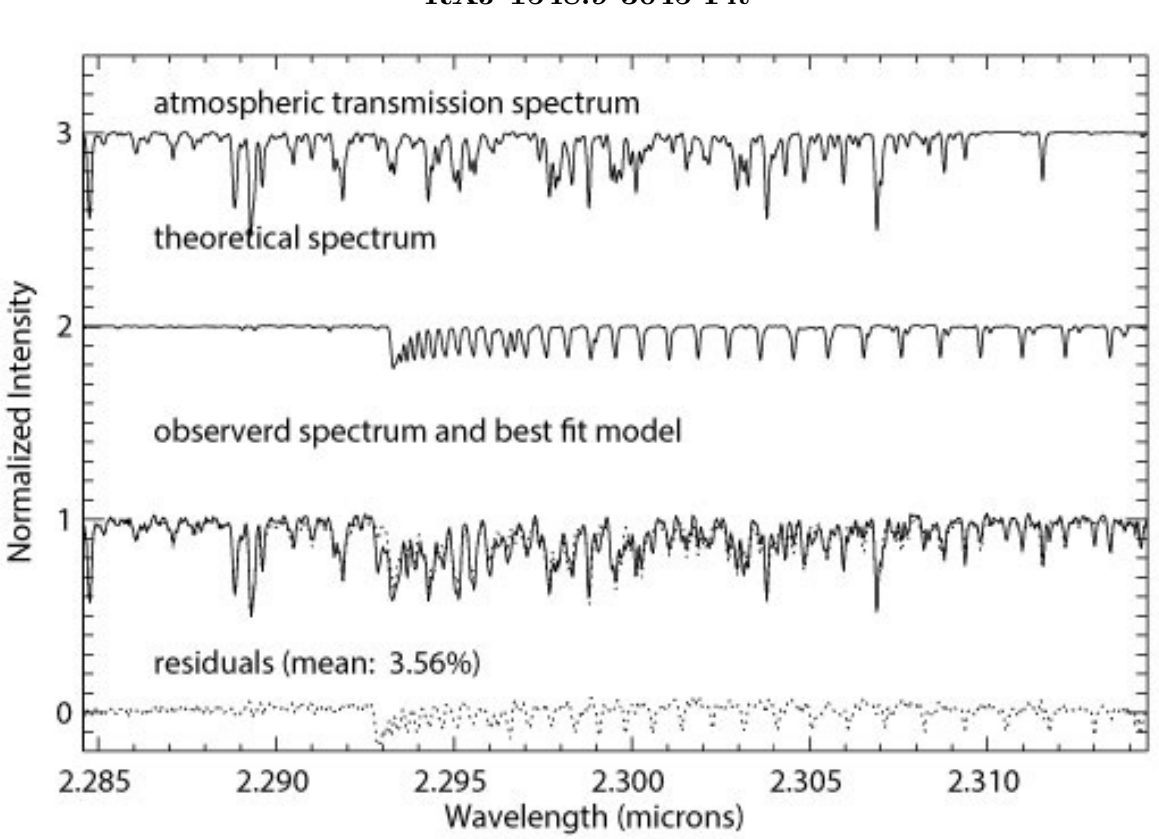

Figure 3.10 An example spectrum fit for RXJ 1548.9-3045. The top solid line show the model telluric spectrum. The second solid line shows the model fit using NexGen spectral models with the best fit parameters. The set of lines shows the observed spectrum (black) and the product of the telluric model and the NexGen Model (dotted). The bottom dotted line shows the residuals and shows clear evidence of a second spectrum.

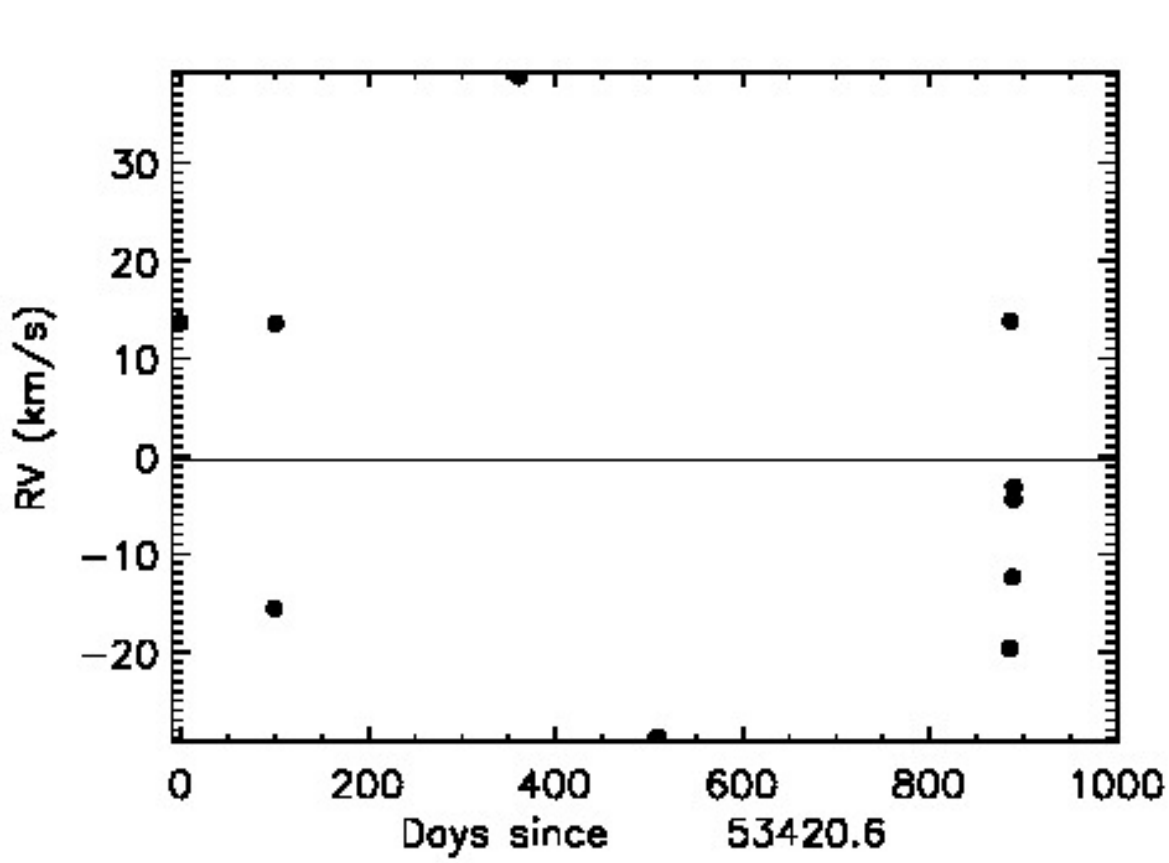

Figure 3.11 The epoch RV (km/s) is plotted with epoch errors for each observing day.

V1096 Tau is an M0 (Riviere-Marichalar et al. 2012) T Tauri star in Taurus-Auriga with a 6.45 day rotation period (Xiao et al. 2012), for which we obtained 8 epochs from November 2004 and January 2007. The RV plot for this Taurus-Auriga member shows significant RV variations (σ_{disp}=9.7 km/s) indicative of a companion (Figure 3.12). In some spectra, a faint companion spectrum was seen in the residuals to the fits, thus identifying this star as a SB2. Again, we used TODCOR to attempt to disentangle the faint companion spectrum and get individual radial velocities for each component, but were unsuccessful as the secondary

spectrum was too faint. Unfortunately, 5 observing runs over a 26 month time frame was insufficient to obtain orbital solutions for this binary.

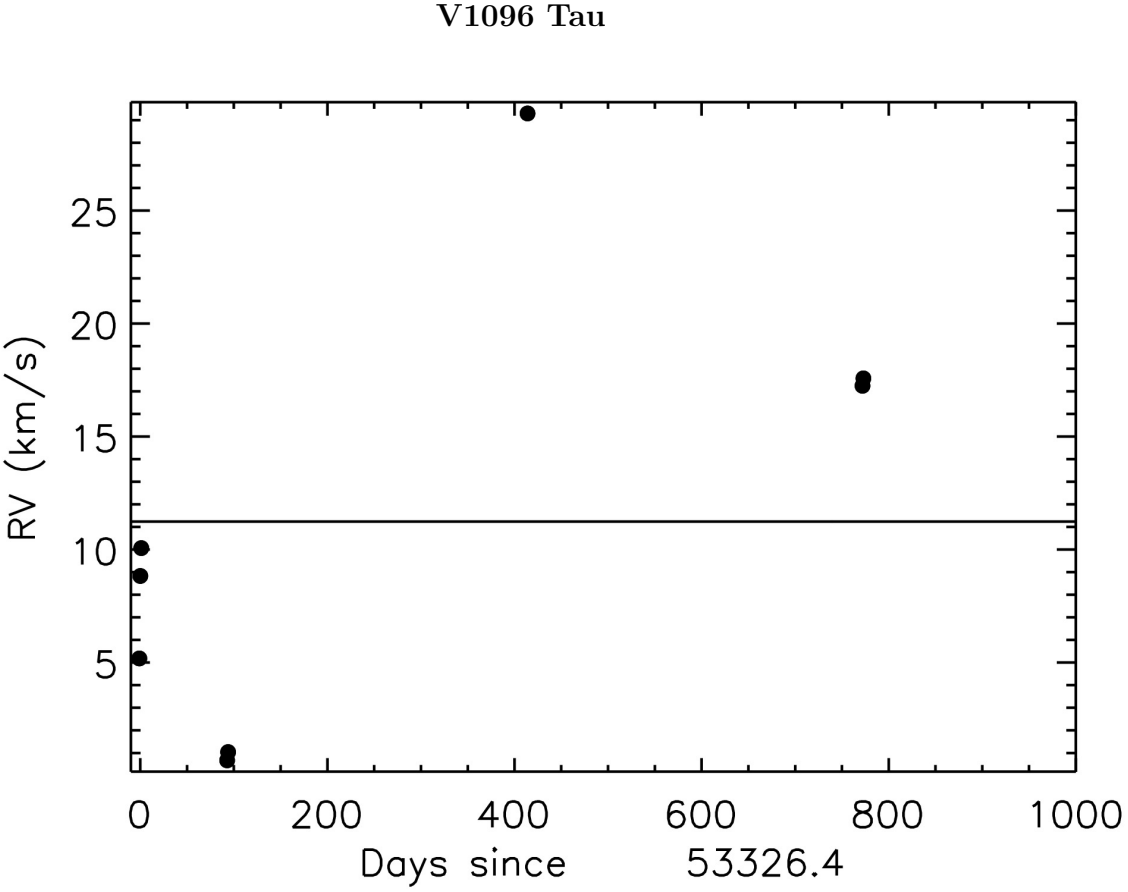

Figure 3.12 The epoch RV (km/s) is plotted with epoch errors for each observing day.

CHAPTER 4

Finding Planets in the Presence of Spots

4.0.1 Age Induced Variability

As discussed in Chapter 2 and Chapter 3, it has long been known that stars exhibiting photospheric activity can cause RV variability that mimics the RV signature of a planet orbiting a star (Queloz et al. 2001; Robertson & Mahadevan 2014; Robertson et al. 2014). Several pioneering surveys have, nevertheless, targeted young stars. This work has shown that stellar jitter has typical amplitudes of $\sim$100 m/s for adolescent (10-100 Myr) age stars (Bailey et al. 2012; Paulson & Yelda 2006; Lagrange et al. 2013), and can be as large as $\sim$1 km/s for T-Tauri age stars (<10 Myr)(Crockett et al. 2012; Johns-Krull et al. 2016; Donati et al. 2016; Yu et al. 2017; Mann et al. 2016; David et al. 2016). Observations in the infrared appear to mitigate these effects compared to optical, but do not eliminate them. The implication is that finding young planets requires more than distinguishing between spots and planets, but rather finding them in the presence of spots. The data obtained here offers new insight in the the potential for this.

With only 3-5 observations, our Gemini Phoenix sample does not provide a robust measure of stellar jitter. However, our Keck NIRSPEC sample consists of stars in two young clusters, 24 stars from Taurus-Auriga at 1-2 Myr and 14 stars from Upper-Sco at $\sim$10 Myr. This study gives us a unique opportunity to investigate RV variability at different ages using the same spectrograph and technique. Additionally Bailey et al. (2012) used the same instrument (NIRSPEC on the Keck telescope) with a nearly identical technique, and over

the same wavelength range for 9 single stars in TWA (∼10 Myr) and 9 single stars in β Pic (23 Myr) to search for young planets; two additional stars were observed but were identified as spectroscopic binaries. The single stars included in this study also have a similar number of measurements. We, therefore, combined our Keck NIRSPEC sample with RV dispersion results from Bailey et al. (2012) to illustrate the difference in the RV dispersions of these four young populations. In Figure 4.1, we plot the standard deviation of the epoch RVs versus $v\sin i$ for 13 Upper Scorpius stars, 23 Taurus-Auriga stars, 9 β Pic stars, and 9 TWA stars; the 4 stars identified in Chapter 2 and Chapter 3 as spectroscopic binaries (RXJ 1548.9-3045, V1096 Tau, GJ 3305, and TWA 23) are not included in Figure 4.1. We note that by plotting standard deviation of the epoch RVs versus $v\sin i$, we are seeing the combination of error terms (e.g., $\sigma_{Internal}, \sigma_{Photon}, \sigma_{Stellar}$). We see that the very young Taurus-Auriga stars at 1-2 Myr show a much higher scatter in RV dispersion (Mean$_{Disp}$=296 m/s; StdDev= 146 m/s) than the older Upper-Sco (Mean$_{Disp}$=161 m/s; StdDev= 126 m/s) at ∼10 Myr, TWA (Mean$_{Disp}$=137 m/s; StdDev= 58 m/s) at ∼10 Myr and β Pic (Mean$_{Disp}$=141 m/s; StdDev= 31 m/s) at 23 Myr. This suggests that the higher RV dispersion in Taurus-Auriga comes from these stars having a much higher stellar jitter.

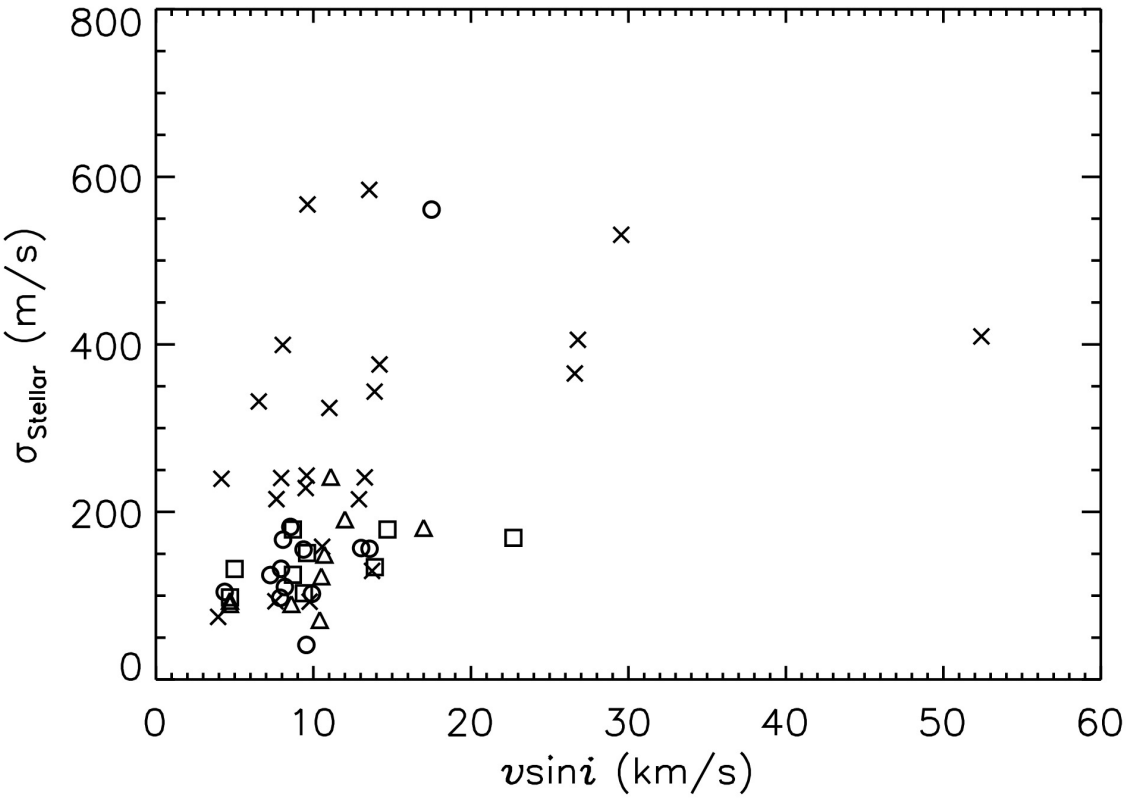

Figure 4.1 The standard deviation (m/s) versus $v$sin$i$ for Upper Scorpius (open circles), Taurus-Auriga ($\times$), β Pic (open squares), and TWA (open triangles).

To quantify the amplitude of the stellar jitter ($\sigma_{Stellar}$) in these young clusters requires removing the other components of the uncertainty in the RV. We do this by calculating the $\sigma_{Stellar}$ for each star by subtracting in quadrature the average epoch uncertainty for each star over the observing period ($< \sigma_{Epoch} >$) from the observed RV dispersion for each star (see Table 3.4) using equation 4.1. As Bailey et al. (2012) provide epoch RVs and errors,we are

able to use this method for β Pic and TWA stars from their work. We exclude the candidate planet host (RXJ 1540.9-3024) from further analysis, as the jitter calculated in Equation 4.1 assumes that the RV dispersion is due solely to stellar jitter, and does not originate from a companion.

$$\sigma_{Stellar} = \sqrt{(RV Dispersion)^2 - (<\sigma_{\star}>)^2} \tag{4.1}$$

In Figure 4.2 we plot these stellar jitter estimates for stars in Upper Scorpius (open circles), Taurus-Auriga ($\times$), β Pic (open squares), and TWA (open triangles) stars observed with Keck/NIRSPEC. The stellar jitter for Upper-Sco stars in our sample ranges from 92-174 m/s with a mean value of 129 m/s (StdDev=30 m/s). For stars in Taurus-Auriga the stellar jitter ranges from 56-584 m/s with a mean value of 293 m/s (StdDev=149 m/s). We see similar jitter values for TWA and Beta Pic as for Upper-Sco, with TWA having values ranging from 68-233 m/s with a mean value of 131 m/s (StdDev= 55 m/s), and Beta Pic having values ranging from 94-172 m/s with a mean value of 135 m/s (StdDev= 30 m/s). A K-S test using the jitter values from these the Keck NIRSPEC sample finds that stars in Taurus-Auriga are statistically distinct from stars in Upper-Sco. However, a K-S test for stars in Upper-Sco compared with stars in β Pic and TWA find that they are not statistically distinct. This implies that stellar jitter appears to decrease significantly in the first 10 Myrs, but declines more slowly in the next 10-15 Myrs.

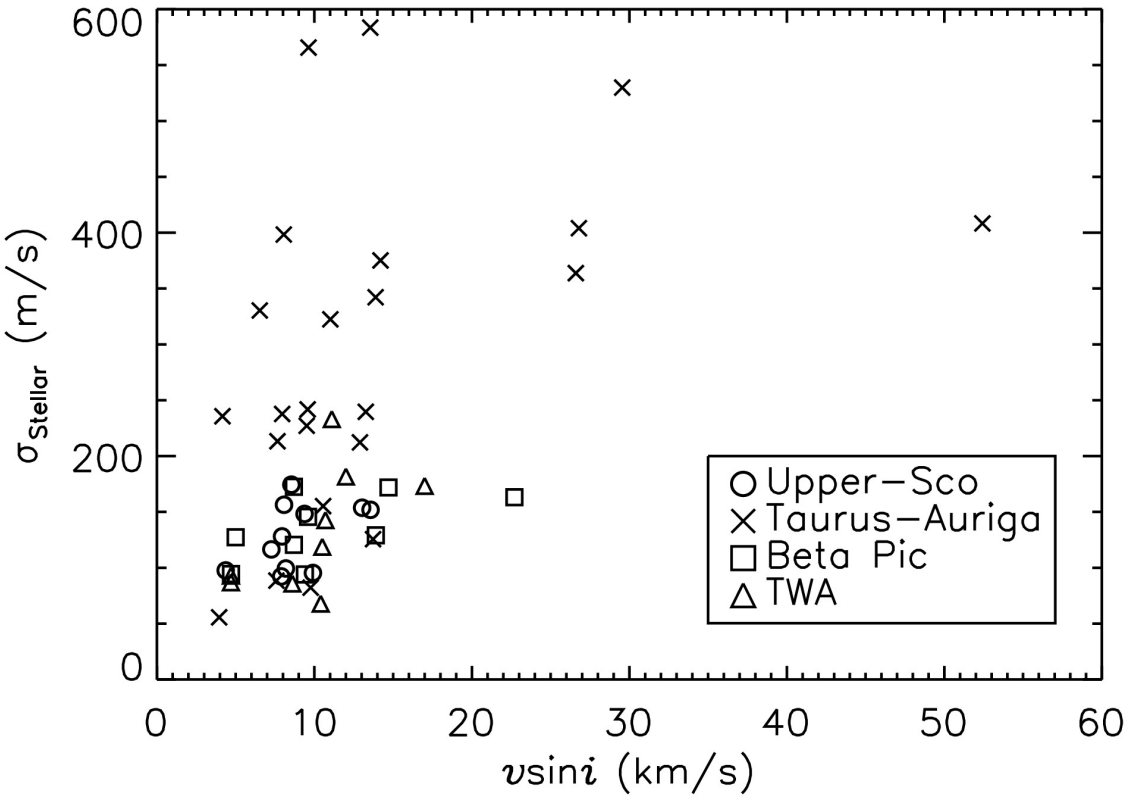

Figure 4.2 Here we plot the stellar jitter calculated using Equation 4.1 for Upper Scorpius (solid circles), Taurus-Auriga (X), β Pic (solid squares), and TWA (solid triangles).

4.0.2 Planets in the Presence of Spots - A Case Study of CIDA-3

Searching for planets orbiting young stars presents very difficult challenges, as photosphereic activity can mimic the RV signature of a planet as it causes a shift in radial velocity as the spot or flare rotates along the surface of the star. The results above show that this can be especially severe for stars with ages $\lesssim$5 Myr. Nevertheless, if we hope to find planets around

the youngest stars, we must be able to find planets in the presence of spots.

CIDA-3 is a M2 T Tauri star in Taurus-Auriga with no literature values for $v\sin i$ or rotation period; we measure a $v\sin i$ value of 9.62±0.98 km/s (see Section 3.2.1). Bulger et al. (2014) show that it has a truncated disk from far-IR observations using Herschel. CIDA-3 stands out in that the 7 observations obtained from Nov 2004 to Jan 2007 show evidence for RV variability using all 3 metrics, with a dispersion of 566 m/s, a Δ of 14.9, and a p-χ^2 of 3.8×10^{-18}. In addition, we see full amplitude RV variations of 1,751 m/s over the 7 observations and ∼1 km/s variations on short (∼2-3 day) timescales. These variations, if identified in an inactive field star, would be interpreted as indicating the presence of a hot Jupiter-like companion. Figure 4.3 shows the RV curve for each epoch observed. CIDA-3 may have a short period giant plant, but the RV variability is likely contaminated by stellar jitter.

Nevertheless, under the assumption that the RV variations are caused by a companion, we use the same Keplerian obit fitting code described in Section 2.1.5.2, to search for orbital solutions that match the observations of CIDA-3. We adopt a stellar mass of 0.32 $M_\odot$ based on the mass estimates from Andrews et al. (2013). The best fit orbital solution corresponds to a highly eccentric (e=0.56), Jupiter mass (msini=2.1 M_J) companion in a 5.6 day period. In Table 4.1, we list the orbital properties for this possible companion to CIDA-3. The phased RV curve is shown in Figure 4.4 with a RMS value of 1 m/s. As the mean stellar jitter for stars in Taurus-Auriga is 293 m/s, and our precision on slowly rotating field stars is ∼30-60 m/s, this RMS value implies that our code is over-fitting our RV data. Additionally,

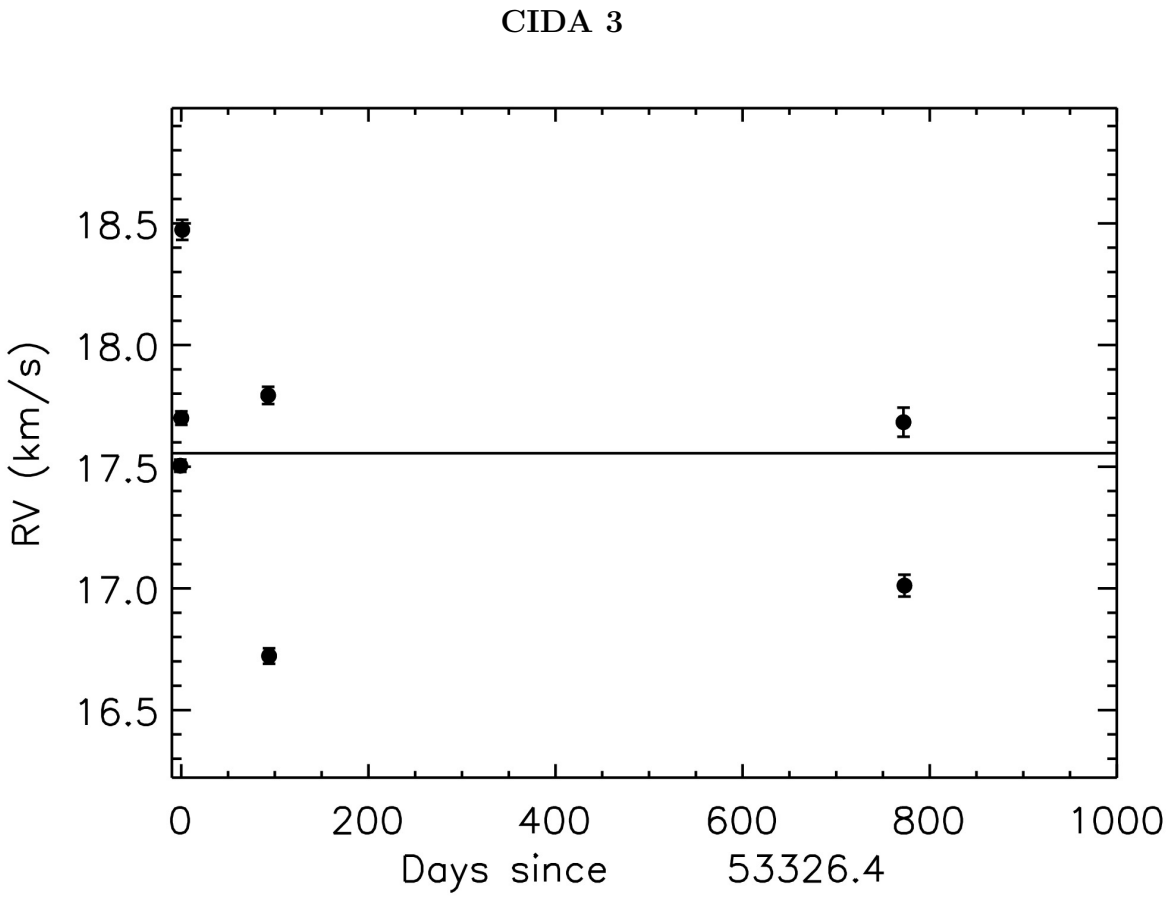

Figure 4.3 The epoch RVs are plotted with epoch RV errors for CIDA 3.

it has been shown that stellar jitter can mimic the RV curve of a highly eccentric companion (e.g.,: Korhonen et al. (2015); Andersen & Korhonen (2015)).

In light of this, we also consider orbital solutions with less severe eccentricities. In Figure 4.5 we show phased RV curves for orbital solutions with e=0.45, e=0.35, e=0.25, and e=0. In these cases the RV curve is not perfectly fit and yields RMS values of 102 m/s, 199 m/s, 270 m/s and 379 m/s, respectively. We list the orbital fit parameters for e=0.45, e=0.35, e=0.25, and e=0 in Table 4.1 as well. We note that the 2 smallest eccentricities considered have RMS

values consistent with the average RV dispersion of Taurus-Auriga stars (296 m/s; Section 4.0.1). If CIDA-3 is orbited by a companion, a lower eccentricity seems more plausible. Ultimately, the high stellar jitter associated with stars as young as those in Taurus-Auriga severely inhibit the ability to discern if the RV shifts are caused by a planet, or by spots based on IR observations alone. Further observations will be needed to identify the cause of the RV variations in CIDA 3.

CIDA 3

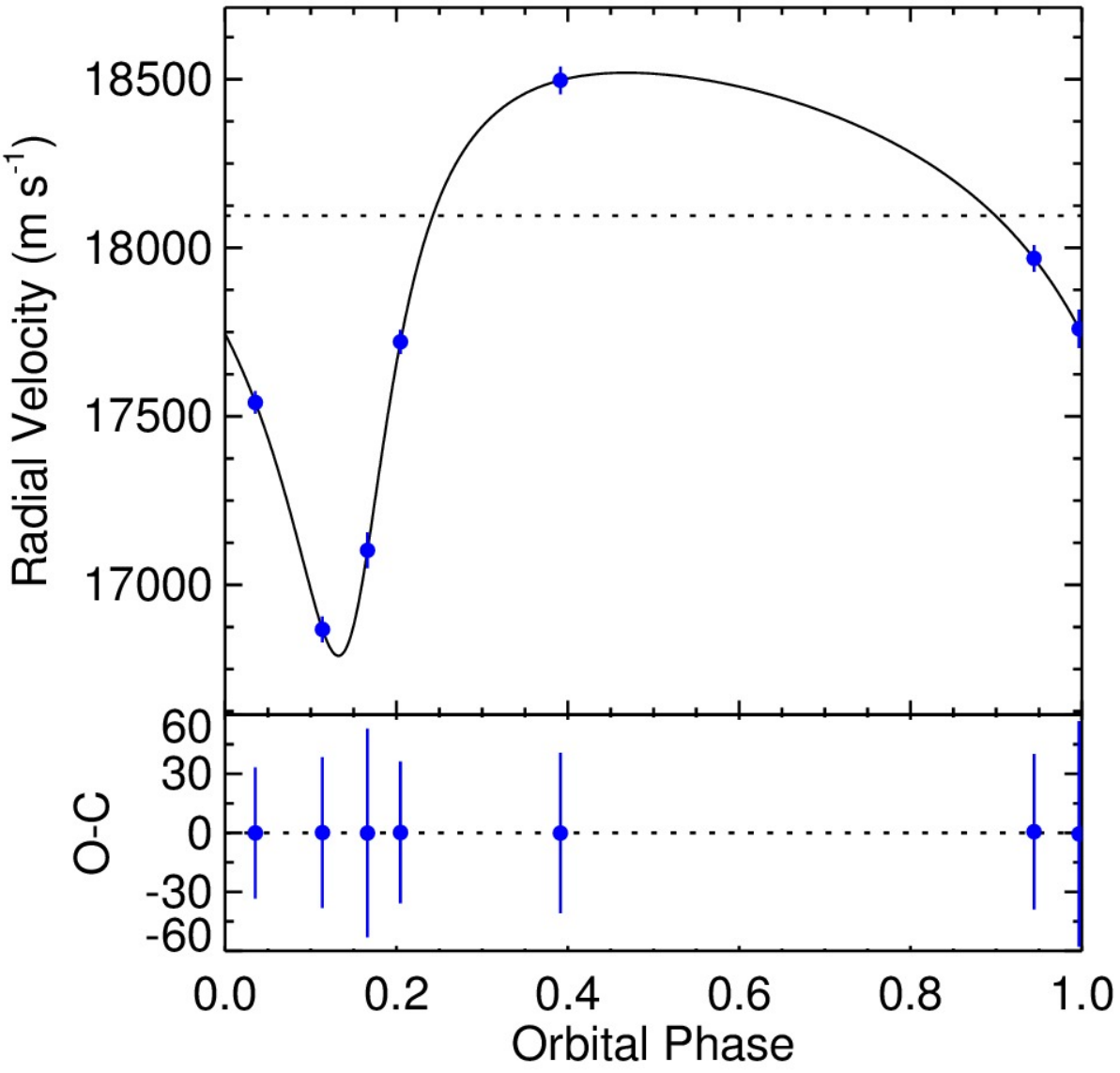

Figure 4.4 The phased RV curve for CIDA 3 with residuals plotted below for the best fit orbital solution.

Table 4.1: Orbital Parameters of CIDA 3 For different Eccentricities

Parameter	Best Fit	e=0.45	e=0.35	e=0.25	e=0.0
P (days)	5.90±0.001	5.90±0.001	5.90±0.001	5.90±0.001	5.90±0.001
T_0	53539.68±0.22	53539.49±0.07	53539.35±0.07	53539.23±0.07	53538.97±0.05
K (m/s)	864.8±109.9	841.4±77.1	856.6±83.7	906.1±99.1	1209.7±122.3
γ (m/s)	18095.1±67.3	18142.0±60.0	18187.9±67.9	18241.3±82.7	18427.3±95.1
e	0.557±0.101	0.45 (fixed)	0.35 (fixed)	0.25 (fixed)	0.00 (fixed)
ω	203.76±11.89	194.82±11.21	188.17±14.63	179.35±21.51	0.00±0.00
M_P (M_J)	2.13±0.47	2.22±0.20	2.38±0.23	2.60±0.28	3.60±0.36
RMS (m/s)	0	102	99	270	397

CIDA 3

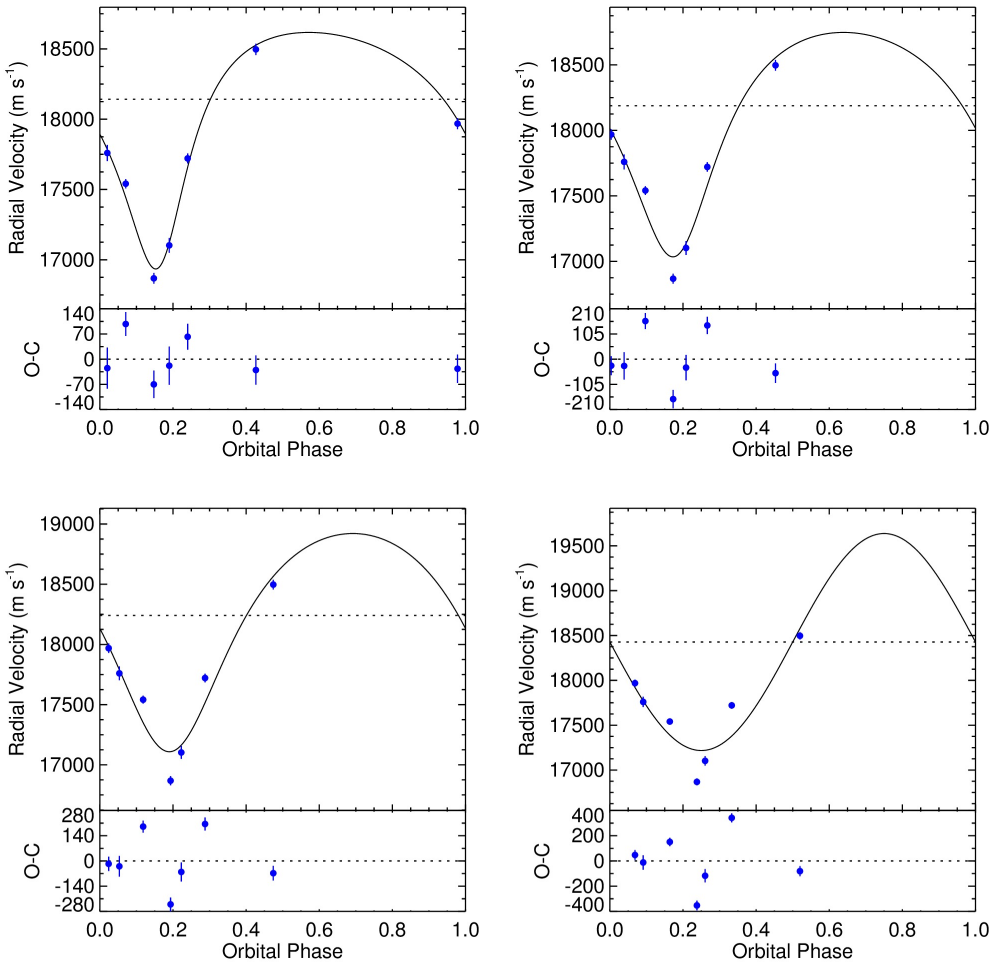

Figure 4.5 The phased RV curve for CIDA 3 with residuals plotted below for e=0.45 (upper left), e=0.35 (upper right), e=0.25 (lower left), and e=0 (lower right). Corresponding RMS values are 102 m/s, 199m/s, 270 m/s and 379 m/s, respectively.

4.1 Companion Mass Detection Rate

We use the multi-epoch, high precision RVs from Chapter 2 and Chapter 3 to determine the fraction of planets that could be detected in these samples. Our empirical precision is 22-31 m/s on slowly rotating field stars with Gemini Phoenix, and the stellar jitter for stars >5 Mys is estimated to be 129 m/s (see Section 4.0.1). By adding those two error sources in quadrature, we can estimate the minimum epoch-to-epoch reflex motion we can detect to be ∼132 m/s. If we assume a circular orbit, we can use Equation 4.2 to calculate the observable velocity shift on a star with mass $M_\star$ by a planet with mass M_P at a given orbital distance a given an inclination i. This corresponds to 133 m/s for a 0.5 $M_\odot$ star (Spectral Type ∼ M1.5) with a 1 M_{Jup} planet with an edge on inclination. However, for the same mass assumptions on a system with a 45° inclination, we would only expect to see a ∼ 30 m/s reflex motion, that, over a 5 day observing period would be just above our detection limits. We provide these analytic results to convey that, given the measured RVs, we should be able to identify trends of any >13M_{Jup} with less than 10 day periods, unless they are nearly face on, for the 17 young stars observed with Gemini Phoenix that have ≥3 epochs of observations and are not identified as RV variable.

$$\begin{aligned} V_{obs} &= V_\star * Sin(i) \\ V_\star &= \frac{M_P}{M_\star} * \sqrt{\frac{(G * M_\star)}{a}} \end{aligned} \tag{4.2}$$

In order to determine our mass detection rates in a more robust way, we use Monte

Carlo statistical model on stars with multi-epoch observations to simulate a range of hot and warm Jupiters to determine our detection limits. 1,000,000 planets are simulated at a specified orbital period and a specified companion mass but with random inclinations (0-90°) and eccentricity values (0-1) to determine the planet detection rate. We define a planet as "detected" if a 3σ detection threshold is reached. For each star we use the observation date, RV uncertainty (σ_{Obs}) and a stellar jitter characteristic of the star's age as input values. We assign the mean value for stellar jitter of 293 m/s for Taurus-Auriga stars, and 129 m/s (the calculated jitter for Upper-Sco) for all other young stars, consistent with Section 4.0.1. For these input values, we used the MJD and σ_{Obs} from Table 2.3, Table 2.8, and Table 3.2 for each star. We use T_{eff}-Mass evolutionary models for pre-main sequence low-mass stars from Baraffe et al. (2015) to assign a stellar mass to each star for our simulations. We assumed a stellar effective temperature (T_{eff}) from the spectral type listed in Table 2.2 using Kraus & Hillenbrand (2007b). From these T_{eff}, we interpolate T_{eff}-Mass models from Baraffe et al. (2015).

The detection probabilities we present in this section are calculated using a P-χ^2 statistic. As such, they are identical to our method for using p-values to determine if RV variations are significant. Furthermore, using these prediction probabilities, we can rule out different mass ranges and periods for stars each sample from Chapter 2 and Chapter 3 that are not identified by our methods as being RV variables.

In Appendix B we show "heat maps" that depict the detection probabilities for companion masses ranging from 0-14 $M_{Jupiter}$ and periods ranging from 0-10 days for all stars in Chapter

2. Representative results from this simulation for young stars stars with ≥3 epochs observed with Gemini Phoenix and VLT CRIRES follow-up are listed in Table 4.2. In this table we show the detection rate (number planets detected/total number of planets simulated) planets with masses 4-5 M_{Jup} and 12-1 $3M_{Jup}$ with 3 and 10 day periods.

Our 5 night observing run on Gemini Phoenix, described in Chapter 2, was designed to identify the RV signature of a short period hot Jupiter-like planets. Due to the short observing period, our companion detection limits are only complete to very short period (<3 day), massive planets 12-13M_{Jup} planets. Our mean detection rate for 12-13M_{Jup} planets in 3 day periods for the young stars observed with Gemini Phoenix is 81%, and, with the exception of RXJ 1219.7-7403 (14%), and RecX 12 (56%), our detection rate is above 76% for the same mass and period range. We note that we did identify 1 star as a candidate RV variable (ScoPMS 13).

We obtained a larger number of observations on 3 stars (TWA 13A, V721 CrA , and TYC 7443-1102-1) with VLT CRIRES follow-up (8-19 epochs over 49-88 days). As such, our detection limits on these 3 stars are more complete. Our overall detection rate for 4-5 M_{Jup} planets with 3 and 10 day periods is above 89% and 77%, respectively, with an average detection rate of 92% and 84%, respectively. The overall detection rate for 12-13 M_{Jup} with 3 and 10 day periods is 97% and 85%, respectively for young stars with an average detection rate of 98% and 96%, respectively. Given these detection rates, we rule out planets >4 M_{Jup} with <10 day periods for stars that are not identified as RV variable.

Star	3 Day Period	10 Day Period
	Detection Rate	Detection Rate
Gemini Phoenix – Young Stars		
$3 < M_{\rm Jup} < 4$		
HIP 23309	0.414	0.048
HIP 29964	0.211	0.016
HD 155555C	0.636	0.157
RecX 4	0.169	0.011
RecX 10	0.122	0.008
RXJ 1005.3-7749	0.251	0.027
RXJ 1204.6-7731	0.513	0.075
TWA 7	0.586	0.109
TWA 13A	0.549	0.125
TWA 13B	0.646	0.162
TWA 10	0.511	0.090
RXJ 1534.3-3300	0.181	0.022
ScoPMS 13	0.519	0.079
RXJ 1557.8-2305	0.118	0.011
SZ 78	0.785	0.292
SZ 96	0.144	0.016
V721CrA	0.150	0.011
HIP 107345	0.519	0.068
$12 < M_{\rm Jup} < 13$		
HIP 23309	0.879	0.471
HIP 29964	0.831	0.325
HD 155555C	0.915	0.718
RecX 4	0.803	0.275

Star	3 Day Period	10 Day Period
RecX 10	0.805	0.238
RXJ 1005.3-7749	0.856	0.443
RXJ 1204.6-7731	0.905	0.626
TWA 7	0.911	0.678
TWA 13A	0.911	0.698
TWA 13B	0.917	0.731
TWA 10	0.893	0.643
RXJ 1534.3-3300	0.760	0.417
ScoPMS 13	0.887	0.589
RXJ 1557.8-2305	0.770	0.223
SZ 78	0.943	0.804
SZ 96	0.812	0.398
V721CrA	0.807	0.263
HIP 107345	0.903	0.642
VLT CRIRES – Young Stars		
$3 < M_{\rm Jup} < 4$		
TWA 13A	0.898	0.827
V721CrA	0.929	0.832
TYC 7443-1102-1	0.928	0.854
1RXS J195602.8320720	0.924	0.839
$12 < M_{\rm Jup} < 13$		
TWA 13A	0.977	0.958
V721CrA	0.978	0.955
TYC 7443-1102-1	0.980	0.963
1RXS J195602.8320720	0.979	0.957

Our Keck NIRSPEC sample described in Chapter 3 was observed over a longer temporal baseline, with each star being having 5-10 observations over >770 days. This gives us greater sensitivity to the detection of companions, including those with a longer orbital period. In Appendix B, we list probabilities for detecting companion masses from 0-14 $M_{Jupiter}$ in 0-30 day periods for all stars in Chapter 3. Additionally, we list a representative detection rate for planets with masses 4-5 M_{Jup} and 12-13 M_{Jup} with 3, 10, and 30 day periods for each of our stars. The results for our companion detection limit simulation for our Keck NIRSPEC sample are listed in Table 4.3. In Figure 4.6, Figure 4.7, and Figure 4.8, we show histograms for detection rates above 95% for planets with masses ranging from 1-50 $M_{Jupiter}$ in 3, 10, and 30 day periods, respectively.

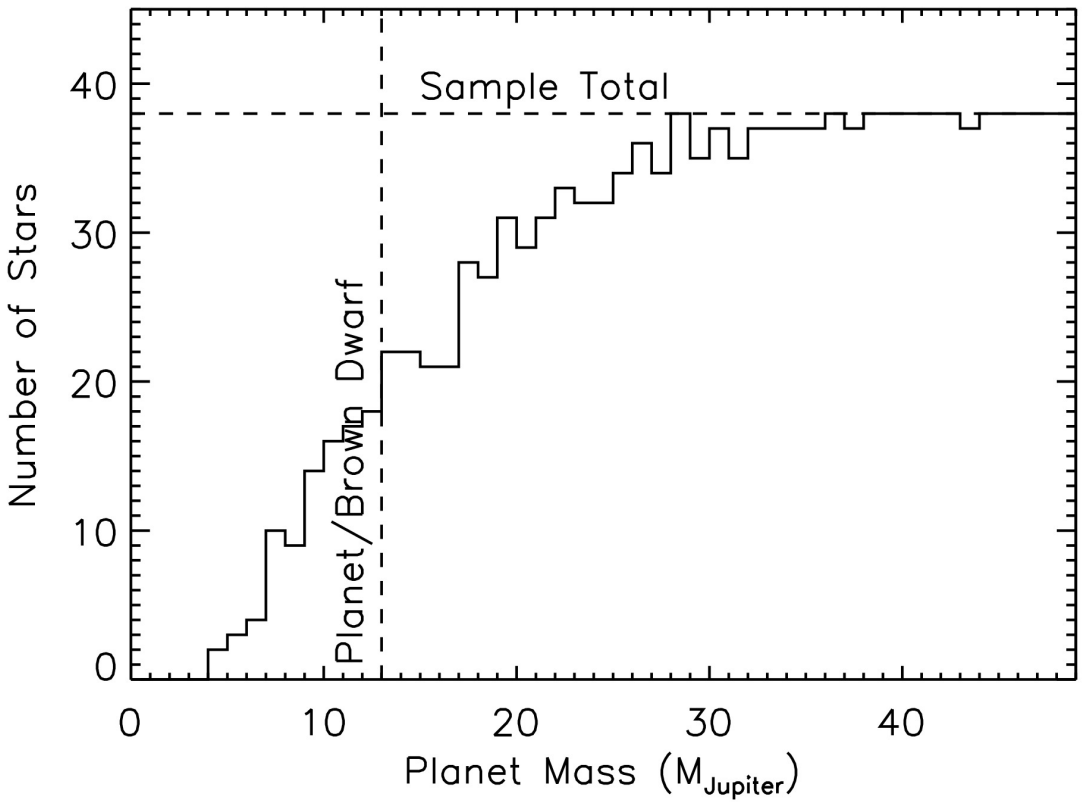

Figure 4.6 A histogram of detection rates above 95% for planets with masses ranging from 1-50 $M_{Jupiter}$ in 3 day periods for all planets in the Keck NIRSPEC sample. The planet/brown dwarf boundary (13 $M_{Jupiter}$; Basri & Brown 2006) is plotted with a vertical dashed line, and the total sample size is plotted with a horizontal dashed line.

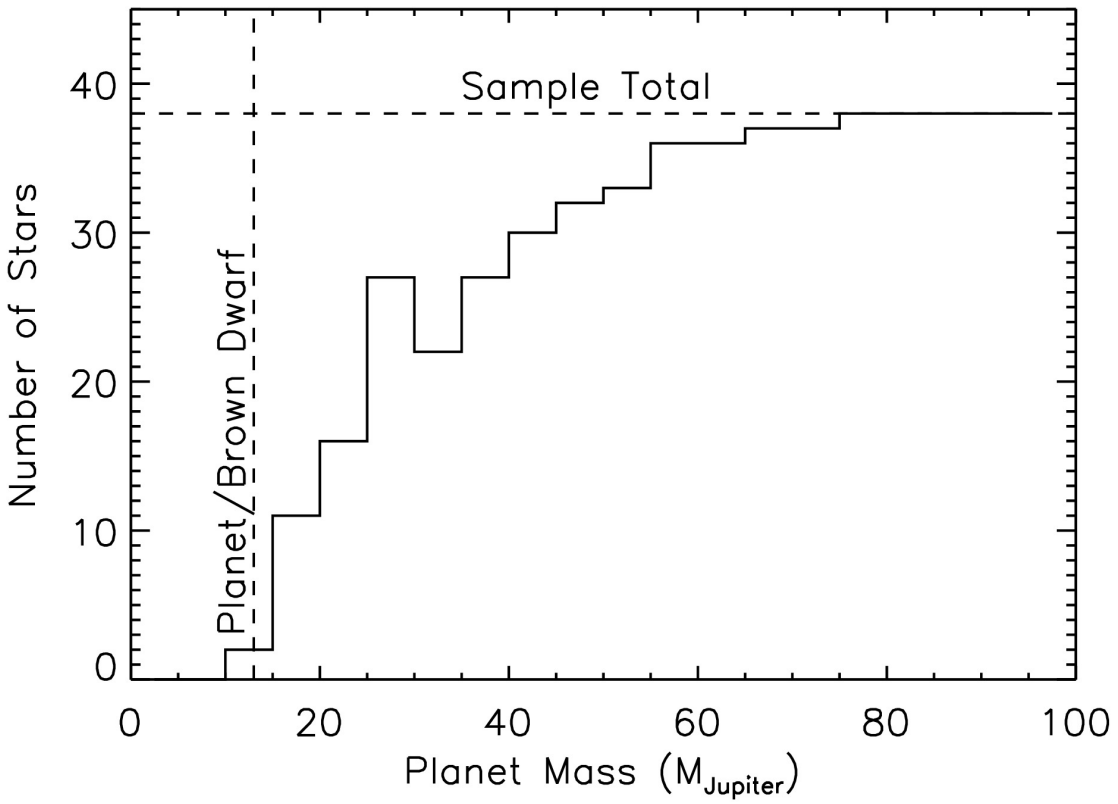

Figure 4.7 A histogram of detection rates above 95% for planets with masses ranging from 1-100 $M_{Jupiter}$ in 10 day periods for all planets in the Keck NIRSPEC sample. The planet/brown dwarf boundary (13 $M_{Jupiter}$; Basri & Brown 2006) is plotted with a vertical dashed line, and the total sample size is plotted with a horizontal dashed line.

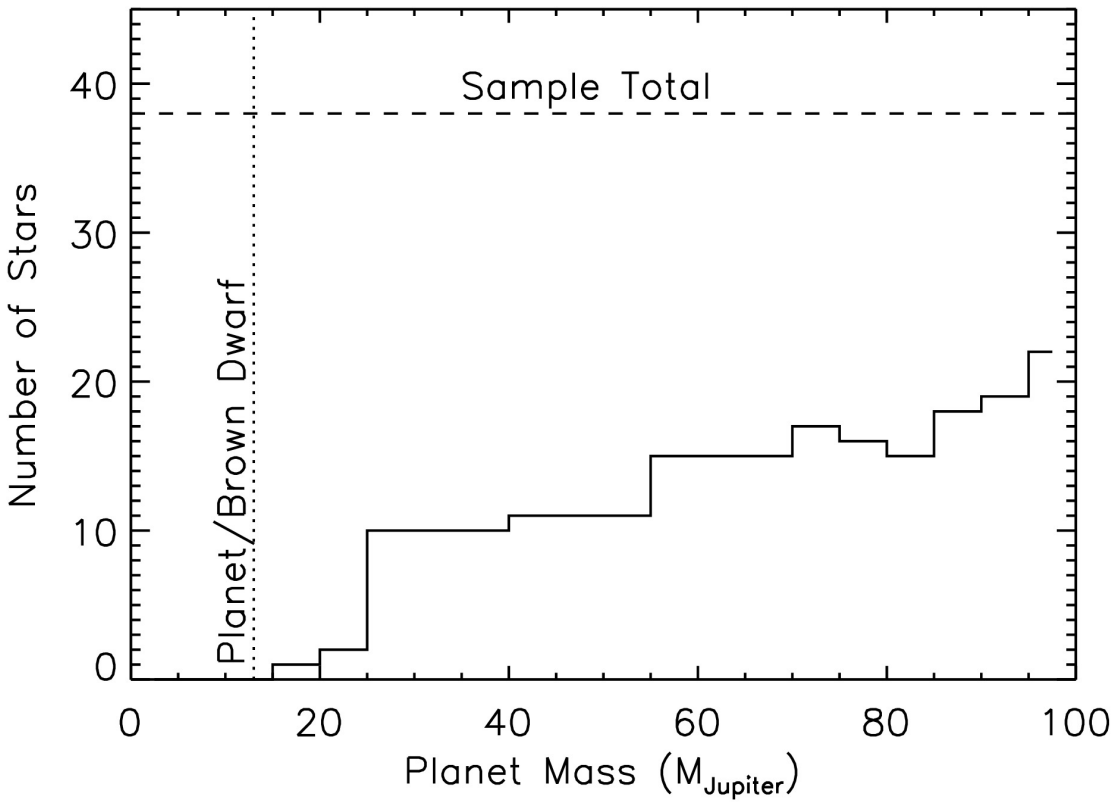

Figure 4.8 A histogram of detection rates above 95% for planets with masses ranging from 1-100 $M_{Jupiter}$ in 30 day periods for all planets in the Keck NIRSPEC sample. The planet/brown dwarf boundary (13 $M_{Jupiter}$; Basri & Brown 2006) is plotted with a vertical dashed line, and the total sample size is plotted with a horizontal dashed line.

For planets with a mass range of 4-5 M_{Jup} our average detection rate for Taurus-Auriga stars with periods of 3, 10, and 30 days is 82%, 34%, and 15%, respectively. For the planets with a mass range of 12-13 M_{Jup}, we our average detection rate for stars observed in Taurus-Auriga is 94%, 84%, and 69% for 3, 10, and 30 day periods. Given these detection rates, we

rule out planets >4 M_{Jup} in < 3 day periods, as well as planets >12 M_{Jup} with periods less than 30 days for stars that are not identified as RV variable in Taurus-Auriga.

For Upper-Sco stars with a planet mass range of 4-5M_{Jup}, we have an average detection rate of 90%, 72%, and 52% for 3, 10, and 30 day periods, respectively. For the planets with a mass range of 12-13M_{Jup}, the average detection rate is 97%, 93%, and 97% for the same periods. We can confidently rule out planets >4M_{Jup} in < 10 day periods, as well as planets >12$_{Jup}$ with periods less than 30 days for stars that are not identified as RV variable in Upper-Sco.

Table 4.3: Detection Limits - Keck NIRSPEC

Star	3 Day Period	10 Day Period	30 Day Period
	Detection Rate	Detection Rate	Detection Rate
Young Stars - Taurus-Auriga			
$3 < M_{Jup} < 4$			
V1306 Tau	0.817	0.439	0.148
V1096 Tau	0.803	0.402	0.125
FN Tau	0.768	0.279	0.079
CY Tau	0.658	0.141	0.032
CIDA 3	0.698	0.158	0.047
V410 X-ray 7	0.683	0.201	0.055
IP Tau	0.679	0.186	0.059
KPNO-Tau 13	0.859	0.591	0.239
DH Tau	0.751	0.268	0.078
IQ Tau	0.934	0.839	0.655
JH 56	0.818	0.452	0.145

J1-665	0.382	0.039	0.012
V1321 Ta	0.770	0.300	0.076
DM Tau	0.490	0.058	0.014
JH 108	0.929	0.782	0.607
DN Tau	0.918	0.743	0.511
RXJ0437.4+1851 A	0.761	0.304	0.078
RXJ0437.4+1851 B	0.701	0.191	0.044
RXJ0438.2+2303	0.623	0.138	0.036
CoKu Tau 4	0.730	0.239	0.061
GM Aur	0.875	0.655	0.387
V1353 Tau	0.719	0.229	0.053
CIDA 10	0.749	0.278	0.071
CIDA 8	0.771	0.307	0.102

$12 < M_{\rm Jup} < 13$

V1306 Tau	0.951	0.867	0.754
V1096 Tau	0.948	0.870	0.741
FN Tau	0.944	0.836	0.774
CY Tau	0.920	0.770	0.520
CIDA 3	0.925	0.785	0.603
V410 X-ray 7	0.931	0.815	0.658
IP Tau	0.924	0.748	0.625
KPNO-Tau 13	0.958	0.908	0.782
DH Tau	0.937	0.839	0.697
IQ Tau	0.984	0.952	0.897
JH 56	0.953	0.894	0.765
J1-665	0.888	0.711	0.434
V1321 Tau	0.943	0.858	0.705
DM Tau	0.895	0.671	0.400
JH 108	0.977	0.942	0.885
DN Tau	0.978	0.930	0.856
RXJ0437.4+1851 A	0.946	0.857	0.701
RXJ0437.4+1851 B	0.935	0.839	0.663
RXJ0438.2+2303	0.921	0.778	0.586
CoKu Tau 4	0.937	0.822	0.666
GM Aur	0.969	0.924	0.843
V1353 Tau	0.934	0.854	0.683
CIDA 10	0.942	0.835	0.710
CIDA 8	0.946	0.849	0.722

Young Stars - Upper Scorpius			
$3 < M_{\rm Jup} < 4$			
RXJ1534.3-3300	0.883	0.694	0.451
RXJ1540.9-3024	0.903	0.785	0.560
RXJ1546.0-2920	0.919	0.804	0.683
RXJ1546.7-3210	0.890	0.698	0.461
RXJ1548.9-3045	0.893	0.748	0.510
RXJ1551.1-2402	0.932	0.797	0.574
RXJ1552.5-2633	0.875	0.573	0.332
RXJ1557.8-2305	0.907	0.748	0.590
RXJ1558.8-2512	0.889	0.612	0.403
RXJ1605.6-2152	0.890	0.662	0.342
RXJ1607.0-2043	0.876	0.623	0.423
ScoPMS 14	0.941	0.861	0.744
ScoPMS 32	0.901	0.731	0.488
ScoPMS 42 B	0.914	0.790	0.656
$12 < M_{\rm Jup} < 13$			
RXJ1534.3-3300	0.964	0.937	0.893
RXJ1540.9-3024	0.974	0.944	0.896
RXJ1546.0-2920	0.977	0.948	0.920
RXJ1546.7-3210	0.971	0.920	0.891
RXJ1548.9-3045	0.970	0.938	0.896
RXJ1551.1-2402	0.980	0.960	0.864
RXJ1552.5-2633	0.967	0.884	0.741
RXJ1557.8-2305	0.972	0.942	0.910
RXJ1558.8-2512	0.967	0.896	0.772
RXJ1605.6-2152	0.967	0.919	0.774
RXJ1607.0-2043	0.966	0.912	0.883
ScoPMS 14	0.985	0.956	0.940
ScoPMS 32	0.972	0.935	0.888
ScoPMS 42 B	0.974	0.956	0.922

4.2 Notable Stars - Keck NIRSPEC

Stars in the Taurus-Auriga star forming region have been studied extensively over the last century; T Tauri itself defined a class of young stars (Joy 1945). Here we discuss in more detail stars observed in this program that are proposed to have stellar companions (IP Tau and CoKuTau 4), that show evidence of their disks being shaped by wider, possibly planetary mass, companions (DM Tau and GM Aurigae), that have directly imaged companion (DH Tau), and that have a with peculiar RV curve (CIDA 8).

IP Tau (K=8.349) is a M0 T Tauri star with a 3.25 day rotation period (Bouvier et al. 1995) and a $v\sin i$ value of 9.51±0.70. Espaillat et al. (2011) conducted a detailed model of the IR (538 μm)emission around IP Tau and classified it harboring a as pre-transitional disk. Simon et al. (2017) measured an inclination of 35° for this disk and Espaillat et al. (2011) find evidence for a 2 AU gap in the disk with an inner wall of 0.07 AU. Additionally, Simon et al. (2017) note that the luminosity and T_{eff} of IP Tau do not agree with the age of the system, and suggest that this star may be an unresolved binary with components of similar mass, although this is based solely on evolutionary models, and no other observational evidence is given.

We obtained 5 epochs from November 2004 and January 2007 and our results show a range of RVs of only 595 m/s and a dispersion of 229 m/s. This is slightly below the average dispersion of Taurus-Auriga (298 m/s). In Figure 4.9 we plot the RV curve for IP Tau. Our data do not show any evidence for RV trends or acceleration that would be expected for a binary with at least modest orbital inclination. We also note that recently Uyama et al.

(2017) conducted a high contrast imaging survey using the Subaru telescope, and their study ruled out companions greater than 14 M_J at orbital distances of 50 AU.

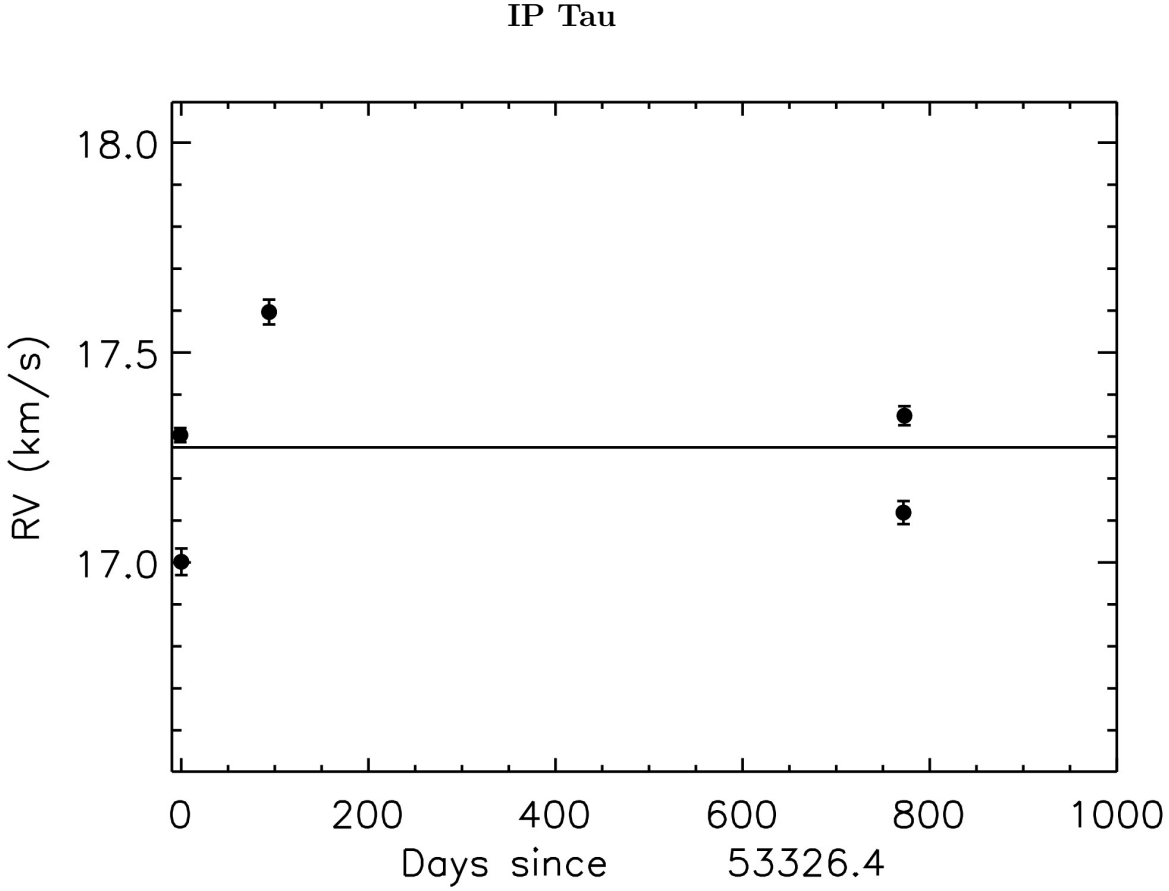

Figure 4.9 The RV curve is plotted with epoch errors for 5 observations.

DH Tau (K=8.178) is a M1 T Tauri star with a 7.2 day period (Bouvier et al. 1995) and a $v\sin i$ value of 7.65±0.39 km/s. Gräfe et al. (2011) observed DH Tau in mid-IR on VLT and concluded DH Tau harbors a disk with an inner disk hole radius of $< 15.5^{+9.0}_{-2.0}$ AU. A substellar companion (30-50 M_{Jup}) was found around DH Tau by Itoh et al. (2005) at a separation of 2.3″ (330 AU) using direct imaging with Subaru/CIAO. Luhman et al. (2006)

revised the mass to 11^{+10}_{-3} M_{Jup}. Although our detection technique would not be able to recover the RV signature of DH Tau b, the presence of this wider companion raises questions about the presence of companions at smaller separations, especially given the inner disk is cleared. Formations scenarios find it difficult to explain a system at this separation without a scattering event (Bryan et al. 2016).

We obtained 8 epochs of DH Tau from November 2004 to January 2007. Figure 4.10 shows the RV curve for DH Tau over the observing period. With an RV range of 722 m/s and a dispersion of 215 m/s, this star did not exhibit an RV signature indicative of a short period planet within our detection limits. In particular, we can exclude, with 95% confidence, > 15 M_{Jup} companions with < 3 day periods. We do however note the presence of a tentative trend in the RV curve (Figure 4.10).

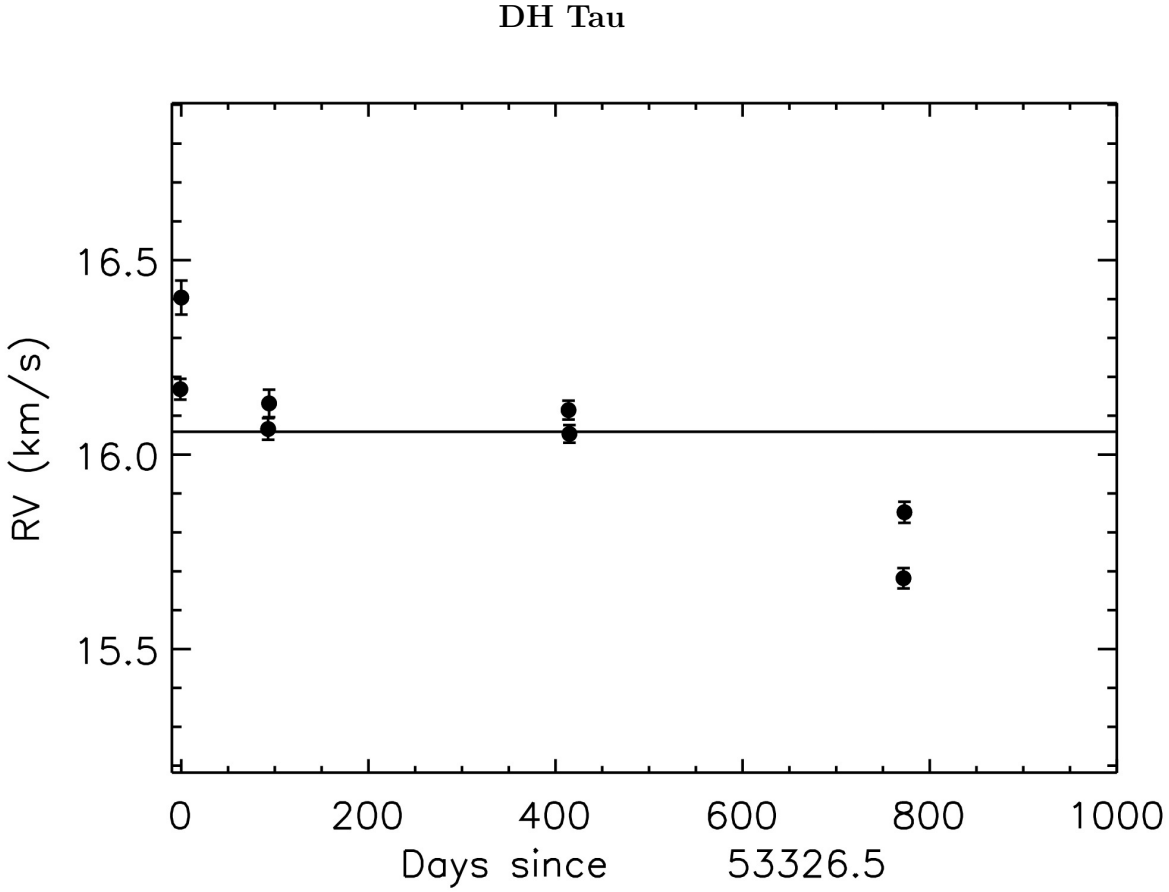

Figure 4.10 The RV curve is plotted with epoch errors for 8 observations.

DM Tau (K=9.522) is a M2 T Tauri star with a 43.5 day period (Hoffman et al. 2009) and a $v\sin i$ value of 4.16±1.20 km/s. Using molecular hydrogen at 112μm, Calvet et al. (2005) determined stellar and disk properties for DM Tau as $M_\star$=0.65 $M_\odot$ and the disk inclination at 35°, which Calvet et al. (2005) and Bergin et al. (2004) propose may be truncated with an inner wall at ∼4 AU.

We obtained 6 epochs of DM Tau between November 2004 and December 2006. In Figure 4.11 we plot the RV curve for DM Tau. We see an RV range of 657 m/s and a dispersion of

249 m/s, slightly below the average dispersion for Taurus-Auriga (298 m/s). Given a disk gap of ∼4 AU, a theoretical planet within that gap would have a period of ∼5.6 yrs, and would not be within detection limits. We can, however, exclude, with 95% confidence, >23 M_{Jup} companions with <4 day periods.

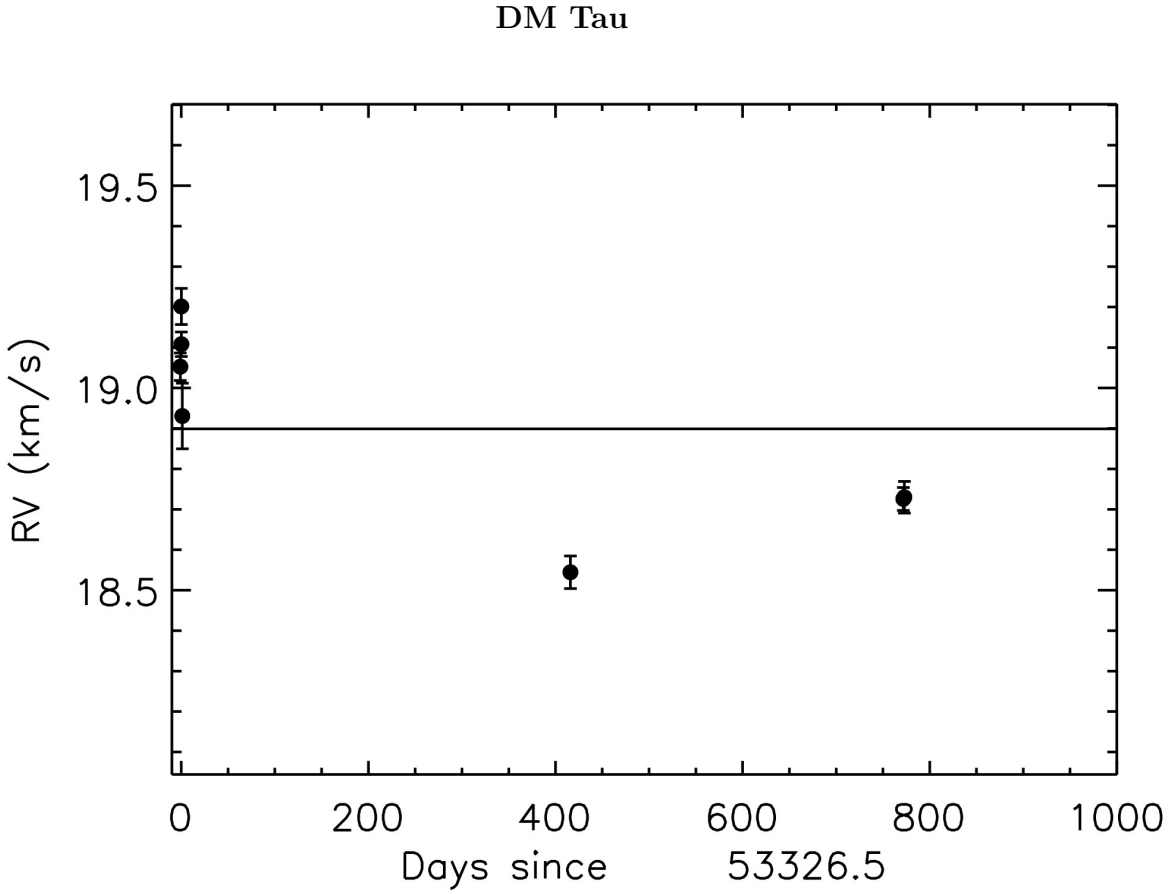

Figure 4.11 The RV curve is plotted with epoch errors for 6 observations.

CoKuTau 4 (K=8.656) is a M1.5 T Tauri star with a disk with no rotation period in the literature and a $v\sin i$ value of 26.6±0.55 km/s. D'Alessio et al. (2005) reported CoKuTau 4 to have a transitional disk of inclination i=50-75°. A later study by Ireland & Kraus (2008)

used adaptive optics to detect a stellar companion of equal mass at 53 mas (8 AU projected separation) within this disk.

We obtained 7 epochs on CokuTau 4 from November 2004 and January 2007. In Figure 4.12 we plot the RV curve for CokuTau 4. We see an RV range of 661 m/s and although the dispersion of CokuTau 4 (365 m/s) is above the average dispersion of Taurus-Auriga (298 m/s), this is far below what we would expect for stellar companion of ≈1-10 km/s. Using Equation 4.2, we calculate the maximum reflex motion for equal (0.5 $M_{\odot}$) mass stars at a separation of 8 AU (Ireland & Kraus 2008) assuming an inclination of 50-75° (D'Alessio et al. 2005). We would expect to see a maximum RV range of 5.4-6.9 km/s over the entire >10 yr (Ireland & Kraus 2008) orbit. We would expect that our observations taken over a 774 day period should show an RV trend and/or acceleration if a equal mass stellar companion was present, unless the system is in a face on orbit or is highly eccentric. Additionally, we were unable to see a second spectrum in the residuals of our fits, although the lack of a second spectrum may be due to the large $v\sin i$ (28 km/s), which broadens the spectral lines and would tend to blend with any companion spectrum. Nevertheless, we note that our observations only cover ∼20% of a 10 year orbit. We can, however, exclude, with 95% confidence, > 17 M_{Jup} companions with < 3 day periods.

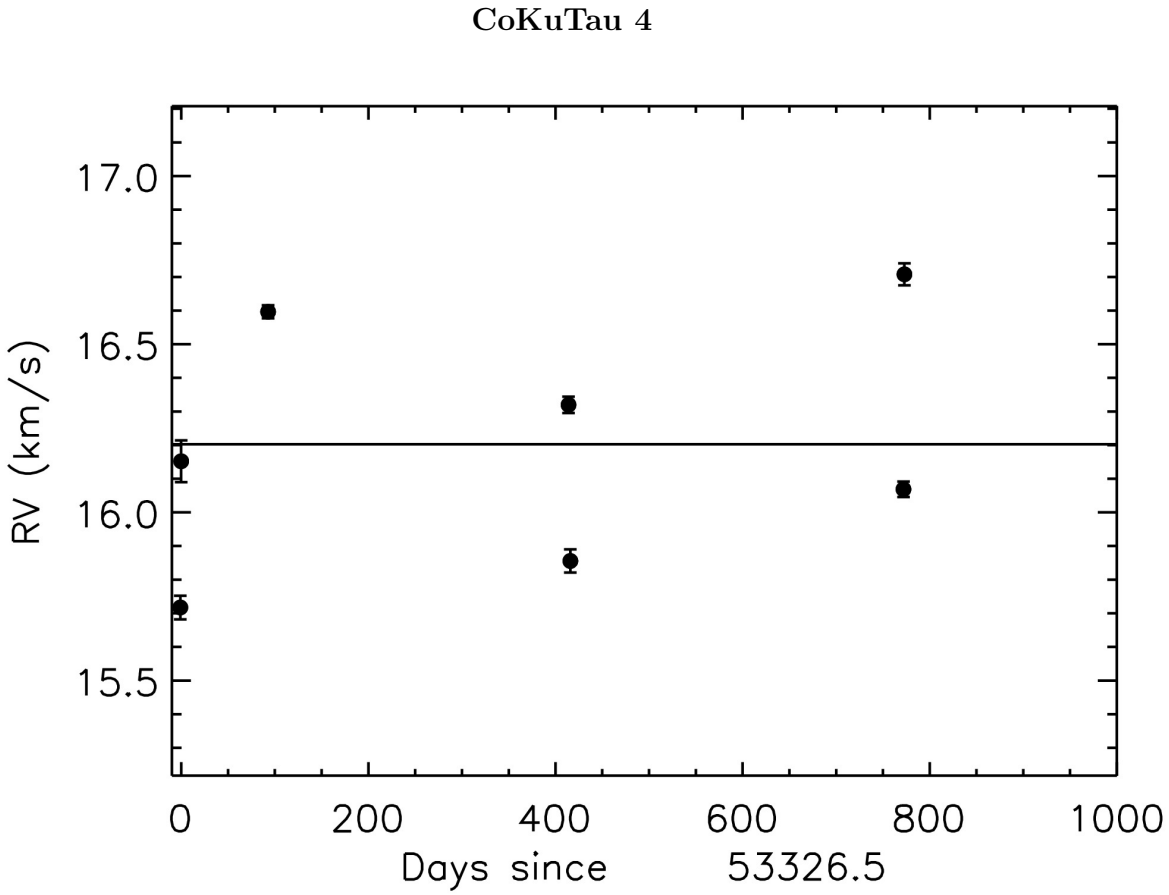

Figure 4.12 The RV curve is plotted with epoch errors for 7 observations.

GM Aurigae (K=8.283) is a K3 T Tauri star with a 12 day period (Bouvier et al. 1995) and a $v\sin i$ value of 13.88±0.30 km/s. The disk surrounding has an inclination of 56° (Dutrey et al. 1998), and it has been suggested that a gap in this disk may be due to a planet clearing a region of the disk. This disk gap has been estimated by several groups using differing methods. Koerner et al. (1993) estimated the gap to be ∼0.4 AU. Rice et al. (2003) suggested that the gap was at 4 AU and would be caused by a 2 M_J planet at 2.5 AU. Bergin et al. (2004) put the gap distance at 6 AU, and Calvet et al. (2005) modeled

a larger gap at 24 AU. Dutrey et al. (2008) report a gap at 19 AU which they posit to be caused by the formation of a low mass companion or planet at 5-15 AU.

We obtained 9 epochs of spectra observations of GM Aurigae between November 2004 and Jan 2007. In Figure 4.13 we plot the RV curve for GM Aurigae. Our results show large ($\sim$ 1 km /s) RV range over the time period sampled. However, with a dispersion of 344 m/s, this is only slightly above the average dispersion for Taurus-Auriga (298 m/s). We can, exclude, with 95% confidence, $>$ 10 M_{Jup} companions with $<$ 4 day periods.

We can estimate a reflex motion on a star by assuming a circular orbit and using a simple Keplerian orbit using Equation 4.2, where V_{obs} is the observed velocity with inclination i, $V_\star$ is the star's velocity, M_P is the mass of the planet, $M_\star$ is the stellar mass, G is the gravitational constant, and a is the semi-major axis. Given a disk inclination of $\sim$50° and a stellar mass of $\sim$1 $M_\odot$ (Dutrey et al. 2008) and assuming a theoretical companion orbiting at 5 AU with the same inclination as the disk, we would expect RV variations of $\sim$10 m/s for 1 M_J, $\sim$100 m/s for 10 M_J, and $\sim$500 m/s for 50 M_J companions. Although our average empirical RV precision for Keck NIRSPEC is 114 m/s, our observing program was designed to find short period (P $\approx$ 100 days) Jupiter-like planets, and as such, this would fall below our detection limits. Given a $v\sin i$ of 14.8 km/s, the short period, high RV dispersion shown in our data is more likely indicative of stellar activity than a companion.

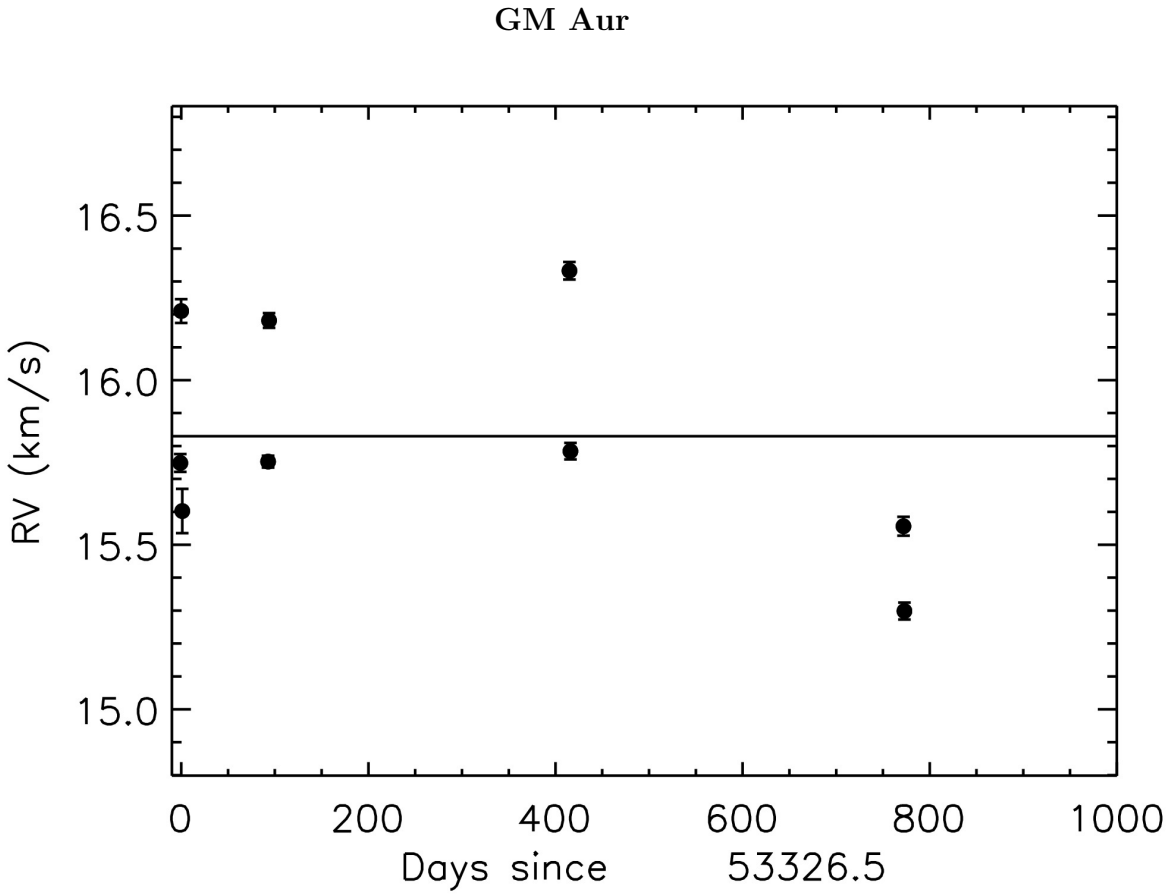

Figure 4.13 The RV curve is plotted with epoch errors for 9 observations.

CIDA 8 (K=9.597) is an M3.5 T Tauri star with a $v\sin i$ value of 29.55±1.03 km/s. We obtained 8 epochs of this star between November 2004 and December 2006 (see Figure 4.14. The RVs range 1.830 km/s over the observing period, and with a dispersion of 531 m/s, CIDA 8 displays a dispersion that is 1.8 times the average dispersion for Taurus-Auriga (298 m/s). Having the second highest $v\sin i$ value of the Taurus-Auriga sample, we expect this star to have a higher than average dispersion. A high $v\sin i$ value implies that it is rapidly rotating and, therefore more likely to have more chromospheric activity. However, in Figure

4.14 the RV for each epoch is shown, and the removal of the a single epoch (MDJ=53741; Day ∼414) changes the dispersion to 265 m/s. Both spectra of CIDA 8 taken on this date showed similar values for RV (17.54 km/s and 17.58 km/s), showed no evidence of cosmic ray hits, and had signal-to-noise values comparable to the rest of the observations (SNR≈200), but were lower than the average value (18.7 km/s) by ∼1.1 km/s. Additionally, observations taken the two following days were within 100 m/s of the average RV. Bailey et al. (2012) noted a similar event in their discussion on TWA 7, and we believe this deviation to likewise be caused by a short duration flare-like event.

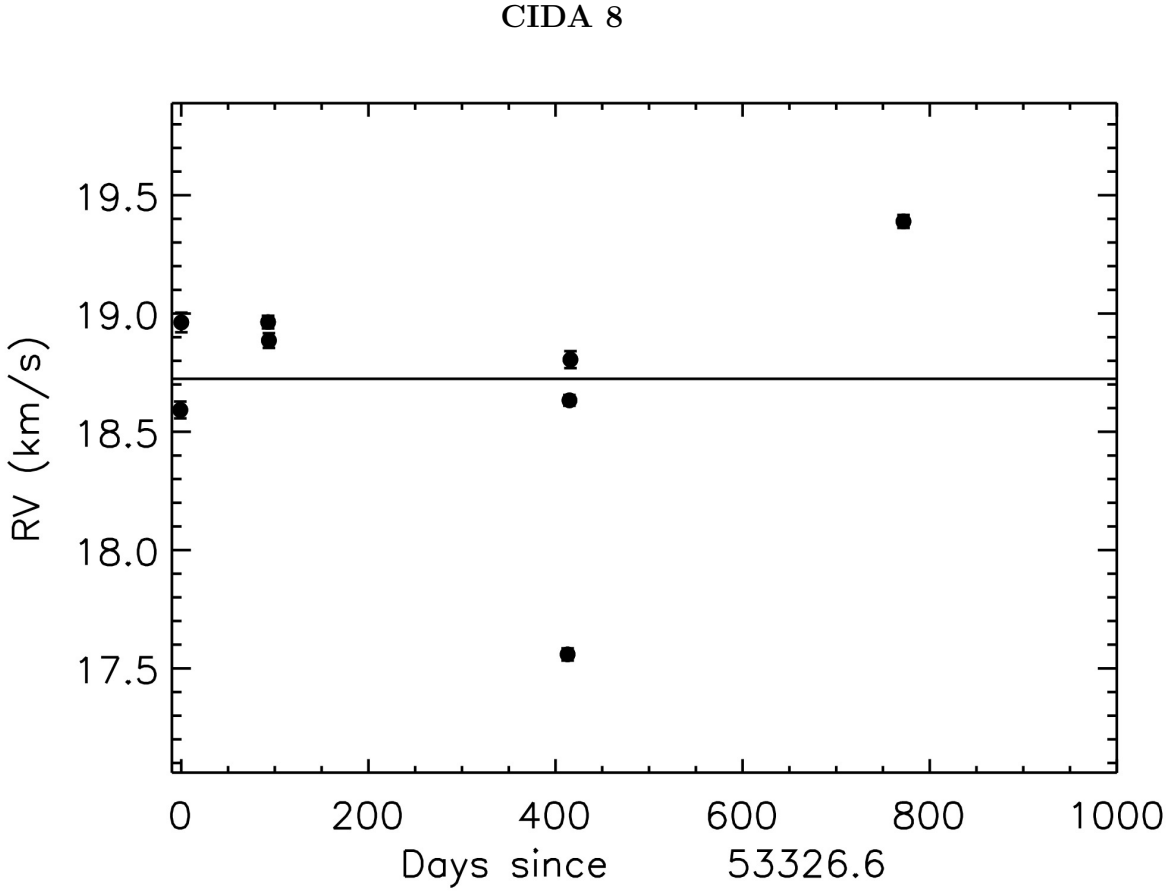

Figure 4.14 The RV curve is plotted with epoch errors for 8 observations.

CHAPTER 5

Habzone

5.1 Motivations for this Study

The work in the previous chapters was an effort to better understand giant planet formation and migration. If we can find Hot-Jupiter planets at a very young age, we can hope to constrain theories on the formation and migration of giant planets. This is important, because it has been posited that gas giant planets are necessary for terrestrial planets to be habitable, so long as they stay in outer orbits.

We do not yet have a detailed understanding of the architectures of all types of planetary systems orbiting various types of stars, although there has been recent progress for planets in close to stars orbital periods less than 50 days around FGKM stars. In this chapter we assume no bias in the final locations of planets around stars, including formation and migration (i.e., we assume the distribution of planets to be uniform in semi-major axis), to assess the integrated EHZs of various types of stars found in the solar neighborhood. We focus on the presence of the *first* habitable planet around a given star, although wider EHZs may of course include more than one planet. This is an important assessment to make given the limited telescope time, funding, and energy of astronomers, so here we focus on the question, "What set of targets might be most appropriate to observe to improve the odds of detecting at least one habitable planet?" This question is posed in wide-ranging arenas, from conversations between students and faculty when developing research projects, to discussions of programmatic directions such as those of NASA's Exoplanet Program Analysis Group and

the NASA/NSF Exoplanet Task Force.

In this chapter we evaluate stars within 10 pc in a consistent fashion to assess what spectral types offer the greatest promise for nearby habitable planets. The nearby sample contains stars that have been characterized carefully, and as a population provide the most accurate snapshot of the stellar content of the Galaxy. Thus, this sample provides the foundation for a realistic understanding of the relative merits of examining different types of stars. Our results, coupled with the planet frequency statistics from the Kepler mission, (e.g.,, Borucki & Koch 2011, Howard et al. 2012, and Dressing & Charbonneau 2013), can provide statistical measures for the of number of habitable planets within larger stellar populations, and particularly among volume-limited samples of nearby stars, as we build to a comprehensive sample of the nearest stars (e.g.,Henry et al. 2006 ; Henry 2012). For example, Howard et al. (2012) show that the number of super-Earth size planets increases with decreasing T_{eff} for orbital periods less than 50 days. Dressing & Charbonneau (2013) show that for cool stars ($T_{eff} < 4000$K) the occurrence rate for planets with 0.5-4 $R_{\oplus}$ is 0.9 planets per star for orbital periods less than 50 days. They also calculate that the lower limit on the occurrence rate of Earth-size planets in the HZ of cool stars is 0.04 with a 95% confidence. Using the population we describe here, this implies that there could be two Earth-size planets within the EHZs of M dwarfs within 5 pc of the Sun. Assuming a constant density of M dwarfs to 10 pc (not all of which have yet been identified) the number of Earth-size planets jumps to 16. One of the primary motivations of this study is to determine, in aggregate, how the odds of finding such planets around M dwarfs compares to other spectral

types.

The results of our habitable real estate calculations, as outlined in this chapter, are particularly valuable in highlighting that the ubiquitous M dwarfs provide many locales meeting the canonical definition for habitability. Current searches for habitable worlds orbiting the nearest stars have yielded many Jovian planets and a few terrestrial worlds, but most of the searches to date have been carried out using the radial velocity technique and have focused on bright FGK stars that provide many photons to spectrographs (and which are in the sweet spot for Kepler). For transit searches, M dwarfs provide higher contrast ratios for a given planet, whereas for radial velocity and astrometric searches they provide larger wobbles for a planet than do more massive FGK stars. Knowing that the M dwarfs, as a group, are important stars to search for habitable worlds helps direct our focus back to the solar neighborhood, in which three-quarters of all stars are red dwarfs. Because of their proximity, these stars hold great promise for the detailed characterization of exoplanets.

5.2 Properties of our Nearest Neighbors

Primary science goals of the Research Consortium on Nearby Stars (RECONS[1]) and the Center for High Angular Resolution Astronomy (CHARA[2]), are to find and determine the fundamental properties of our nearest stellar neighbors. This has led to the most complete assessment to date of stars within 5 pc of the Sun.

[1] `http://recons.org`
[2] `http://www.chara.gsu.edu/CHARA/`

5.2.1 The 5 pc Sample

The modern sample of all known stars and brown dwarfs within 5 pc of the Sun (Henry 2010; Henry 2012), listed in Table 5.1 (assembled photometry in Table 5.2) was first published in the *Observer's Handbook 2010*. The sample, which is updated yearly, was created using the combination of several ground-based and space-based parallax programs, including the General Catalogue of Trigonometric Stellar Parallaxes (van Altena et al. 1995), Hipparcos (Perryman et al. 1997), RECONS (Henry et al. 1997; Henry et al. 2006; Deacon et al. 2005; Jao et al. 2005; Costa et al. 2005), HST (Benedict et al. 1999; Benedict et al. 2002), Gatewood (1989), Gatewood (1994), and Gatewood et al. (1992). To be included in the sample, a system must have a weighted mean trigonometric parallax measurement of 200 mas or greater with an error of 10 mas or less. To create this sample the parallaxes compiled were combined and weighted based on the individual measurement errors. The spectral type, with reference, for each star or star system is given with the astrometric data, including RA, Dec, the weighted mean trigonometric parallax, and the number of parallaxes included in the weighted mean, in Table 5.1. The closing date for the sample is 2012.0.

Table 5.1: Five Parsec Sample

Name	LHS	RA 2000.0	DEC	π	err	# of π	SpType	Ref
Sun	···	···	···	···	···	···	G2.0V	···
GJ 1	1	00 05 24.4	−37 21 27	.23032	.00090	2	M1.5V	Hen10
GJ 1002	2	00 06 43.2	−07 32 17	.21300	.00360	1	M5.0V	Hen94
GJ 15 A	3	00 18 22.9	+44 01 23	.27987	.00060	3	M1.5V	Hen94
GJ 15 B	4	00 18 22.9	+44 01 23	.27987	.00060	3	M3.5V	Hen94
GJ 35	7	00 49 09.9	+05 23 19	.23270	.00181	2	DZ7	YPC95
GJ 54.1	138	01 12 30.6	−16 59 57	.26908	.00299	2	M4.5V	Hen94
GJ 65 A	9	01 39 01.3	−17 57 01	.37370	.00270	1	M5.5V	Hen94
GJ 65 B	10	01 39 01.3	−17 57 01	.37370	.00270	1	M6.0V	Hen94
GJ 71	146	01 44 04.1	−15 56 15	.27397	.00017	2	G8.5V	Gra06
GJ 83.1	11	02 00 13.2	+13 03 08	.22480	.00290	1	M4.5V	Hen94
SO 0253+1652	···	02 53 00.9	+16 52 53	.25941	.00089	3	M7.0V	Hen04
DEN 0255-4700	···	02 55 03.7	−47 00 52	.20137	.00389	1	L7.5V	Cos06
GJ 144	1557	03 32 55.8	−09 27 30	.31122	.00009	3	K2.0V	Gra06
GJ 1061	1565	03 36 00.0	−44 30 46	.27201	.00130	2	M5.0V	Hen06
LP 944-020	···	03 39 35.2	−35 25 41	.20140	.00421	1	M9.0V	Sch07
GJ 166 A	23	04 15 16.3	−07 39 10	.20065	.00023	2	K0.5V	Gra06
GJ 166 B	24	04 15 22.0	−07 39 35	.20065	.00023	2	DA4	CNS91
GJ 166 C	25	04 15 22.0	−07 39 35	.20065	.00023	2	M4.5V	Hen94
GJ 191	29	05 11 40.6	−45 01 06	.25567	.00091	2	M2.0VI	Jao08

Table 5.1: Five Parsec Sample

Name	LHS	RA 2000.0	DEC	π	err	# of π	SpType	Ref
GJ 234 A	1849	06 29 23.4	−02 48 50	.24444	.00092	3	M4.0V	Mon01
GJ 234 B	1850	06 29 23.4	−02 48 50	.24444	.00092	3	M5.5V	Rei04
GJ 244 A	219	06 45 08.9	−16 42 58	.38002	.00128	2	A1.0V	Joh53
GJ 244 B	···	06 45 08.9	−16 42 58	.38002	.00128	2	DA2	CNS91
GJ 273	33	07 27 24.5	+05 13 33	.26623	.00066	3	M3.5V	Hen94
GJ 280 A	233	07 39 18.1	+05 13 30	.28517	.00064	4	F5.0IV−V	Gra01
GJ 280 B	···	07 39 18.1	+05 13 30	.28517	.00064	4	DA	CNS91
GJ 1111	248	08 29 49.5	+26 46 37	.27580	.00300	1	M6.0V	Rei95
GJ 380	280	10 11 22.1	+49 27 15	.20553	.00049	2	K7.0V	Hen94
GJ 388	5167	10 19 36.4	+19 52 10	.20460	.00280	1	M3.0V	Hen94
LHS 288	288	10 44 21.2	−61 12 36	.20970	.00265	2	M5.5V	Hen04
LHS 292	292	10 48 12.6	−11 20 14	.22030	.00360	1	M6.5V	Rei95
DEN 1048-3956	···	10 48 14.6	−39 56 07	.24853	.00118	3	M8.5V	Hen04
GJ 406	36	10 56 29.2	+07 00 53	.41910	.00210	1	M6.0V	Hen94
GJ 411	37	11 03 20.2	+35 58 12	.39325	.00057	2	M2.0V	Hen94
GJ 412 A	38	11 05 28.6	+43 31 36	.20567	.00093	2	M1.0V	Hen94
GJ 412 B	39	11 05 30.4	+43 31 18	.20567	.00093	2	M5.5V	Hen94
GJ 440	43	11 45 42.9	−64 50 29	.21612	.00109	3	DQ6	CNS91
GJ 447	315	11 47 44.4	+00 48 16	.29814	.00137	2	M4.0V	Hen94
GJ 473 A	333	12 33 17.2	+09 01 15	.22790	.00460	1	M5.0V	Hen10

Table 5.1: Five Parsec Sample

Name	LHS	RA 2000.0	DEC	π	err	# of π	SpType	Ref
GJ 473 B	···	12 33 17.2	+09 01 15	.22790	.00460	1	M7.0V	CNS91
GJ 551	49	14 29 43.0	−62 40 46	.76885	.00029	4	M5.0V	CNS91
GJ 559 A	50	14 39 36.5	−60 50 02	.74723	.00117	1	G2.0V	Gra06
GJ 559 B	51	14 39 35.1	−60 50 14	.74723	.00117	1	K0.0V	CNS91
GJ 628	419	16 30 18.1	−12 39 45	.23438	.00150	2	M3.0V	Hen94
GJ 674	449	17 28 39.9	−46 53 43	.22011	.00139	2	M2.5V	Mon01
GJ 687	450	17 36 25.9	+68 20 21	.22047	.00083	2	M3.0V	Hen94
GJ 699	57	17 57 48.5	+04 41 36	.54551	.00029	2	M4.0V	Hen94
GJ 725 A	58	18 42 46.7	+59 37 49	.28383	.00146	3	M3.0V	Hen94
GJ 725 B	59	18 42 46.9	+59 37 37	.28383	.00146	3	M3.5V	Hen94
SCR 1845-6357 A	···	18 45 02.6	−63 57 52	.25950	.00111	2	M8.5V	Hen04
SCR 1845-6357 B	···	18 45 02.6	−63 57 52	.25950	.00111	2	T5.5V	Bil06
GJ 729	3414	18 49 49.4	−23 50 10	.33722	.00197	2	M3.5V	Hen10
GJ 1245 A	3494	19 53 54.2	+44 24 55	.22020	.00100	1	M5.5V	Hen94
GJ 1245 B	3495	19 53 55.2	+44 24 56	.22020	.00100	1	M6.0V	Hen94
GJ 1245 C	···	19 53 54.2	+44 24 55	.22020	.00100	1	M7.0V	Rei04
GJ 820 A	62	21 06 53.9	+38 44 58	.28608	.00048	3	K5.0V	Hen94
GJ 820 B	63	21 06 55.3	+38 44 31	.28608	.00048	3	K7.0V	Hen94
GJ 825	66	21 17 15.3	−38 52 03	.25344	.00080	2	M0.0V	Tor06
GJ 832	3685	21 33 34.0	−49 00 32	.20203	.00100	2	M1.5V	Joh10

Table 5.1: Five Parsec Sample

Name	LHS	RA 2000.0	DEC	π	err	# of π	SpType	Ref
GJ 845 A	67	22 03 21.7	−56 47 10	.27607	.00028	2	K4.0V	Gra06
GJ 845 B	···	22 04 10.5	−56 46 58	.27607	.00028	2	T1.0V	McC04
GJ 845 C	···	22 04 10.5	−56 46 58	.27607	.00028	2	T6.0V	McC04
GJ 860 A	3814	22 27 59.5	+57 41 45	.24806	.00139	2	M3.0V	Hen94
GJ 860 B	3815	22 27 59.5	+57 41 45	.24806	.00139	2	M4.0V	Hen94
GJ 866 A	68	22 38 33.4	−15 18 07	.28950	.00440	1	M5.0V	Hen02
GJ 866 B	···	22 38 33.4	−15 18 07	.28950	.00440	1	M	···
GJ 866 C	···	22 38 33.4	−15 18 07	.28950	.00440	1	M	···
GJ 876	530	22 53 16.7	−14 15 49	.21447	.00057	3	M4.0V	Mon01
GJ 887	70	23 05 52.0	−35 51 11	.30508	.00070	2	M2.0V	Tor06
GJ 905	549	23 41 55.0	+44 10 38	.31637	.00055	3	M5.5V	Hen94

Bil06 Biller et al. (2006)
CNS91 Gliese & Jahreiß (1991)
Cos06 Costa et al. (2006)
Gra01 Gray et al. (2001)
Gra06 Gray et al. (2006)
Hen94 Henry et al. (1994)
Hen02 Henry et al. (2002a)
Hen04 Henry et al. (2004)
Hen06 Henry et al. (2006)
Hen10 Henry (2010)
Jao08 Jao et al. (2008)
Joh53 Johnson & Morgan (1953)
Joh10 Johnson et al. (2010)
McC04 McCaughrean et al. (2004)
Mon01 Montes et al. (2001)
Rei95 Reid et al. (1995)
Rei04 Reid et al. (2004)
Sch07 Schmidt et al. (2007)
Tor06 Torres et al. (2006)
YPC95 van Altena et al. (1995)

Table 5.2: Five Parsec Sample: Photometry

Name	U	Uref	B	Bref	V	Vref	R	Rref	I	Iref	J	err	H	err	K	err	Notes
Sun	−25.97	A95	−26.10	A95	−26.75	A95	−27.27	A95	−27.56	A95	−27.928	A95	−28.211	A95	−28.274	A95	···
GJ 1	···	···	10.02	B90	8.54	B90	7.57	B90	6.41	B90	5.328	0.019	4.828	0.076	4.523	0.017	···
GJ 1002	17.61	Le92	15.73	W96	13.77	B91	12.16	B91	10.15	B91	8.323	0.019	7.792	0.034	7.439	0.021	···
GJ 15 A	10.87	Le92	9.63	Le92	8.08	Le92	···	···	5.94	Le92	5.252	0.264	4.476	0.200	4.018	0.020	···
GJ 15 B	14.26	Le92	12.88	W96	11.06	W96	9.83	W96	8.24	W96	6.789	0.024	6.191	0.016	5.948	0.024	···
GJ 35	···	···	12.94	B90	12.40	B90	12.14	B90	11.91	B90	11.688	0.022	11.572	0.024	11.498	0.025	···
GJ 54.1	15.24	Le92	13.95	B90	12.10	B90	10.73	B90	8.95	B90	7.258	0.020	6.749	0.033	6.420	0.017	···
GJ 65 A	14.96	Le92	13.95	B90	12.61*	H99	10.40	B90	8.34	B90	6.86*	H93	6.30*	H93	5.91*	H93	joint UBRI
GJ 65 B	···	···	···	···	13.06*	H99	···	···	···	···	7.24*	H93	6.60*	H93	6.31*	H93	···
GJ 71	4.42	J66	4.21	B90	3.49	B90	3.06	B90	2.67	B90	2.06	J66	1.800	0.234	1.68	J66	···
GJ 83.1	15.47	Le92	14.14	B90	12.31	B90	10.95	B90	9.21	B90	7.514	0.017	6.970	0.027	6.648	0.017	···
SO 0253+1652	···	···	···	···	15.13	H06	13.03	H06	10.65	H06	8.394	0.027	7.883	0.040	7.585	0.046	···
DEN 0255-4700	···	···	···	···	22.92	C06	19.90	C06	17.45	C06	13.246	0.027	12.204	0.024	11.558	0.024	···
GJ 144	···	···	4.61	B90	3.73	B90	3.22	B90	2.79	B90	2.20	G75	1.75	G75	1.65	G75	···
GJ 1061	···	···	···	···	13.09	H06	11.45	H06	9.46	H06	7.523	0.020	7.015	0.044	6.610	0.021	···
LP 944-020	···	···	···	···	···	···	···	···	13.29	D07	10.725	0.021	10.017	0.021	9.548	0.023	···
GJ 191	···	···	10.41	B90	8.85	B90	7.90	B90	6.90	B90	5.821	0.025	5.316	0.027	5.049	0.021	···
GJ 234 A	14.03	Le92	12.81	B90	11.18*	H99	9.78	B90	8.08	B90	6.57*	H93	5.97*	H93	5.73*	H93	joint UBRI
GJ 234 B	···	···	···	···	14.26*	H99	···	···	···	···	8.36*	H93	7.60*	H93	7.23*	H93	···
GJ 244 AB	−1.4 1	J66	−1.43	B90	−1.43	B90	−1.42	B90	−1.41	B90	−1.391	0.109	−1.391	0.184	−1.390	0.214	joint
GJ 273	12.59	W93	11.42	B90	9.85	B90	8.70	B90	7.16	B90	5.714	0.032	5.219	0.063	4.857	0.022	···
GJ 280 AB	0.82	J66	0.79	B90	0.37	B90	0.12	B90	−0.12	B90	−0.40	G75	−0.60	G75	−0.65	G75	joint
GJ 1111	···	···	16.95	B90	14.90	B90	12.90	B90	10.64	B90	8.235	0.021	7.617	0.018	7.260	0.024	···
GJ 380	9.25	Le92	7.97	Le92	6.59	Le92	5.74	Le92	4.97	Le92	3.98	G75	3.32	G75	3.19	G75	···
GJ 388	11.91	Le92	10.85	Le92	9.32	Le92	8.23	Le92	6.81	Le92	5.449	0.027	4.843	0.020	4.593	0.017	···
LHS 288	···	···	···	···	13.92	B91	12.33	B91	10.31	B91	8.492	0.021	8.054	0.044	7.728	0.027	···
LHS 292	···	···	17.70	Le92	15.73	B91	13.67	B91	11.33	B91	8.857	0.021	8.263	0.036	7.926	0.033	···
DEN 1048-3956	···	···	···	···	17.39	J05	15.05	J05	12.55	J05	9.538	0.022	8.905	0.044	8.447	0.023	···
GJ 406	17.03	Le92	15.52	B90	13.53	B90	11.67	B90	9.50	B90	7.085	0.024	6.482	0.042	6.084	0.017	···
GJ 411	10.12	Le92	8.98	Le92	7.47	Le92	6.46	Le92	5.32	Le92	4.13	G75	3.56	G75	3.20	G75	···
GJ 412 A	11.48	Le92	10.34	W96	8.77	W96	7.79	W96	6.70	W96	5.538	0.019	5.002	0.021	4.769	0.020	···
GJ 412 B	···	···	16.53	B90	14.44	B90	12.77	B90	10.68	B90	8.742	0.025	8.177	0.024	7.839	0.026	···

Table 5.2: Five Parsec Sample: Photometry

Name	U	Uref	B	Bref	V	Vref	R	Rref	I	Iref	J	err	H	err	K	err	Notes
GJ 440	11.04	La92	11.68	La92	11.50	S09	11.34	S09	11.20	S09	11.188	0.024	11.130	0.025	11.104	0.026	···
GJ 447	14.22	Le92	12.92	B90	11.16	B90	9.85	B90	8.17	B90	6.505	0.023	5.945	0.024	5.654	0.024	···
GJ 473 A	···	···	15.06*	T99	13.25*	T99	···	···	···	···	7.69*	T99	7.06*	T99	6.59*	T99	···
GJ 473 B	···	···	15.11*	T99	13.24*	T99	···	···	···	···	7.82*	T99	7.26*	T99	7.03*	T99	···
GJ 551	14.36	Le92	12.88	B90	11.05	B90	9.43	B90	7.43	B90	5.357	0.023	4.835	0.057	4.384	0.033	···
GJ 559 A	···	···	0.64	B90	0.01	B90	−0.35	B90	−0.68	B90	···	···	···	···	···	···	···
GJ 559 B	···	···	2.18	B90	1.34	B90	0.87	B90	0.46	B90	···	···	···	···	···	···	···
GJ 628	12.82	W93	11.68	B90	10.10	B90	8.94	B90	7.42	B90	5.950	0.024	5.373	0.040	5.075	0.024	···
GJ 674	···	···	10.90	B90	9.37	B90	8.30	B90	6.97	B90	5.711	0.019	5.154	0.033	4.855	0.018	···
GJ 687	11.76	Le92	10.64	W96	9.17	W96	8.08	W96	6.68	W96	5.335	0.021	4.766	0.033	4.548	0.021	···
GJ 699	12.54	Le92	11.31	B90	9.57	B90	8.35	B90	6.79	B90	5.244	0.020	4.834	0.034	4.524	0.020	···
GJ 725 A	11.55	Le92	10.42	W96	8.90	W96	7.83	W96	6.48	W96	5.189	0.017	4.741	0.036	4.432	0.020	···
GJ 725 B	12.41	Le92	11.28	W96	9.69	W96	8.57	W96	7.13	W96	5.721	0.020	5.197	0.024	5.000	0.022	···
SCR 1845-6357 AB	···	···	···	···	17.39	H06	14.99	H06	12.46	H06	9.544	0.023	8.967	0.027	8.508	0.020	joint
GJ 729	···	···	12.18	B90	10.44	B90	9.21	B90	7.65	B90	6.222	0.018	5.655	0.034	5.370	0.016	···
GJ 1245 A	···	···	15.31	Le92	13.46*	H99	11.81	W96	9.78	W96	8.09*	H93	7.53*	H93	7.21*	H93	joint BRI
GJ 1245 C	···	···	···	···	16.75*	H99	···	···	···	···	9.35*	H93	8.61*	H93	8.24*	H93	···
GJ 1245 B	···	···	15.98	Le92	14.01	W96	12.36	W96	10.27	W96	8.275	0.025	7.728	0.031	7.387	0.018	···
GJ 820 A	8.63	J66	7.40	J66	6.03	J66	4.86	J66	4.03	J66	3.114	0.268	2.540	0.198	2.248	0.318	···
GJ 820 B	8.62	Le92	7.40	Le92	6.03	Le92	···	···	4.41	Le92	3.546	0.278	2.895	0.218	2.544	0.328	···
GJ 825	9.29	Le192	8.09	B90	6.67	B90	5.77	B90	4.91	B90	3.915	M76	3.270	M76	3.075	M76	···
GJ 832	11.36	Le92	10.18	B90	8.66	B90	7.66	B90	6.47	B90	5.349	0.032	4.766	0.256	4.501	0.018	···
GJ 845 A	6.74	J66	5.73	B90	4.68	B90	4.06	B90	3.53	B90	2.894	0.292	2.349	0.214	2.237	0.240	···
GJ 845 BC	···	···	···	···	···	···	···	···	···	···	11.010	0.020	11.306	0.024	11.208	0.024	joint
GJ 860 A	···	···	···	···	9.86*	H93	···	···	···	···	5.91*	H93	5.33*	H93	5.02*	H93	···
GJ 860 B	···	···	···	···	11.41*	H93	···	···	···	···	7.10*	H93	6.47*	H93	6.39*	H93	···
GJ 866 AC	15.83	Le92	14.33	B90	12.94*	H99	10.70	B90	8.64	B90	7.06*	L90	6.46*	L90	6.05*	L90	joint UBRI
GJ 866 B	···	···	···	···	13.34*	H99	···	···	···	···	7.62*	L90	7.02*	L90	6.61*	L90	···
GJ 876	12.90	W93	11.76	B90	10.18	B90	9.00	B90	7.43	B90	5.934	0.019	5.349	0.049	5.010	0.021	···
GJ 887	···	···	8.84	B90	7.34	B90	6.37	B90	5.32	B90	4.338	0.258	3.608	0.230	3.465	0.200	···
GJ 905	15.65	Le92	14.20	W96	12.29	W96	10.77	W96	8.82	W96	6.884	0.025	6.247	0.027	5.929	0.020	···
GJ 166 A	···	···	···	···	4.43	B90	3.96	B90	3.54	B90	3.013	0.238	2.594	0.198	2.498	0.236	···

Table 5.2: Five Parsec Sample: Photometry

Name	U	Uref	B	Bref	V	Vref	R	Rref	I	Iref	J	err	H	err	K	err	Notes
GJ 166 B	8.88	K91	9.56	K91	9.53	K91	···	···	···	···	9.849	0.029	9.986	0.039	9.861	0.071	···
GJ 166 C	···	···	12.84	R04	11.17	R04	···	···	···	···	6.747	0.020	6.278	0.040	5.962	0.026	···

JHK & err from 2MASS unless otherwise noted.
* deconvolved using flux ratios from references given and available optical and infrared photometry
"joint" indicates unresolved photometry.
A95 Alonso et al. (1995)
B90 Bessel (1990)
B91 Bessell (1991)
C06 Costa et al. (2006)
D07 Deacon & Hambly (2007)
G75 Glass (1975)
H93 Henry & McCarthy (1993)
H99 Henry et al. (1999)
H06 Henry et al. (2006)
J05 Jao et al. (2005)
J66 Johnson et al. (1966)
K91 Kidder et al. (1991)
La92 Landolt (1992)
Le92 Leggett (1992)
L90 Leinert et al. (1990)
M76 Mould & Hyland (1976)
R04 Reid et al. (2004)
S09 Subasavage et al. (2009)
W93 Weis (1993)
W96 Weis (1996)
T99 Torres et al. (1999)

The 5 pc sample contains 67 stars, including the Sun, and 4 presumed brown dwarfs (spectral types L or T) in 50 systems. Of the 50 systems, 34 are single, 11 are binaries, and 5 are triples, giving a multiplicity fraction of 32%. This fraction is consistent with previous volume limited surveys (35%; Reid & Gizis 1997). The majority (85%) of the sample are main sequence stars; the exceptions include Procyon (GJ 280A), which has a slightly evolved spectral type of F5IV-V, 5 white dwarfs, and the 4 L/T dwarfs. The spectral type breakdown includes 1 A, 1 F, 3 G's (including the Sun), 7 K's, 50 M's, 1 L, 3 T's, and 5 white dwarfs. We do not include white dwarfs and brown dwarfs in subsequent calculations of habitable real estate, as they are objects that are cooling continually, resulting in unsustainable HZs on long (∼Gyr) timescales.

5.2.2 An Estimated 10 pc Sample

Due to the sparse population of all but the M stars in the 5 pc sample, it is difficult to draw meaningful statistics to estimate which stellar spectral types possess the most habitable real estate. Therefore, we extend our sample to 10 pc for A, F, G and K stars. Using the Hipparcos Catalog, which is complete to V=9 (Perryman et al. 1997) , we selected all objects with a parallax greater than 100 mas for inclusion into the sample. We expect that the extended 10 pc sample is complete for spectral types A through K, given M_v=9.0 for a M0.0V star (Henry et al. 2006). However, rather than using spectral type as a selection criterion, we used a color cutoff of $V - K \leq 3.5$ as the dividing line between K and M dwarfs (Kenyon & Hartmann 1995). As with the 5 pc sample, weighted mean parallaxes from the General Catalogue of Trigonometric Stellar Parallaxes, The Hipparcos Catalog and other

sources are listed with the astrometry data for the extended 10 pc sample in Table 5.3, as well as spectral types and references. Available photometric data are listed in Table 5.4. We note that there are no O type or B type stars within 10 pc. Because the M star population is not complete out to 10 pc (Henry et al. 2006), we approximate the total M star population by scaling by a factor of eight from the 5 pc sample. For clarity, we refer to the additional AFGK stars from 5-10 pc as the "extended 10 pc sample" and our estimates of all AFGKM stars within 10 pc as the "estimated 10 pc sample". In total, the stellar population of the estimated 10 pc sample consists of 66 AFGK stars in 57 systems. Broken down by spectral type, the sample contains 4 A stars, 6 F stars, 21 G stars, 35 K stars and an estimated 400 M stars within 10 pc.

Name	LHS	RA 2000.0	DEC	π	err	# of π	SpType	Ref
GJ 17	5	00 20 04.2	−64 52 29	.11647	.00016	2	F9.5V	Gra06
GJ 19	6	00 25 45.1	−77 15 15	.13407	.00011	2	G0.0V	Gra06
GJ 33	121	00 48 23.0	+05 16 50	.13426	.00049	2	K2.5V	Gra06
GJ 34 A	123	00 49 06.3	+57 48 55	.16823	.00046	2	G3.0V	Mon01
GJ 53 A	8	01 08 16.4	+54 55 13	.13267	.00074	2	G5.0V	Joh53
GJ 66 A	···	01 39 47.6	−56 11 47	.12999	.00208	2	K5.0V	Mon01
GJ 66 B	···	01 39 47.6	−56 11 36	.12999	.00208	2	K5.0V	Mon01
GJ 68	1287	01 42 29.8	+20 16 07	.13275	.00049	2	K1.0V	Gra06
GJ 105 A	15	02 36 04.9	+06 53 13	.13906	.00044	2	K3.0V	Gra06
GJ 139	19	03 19 55.7	−43 04 11	.16547	.00019	2	G8.0V	Pas94
GJ 150	1581	03 43 14.9	−09 45 48	.11063	.00022	2	K1.0III-IV	Gra06
GJ 178	···	04 49 50.4	+06 57 41	.12393	.00017	2	F6.0V	Mon01
GJ 183	200	05 00 49.0	−05 45 13	.11477	.00048	2	K3.0V	CNS91
GJ 216 A	···	05 44 27.8	−22 26 54	.11204	.00018	2	F6.0V	Mon01
GJ 216 B	···	05 44 26.5	−22 25 19	.11204	.00018	2	K2.0V	CNS91
GJ 222 A	···	05 54 23.0	+20 16 34	.11522	.00025	3	G0.0V	CNS91
GJ 250 A	1875	06 52 18.1	−05 10 25	.11465	.00043	2	K3.0V	CNS91
GJ 423 A	2390	11 18 10.9	+31 31 45	.11951	.00079	2	G0.0V	Bat89
GJ 423 B	2391	11 18 11.0	+31 31 46	.11951	.00079	2	G5.0V	Bat89

Name	LHS	RA 2000.0	DEC	π	err	# of π	SpType	Ref
GJ 432 A	308	11 34 29.5	−32 49 53	.10461	.00037	2	K0.0V	CNS91
GJ 434	···	11 41 03.0	+34 12 06	.10416	.00026	2	G8.0V	CNS91
GJ 442 A	311	11 46 31.1	−40 30 01	.10844	.00022	2	G2.0V	Gra06
GJ 451	44	11 52 58.8	+37 43 07	.11013	.00040	2	G8.0V	Joh53
GJ 475	2579	12 33 44.5	+41 21 27	.11848	.00020	2	G0.0V	CNS91
GJ 502	348	13 11 52.4	+27 52 41	.10952	.00017	2	G0.0V	CNS91
GJ 506	349	13 18 24.3	−18 18 40	.11690	.00022	2	G7.0V	Gra06
GJ 566 A	···	14 51 23.4	+19 06 02	.14757	.00072	2	G8.0V	Ruc95
GJ 566 B	···	14 51 23.4	+19 06 02	.14757	.00072	2	K4.0V	Mon99
GJ 570 A	387	14 57 28.0	−21 24 56	.17062	.00067	3	K4.0V	Gra06
GJ 631	3224	16 36 21.4	−02 19 29	.10249	.00040	2	K2.0V	Mon01
GJ 638	···	16 45 06.4	+33 30 33	.10195	.00070	2	K7.0V	CNS91
GJ 663 A	437	17 15 20.9	−26 36 09	.16812	.00040	4	K1.0V	CNS91
GJ 663 B	438	17 15 21.0	−26 36 10	.16812	.00040	4	K1.0V	CNS91
GJ 664(C)*	439	17 16 13.4	−26 32 46	.16812	.00040	4	K5.0V	CNS91
GJ 667 A	442	17 18 57.2	−34 59 23	.13822	.00070	2	K3.0V	CNS91
GJ 667 B	443	17 19 01.9	−34 59 33	.13822	.00070	2	K5.0V	CNS91
GJ 666 A	444	17 19 03.8	−46 38 10	.11371	.00069	2	G8.0V	CNS91
GJ 673	447	17 25 45.2	+02 06 41	.12987	.00071	2	K7.0V	CNS91

Name	LHS	RA 2000.0	DEC	π	err	# of π	SpType	Ref
GJ 695 A	3326	17 46 27.5	+27 43 14	.12032	.00016	2	G5.0IV	CNS91
GJ 702 A	458	18 05 27.4	+02 29 59	.19596	.00087	2	K0.0V	CNS91
GJ 702 B	459	18 05 27.4	+02 29 56	.19596	.00087	2	K5.0V	CNS91
GJ 713 A	3379	18 21 03.4	+72 43 58	.12343	.00044	3	F7.0V	CNS91
GJ 713 B	···	18 21 03.4	+72 43 58	.12343	.00044	3	G8.0V	Far10
GJ 721	···	18 36 56.3	+38 47 01	.12985	.00032	3	A0.0V	CNS91
GJ 764	447	19 32 21.6	+69 39 40	.17379	.00018	2	K0.0V	CNS91
GJ 768	3490	19 50 47.0	+08 52 06	.19540	.00046	3	A7.0V	CNS91
GJ 780	485	20 08 43.6	−66 10 55	.16371	.00017	2	G8.0IV	Gra06
GJ 783 A	486	20 11 11.9	−36 06 04	.16626	.00027	2	K2.5V	Gra06
GJ 785	488	20 15 17.4	−27 01 59	.11222	.00030	2	K2.0V	Gra06
GJ 827	3674	21 26 26.6	−65 21 58	.10797	.00019	2	F9.0V	Gra06
GJ 881(A)	···	22 57 39.0	−29 37 20	.13042	.00037	4	A4.0V	Gra06
GJ 879(B)*	···	22 56 24.1	−31 33 56	.13042	.00037	4	K5.0V	CNS91
GJ 884	3885	23 00 16.1	−22 31 28	.12175	.00069	2	K7.0V	Gra06
GJ 892	71	23 13 17.0	+57 10 06	.15284	.00028	2	K3.0V	CNS91

* Designates component to above system with different GJ number.
Bat89 Batten et al. (1989)

CNS91 Gliese & Jahreiß (1991)
Far10 Farrington et al. (2010)
Gra06 Gray et al. (2006)
Mon99 Montes et al. (1999)
Mon01 Montes et al. (2001)
Pas94 Pasquini et al. (1994)
Ruc95 Ruck & Smith (1995)
Joh53 Johnson & Morgan (1953)

Table 5.4: Extended Ten Parsec Sample: Photometry

Name	U	Uref	B	Bref	V	Vref	R	Rref	I	Iref	J	err	H	err	K	err	Notes
GJ 17	4.82	Joh66	4.80	Bes90	4.22	Bes90	3.89	Bes90	3.57	Bes90	3.17	Gla75	2.87	Gla75	2.78	Gla75	···
GJ 19	3.53	Joh66	3.42	Bes90	2.80	Bes90	2.45	Bes90	2.12	Bes90	1.72	Gla75	1.40	Gla75	1.32	Gla75	···
GJ 33	···	···	6.60	Bes90	5.72	Bes90	5.21	Bes90	4.76	Bes90	4.24	Joh68	3.72	Joh68	3.48	Joh68	···
GJ 34 A	4.04	Joh66	4.02	Joh66	3.44	Joh66	3.1	USNOB	2.8	USNOB	2.109	0.570	2.086	0.504	1.988	···	···
GJ 53 AB	5.96	Joh66	5.87	Joh66	5.18	Joh66	4.7	USNOB	4.4	USNOB	3.86	Joh68	3.39	Joh68	3.36	Joh68	joint
GJ 66 A	···	···	6.69	Hog00	5.80	Hog00	···	···	···	···	4.043	0.378	···	···	3.510	0.282	···
GJ 66 B	···	···	6.84	Mer86	5.96	Mer86	···	···	···	···	3.573	···	···	···	3.558	0.270	···
GJ 68	6.57	Joh66	6.08	Joh66	5.24	Joh66	4.7	USNOB	4.3	USNOB	3.855	0.24	3.391	0.226	3.285	0.266	···
GJ 105 AC	···	···	6.78	Bes90	5.81	Bes90	5.24	Bes90	4.74	Bes90	4.07	Gla75	3.52	Gla75	3.45	Gla75	joint
GJ 139	5.19	Joh66	4.97	Bes90	4.26	Bes90	3.85	Bes90	3.47	Bes90	2.95	Gla75	2.59	Gla75	2.52	Gla75	···
GJ 150	···	···	4.45	Bes90	3.53	Bes90	3.03	Bes90	2.59	Bes90	1.99	Gla75	1.53	Gla75	1.45	Gla75	···
GJ 178	3.64	Joh66	3.65	Bes90	3.19	Bes90	2.92	Bes90	2.67	Bes90	2.35	Gla75	2.15	Gla75	2.07	Gla75	···
GJ 183	···	···	7.29	Bes90	6.23	Bes90	5.44	Bes90	4.69	Bes90	4.389	0.244	3.797	0.214	3.706	0.228	···
GJ 216 A	4.07	Joh66	4.06	Bes90	3.59	Bes90	3.30	Bes90	3.02	Bes90	2.804	0.276	2.606	0.236	2.508	0.228	···
GJ 216 B	···	···	7.12	Bes90	6.18	Bes90	5.63	Bes90	5.17	Bes90	4.845	0.198	4.158	0.202	4.131	0.264	···
GJ 222 AB	5.04	Joh66	5.00	Joh66	4.41	Joh66	4.0	USNOB	3.8	USNOB	3.34	Joh68	3.04	Joh68	2.97	Joh68	joint
GJ 250 A	···	···	7.64	Bes90	6.59	Bes90	5.98	Bes90	5.45	Bes90	5.013	0.252	4.294	0.258	4.107	0.036	···
GJ 423 AC	···	···	4.78	Lep05	4.27	Lep05	3.9	USNOB	3.7	USNOB	2.462	0.294	2.231	0.204	2.142	0.230	joint
GJ 423 BD	···	···	5.36	Lep05	4.74	Lep05	4.4	USNOB	4.0	USNOB	···	···	···	···	···	···	joint

Table 5.4: Extended Ten Parsec Sample: Photometry

Name	U	Uref	B	Bref	V	Vref	R	Rref	I	Iref	J	err	H	err	K	err	Notes
GJ 432 A	···	···	6.78	Bes90	5.97	Bes90	5.52	Bes90	5.10	Bes90	4.784	0.228	4.138	0.214	4.022	0.036	···
GJ 434	6.28	Joh66	6.05	Bes90	5.33	Bes90	4.9	USNOB	4.5	USNOB	3.99	Joh68	3.61	Joh68	3.60	Joh68	···
GJ 442 A	···	···	5.56	Bes90	4.90	Bes90	4.5	USNOB	4.2	USNOB	3.931	0.276	3.490	0.238	3.489	0.278	···
GJ 451	7.37	Joh66	7.20	Joh66	6.45	Joh66	6.0	USNOB	5.6	USNOB	4.89	Gla75	4.43	Gla75	4.37	Gla75	···
GJ 475	4.91	Joh66	4.86	Joh66	4.27	Joh66	3.9	USNOB	3.6	USNOB	3.23	Joh66	2.905	0.198	2.84	Joh66	···
GJ 502	4.92	Joh66	4.84	Joh66	4.26	Joh66	3.9	USNOB	3.6	USNOB	3.24	Gla75	2.90	Gla75	2.87	Gla75	···
GJ 506	5.69	Joh66	5.43	Bes90	4.72	Bes90	4.33	Bes90	3.97	Bes90	3.334	0.200	2.974	0.176	2.956	0.236	···
GJ 566 A	5.68	Lut71	5.44	Lut71	4.72	Lut71	4.52	Bre64	4.24	Bre64	2.660	0.448	2.253	0.698	1.971	0.600	joint JHK
GJ 566 B	9.29	Lut71	8.14	Lut71	6.97	Lut71	6.30	Bre64	5.86	Bre64	···	···	···	···	···	···	···
GJ 570 A	7.88	Joh66	6.82	Joh66	5.71	Joh66	···	···	···	···	3.663	0.258	3.085	0.196	3.048	0.224	···
GJ 631	···	···	6.57	Bes90	5.76	Bes90	5.31	Bes90	4.9	Bes90	4.33	Joh66	4.053	0.208	3.87	Joh66	···
GJ 638	···	···	9.48	Joh53	8.11	Joh65	7.3	USNOB	6.6	USNOB	5.48	0.023	4.878	0.018	4.712	0.021	···
GJ 663 AB	···	···	5.93	Tor06	5.08	Tor06	···	···	···	···	···	···	···	···	···	···	joint
GJ 664(C)*	···	···	7.48	Bes90	6.32	Bes90	5.62	Bes90	5.04	Bes90	4.155	0.25	···	···	3.466	0.256	···
GJ 667 AB	7.77	Joh66	6.95	Joh66	5.91	Joh66	4.97	Joh66	4.38	Joh66	3.903	0.262	3.230	0.206	3.123	0.278	joint
GJ 666 A	···	···	6.35	Bes90	5.47	Bes90	5.00	Bes90	4.54	Bes90	4.077	0.996	3.146	0.664	3.421	0.282	···
GJ 673	···	···	8.89	Bes90	7.53	Bes90	6.69	Bes90	5.94	Bes90	4.934	0.024	4.341	0.044	4.14	Gla75	···
GJ 695 AD	4.56	Joh66	4.17	Joh66	3.42	Joh66	2.9	USNOB	2.6	USNOB	2.13	Joh66	1.559	0.184	1.77	Joh66	joint
GJ 702 A	5.31	Egg65	4.98	Egg65	4.20	Egg65	3.87	Bre64	3.61	Bre64	2.343	0.296	1.876	0.244	1.791	0.304	joint JHK

Table 5.4: Extended Ten Parsec Sample: Photometry

Name	U	Uref	B	Bref	V	Vref	R	Rref	I	Iref	J	err	H	err	K	err	Notes
GJ 702 B	···	···	7.15	Egg65	6.00	Egg65	5.26	Bre64	4.82	Bre64	···	···	···	···	···	···	···
GJ 713 AB	4.01	Joh66	4.07	Joh66	3.58	Joh66	3.3	USNOB	3.0	USNOB	2.588	0.260	2.372	0.188	2.216	0.252	joint
GJ 721	0.02	Joh66	0.02	Bes90	0.03	Bes90	0.04	Bes90	0.04	Bes90	0.02	Joh66	−0.029	0.146	0.02	Joh66	···
GJ 764	5.86	Oja84	5.46	Oja93	4.68	Oja93	4.2	USNOB	3.8	USNOB	3.32	Joh66	3.039	0.214	2.78	Joh66	···
GJ 768	1.07	Joh66	0.99	Bes90	0.77	Bes90	0.64	Bes90	0.50	Bes90	0.39	Joh66	0.102	0.220	0.26	Joh66	···
GJ 780	4.76	Joh66	4.31	Bes90	3.55	Bes90	3.14	Bes90	2.79	Bes90	2.35	Gla75	2.03	Gla75	1.93	Gla75	···
GJ 783 A	···	···	6.19	Joh66	5.32	Joh66	···	···	···	···	3.518	0.300	2.999	0.422	3.008	0.602	···
GJ 785	···	···	6.61	Bes90	5.73	Bes90	5.23	Bes90	4.81	Bes90	4.112	0.294	3.582	0.266	3.501	0.232	···
GJ 827	4.58	Joh66	4.71	Bes90	4.22	Bes90	3.92	Bes90	3.61	Bes90	3.27	Gla75	3.00	Gla75	2.90	Gla75	···
GJ 881(A)	1.30	Joh66	1.24	Bes90	1.15	Bes90	1.10	Bes90	1.07	Bes90	1.02	Gla75	1.03	Gla75	0.99	Gla75	···
GJ 879(B)*	···	···	7.56	Bes90	6.46	Bes90	5.8	Bes90	5.78	Bes90	4.533	0.037	3.804	0.210	3.805	0.240	···
GJ 884	···	···	9.25	Bes90	7.86	Bes90	7.00	Bes90	6.23	Bes90	5.346	0.021	4.696	0.076	4.478	0.016	···
GJ 892	7.46	Oja84	6.56	Oja93	5.57	Oja93	4.9	USNOB	4.5	USNOB	3.80	Gla75	3.27	Gla75	3.18	Gla75	···

* Designates component to above system with different GJ number.
JHK & err from 2MASS unless otherwise noted.
"joint" indicates unresolved photometry.

Bes90 Bessel (1990)
Bre64 Breckinridge & Kron (1964)
Egg65 Eggen (1965)
Gla75 Glass (1975)
Hog00 Høg et al. (2000)
Joh53 Johnson & Morgan (1953)
Joh66 Johnson et al. (1966)
Joh68 Johnson et al. (1968)
Lep05 Lépine & Shara (2005)
Lut71 Lutz (1971)
Mer86 Mermilliod (1986)
Oja84 Oja (1984)
Oja93 Oja (1993)
Tor06 Torres et al. (2006)
USNOB Monet et al. (2003)

5.2.3 Photometry and Energy Distributions

The $UBVRI$ photometry used in this chapter, listed in Tables 5.2 and 5.4, was extracted from sources in the literature with preference given to large surveys and measurements consistent with photometry obtained as part of the CTIO Parallax (CTIOPI) program, which uses the Johnson-Kron-Cousins system. R and I magnitudes from the USNO-B1.0 catalog (Monet et al. 2003) are incorporated in the extended 10 pc sample and both are rounded to the nearest 0.1 mag. R magnitudes are averaged from the first and second epochs.

The majority of JHK photometry is taken from the 2MASS database, identified as those values with errors listed explicitly in Tables 5.2 and 5.4 (Cutri et al. 2003). In cases of close binaries with magnitude difference measurements in the literature (e.g.,, Henry & McCarthy 1993 and Henry et al. 1999), the optical and 2MASS photometry is used with the published magnitude differences to split the component fluxes into individual magnitudes. Note that stars brighter than $\sim$5 mag are saturated in 2MASS images and typically have relatively large photometric errors ($\geq$ 0.2 mag). Where possible, we use JHK measurements in the literature for these stars (Johnson et al. 1966; Johnson et al. 1968 ; Glass 1975; Mould & Hyland 1976). These magnitudes, listed in their unconverted form in Tables 5.2 & 5.4 and with specific references listed in the error columns, were then converted to 2MASS magnitudes using color transformations from Carpenter (2001). Of the 16 multiple systems in the 5 pc sample, eight have spatially unresolved photometry in some or all passbands and are marked as "Joint" in the Notes section of Table 5.2. Similarly, 10 of the 19 multiple systems in the extended 10 pc sample have spatially unresolved photometry in some or all

passbands and are listed as "Joint" in the Notes section of Table 5.4.

5.3 Habitable Zones

The term "habitable zone" was first coined by Huang (1959) as a region around a star where a planet could support life. Since then, there have been many definitions of habitability, most based on the presence of liquid water on the surface of a planet. These planets could be terrestrial in nature, which are known to exist (Borucki & for the Kepler Team 2010), or perhaps moons of gas-giant planets, which are suspected to exist (Weidner & Horne 2010). Examples of nearby stars hosting potentially habitable super-Earths include GJ 581, an M dwarf with potentially two planets in its habitable zone (Mayor et al. 2009; Vogt et al. 2010a) and GJ 667C, another M dwarf with one planet in its habitable zone (Anglada-Escudé et al. 2012).

Kasting et al. (1993) did pioneering work in describing habitable zones (HZs) around main sequence stars. To approximate the location of the HZ, they introduced a one-dimensional climate model that yields the distances from main sequence stars where liquid water would be present, given an initial assumption of a $CO_2/H_2O/N_2$ atmosphere and an Earth-sized planet. They describe the inner boundary of their model as the point at which the atmosphere becomes saturated with H_2O, causing a loss of water via photolysis and hydrogen escape; the outer boundary is marked by the formation of CO_2 clouds that cool a planet's surface by increasing its albedo and lowering its convective lapse rate. They give an equation for the distance from a star, D, of the HZ in AU based on the incident flux that a planet receives,

$L/L_{\odot}$, the star's luminosity relative to that of the Sun, and S_{eff}, the ratio of outgoing IR flux to the incoming incident flux at the top of the planet's atmosphere:

$$D = 1AU\Big(\frac{L/L_{\odot}}{S_{eff}}\Big) \tag{5.1}$$

Using more explicit terms, Equation 5.1 can be used to show the distance from a star at which a planet would have a given temperature, based on energy balance (Kaltenegger et al. 2002). Equation 5.2 can then be used to show that the equilibrium temperature, T_P, of a planet at a distance, D, from its host star is a function of the stellar effective temperature, T_{eff}, stellar radius, $R_{\star}$, and the planet's Bond albedo, A. Thus, if the stellar T_{eff} and $R_{\star}$ are known, we can calculate the range of distances where a planet with given albedo[3] would have a surface temperature suitable for liquid water, as described by the planet's temperature, T_P:

$$T_P = T_{eff}\Big(\frac{R_{\star}}{2D}\Big)^{1/2}(1-A)^{1/4} \tag{5.2}$$

5.4 Methodology to Derive the EHZ

The HZ around a star is primarily a function of the total energy output of a star that reaches the surface of a planet. This can be determined if the stellar temperature and radius are known, which we calculate for our sample of stars as described in Section 5.4.1. However, a range of other factors, such as atmospheric pressure, composition, and cloud cover play roles

[3] $A = 0.3$ for the hypothetical planets used in this paper. R. et al. ????

in determining the surface temperature of a planet. To account for this, in Section 5.4.2 we follow previous studies and approximate these effects by using empirical temperature constraints provided by planets in the Solar System.

5.4.1 SED Fitting used to Derive Stellar Temperature and Radius

Although spectral types are often used to estimate stellar effective temperatures, the various methods for determining spectral types are inhomogeneous and often depend upon the spectral range used. As an alternative, we fit synthetic stellar spectra to broad-band energy distributions to determine effective temperatures and radii. In particular, we use photometric measurements spanning $UBVRIJHK$ (0.3 to 2.4 μm) in conjunction with model spectra generated using the PHOENIX code (Hauschildt et al. 1999). This prescription is only used for single stars and for stars in multiple systems in the 5 pc and extended 10 pc samples with at least four spatially resolved photometric measurements in different filter bandpasses. Estimates for unresolved multiples are discussed in Section 5.4.3.

These available models span the temperature ranges of T_{eff} of 10,000 K to 7000 K in 200 K increments and 6900 K to 2000 K in 100 K increments. The model spectra have a resolution of 2 Å and range from 10 Å to 500 μm. The models were convolved with $UBVRIJHK$ filter responses to create synthetic photometry. For the $UBVRI$ synthetic photometry, we took zero points from Bessell et al. (1998) and filter responses from CTIO[4]. JHK filter responses and zero points were from 2MASS[5]. The zero points adopted are listed in Table 5.5. We adopt log g values of 4.5 or 5.0 for all stars.

[4] `http://www.ctio.noao.edu/instruments/filters/`
[5] `http://www.ipac.caltech.edu/2mass/releases/allsky/doc/`

Table 5.5: $UBVRIJHK$ Zero Points

Filter	Zero Point	λ_{eff}(Å)	Ref
U	4.18e-9	3660	Bessell et al. (1998)
B	6.32e-9	4380	Bessell et al. (1998)
V	3.63e-9	5450	Bessell et al. (1998)
R	2.18e-9	6410	Bessell et al. (1998)
I	1.13e-9	7980	Bessell et al. (1998)
J	3.14e-10	12350	Cohen et al. (2003)
H	1.11e-10	16620	Cohen et al. (2003)
K	4.29e-11	21590	Cohen et al. (2003)

Zero points have units of ergs cm^2 sec^{-1} Å^{-1}.

Solar metallicity is adopted for all stars except GJ 191 (Fe/H = −0.98; Woolf & Wallerstein 2005) and GJ 451 (Fe/H = −1.16; Valenti & Fischer 2005), for which we adopt metallicities of −1.0. The assumption of solar metallicity for the remainder of our 10 pc sample is based on the 36 FGK stars that overlap with Valenti & Fischer (2005). These stars have an average metallicity of Fe/H = −0.048 with a standard deviation of 0.168 dex.

The flux values in the model spectra are given as a surface flux that must be scaled by a radius to a known distance for fitting with observed integrated flux values. A stellar radius grid from 0.001 $R_\odot$ to 3.00 $R_\odot$ with a step size of 0.001 $R_\odot$ is calculated for each model spectrum. Each spectrum and radius combination is then convolved with filter response and the zero point data referenced above to derive consequent fluxes observed at Earth. These integrated fluxes are then fit via a χ^2 minimization routine, written in IDL and

described in Equation 5.3, to compare the model flux with the observed flux across each filter bandpass. Here, O is the observed integrated flux from the photometric measurements, E is the estimated integrated flux from the model grids, ν is the number of photometric points (degrees of freedom), and σ is the average error in the photometric measurement. Examples of fits for AFGKM stars in the 5 pc sample are shown in Figure 5.1.

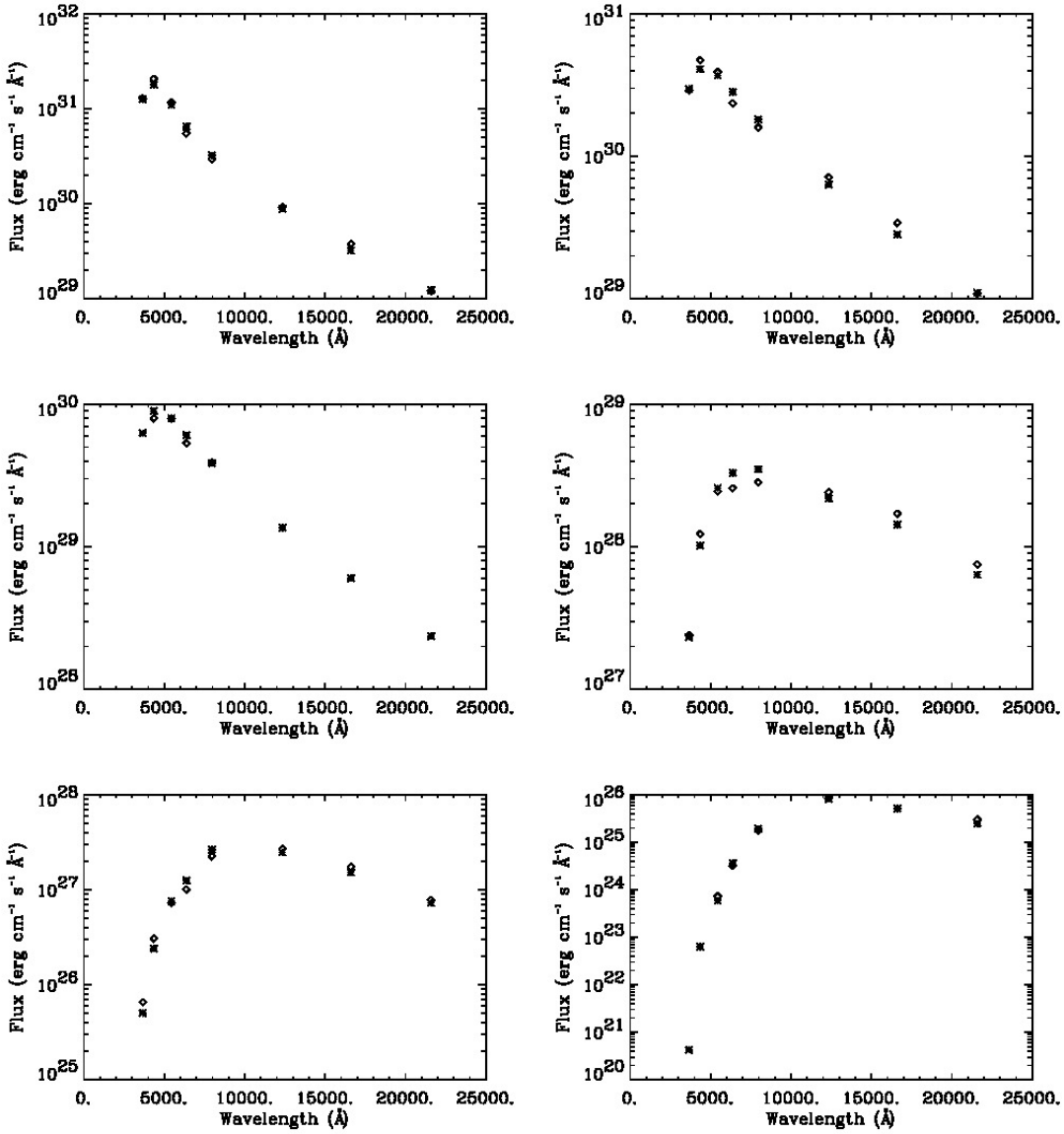

Figure 5.1 Examples of model ($*$) and observed ($\Diamond$) flux values are shown for (*top-left to right*) GJ 244A (A1.0V), GJ 280A (F5.0IV−V), (*middle-left to right*) GJ 599A (G2.0V), GJ 380 (K7.0V), (*bottom-left to right* GJ 273 (M3.5V), SCR 1845-6357A (M8.5V). In each case the points represent $UBVRIJHK$ photometry. Model values for stars with incomplete photometry, e.g.,, GJ 559A missing UJHK and SCR 1845-6357A missing UB, are plotted for completeness.

$$\chi^2_{\rm red} = \frac{\chi^2}{\nu} = \frac{1}{\nu}\sum\frac{(O-E)^2}{\sigma^2} \tag{5.3}$$

The output is an effective temperature from the model and a radius that best fits the measured photometric data for a given distance. We assume no interstellar extinction for our sample, and choose four photometric points as the minimum number needed to make a fit. When deriving radii, all stars in the sample are assumed to be spherical and radiate isotropically, which is not the case for rapidly rotating stars that may be oblate and experience gravity darkening (e.g.,, Altair, see Monnier et al. 2007; Vega, see Aufdenberg et al. 2006). This is most common among stars earlier than mid-F spectral type, as these stars are fully radiative and consequently do not possess an efficient rotational braking mechanism (e.g.,, Wilson 1966). However, all but one early type star (i.e., earlier than spectral type F5) within 10 pc have projected rotational velocities less than 100 km/s, which correspond to projected oblateness values $\lesssim$2% (Absil et al. 2008). These apparently slow rotating stars include Sirius A (GJ 244, A1V, 16 km/s; Royer et al. 2002), Procyon A (GJ 280, F5V-IV, 4.9 km/s; Fekel 1997), Vega (GJ 721, A0V, 24 km/s; Royer et al. 2007), and Fomalhaut (GJ 881, A4V, 93 km/s; Royer et al. 2007). We note that despite having a small $v\sin i$ value, Vega is believed to be rapidly rotating with a nearly pole on orientation (Aufdenberg et al. 2006). An additional rapidly rotating star is Altair (GJ 768, A7V, 217 km/s; Royer et al. 2007) which has an oblateness of 18% determined from interferometric measurements by the CHARA Array (Monnier et al. 2007). As expected, our derived radii and effective temperatures for Altair and Vega are intermediate to the polar and equatorial values listed

in Monnier et al. (2007) and Aufdenberg et al. (2006), respectively. Because the EHZ boundaries are a function of the square root of the total luminosity (see Section 5.4.2), our adopted methodology should yield reliable estimates of the habitable real estate these stars provide, even if the stellar temperatures vary with stellar latitude.

As a consequence of the limited temperature resolution of the PHOENIX grids used (ΔT=200K from 10000K to 7000K and ΔT=100K from 6900K to 2000K), the fitting routine can determine a slightly larger radius coupled with a cooler temperature, or vice versa. Systematic uncertainties in the PHOENIX models are such that a ΔT of less than 100K are unreliable (Hauschildt, priv. comm.). As the Stefan-Boltzmann law shows $R_\star{}^2 T_{eff}{}^4 \sim L_\star$, the luminosity determined from the SED remains the same as long as the radii and effective temperatures move in opposite directions, and therefore the EHZ, being a function of the square root of the luminosity, does not change. Of key importance, the output radii and temperatures determined here allow us to compare our results directly to those found via interferometric techniques.

Of the stars investigated, 28 have spatially resolved angular diameters from long baseline interferometric instruments such as CHARA, PTI, and VLTI (Table 5.6). Fifteen of these measurements are from the recent effort of Boyajian et al. (2012). Because these measurements determine sizes to within a few percent, we use them to test the accuracy of the radii determined in our fitting process. The published radii are on average 7.4% larger than our derived radii, which shows a systematic effect. Our derived model T_{eff} are on average 2.4% hotter than derived from interferometric measurements. A comparison of our model

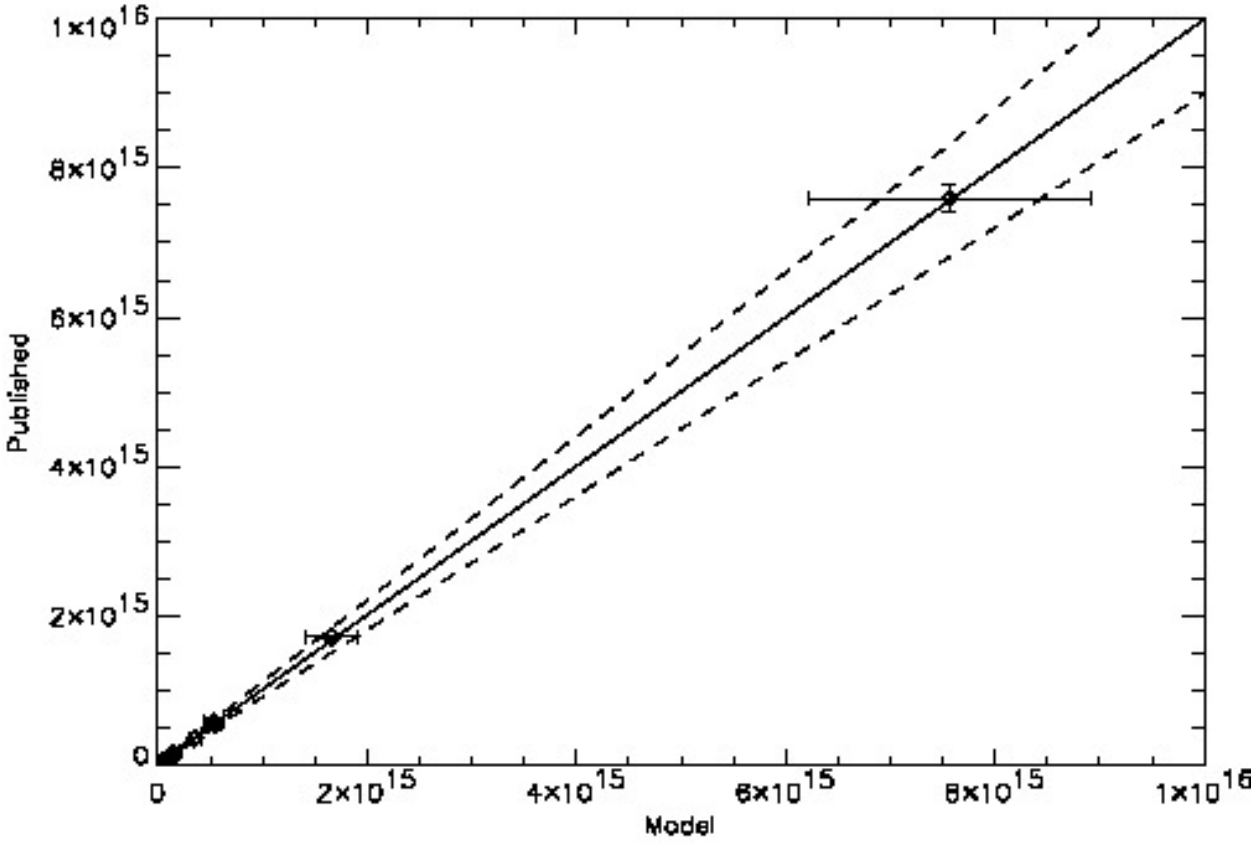

Figure 5.2 Model fits vs published $(R/R_{\odot})^2T^4$ values. The solid line illustrates 1:1 agreement and the dashed lines represent 10% offsets. Error bars are 1σ for the model and given errors for the interferometrically derived values used to derive the published values.

versus published values is shown in Figure 5.2. The temperature uncertainties correspond to spectral type uncertainties of 1-2 spectral subclasses, similar to the error associated with most spectral classification methods. As the average values indicate, the over-prediction of temperature leads to the expected under-prediction of radius, and the combination yields a more accurate luminosity, and thus consistent EHZ. Given this agreement, we adopt our model values for T_{eff} and $R/R_{\odot}$ in final calculations of the habitable real estate.

Table 5.6: Comparison of Derived Temperatures and Radii for Nearby Stars Using Our SED Fits and Interferometric Results

Star	SpType	V-K	$T_{\rm eff}$Model	$T_{\rm eff}$ModelFixR	$T_{\rm eff}$Published	$R/R_{\odot Model}$	$R/R_{\odot Pub}$	Ref.
GJ 244 A	A1.0V	−0.040	10000	9600	9900±200	1.645	1.711± 0.013	Kervella et al. (2003b)
GJ 280 A	F5.0IV-V	1.028	6700	6500	6524	1.898	2.048± 0.025	Kervella et al. (2003a)
GJ 559 A	G2.0V	1.490	6000	5700	5810±50	1.103	1.224± 0.003	Kervella et al. (2003a)
GJ 71	G8.5V	1.696	5700	5400	5264±100	0.708	0.816± 0.013	Di Folco et al. (2004)
GJ 631	K2.0V	1.890	5500	5300	5337±41	0.710	0.759± 0.012	Boyajian et al. (2012)
GJ 166 A	K0.5V	1.932	5200	5100	5143±14	0.735	0.806± 0.004	Boyajian et al. (2012)
GJ 559 B	K0.0V	1.940	5400	5100	5260±50	0.775	0.863± 0.005	Kervella et al. (2003a)
GJ 144	K2.0V	1.954	5200	5000	5135±100	0.689	0.743± 0.005	Di Folco et al. (2004)
GJ 33	K2.5V	2.240	5200	5000	4950±14	0.643	0.695± 0.004	Boyajian et al. (2012)
GJ 105 A	K3.0V	2.360	5000	4700	4662±17	0.677	0.795± 0.006	Boyajian et al. (2012)
GJ 892	K3.0V	2.390	5000	4800	4699±16	0.698	0.778± 0.005	Boyajian et al. (2012)
GJ 702 A	K0.0V	2.409	5500	5700	5407±52	0.754	0.831± 0.004	Boyajian et al. (2012)
GJ 845 A	K5.0V	2.443	4900	4600	5468±59	0.608	0.732± 0.007	Demory et al. (2009)
GJ 570 A	K4.0V	2.662	4700	4700	4507±58	0.734	0.739± 0.019	Boyajian et al. (2012)
GJ 820 B	K7.0V	3.486	4300	4200	4040±80	0.530	0.595± 0.008	Kervella et al. (2008)
GJ 380	K7.0V	3.628	4200	4200	4081±15	0.599	0.642± 0.005	Boyajian et al. (2012)

Table 5.6: Comparison of Derived Temperatures and Radii for Nearby Stars Using Our SED Fits and Interferometric Results

Star	SpType	V-K	$T_{\rm eff}$Model	$T_{\rm eff}$ModelFixR	$T_{\rm eff}$Published	$R/R_{\odot Model}$	$R/R_{\odot Pub}$	Ref.
GJ 820 A	K5.0V	3.782	4000	4100	4400±100	0.709	0.665± 0.005	Kervella et al. (2008)
GJ 702 B*	K5.0V	···	···	···	4393±149	···	0.670± 0.009	Boyajian et al. (2012)
GJ 191	M2.0VI	3.801	3800	3600	3570±156	0.249	0.291± 0.025	Ségransan et al. (2003)
GJ 887	M2.0V	3.875	3800	3700	3797±45	0.414	0.459± 0.011	Demory et al. (2009)
GJ 411	M2.0V	3.969	3700	3500	3465±17	0.338	0.392± 0.004	Boyajian et al. (2012)
GJ 412 A	M1.0V	4.001	3700	3600	3497±39	0.353	0.398± 0.009	Boyajian et al. (2012)
GJ 15 A	M1.5V	4.062	3800	3700	3730±49	0.323	0.379± 0.006	Berger et al. (2006)
GJ 725 A	M3.0V	4.468	3400	3400	3407±15	0.344	0.356± 0.004	Boyajian et al. (2012)
GJ 687	M3.0V	4.622	3400	3200	3413±28	0.406	0.418± 0.007	Boyajian et al. (2012)
GJ 725 B	M3.5V	4.690	3300	3200	3104±28	0.275	0.323± 0.006	Boyajian et al. (2012)
GJ 699	M4.0V	5.046	3100	3100	3224±10	0.198	0.187± 0.001	Boyajian et al. (2012)
GJ 551	M5.0V	6.666	2700	2900	3098±56	0.167	0.141± 0.007	Demory et al. (2009)

$T_{\rm eff}$Model refers to temperatures from our model, while, $T_{\rm eff}$ModelFixR refers to temperatures derived while holding the radius to values obtained through long baseline interferometry.

* GJ 702B does not have enough resolved photometry for a model solution.

A few stars are worthy of note. Procyon is slightly evolved (F5.0IV-V) and has a highly constrained log g of 4.05±0.04 (Fuhrmann et al. 1997) measured via high resolution spectroscopy in concert with masses determined using astrometry from the Procyon-white dwarf orbit. We adjusted the log g to 4.0 for this star and recomputed the T_{eff} and R. This, nevertheless, yielded identical values within the model grid resolution as those of log g=4.5. The model spectra used in this work have a low temperature limit of 2000 K, which is the value derived for the three intrinsically faintest stars in this sample: SCR 1845-6357A (M8.5V), DEN 1048-3956 (M8.5V), and LP 944-020 (M9.0V).

5.4.2 Habitable Zones of Single Stars

Kasting et al. (1993) use a one-dimensional climate model to calculate HZs around single main sequence stars. A one-dimensional climate model characterizes a planet's global temperature by dividing the planet into latitudinal bands, and treats the planet as uniform with respect to longitude. These one-dimensional radiative-convective models are a good approximation of global temperature, but more complicated 3-D global climate models are needed to account for the complex physical interactions associated with oceans, clouds, and land surface processes. These inputs add parameters such as land/ocean surface coverage and clouds, which can vary from planet to planet, complicating the overall goal to characterize the EHZ of a star. Here we use the one-dimensional model to generalize the EHZ, and adopt a modified version of the one-dimensional model based on the "Venus and early Mars criterion" from Selsis et al. (2007). In that work, they argue that empirical evidence shows that Venus has not had water on its surface for at least one billion years, and Mars

had water on its surface around 4 billion years ago. The solar fluxes at those times were 8% and 28% lower, respectively (Baraffe et al. 1998). Venus (0.72 AU today) and Mars (1.52 AU today) would need to be at distances of ∼0.75 AU and ∼1.77 AU, respectively, to receive these levels of solar flux today.

Selsis et al. (2007) provide a method for estimating the inner and outer edges of HZs for stars with T_{eff} = 3700K-7200K. The stars in the sample discussed here range in temperatures from 2000K to 10000K. We have therefore chosen to derive new relations for the HZ boundaries that span the entire stellar temperature regime of our sample, and thereby provide a consistent methodology for all stars in the sample.

In defining our EHZ inner and outer boundaries, we assume a planet with an atmosphere, radius, mass, and Bond albedo (0.3) that matches Earth (Kasting 1996). This leads to the EHZ Equations 5.4 and 5.5, used to determine the empirical surface temperature of an Earth-like planet that satisfies the "Venus criterion" (we adopt 0.80 AU on the suggestion of Kasting, priv. comm.) and "Mars criterion" (1.77 AU). The resulting inner and outer radii of the EHZ correspond to equilibrium temperatures of 285 K to 195 K, respectively.

$$R_{EHZinner} = \frac{R_\star}{2}(0.7)^{1/2}\Big(\frac{T_{eff}}{285K}\Big)^2 \tag{5.4}$$

$$R_{EHZouter} = \frac{R_\star}{2}(0.7)^{1/2}\Big(\frac{T_{eff}}{195K}\Big)^2 \tag{5.5}$$

Note that these only depend on $R_\star$ and T^2_{eff}, or essentially the square root of the star's

luminosity. Values for both samples are listed in Tables 5.7 and 5.8. Only stars used in the cumulative EHZ calculations are listed, except for the cases of Sirius (GJ 244A) and Procyon (GJ 280A), which provide useful benchmarks.

Table 5.7: Empirical Habitable Zones (EHZs) for the Five Parsec Sample

		Model					Model FixR				
Name	SpType	R	$T_{\rm eff}$	EHZ Inner R	EHZ Outer R	EHZ Lin	R	$T_{\rm eff}$	EHZ Inner R	EHZ Outer R	EHZ Lin
		$(R/R_{\odot})$	(K)	(AU)	(AU)	(AU)	$(R/R_{\odot})$	(K)	(AU)	(AU)	(AU)
Sun	G2.0V	0.917	6000	0.789	1.686	0.897	1.00	5800	0.804	1.718	0.914
DEN 1048-3956	M8.5V	0.134	2000	0.013	0.027	0.014	···	···	···	···	···
GJ 1	M1.5V	0.349	3700	0.114	0.244	0.130	···	···	···	···	···
GJ 15 A	M1.5V	0.323	3800	0.112	0.239	0.127	0.387	3700	0.127	0.271	0.144
GJ 15 B	M3.5V	0.197	3200	0.048	0.103	0.055	···	···	···	···	···
GJ 54.1	M4.5V	0.181	2900	0.036	0.078	0.042	···	···	···	···	···
GJ 65 A	M5.5V	0.248	2600	0.040	0.086	0.046	···	···	···	···	···
GJ 65 B	M6.0V	0.225	2700	0.039	0.084	0.045	···	···	···	···	···
GJ 71	G8.0V	0.700	5700	0.545	1.164	0.619	0.816	5400	0.570	1.218	0.648
GJ 83.1	M4.5V	0.195	2900	0.039	0.084	0.045	···	···	···	···	···
GJ 144	K2.0V	0.630	5400	0.440	0.940	0.500	0.735	5000	0.440	0.941	0.500
GJ 166 A	K0.5V	0.735	5200	0.476	1.017	0.541	0.806	5000	0.483	1.031	0.549

Table 5.7: Empirical Habitable Zones (EHZs) for the Five

Parsec Sample

		Model					Model FixR				
Name	SpType	R	$T_{\rm eff}$	EHZ Inner R	EHZ Outer R	EHZ Lin	R	$T_{\rm eff}$	EHZ Inner R	EHZ Outer R	EHZ Lin
		$(R/R_{\odot})$	(K)	(AU)	(AU)	(AU)	$(R/R_{\odot})$	(K)	(AU)	(AU)	(AU)
GJ 166 C	M4.5V	0.249	3200	0.061	0.130	0.069	···	···	···	···	···
GJ 191	M1.5VI	0.240	3800	0.083	0.177	0.094	0.291	3500	0.085	0.182	0.097
GJ 234 A	M4.0V	0.287	3000	0.062	0.132	0.070	···	···	···	···	···
GJ 234 B	M5.5V	0.155	2700	0.027	0.058	0.031	···	···	···	···	···
GJ 244 A*	A1.0V	1.645	10000	3.942	8.420	4.478	1.711	9600	3.779	8.071	4.293
GJ 273	M3.5V	0.316	3200	0.077	0.165	0.088	···	···	···	···	···
GJ 280 A*	F5.0IV-V	1.906	6700	2.050	4.380	2.329	2.048	6500	2.073	4.429	2.356
GJ 380	K7.0V	0.648	4100	0.261	0.558	0.297	0.642	4100	0.259	0.552	0.294
GJ 388	M3.0V	0.452	3300	0.118	0.251	0.133	···	···	···	···	···
GJ 406	M6.0V	0.162	2500	0.024	0.052	0.028	···	···	···	···	···
GJ 411	M2.0V	0.338	3700	0.111	0.237	0.126	0.392	3500	0.115	0.246	0.130
GJ 412 A	M1.0V	0.353	3700	0.116	0.247	0.131	0.398	3600	0.124	0.264	0.140

Table 5.7: Empirical Habitable Zones (EHZs) for the Five

Parsec Sample

		Model					Model FixR				
Name	SpType	R	$T_{\rm eff}$	EHZ Inner R	EHZ Outer R	EHZ Lin	R	$T_{\rm eff}$	EHZ Inner R	EHZ Outer R	EHZ Lin
		$(R/R_{\odot})$	(K)	(AU)	(AU)	(AU)	$(R/R_{\odot})$	(K)	(AU)	(AU)	(AU)
GJ 412 B	M5.5V	0.152	2600	0.025	0.053	0.028	···	···	···	···	···
GJ 447	M4.0V	0.213	3000	0.046	0.098	0.052	···	···	···	···	···
GJ 473 A	M5.0V	0.212	2700	0.037	0.079	0.042	···	···	···	···	···
GJ 473 B	M7.0V	0.177	2900	0.036	0.076	0.040	···	···	···	···	···
GJ 551	M5.5V	0.167	2700	0.029	0.062	0.033	0.141	2900	0.028	0.061	0.032
GJ 559 A	G2.0V	0.884	6700	0.951	2.031	1.080	1.224	5700	0.953	2.036	1.083
GJ 559 B	K0.0V	0.774	5400	0.541	1.155	0.614	0.863	5200	0.559	1.194	0.635
GJ 628	M3.0V	0.321	3200	0.079	0.168	0.089	···	···	···	···	···
GJ 674	M2.5V	0.355	3400	0.098	0.210	0.112	···	···	···	···	···
GJ 687	M3.0V	0.406	3400	0.112	0.240	0.128	0.418	3400	0.116	0.247	0.132
GJ 699	M4.0V	0.198	3100	0.046	0.097	0.051	0.187	3100	0.043	0.092	0.048
GJ 725 A	M3.0V	0.344	3400	0.095	0.204	0.109	0.356	3400	0.099	0.211	0.112

Table 5.7: Empirical Habitable Zones (EHZs) for the Five

Parsec Sample

		Model					Model FixR				
Name	SpType	R	$T_{\rm eff}$	EHZ Inner R	EHZ Outer R	EHZ Lin	R	$T_{\rm eff}$	EHZ Inner R	EHZ Outer R	EHZ Lin
		$(R/R_{\odot})$	(K)	(AU)	(AU)	(AU)	$(R/R_{\odot})$	(K)	(AU)	(AU)	(AU)
GJ 725 B	M3.5V	0.275	3300	0.072	0.153	0.081	0.323	3200	0.079	0.169	0.090
GJ 729	M3.5V	0.214	3100	0.049	0.105	0.056	···	···	···	···	···
GJ 820 A	K5.0V	0.709	4000	0.272	0.581	0.309	0.665	4100	0.268	0.572	0.304
GJ 820 B	K7.0V	0.530	4300	0.235	0.502	0.267	0.595	4200	0.252	0.537	0.286
GJ 825	M0.0V	0.516	4100	0.208	0.444	0.236	···	···	···	···	···
GJ 832	M1.5V	0.423	3600	0.131	0.280	0.149	···	···	···	···	···
GJ 845 A	K5.0V	0.608	4900	0.350	0.747	0.397	0.732	4600	0.371	0.793	0.422
GJ 860 A	M3.0V	0.328	3300	0.085	0.183	0.098	···	···	···	···	···
GJ 860 B	M4.0V	0.194	3200	0.048	0.102	0.054	···	···	···	···	···
GJ 866 B	MV	0.215	2700	0.037	0.080	0.043	···	···	···	···	···
GJ 876 A	M4.0V	0.390	3100	0.090	0.191	0.101	···	···	···	···	···
GJ 887	M1.5V	0.414	3800	0.143	0.306	0.163	0.491	3700	0.161	0.344	0.183

Table 5.7: Empirical Habitable Zones (EHZs) for the Five Parsec Sample

		Model					Model FixR				
Name	SpType	R	$T_{\rm eff}$	EHZ Inner R	EHZ Outer R	EHZ Lin	R	$T_{\rm eff}$	EHZ Inner R	EHZ Outer R	EHZ Lin
		$(R/R_{\odot})$	(K)	(AU)	(AU)	(AU)	$(R/R_{\odot})$	(K)	(AU)	(AU)	(AU)
GJ 905	M5.5V	0.216	2700	0.038	0.080	0.042	···	···	···	···	···
GJ 1002	M5.0V	0.142	2900	0.029	0.061	0.032	···	···	···	···	···
GJ 1061	M5.0V	0.178	2700	0.031	0.066	0.035	···	···	···	···	···
GJ 1111	M6.0V	0.162	2400	0.022	0.048	0.026	···	···	···	···	···
GJ 1245 A	M5.5V	0.194	2700	0.034	0.072	0.038	···	···	···	···	···
GJ 1245 B	M6.0V	0.150	2700	0.026	0.056	0.030	···	···	···	···	···
GJ 1245 C	M7.0V	0.171	2100	0.018	0.039	0.021	···	···	···	···	···
LHS 288	M5.5V	0.150	2700	0.026	0.056	0.030	···	···	···	···	···
LHS 292	M6.5V	0.146	2400	0.020	0.043	0.023	···	···	···	···	···
LP 944-020	M9.0V	0.091	2000	0.009	0.019	0.010	···	···	···	···	···
SCR 1845-6357 A	M8.5V	0.129	2000	0.012	0.026	0.014	···	···	···	···	···
SO 0253+1652	M7.0V	0.156	2400	0.022	0.046	0.024	···	···	···	···	···

This table shows model radius, temperature, inner and outer HZ radius, and the HZ width in AU in columns 3-7. Columns 8-12 show radius, temperature, inner and outer HZ radius, and the HZ width in AU based on the method of holding the stellar radius to the values obtained through long baseline interferometry (see Table 6). * Sirius (GJ 244A) and Procyon (GJ 280A) are included as benchmarks, but are not used in final EHZ calculations because of companion white dwarfs.

Table 5.8: Empirical Habitable Zones (EHZs) for the Extended Ten Parsec Sample

		Model					Model FixR				
Name	SpType	R	$T_{\rm eff}$	EHZ Inner R	EHZ Outer R	EHZ Lin	R	$T_{\rm eff}$	EHZ Inner R	EHZ Outer R	EHZ Lin
		$(R/R_{\odot})$	(K)	(AU)	(AU)	(AU)	$(R/R_{\odot})$	(K)	(AU)	(AU)	(AU)
GJ 17	F9.5V	0.989	6100	0.882	1.884	1.002	···	···	···	···	···
GJ 19	G0.0V	1.709	6000	1.474	3.149	1.675	···	···	···	···	···
GJ 33	K2.5V	0.643	5200	0.417	0.890	0.473	0.695	5000	0.416	0.889	0.473
GJ 34 A	G3.0V	0.989	6100	0.882	1.884	1.002	···	···	···	···	···
GJ 66 A	K5.0V	0.740	5100	0.461	0.985	0.524	···	···	···	···	···
GJ 66 B	K5.0V	0.794	4900	0.457	0.976	0.519	···	···	···	···	···
GJ 68	K1.0V	0.739	5400	0.516	1.103	0.587	···	···	···	···	···
GJ 105 A	K3.0V	0.677	5000	0.406	0.866	0.460	0.795	4700	0.421	0.899	0.478
GJ 139	G8.0V	0.812	5700	0.632	1.350	0.718	···	···	···	···	···
GJ 178	F6.0V	1.244	6600	1.299	2.774	1.475	···	···	···	···	···
GJ 183	K3.0V	0.791	4800	0.437	0.933	0.496	···	···	···	···	···
GJ 216 A	F6.0V	1.137	6600	1.187	2.534	1.347	···	···	···	···	···

Table 5.8: Empirical Habitable Zones (EHZs) for the Extended Ten Parsec Sample

		Model					Model FixR				
Name	SpType	R	$T_{\rm eff}$	EHZ Inner R	EHZ Outer R	EHZ Lin	R	$T_{\rm eff}$	EHZ Inner R	EHZ Outer R	EHZ Lin
		$(R/R_{\odot})$	(K)	(AU)	(AU)	(AU)	$(R/R_{\odot})$	(K)	(AU)	(AU)	(AU)
GJ 216 B	K2.0V	0.593	5300	0.399	0.853	0.454	···	···	···	···	···
GJ 250 A	K3.0V	0.597	4900	0.344	0.734	0.390	···	···	···	···	···
GJ 432 A	K0.0V	0.627	5500	0.455	0.971	0.516	···	···	···	···	···
GJ 434	G8.0V	0.793	5700	0.617	1.319	0.702	···	···	···	···	···
GJ 442 A	G2.0V	0.792	6000	0.683	1.459	0.776	···	···	···	···	···
GJ 451	G8.0V	0.542	5400	0.378	0.807	0.429	···	···	···	···	···
GJ 475	G0.0V	0.952	6100	0.849	1.813	0.964	···	···	···	···	···
GJ 502	G0.0V	1.029	6100	0.918	1.960	1.042	···	···	···	···	···
GJ 506	G7.0V	0.927	5700	0.722	1.542	0.820	···	···	···	···	···
GJ 566 A	G8.0V	0.534	6200	0.491	1.049	0.558	···	···	···	···	···
GJ 566 B	K4.0V	0.376	5000	0.225	0.481	0.256	···	···	···	···	···
GJ 570 A	K4.0V	0.734	4700	0.389	0.830	0.441	0.739	4700	0.391	0.836	0.444

Table 5.8: Empirical Habitable Zones (EHZs) for the Extended Ten Parsec Sample

		Model					Model FixR				
Name	SpType	R	$T_{\rm eff}$	EHZ Inner R	EHZ Outer R	EHZ Lin	R	$T_{\rm eff}$	EHZ Inner R	EHZ Outer R	EHZ Lin
		$(R/R_{\odot})$	(K)	(AU)	(AU)	(AU)	$(R/R_{\odot})$	(K)	(AU)	(AU)	(AU)
GJ 631	K2.0V	0.710	5500	0.515	1.099	0.584	0.759	5300	0.511	1.091	0.580
GJ 638	K7.0V	0.620	4100	0.250	0.534	0.284	···	···	···	···	···
GJ 663 A	K1.0V	···	···	0.523	1.118	0.595	···	···	···	···	···
GJ 663 B	K1.0V	···	···	0.523	1.118	0.595	···	···	···	···	···
GJ 664 (C)*	K5.0V	0.581	4600	0.295	0.629	0.334	···	···	···	···	···
GJ 666 A	G8.0V	0.841	5200	0.545	1.164	0.619	···	···	···	···	···
GJ 667 A	K3.0V	···	···	0.399	0.853	0.454	···	···	···	···	···
GJ 667 B	K5.0V	···	···	0.285	0.607	0.322	···	···	···	···	···
GJ 673	K7.0V	0.644	4100	0.259	0.554	0.295	···	···	···	···	···
GJ 702 A	K0.0V	0.754	5500	0.547	1.168	0.621	0.670	5700	0.522	1.114	0.593
GJ 702 B	K5.0V	0.411	5100	0.256	0.735	0.479	···	···	···	···	···
GJ 721	A0.0V	2.543	9800	5.852	12.50	6.648	···	···	···	···	···

Table 5.8: Empirical Habitable Zones (EHZs) for the Extended Ten Parsec Sample

		Model					Model FixR				
Name	SpType	R	$T_{\rm eff}$	EHZ Inner R	EHZ Outer R	EHZ Lin	R	$T_{\rm eff}$	EHZ Inner R	EHZ Outer R	EHZ Lin
		$(R/R_{\odot})$	(K)	(AU)	(AU)	(AU)	$(R/R_{\odot})$	(K)	(AU)	(AU)	(AU)
GJ 764	K0.0V	0.694	5500	0.503	1.075	0.572	···	···	···	···	···
GJ 768	A7.0V	1.701	7800	2.480	5.297	2.817	···	···	···	···	···
GJ 783 A	K2.5V	0.751	5000	0.450	0.961	0.511	···	···	···	···	···
GJ 785	K2.0V	0.802	5100	0.450	1.068	0.618	···	···	···	···	···
GJ 827	F9.0V	0.970	6400	0.952	2.034	1.082	···	···	···	···	···
GJ 879 (B)*	K5.0V	0.592	4700	0.313	0.669	0.356	···	···	···	···	···
GJ 881 (A)	A4.0V	1.635	9200	3.316	7.084	3.768	···	···	···	···	···
GJ 884	K7.0V	0.553	4200	0.234	0.499	0.265	···	···	···	···	···
GJ 892	K3.0V	0.698	5000	0.418	0.893	0.475	0.778	4800	0.430	0.918	0.488

* Designates wide component to above system with different GJ number.

This table shows model radius, temperature, inner and outer HZ radius, and the HZ width in AU in columns 3-7 for the extended 10 pc sample.
HZs for GJ 663A, GJ 663B, GJ 667A, and GJ 667B are estimated using the V-K relationship (see Section 5.5.2).

5.4.3 Habitable Zones of Multiple Star Systems

Although stars in multiple systems are often avoided in planet searches, planets have been found in binary and multiple systems (e.g., Patience et al. 2002; Raghavan et al. 2006; Eggenberger et al. 2007). The potentially dynamically disruptive effects of any close stellar companion must be considered when assessing the possibility of formation, long-term dynamical stability, and ultimately the habitability of planets in multiple star systems. The α Centauri triple system, at a distance from the Sun of 1.34 pc for the G2V-K0V pair (GJ 559 AB) and 1.30 pc for the wide M5V companion (GJ 551), includes the nearest set of Sun-like stars, and provides a test case to study the habitability of multiple stars. The G-K pair has an orbit with a semimajor axis of $17\farcs57$ and eccentricity of 0.518 (Pourbaix et al. 2002). This gives periastron and apastron distances of 11.33 AU and 26.67 AU, respectively. Barbieri et al. (2002) show for α Centauri A that planets can form in stable orbits on a timescale of 5 Myr. Using numerical simulations, they show that not only could planets form, but in some models they formed directly in the habitable zone. Quintana et al. (2007) similarly find that binary separations greater than 10 AU did not inhibit the formation of terrestrial planets at 2 AU. Consistent with this, Wiegert & Holman (1997) show that the orbit of a planet can be stable as long as the ratio of the semimajor axis of the binary to that of the planet is more than 5:1.

The 36 multiple systems in the 5 pc and extended 10 pc samples consist of 27 binaries, 6 triples, and 3 quadruple systems (GJ 423, GJ 570, and GJ 695), for a total of 84 stars/brown dwarfs. However, nine are not main sequence stars, and excluded because of their evolu-

tionary states (e.g.,, sub-giants, white dwarfs, and brown dwarfs). Additionally, 16 are M star companions in the extended 10 pc AFGK sample. Because the habitable real estate of M stars out to 10 pc is estimated by scaling the 5 pc results, we do not consider these M stars in our EHZ calculations. This leaves 59 stars in multiple systems with potential habitable zones. For clarity, we emphasize that the EHZ of each star in a system is calculated separately.

Of the 59 stars, 43 (73%) have at least 4 spatially resolved photometric measurements in different filter bandpasses. For these stars, the same prescription used in Section 5.4.2 is used to calculate the EHZs. For the 16 stars that are not photometrically spatially resolved from their nearest companion(s), we estimate the EHZ locations based on spectral type information for the components. Using the assembled spectral types listed in Tables 5.1 & 5.3, we estimate the components' $V - K$ color using the spectral type versus $V - K$ colors relations of Kenyon & Hartmann (1995), and estimate the location of the EHZs using the relations described in Section 5.5.2.

To assess the dynamical stability of any planets in these EHZs, we compare the locations of the outer EHZ boundaries to the binary separations listed in Table 5.9. We consider a planet to be dynamically stable if the periastron distance of a star's nearest companion is greater than five times the outer EHZ boundary. In cases where the periastron distance cannot be calculated (because its full orbit solution is not known), we use the projected separation. Fortunately, these exceptions are all large separation multiples, and thus minor errors in the adopted separation are likely irrelevant for dynamical stability considerations.

The ratios of periastron distances to outer EHZ boundaries are illustrated in Figure 5.3. For each star and its nearest companion, the ratios range from 0.001 to 164107. 49 of the 59 stars have ratios greater than 5 to their nearest companions, and thus EHZs in which planets should be in dynamically stable orbits. The remaining 10 stars (GJ 53A, GJ 222A, GJ 244A, GJ 280A, GJ 423A, GJ 423B, GJ 713A, GJ 713B, GJ 866A, and GJ 866C) are considered to have EHZs in which planets would not be in dynamically stable orbits, so are excluded in our estimate of total EHZ real estate. Seven of these have ratios less than 1.0, hinting at the possibility of circumbinary planets. However, the majority of the EHZ outer radii are only a few times the binary separations, making it unlikely that these systems would have dynamically stable circumbinary planets in the EHZ. Nonetheless, it is worth noting that a few massive planets have been reported in circumbinary orbits (Lee et al. 2009; Qian et al. 2010).

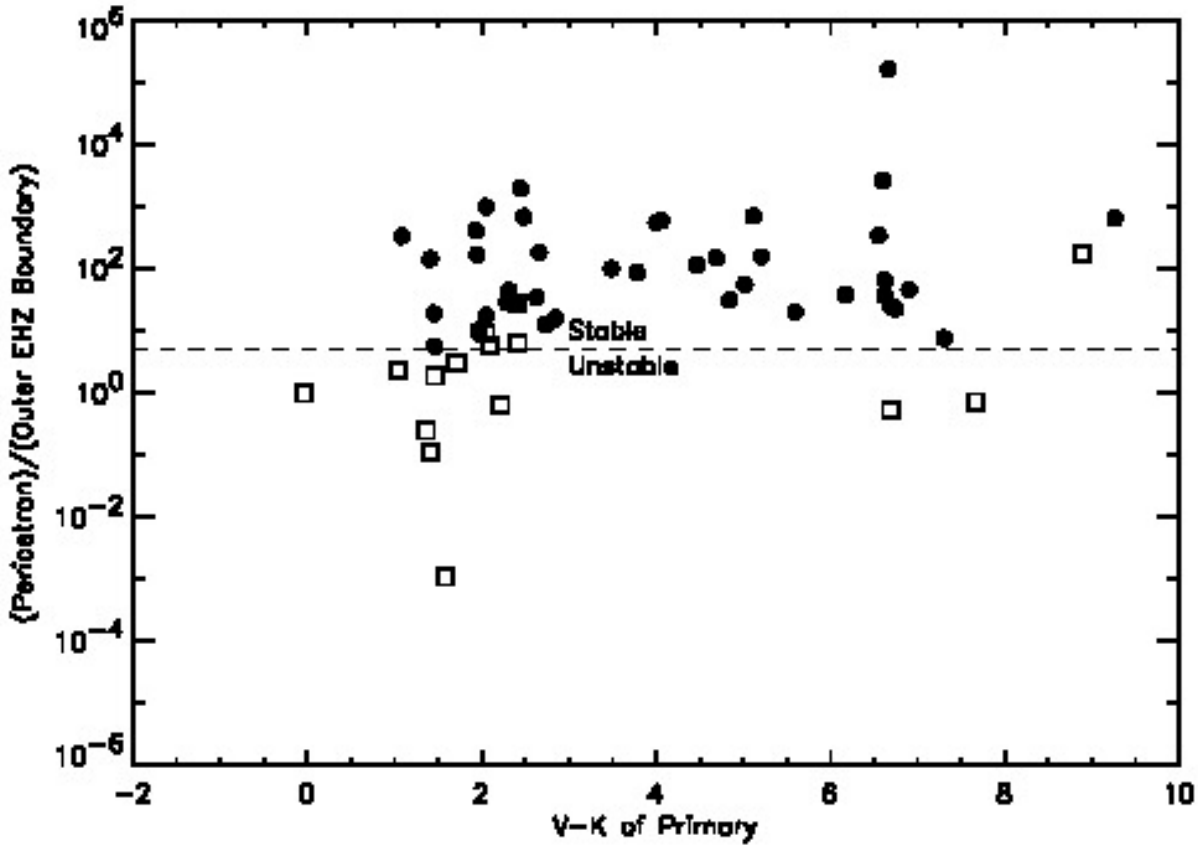

Figure 5.3 The closest approach of a companion star to the outer radius of the EHZ is plotted versus the primary's V-K value. Photometrically unresolved multiples are plotted as *open squares*, while resolved components are plotted as *filled circles*. Stars with companions that get closer than 5 times the outer EHZ boundary (*dashed line*) are considered dynamically unstable planet hosts, and are not included in the total habitable real estate calculations. GJ 663AB and GJ 663BA are plotted as the same point as their ΔV and ΔK = 0. The open square at $V - K = 8.88$, ratio = 173, is SCR 1845-6357, an M dwarf with a brown dwarf companion in a highly uncertain orbit.

Table 5.9: Orbital Properties of Multiple Systems

Star	Sep	a	e	i (°)	Ω(°)	ω(°)	P(yr)	T	Ref
GJ 15 AB	40″	···	···	···	···	···	···	···	E96
GJ 34 AB	···	11.″99	0.497	34.76	98.43	88.59	480	1889.6	S69
GJ 53 AB	···	1.″01	0.561	106.8	47.3	152.7	21.75	1975.74	D95
GJ 65 AB	···	2.″06	0.615	127.3	150.5	285.4	26.52	1971.88	W73
GJ 66 AB	···	7.″82	0.534	142.8	13.1	18.37	483.66	1813.5	V57
GJ 105 AC-B	165″	···	···	···	···	···	···	···	G00
GJ 105 AC	3.″3	···	···	···	···	···	···	···	G00
GJ 166 A-BC	83″	···	···	···	···	···	···	···	B89
GJ 166 BC	6.″94	···	0.410	108.9	150.9	327.8	252.1	1849.6	H74
GJ 216 AB	95″	···	···	···	···	···	···	···	E56
GJ 222 AB	···	0.″688	0.451	95.94	126.36	111.57	14.11	1999.9	Ha02
GJ 234 AB	···	1.″04	0.371	51.8	30.7	223	16.12	1999.38	S00
GJ 244 AB	···	7.″56	0.592	136.5	55.57	147.27	50.09	1894.13	G78
GJ 250 AB	58″	···	···	···	···	···	···	···	E56
GJ 280 AB	···	4.″496	0.365	31.9	284.8	88.8	40.38	1967.86	I92
GJ 412 AB	28″	···	···	···	···	···	···	···	G03
GJ 423 AC-BD	···	2.″533	0.421	112.1	101.3	127.3	59.84	1995.05	H96
GJ 423 AC	···	0.″056	0.53	94.9	263.5	143.0	1.832	1986.50	M95
GJ 423 BD	*	···	···	···	···	···	0.015	···	M95
GJ 432 AB	17″	···	···	···	···	···	···	···	He02
GJ 442 AB	25.″4	···	···	···	···	···	···	···	P94
GJ 473 AB	···	0.″926	0.295	103.00	143.48	347.2	15.64	1992.30	T99
GJ 559 AB	···	17.″57	0.518	79.2	204.85	231.65	79.91	1875.66	P02
GJ 551-GJ 559 AB	2.°18	···	···	···	···	···	···	···	P94
GJ 566 AB	···	4.″94	0.51	139	347	203	151.6	1909.3	S99
GJ 570 A-BC	···	32.″34	0.20	72.53	317.31	252.1	2130	1689	Ha94

Table 5.9: Orbital Properties of Multiple Systems

Star	Sep	a	e	i (°)	Ω(°)	ω(°)	P(yr)	T	Ref
GJ 570 BC	···	0.″151	0.756	107.6	195.9	127.56	0.846	1996.51	F99
GJ 570 ABC-D	258.″3	···	···	···	···	···	···	···	B00
GJ 663 AB	···	13.″0	0.916	99.79	-85.8	-90.2	470.9	1677.9	I96
GJ 663 AB-GJ 664	74.″2	···	···	···	···	···	···	···	L57
GJ 666 AB	···	10.″42	0.779	35.64	131.78	333.44	693.24	1907.2	W57
GJ 667 AB	···	1.″81	0.58	128	313	247	42.15	1975.9	S99
GJ 695 AD	1.″43	···	0.32	68.0	81.8	92	65	1951.0	T01;He94
GJ 695 AD-BC	34″	···	···	···	···	···	···	···	R10
GJ 695 BC	···	1.″36	0.178	66.2	60.7	174.0	43.2	1965.4	C59
GJ 702 AB	···	4.″55	0.499	121.16	302.12	14.0	88.38	1895.94	P00
GJ 713 AB	···	0.″124	0.428	74.42	230.30	119.3	0.768	1984.83	F10
GJ 725 AB	···	13.″88	0.53	66.0	136.9	234.6	408	1775.0	H87
GJ 783 AB	7.″1	···	···	···	···	···	···	···	P94
GJ 820 AB	···	24.″43	0.414	52.7	173.4	153.17	691.61	1689.14	B50
GJ 845 A-BC	402.″3	···	···	···	···	···	···	···	S03
GJ 845 BC	0.″732	···	···	···	···	···	···	···	M04
GJ 860 AB	···	2.″383	0.410	167.2	154.5	211.0	44.67	1970.22	H86
GJ 866 AC	···	∼0.″01	0.000	∼117	···	···	···	1991.71	D99
GJ 866 AC-B	···	0.″346	0.446	112	161.5	337.6	2.25	1997.53	D99
GJ 881-GJ 879	1.°97	···	···	···	···	···	···	···	P94
GJ 1245 AC-B	7.″969	···	0.320	135.0	80.0	38.0	15.22	1983.1	T97
GJ 1245 AC	0.″800	···	···	···	···	···	···	···	T97
SCR 1845-6357 AB	1.″170	···	···	···	···	···	···	···	B06

* asin(i)=274,000 km
B00 Burgasser et al. (2000)
B06 Biller et al. (2006)
B50 Baize (1950)
B89 Baize & Petit (1989)
C59 Couteau (1960)
D95 Drummond et al. (1995)
D99 Delfosse et al. (1999)
E56 Eggen (1956)
E96 Eggen (1996)
F10 Farrington et al. (2010)
F99 Forveille et al. (1999)
G00 Golimowski et al. (2000)
G03 Gould (2003)
G78 Gatewood & Gatewood (1978)
Ha02 Han & Gatewood (2002)
He02 Henry et al. (2002b)
H74 Heintz (1974)
H86 Heintz (1986)
H87 Heintz (1987)
Ha94 Hale (1994)
he94 Heintz (1994)
H96 Heintz (1996)
I92 Irwin et al. (1992)
I96 Irwin et al. (1996)
L57 Luyten (1957)
M04 McCaughrean et al. (2004)
M95 Mason et al. (1995)
P00 Pourbaix (2000)
P02 Pourbaix et al. (2002)
P94 Poveda et al. (1994)
R10 Raghavan et al. (2010)
S00 Ségransan et al. (2000)
S03 Scholz et al. (2003)
S69 Strand (1969)
S99 Söderhjelm (1999)
T01 Turner et al. (2001)
T97 Tokovinin (1997)
T99 Torres et al. (1999)
V57 van Albada (1957)
W57 Wieth-Knudsen (1957)
W73 Worley & Behall (1973)

5.5 Discussion

The described HZ calculations are used to assess the total habitable real estate in the solar neighborhood and to determine the amount of habitable real estate as a function of spectral type. Evolved stars, brown dwarfs, and multiple stars with separations detrimental to the orbital stability of a planet in the EHZ, as described above, are excluded in these assessments. In the 5 pc sample, stars removed from the analysis due to close companions include GJ 244A, GJ 244B, GJ 280A, GJ 280B, GJ 866A, and GJ 866C. The distribution by spectral type, after the removal of these stars in the 5 pc sample is as follows: 0 A, 0 F, 3 G, 7 K, and 48 M stars. Similarly, stars removed from the extended 10 pc sample analysis due to close

companions include GJ 53A, GJ 53B, GJ 222A, GJ 222B, GJ 423A, GJ 423 B, GJ 423C, GJ 423D, GJ 713A, and GJ 713B. Stars with evolved spectral types such as GJ 150, GJ 695A, and GJ 780 are also removed from subsequent calculations. By spectral type, the total stellar samples considered in the final EHZ assessment are 3 A, 4 F, 14 G, 34 K, and an estimated 384 M stars.

5.5.1 The EHZ "Width"

Using our initial assumptions of a terrestrial "Earth-like" planet as the basis for our EHZ, we estimate the habitable real estate using linear AU separations from the central star, essentially the width of the EHZ. In Table 5.10 we present the EHZ width totals for each spectral type in the 5 pc and total 10 pc samples.

Table 5.10: Total EHZ by Spectral Type

	5 pc Sample		Total 10 pc Sample	
SpType	# of stars	EHZ AU	# of stars	EHZ AU
A	0(1)	···	3 (4)	13.2
F	0(1)	···	4 (6)	4.9
G	3	2.6	14 (21)	11.9
K	7	2.9	34 (35)	15.4
M	48(50)	3.3	384*(400)*	26.1*

The numbers used in the table reflect the number of stars in each sample for which the EHZ was calculated (and include the Sun). Photometrically unresolved binaries, evolved

stars, and substellar objects for which EHZs were not calculated are excluded from these totals. *The totals for the M type population to 10 pc are a factor of eight greater than the population within 5 pc, estimated via scaling by the volume (R^3). Numbers in parentheses are totals including photometrically unresolved binaries and evolved stars.

The cumulative EHZ width for stars in the 5 pc subsample is 8.8 AU, including 2.6 AU for the 3 G stars (including the Sun) and 2.9 AU for the 7 K stars. The 48 M dwarfs in the 5 pc sample *en masse* provide 3.3 linear AU available for habitable planets, or 38% of the available EHZ. The dominant contribution of M dwarfs to the EHZ width is demonstrated clearly using the estimated 10 pc sample. The total EHZ width for the estimated 10 pc sample is 71.5 AU, including 13.2 AU for the 3 A, 4.9 AU for the 4 F stars, 11.9 AU for the 14 G stars, and 15.4 AU for the 34 K stars. The estimated 384 M stars *en masse* provide 26.1 AU of linear EHZ. This accounts for 36.5% of the total EHZ. Thus, by spectral type, M stars *en masse* provide the largest EHZ real estate.

5.5.2 Predicting the Size of the Habitable Zone from $V - K$ Colors

Given the rapid pace of exoplanet discovery, it would be helpful to have a tool to easily and accurately predict the location of the EHZ to determine whether or not a planet resides within it. Predicting the EHZ of a star based on spectral classification can be problematic due to the inhomogeneity in classification and spectral types being determined over different wavelength ranges. As shown in Henry et al. (2006), the $V - K$ color is a useful temperature diagnostic for the A through M stars that dominate the solar neighborhood. This relation can also be very helpful in determining a rough estimate of the EHZ based on observable

photometry, and may be easily scaled to larger populations.

We use the results from the 5 pc and extended 10 pc samples to derive a relation between $V-K$ color and the size and location of the EHZ. As in the computation of total habitable real estate, we removed binary stars with unresolved photometry, as well as stars known to be evolved. We do, however, use stars such as Sirius (GJ 244) and Procyon (GJ 280) for which EHZs have been determined, even though their companions corrupt their EHZs. Their white dwarf companions do not significantly contribute to their luminosities or $V-K$, and their inclusion improves the statistics of our fit. We fit a second order polynomial, described by Equation 5.6, to the $V-K$ colors and computed EHZ widths shown in Figure 5.4.

$$Log(EHZ_{\text{width(AU)}}) = 0.648 - 0.457(V-K) + 0.021(V-K)^2 \tag{5.6}$$

Using the same method, a relationship for $V-K$ color and the inner and outer radii of the EHZs are described by Equations 5.7 and 5.8, respectively. These relations are only valid for main sequence stars.

$$Log(EHZ_{\text{inner(AU)}}) = 0.593 - 0.457(V-K) + 0.021(V-K)^2 \tag{5.7}$$

$$Log(EHZ_{\text{outer(AU)}}) = 0.922 - 0.457(V-K) + 0.021(V-K)^2 \tag{5.8}$$

As a check on these relations, we use these to calculate the total EHZ width by spectral type of the estimated 10 pc sample and compare these values to the direct calculations

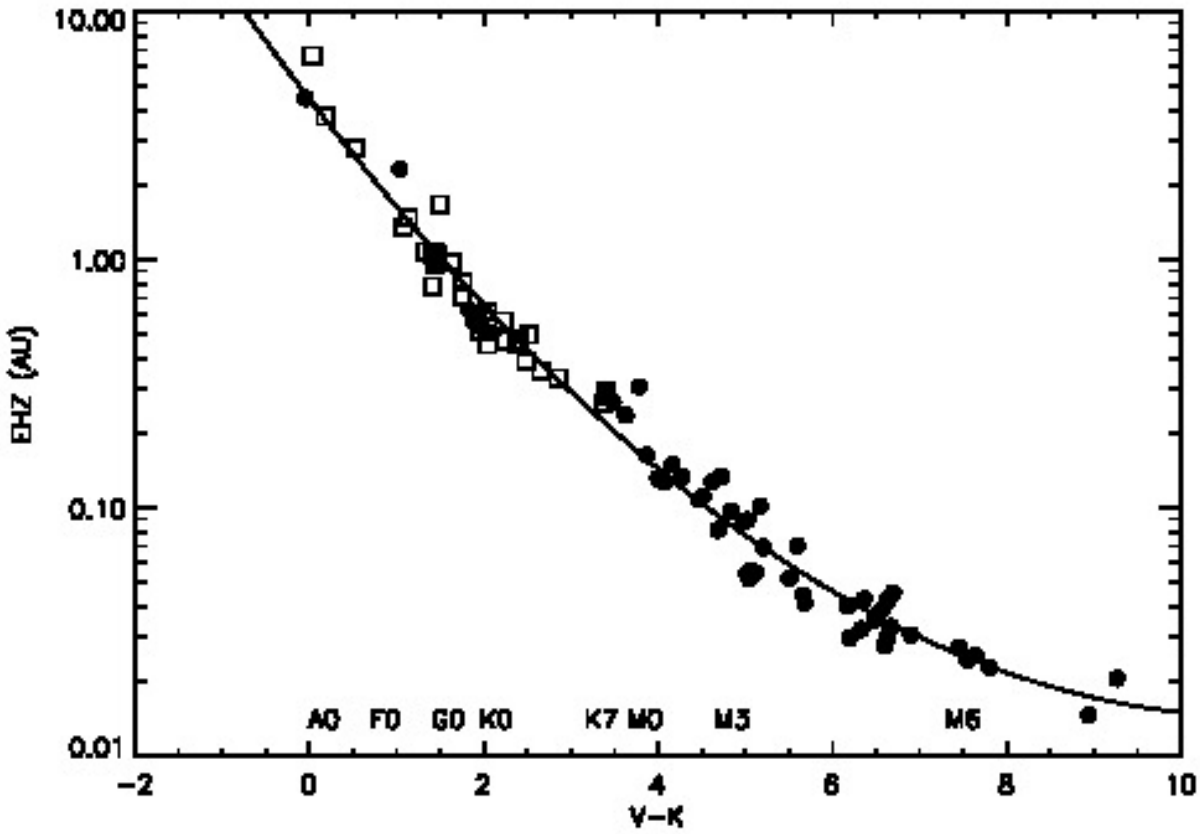

Figure 5.4 Empirical habitable zone (EHZ) widths for the 5 pc (*filled circles*) and extended 10 pc samples (*open squares*). The best fit relation (Equation 5.6 in text) is overplotted.

described in Sections 5.4.2 & 5.4.3. We find the total EHZ widths from the empirical relations differ on average from the calculated total widths by −12.7%, −6.4%, 1.6%, 4.7%, and 0.3% for A, F, G, K, and M stars respectively; negative values correspond to underpredictions of the EHZ width totals. The higher percentage differences for A type and F type totals are due to the relatively small populations within 10 pc and the effects of large 2MASS photometric errors due to brightness. The results imply that this relation is useful for quickly estimating the amount of habitable real estate for a population with known $V - K$ values. We also test

how well the predicted inner and outer boundaries from our relations agree for any given star. On average, these predictions yield values consistent to 3% with a dispersion of 22% for both inner and outer boundaries for AFGKM stars in our samples. These dispersions can be interpreted as the uncertainty in the locations of these boundaries from these relations.

5.5.3 Planets in the EHZs of Nearby Stars

Of the 15 confirmed planetary systems within 10 pc of the Sun for which orbits have been determined, five contain multiple planets (GJ 139, GJ 506, GJ 581, GJ 667C, and GJ 876). All 15 systems are listed in Table 5.11 with published values for semimajor axis and eccentricity, as well as calculated inner and outer radii of the EHZ from this work. Three of the systems, GJ 581, GJ 667C, and GJ 876 have planets in the EHZ.

Table 5.11: Exoplanets within Ten Parsecs

Star	Planet	Semimajor Axis	e	Ref	HZinner	HZouter
		(AU)			(AU)	(AU)
GJ 15 A	a	0.0717±0.0034	0.0	Howard et al. (2014)	0.112	0.239
GJ 139	b	0.1207±0.0020	0.0	Pepe et al. (2011)	0.632	1.350
GJ 139	c	0.2036±0.0034	0.0	Pepe et al. (2011)	0.632	1.350
GJ 139	d	0.3499±0.0059	0.0	Pepe et al. (2011)	0.632	1.350
GJ 144	b	3.39±0.36	0.702±0.039	Benedict et al. (2006)	0.439	0.938
GJ 176	b	0.066	0	Forveille et al. (2009)	0.136	0.290
GJ 442 A	b	0.46±0.04	0.34±0.14	Tinney et al. (2011)	0.689	1.472
GJ 506	b	0.05±5.0e-6	0.12±0.11	Vogt et al. (2010b)	0.689	1.472
GJ 506	c	0.2175±0.0001	0.14±0.06	Vogt et al. (2010b)	0.719	1.537
GJ 506	d	0.476±0.001	0.35±0.09	Vogt et al. (2010b)	0.719	1.537
GJ 559 B	b*	0.04185±0.0003	0	Dumusque et al. (2012)	0.541	1.155
GJ 581	b	0.04	0	Mayor et al. (2009)	0.083	0.179
GJ 581	c	0.07	0.17±0.07	Mayor et al. (2009)	0.083	0.179
GJ 581	**d**	**0.22**	**0.38±0.09**	**Mayor et al. (2009)**	**0.083**	**0.179**
GJ 581	e	0.03	0	Mayor et al. (2009)	0.083	0.179
GJ 581	f*	0.758±0.015	···	Vogt et al. (2010a)	0.083	0.179
GJ 581	**g***	**0.1460±1.4e-4**	···	**Vogt et al. (2010a)**	**0.083**	**0.179**

Table 5.11: Exoplanets within Ten Parsecs

Star	Planet	Semimajor Axis	e	Ref	HZinner	HZouter
		(AU)			(AU)	(AU)
GJ 667 C	b	0.049	0.172±0.043	Anglada-Escudé et al. (2012)	0.096	0.205
GJ 667 C	**c**	**0.123±0.020**	**< 0.27**	**Anglada-Escudé et al. (2012)**	**0.096**	**0.205**
GJ 674	b	0.039	0.20±0.02	Bonfils et al. (2007)	0.098	0.210
GJ 785	b	0.310±0.005	0.30±0.09	Howard et al. (2011)	0.500	1.068
GJ 832	b	3.4±0.4	0.12±0.11	Bailey et al. (2009)	0.131	0.280
GJ 849	b	2.35	0.06±0.09	Butler et al. (2006)	0.136	0.290
GJ 876	b	0.2083±2.0e-5	0.0292±1.5e-3	Rivera et al. (2010)	0.090	0.191
GJ 876	**c**	**0.1296±2.6e-5**	**0.2549±8.0e-4**	**Rivera et al. (2010)**	**0.090**	**0.191**
GJ 876	d	0.0208±1.5e-7	0.207±0.055	Rivera et al. (2010)	0.090	0.191
GJ 876	e	0.3443±0.0013	0.055±0.012	Rivera et al. (2010)	0.090	0.191
GJ 881	b	115	0.11	Kalas et al. (2008)	3.316	7.084

Bold rows indicate the planet is in the EHZ for at least part of its orbit.

* Planet detection controversial.

GJ 581, an M2.5V star at a distance of 6.25 pc, has six proposed planets, but the existence of GJ 581g and GJ 581f are currently debated (see: Vogt et al. 2010a; Andrae et al. 2010; Gregory 2011; Anglada-Escudé & Dawson 2010; Tuomi 2011). If real, GJ 581g, with a semimajor axis of 0.146 AU, orbits in the EHZ in a presumed circular orbit. Using the CHARA Array, von Braun et al. (2011) recently measured the size of the star and derived HZ boundaries of R_{in}= 0.11 AU and R_{out}= 0.21 AU. Our EHZ is somewhat closer in to the star, R_{in}= 0.083 AU and R_{out}= 0.179 AU, but still places GJ 581g in the EHZ. The differences are due to our calculated luminosity (L= $0.11 L_{\odot}$) being 8% lower than von Braun et al. (2011), as they adopted an extinction of A_V= 0.174 for GJ 581, which they note as unexpected for a star at this distance. GJ 581d, with semimajor axis of 0.22 AU and eccentricity of 0.38, also moves in and out of the EHZ of GJ 581.

GJ 667C, an M1.5V star at a distance of 7.23 pc, hosts two planets, and possibly four (Anglada-Escudé et al. 2012). Although GJ 667Cb does not lie within the EHZ, GJ 667Cc (m sin i of 4.5 $M_{\oplus}$) lies within the EHZ for the majority of its orbit. With a semimajor axis of 0.123 AU and eccentricity <0.27, it may lie completely within the EHZ once the eccentricity is more highly constrained.

GJ 876, an M3.5V star at a distance of 4.66 pc, hosts four planets (Rivera et al. 2010). Our calculations show an EHZ spanning 0.090-0.191 AU. Rivera et al. (2010) report orbital fits for two planets near the EHZ with semimajor axes of 0.13 AU (GJ 876c) and 0.21 AU (GJ 876b), and eccentricities of 0.25 and 0.03, respectively. As shown in Figure 5.5, this allows for GJ 876c to be in the EHZ of its host star for the full duration of its orbit, while GJ

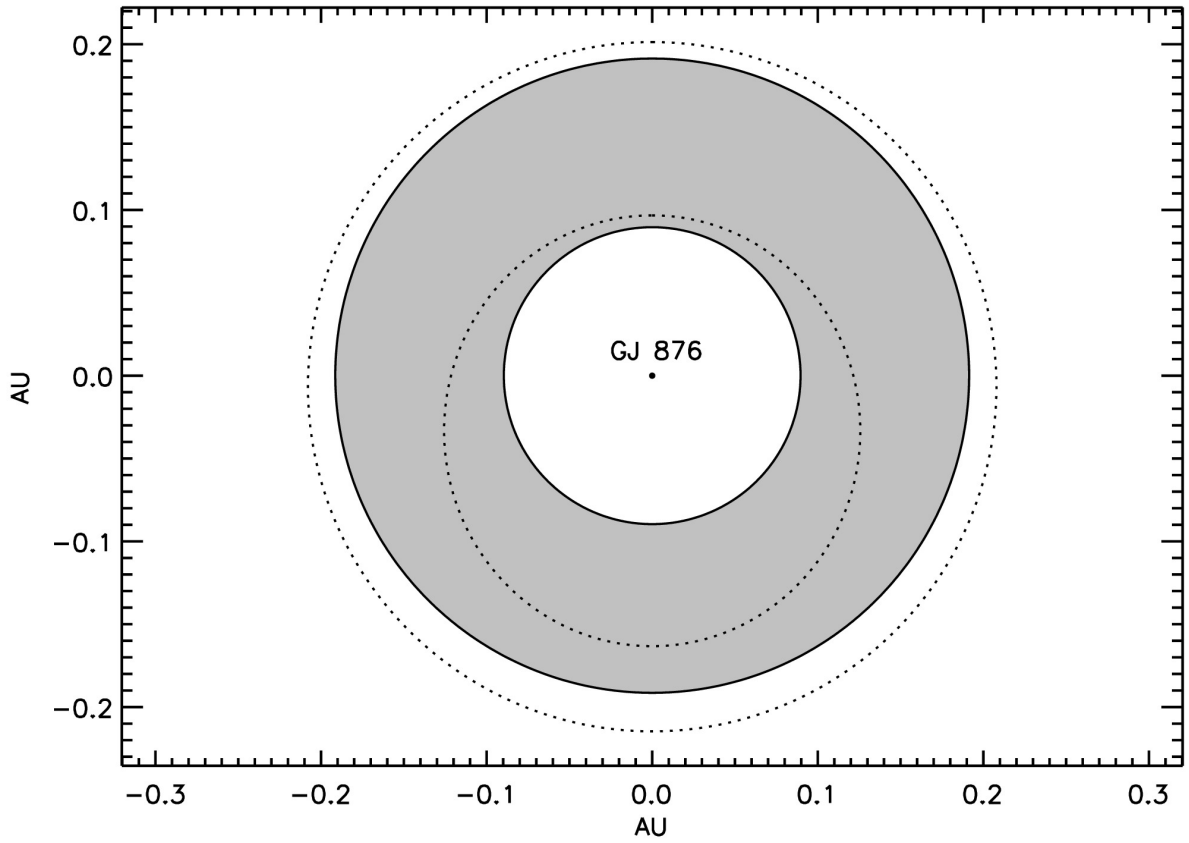

Figure 5.5 The EHZ in this figure is shown as a shaded disk, along with the orbits of the two planets (dotted circles) in the GJ 876 system nearest the EHZ.

876b lies just outside the EHZ. Although these planets are not considered terrestrial ($m \sin i$ of 0.56 and 1.89 M_J), the possibility exists that they could have terrestrial-like moons that could be habitable.

5.5.4 Complications to Habitability

The previous sections provide estimates of EHZs based on the requirement of liquid water on a planetary surface. Of course, a planet's location in the EHZ of a host star does not

guarantee its habitability. A host of other factors, such as planet size, atmosphere, magnetic fields, and even plate tectonics, play vital roles in determining the habitability of a planet in the EHZ. Without a sufficiently thick atmosphere, biologically harmful radiation can penetrate to the surface of a planet. On Earth, atmospheric CO_2 levels are kept in check by the carbon-silicate cycle. Known to regulate climate temperatures through a negative feedback, this cycle allows for as much as 60 bars (Kasting 1996) of CO_2 to be locked away in rock and sediments. This slow carbon-silicate cycle requires that water be present, because without water, the atmospheric CO_2 cannot be sequestered as carbonate. A magnetosphere on Earth also plays an important role by deflecting harmful charged particles. Tectonic activity may be one of the key factors in keeping a planet habitable (Doyle et al. 1998). Without water, the lithosphere of a planet may become a stagnant lid, halting tectonic activity and the sequestration of CO_2.

There is a temporal constraint on habitability as well, as the HZ may change considerably over the lifetime of a star (Kasting et al. 1993; Kasting 1996; Tarter et al. 2007; Selsis et al. 2007). Putting these complications aside, the requirement of liquid water on the surface of a planet is a good first order approximation to habitability.

CHAPTER 6

Summary

In human-kind's search to quantify elements of the Drake Equation, we first need to know how gas giant planets form and migrate, since gas giant planets can dynamically scatter debris in the solar system, potentially clearing out large life-sterilizing impactors as well as capturing and clearing remaining comets and asteroids. Of similar importance is quantifying the amount of habitable area for nearby stars to better understand how much habitable real estate is available. With this, and a mass function, we can better predict how much habitable real estate there might be in the galaxy. This dissertation is focused on addressing these two topics.

Finding young Hot Jupiters is key to understanding formation and migration scenarios for giant planets, since the timescale to distinguish between different models diverge at ages between 1-10 Myr. Nevertheless, young chromospherically active stars have been traditionally avoided in high-precision radial velocity (RV) surveys because of the time-dependent warping of stellar absorption features caused by starspots. Although these distortions can be identified in very high spectral resolution observations (R >50K), if left unaccounted for they can give the appearance of periodic RV shifts that can be misinterpreted as a planet (Queloz et al. 2001).

In this work, we used high resolution infrared (R=30-50K) to search for planets around young stars in the northern and southern hemisphere. By targeting this wavelength range, we hoped to mitigate the stellar jitter caused by the chromospheric activity on the surface of

these stars as the spot contrast in the infrared is much lower. In this Chapter, we summarize the results of our two surveys.

Additionally, we presented the ensemble results for the estimated habitable real estate around all known stars and brown dwarfs within 5 pc of the Sun, and an extended sample of A, F, G and K stars out to 10 pc.

6.1 Gemini Phoenix and VLT CRIRES

In Chapter 2, we demonstrated the RV precision of our technique on 25 young ($\sim$10 Myr) stars observed in with the high dispersion infrared Phoenix spectrograph on the Gemini South telescope and CRIRES on the VLT. These stars include members of nearby Moving Groups β Pictoris, Tucana-Horologium, η Chamaeleontis, TW Hydrae, Chamaeleon, Upper-Scorpius, Lupus, and Corona Australus. Using telluric lines as a wavelength calibration reference, we were able to achieve empirical RV precisions as low as 21-31 m/s with Gemini Phoenix and 32-63 m/s with VLT CRIRES on RV standards.

6.1.1 Gemini Phoenix

With Gemini Phoenix, we applied this technique to young stars to measure the multi-epoch RVs, and fit for $v\sin i$ and absolute systemic RV for each star. Using 18 free parameters to characterize the convolution of a telluric and synthetic model, we fit for instrumental profile (a 9 Gaussian model), the wavelength solution (quadratic), depth of telluric features, the depth of stellar features, the projected rotational velocity ($v\sin i$), a linear (2 parameter) continuum normalization offset, and the star's RV. These $v\sin i$ values range from 0.30 km/s

to 15 km/s and agree to within 18% of published values, but we caution that our velocity resolution ($\sim$6 km/s) can only put upper limits on $v\sin i$ values below <3 km/s.

Although there is not standard prescription for identifying companion induced RV variability for young stars, we investigated the empirical variability by comparing the $v\sin i$ to the standard deviation in the epoch RV for stars in our sample, and the statistical P-χ^2 test. For young stars in the Gemini Phoenix sample, the majority of young stars (15) show similar RV dispersion ($\lesssim$100 m/s) independent of $v\sin i$ over a range of $v\sin i$ values (0.3 - 15 km/s), with an average dispersion of 63 m/s. However, we found four young stars with significantly (5σ) above the average standard deviation. These include SZ96 (359 m/s), RXJ 1557.8-2305 (201 m/s), TWA 13A (353 m/s), and ScoPMS 13 (353 m/s).

Although SZ 96 and RXJ 1557.8-2305 showed high RV dispersions, with SNR values of 52-63 and 55-76 respectively, were below the average SNR value for the sample (SNR_{Avg}=82). Additionally, the p-values for these stars (SZ 96 - 0.43; RXJ 1557.8-2305 - 0.55) did not show statistically significant variation. As such, we did not identify these as intrinsically variable, as their variations were likely due to their low SNR values.

TWA 13A had been previously identified as a candidate RV variable in Bailey et al. (2012), and showed a higher than average RV dispersion in our data. However, the p-value for our 4 epochs of data was 0.21, signifying that the RV variability was not significant. Nevertheless, we did follow-up this star with VLT CRIRES.

ScoPMS 13 showed an unusually large dispersion of 353 m/s, and a p-value of 0.024. We caution that this is based on only 3 epochs of observation. It has a spatially resolved

companion with a projected separation of ∼21 AU that would not cause large RV dispersions in short timescales. ScoPMS 13 will need to have follow-up RV observations to determine if the RV variability is due to stellar jitter, or a companion. Nevertheless, we classify it as a candidate RV variable.

In addition to the four stars mentioned above, RXJ1204.6-7731 was identified as a spectroscopic binary with a standard deviation of the RV measurements of more than 2 orders of magnitude above the average standard deviation (σ=8,825 m/s), and a P-χ^2 value of <0.0001. Since our code is not designed to model a composite spectrum, we used TODCOR to determine the RVs of both components. With the resulting RV's from TODCOR, we fit Keplerian orbits to each component separately utilizing a Markov Chain Monte Carlo (MCMC) algorithm described in Quinn et al. (2015). Although the best orbital fit is preliminary, we report the system to be a 5.6 day SB2 component RV amplitudes of RXJ1204.6-7731A (10.8 km/s) and RXJ1204.6-7731B (29.6 km/s) correspond to a mass ratio of K_A/K_B= 0.37.

6.1.2 VLT CRIRES

We were granted queue observing time on VLT CRIRES to monitor the RVs of four young stars in greater detail over a longer (2-3 month) temporal baseline. We targeted TWA 13A and V721 CrA from the Gemini Phoenix sample for additional observations with VLT CRIRES, as well as two additional stars, TYC 7443-1102-1 and 1RXS J195602.8320720 from β Pic. Our follow-up observations were setup to give nearly the same wavelength range and resolution as the Gemini Phoenix dataset. The analysis used the same prescription as the

Gemini Phoenix sample.

TWA 13A was chosen for follow-up due to its RV variability noted in Bailey et al. (2012) and the large (but not statistically significant) RV variations seen in our Gemini Phoenix observations. V721 CrA was chosen to ascertain our empirical precision on a young star with similar spectral type and $v\sin i$. We observed the young common proper motion pair, TYC 7443-1102-1 and 1RXS J195602.8320720, as it gave us an additional opportunity to study a young coeval pair.

Two of these four stars, V721 CrA (10 epochs) and TYC 7443-1102-1 (19 epochs) had RV dispersions (88 m/s and 58 m/s respectively) near the average dispersion of 63 m/s for the Gemini Phoenix sample. We measure low p-values for both V721 CrA and TYC 7443-1102-1 (0.06 and 0.99 respectively), we do not consider these stars to be short period RV variables.

TWA 13A (8 epochs) exhibited a slightly lower standard deviation of 171 m/s than the fits from Gemini Phoenix, however, a P-χ^2 test indicated the RV variations were statistically significant, with a p-value of 0.004. Although Bailey et al. (2012) and this work both indicated that TWA 13A is an RV variable, we were unable to determine the underlying cause of this elevated RV dispersion.

1RXS J195602.8320720 (18 epochs) showed very high standard deviation (15,794 m/s) indicative of a stellar companion, and a p-value of $<<0.0001$. Additionally, the companion spectrum is seen in the residuals of our fits, and thus we classified this as a double-lined spectroscopic binary. We, again, used TODCOR to fit individual RV measurements for each component, and we attempted fit Keplerian orbits to the individual components, but were

unable to come up with a solution which had a residuals <4 km/s. The best fit orbital solution appears to be a ∼19 day period binary with nearly equal mass (K_A/K_B=0.97) components. We also notice a trend in the mean velocities showing some acceleration (i.e. not linear) that could be caused by a wider companion.

6.2 Keck NIRSPEC

We conducted a high precision RV search for planets using Keck NIRSPEC on 24 young stars in Taurus-Auriga (∼1-2 Myr) and 14 young stars in Upper Scorpius (∼10 Myr), with a temporal baseline ranging from 2-5 years, using the high dispersion infrared spectrograph NIRSPEC on the W.M. Keck telescope. We used the same technique described in Chapter 2 to obtain RVs and $v\sin i$ values for each star. In total, we obtained 29 nights (Nov 18 2004 to July 24 2010) giving us sensitivity to longer period RV variations. Using this technique, we were able to achieve empirical an RV precision of 75-115 m/s on RV standard stars.

Again, we assessed the variability empirically by comparing the $v\sin i$ to the standard deviation in the epoch RV for stars in our sample. The RV dispersions of Upper-Sco stars at ∼10 Myr and Taurus-Auriga stars at ∼1-2 Myr showed a pronounced difference, and we will discuss them separately below. We used the statistical P-χ^2 test, and new test to assess how statistically significant the RV dispersions are, which we call Δ. Δ is defined as the RV dispersion divided by the average error ($< \sigma_{Epoch} >$) for that star.

In the following discussion in Sections 6.2.1 and 6.2.2, we will exclude newly discovered spectroscopic binaries. These discoveries will be discussed in Section 6.2.4.

6.2.1 Taurus-Auriga

The stars in the very young (1-2 Myr) Taurus-Auriga sample showed a wide range of RV dispersion values between 75-584 m/s with an average of 296 m/s and $v\sin i$ values between 4-52 km/s with an average of 14 km/s. Taurus-Auriga stars show a large spread in Δ values between 1.5-19.3 with an average value of 9.4 and a standard deviation of 4.8. Taurus-Auriga stars showed a high fraction of low p-values with 16 out of 24 stars having a p-values less than 0.01. Using all three metrics, a large fraction of stars in Taurus-Auriga stars exhibit evidence of having statistically significant RV variability. However, since we do not expect the majority of these stars to have hot Jupiter-like companions, we interpret this as Taurus-Auriga stars having large amplitude stellar induced RV variations. Consequently, we do not identify any of these stars as candidate planet hosts.

6.2.2 Upper-Sco

The stars in Upper-Sco showed a range of RV dispersions between 41-561 m/s with an average of 161 m/s and $v\sin i$ fit values that range from 4-18 km/s with an average of 10 km/s. RXJ1540.9-3024 was at the upper end of that dispersion range, with an average RV dispersion of 561 m/s. The remaining 12 stars in Upper-Sco have a much smaller range in RV dispersions than Taurus-Auriga, with RV dispersions between 41-182 m/s with an average of 127 m/s. Excluding RXJ 1540.9-3024, there is a concentration of Δ values objects between 0.9-5.1 with an average value of 3.2 and a standard deviation of 1.1. RXJ 1540.9-3024 has a Δ value of 12.4, implying that the large RV dispersion for this star is not a consequence of

large RV errors. Again, with the exception of RXJ 1540.9-3024 with a p-value of 2.2×10^{-25}, the ensemble of Upper-Sco stars exhibited a flat distribution between zero and one. This is consistent with a population of RV non-variable stars. All three metrics point to RXJ1540.9-3024 being an RV variable.

6.2.3 Known Planet Host and Planet Candidate

6.2.3.1 GJ 876

We showed the ability of our code to recover the largest planet in the GJ 876 system, a nearby M-dwarf with 5 known planets. Using a Keplerian orbit fitting code, we were able to fit for the orbital properties of GJ 876a by adopting the stellar mass ($M_\star$= 0.32 $M_\odot$) and eccentricity (e=0.27) values from Marcy et al. (1998). Our fit for period of 61.97±0.51 days and planet mass of 1.7±0.4 M_J are in agreement with values from Delfosse et al. (1998) (P=60.97±0.19 days ; M_P=2 M_J) and Marcy et al. (1998) (P=2.11±0.01 M_J; M_P=60.85±0.15 days).

6.2.3.2 RXJ 1540.9-3024

We identified RXJ 1540.9-3024 as young planet candidate with a dispersion of 561 m/s and full amplitude variations of 1,594 m/s over the time period observed. Using a Keplerian orbit fitting code we obtained a best fit orbital solution which corresponds to a Jupiter mass ($m\sin i$=5.4 M_J) companion in a 10.7 day period, and an eccentricity of e=0.28. At ∼10 Myr, this star may harbor one of the youngest planets ever discovered. We are currently conducting observations of this star to confirm the presence of a giant planet and hopefully better constrain the planet mass and orbital properties of this very young system.

6.2.4 Spectroscopic Binaries

We identified two stars, RXJ 1548.9-3045 in Upper Scorpius and V1096 Tau in Taurus-Auriga, as double lined spectroscopic binaries. In both cases, the spectrum of the secondary was seen in the residuals of our fits, and we recovered the RVs for individual components using TODCOR. Unfortunately, the sparse sampling of the observations, 10 epochs over 29 months for RXJ 1548.9-3045 and 5 epochs over a 26 months for V1096 Tau, inhibited us from obtaining orbital solutions for these binaries.

6.3 Finding Planets in the Presence of Spots

It has long been known that stars exhibiting chromospheric activity can cause RV variability that mimics the RV signature of a planet orbiting a star. Observations in the infrared appear to mitigate these effects compared to optical, but do not eliminate them. The implication is that finding young planets requires more than distinguishing between spots and planets, but rather finding them in the presence of spots.

We quantified the magnitude of stellar jitter ($\sigma_{Stellar}$) for young stars from our Keck NIRSPEC sample by subtracting in quadrature the average epoch uncertainty for each star over the observing period ($< \sigma_{Epoch} >$) from the observed RV dispersion for each star. We chose to use the Keck NIRSPEC samples as a template for young stars, as it contains two young clusters at different ages (Upper-Sco, $\sim$10 Myr and Taurus-Auriga, $\sim$1-2 Myr). Our Gemini Phoenix sample, with only 3-5 observations, and our VLT CRIRES sample, with only four stars, did not provide a robust measure of stellar jitter.

The stellar jitter for Upper-Sco stars in our sample ranges from 92-174 m/s with a mean value of 129 m/s (StdDev=30 m/s). For stars in Taurus-Aurigia, the stellar jitter ranges from 56-584 m/s with a mean value of 293 m/s (StdDev=149 m/s). We note a large difference in RV dispersion between Taurus-Auriga ($\sim$1-2 Myr) and Upper-Scorpius ($\sim$10 Myr) regardless of $v\sin i$. We interpret this as evidence for stellar jitter declining significantly from 1-2 to 10 Myr.

We showed how CIDA 3 is a good example of a high dispersion (566 m/s) star that shows RV variability that could be misinterpreted as motion due to a high eccentricity planet. Using orbit fitting analysis, we can match the RVs to a highly eccentric (e=0.56) Jupiter mass ($m\sin i$=2.1 M_J) companion in a 5.6 day period. However, given the high dispersion (296 m/s) and high stellar jitter of Taurus-Auriga stars (293 m/s), it is difficult at such a young age to distinguish the stellar RV variability from RV variability induced by an orbiting companion.

Additionally, we used used Monte Carlo statistical model on stars from Chapter 2 and Chapter 3 with multi-epoch observations along with the average stellar jitter of 293 m/s for Taurus-Auriga stars, and 129 m/s (the calculated jitter for Upper-Sco) for all other young stars to determine companion detection limits.

The mean probability for detecting for 12-13M_{Jup} planets in 3 day periods for the young stars observed with Gemini Phoenix was 81%, and, with the exception of RXJ 1219.7-7403 (14%), and RecX 12 (56%), our detection rate for all stars is above 76% for the same mass and period range.

Since our VLT CRIRES follow-up had more observations taken over a longer time period (8-19 epochs over 49-88 days), we were more sensitive to lower mass companions. Our overall detection rate for 4-5 M_{Jup} planets with 3 and 10 day periods is above 89% and 77%, respectively, for all young stars in this sample, with an average detection rate of 92% and 84%, respectively. The overall detection rate for 12-13 M_{Jup} with 3 and 10 day periods is 97% and 85%, respectively, for young stars with an average detection rate of 98% and 96%, respectively. Given these detection rates, we rule out planets >4 M_{Jup} with <10 day periods for stars that are not identified as RV variable.

Our Keck NIRSPEC sample described in Chapter 3 was observed over a longer temporal baseline, with each star being having 5-10 observations over >770 days. For this reason, we were sensitive to the detection of short (<10 day) and long (10-30 day) period companions.

For Taurus-Auriga stars, our average detection rate for planets with a mass range of 4-5 $M_{\rm Jup}$ for periods of 3,10, and 30 days is 82%, 34%, and 15%, respectively. Given these detection rates, we rule out planets >4 M_{Jup} in < 3 day periods, as well as planets >12 M_{Jup} with periods less than 30 days for stars that are not identified as RV variables.

For Upper-Sco stars with a planet mass range of 4-5$M_{\rm Jup}$, we have an average detection rate of 90%, 72%, and 52% for 3, 10, and 30 day periods, respectively. For the planets with a mass range of 12-13M_{Jup}, the average detection rate is 97%, 93%, and 97% for the same periods. We can confidently rule out planets >4M_{Jup} in < 10 day periods, as well as planets >12$_{Jup}$ with periods less than 30 days for stars that are not identified as RV variable in Upper-Sco.

The hot Jupiter frequency for field FGK stars is 1.2% (Wright et al. 2012), and it is even lower for M stars ($\lesssim$1%; Bonfils et al. 2013. Given these frequencies, it would be statistically consistent with the field if we found $\lesssim$1 hot Jupiter in the 61 stars surveyed using Gemini Phoenix, VLT CRIRES and Keck NIRSPEC.

6.4 Habitable Zones around Nearby Stars

In Chapter 5, we assessed the sample of stars currently known to be within 5 pc of the Sun for the purpose of determining the habitable real estate and its dependence on spectral type. Because of the sparse population of high mass stars within 5 pc of the Sun, we expand this sample for AFGK stars to 10 pc; there are no O or B stars within 10 pc of the Sun. After eliminating evolved stars, substellar objects, and close multiples in which planets in HZs would be dynamically unstable, we use the final sample to estimate the EHZs for stars in both the 5 pc and extended 10 pc samples. We do not consider circumbinary habitable zones in this work, but EHZs are calculated in the same fashion as single stars for each of the 49 components in multiple systems that satisfy our dynamical stability constraint.

Using PHOENIX models convolved with filter response curves, we fit observed $UBVRIJHK$ photometry for each object, assuming spherical, non-rapidly rotating stars with solar metallicity and log g values of 4.0 to 5.0, with the 2 exceptions being the metal poor stars GJ 191 and GJ 451. This fitting process allows us to determine a radius and T_{eff} for each star that is then used to determine its surrounding EHZ, calculated using a modified "Venus and early Mars criterion" from Selsis et al. (2007).

We used estimates of linear AU to map the EHZ of each star and sum by spectral type *en masse*: 48 M dwarf stars used in the 5 pc sample provide more habitable real estate (3.3 AU) than the three G dwarfs stars (2.6 AU) and seven K stars (2.9 AU) found within 5 pc of the Sun. Even after extending the sample of AFGK stars to 10 pc, the anticipated sample of M dwarfs within 10 pc (not all have yet been identified) possess more EHZ real estate than any other spectral type, spanning ∼26 AU compared to 13.2 AU, 11.9 AU, and 15.4 AU for each of the A, G, and K types (the F stars provide only 4.9 linear AU of EHZ). The result is a natural consequence of the large relative numbers of M dwarfs, and the frequency of close companions that declines with mass.

As a population M dwarfs provide more options and more habitable real estate than their more massive counterparts. Furthermore, recent results from Kepler show that for stars with $T_{eff} > 4000$K within 5 pc of the Sun, there is likely to be at least 2 Earth-size planets in the HZ. That number increases to 16 within 10 pc (Dressing & Charbonneau 2013).

Using the 5 pc and extended 10 pc samples, we derived relations between $V - K$ color and EHZ width and inner and outer limits. Comparisons of color predicted locations suggest they are comparable to uncertainties associated with habitability assumptions (e.g.,, Section 5.4.2). Thus, these color relations are practical tools for estimating the EHZs of stars using commonly available photometric measurements. The relations for the inner and outer radii of the EHZ are helpful for quickly estimating whether or not a known planet or disk is within the EHZ. The relation for EHZ size is useful in predicting the habitable real estate available in a stellar population. In particular, we considered the results for the 14 extrasolar

planetary systems known within 10 pc of the Sun. The three systems with planets in the calculated EHZs — GJ 581, GJ 667C, and GJ 876 — are all M dwarfs. In total, as many as four planets circling these stars spend at least part of their time in the EHZs, providing an ideal set of targets for future efforts to detect biosignatures.

6.5 Appendix A

RV curves for all stars from Chapters 2 and 3 are shown in Appendix A. These are organized by survey, with Gemini Phoenix young stars and RV standards shown first, followed by VLT CRIRES young stars and RV standards, and conclude with Keck Nirspec young stars (Taurus-Auriga and Upper-Sco) and RV standards.

6.6 Appendix B

In Appendix B our detection rates for companion masses from 0-14 $M_{Jupiter}$ in 0-10 day periods for all stars in Chapter 2. For stars in Chapter 3, we show probabilities for detecting companion masses from 0-14 $M_{Jupiter}$ in 0-30 day periods for all stars in Chapter 3

Appendices

A RV Curves for All Stars

A Gemini South Phoenix

A.1 Young Stars – Gemini Phoenix

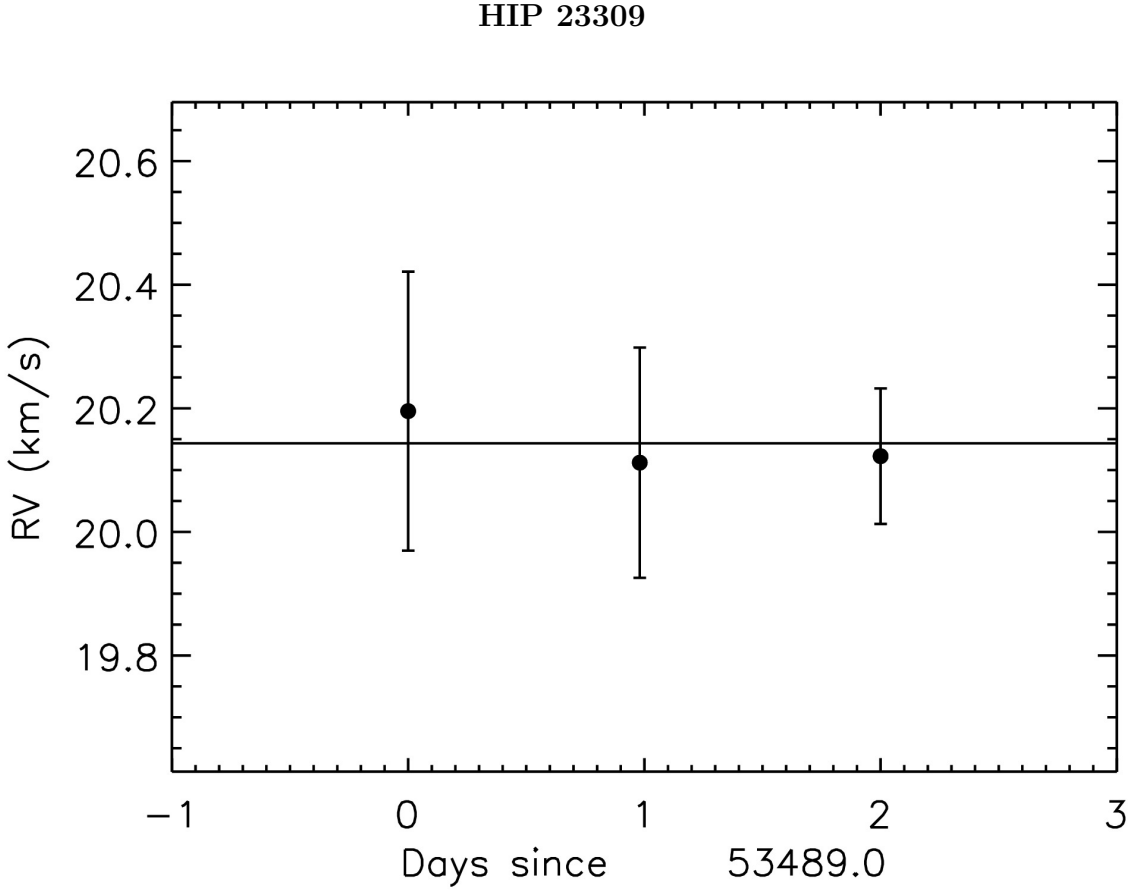

Figure 1 The RV curve is plotted with epoch errors for each observing day.

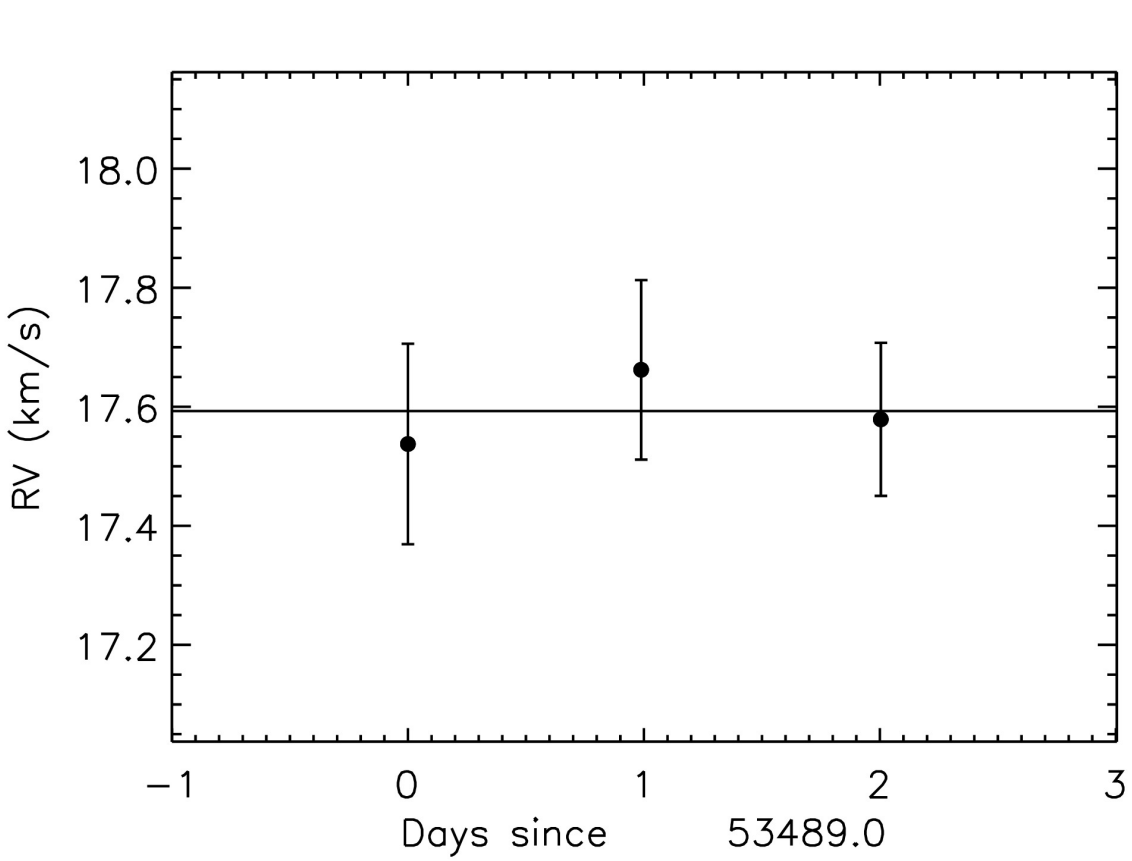

Figure 2 The RV curve is plotted with epoch errors for each observing day.

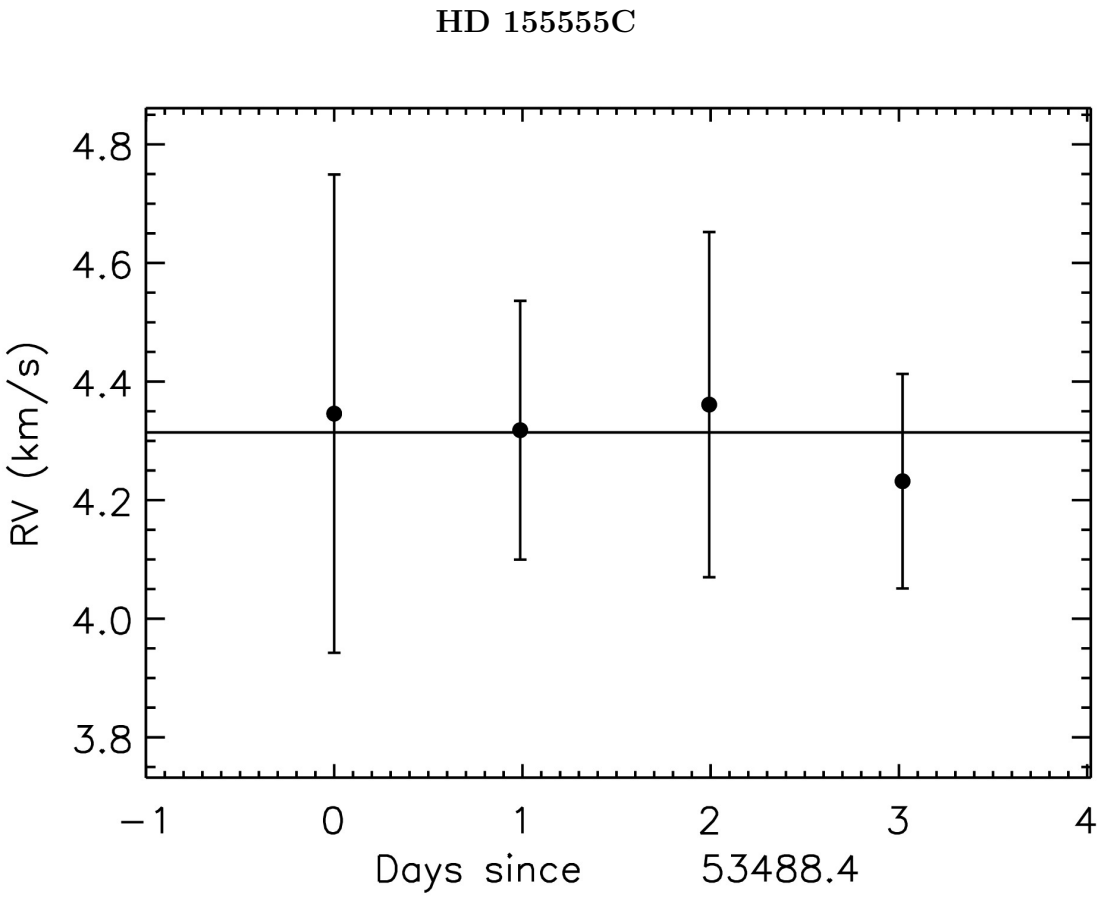

Figure 3 The RV curve is plotted with epoch errors for each observing day.

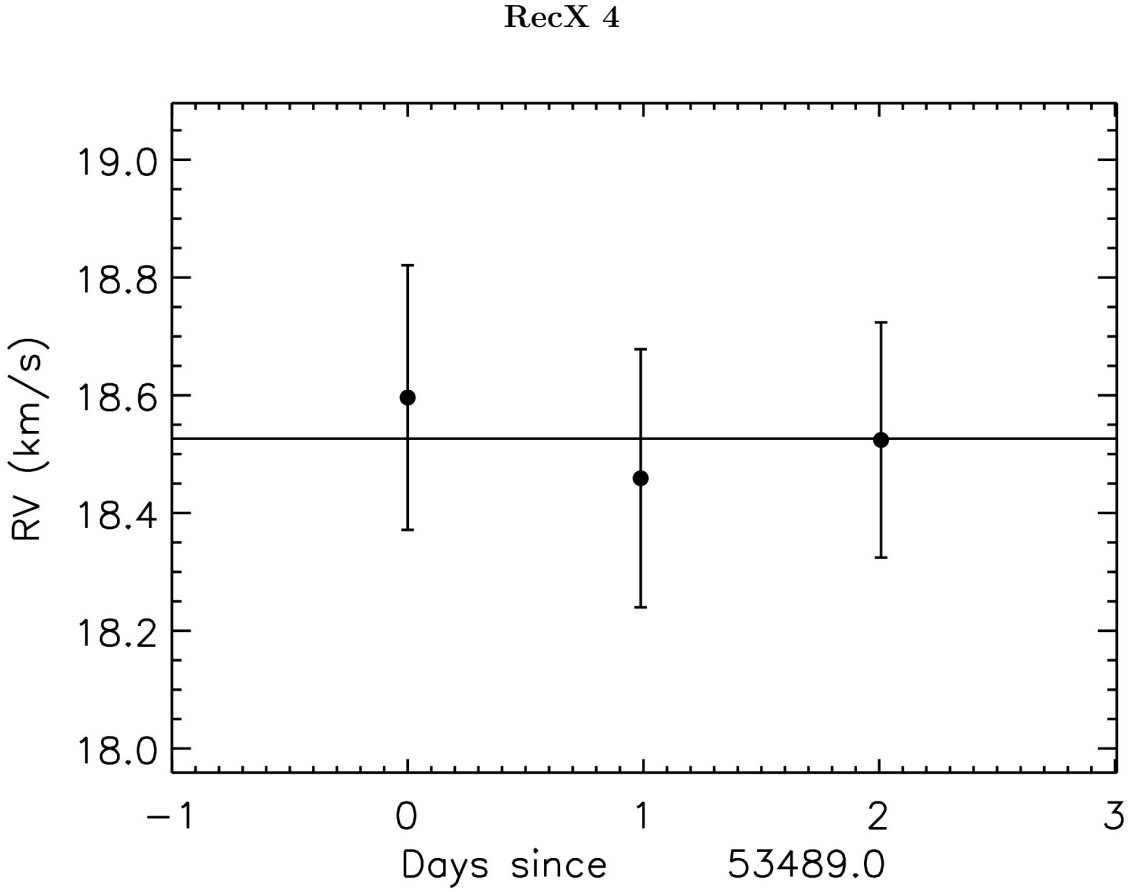

Figure 4 The RV curve is plotted with epoch errors for each observing day.

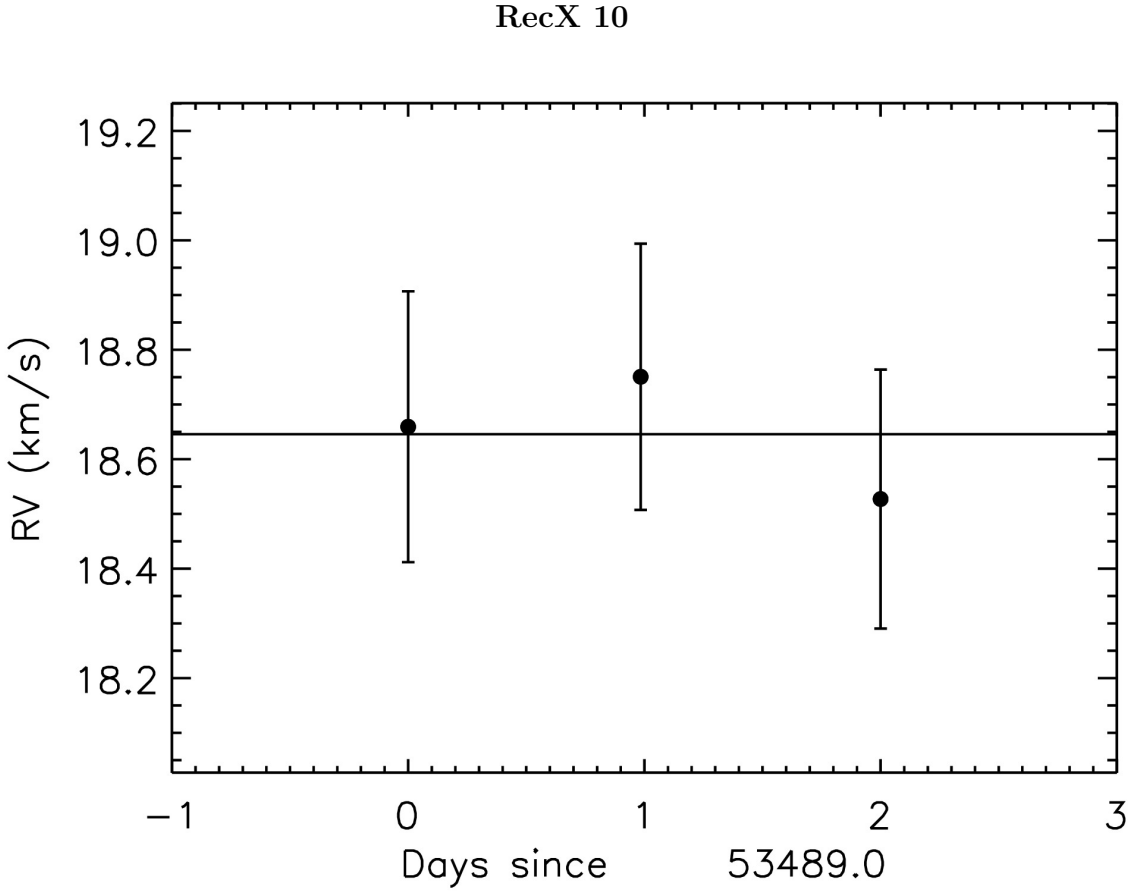

Figure 5 The RV curve is plotted with epoch errors for each observing day.

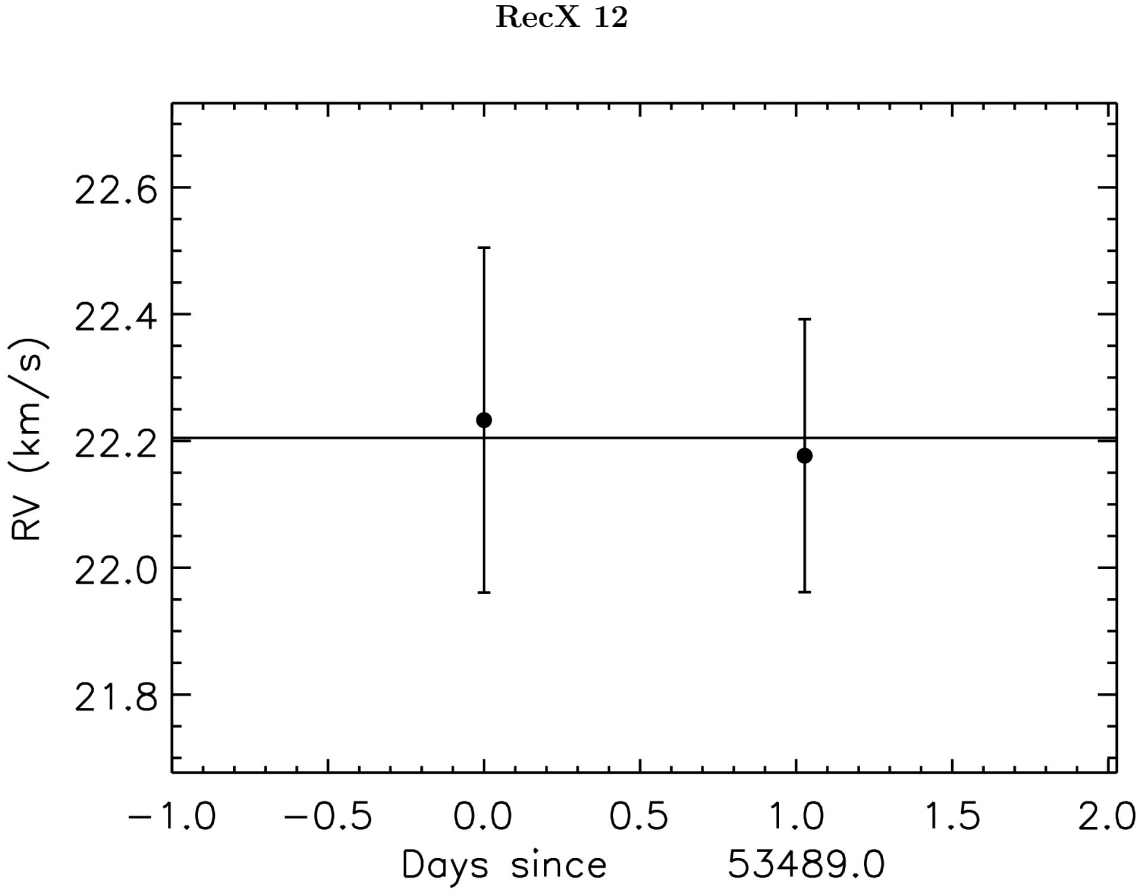

Figure 6 The RV curve is plotted with epoch errors for each observing day.

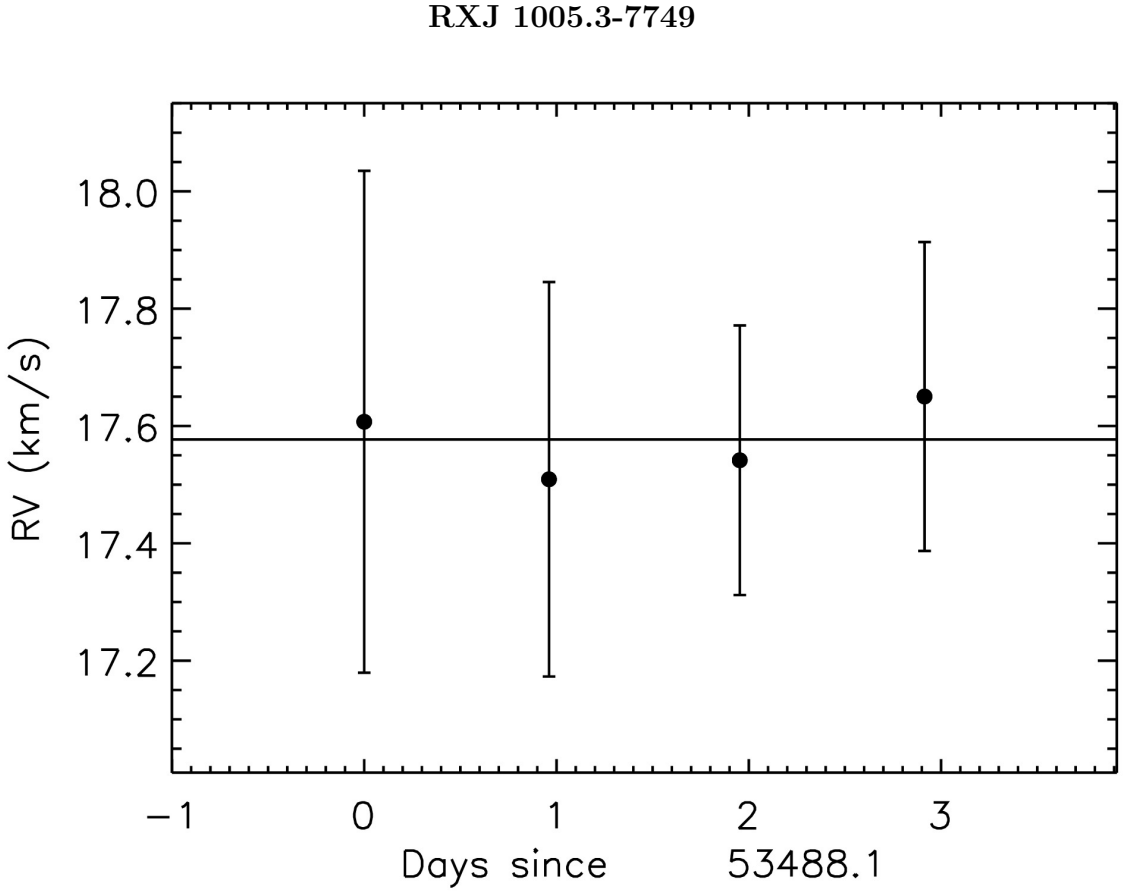

Figure 7 The RV curve is plotted with epoch errors for each observing day.

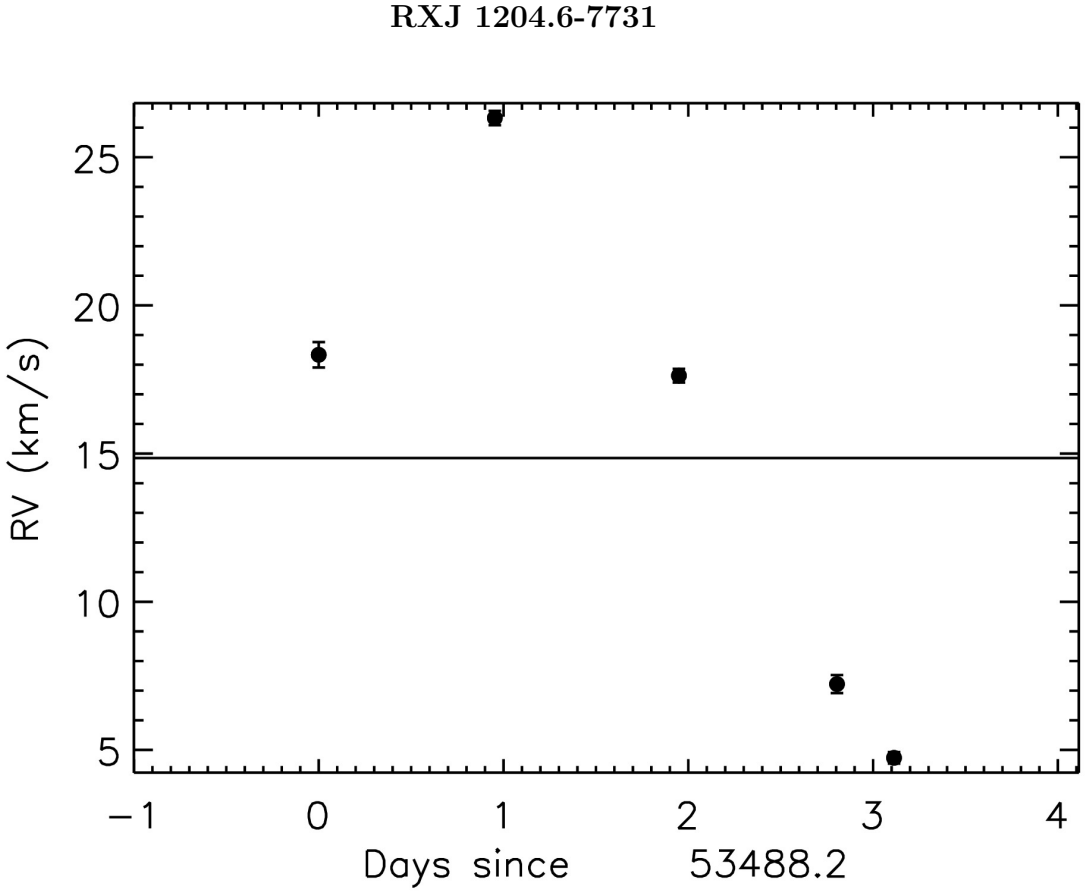

Figure 8 The RV curve is plotted with epoch errors for each observing day.

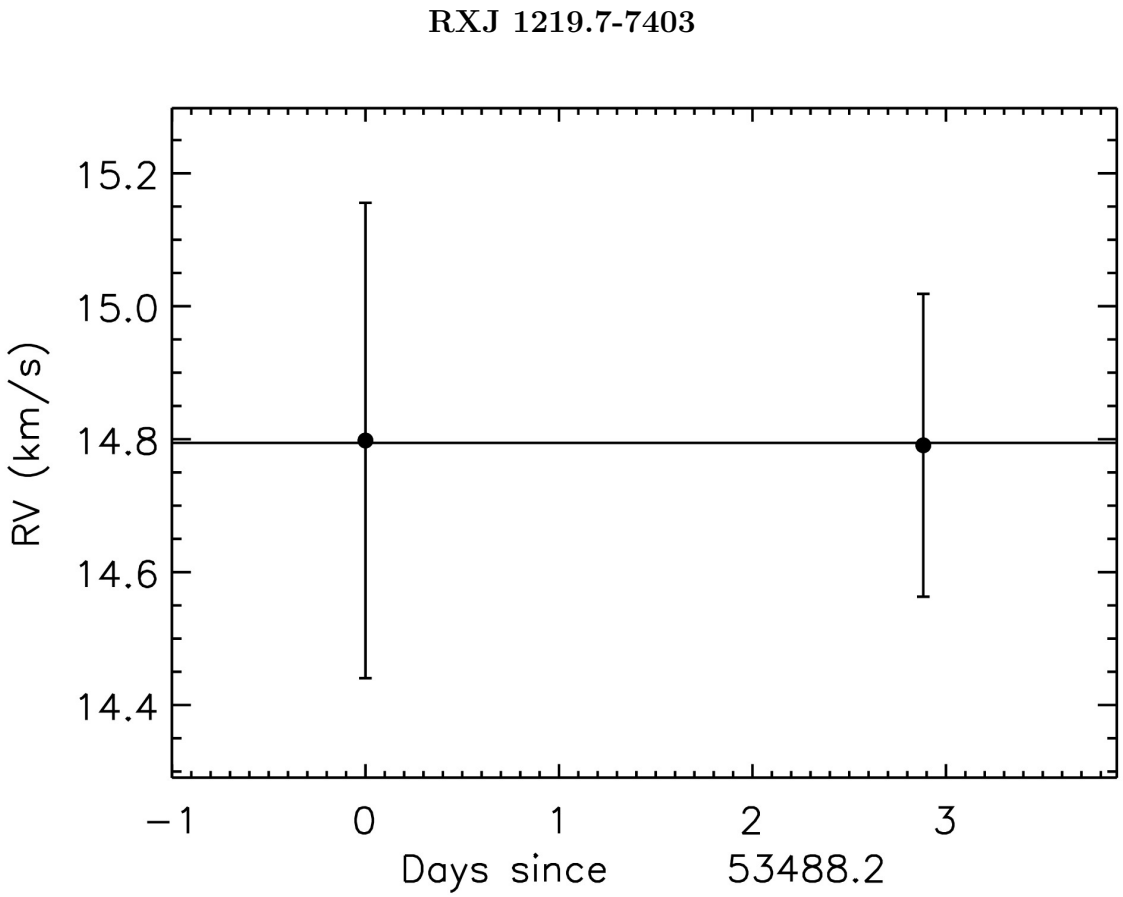

Figure 9 The RV curve is plotted with epoch errors for each observing day.

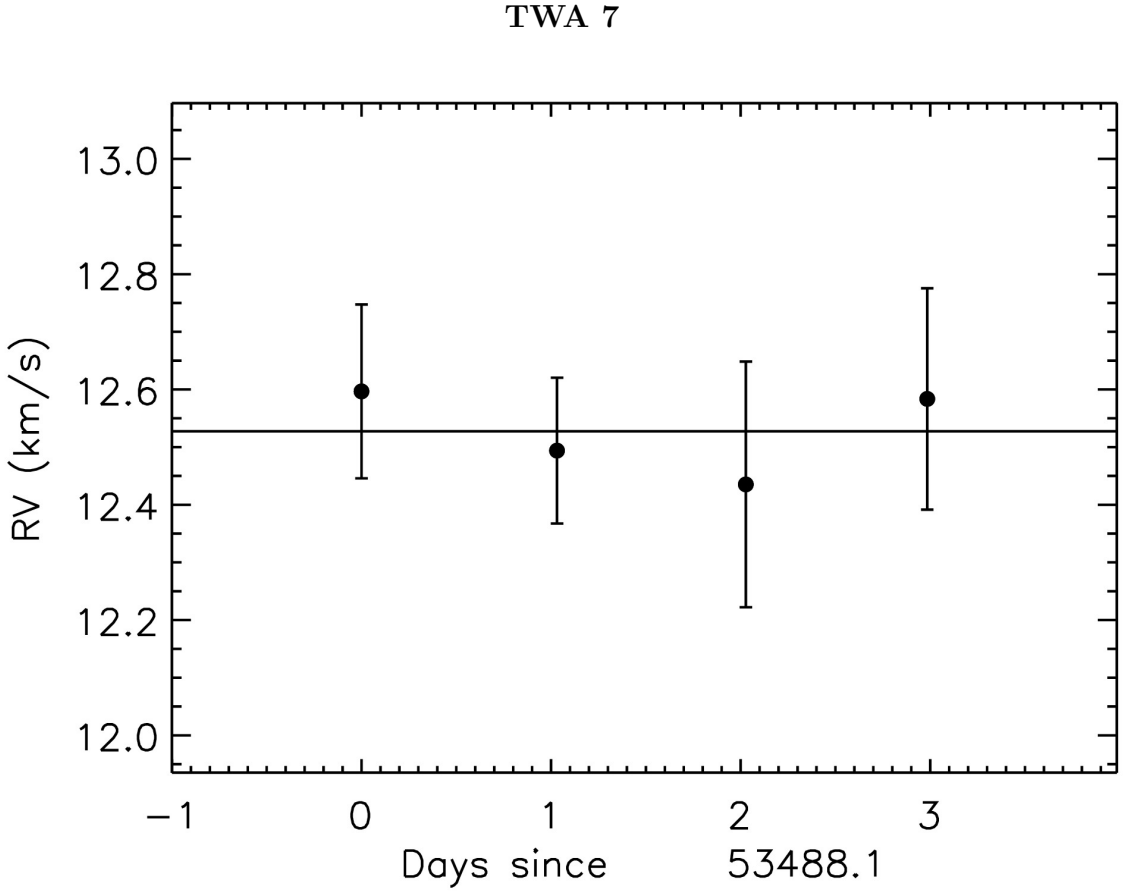

Figure 10 The RV curve is plotted with epoch errors for each observing day.

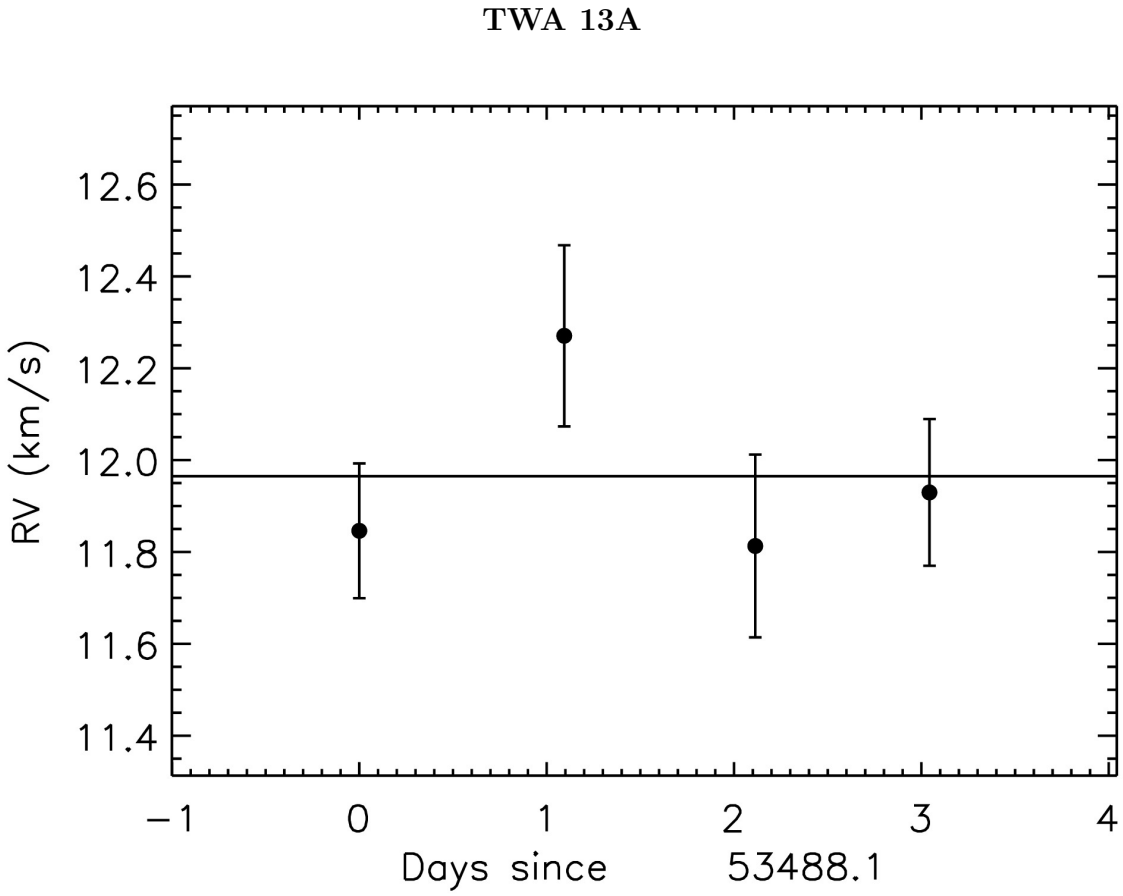

Figure 11 The RV curve is plotted with epoch errors for each observing day.

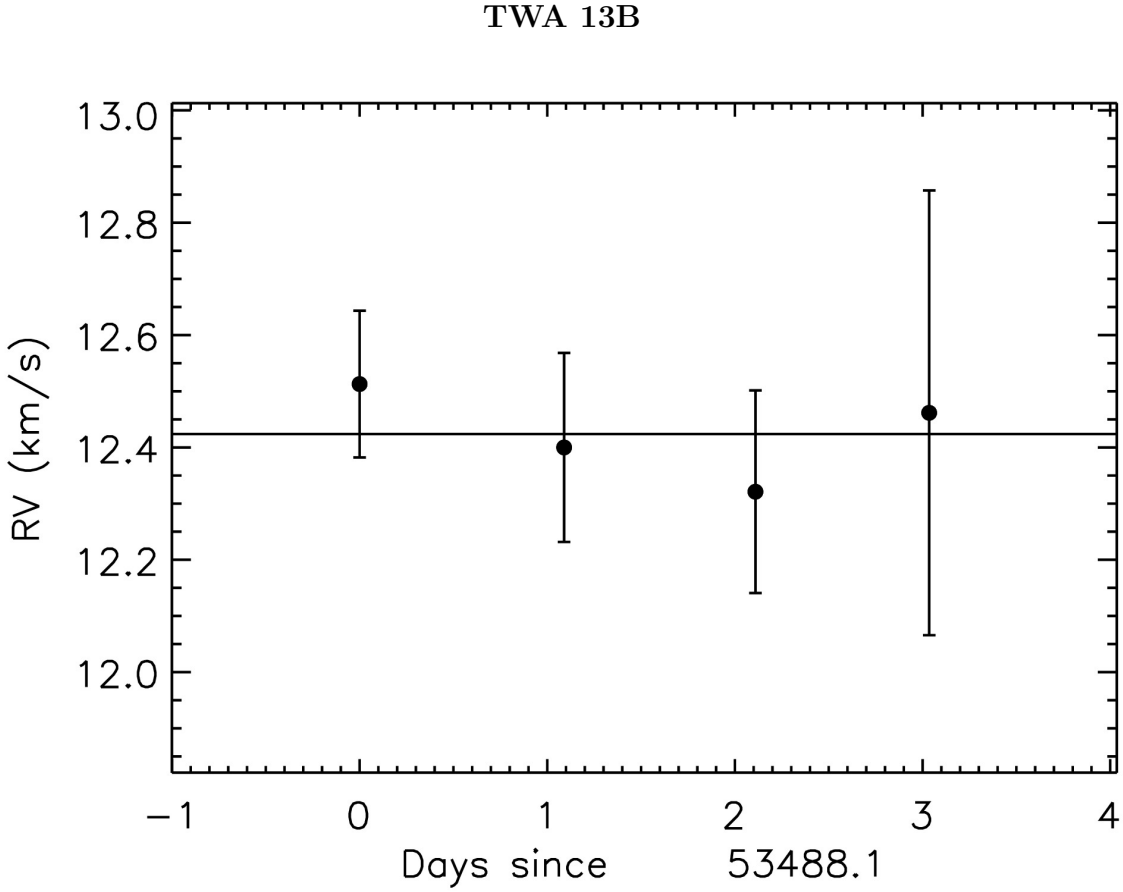

Figure 12 The RV curve is plotted with epoch errors for each observing day.

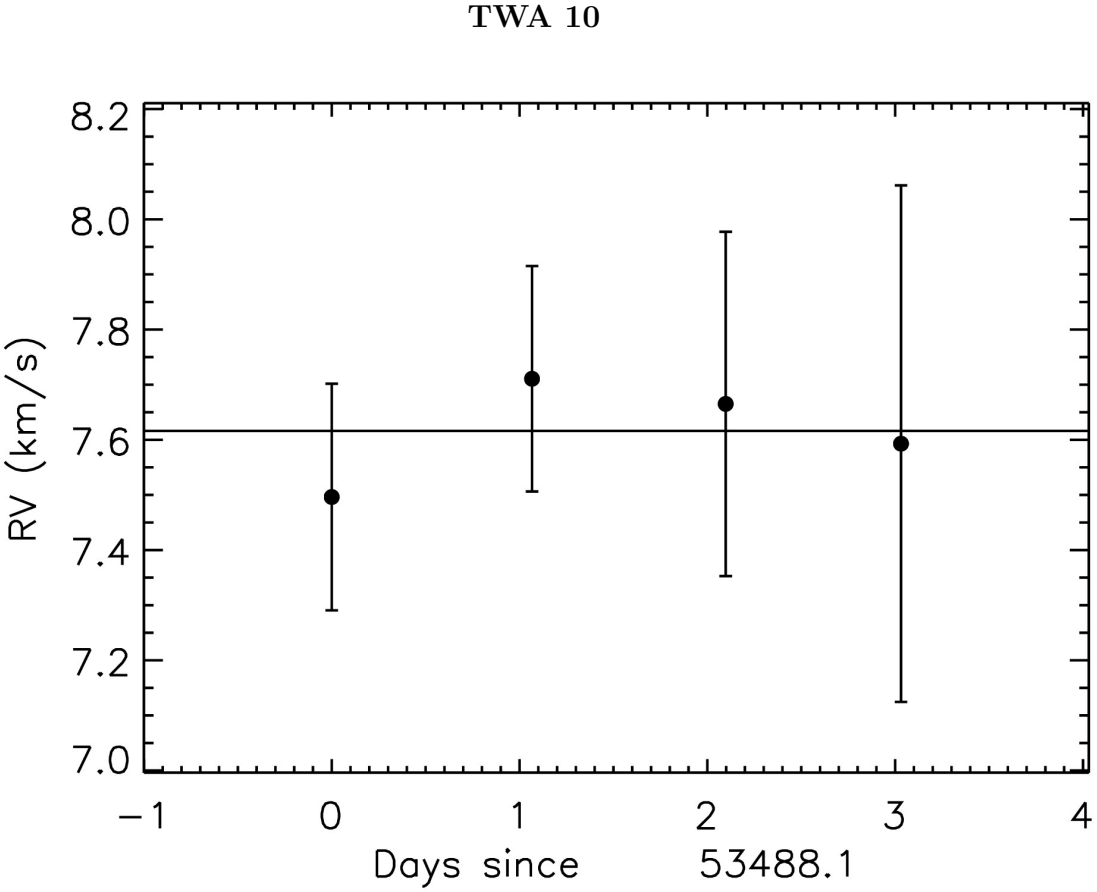

Figure 13 The RV curve is plotted with epoch errors for each observing day.

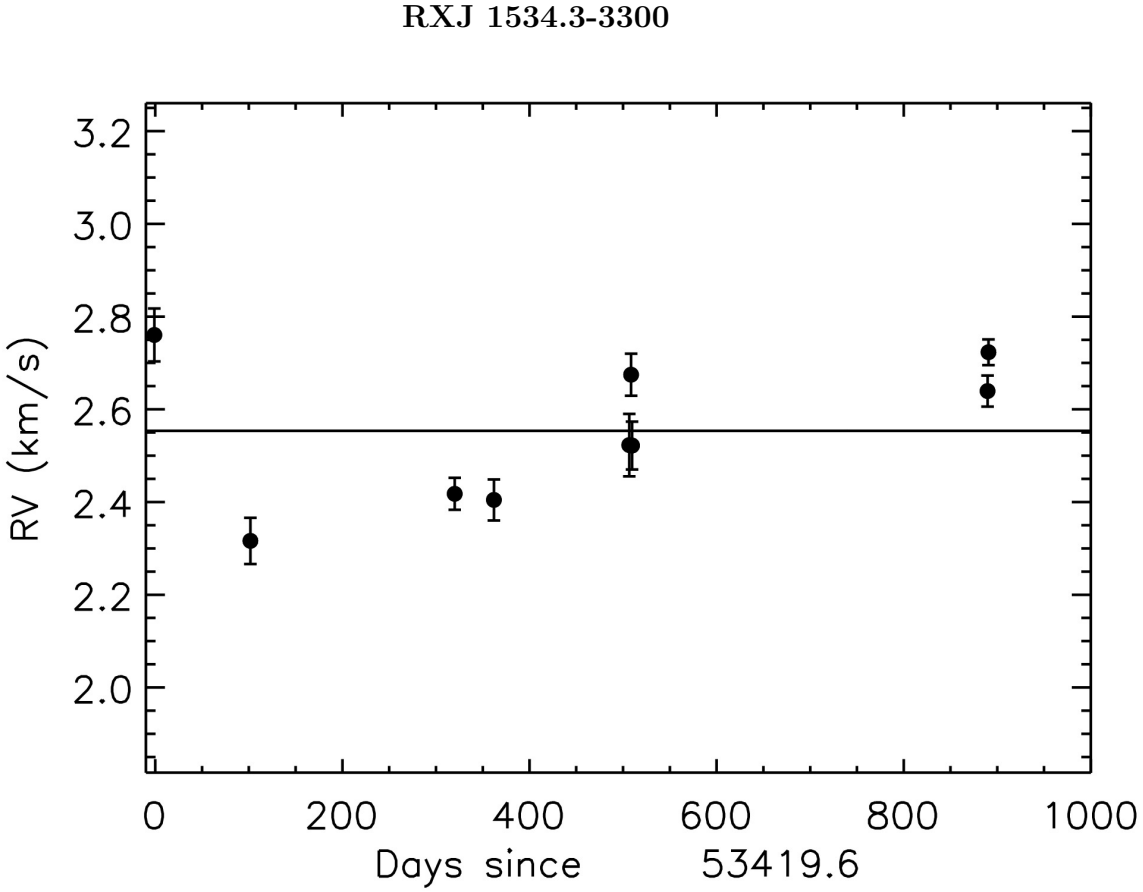

Figure 14 The RV curve is plotted with epoch errors for each observing day.

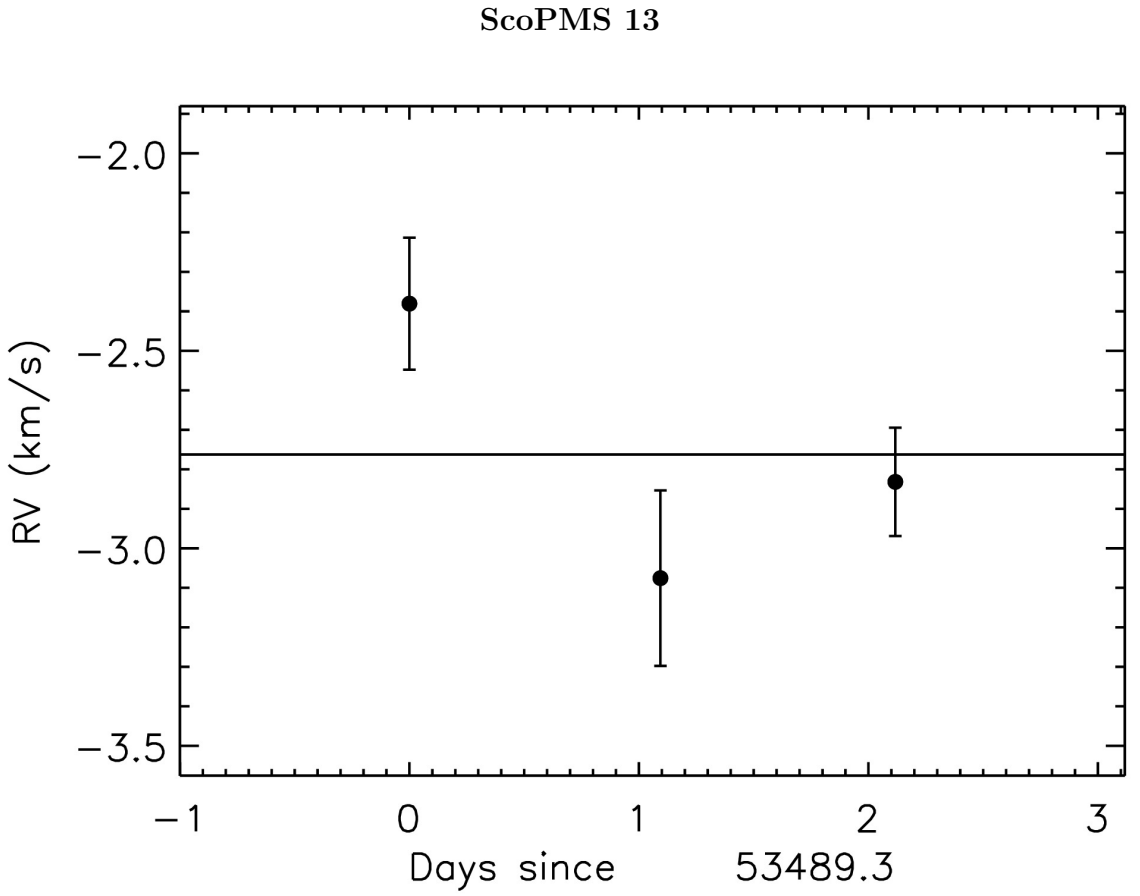

Figure 15 The RV curve is plotted with epoch errors for each observing day.

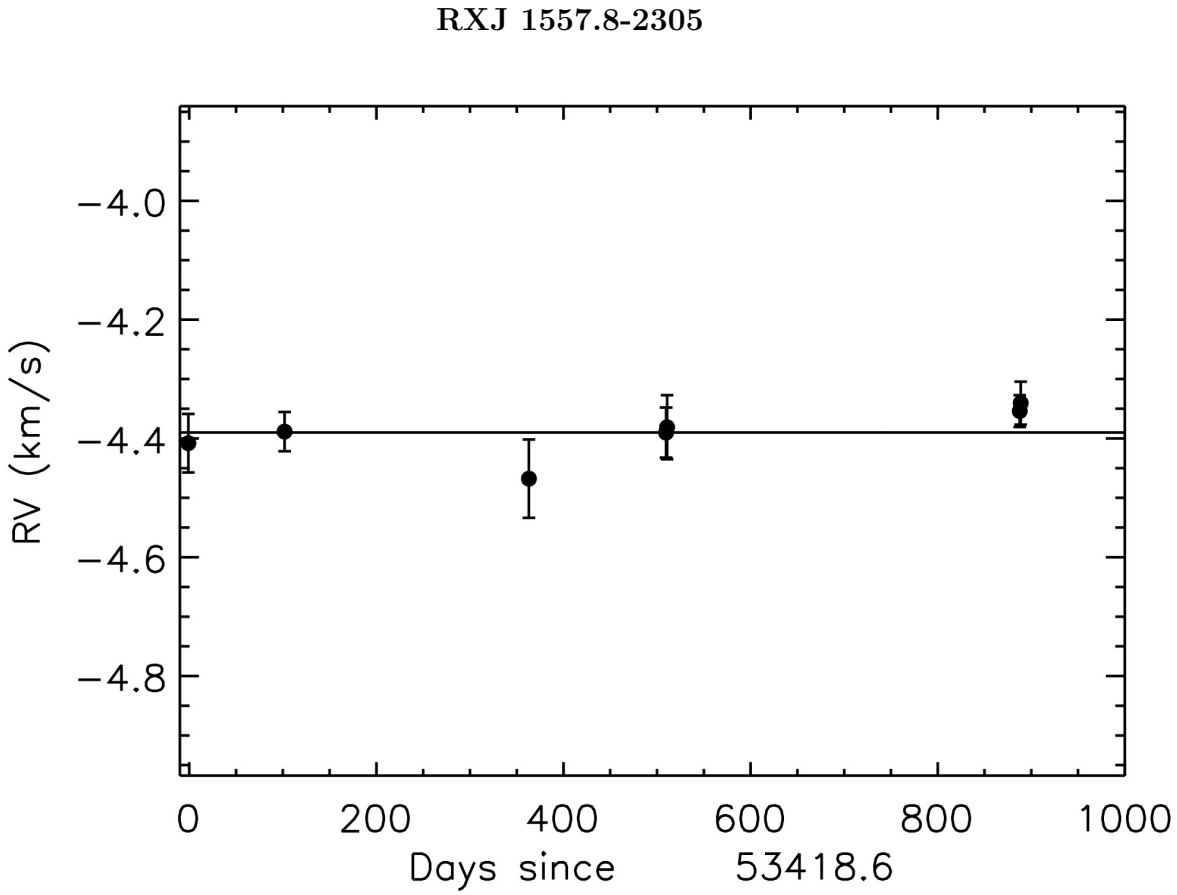

Figure 16 The RV curve is plotted with epoch errors for each observing day.

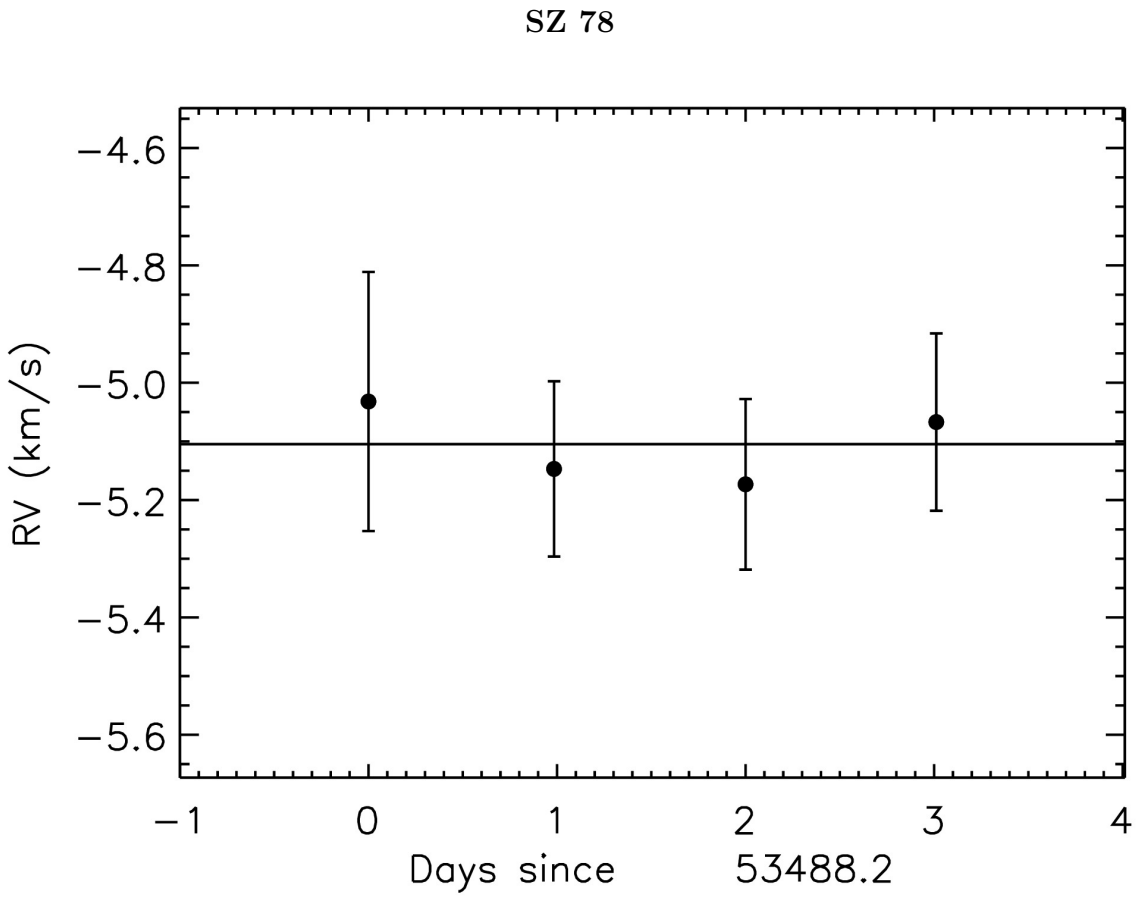

Figure 17 The RV curve is plotted with epoch errors for each observing day.

SZ 96

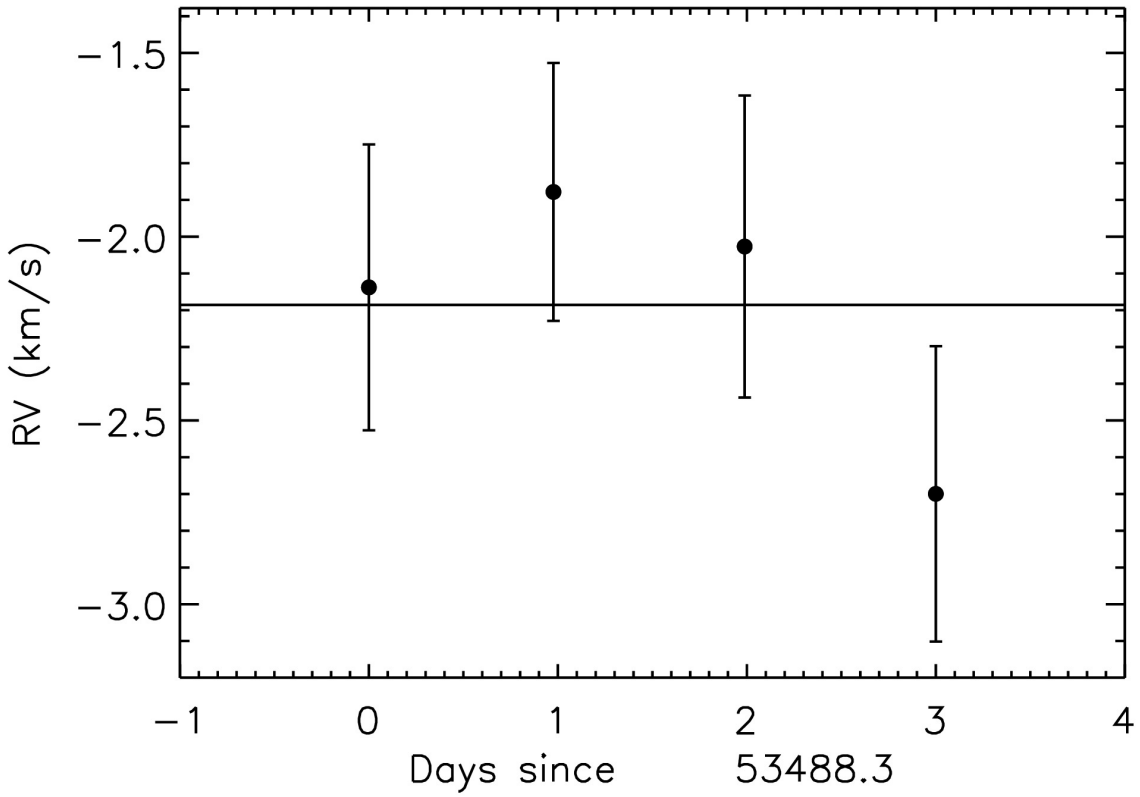

Figure 18 The RV curve is plotted with epoch errors for each observing day.

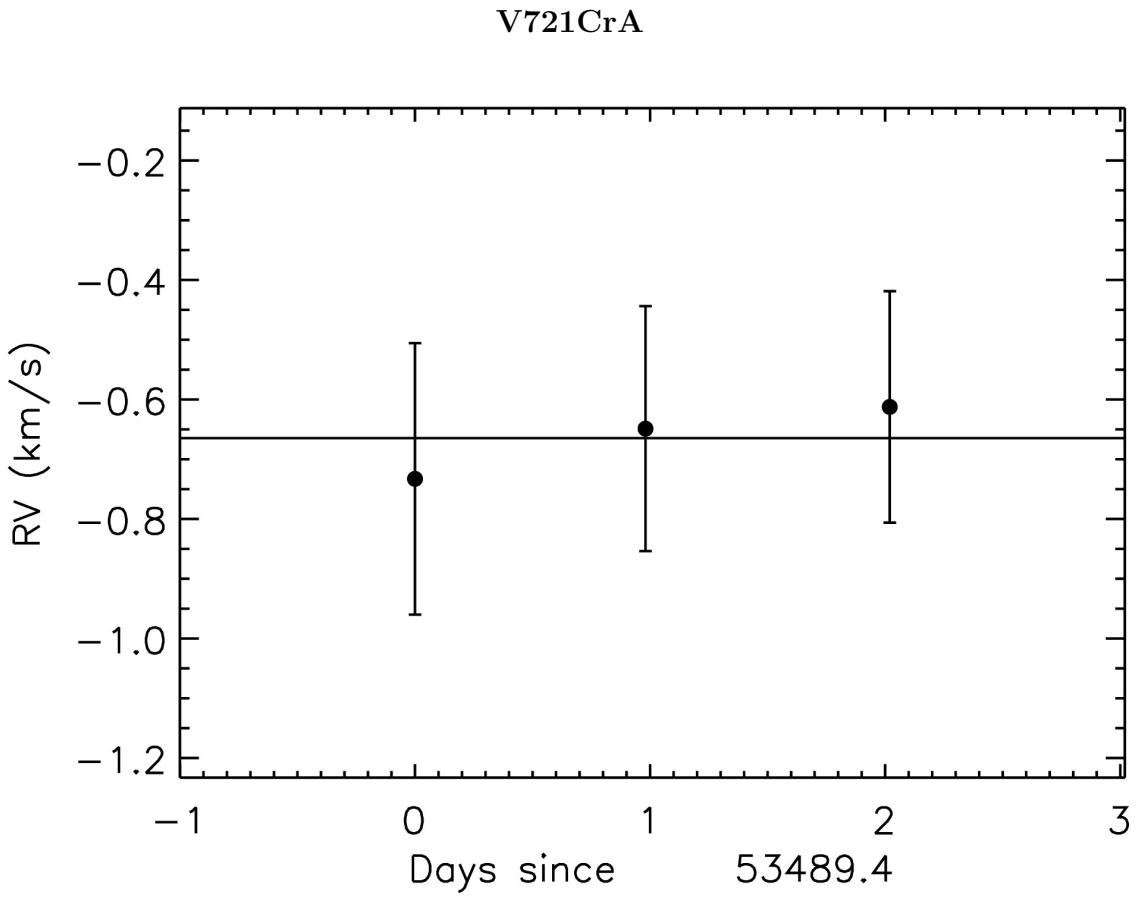

Figure 19 The RV curve is plotted with epoch errors for each observing day.

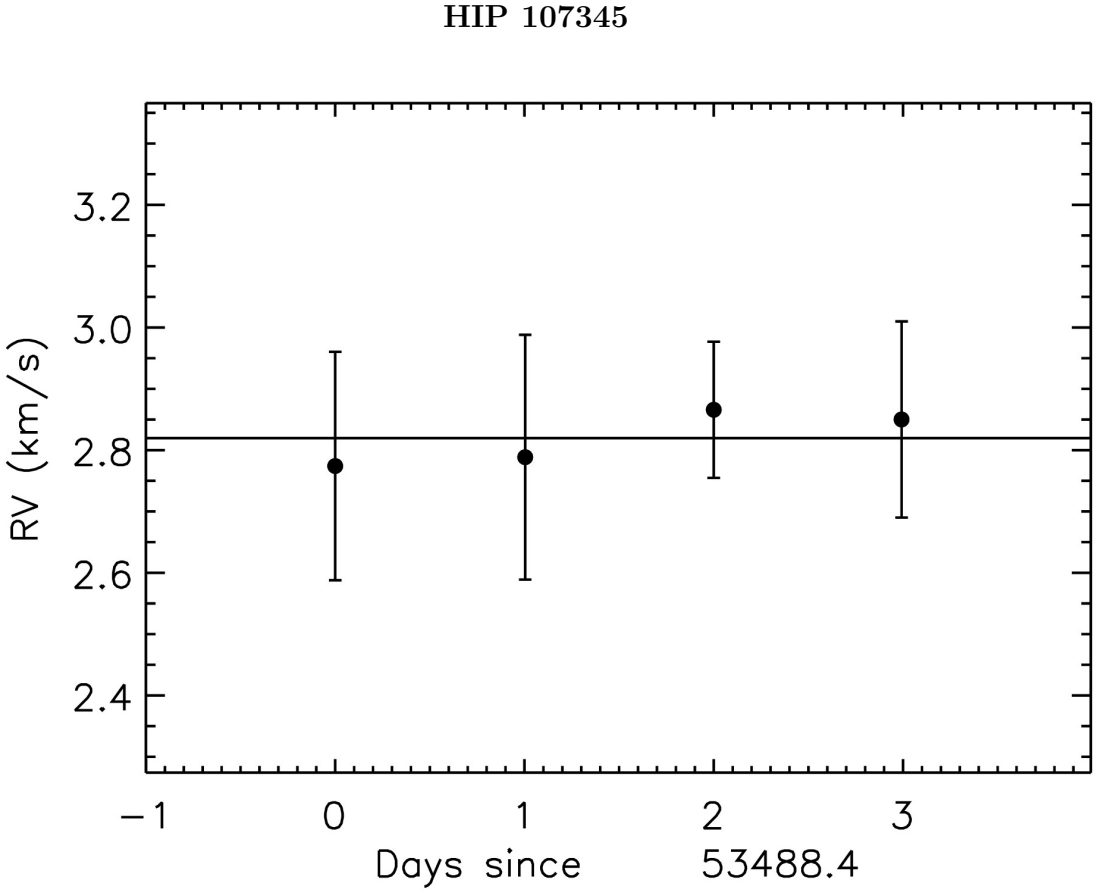

Figure 20 The RV curve is plotted with epoch errors for each observing day.

A.2 Radial Velocity Standards – Gemini Phoenix

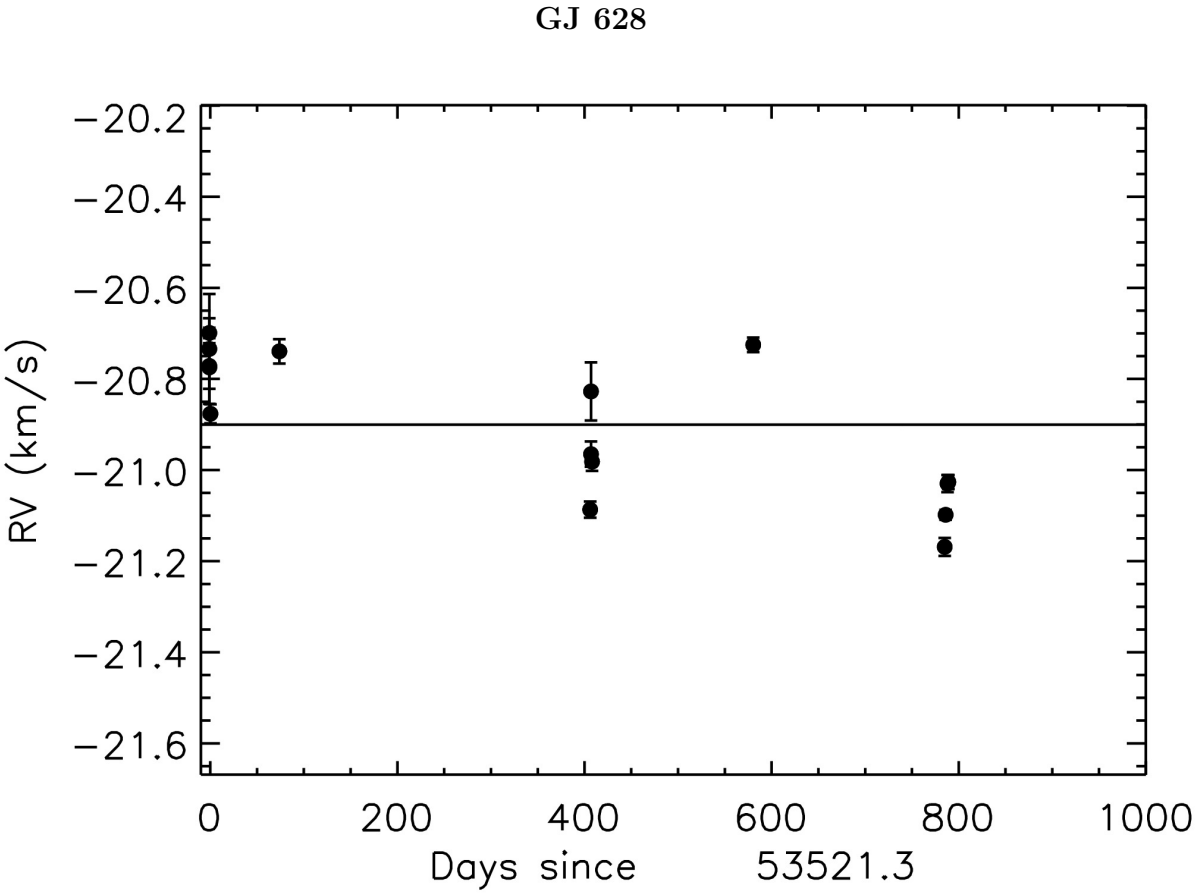

Figure 21 The RV curve is plotted with epoch errors for each observing day.

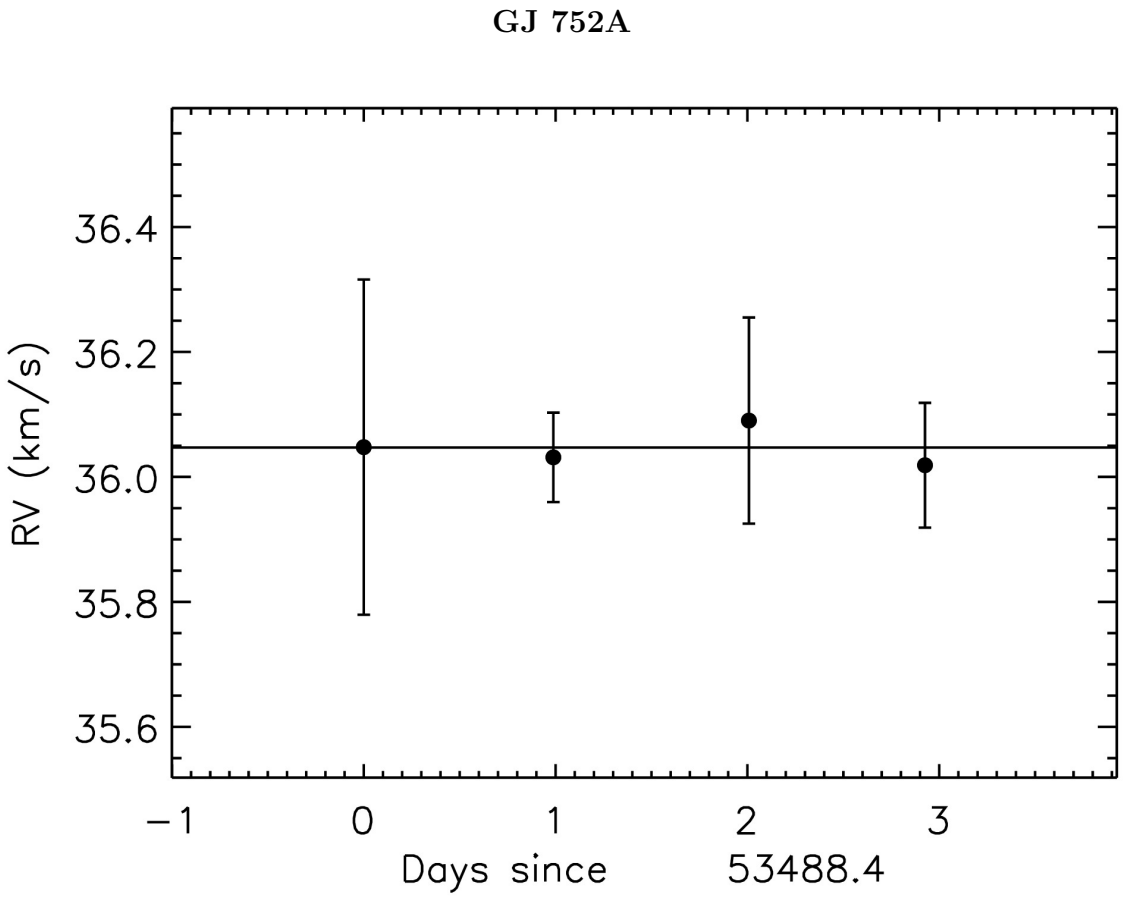

Figure 22 The RV curve is plotted with epoch errors for each observing day.

B VLT CRIRES

B.1 Young Stars – VLT CRIRES

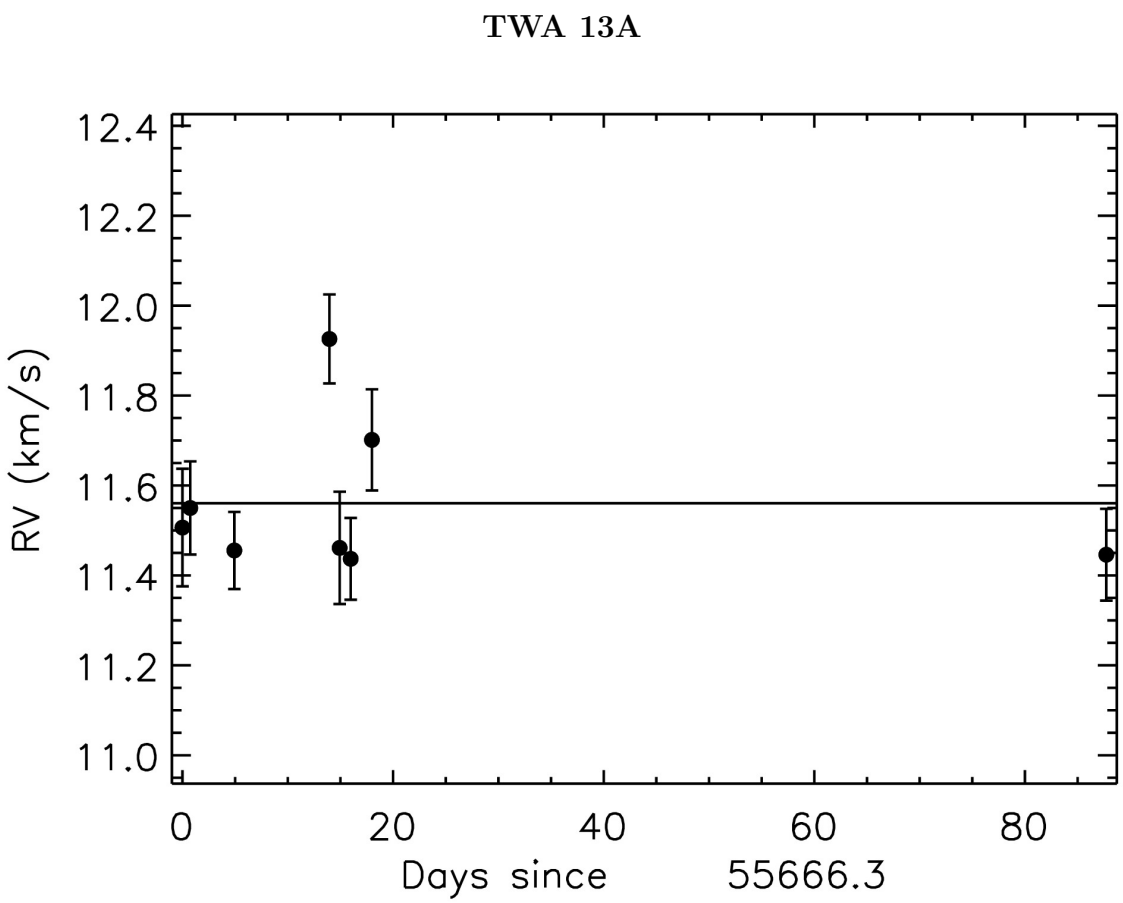

Figure 23 The RV curve is plotted with epoch errors for each observing day.

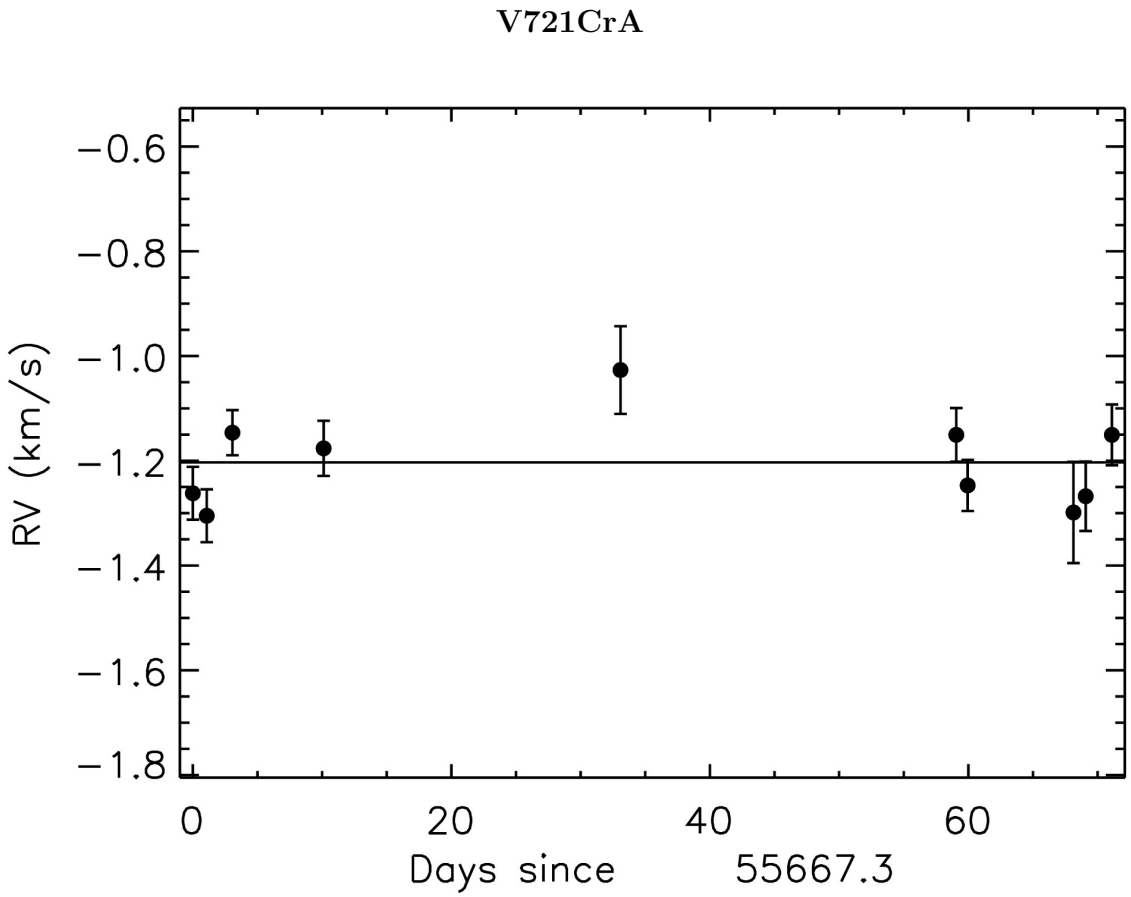

Figure 24 The RV curve is plotted with epoch errors for each observing day.

TYC 7443-1102-1

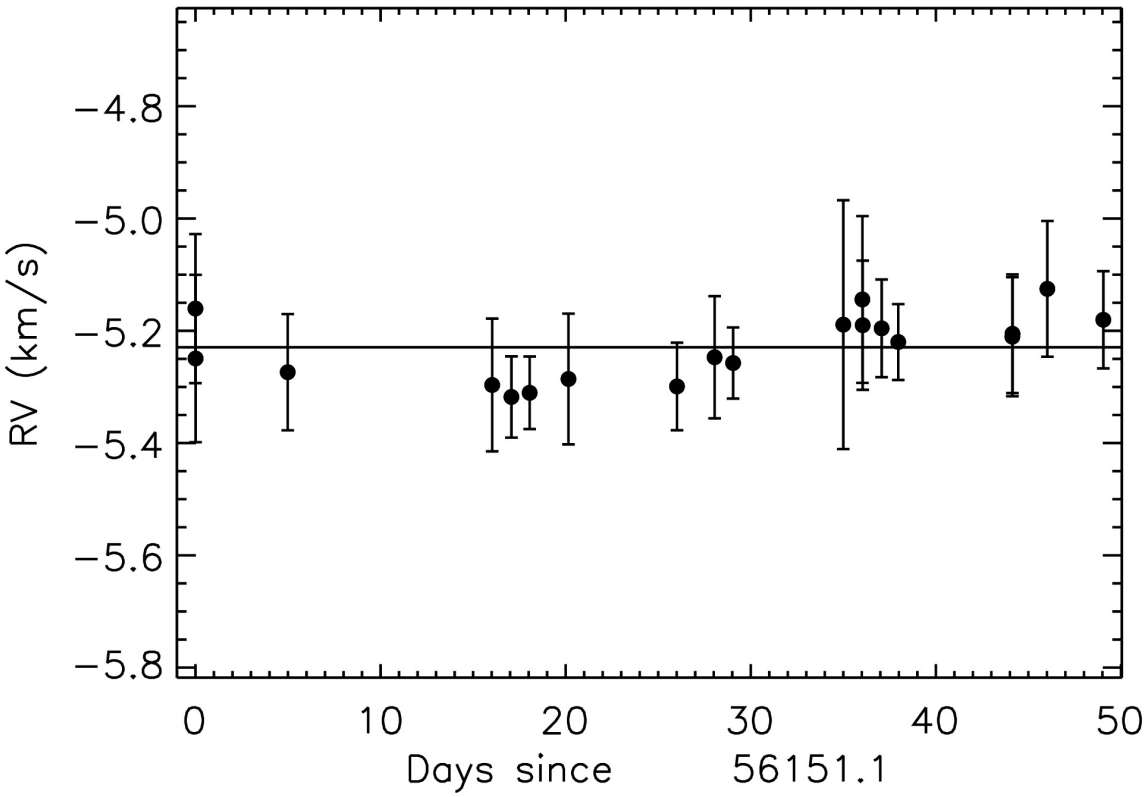

Figure 25 The RV curve is plotted with epoch errors for each observing day.

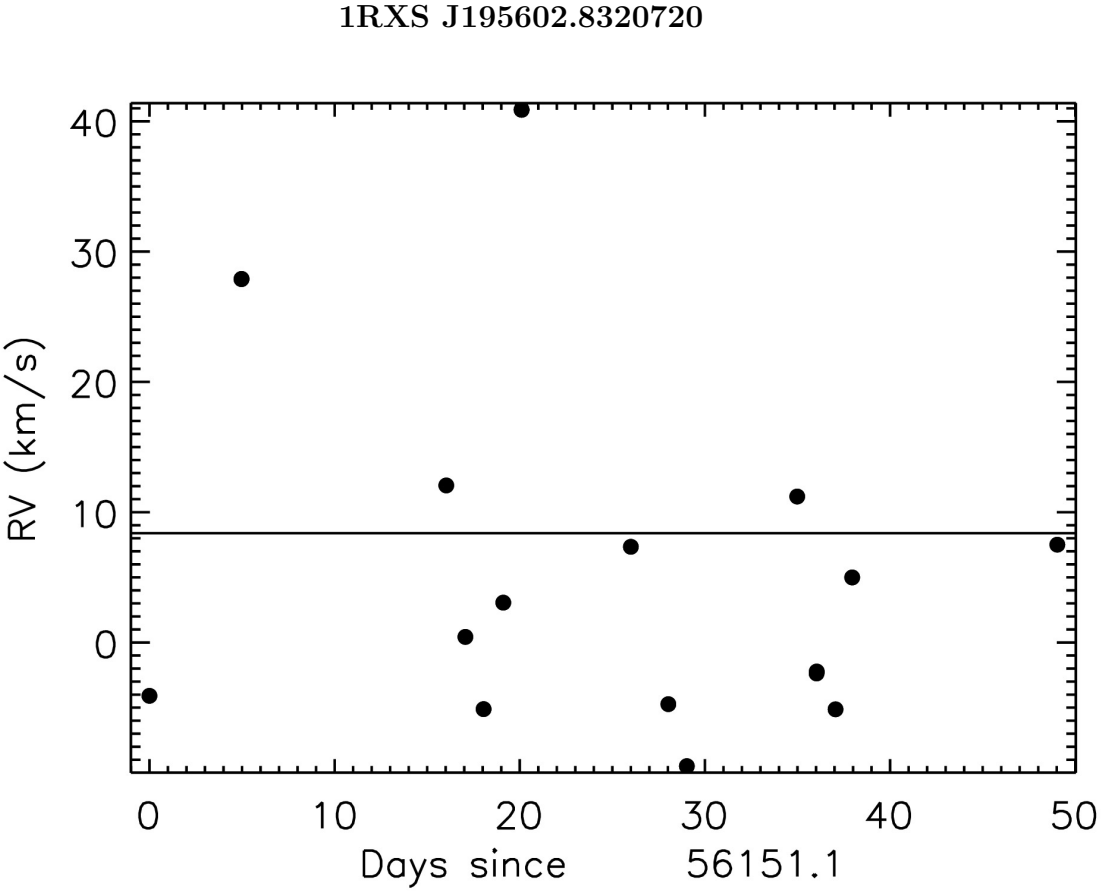

Figure 26 The RV curve is plotted with epoch errors for each observing day.

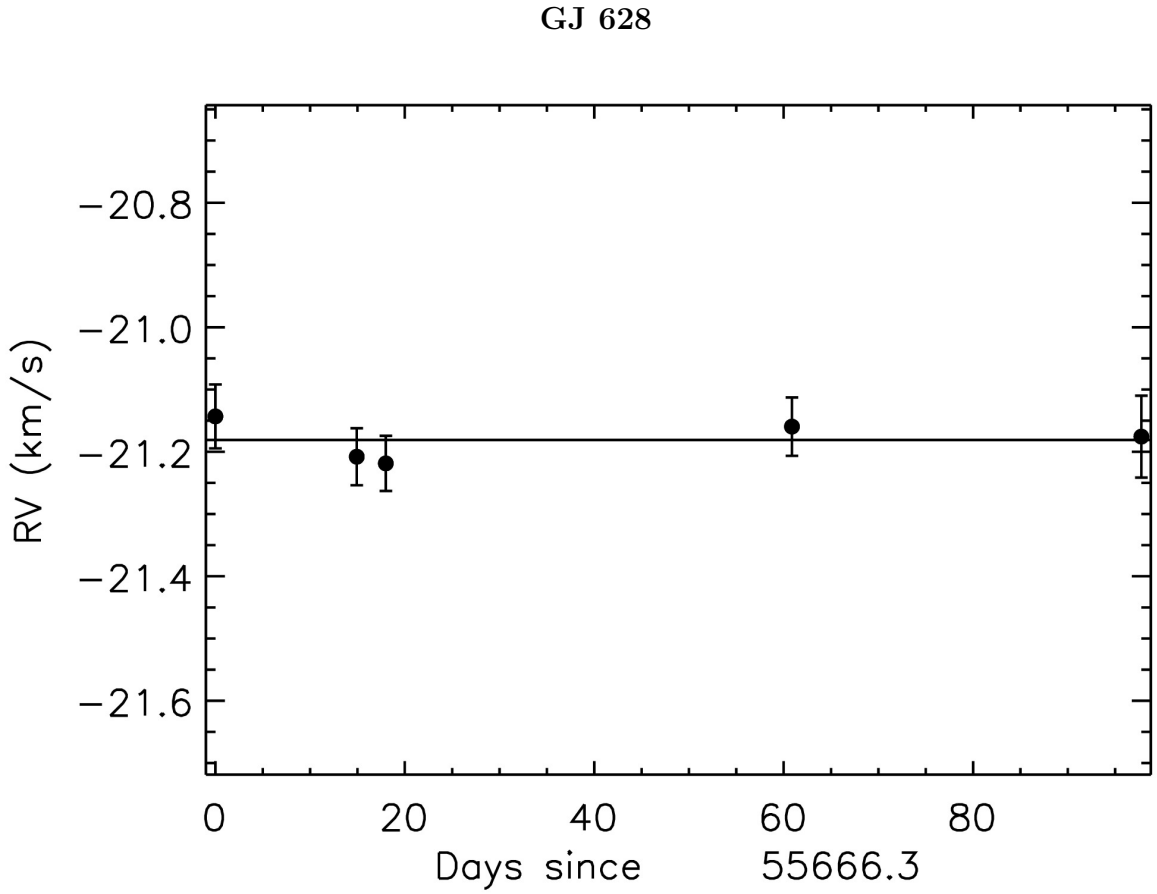

Figure 27 The RV curve is plotted with epoch errors for each observing day.

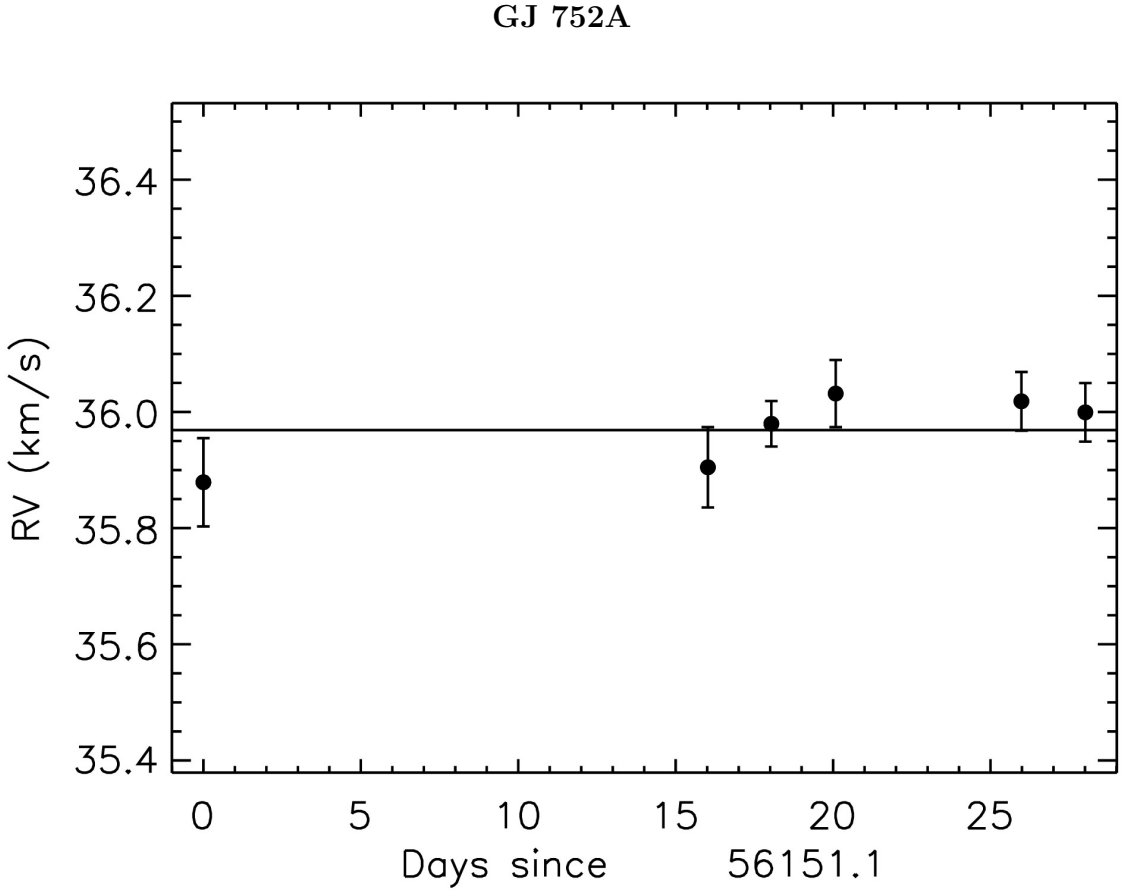

Figure 28 The RV curve is plotted with epoch errors for each observing day.

C Keck NIRSPEC

C.1 Taurus-Auriga

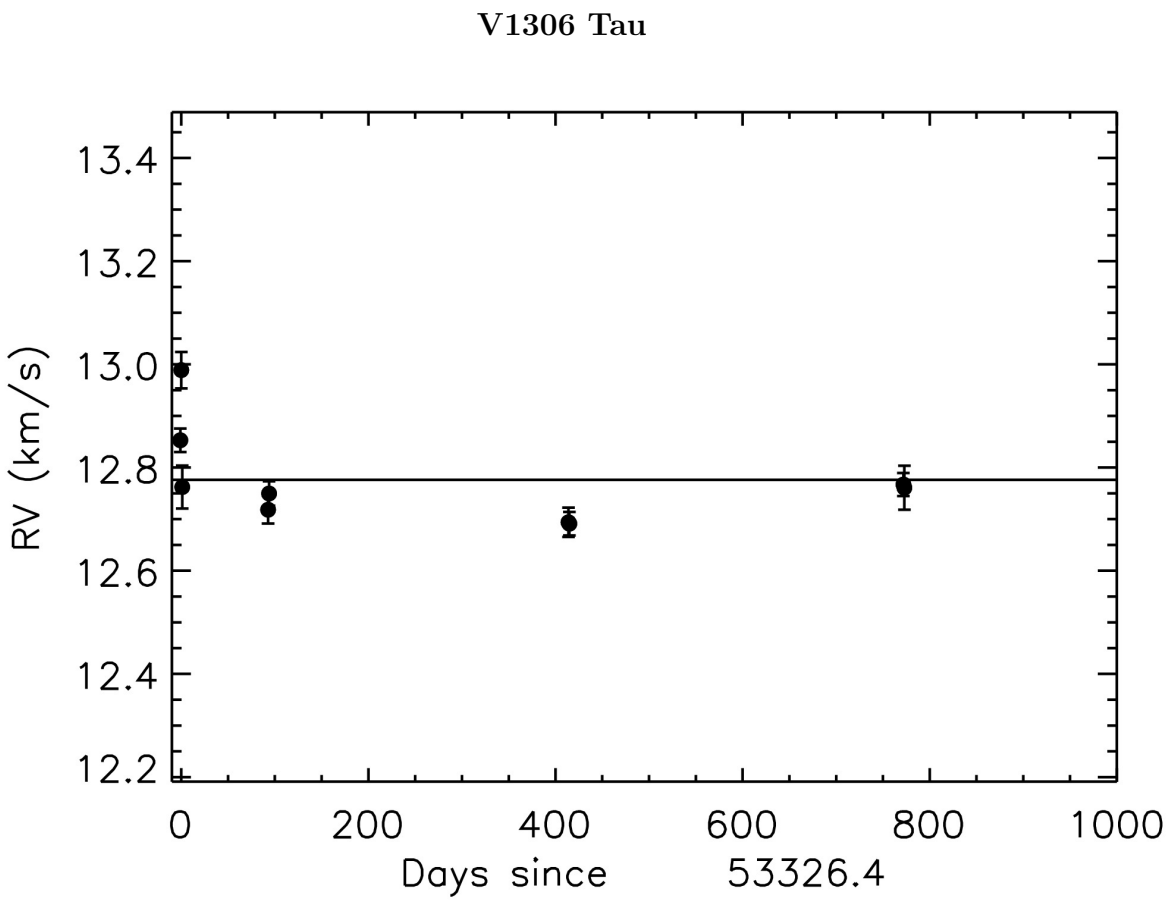

Figure 29 The RV curve is plotted with epoch errors for each observing day.

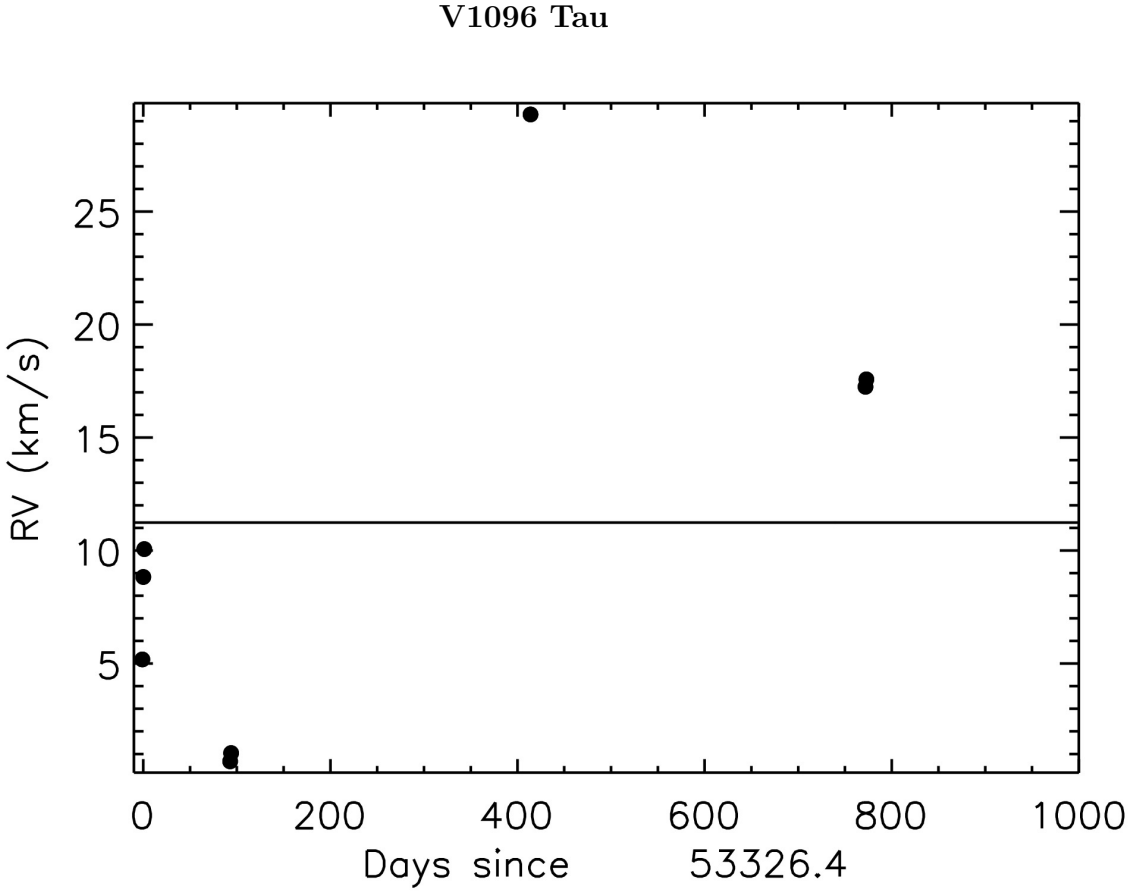

Figure 30 The RV curve is plotted with epoch errors for each observing day.

CIDA 3

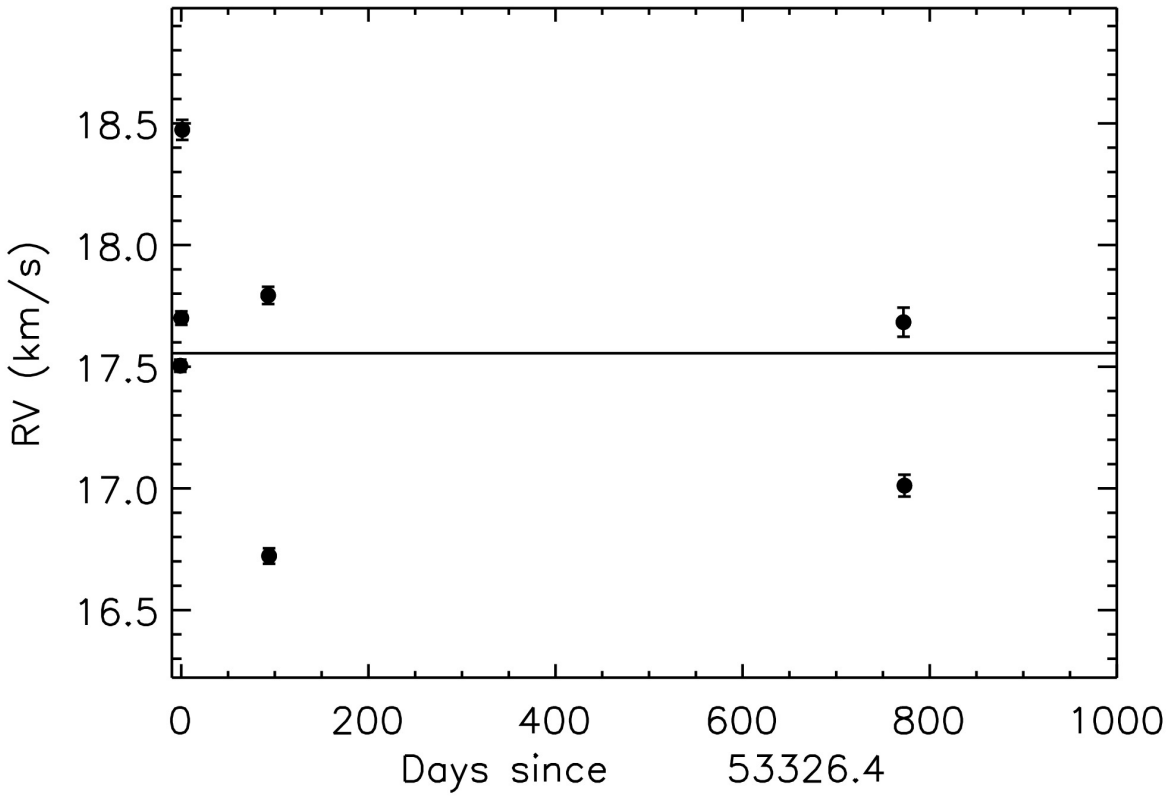

Figure 31 The RV curve is plotted with epoch errors for each observing day.

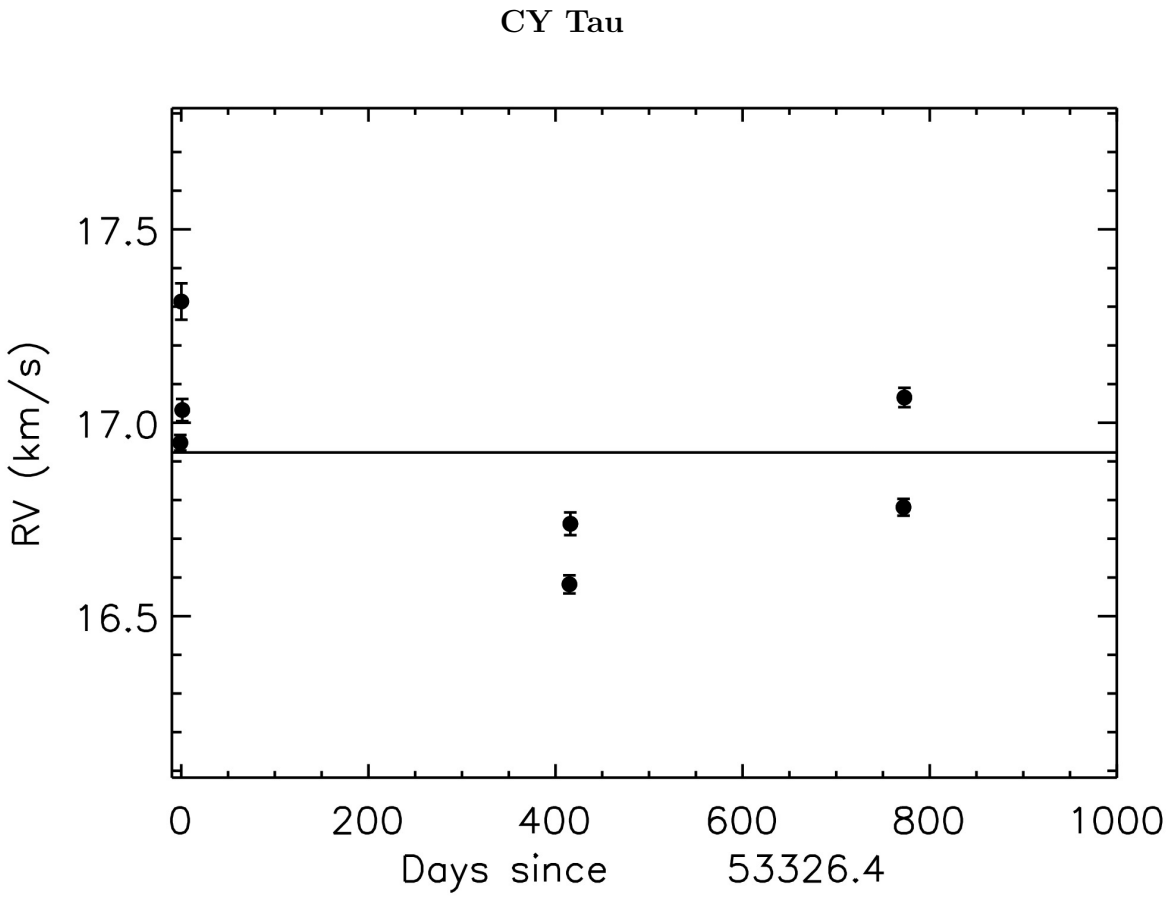

Figure 32 The RV curve is plotted with epoch errors for each observing day.

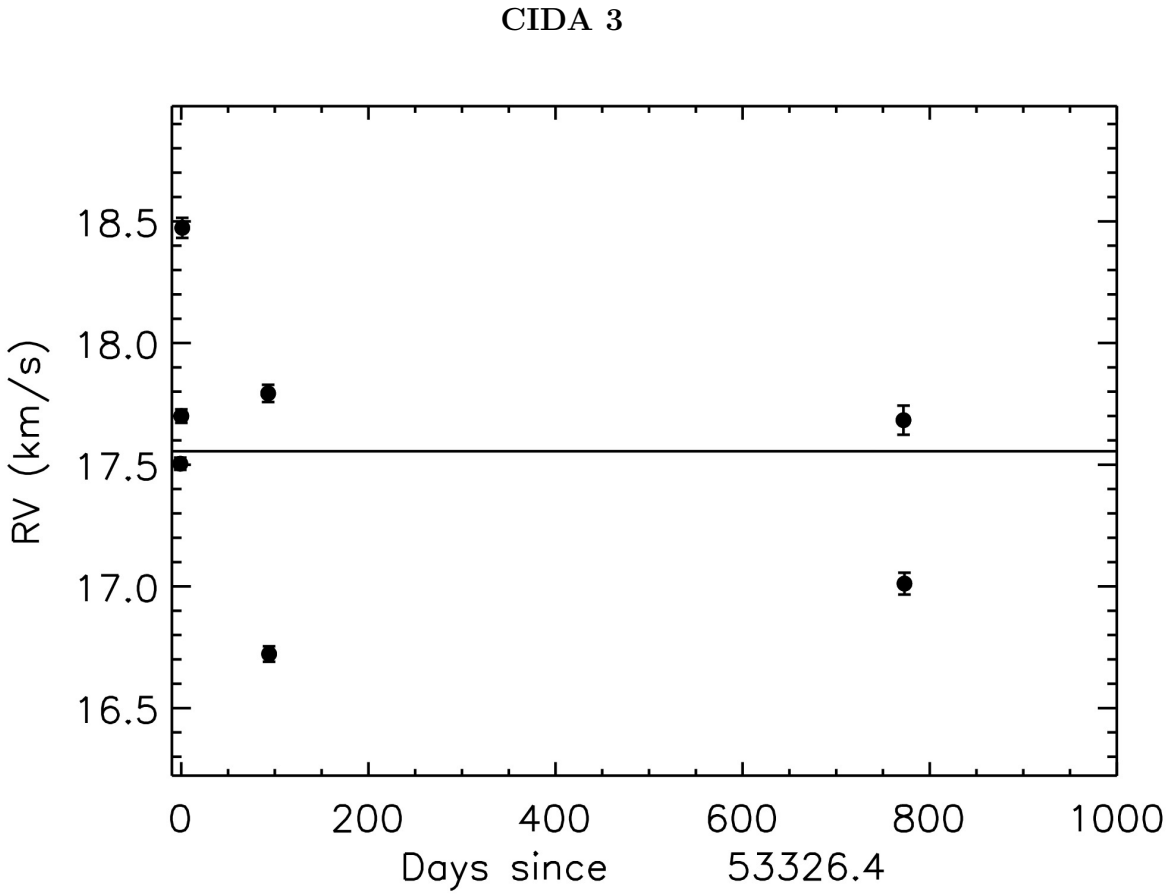

Figure 33 The RV curve is plotted with epoch errors for each observing day.

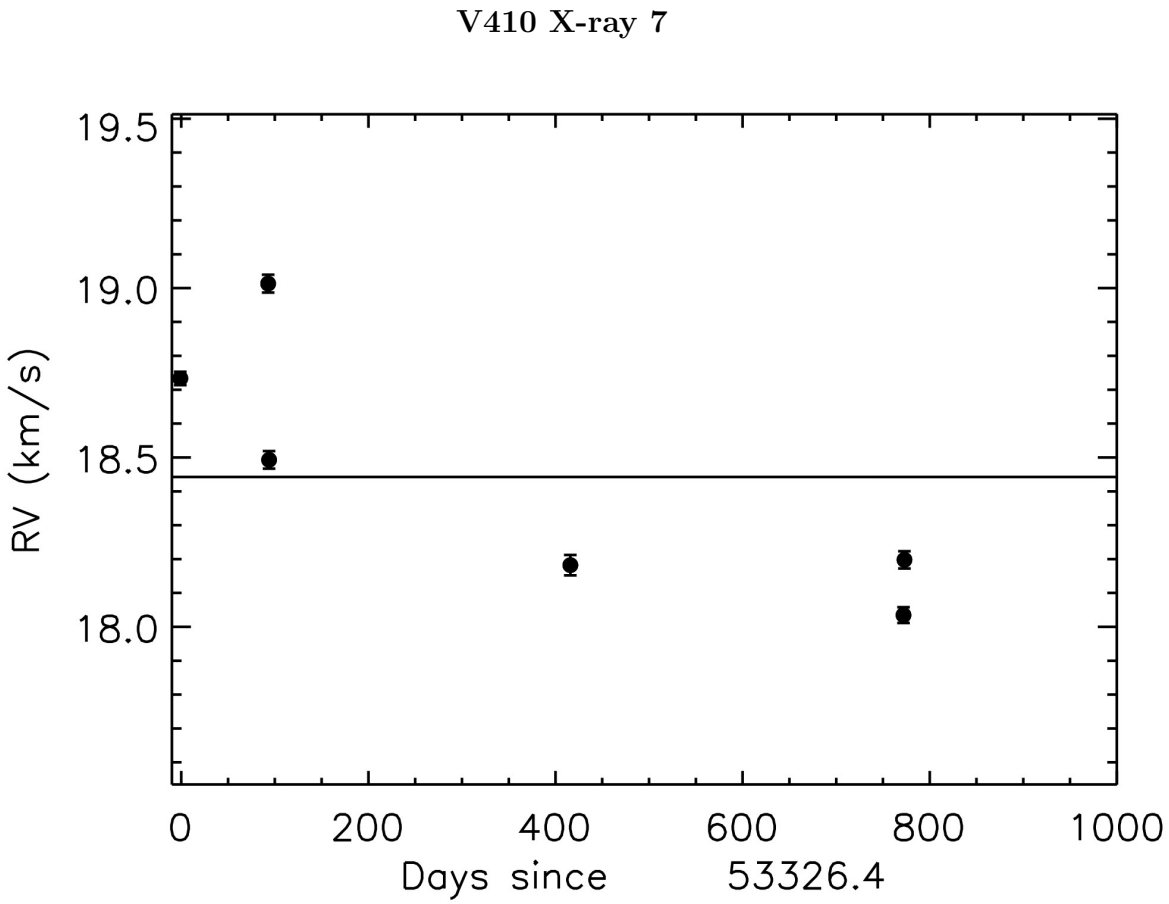

Figure 34 The RV curve is plotted with epoch errors for each observing day.

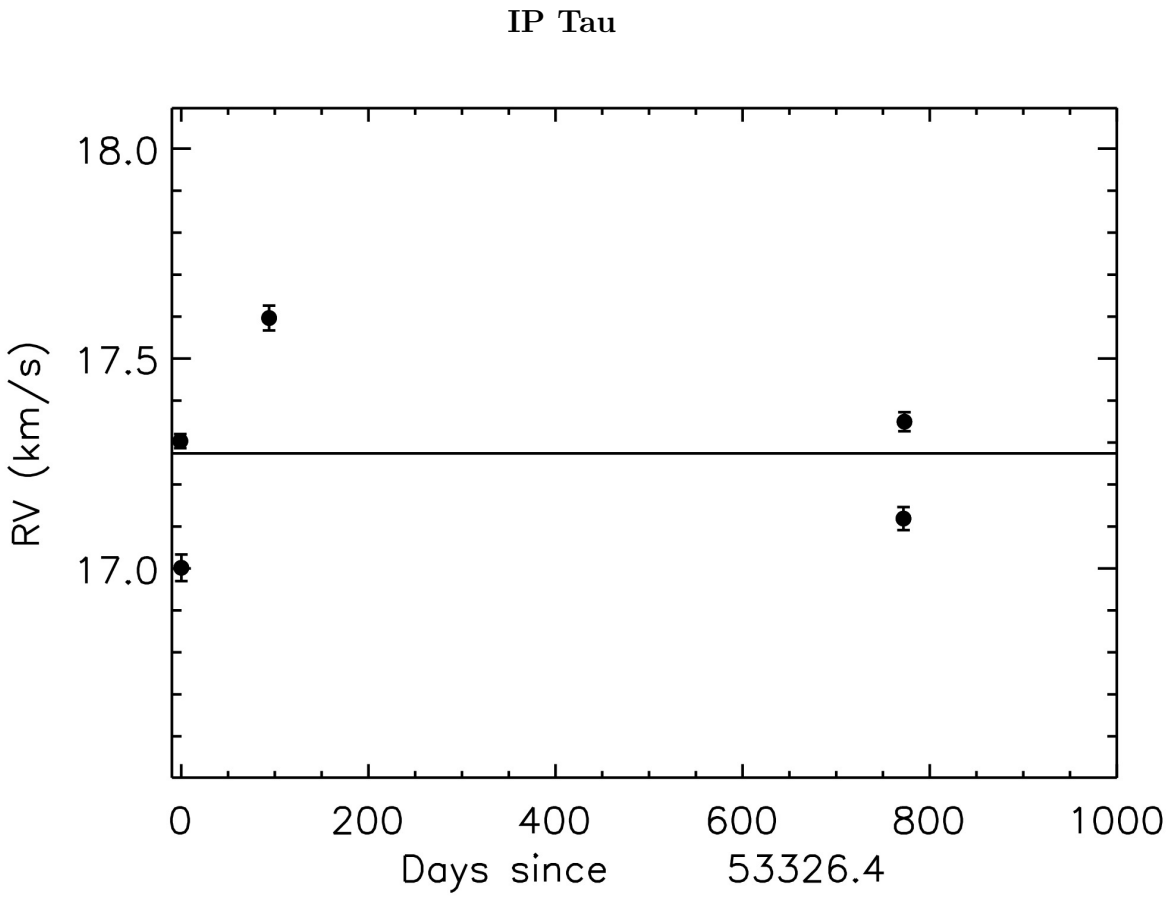

Figure 35 The RV curve is plotted with epoch errors for each observing day.

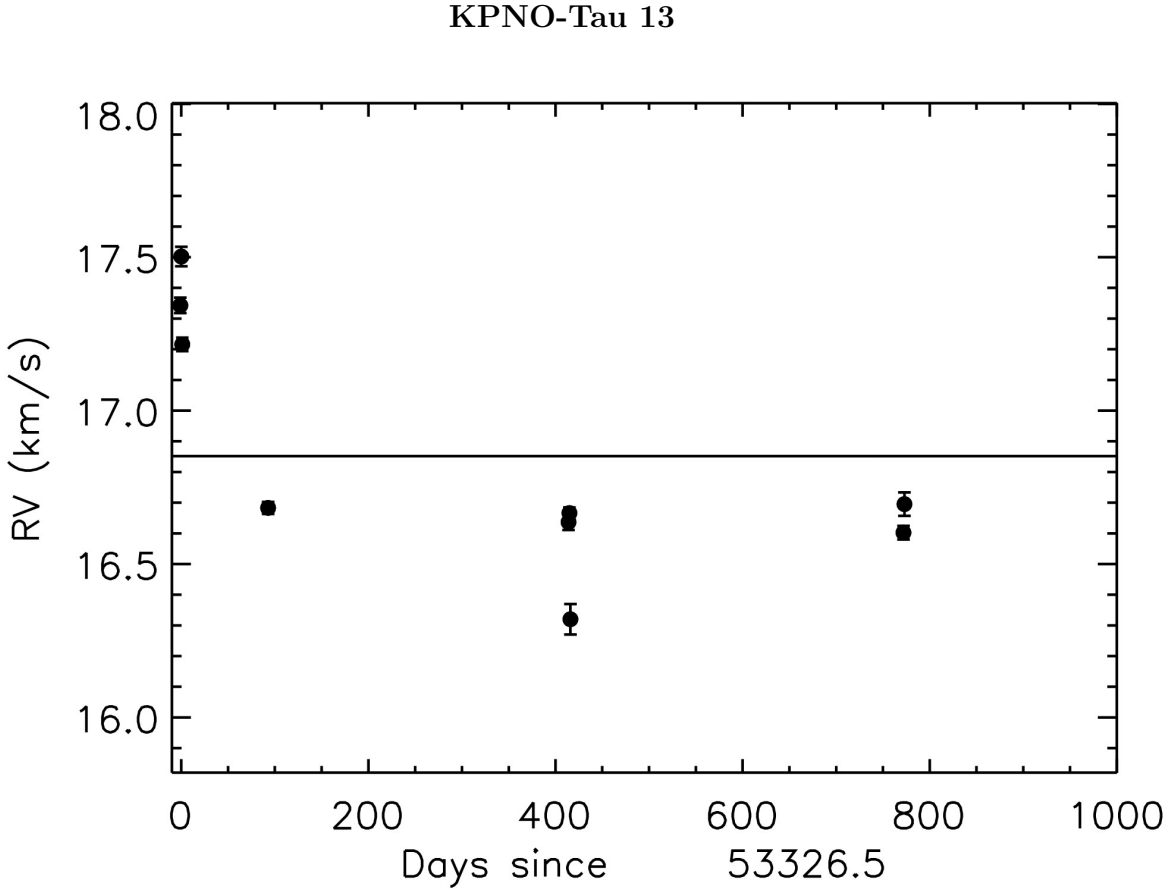

Figure 36 The RV curve is plotted with epoch errors for each observing day.

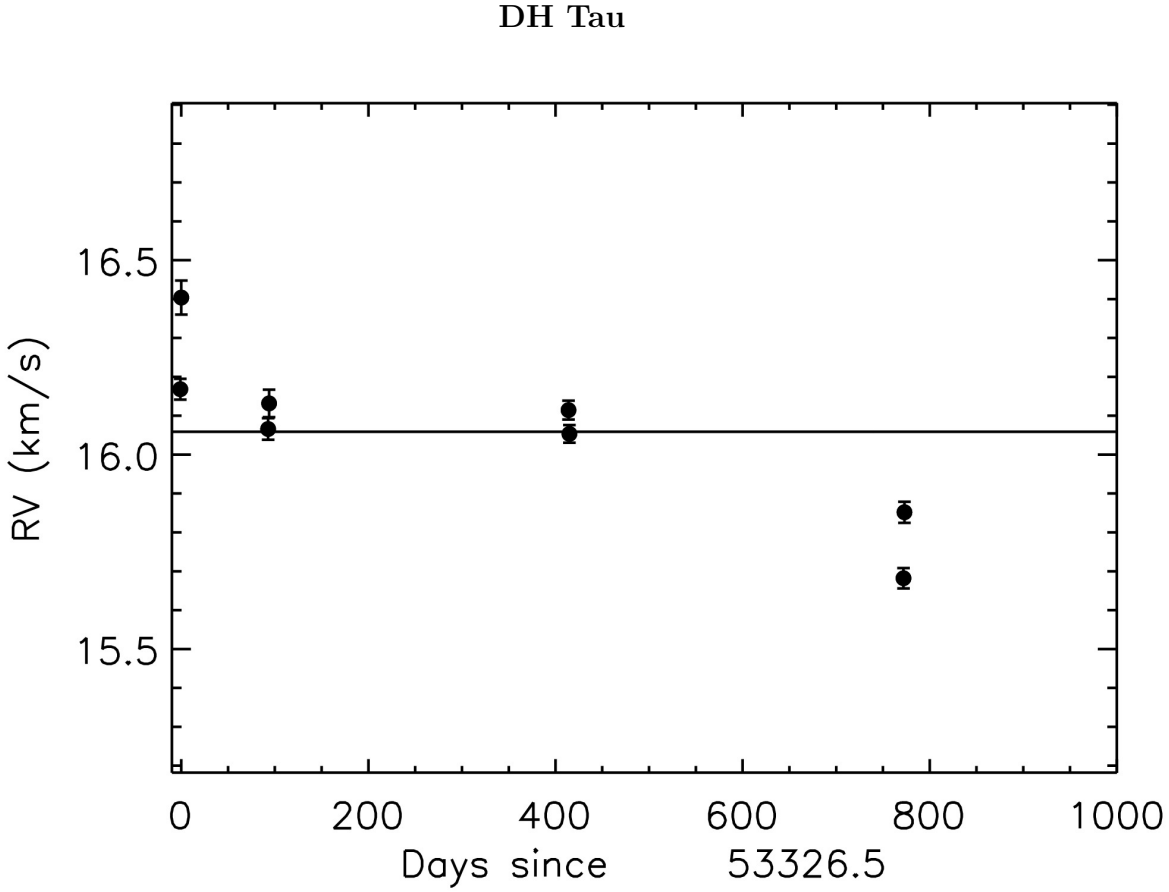

Figure 37 The RV curve is plotted with epoch errors for each observing day.

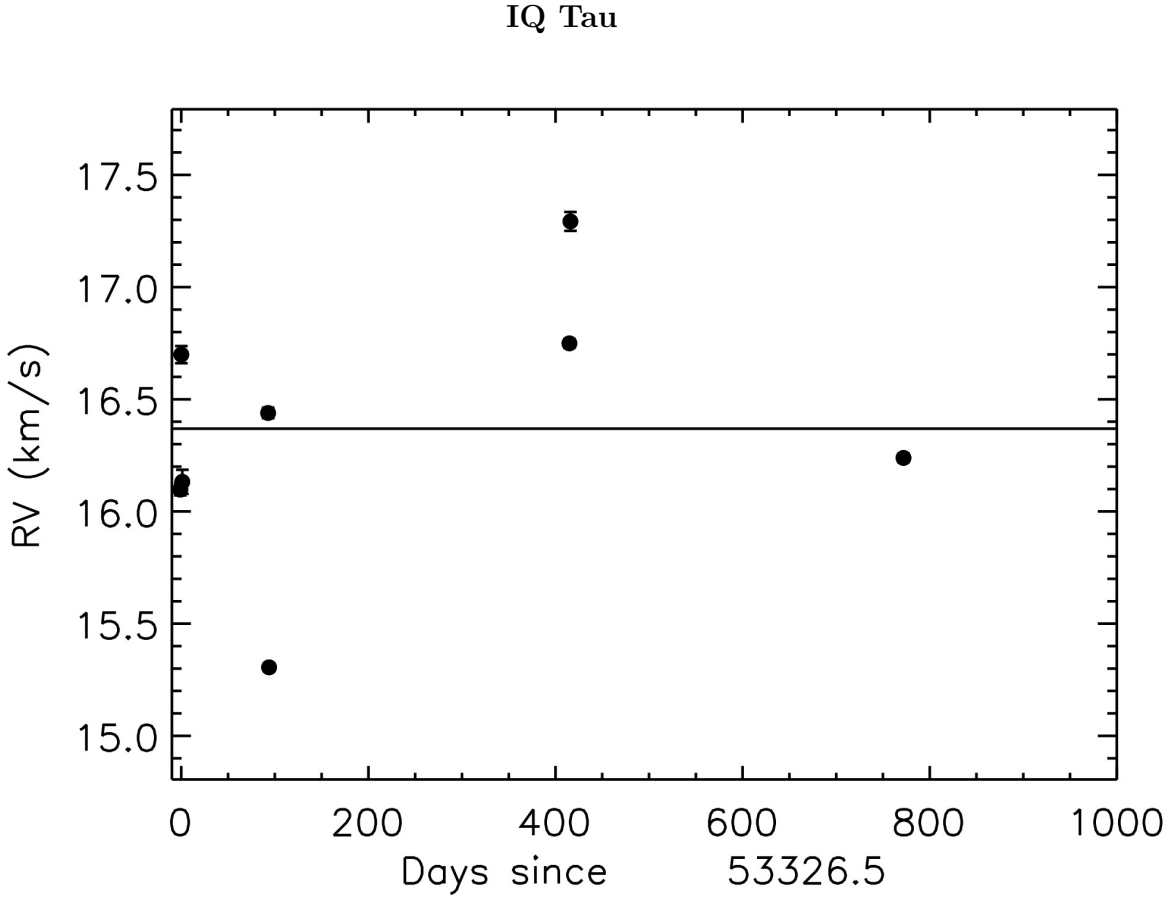

Figure 38 The RV curve is plotted with epoch errors for each observing day.

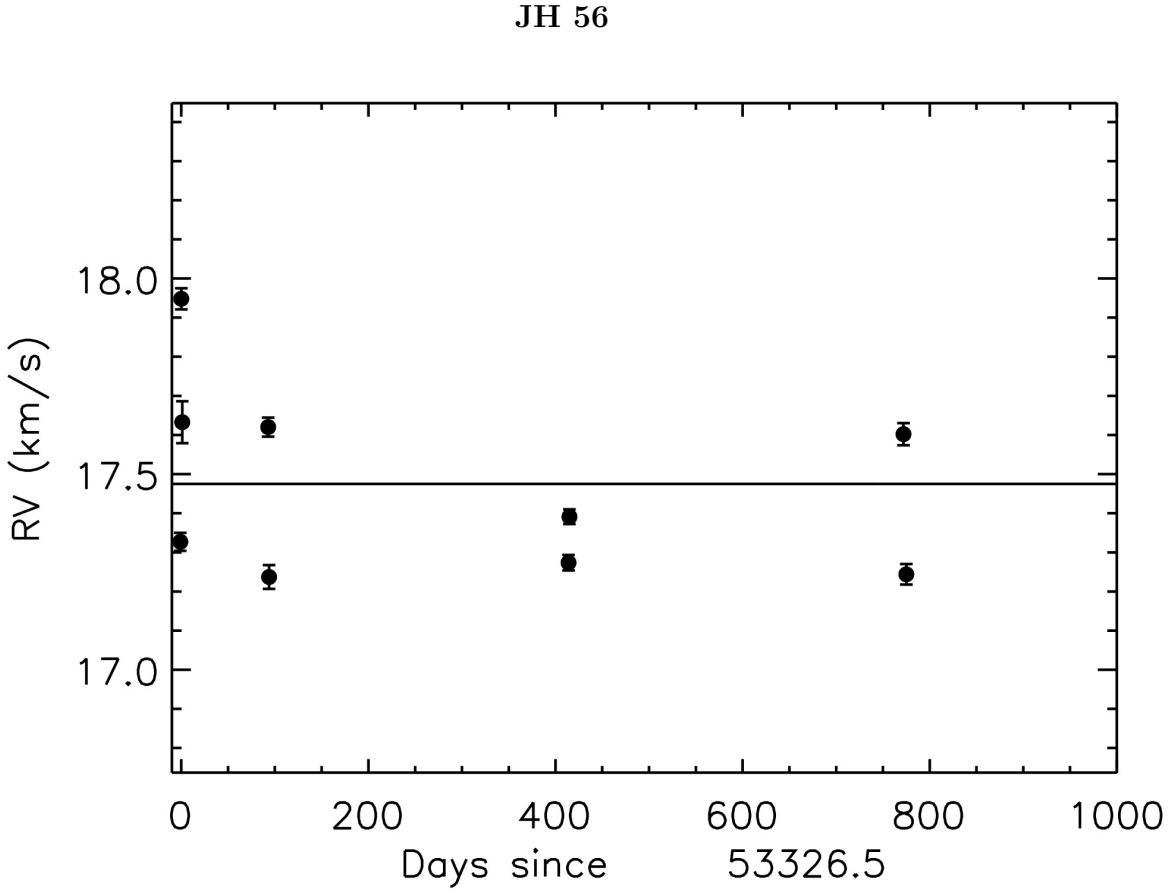

Figure 39 The RV curve is plotted with epoch errors for each observing day.

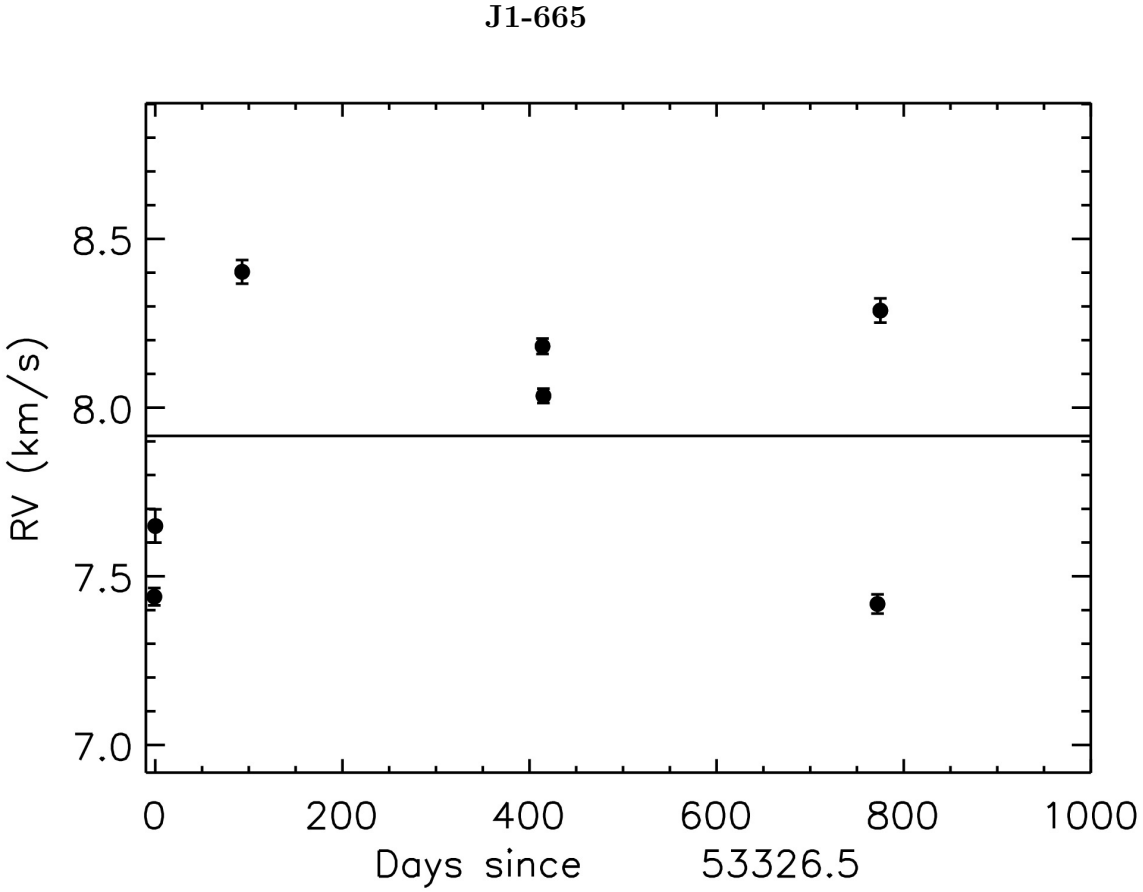

Figure 40 The RV curve is plotted with epoch errors for each observing day.

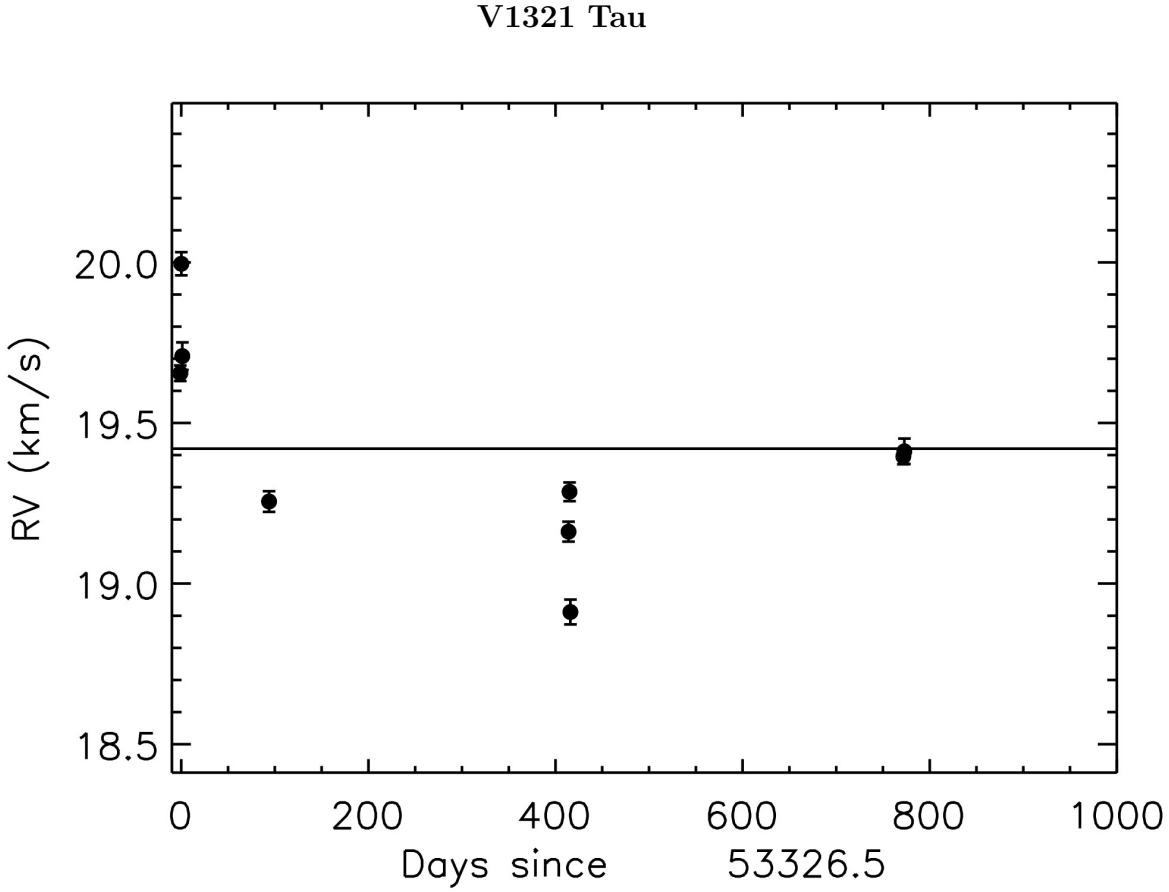

Figure 41 The RV curve is plotted with epoch errors for each observing day.

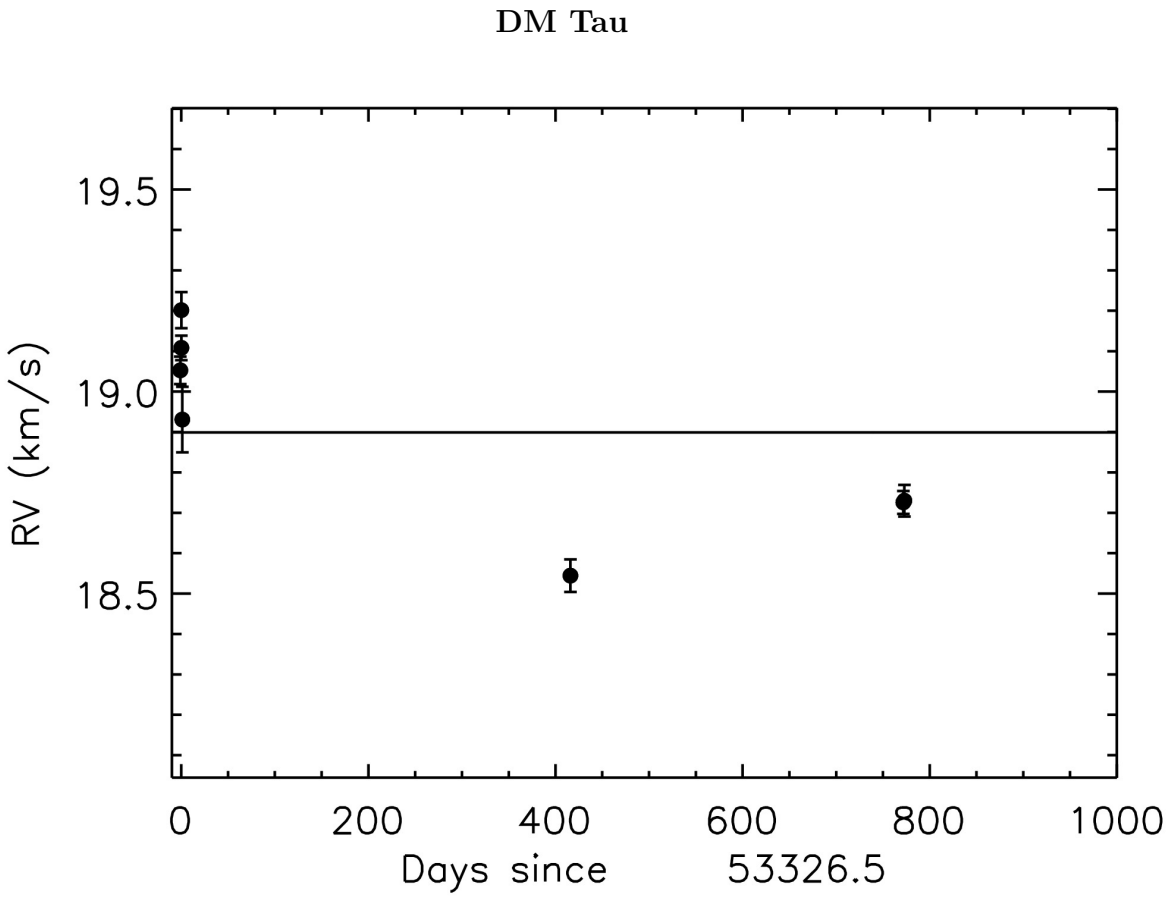

Figure 42 The RV curve is plotted with epoch errors for each observing day.

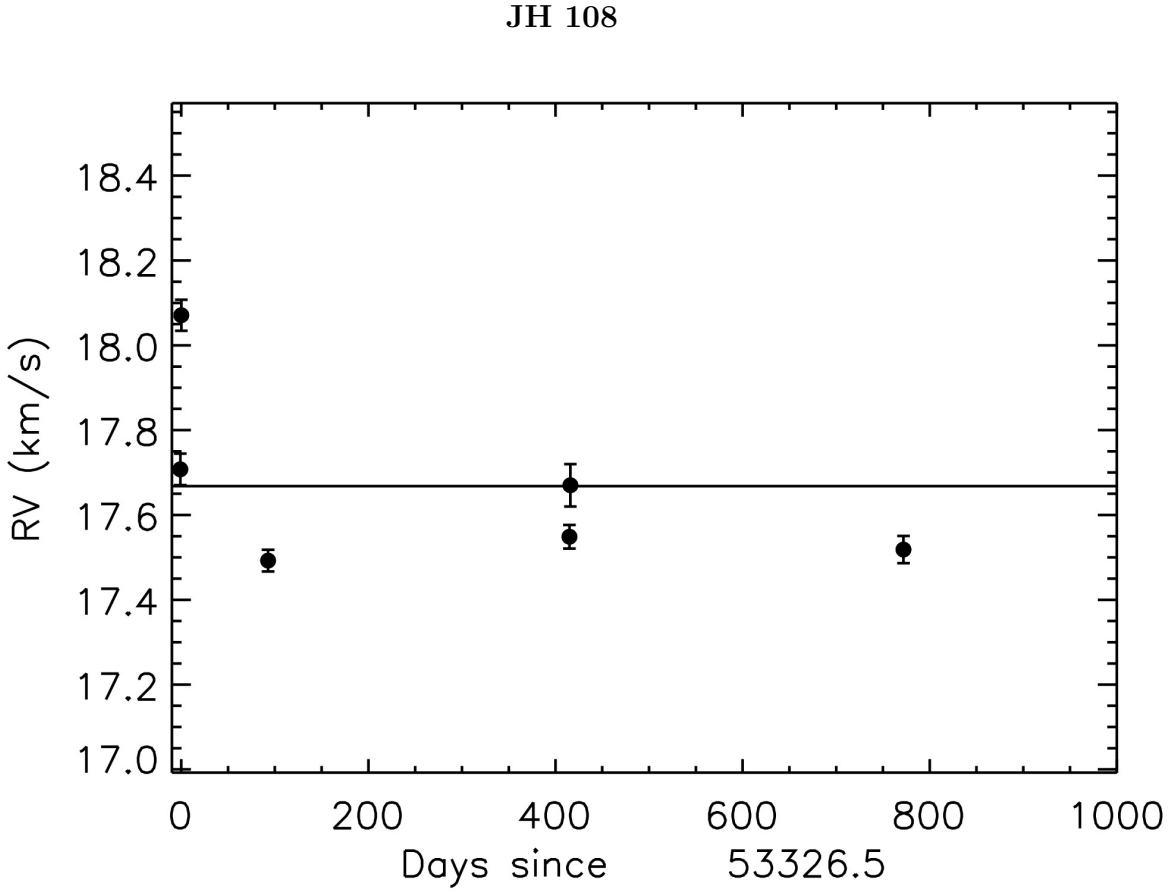

Figure 43 The RV curve is plotted with epoch errors for each observing day.

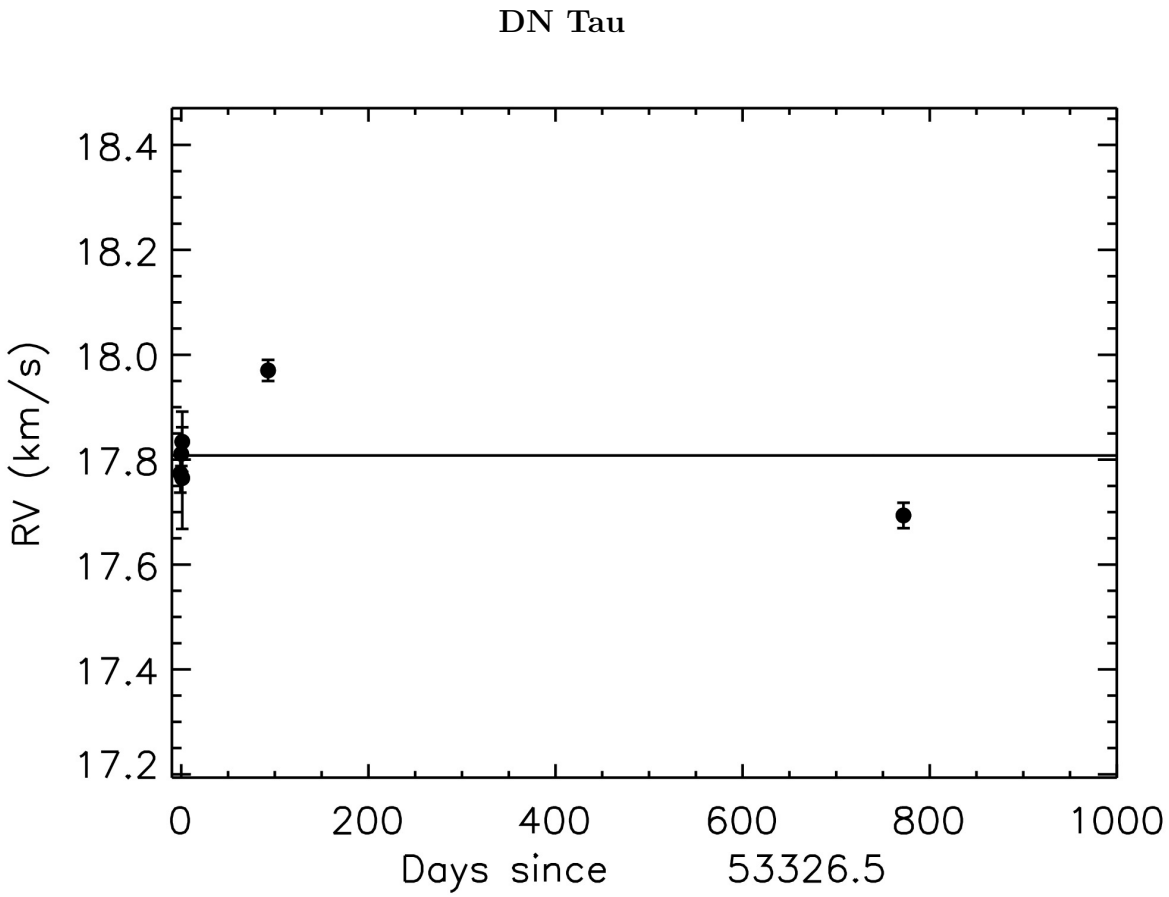

Figure 44 The RV curve is plotted with epoch errors for each observing day.

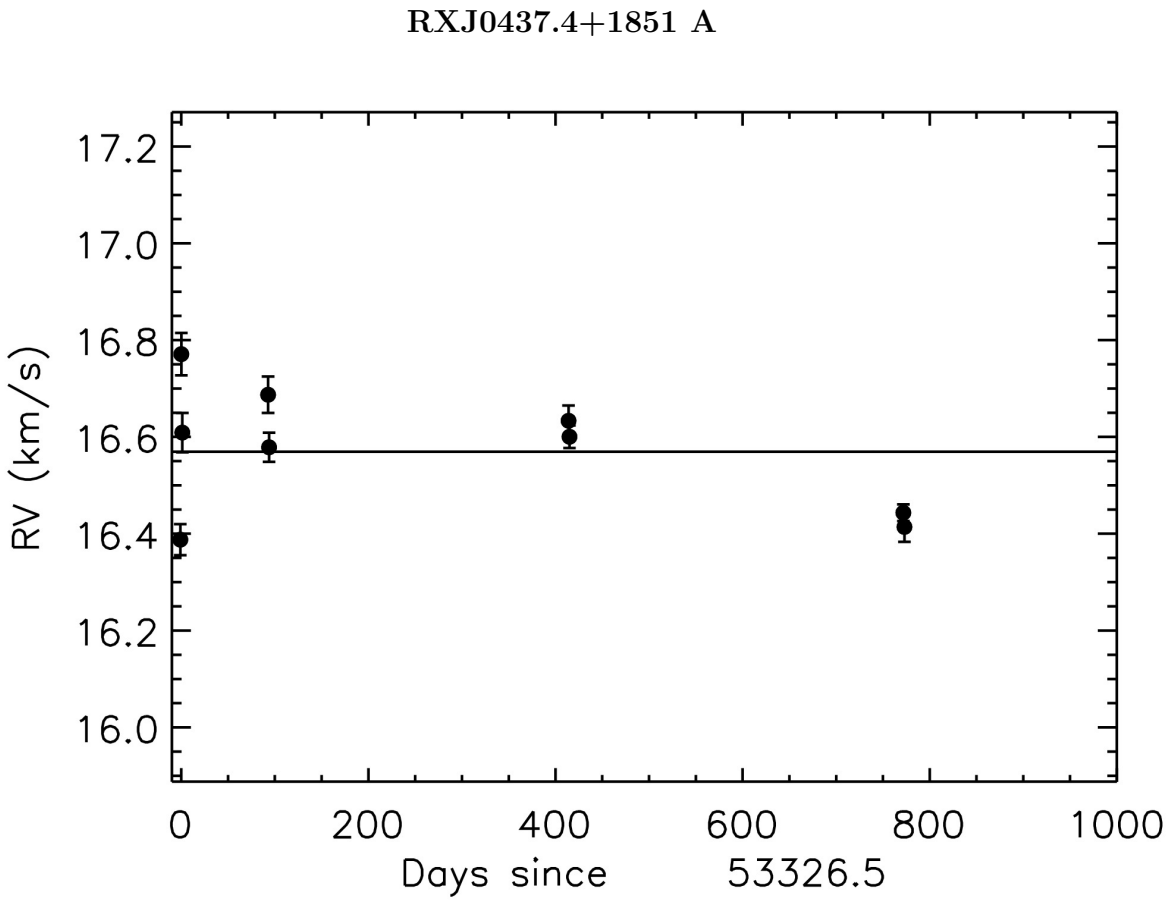

Figure 45 The RV curve is plotted with epoch errors for each observing day.

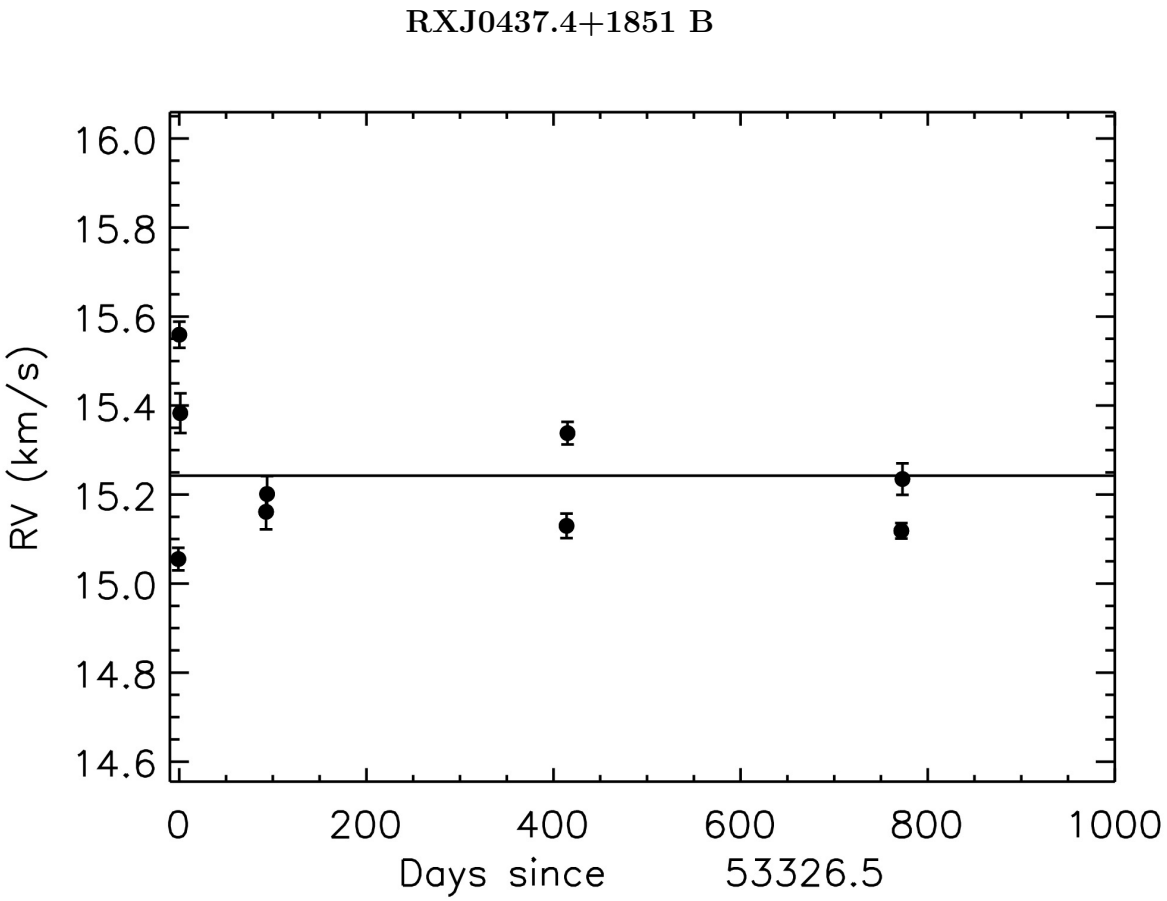

Figure 46 The RV curve is plotted with epoch errors for each observing day.

RXJ0438.2+2303

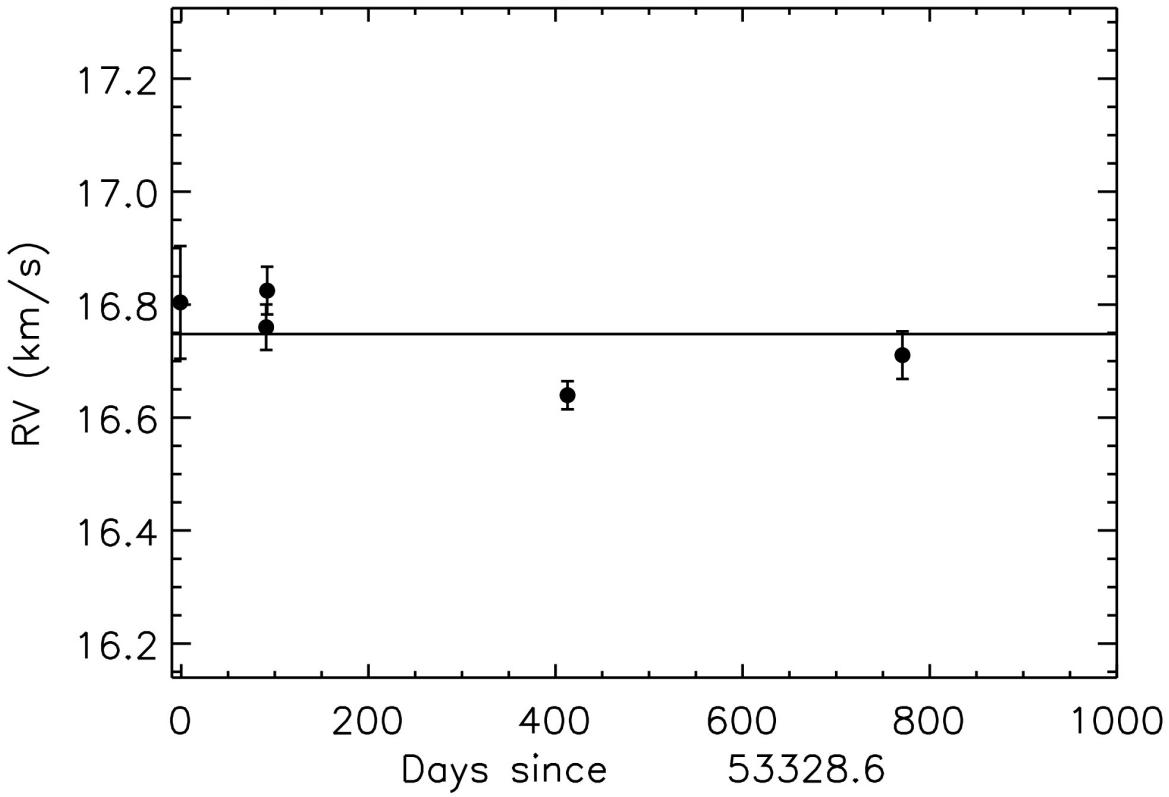

Figure 47 The RV curve is plotted with epoch errors for each observing day.

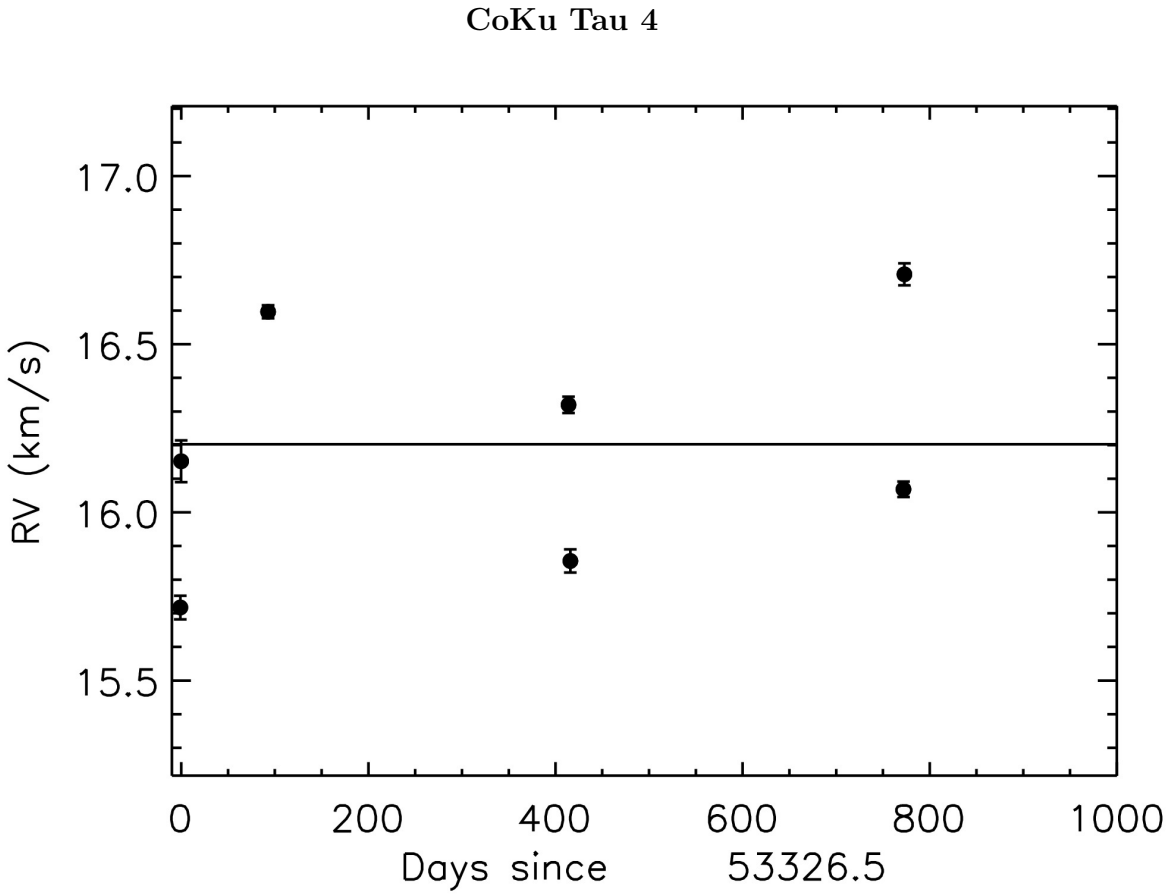

Figure 48 The RV curve is plotted with epoch errors for each observing day.

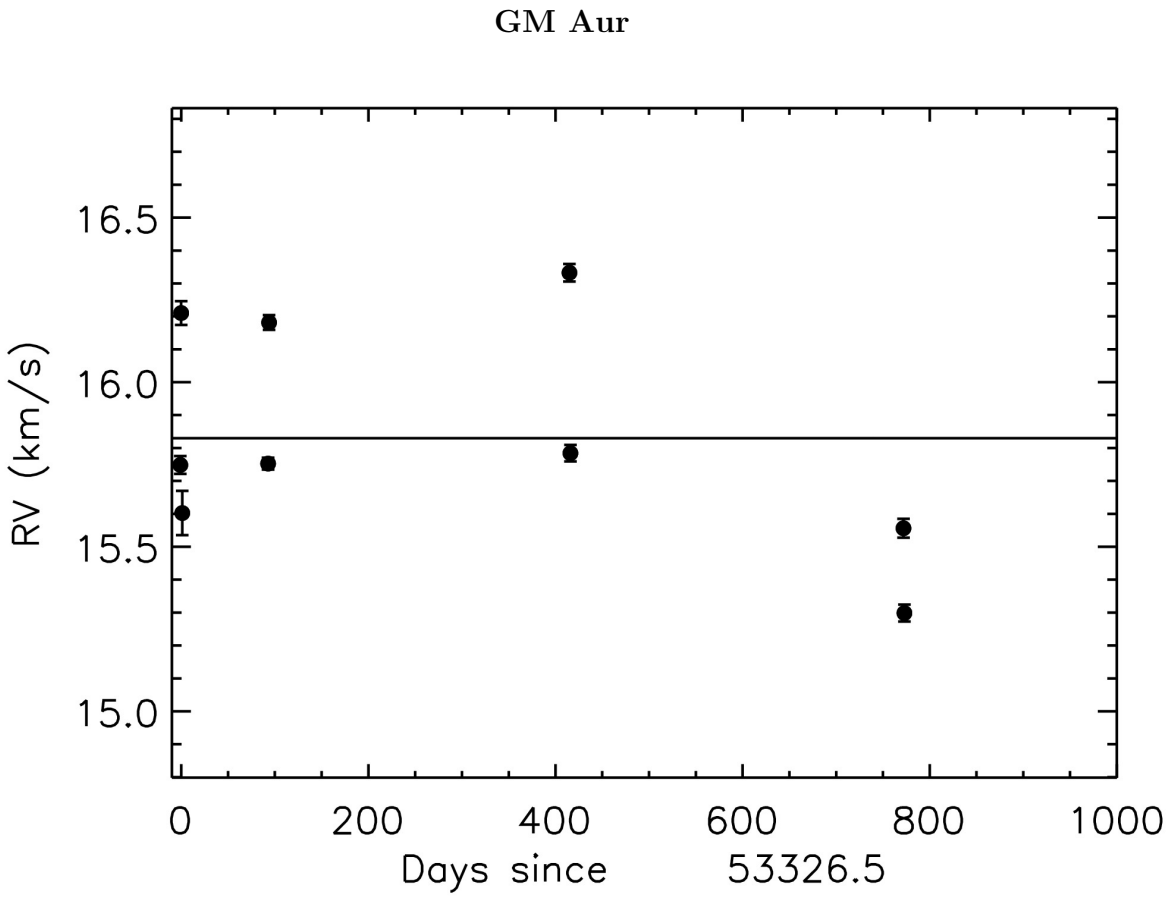

Figure 49 The RV curve is plotted with epoch errors for each observing day.

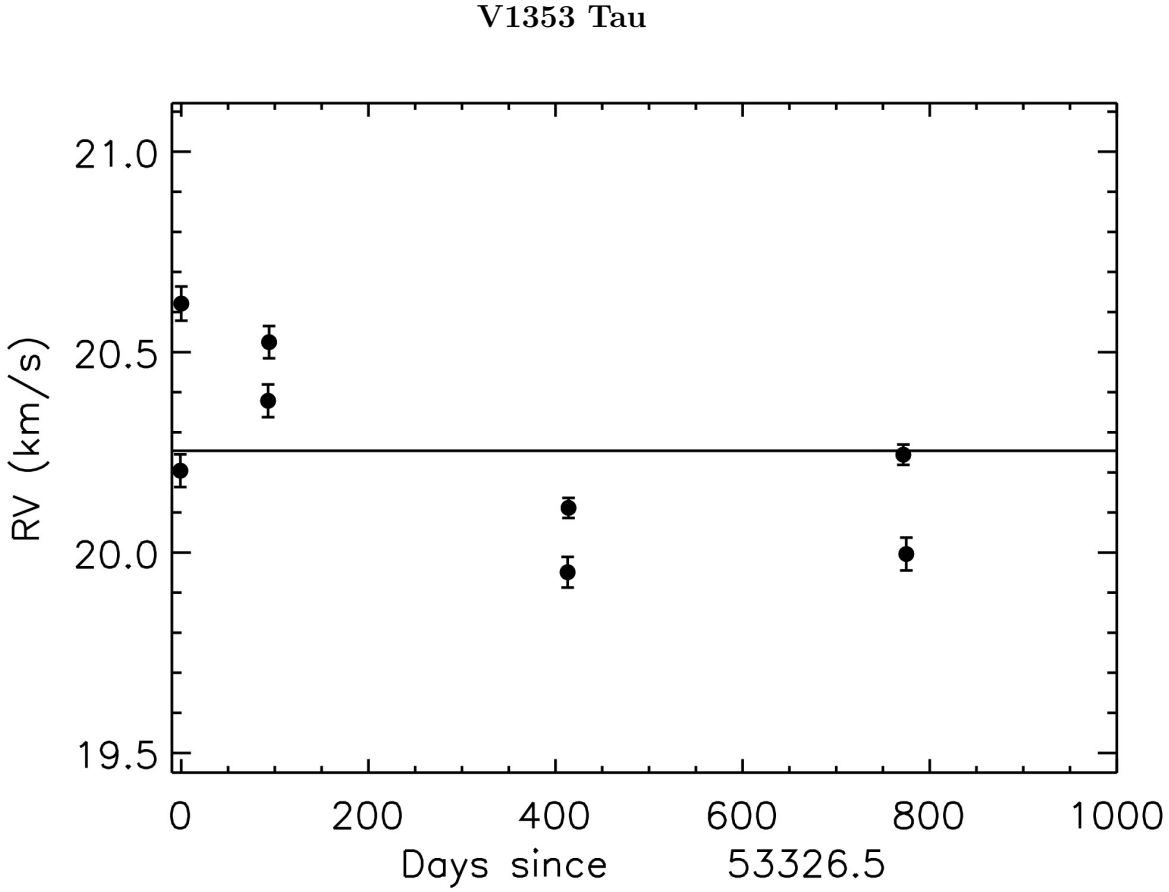

Figure 50 The RV curve is plotted with epoch errors for each observing day.

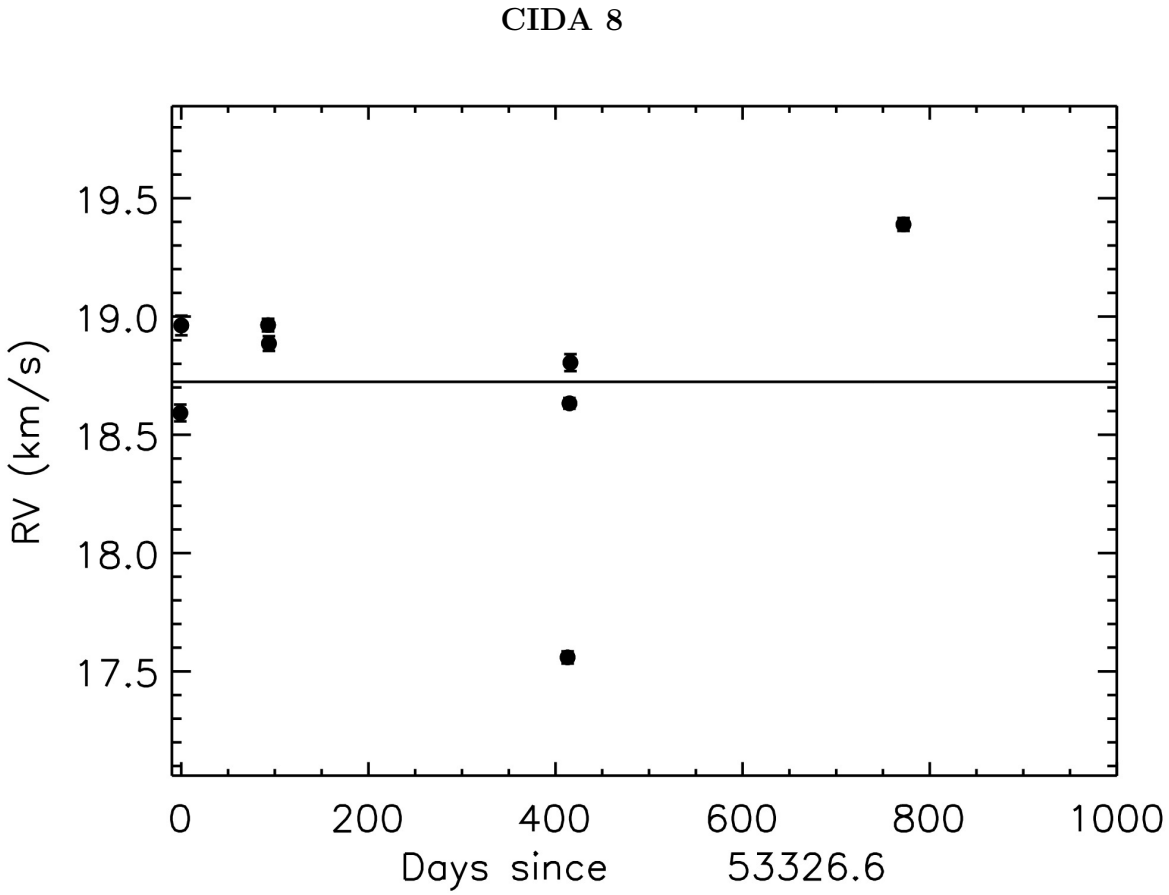

Figure 51 The RV curve is plotted with epoch errors for each observing day.

CIDA 10

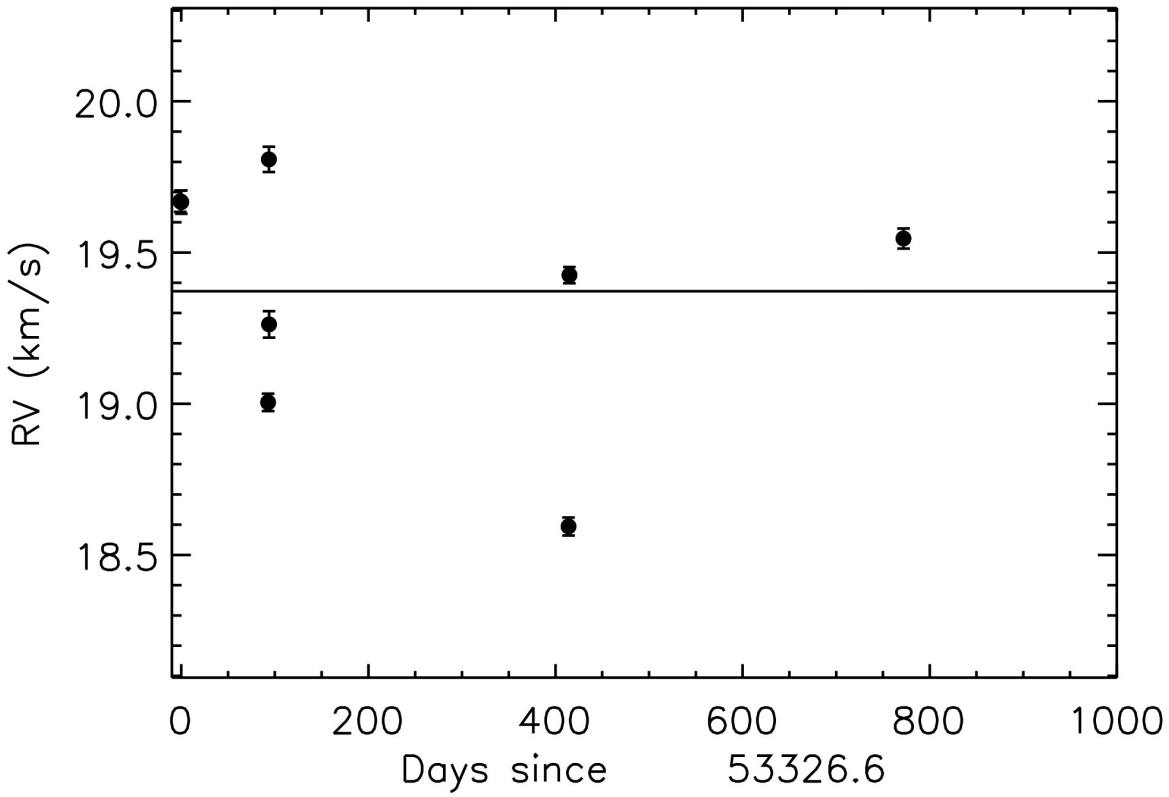

Figure 52 The RV curve is plotted with epoch errors for each observing day.

C.2 Upper Scorpius

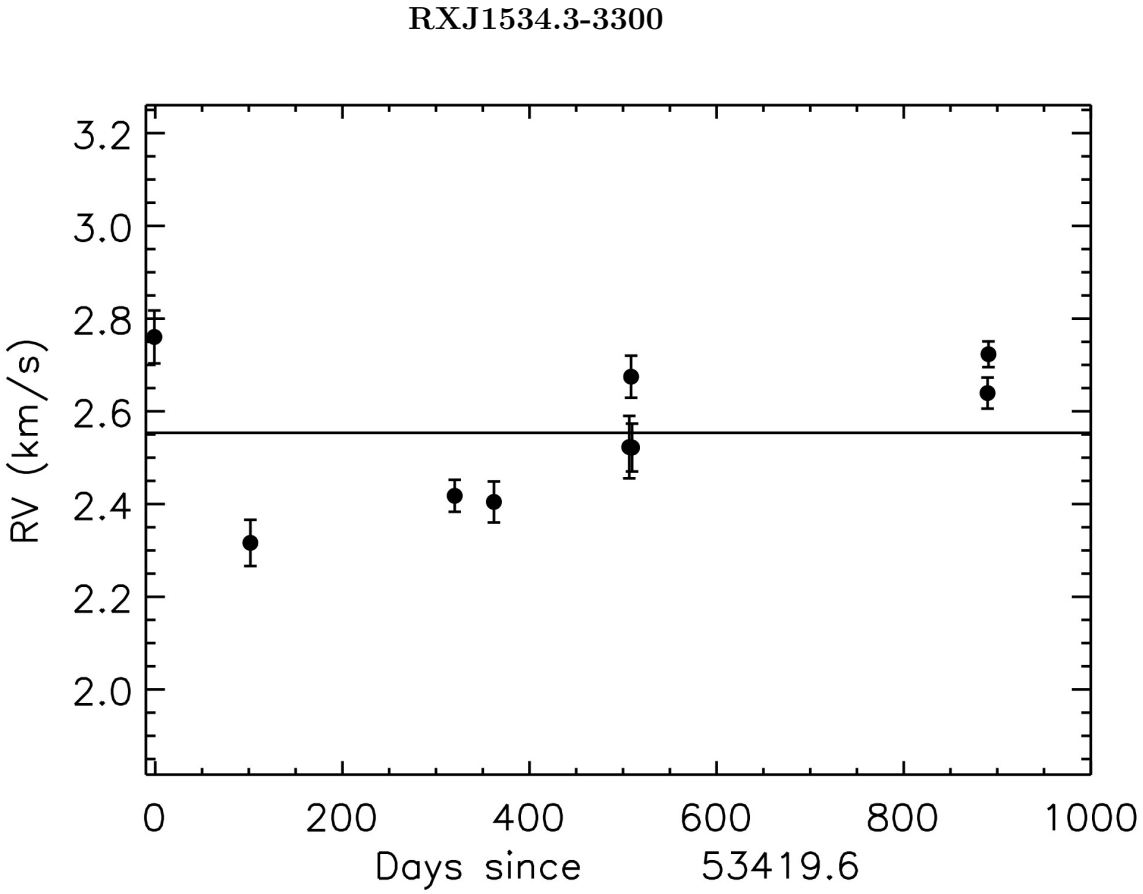

Figure 53 The RV curve is plotted with epoch errors for each observing day.

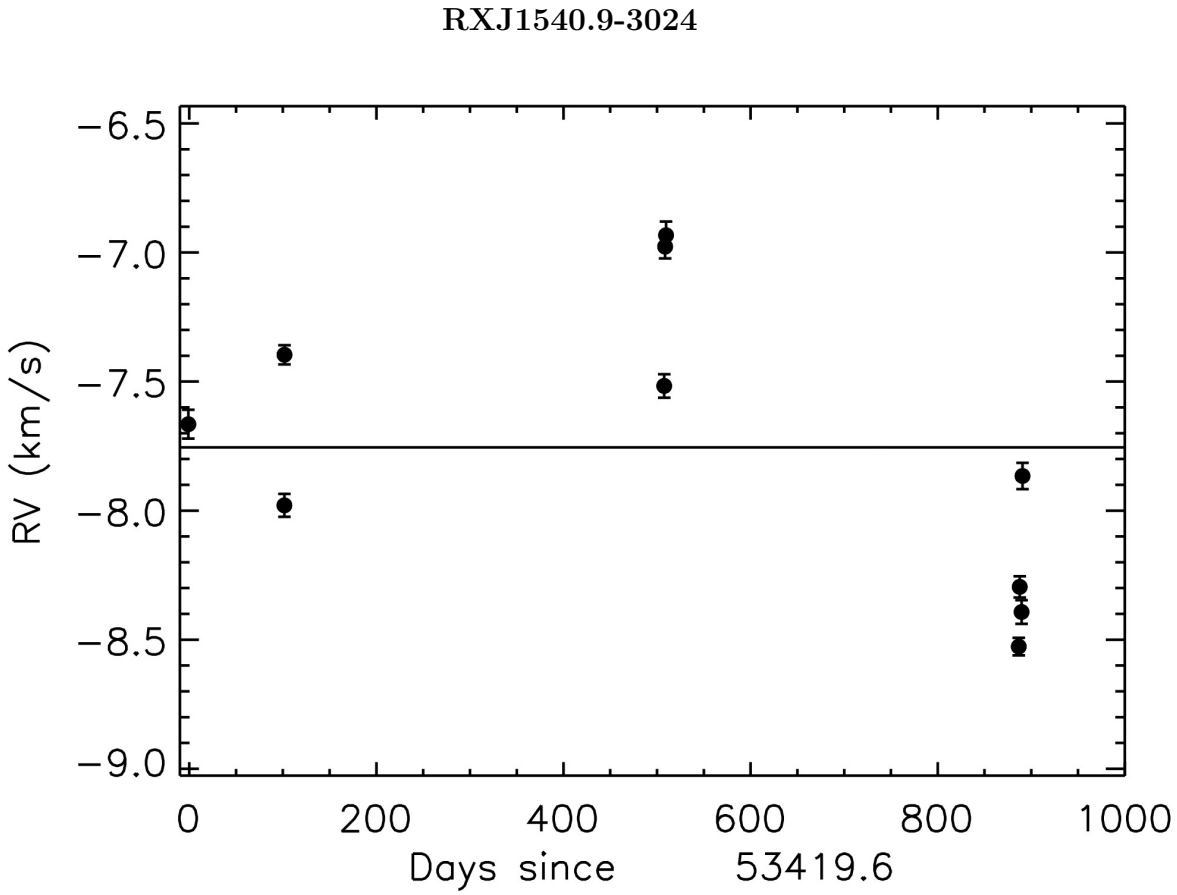

Figure 54 The RV curve is plotted with epoch errors for each observing day.

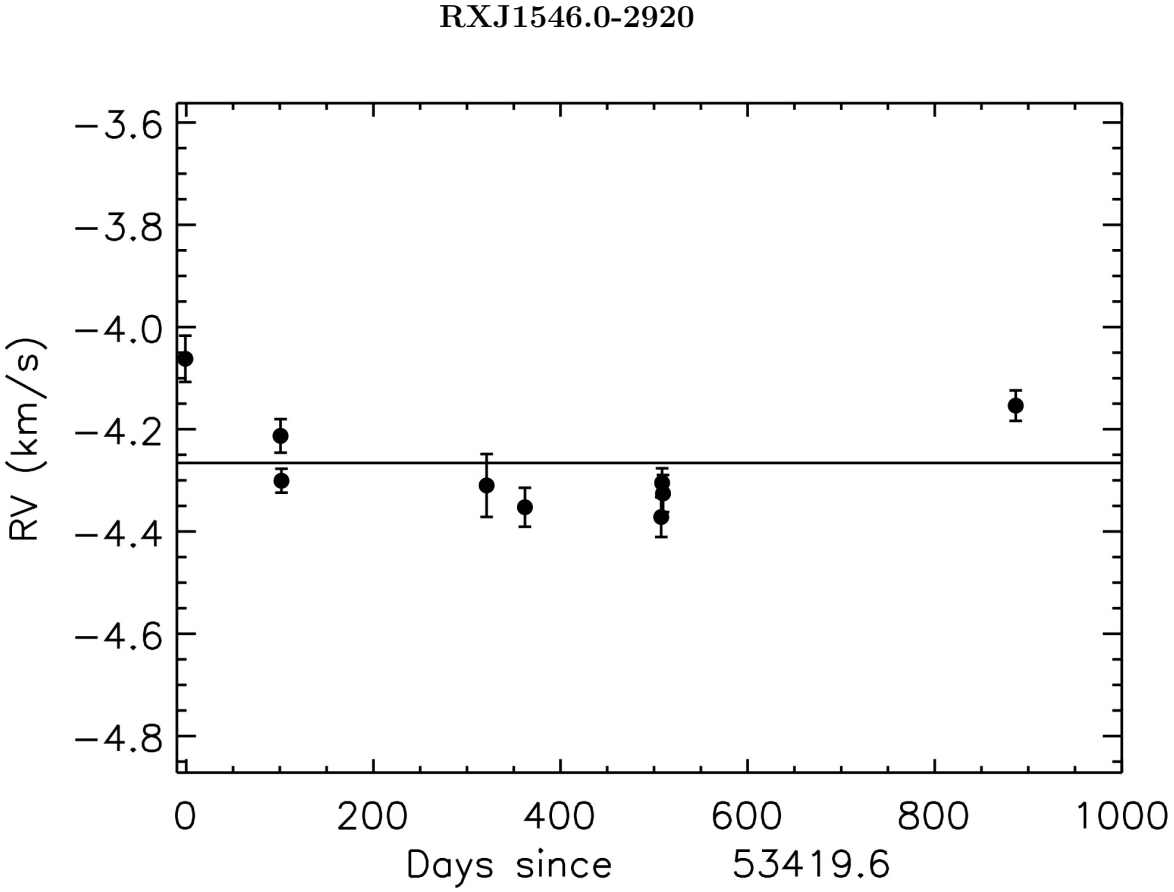

Figure 55 The RV curve is plotted with epoch errors for each observing day.

RXJ1546.7-3210

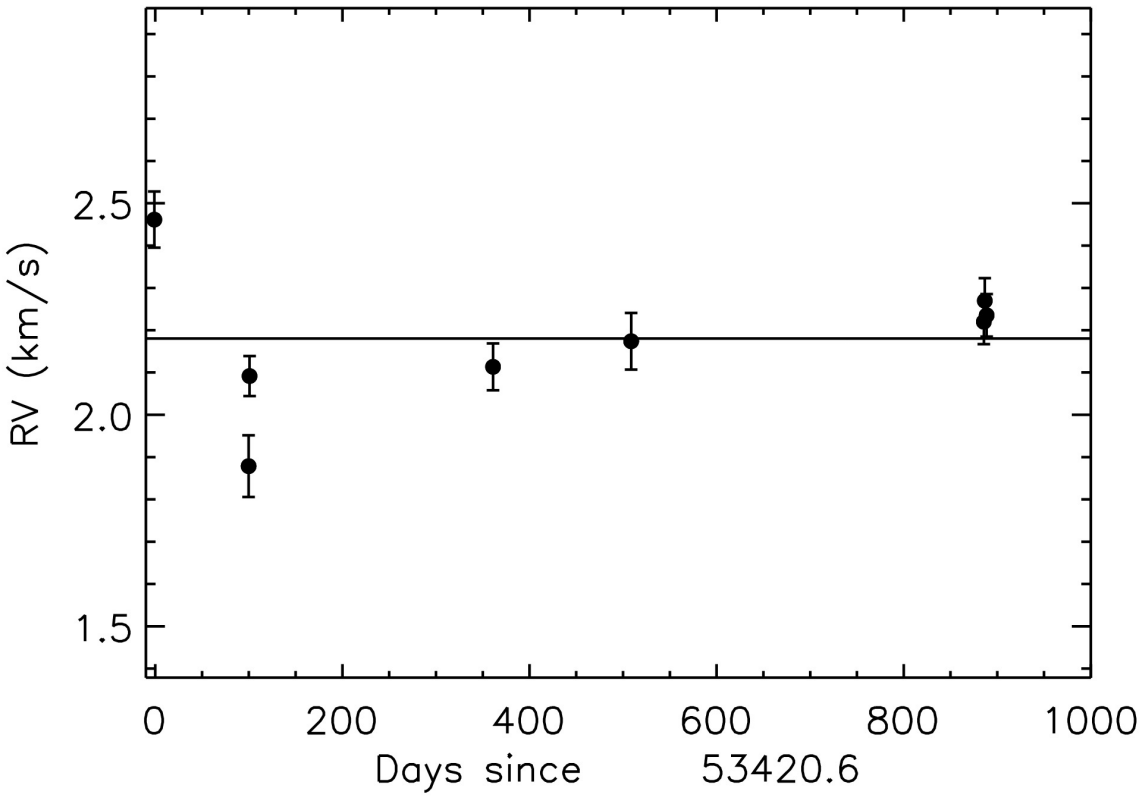

Figure 56 The RV curve is plotted with epoch errors for each observing day.

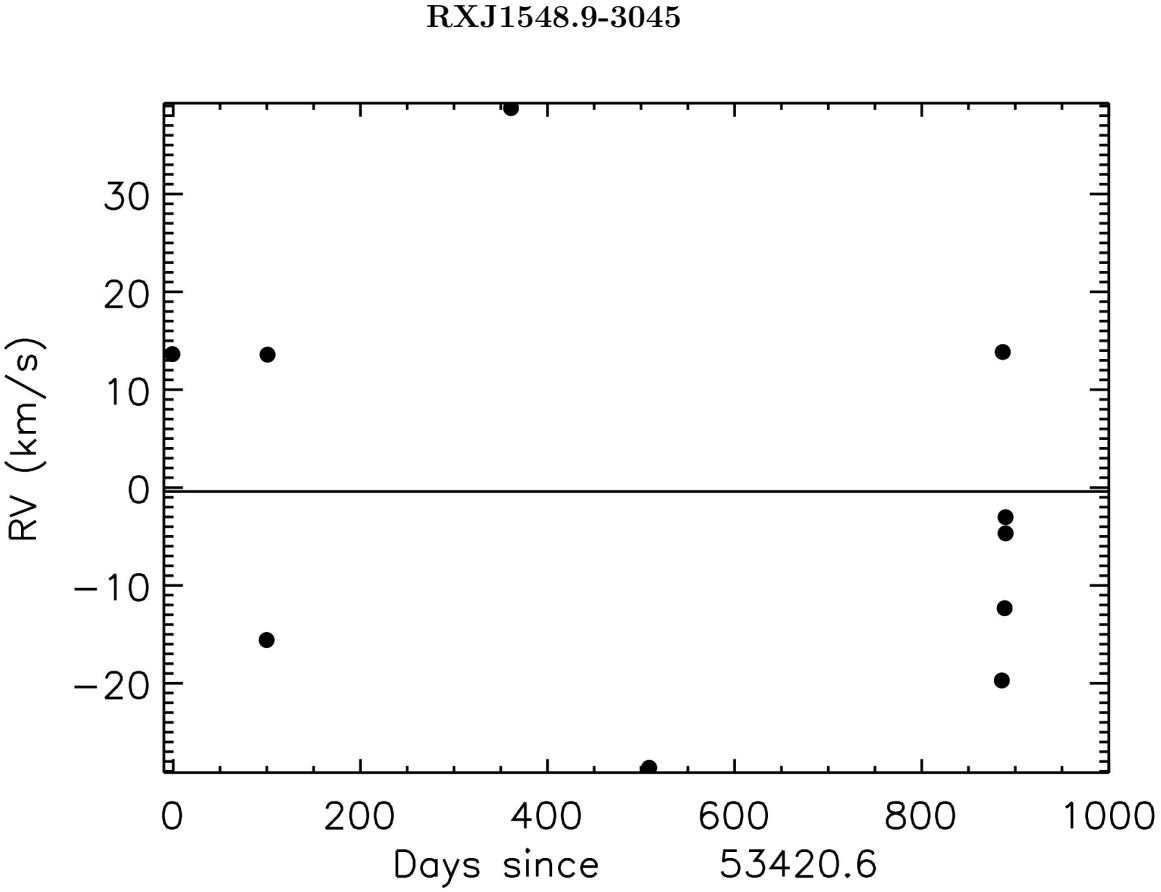

Figure 57 The RV curve is plotted with epoch errors for each observing day.

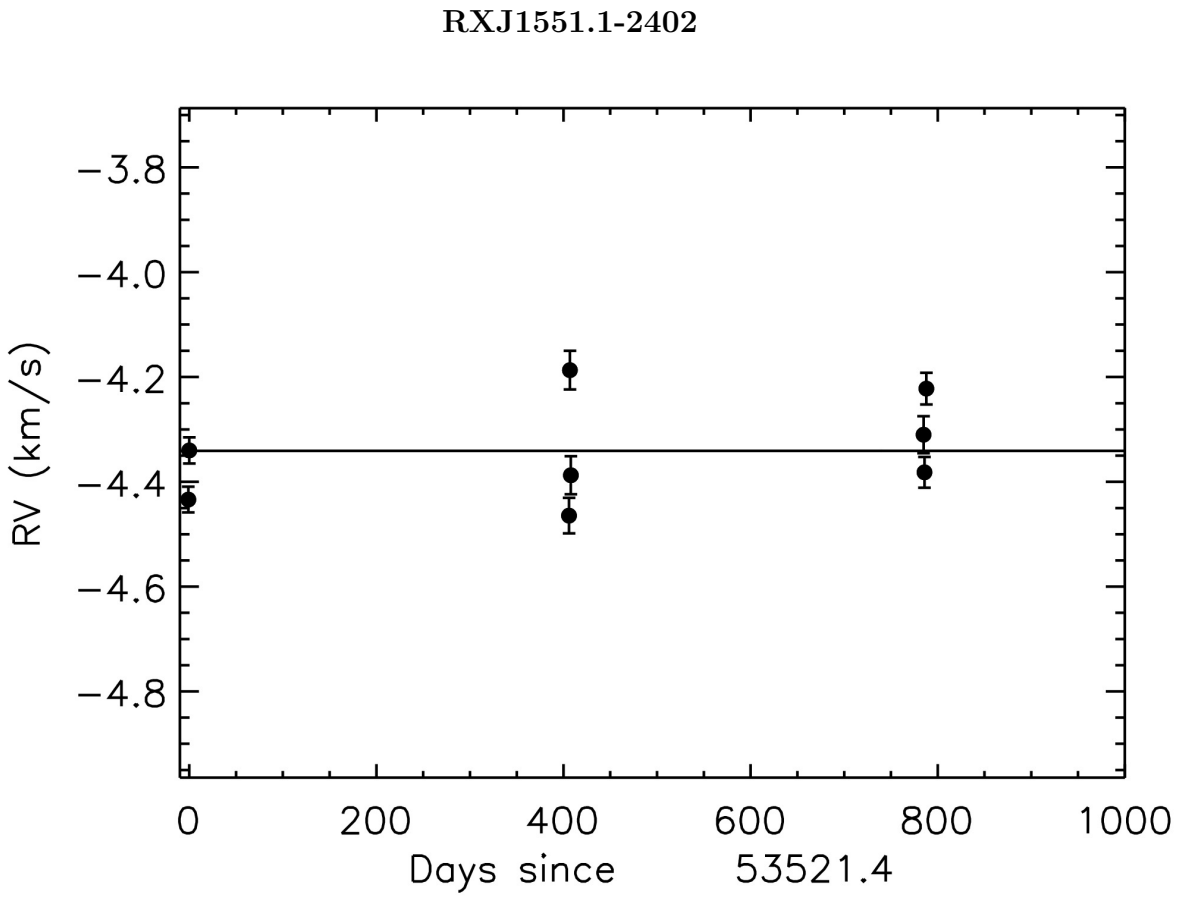

Figure 58 The RV curve is plotted with epoch errors for each observing day.

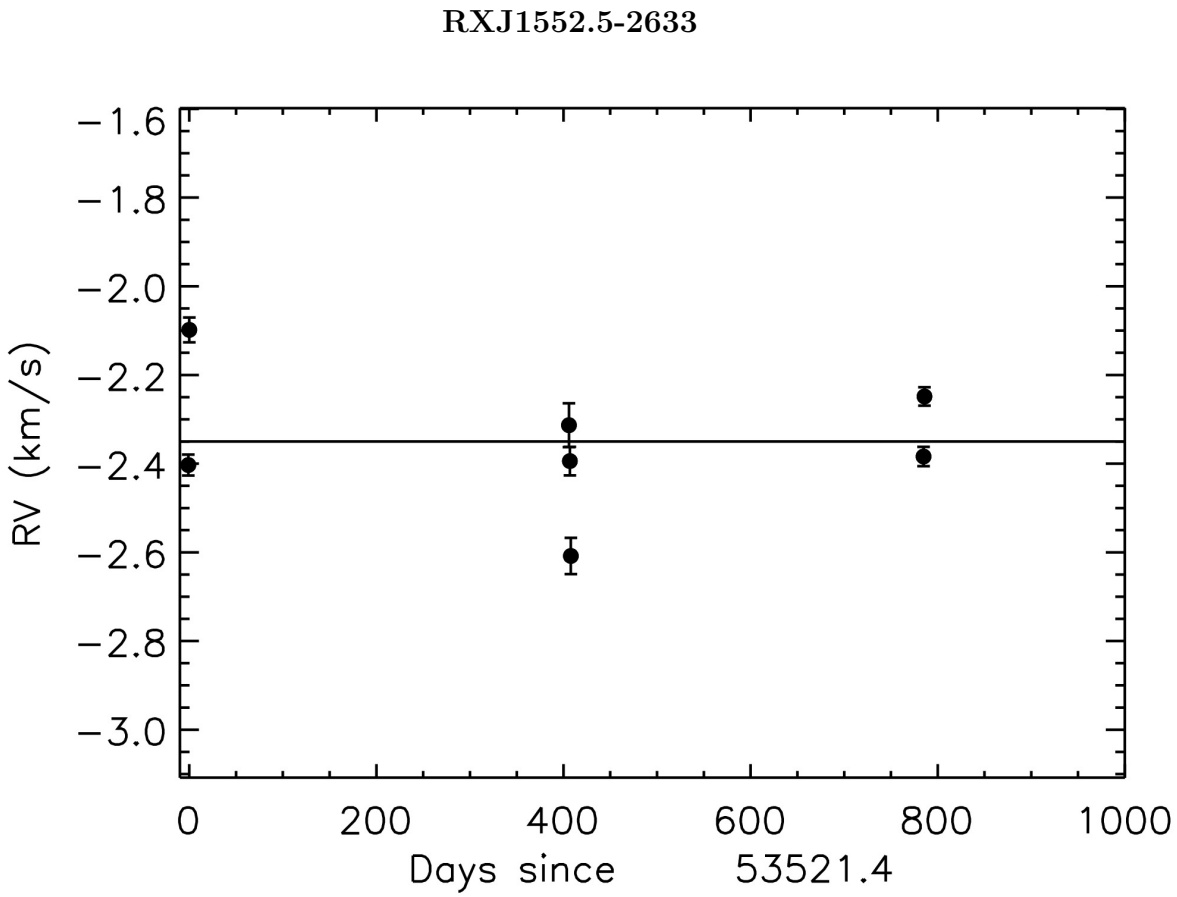

Figure 59 The RV curve is plotted with epoch errors for each observing day.

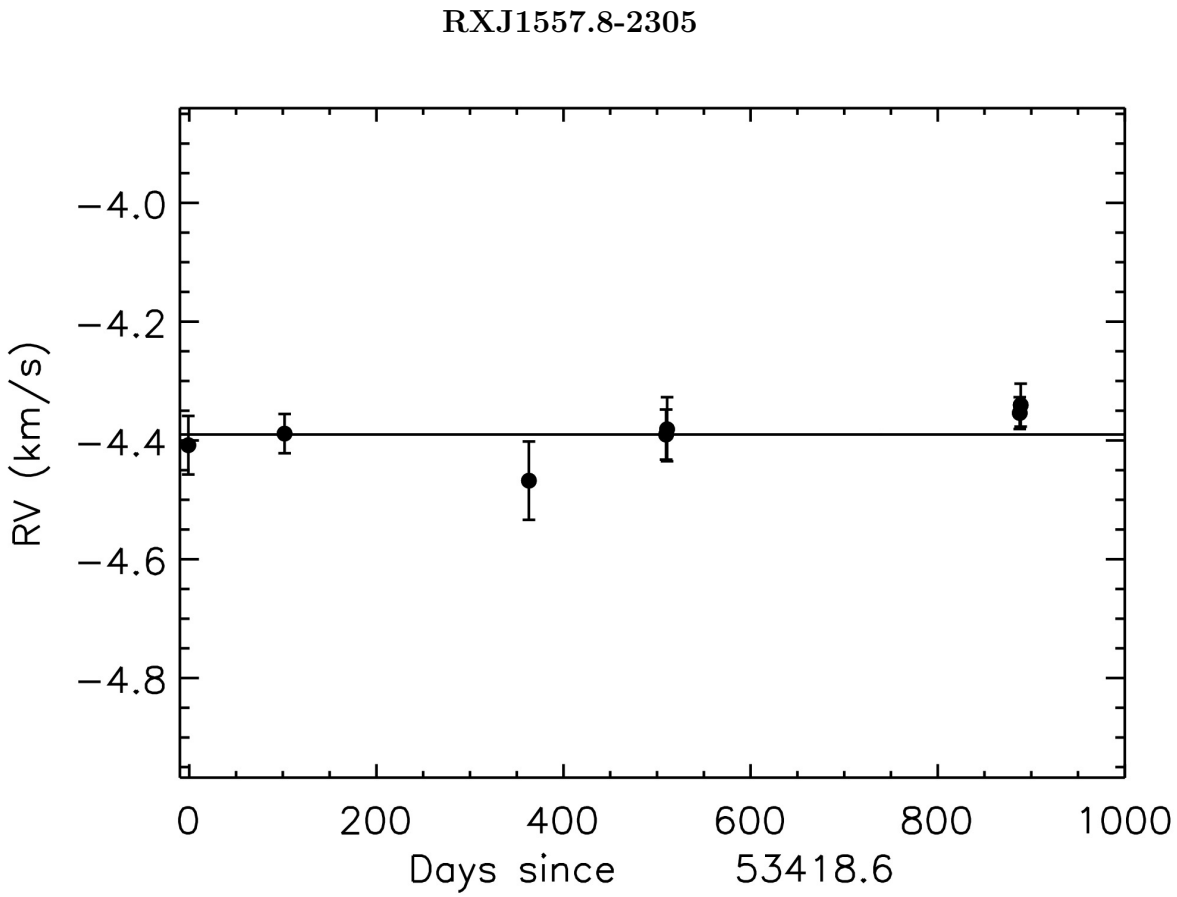

Figure 60 The RV curve is plotted with epoch errors for each observing day.

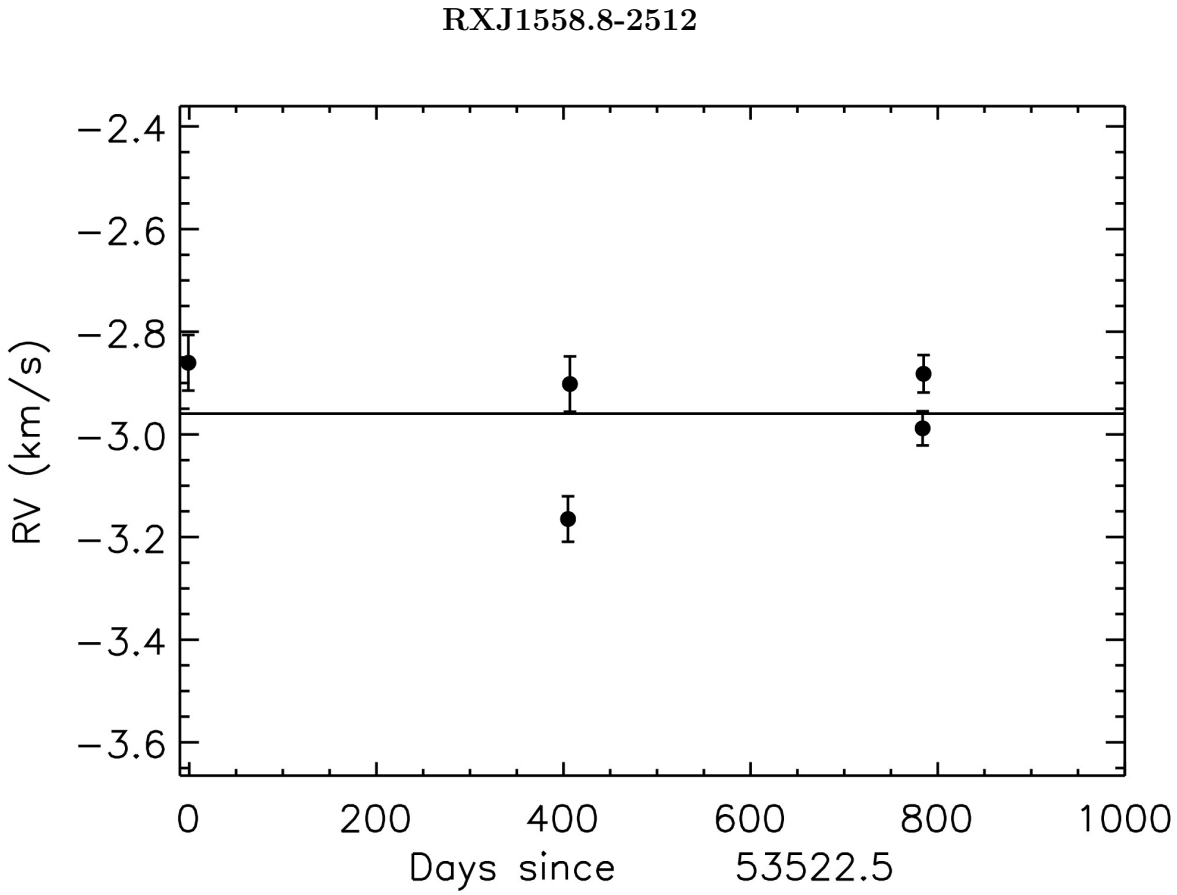

Figure 61 The RV curve is plotted with epoch errors for each observing day.

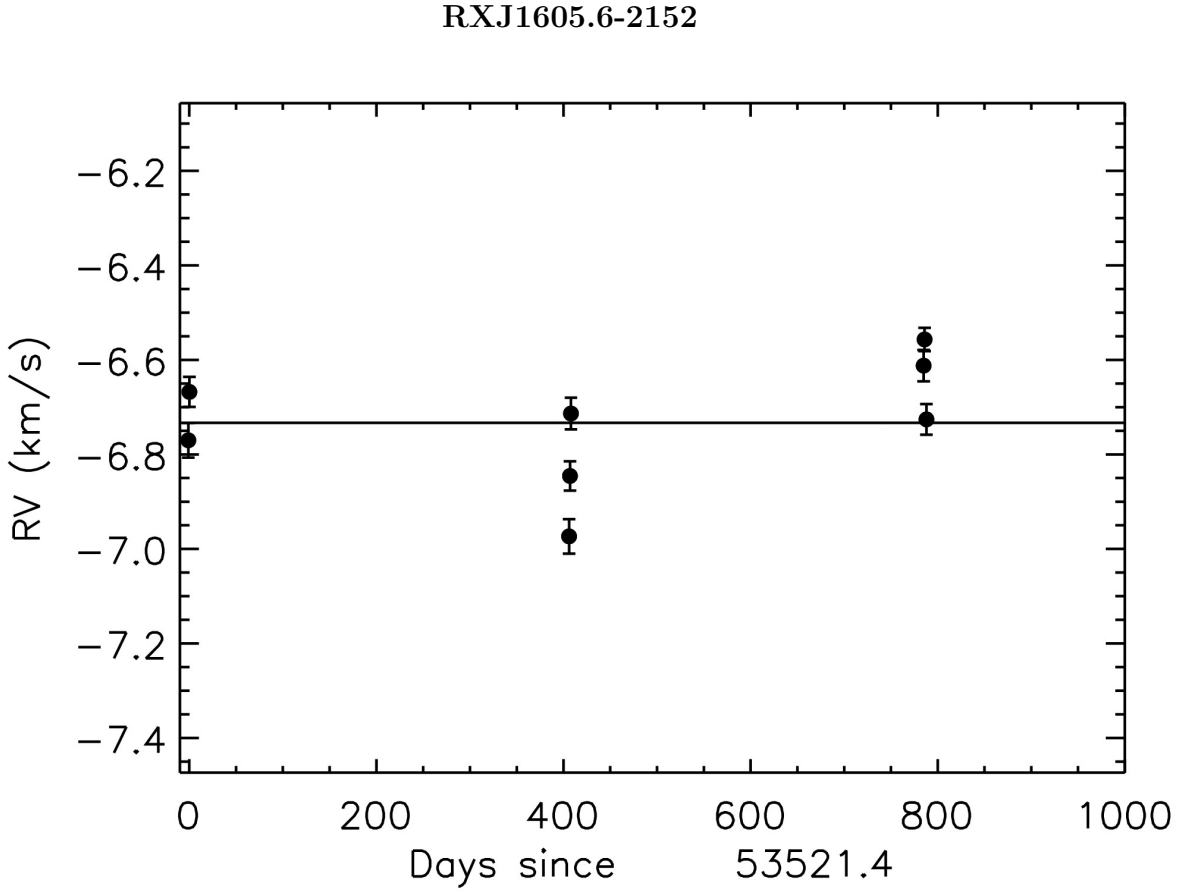

Figure 62 The RV curve is plotted with epoch errors for each observing day.

RXJ1607.0-2043

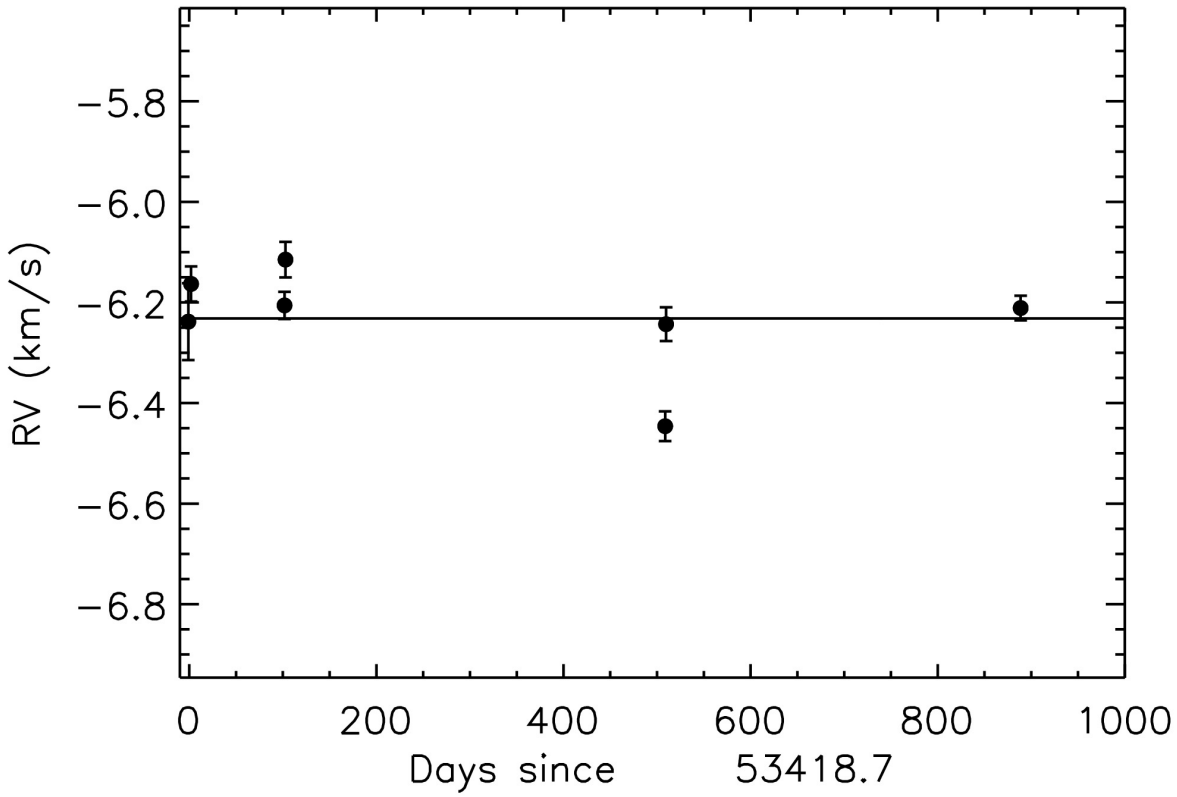

Figure 63 The RV curve is plotted with epoch errors for each observing day.

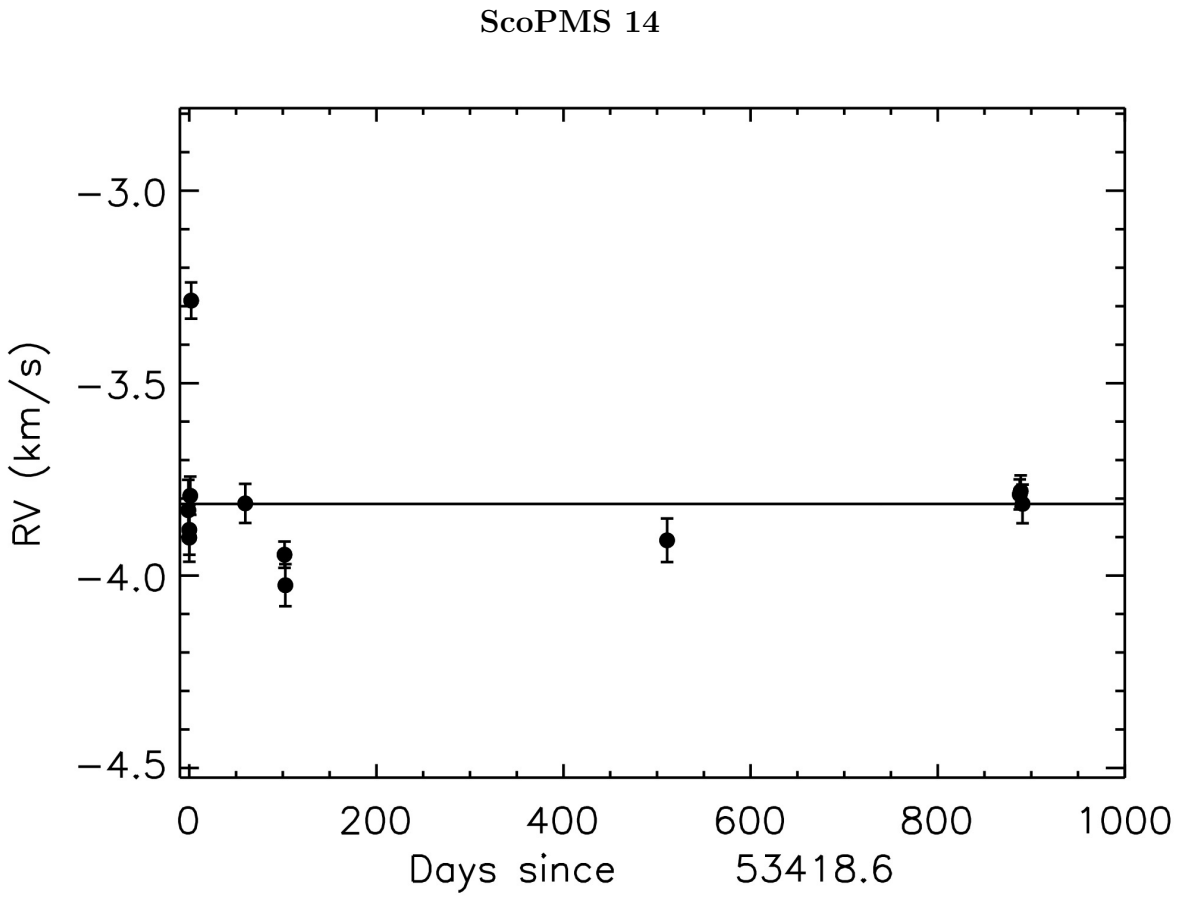

Figure 64 The RV curve is plotted with epoch errors for each observing day.

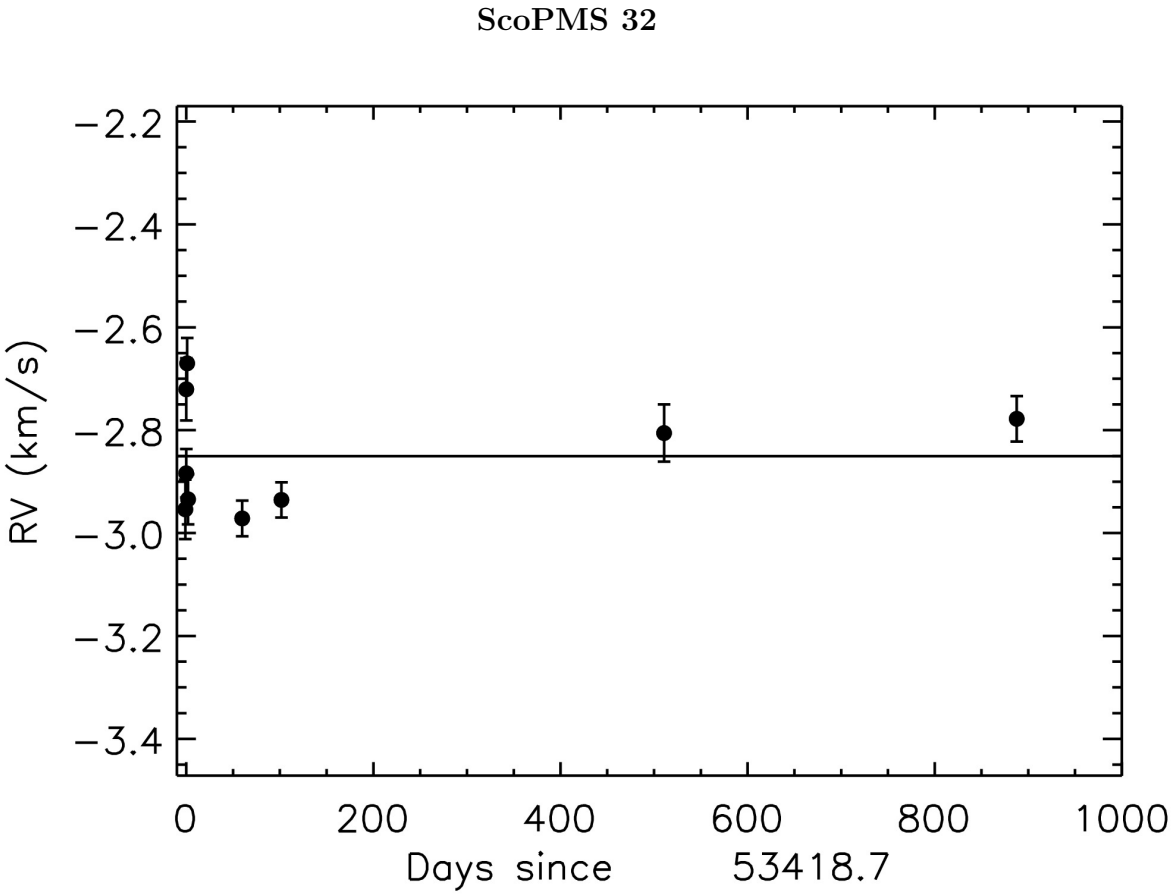

Figure 65 The RV curve is plotted with epoch errors for each observing day.

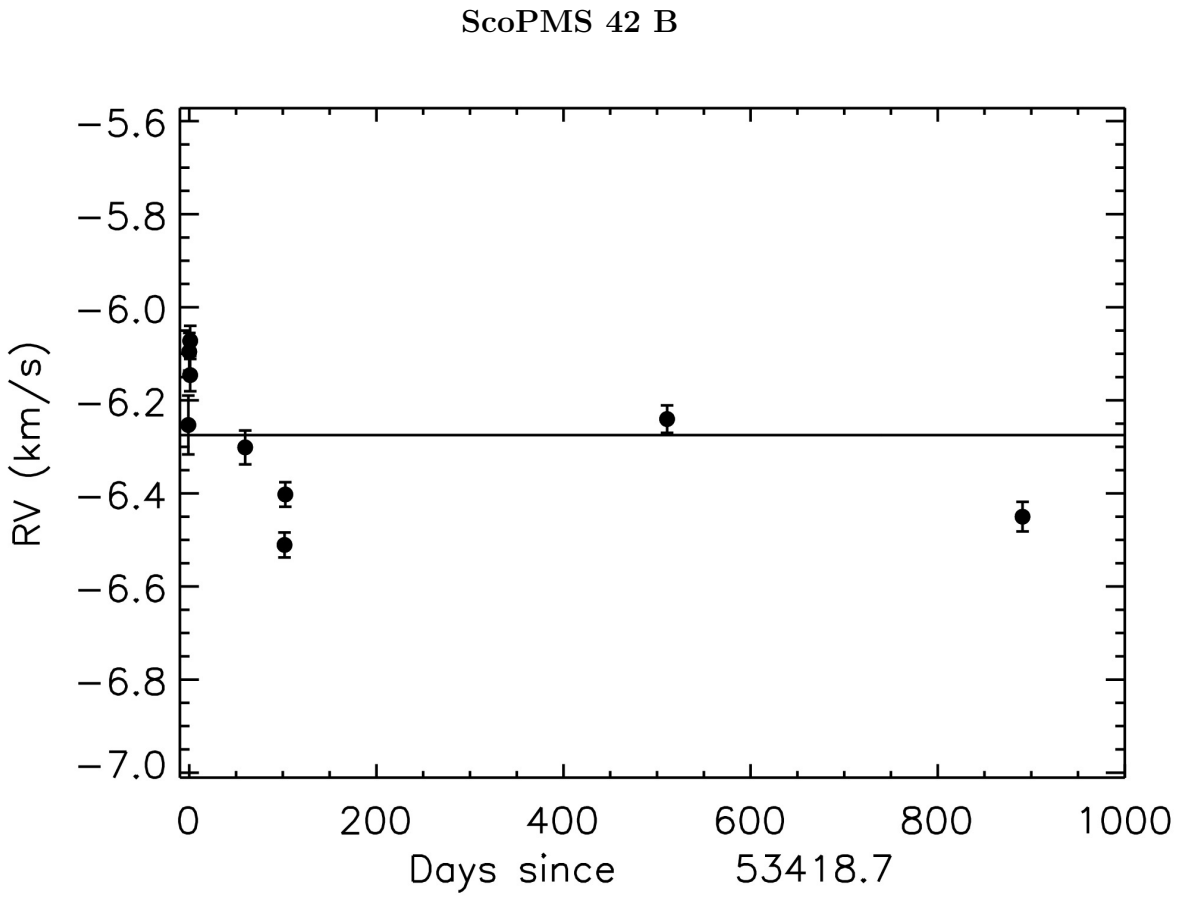

Figure 66 The RV curve is plotted with epoch errors for each observing day.

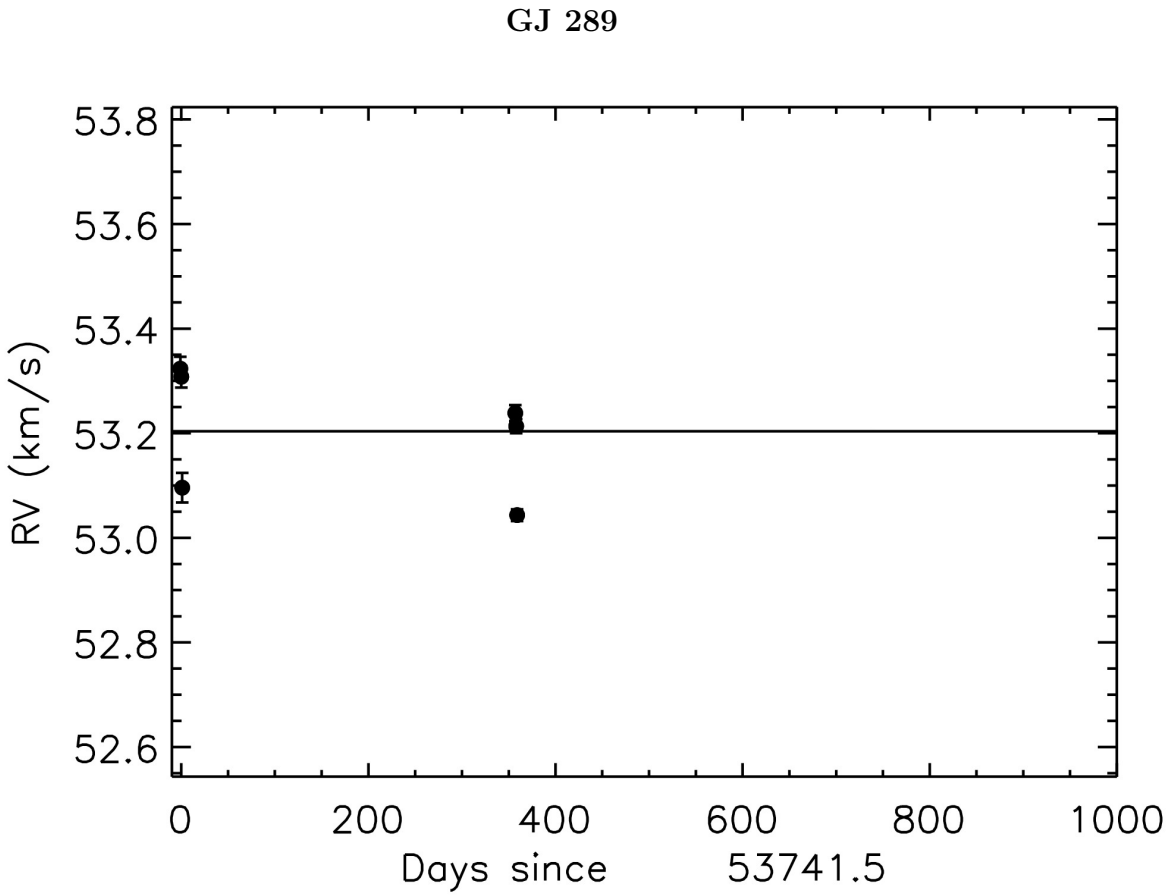

Figure 67 The RV curve is plotted with epoch errors for each observing day.

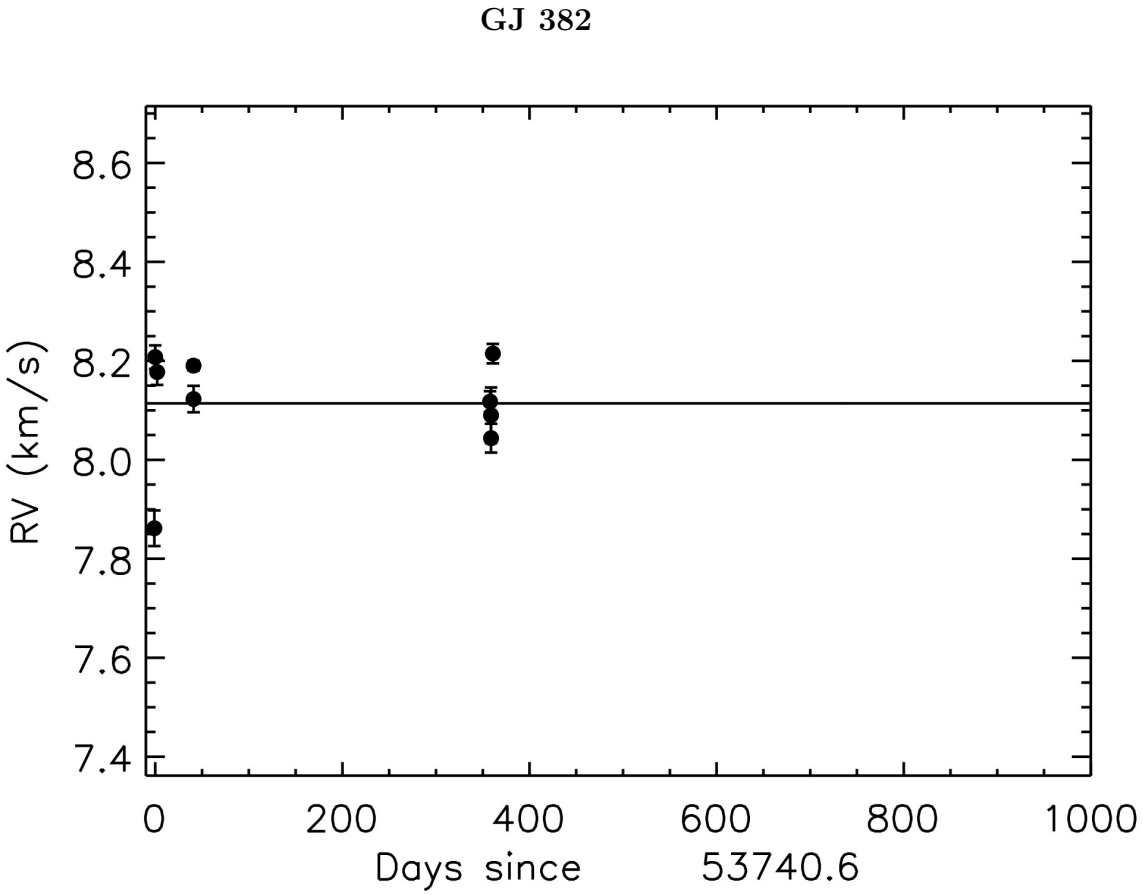

Figure 68 The RV curve is plotted with epoch errors for each observing day.

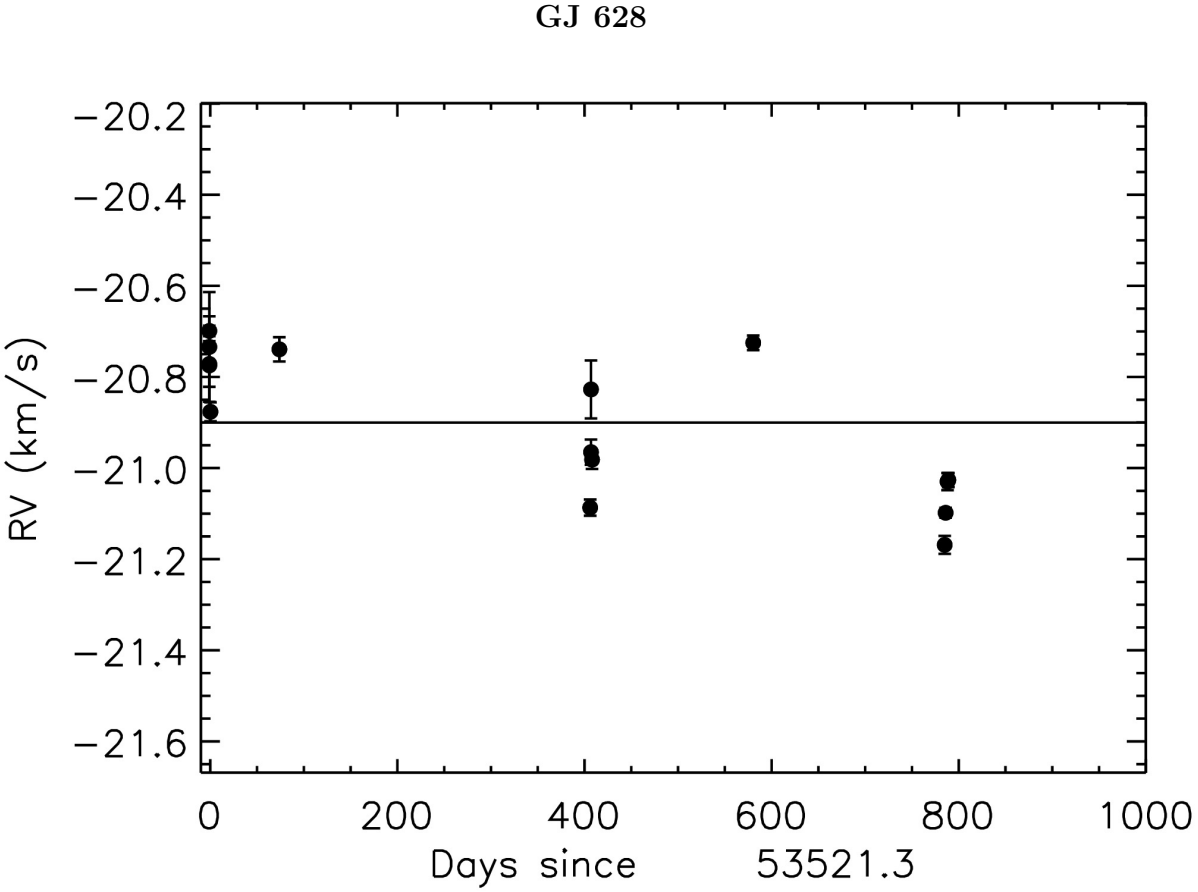

Figure 69 The RV curve is plotted with epoch errors for each observing day.

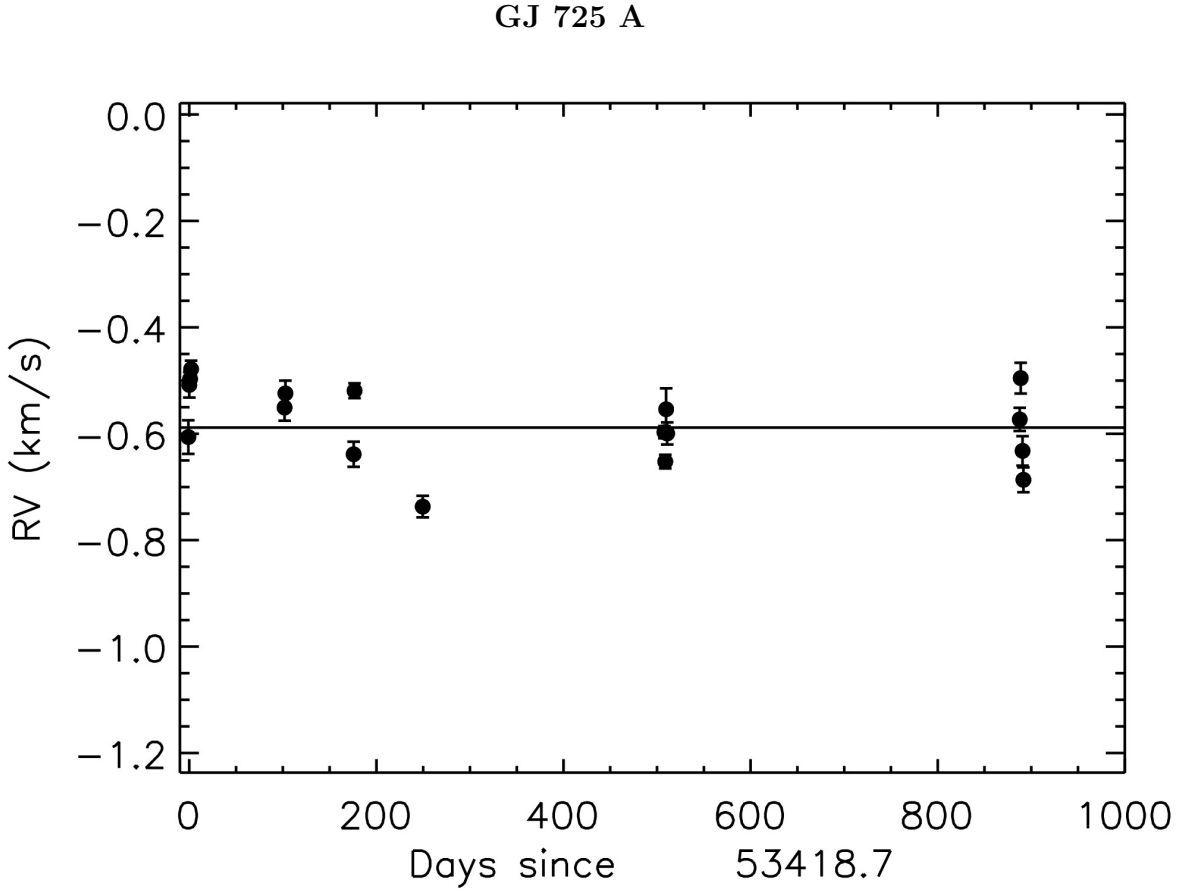

Figure 70 The RV curve is plotted with epoch errors for each observing day.

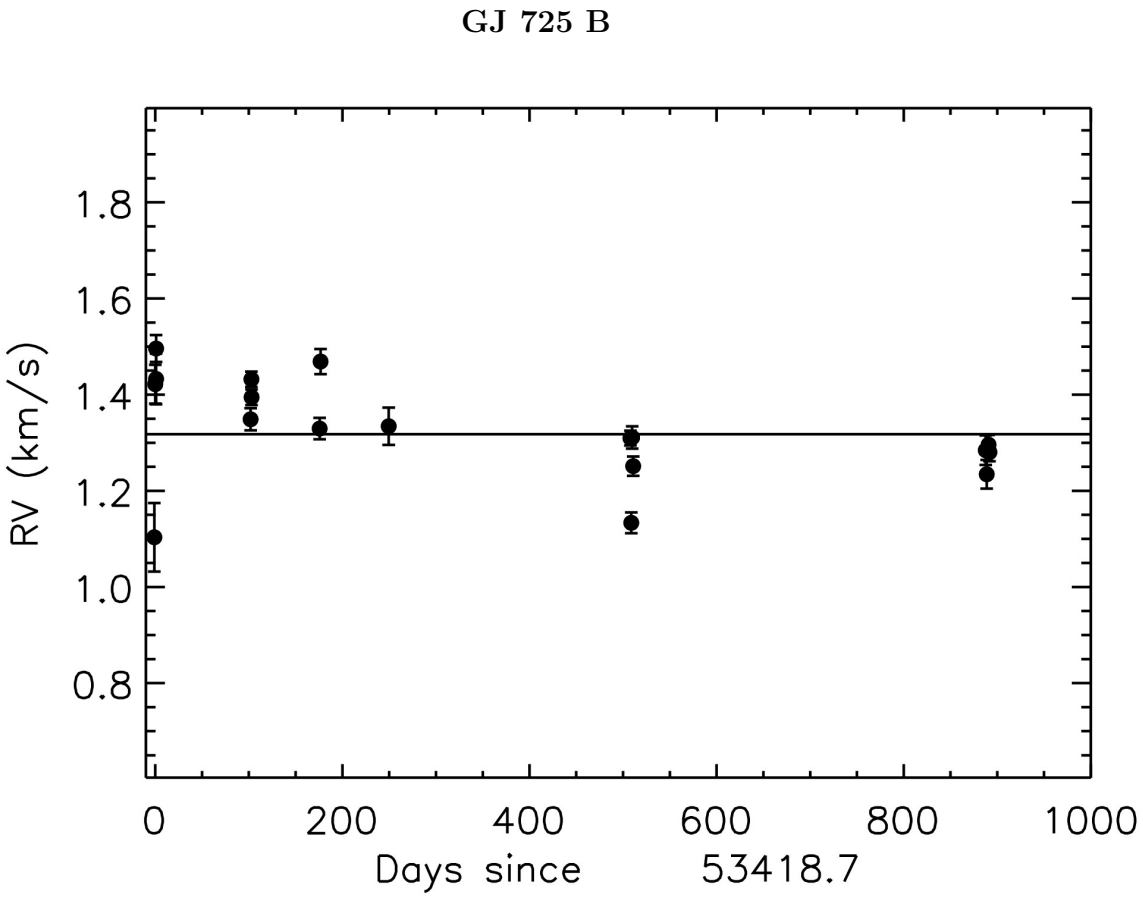

Figure 71 The RV curve is plotted with epoch errors for each observing day.

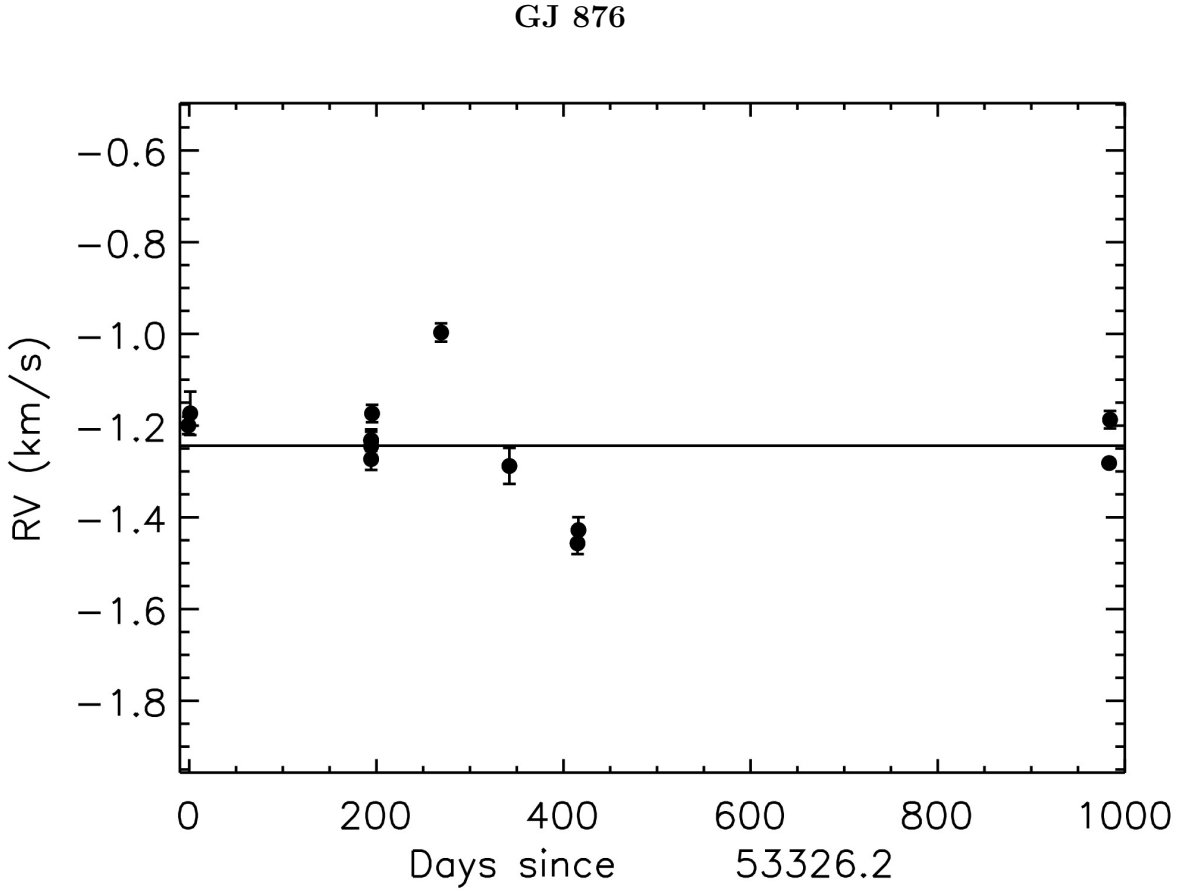

Figure 72 The RV curve is plotted with epoch errors for each observing day.

B Detection Limits

A Gemini South Phoenix

A.1 Young Stars – Gemini Phoenix

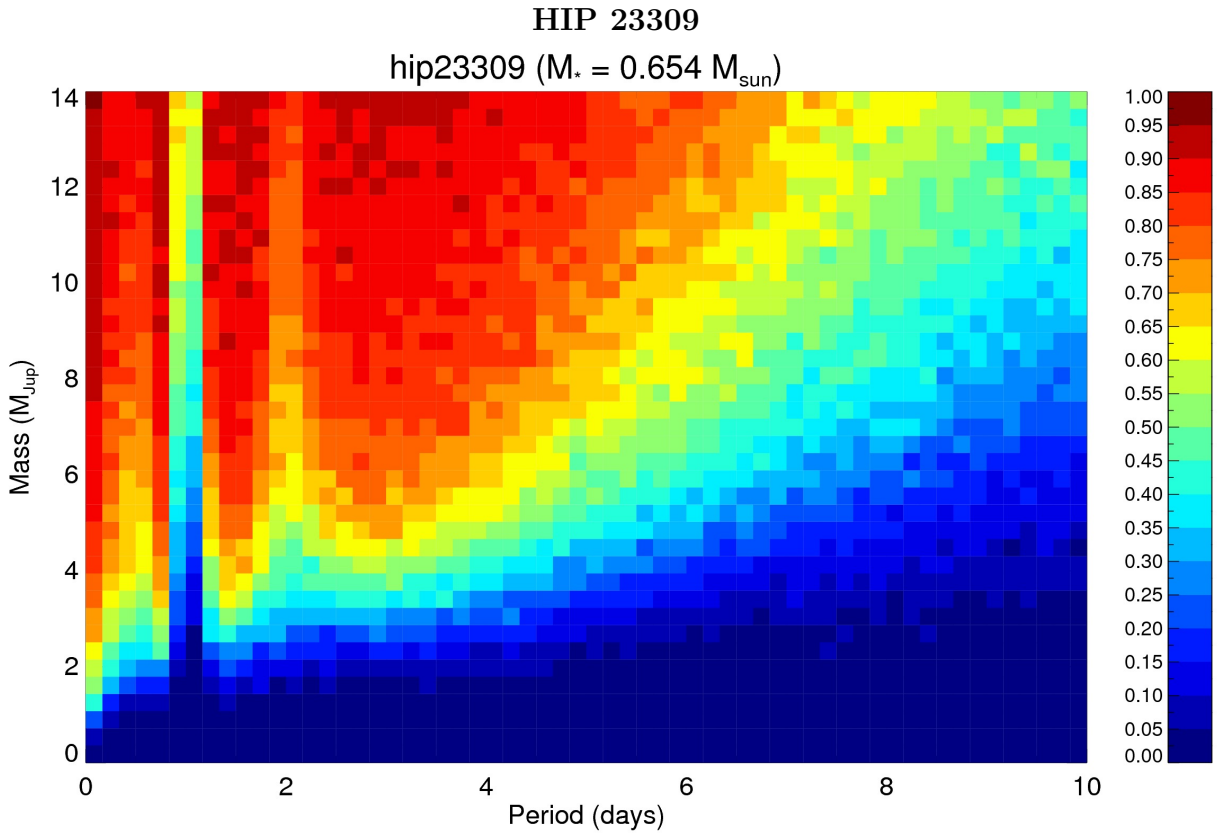

Figure 73 The detection limits are plotted for simulated planets from 0-14 M_{Jup} in 0-10 day orbital periods, with blue (0%) to maroon (100%).

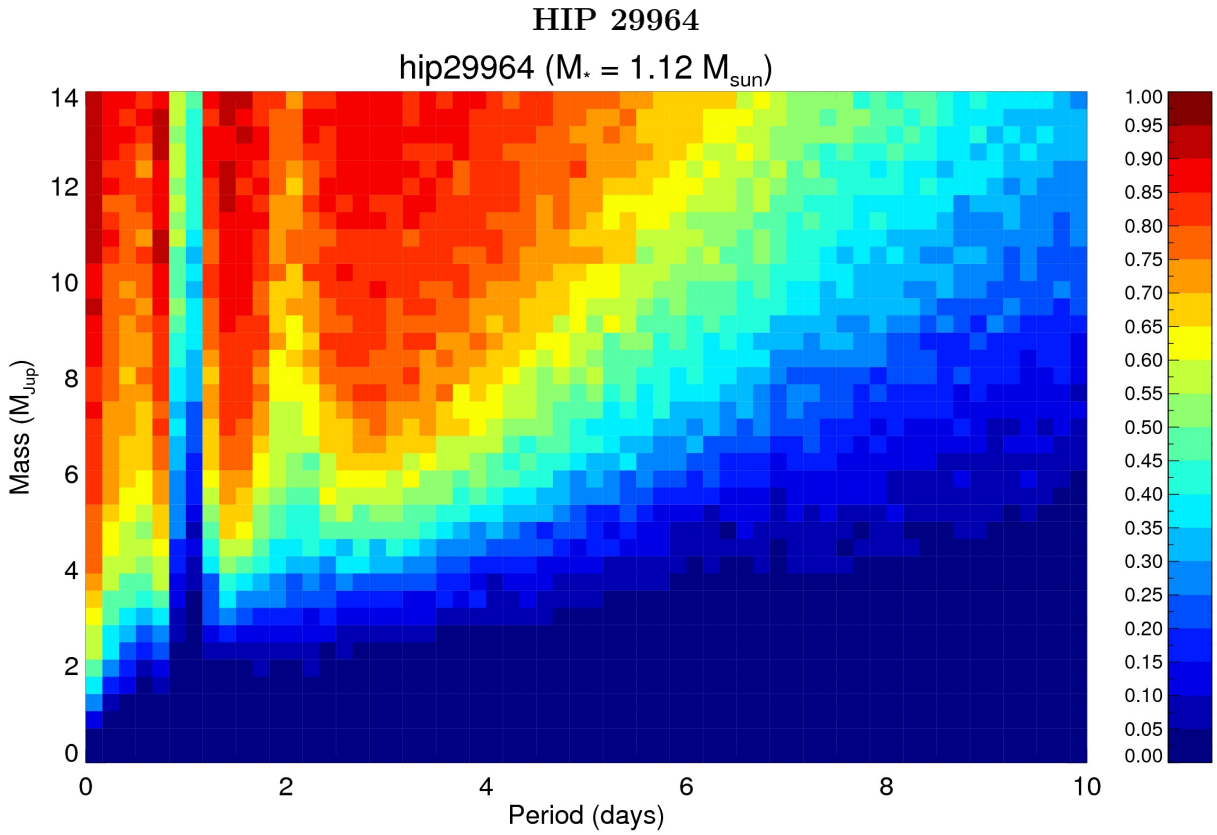

Figure 74 The detection limits are plotted for simulated planets from 0-14 M_{Jup} in 0-10 day orbital periods, with blue (0%) to maroon (100%).

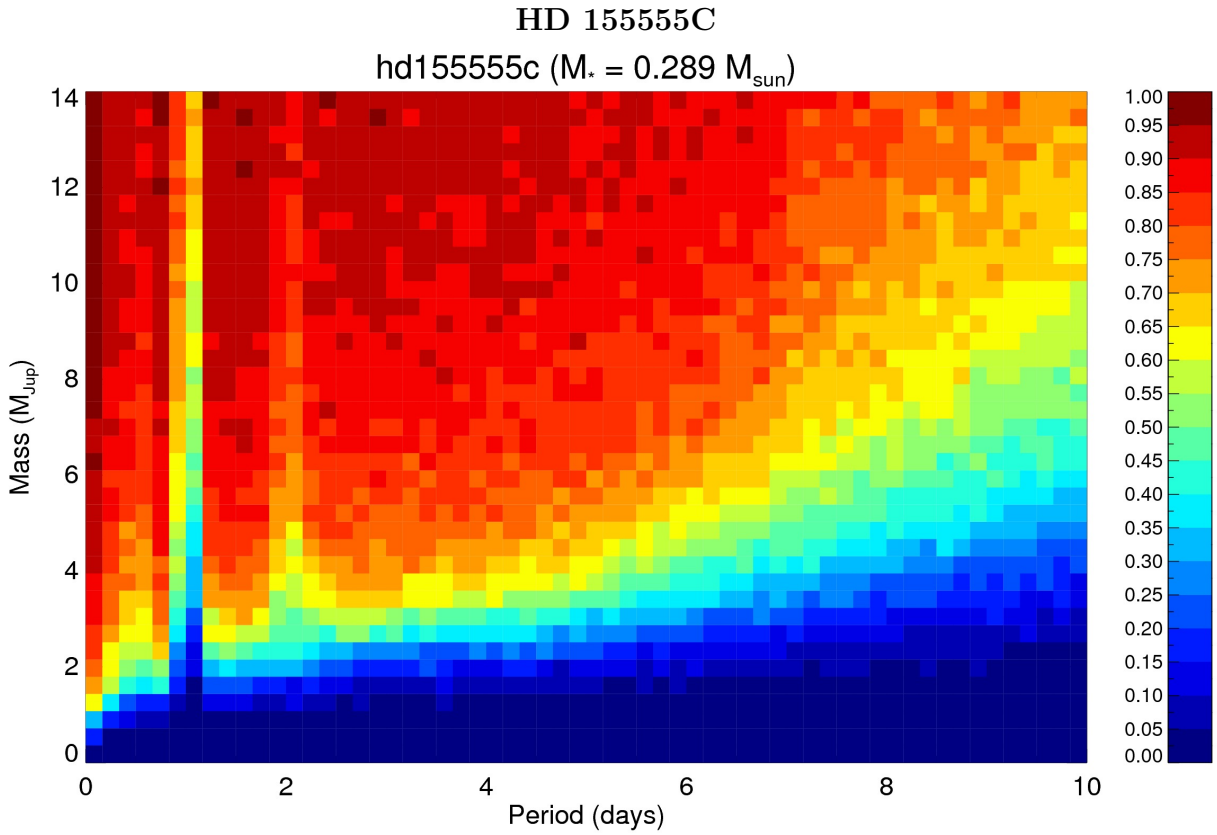

Figure 75 The detection limits are plotted for simulated planets from 0-14 M_{Jup} in 0-10 day orbital periods, with blue (0%) to maroon (100%).

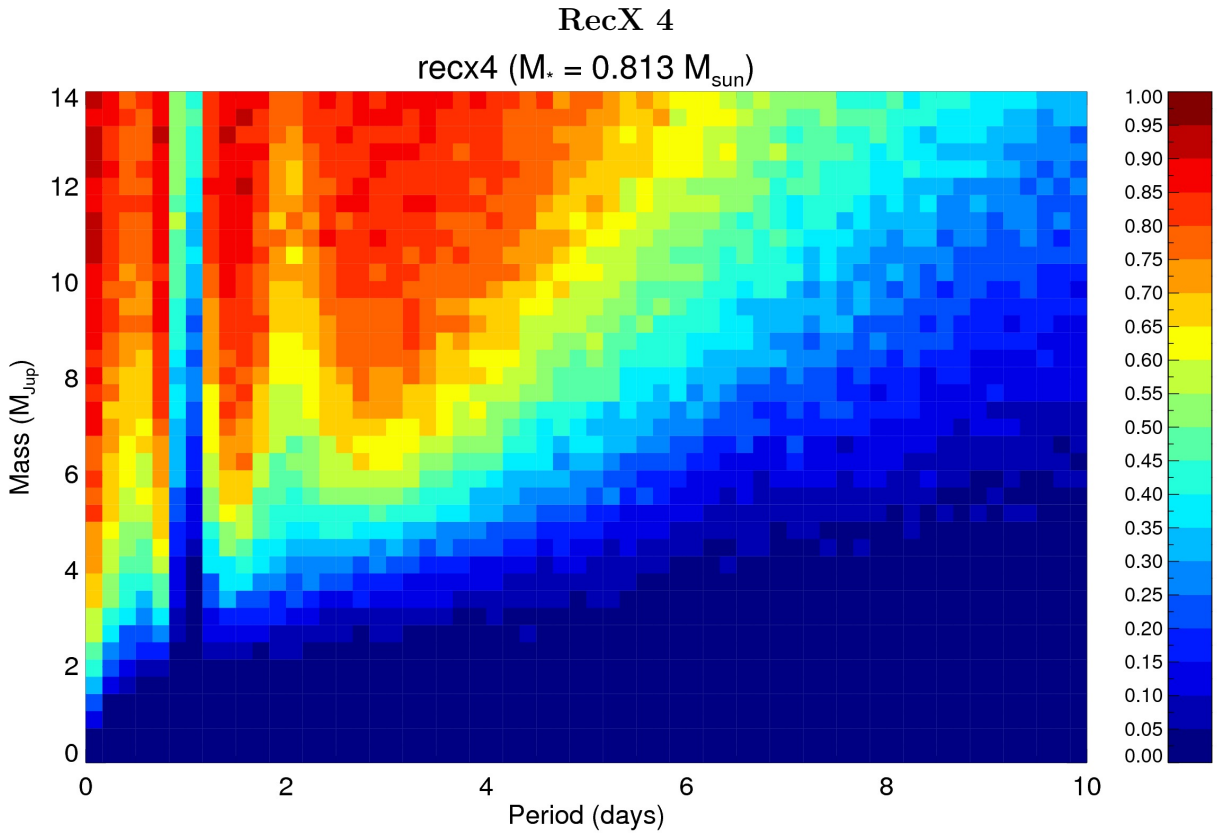

Figure 76 The detection limits are plotted for simulated planets from 0-14 M_{Jup} in 0-10 day orbital periods, with blue (0%) to maroon (100%).

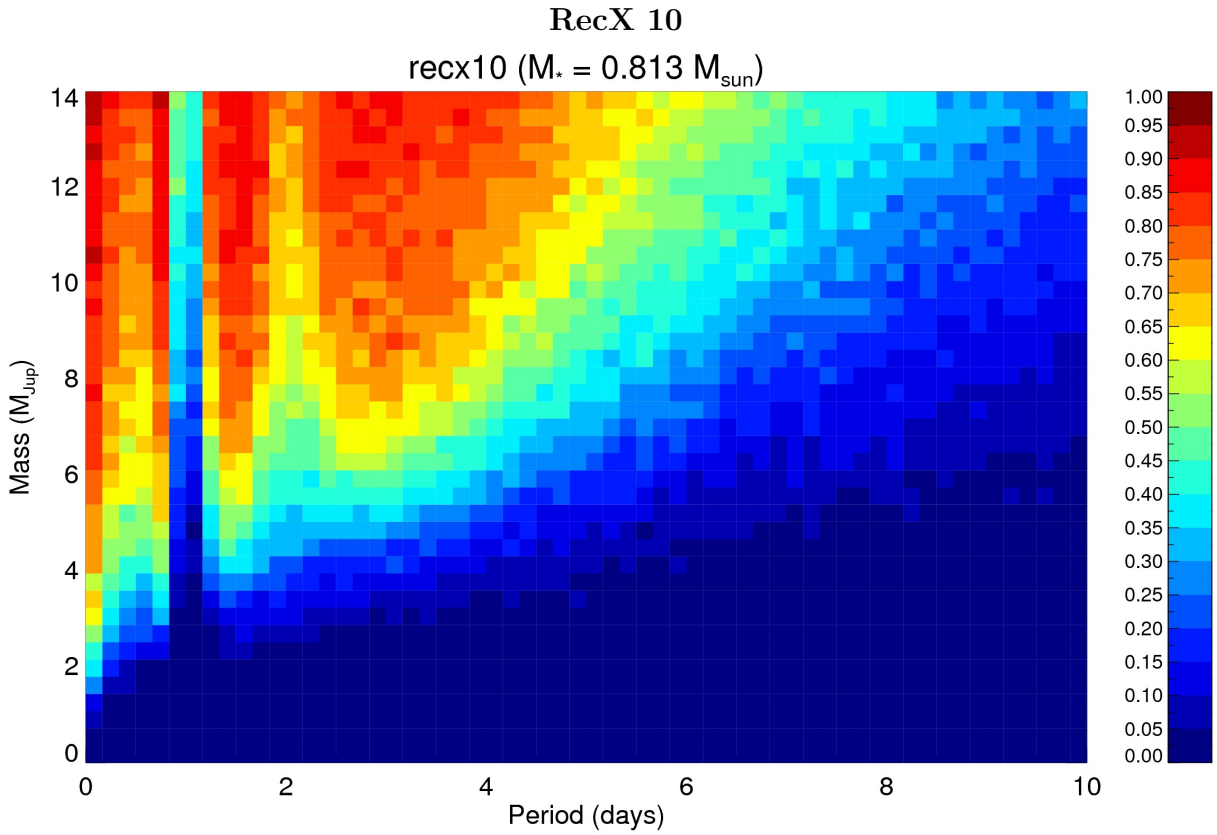

Figure 77 The detection limits are plotted for simulated planets from 0-14 M_{Jup} in 0-10 day orbital periods, with blue (0%) to maroon (100%).

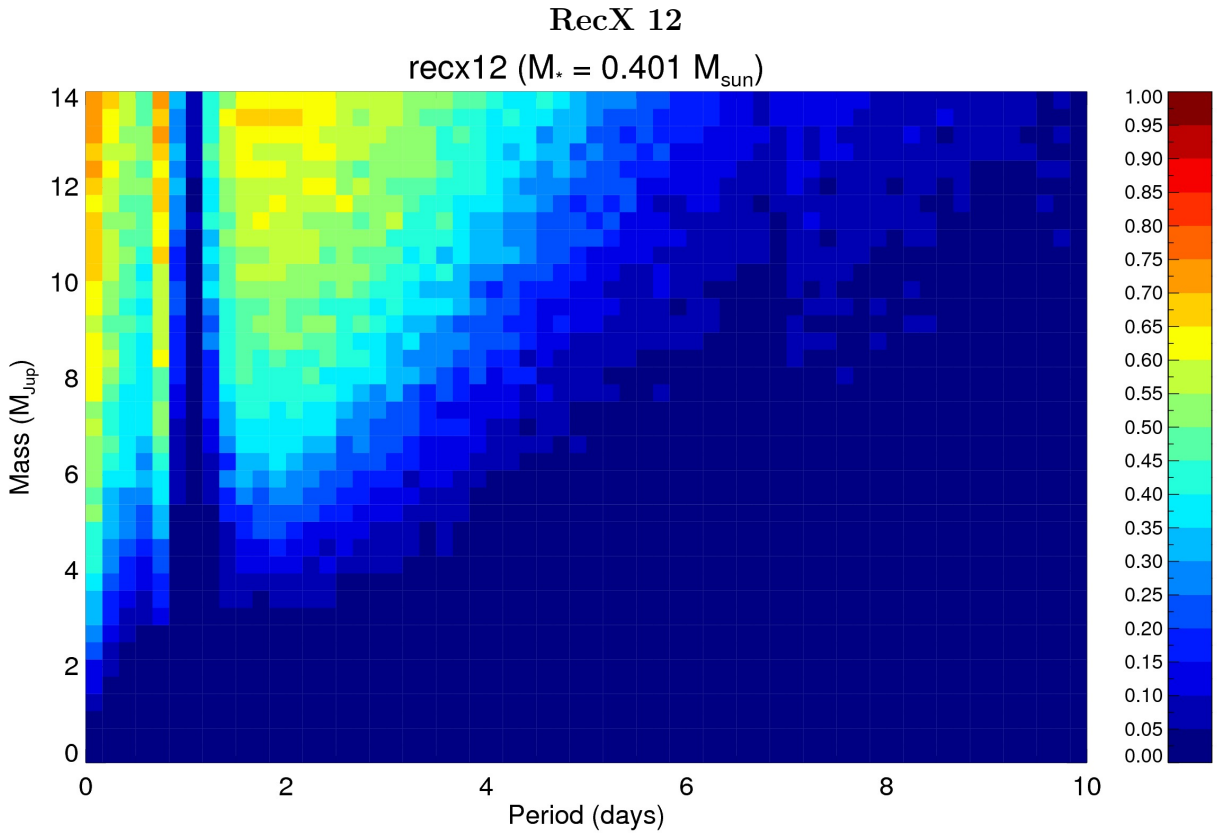

Figure 78 The detection limits are plotted for simulated planets from 0-14 M_{Jup} in 0-10 day orbital periods, with blue (0%) to maroon (100%).

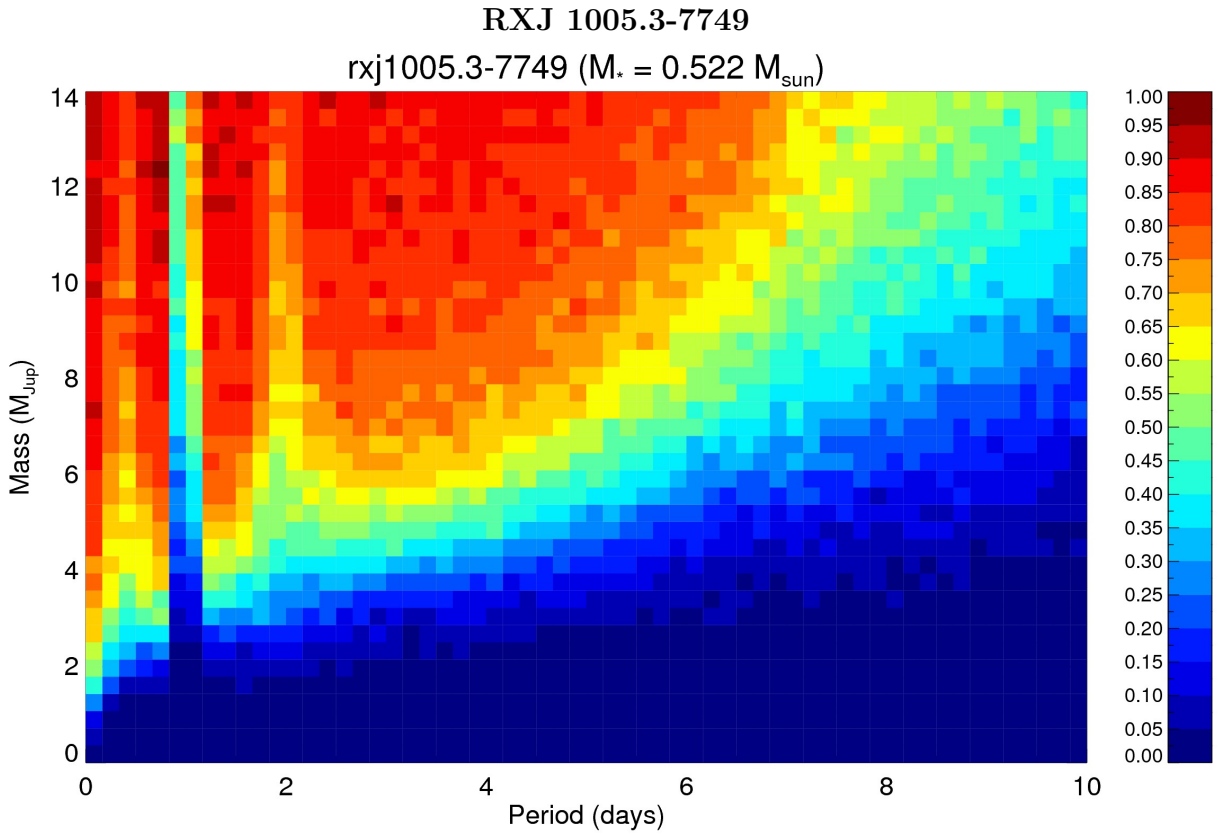

Figure 79 The detection limits are plotted for simulated planets from 0-14 M_{Jup} in 0-10 day orbital periods, with blue (0%) to maroon (100%).

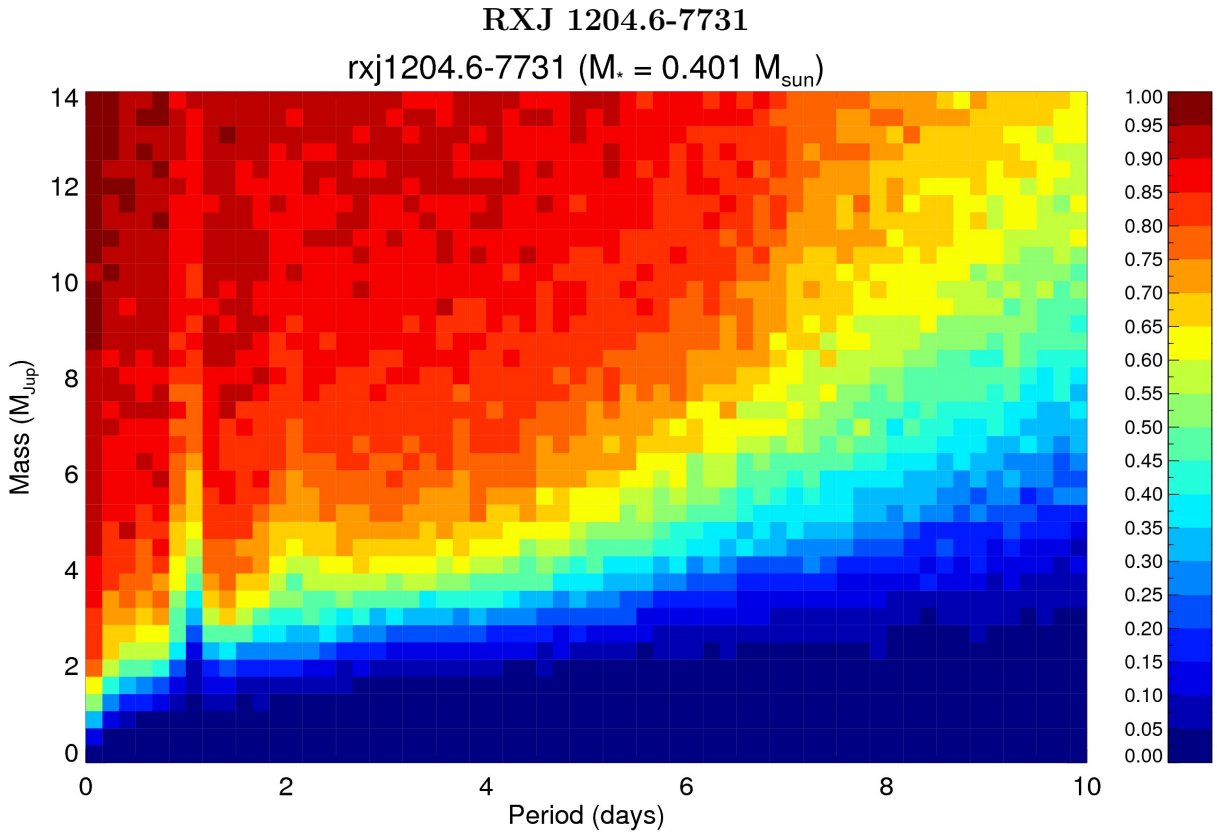

Figure 80 The detection limits are plotted for simulated planets from 0-14 M_{Jup} in 0-10 day orbital periods, with blue (0%) to maroon (100%).

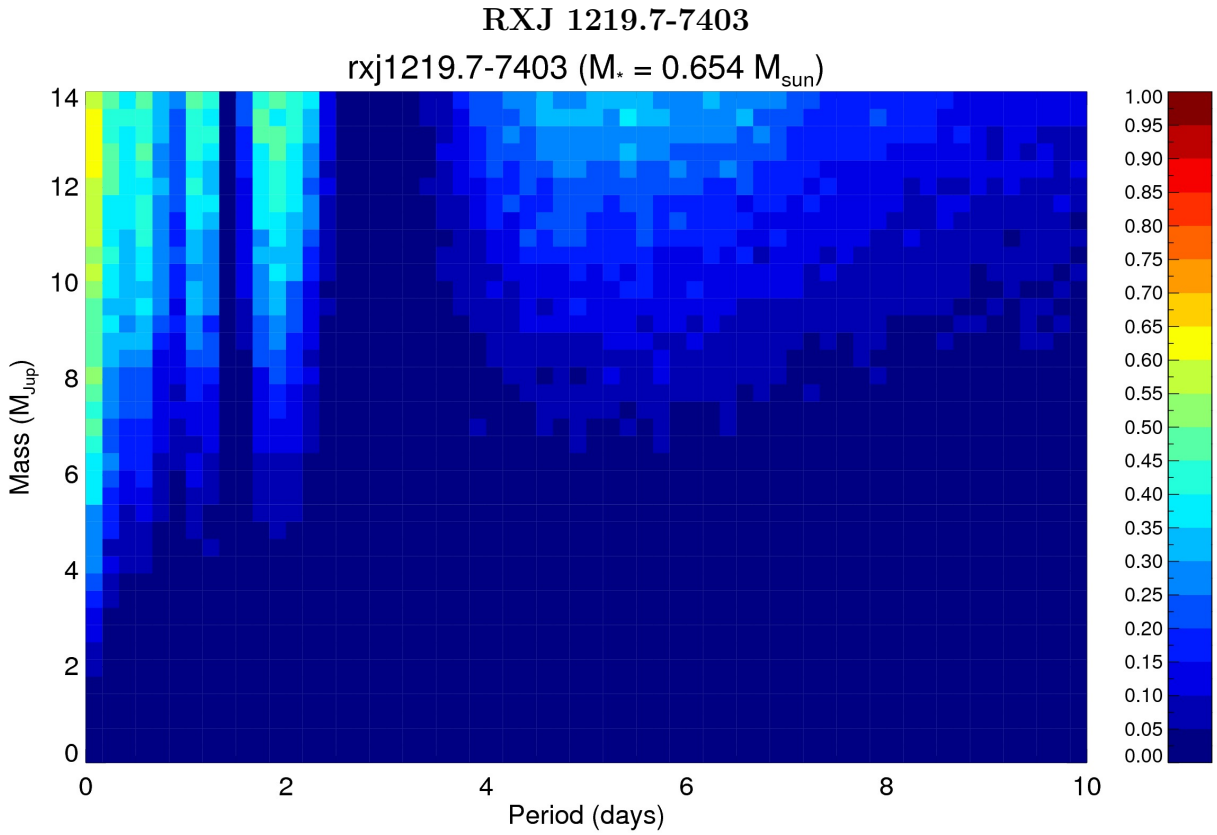

Figure 81 The detection limits are plotted for simulated planets from 0-14 M_{Jup} in 0-10 day orbital periods, with blue (0%) to maroon (100%).

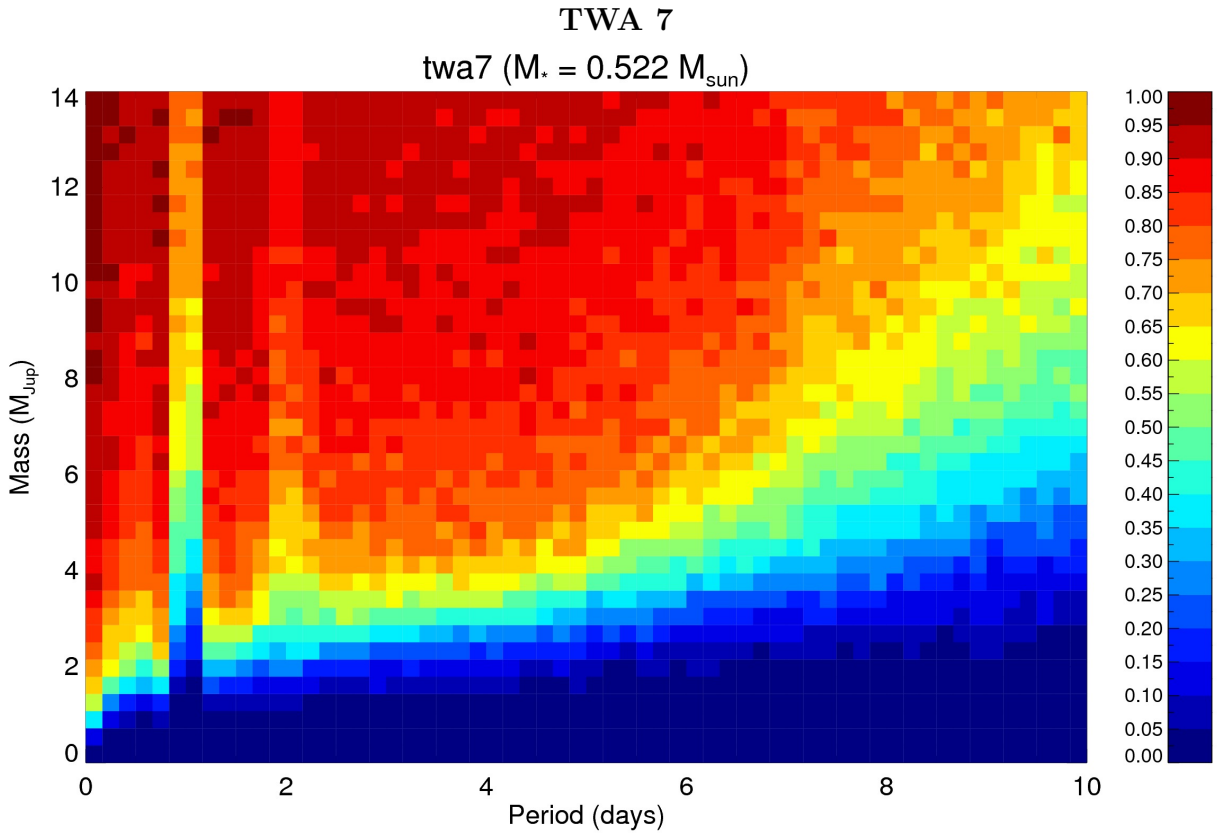

Figure 82 The detection limits are plotted for simulated planets from 0-14 M_{Jup} in 0-10 day orbital periods, with blue (0%) to maroon (100%).

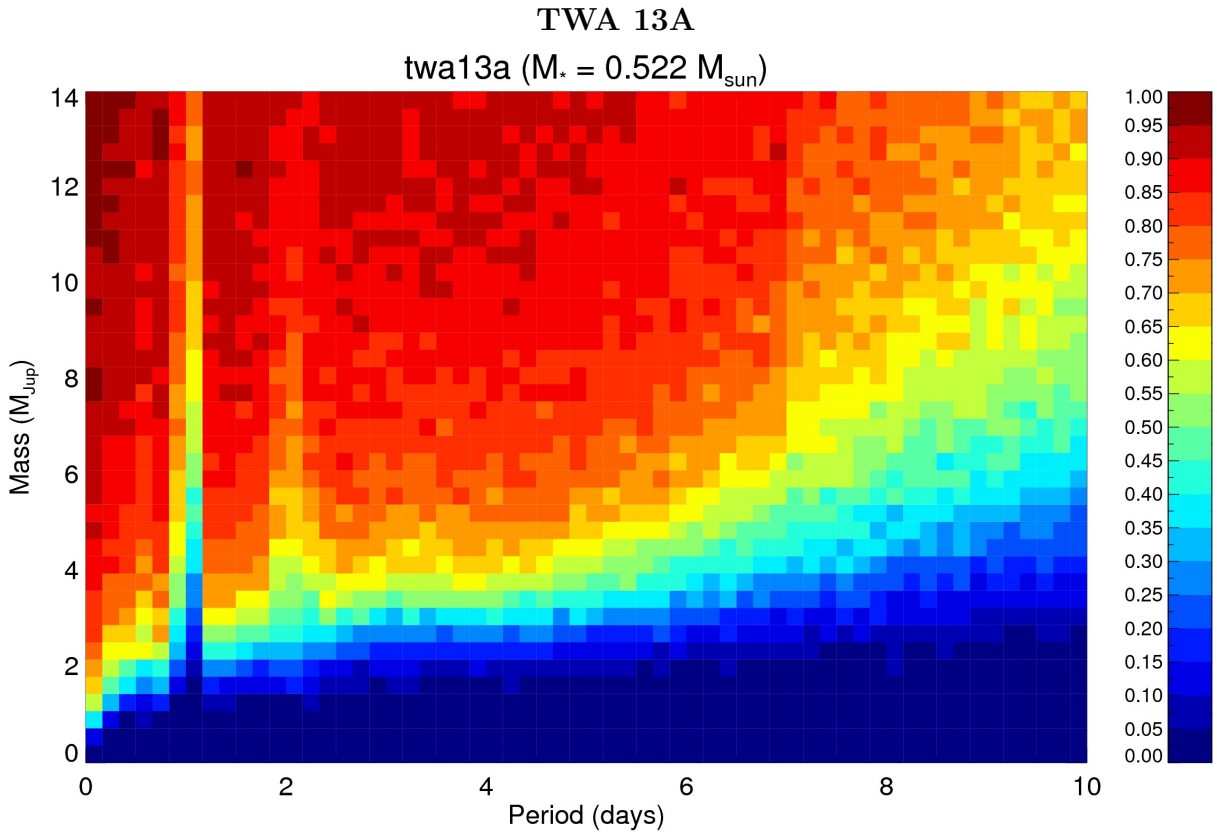

Figure 83 The detection limits are plotted for simulated planets from 0-14 M_{Jup} in 0-10 day orbital periods, with blue (0%) to maroon (100%).

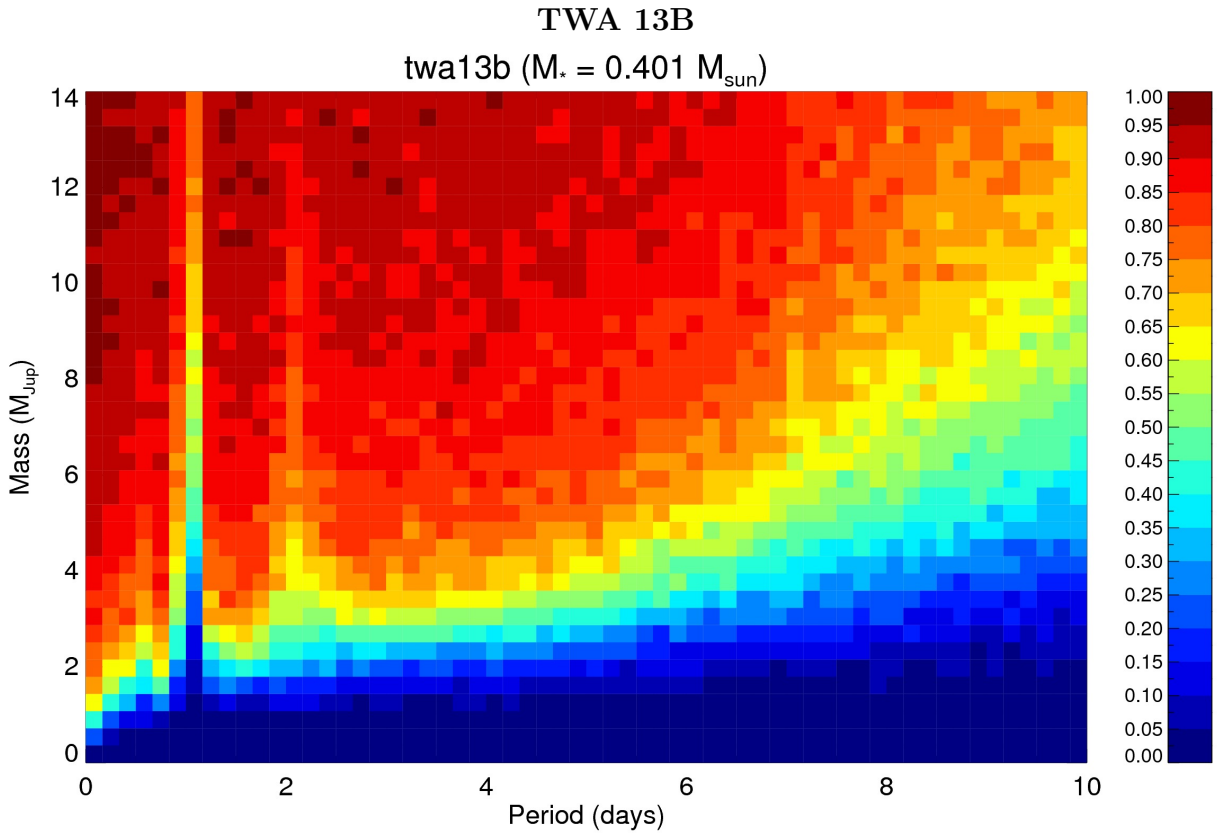

Figure 84 The detection limits are plotted for simulated planets from 0-14 M_{Jup} in 0-10 day orbital periods, with blue (0%) to maroon (100%).

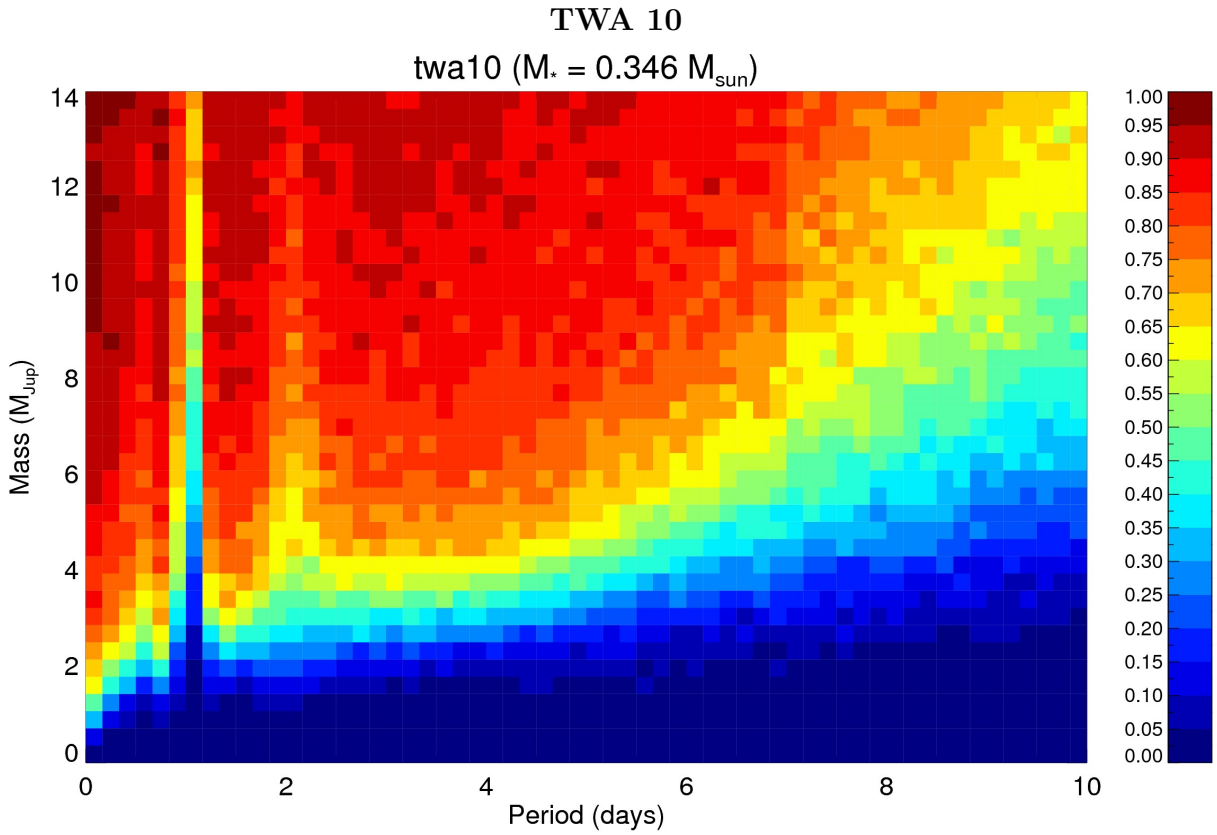

Figure 85 The detection limits are plotted for simulated planets from 0-14 M_{Jup} in 0-10 day orbital periods, with blue (0%) to maroon (100%).

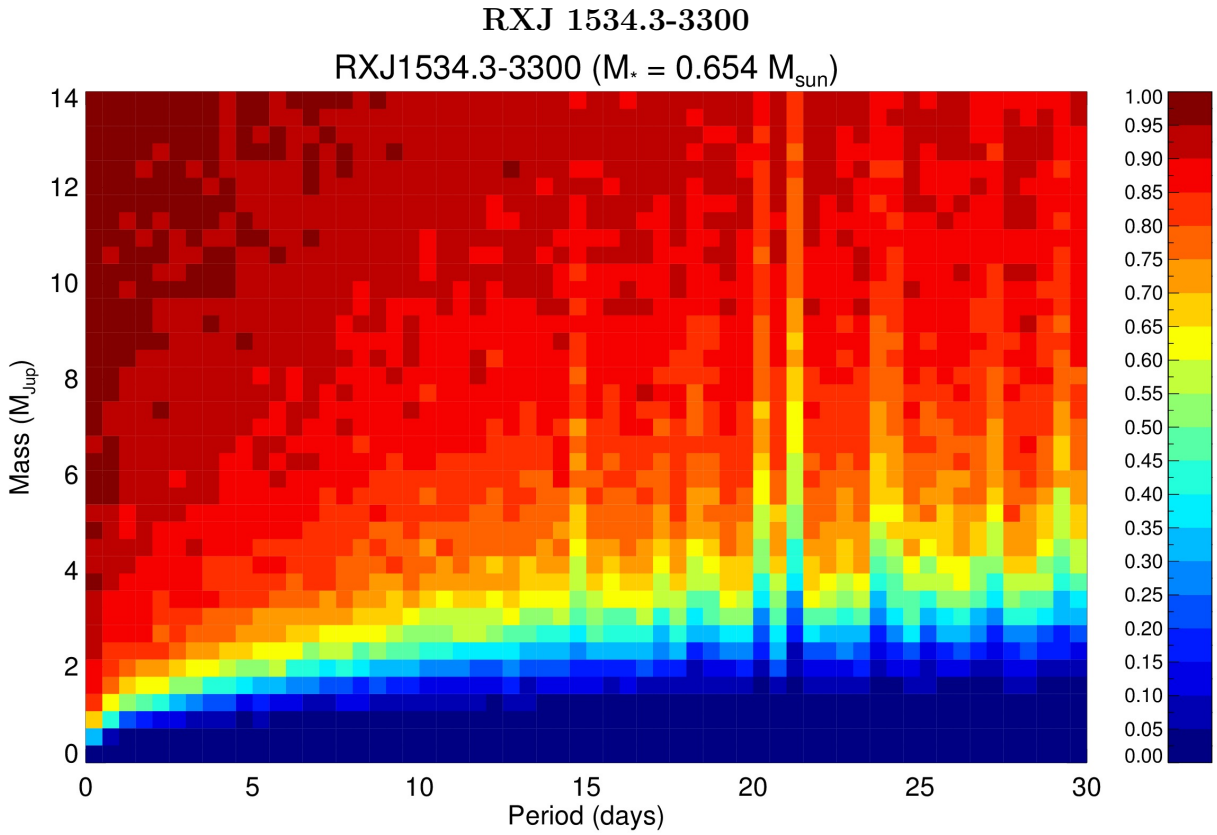

Figure 86 The detection limits are plotted for simulated planets from 0-14 M_{Jup} in 0-10 day orbital periods, with blue (0%) to maroon (100%).

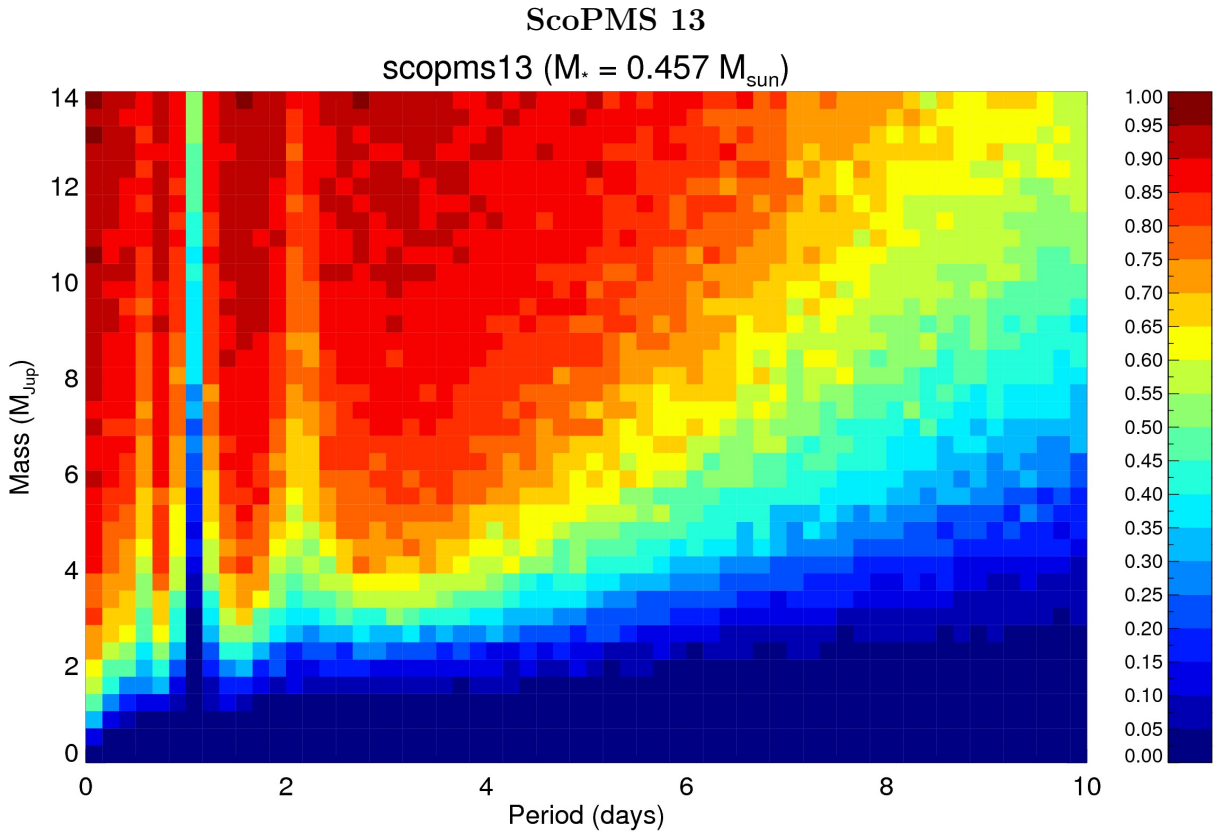

Figure 87 The detection limits are plotted for simulated planets from 0-14 M_{Jup} in 0-10 day orbital periods, with blue (0%) to maroon (100%).

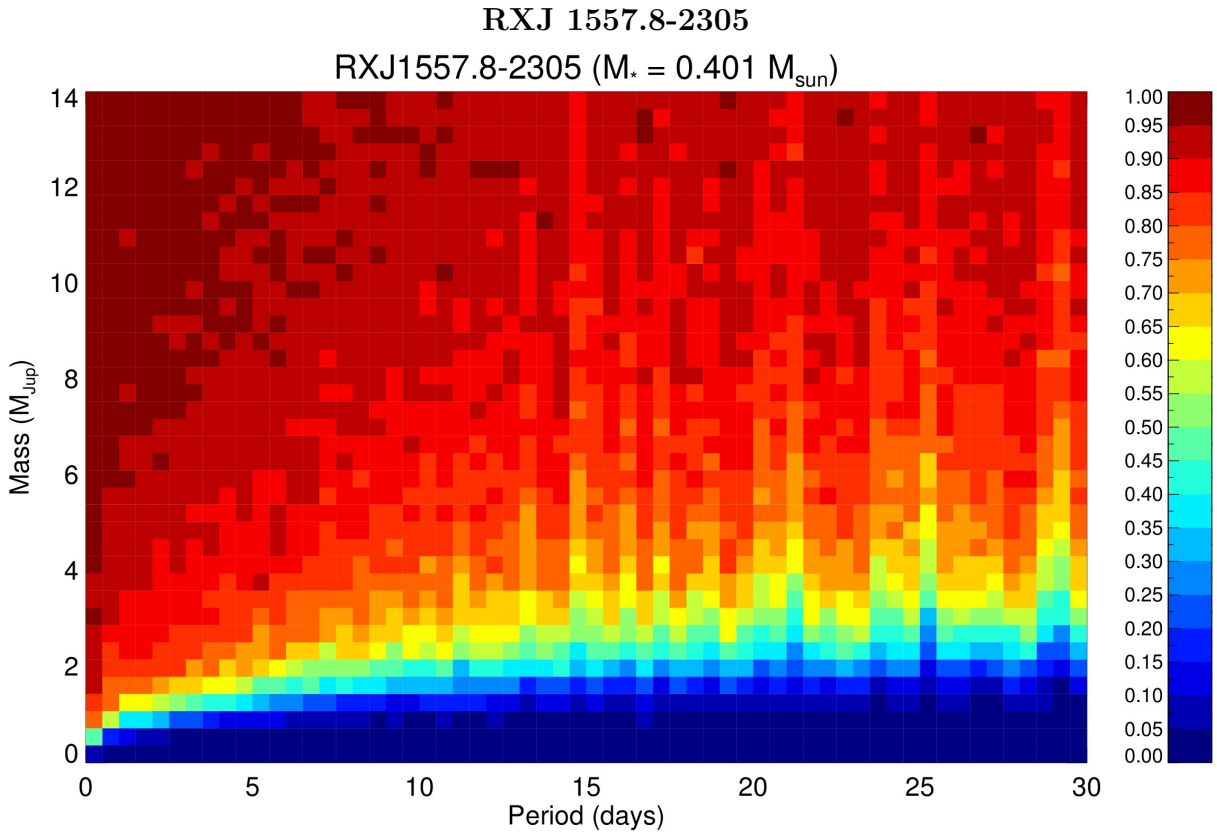

Figure 88 The detection limits are plotted for simulated planets from 0-14 M_{Jup} in 0-10 day orbital periods, with blue (0%) to maroon (100%).

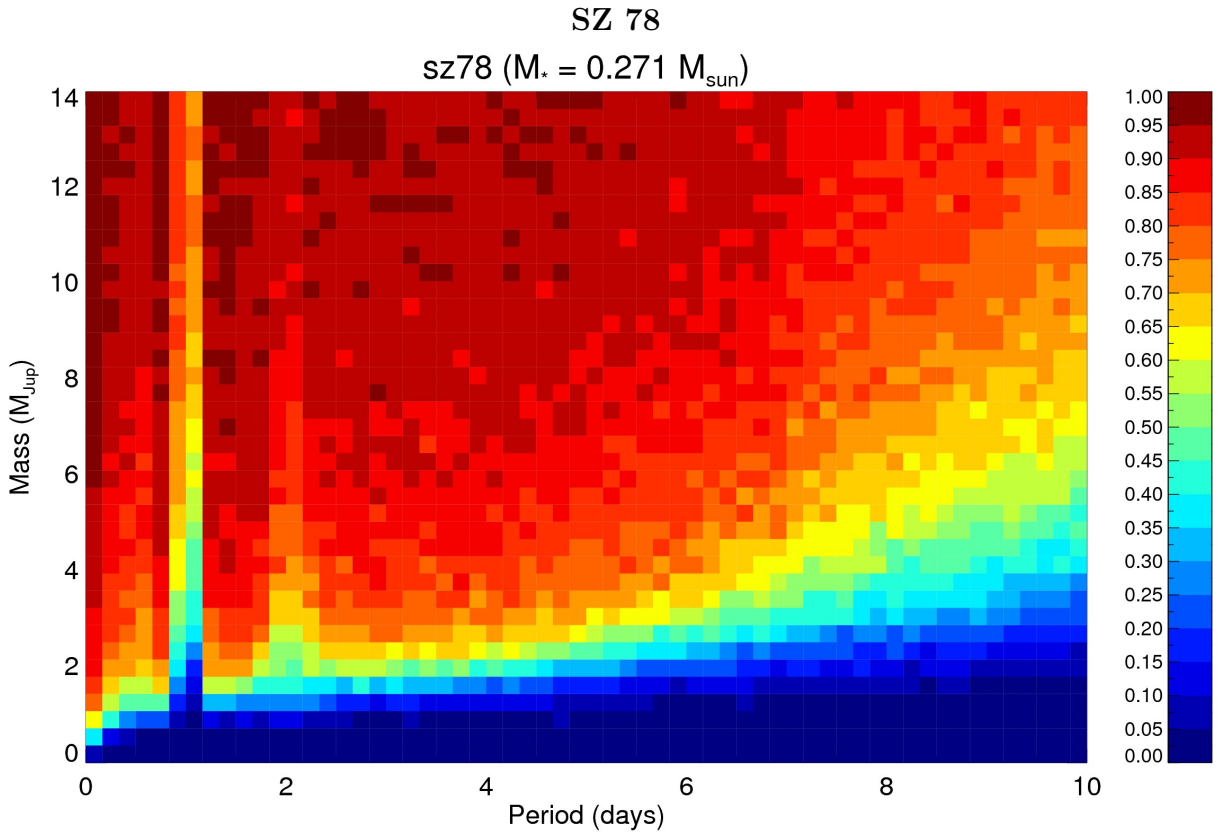

Figure 89 The detection limits are plotted for simulated planets from 0-14 M_{Jup} in 0-10 day orbital periods, with blue (0%) to maroon (100%).

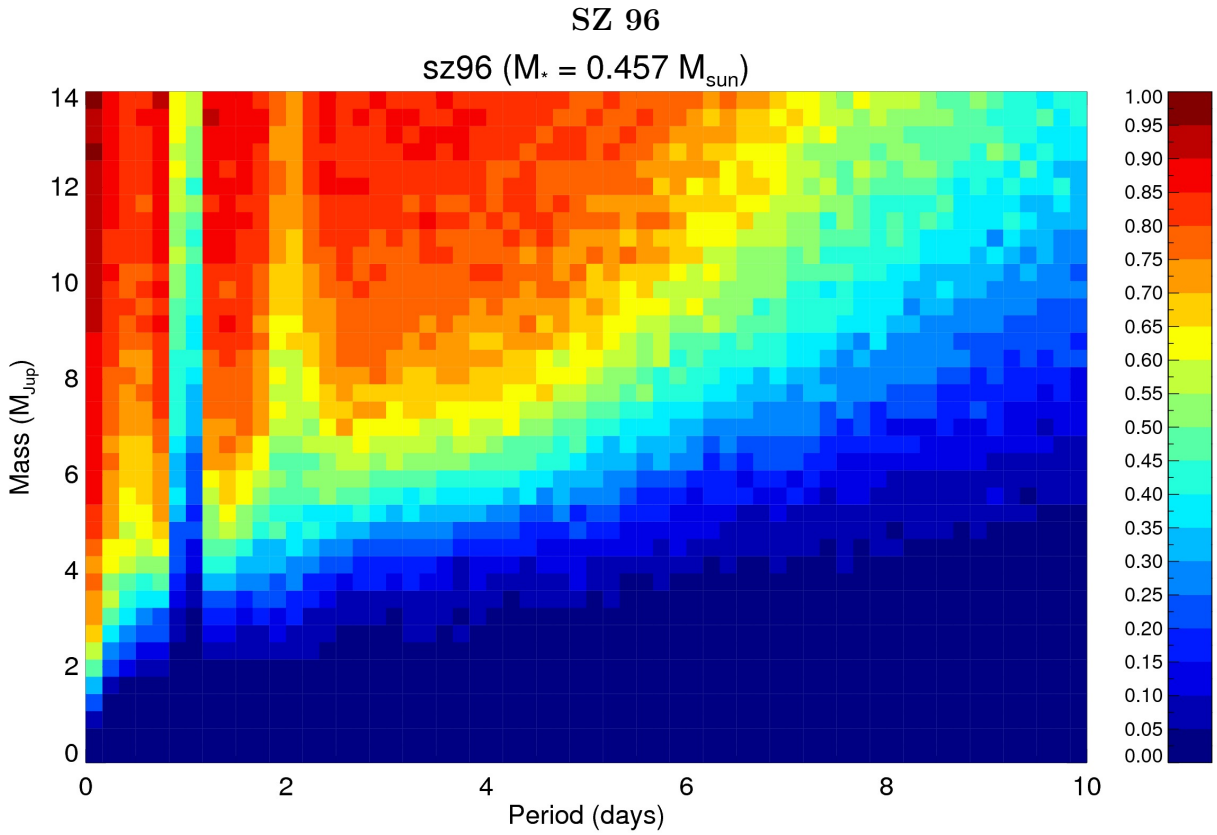

Figure 90 The detection limits are plotted for simulated planets from 0-14 M_{Jup} in 0-10 day orbital periods, with blue (0%) to maroon (100%).

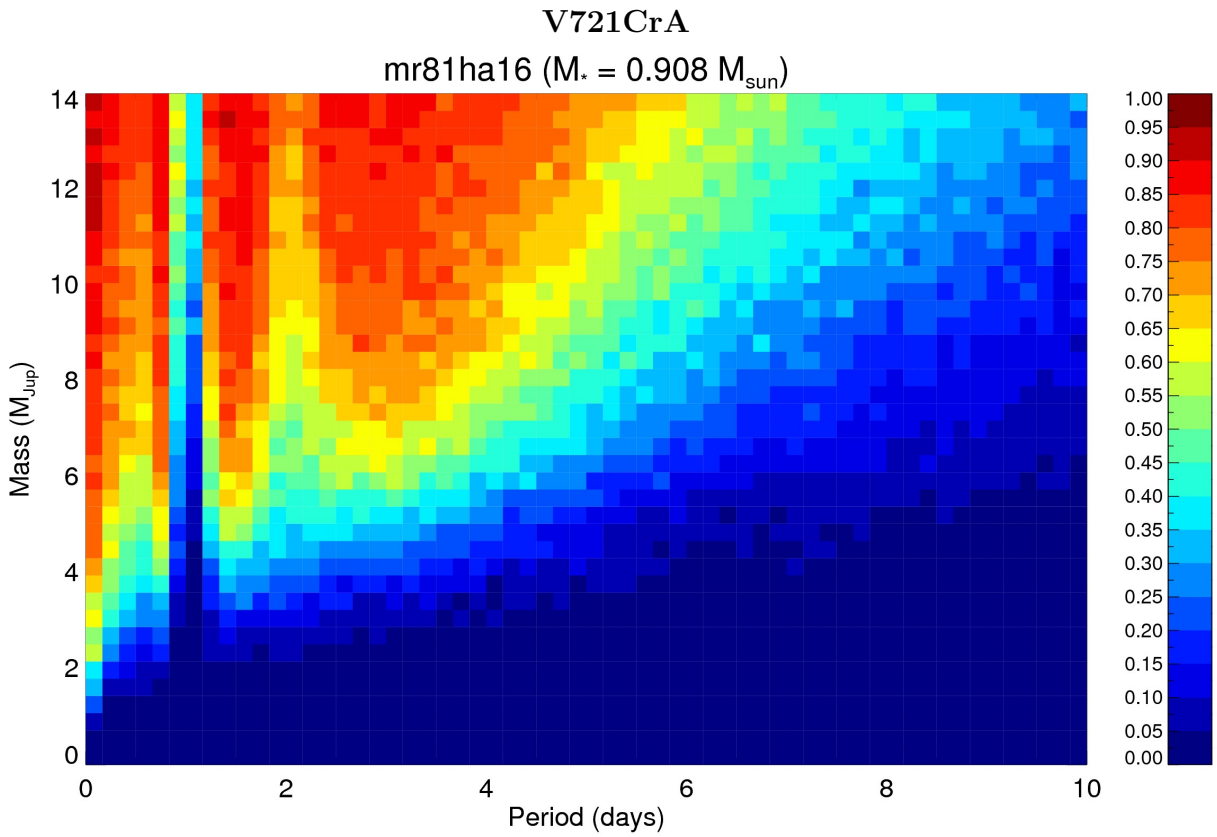

Figure 91 The detection limits are plotted for simulated planets from 0-14 M_{Jup} in 0-10 day orbital periods, with blue (0%) to maroon (100%).

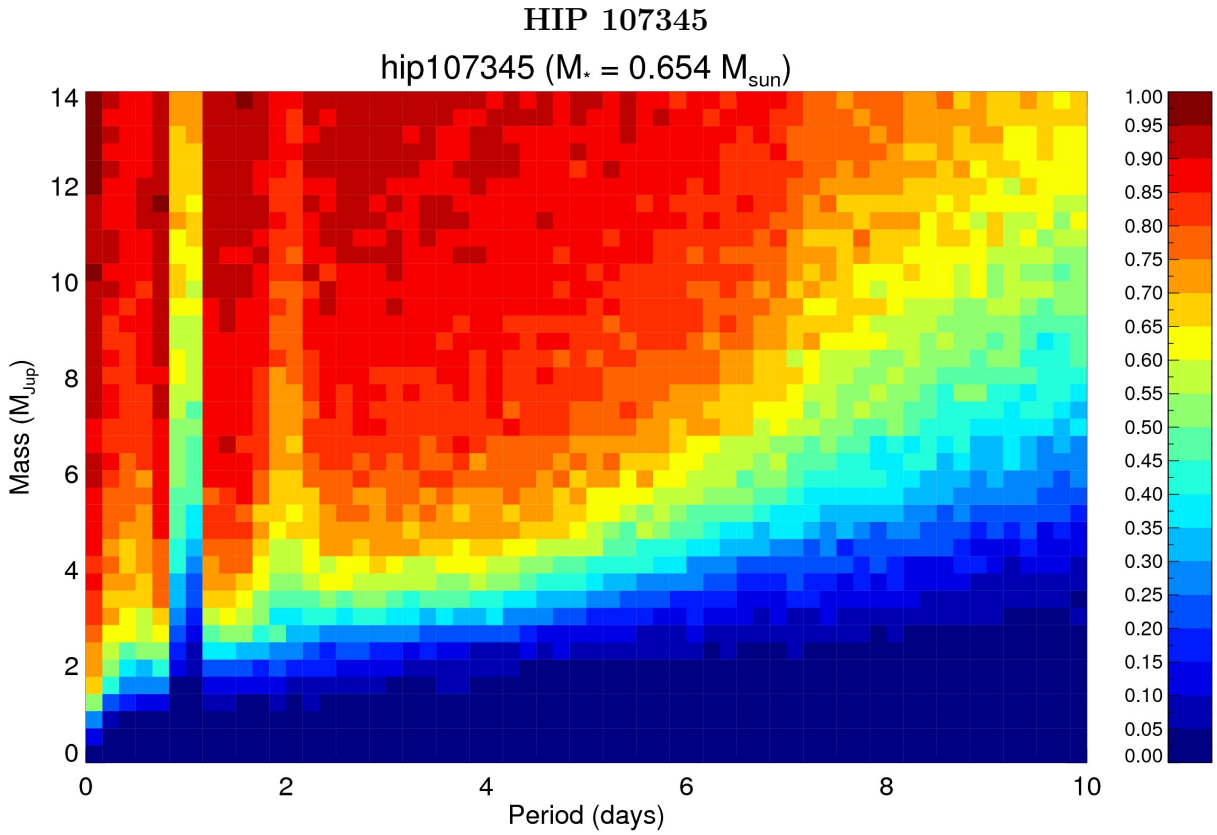

Figure 92 The detection limits are plotted for simulated planets from 0-14 M_{Jup} in 0-10 day orbital periods, with blue (0%) to maroon (100%).

A.2 Radial Velocity Standards – Gemini Phoenix

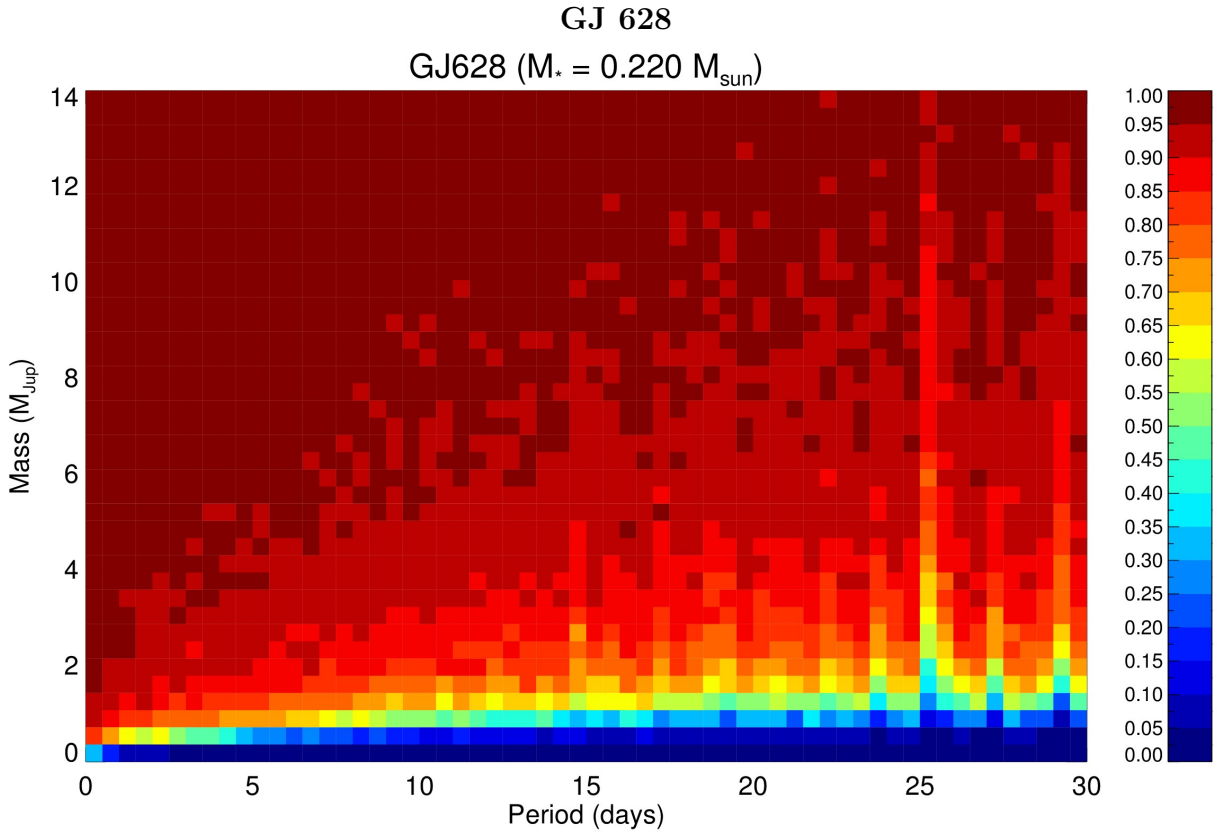

Figure 93 The detection limits are plotted for simulated planets from 0-14 M_{Jup} in 0-10 day orbital periods, with blue (0%) to maroon (100%).

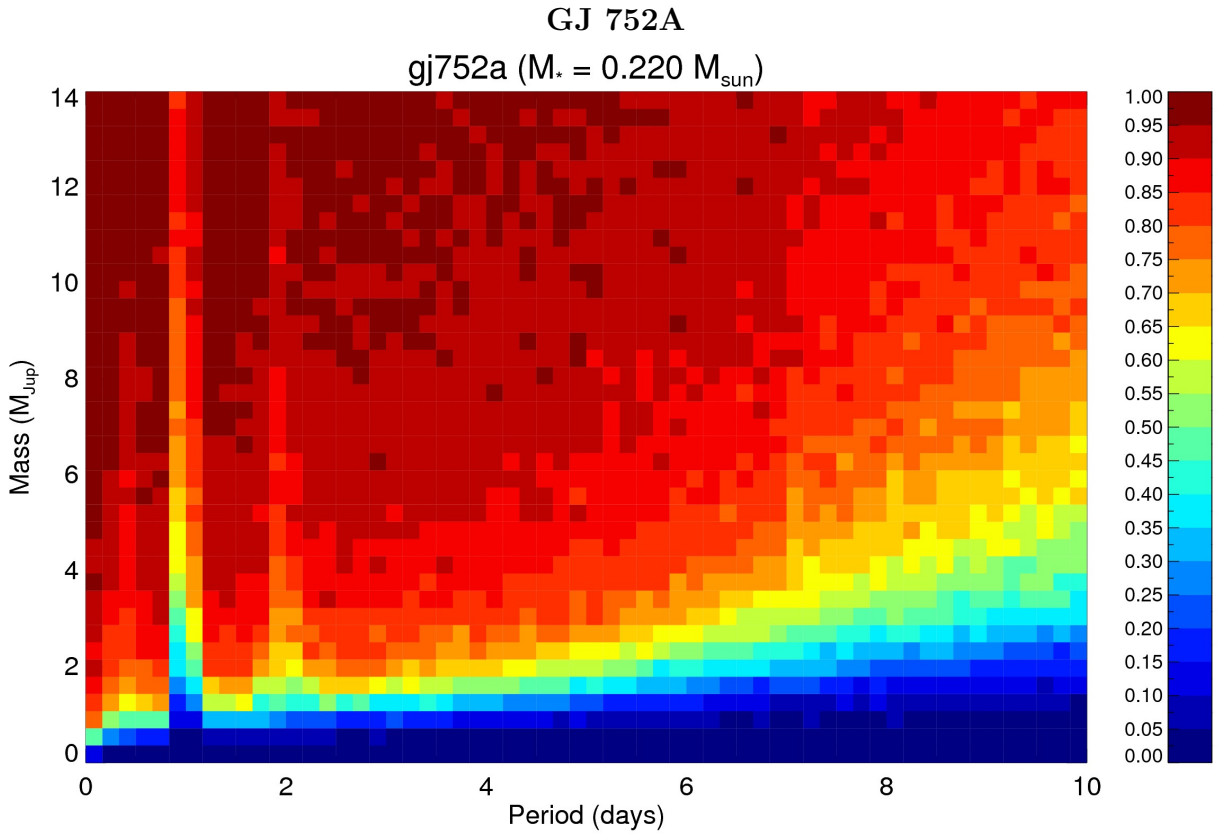

Figure 94 The detection limits are plotted for simulated planets from 0-14 M_{Jup} in 0-10 day orbital periods, with blue (0%) to maroon (100%).

B VLT CRIRES

B.1 Young Stars – VLT CRIRES

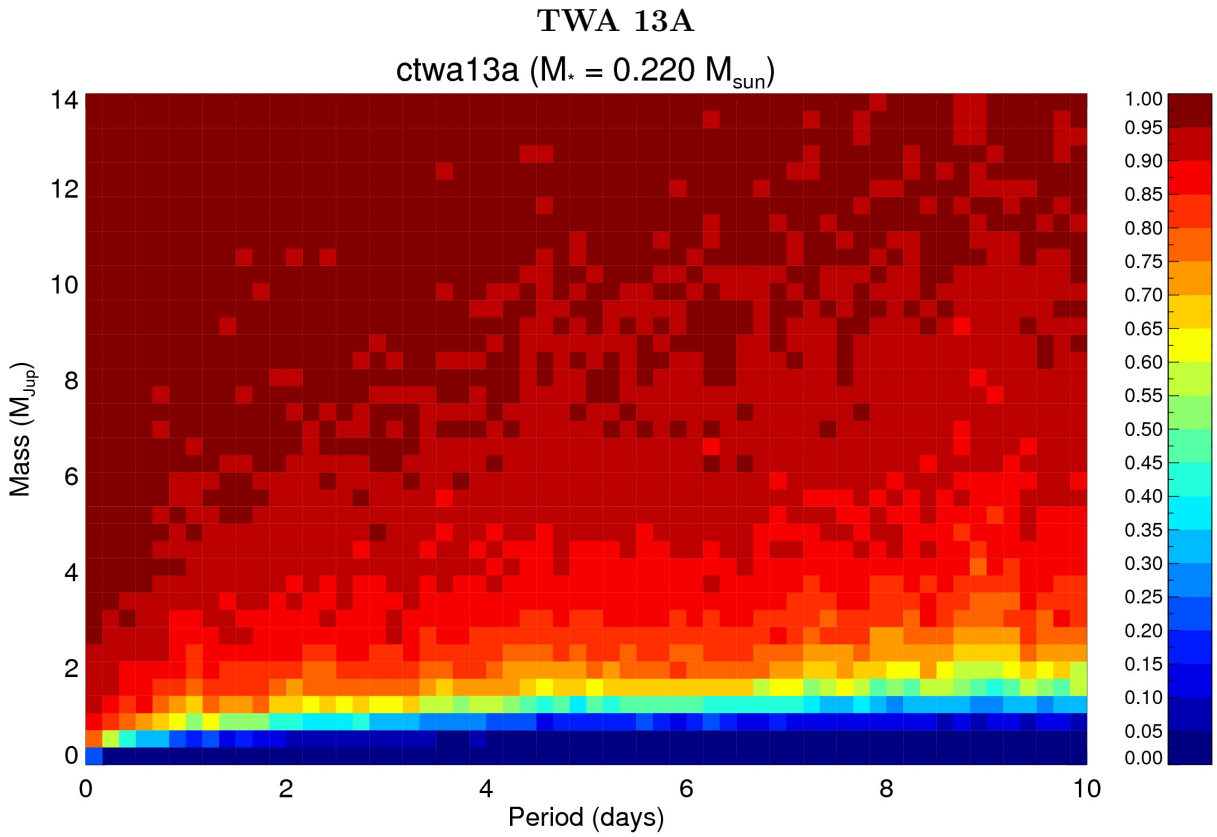

Figure 95 The detection limits are plotted for simulated planets from 0-14 M_{Jup} in 0-10 day orbital periods, with blue (0%) to maroon (100%).

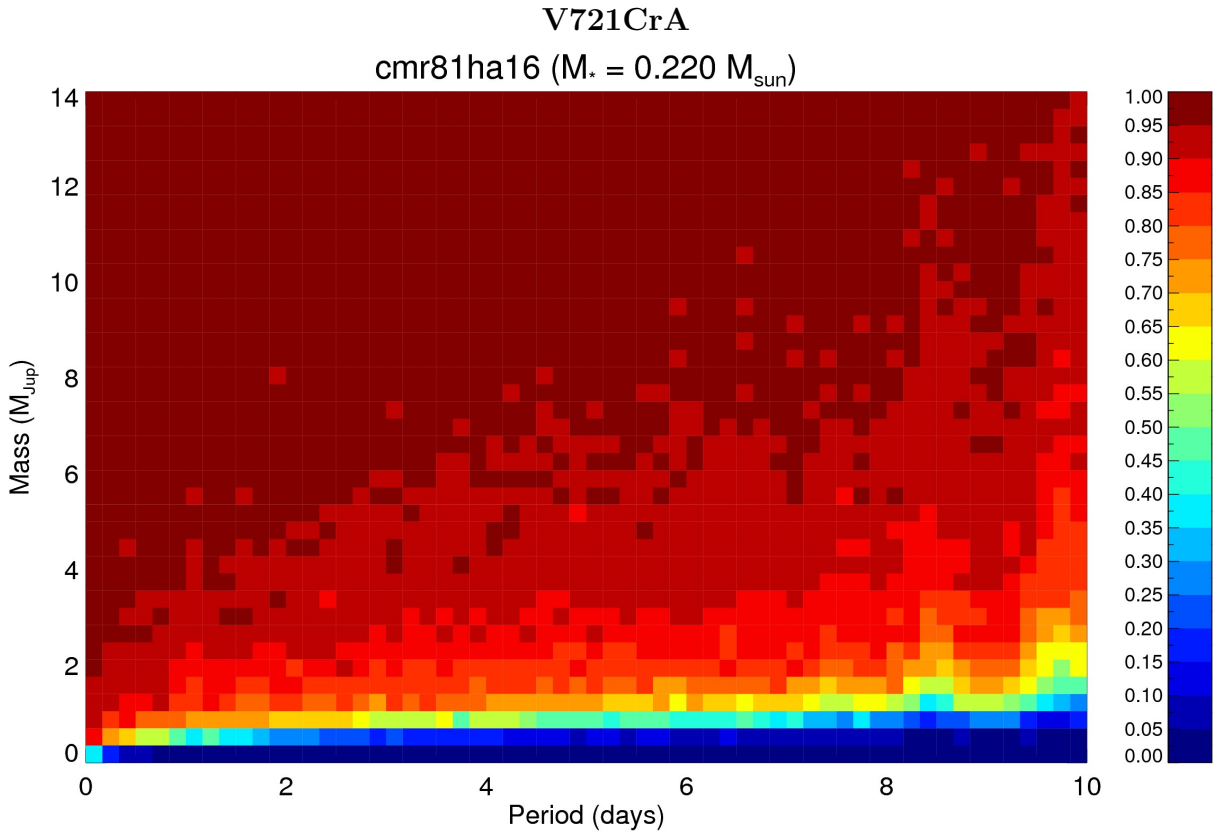

Figure 96 The detection limits are plotted for simulated planets from 0-14 M_{Jup} in 0-10 day orbital periods, with blue (0%) to maroon (100%).

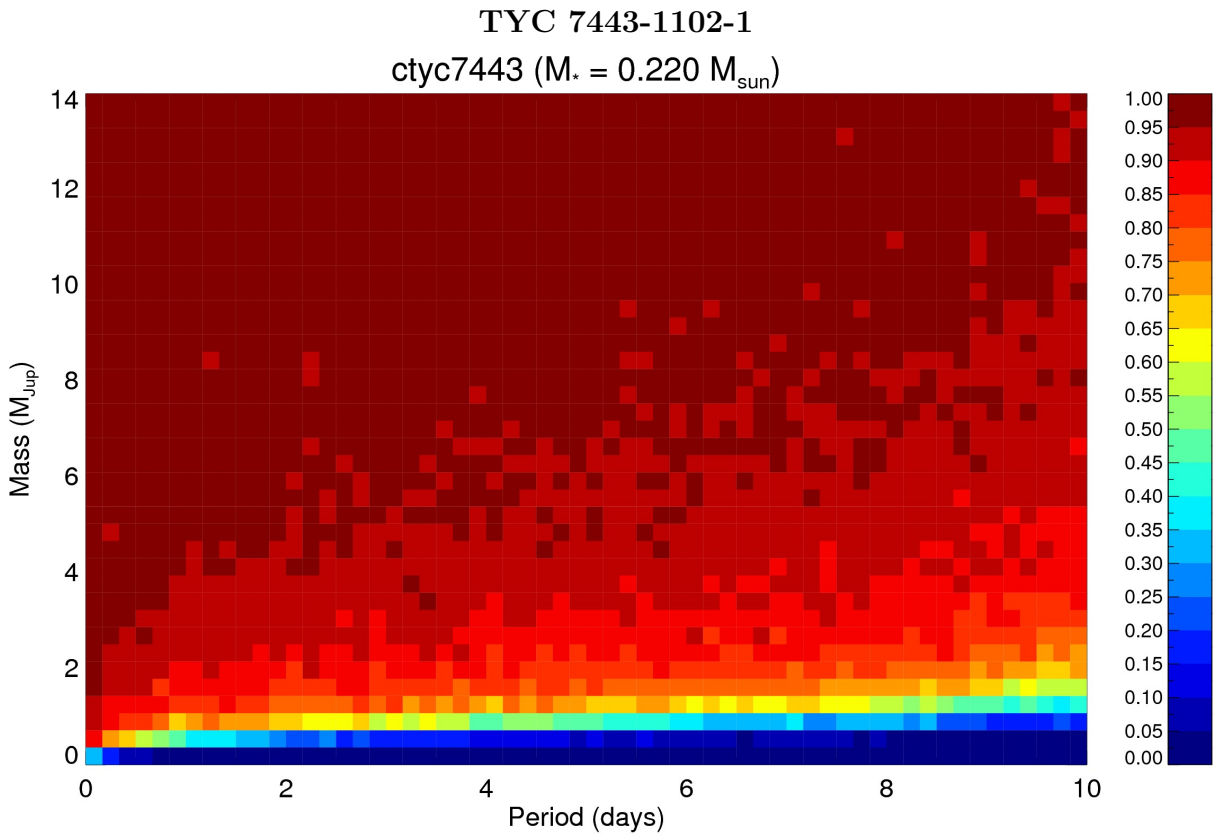

Figure 97 The detection limits are plotted for simulated planets from 0-14 M_{Jup} in 0-10 day orbital periods, with blue (0%) to maroon (100%).

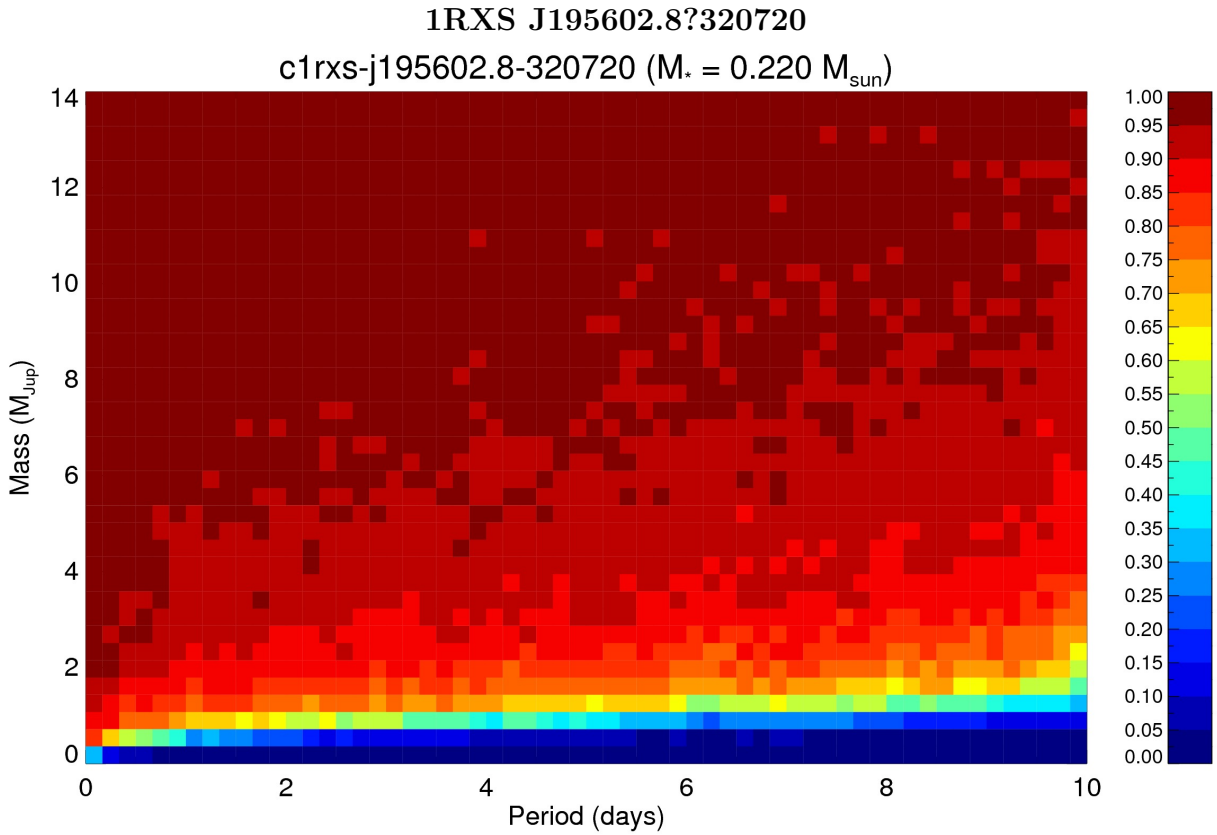

Figure 98 The detection limits are plotted for simulated planets from 0-14 M_{Jup} in 0-10 day orbital periods, with blue (0%) to maroon (100%).

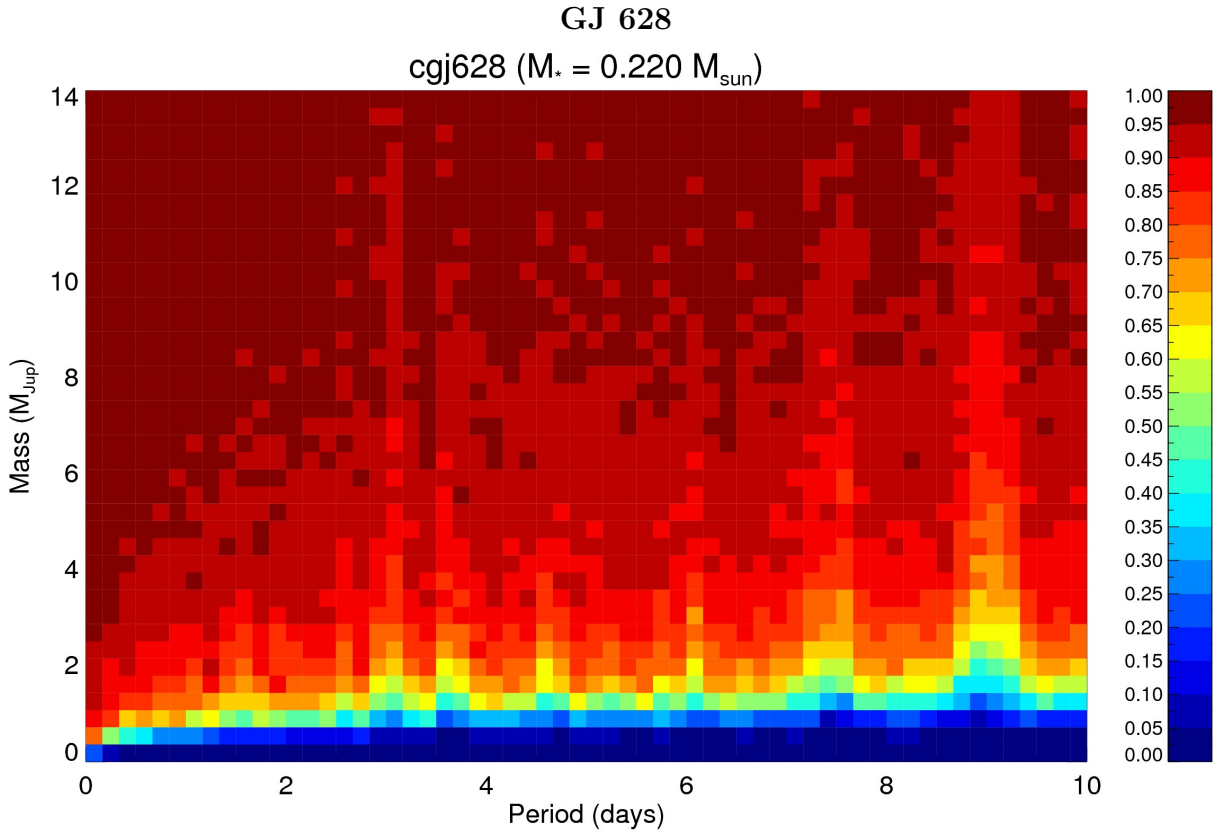

Figure 99 The detection limits are plotted for simulated planets from 0-14 M_{Jup} in 0-10 day orbital periods, with blue (0%) to maroon (100%).

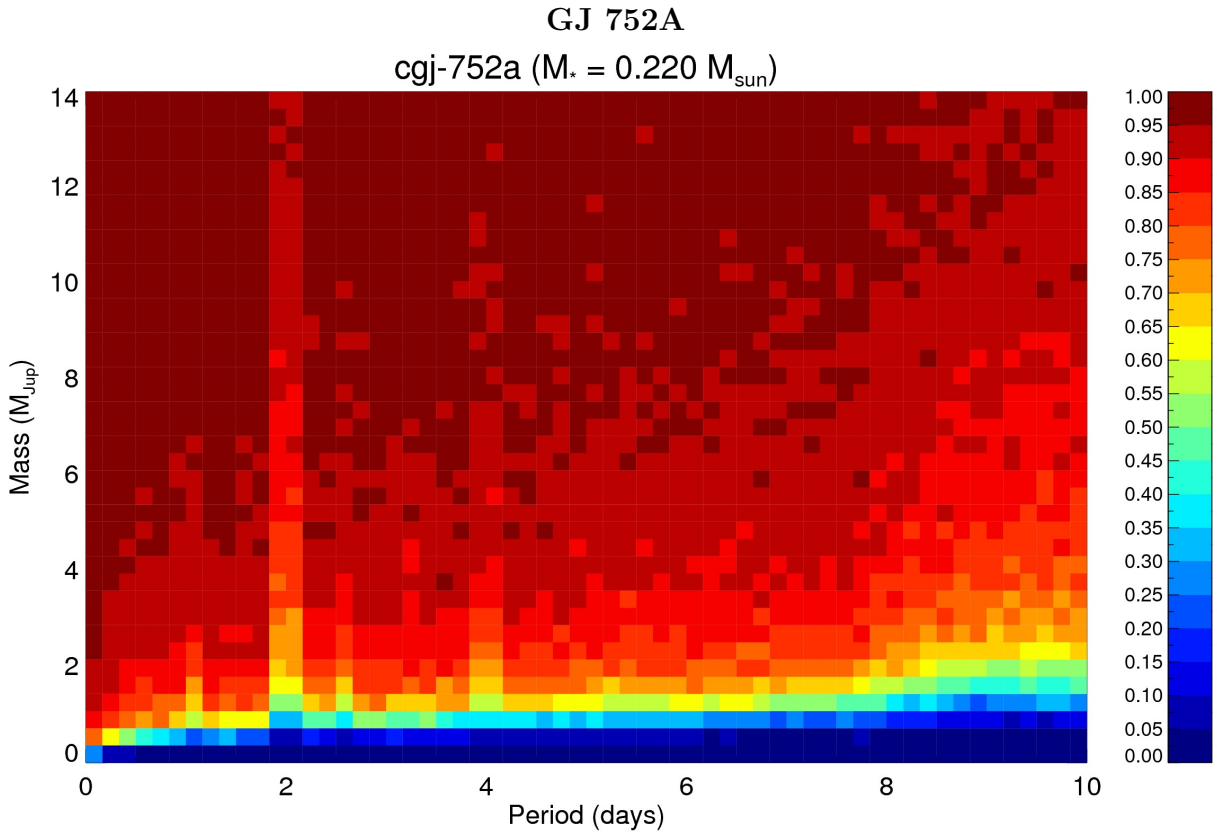

Figure 100 The detection limits are plotted for simulated planets from 0-14 M_{Jup} in 0-10 day orbital periods, with blue (0%) to maroon (100%).

C Keck NIRSPEC

A Taurus-Auriga

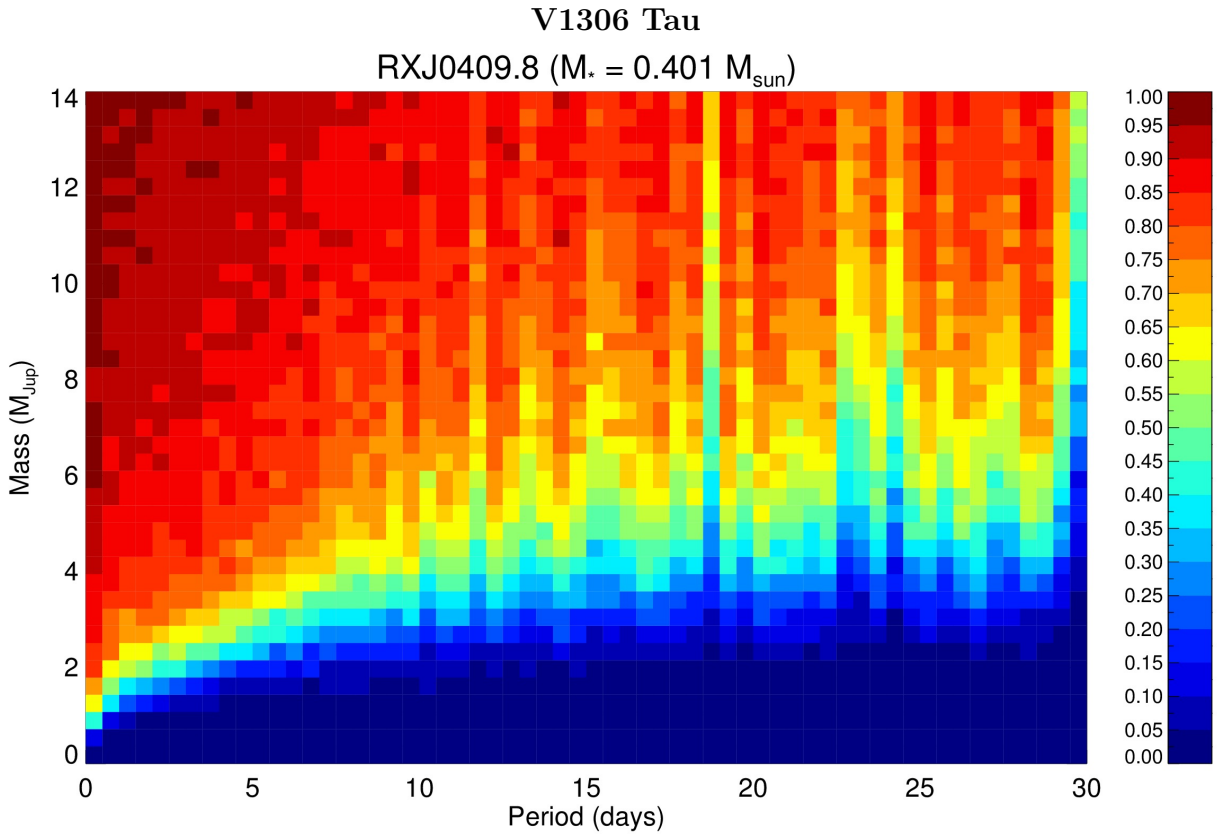

Figure 101 The detection limits are plotted for simulated planets from 0-14 M_{Jup} in 0-30 day orbital periods, with blue (0%) to maroon (100%).

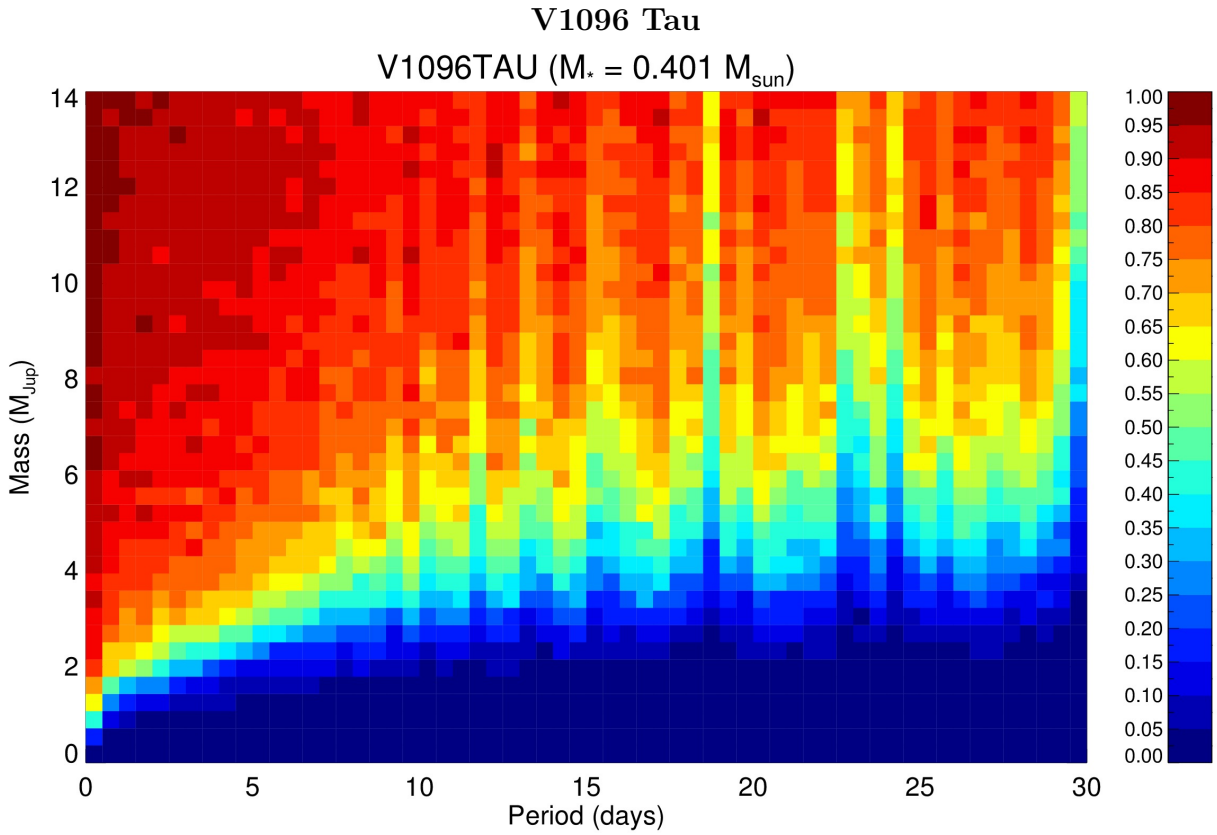

Figure 102 The detection limits are plotted for simulated planets from 0-14 M_{Jup} in 0-30 day orbital periods, with blue (0%) to maroon (100%).

FN Tau

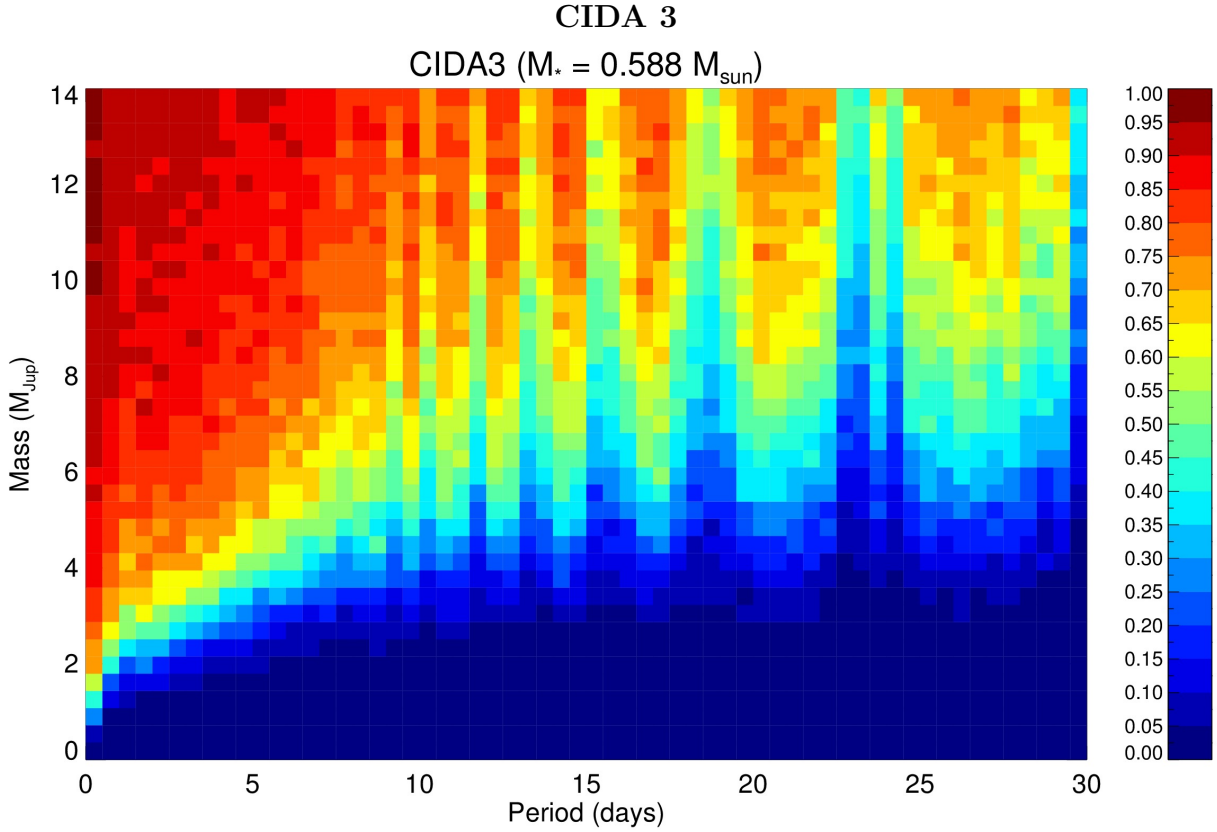

Figure 103 The detection limits are plotted for simulated planets from 0-14 M_{Jup} in 0-30 day orbital periods, with blue (0%) to maroon (100%).

CY Tau

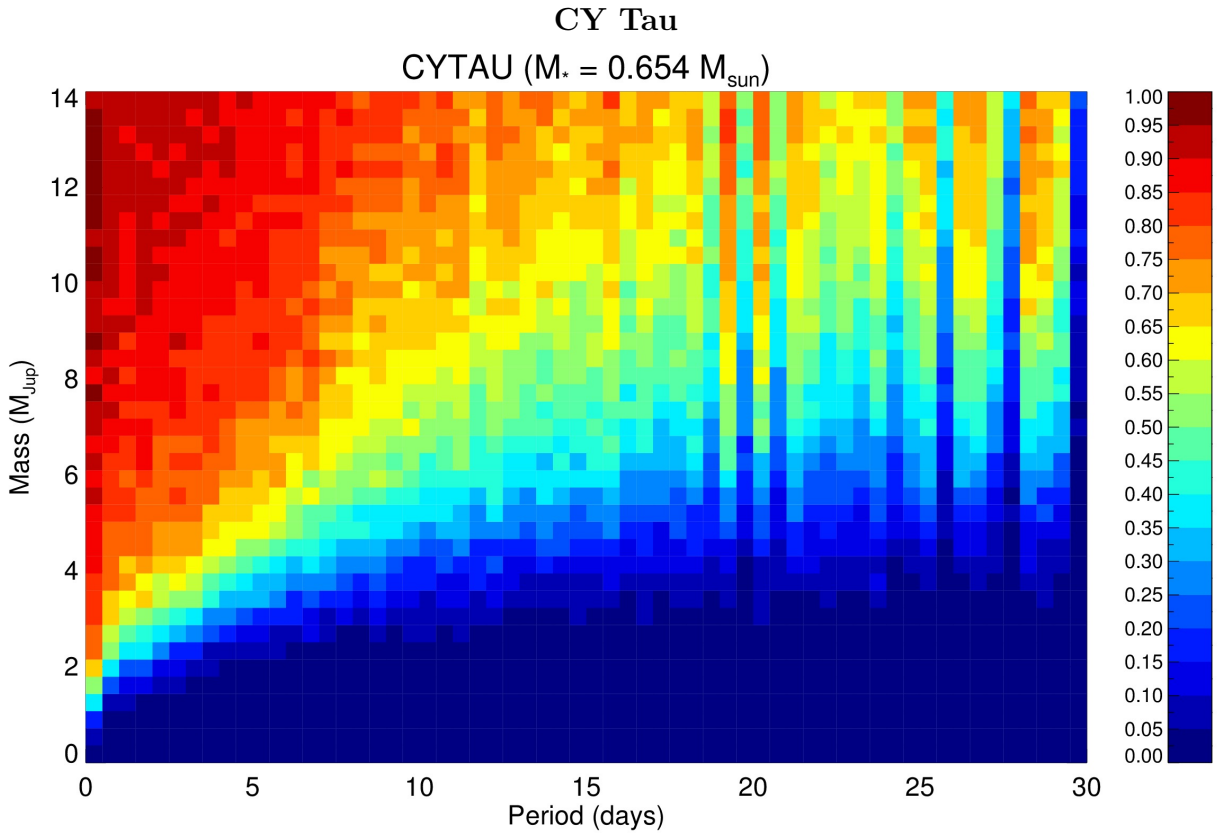

Figure 104 The detection limits are plotted for simulated planets from 0-14 M_{Jup} in 0-30 day orbital periods, with blue (0%) to maroon (100%).

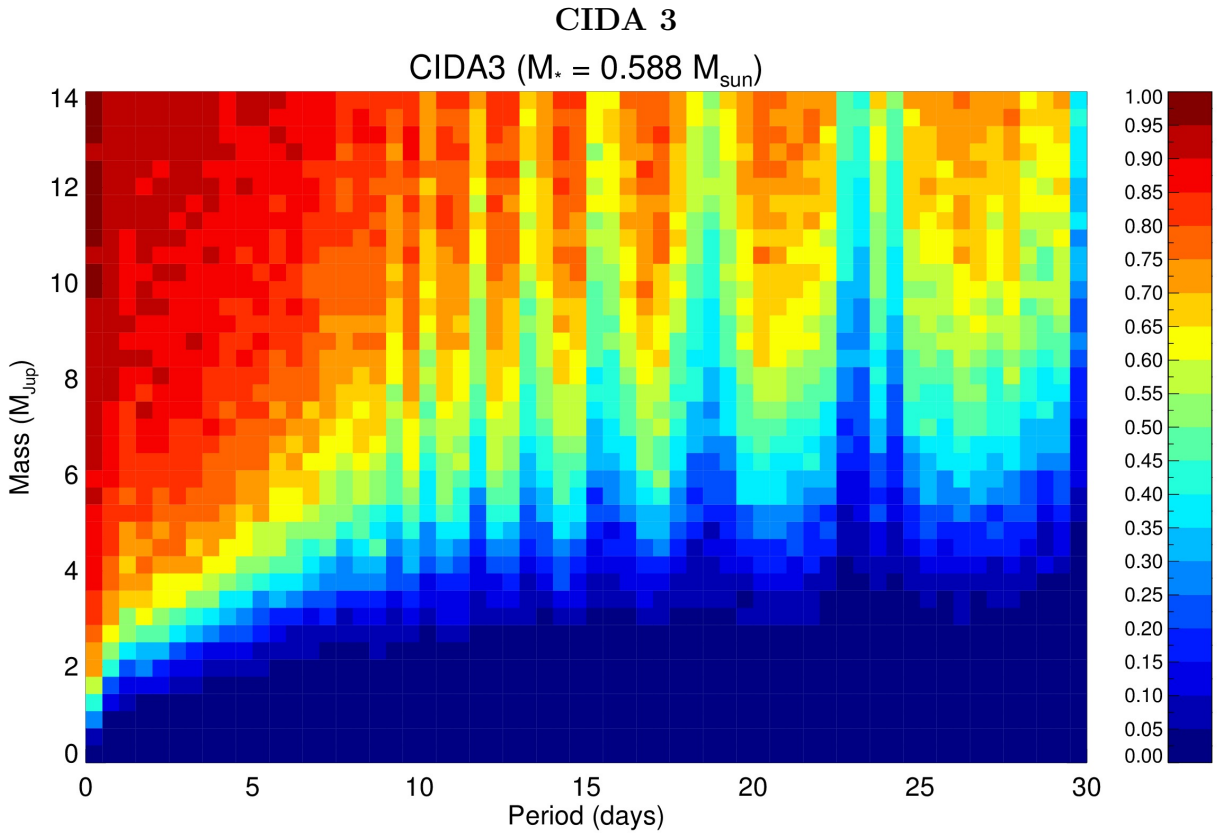

Figure 105 The detection limits are plotted for simulated planets from 0-14 M_{Jup} in 0-30 day orbital periods, with blue (0%) to maroon (100%).

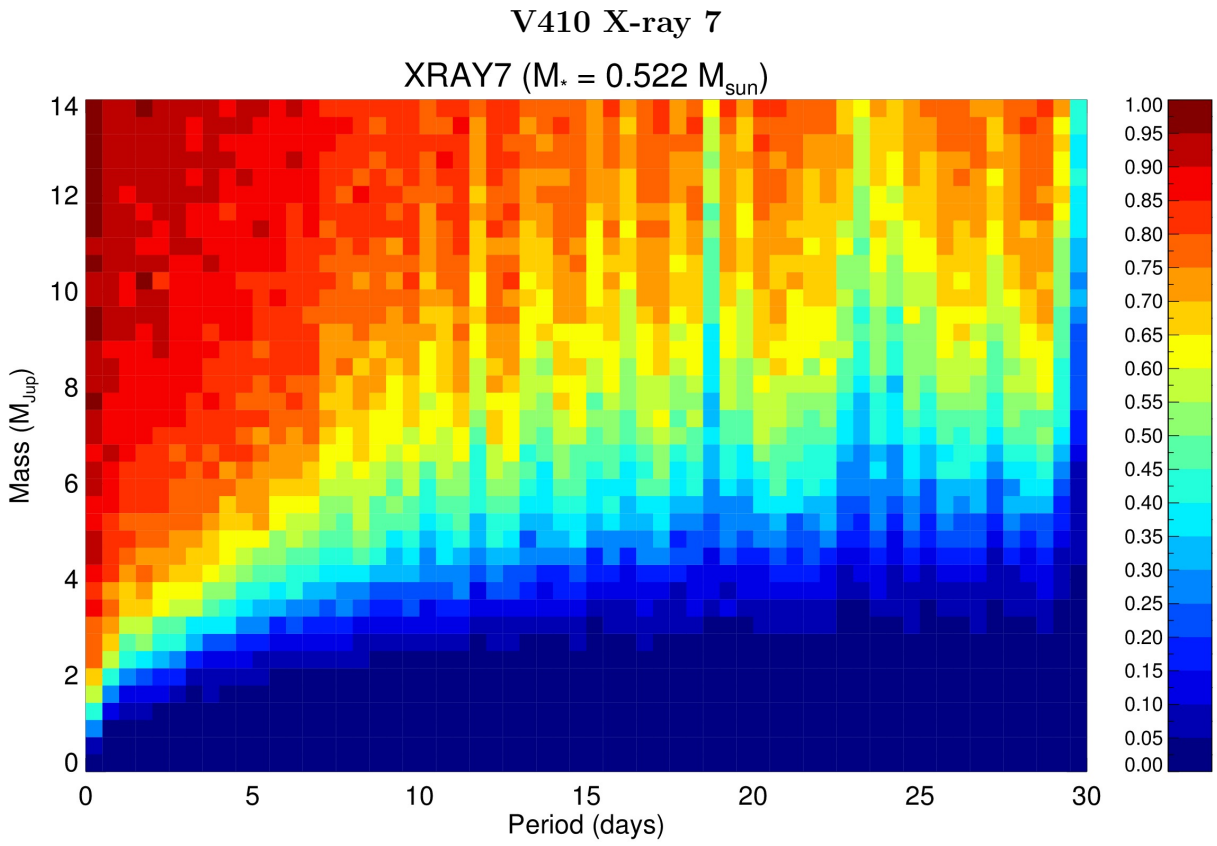

Figure 106 The detection limits are plotted for simulated planets from 0-14 M_{Jup} in 0-30 day orbital periods, with blue (0%) to maroon (100%).

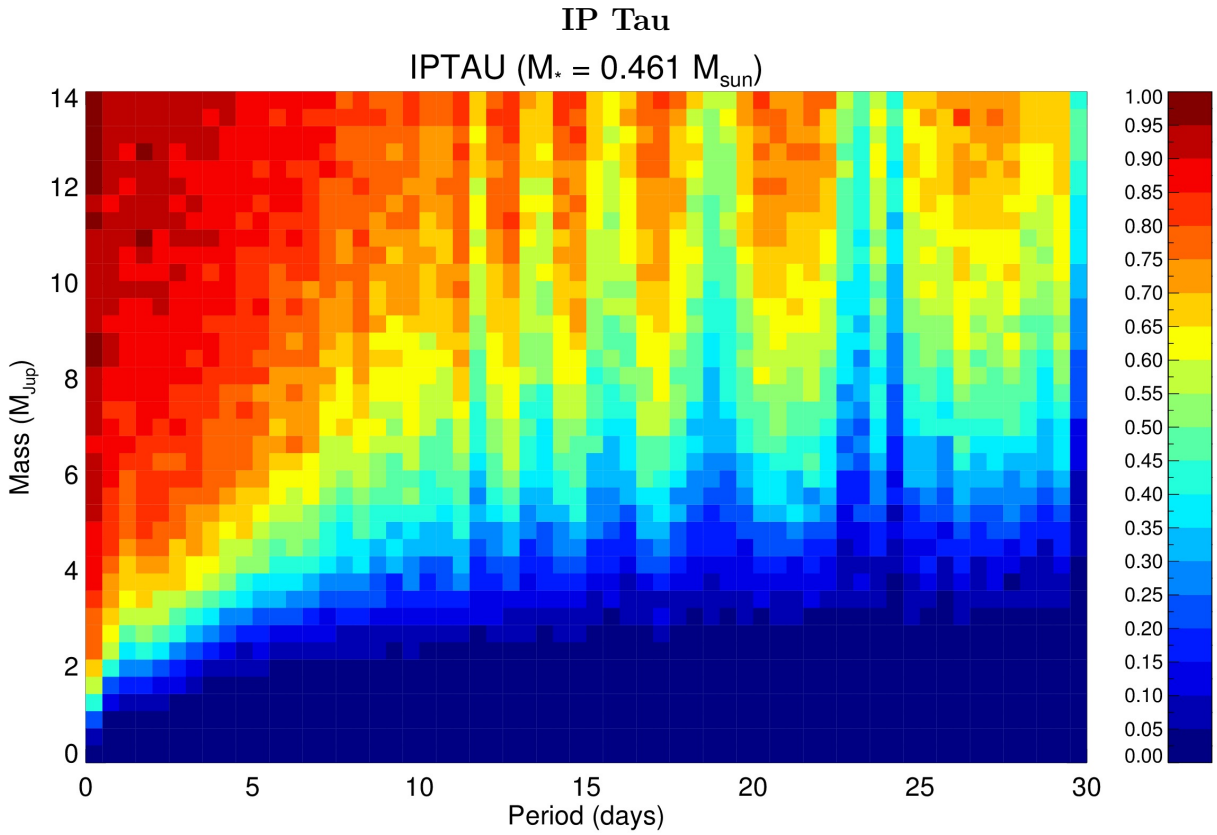

Figure 107 The detection limits are plotted for simulated planets from 0-14 M_{Jup} in 0-30 day orbital periods, with blue (0%) to maroon (100%).

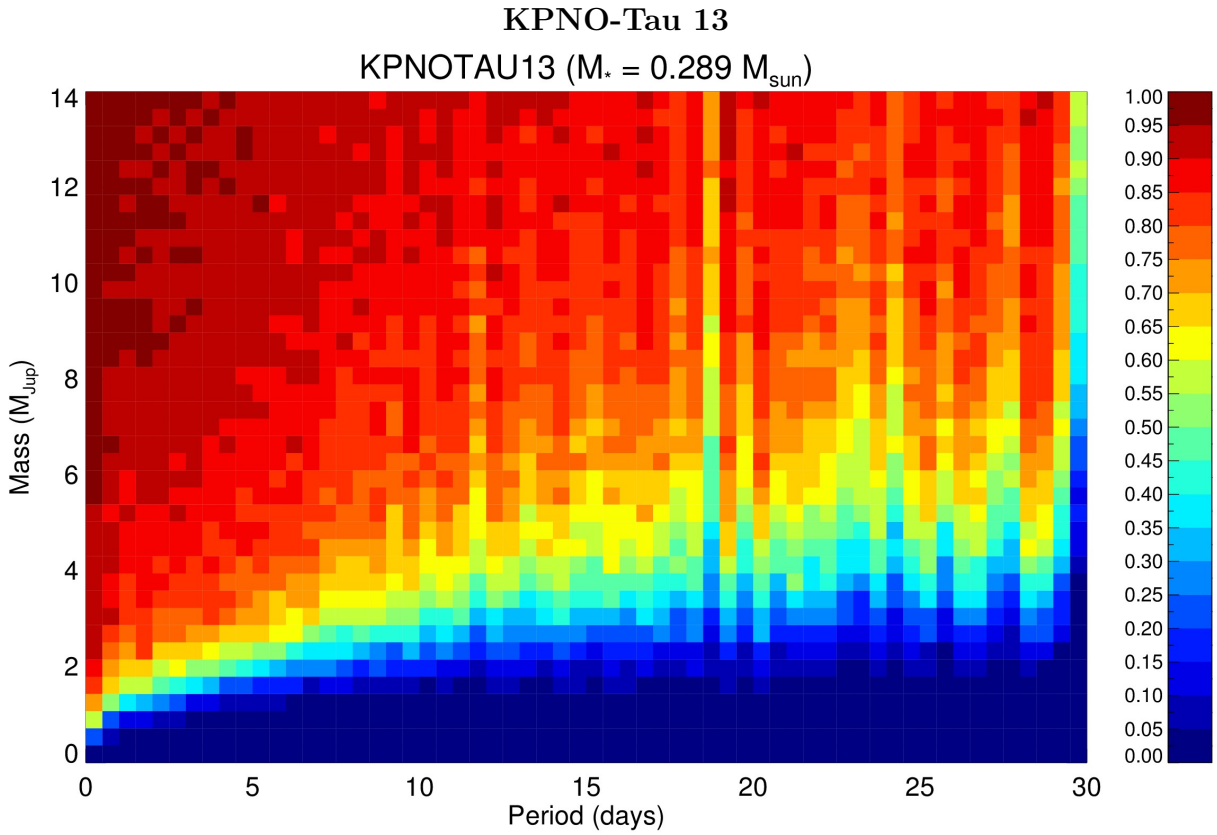

Figure 108 The detection limits are plotted for simulated planets from 0-14 M_{Jup} in 0-30 day orbital periods, with blue (0%) to maroon (100%).

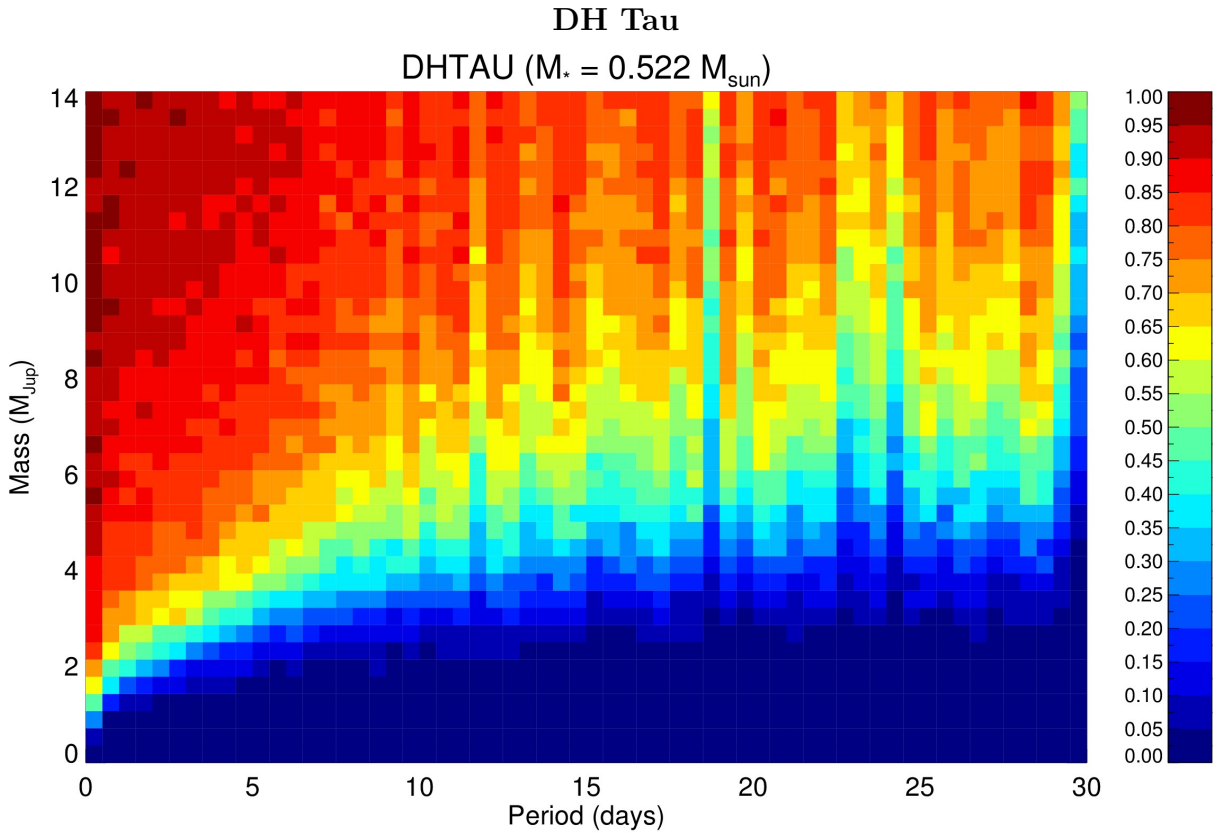

Figure 109 The detection limits are plotted for simulated planets from 0-14 M_{Jup} in 0-30 day orbital periods, with blue (0%) to maroon (100%).

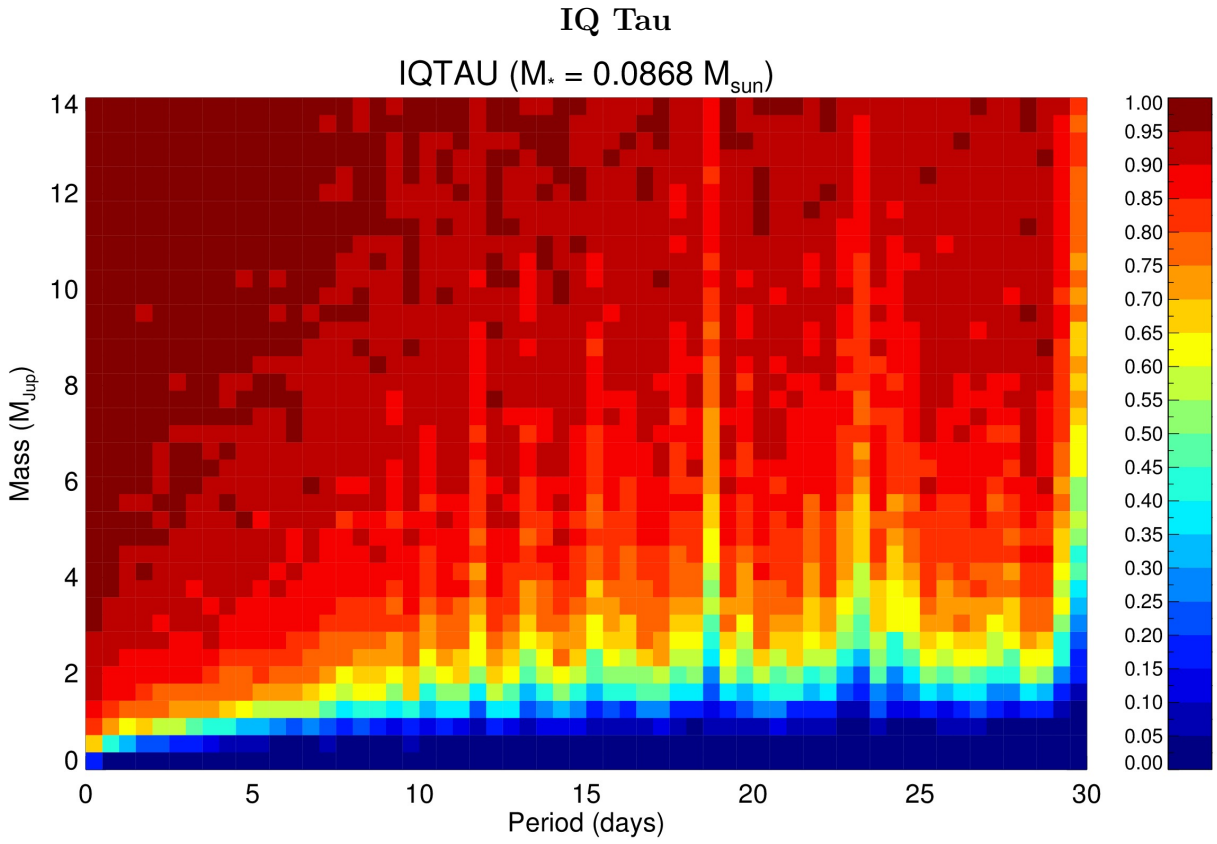

Figure 110 The detection limits are plotted for simulated planets from 0-14 M_{Jup} in 0-30 day orbital periods, with blue (0%) to maroon (100%).

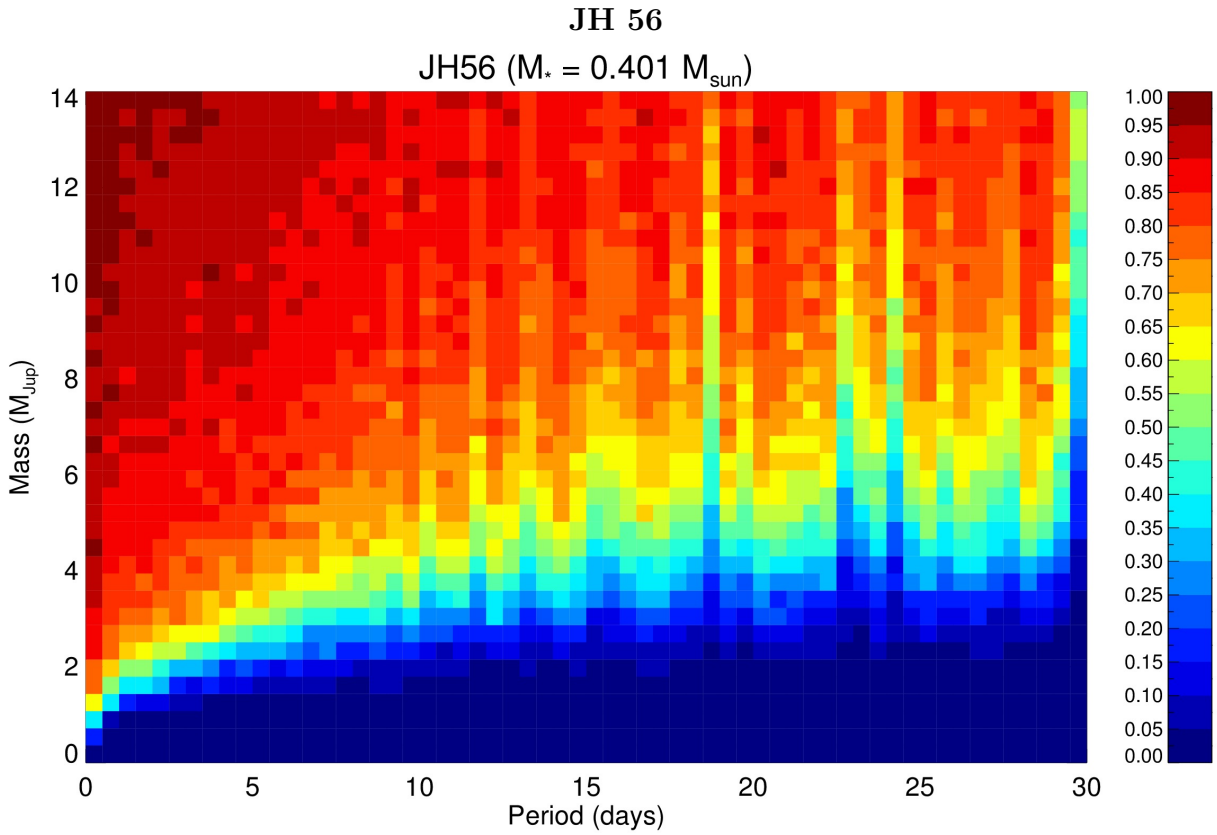

Figure 111 The detection limits are plotted for simulated planets from 0-14 M_{Jup} in 0-30 day orbital periods, with blue (0%) to maroon (100%).

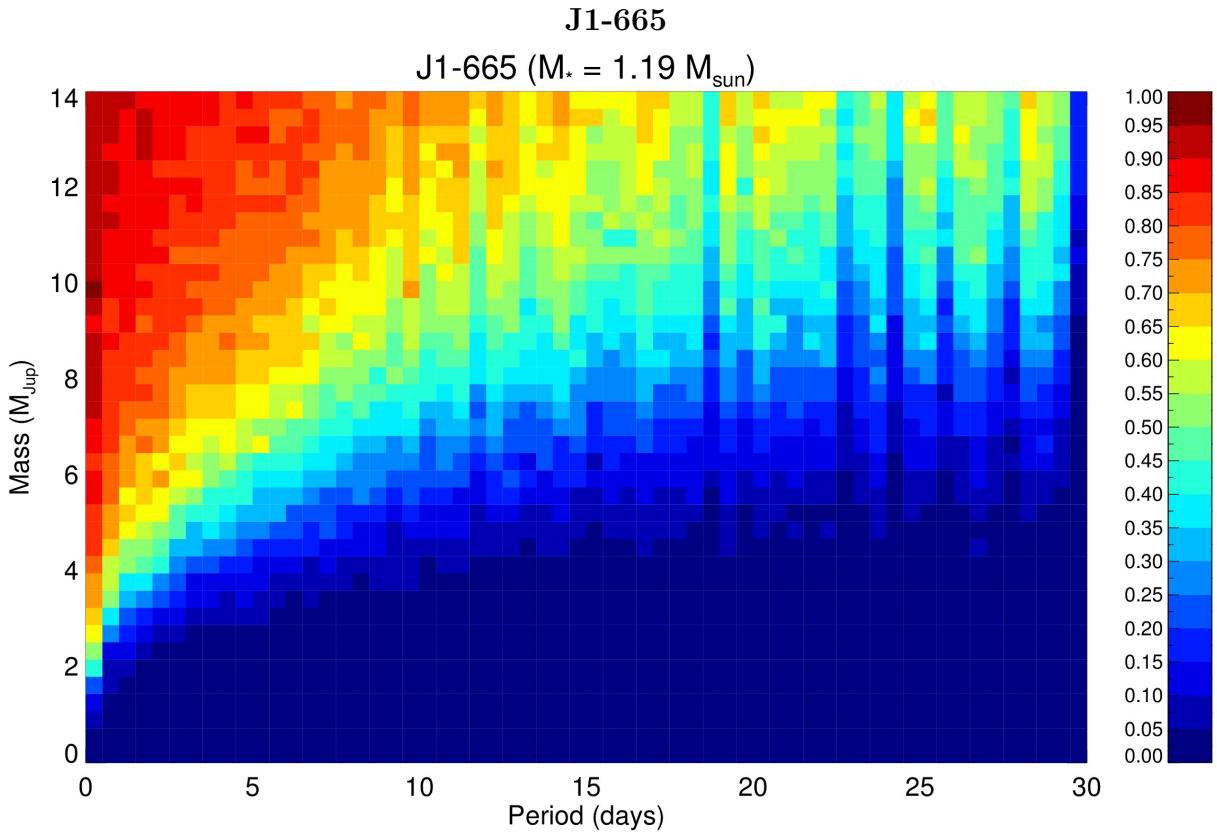

Figure 112 The detection limits are plotted for simulated planets from 0-14 M_{Jup} in 0-30 day orbital periods, with blue (0%) to maroon (100%).

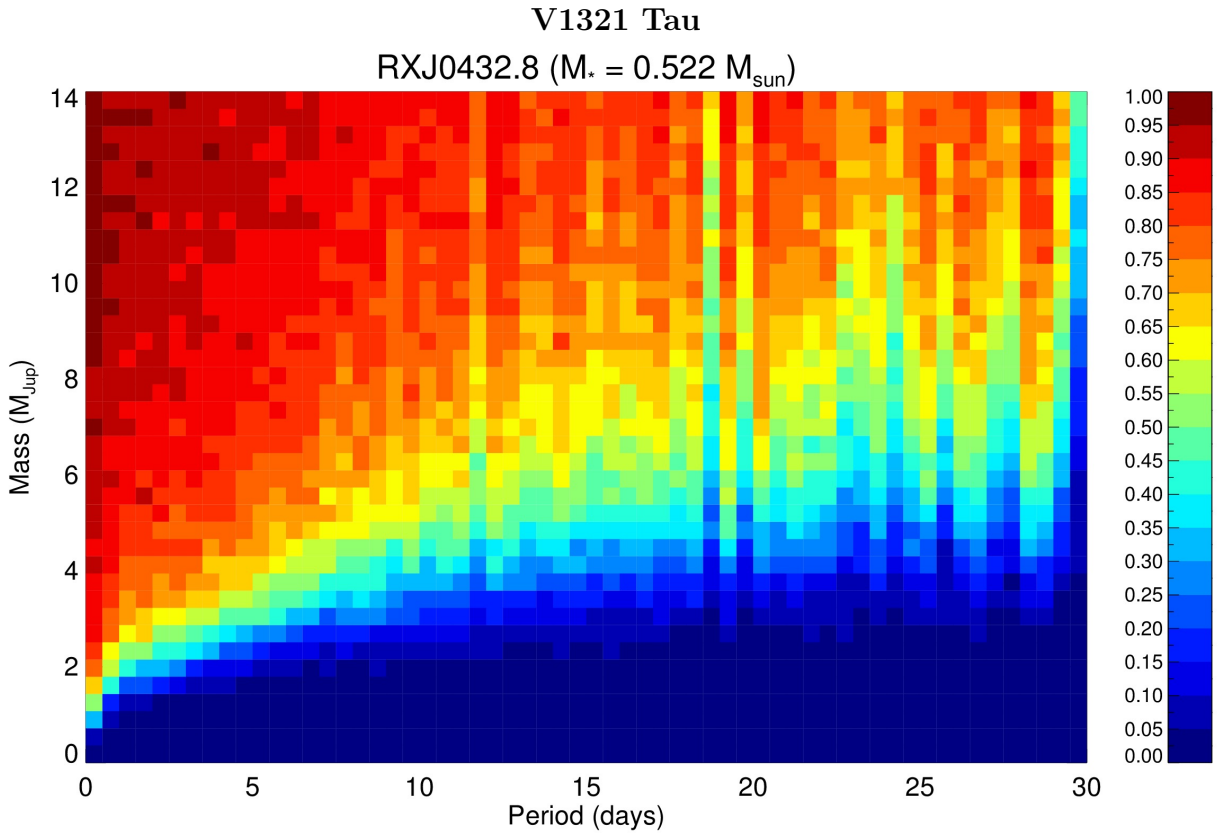

Figure 113 The detection limits are plotted for simulated planets from 0-14 M_{Jup} in 0-30 day orbital periods, with blue (0%) to maroon (100%).

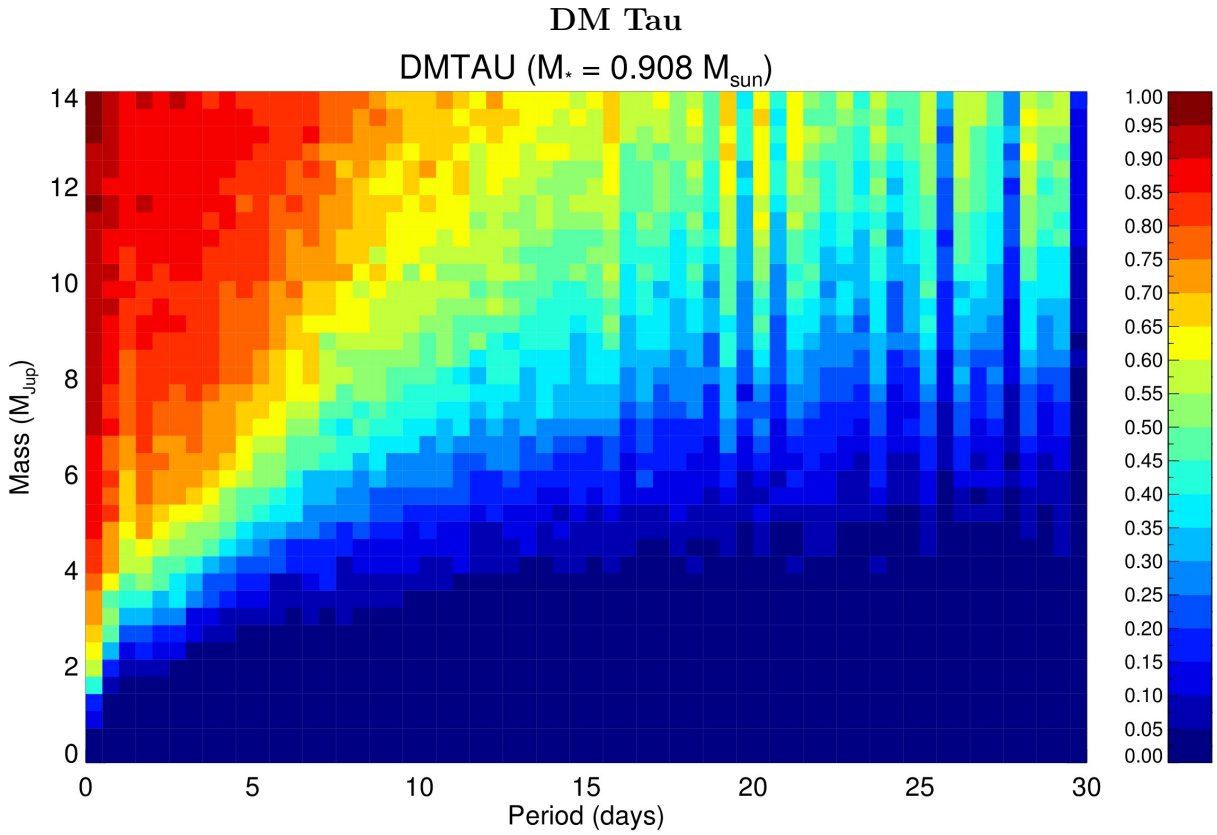

Figure 114 The detection limits are plotted for simulated planets from 0-14 M_{Jup} in 0-30 day orbital periods, with blue (0%) to maroon (100%).

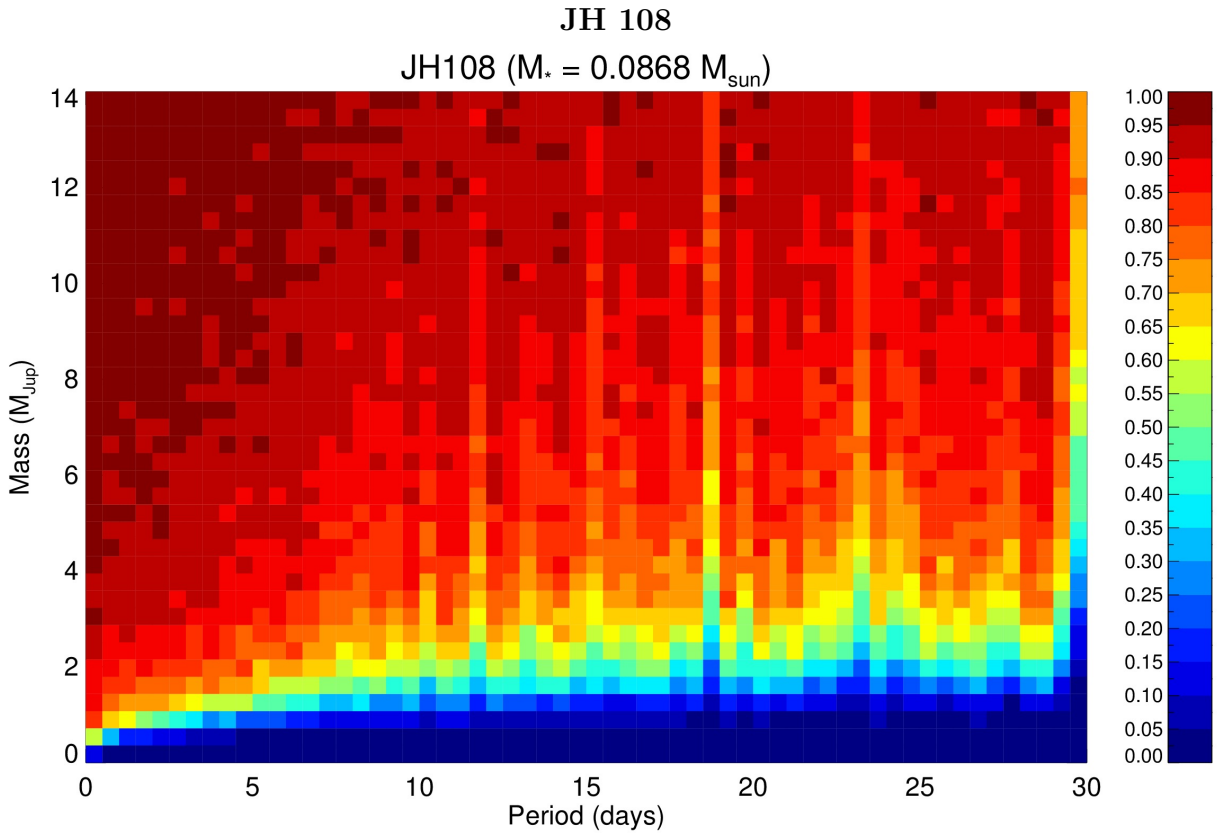

Figure 115 The detection limits are plotted for simulated planets from 0-14 M_{Jup} in 0-30 day orbital periods, with blue (0%) to maroon (100%).

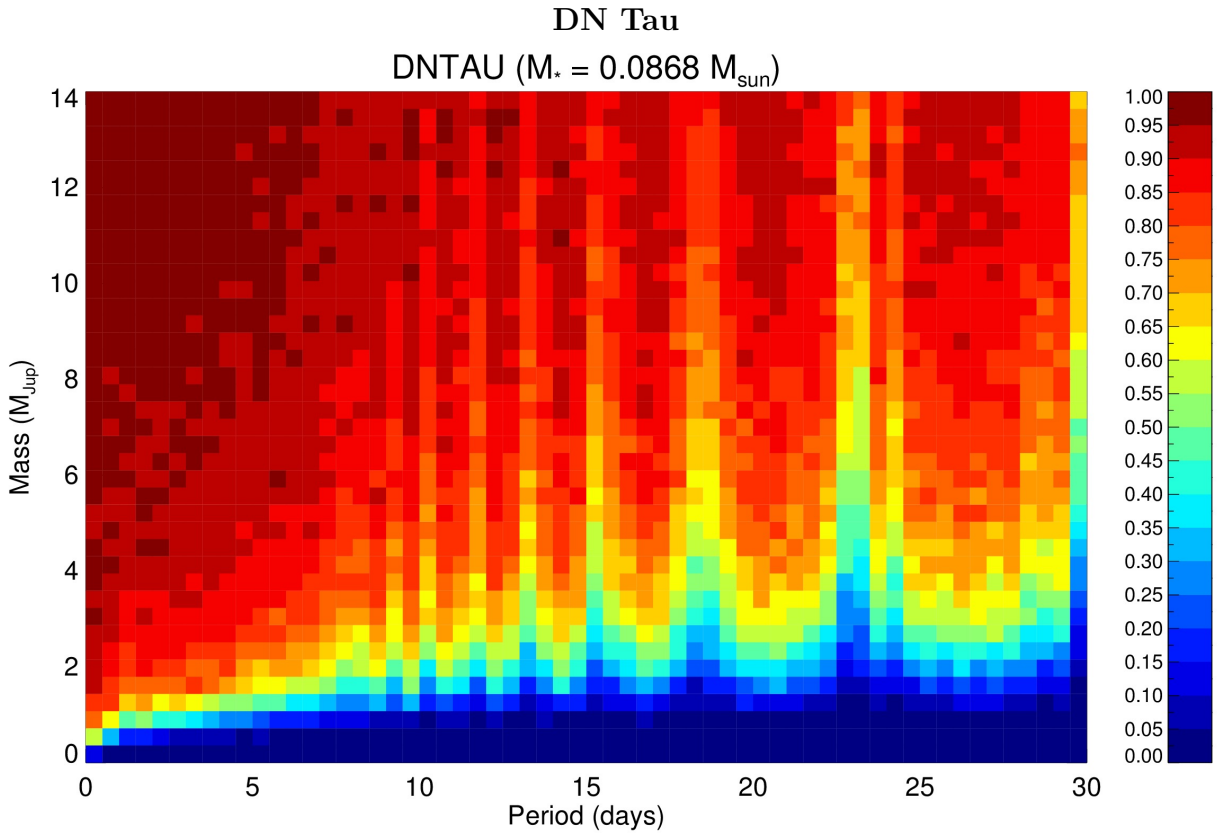

Figure 116 The detection limits are plotted for simulated planets from 0-14 M_{Jup} in 0-30 day orbital periods, with blue (0%) to maroon (100%).

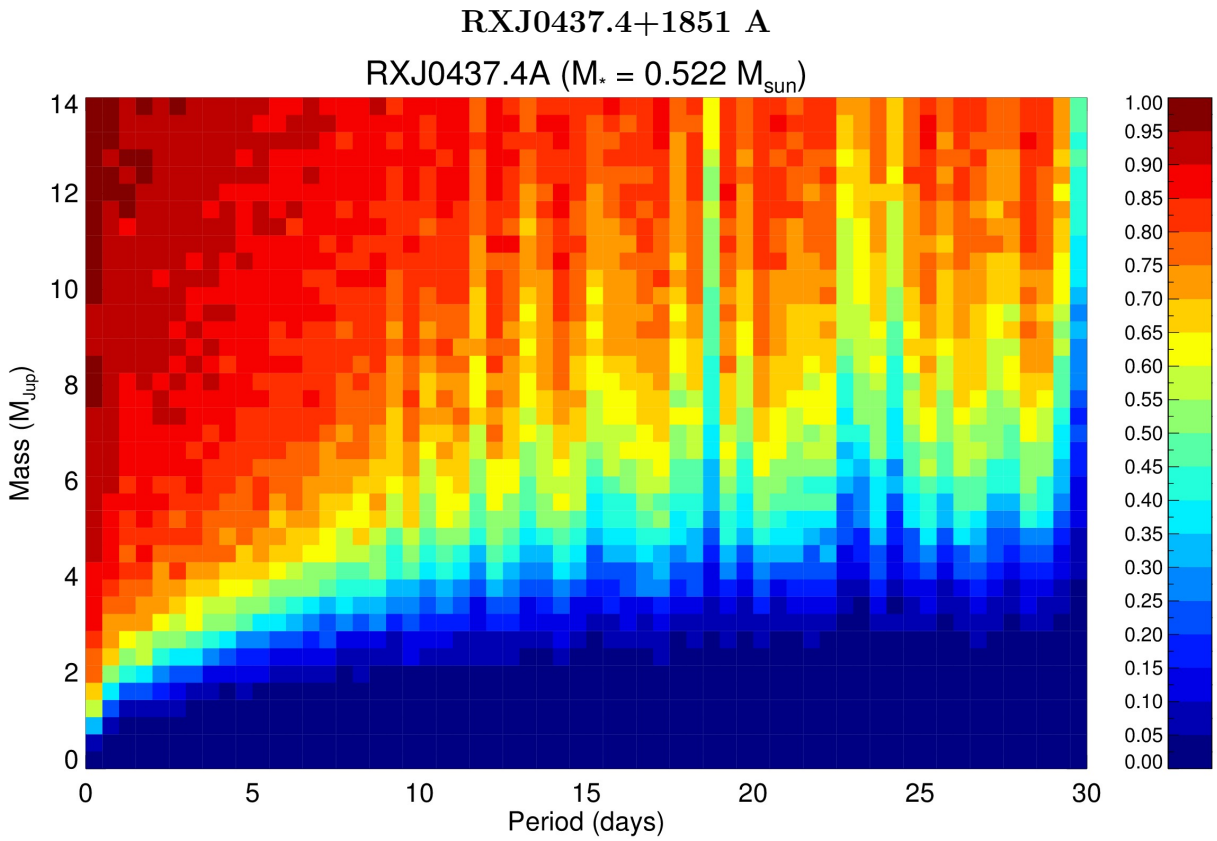

Figure 117 The detection limits are plotted for simulated planets from 0-14 M_{Jup} in 0-30 day orbital periods, with blue (0%) to maroon (100%).

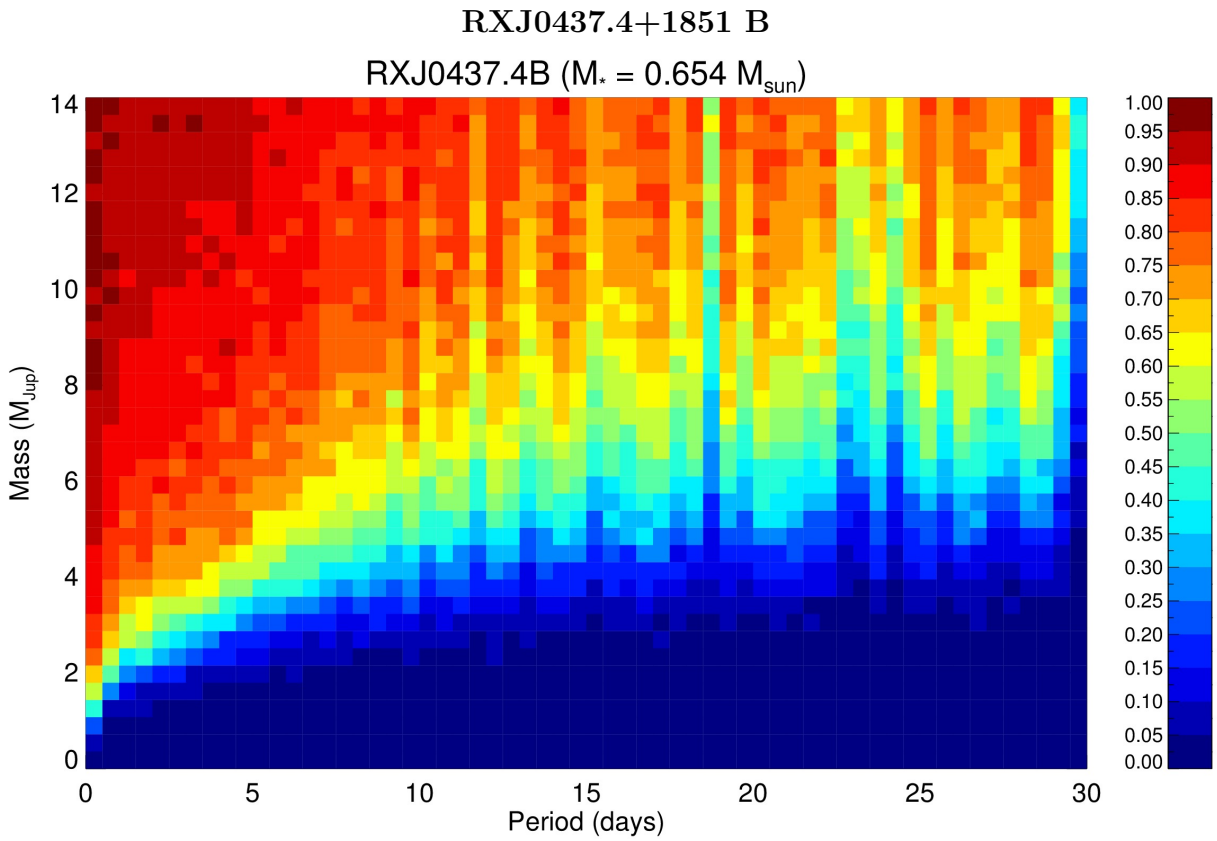

Figure 118 The detection limits are plotted for simulated planets from 0-14 M_{Jup} in 0-30 day orbital periods, with blue (0%) to maroon (100%).

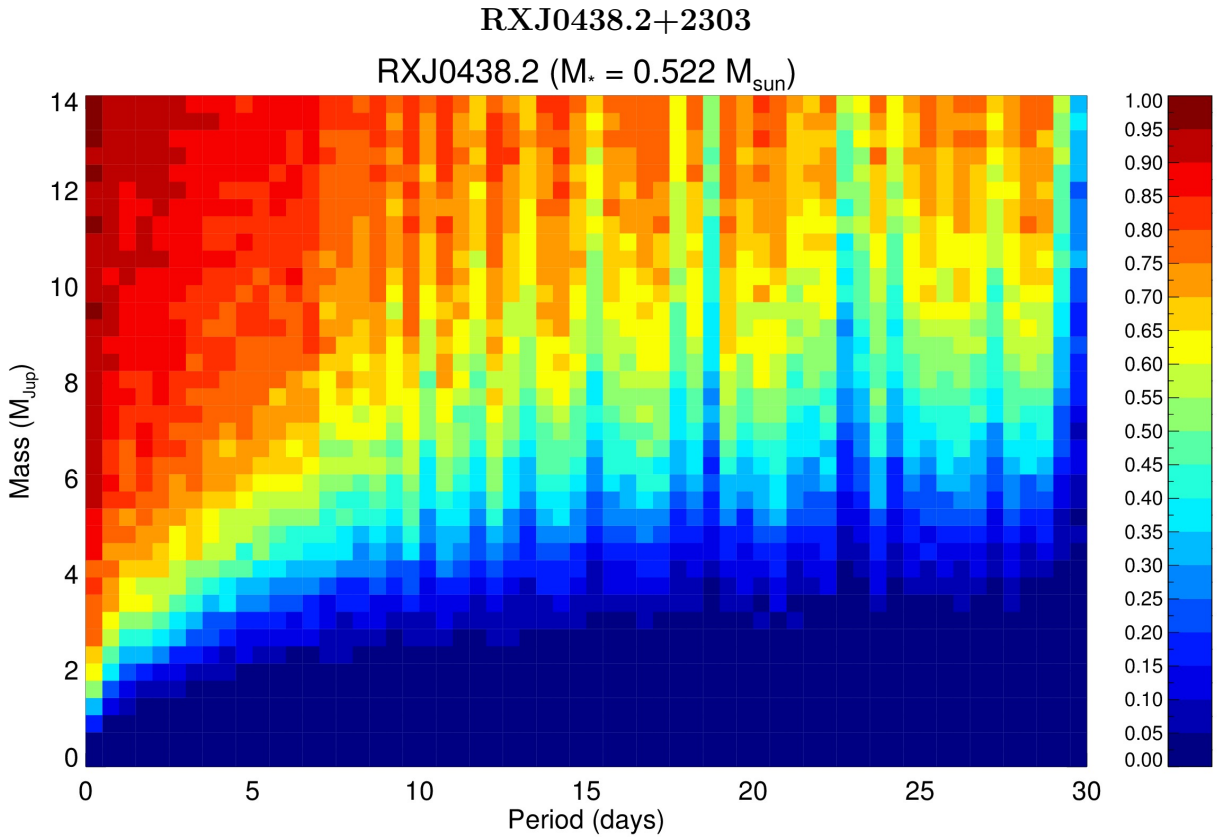

Figure 119 The detection limits are plotted for simulated planets from 0-14 M_{Jup} in 0-30 day orbital periods, with blue (0%) to maroon (100%).

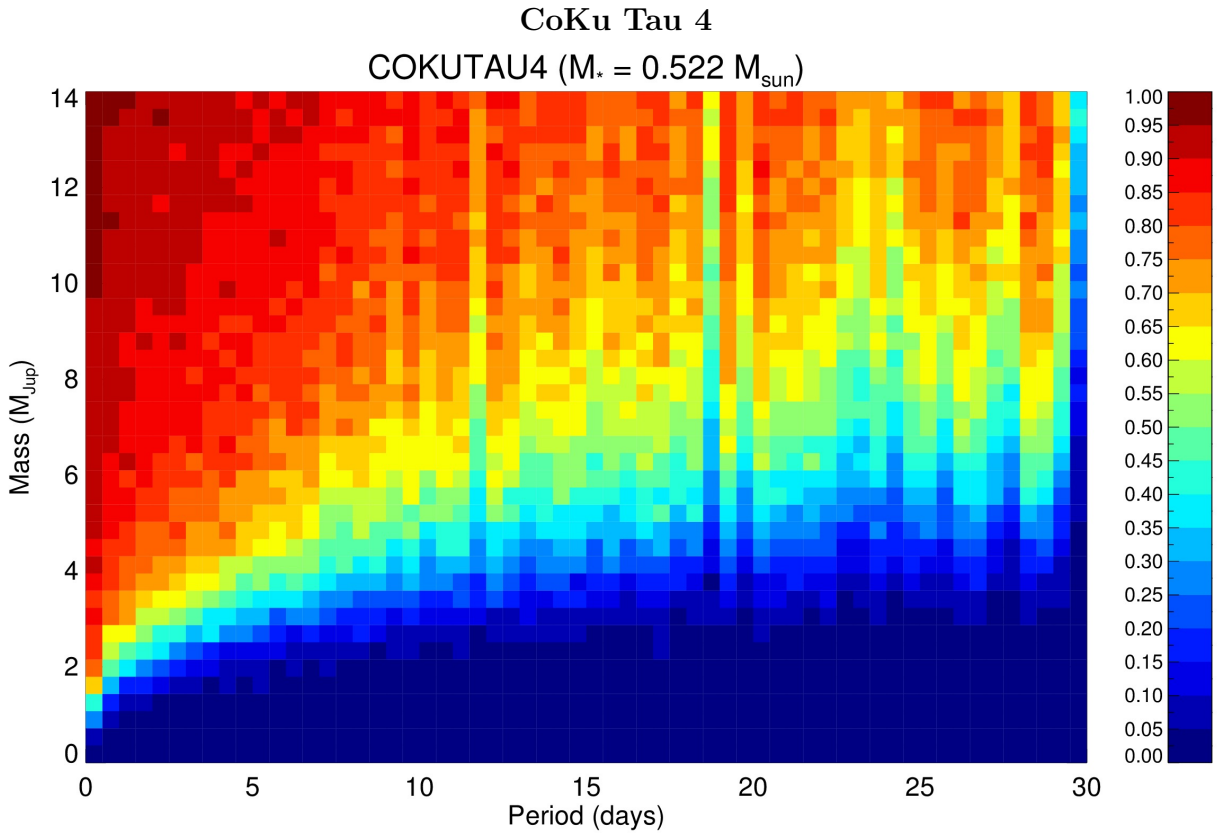

Figure 120 The detection limits are plotted for simulated planets from 0-14 M_{Jup} in 0-30 day orbital periods, with blue (0%) to maroon (100%).

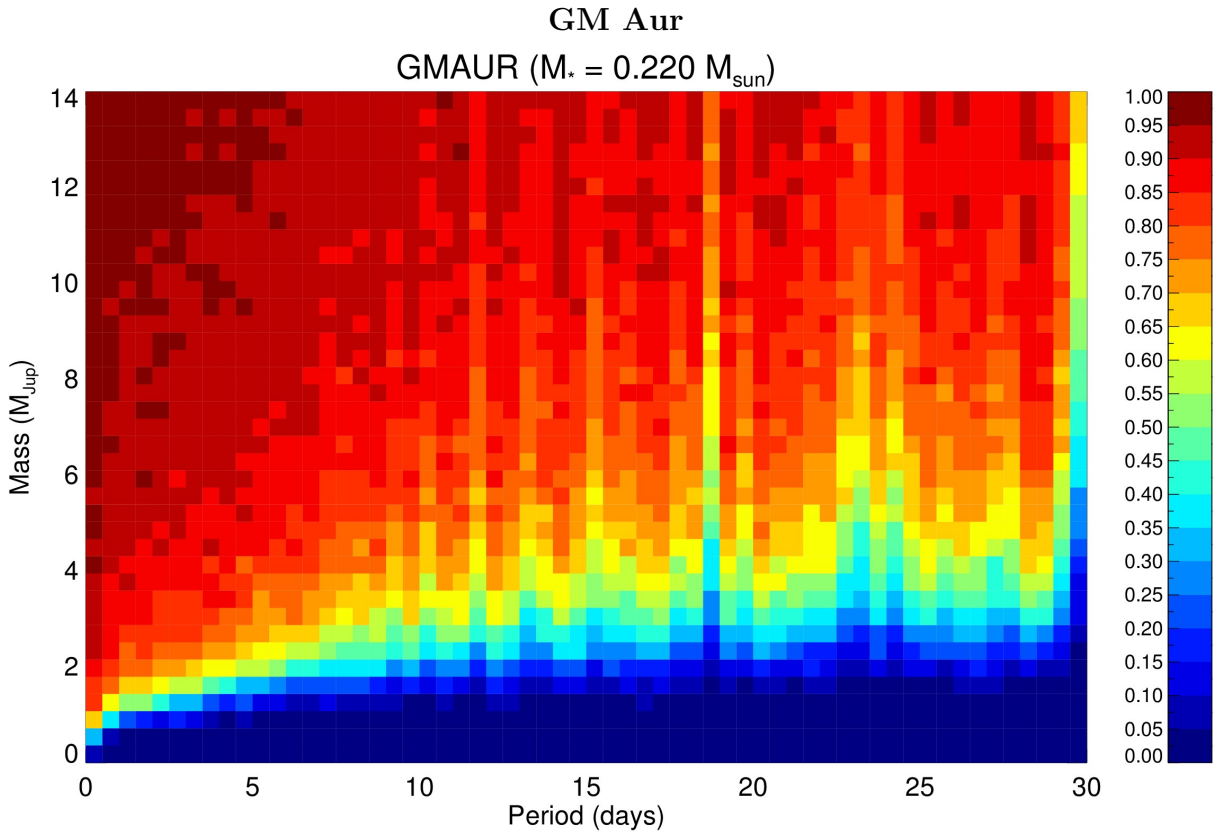

Figure 121 The detection limits are plotted for simulated planets from 0-14 M_{Jup} in 0-30 day orbital periods, with blue (0%) to maroon (100%).

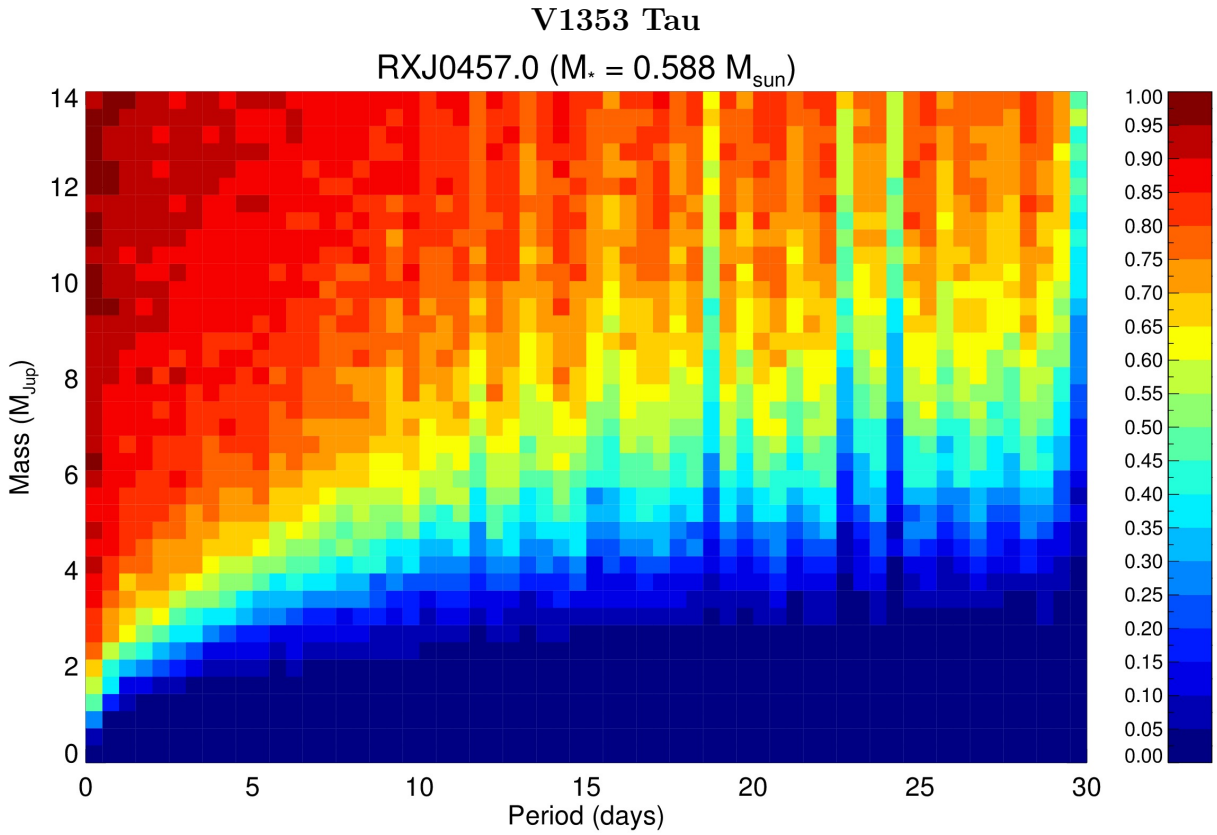

Figure 122 The detection limits are plotted for simulated planets from 0-14 M_{Jup} in 0-30 day orbital periods, with blue (0%) to maroon (100%).

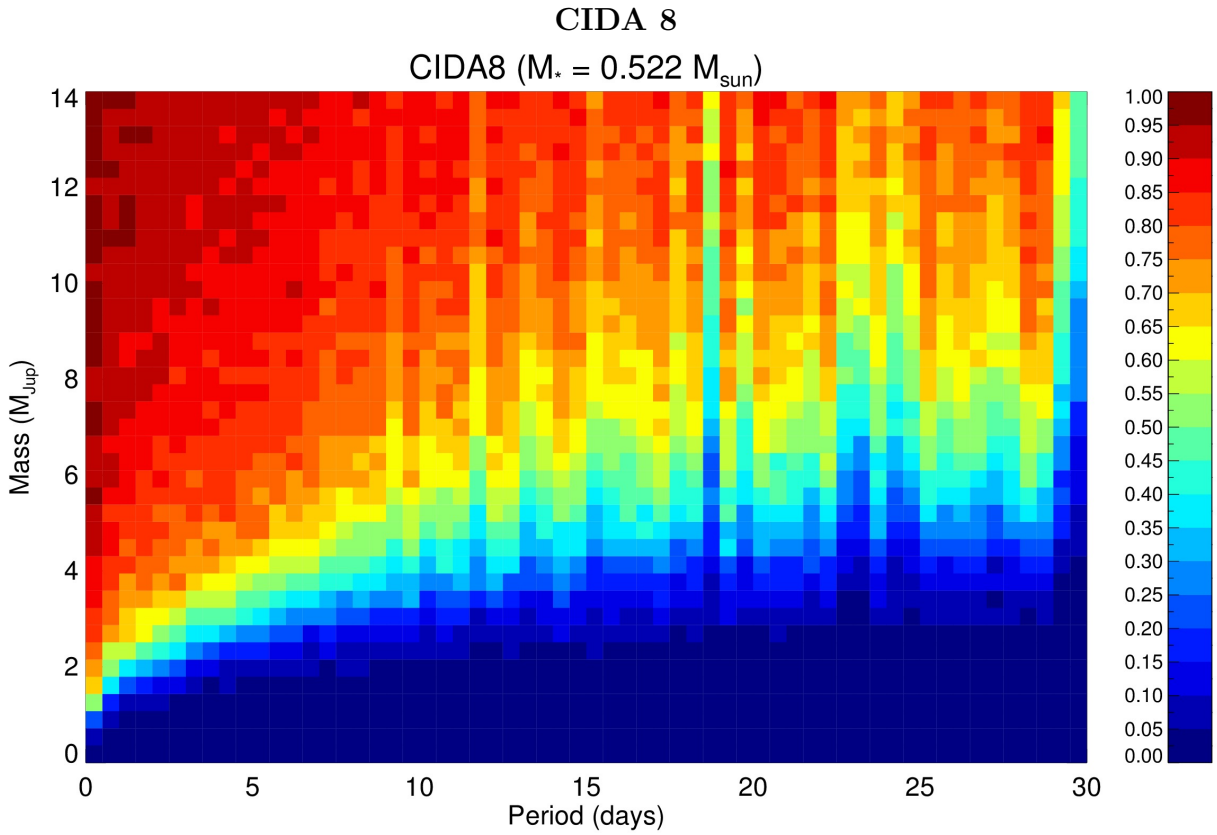

Figure 123 The detection limits are plotted for simulated planets from 0-14 M_{Jup} in 0-30 day orbital periods, with blue (0%) to maroon (100%).

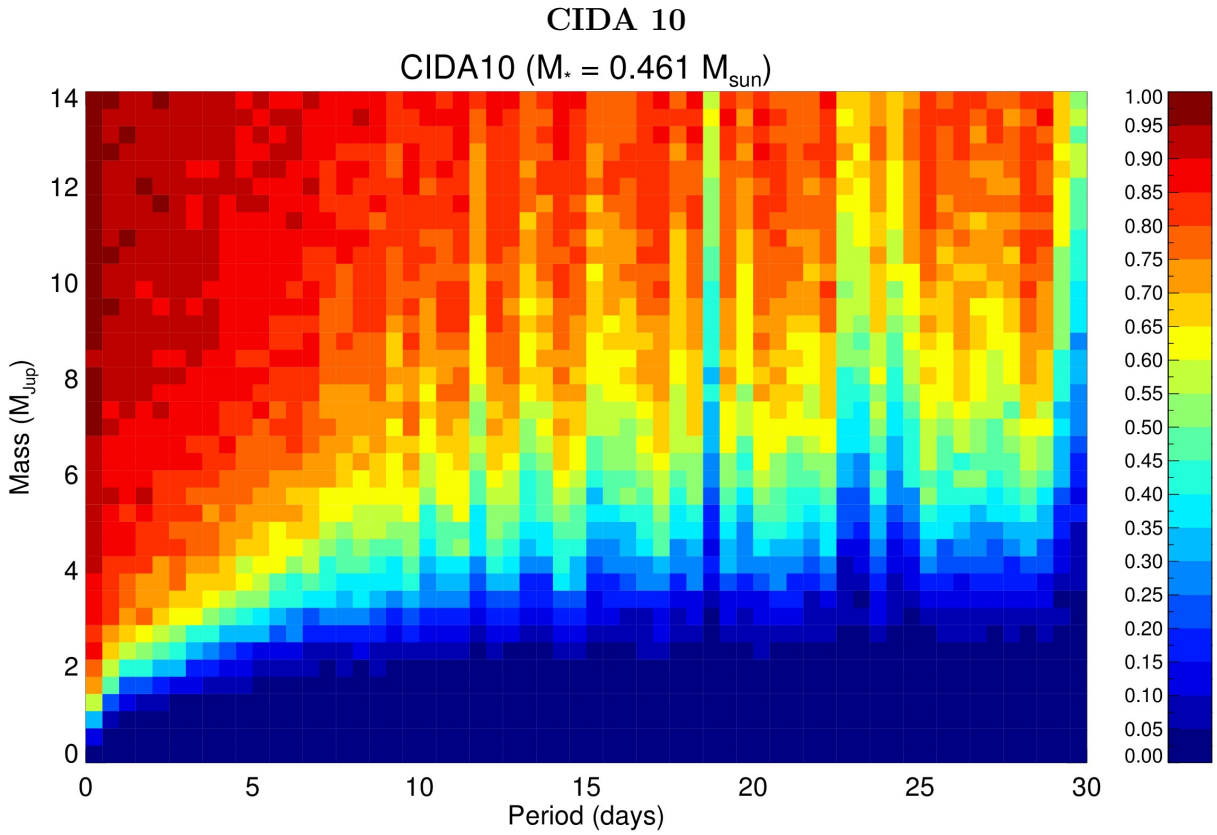

Figure 124 The detection limits are plotted for simulated planets from 0-14 M_{Jup} in 0-30 day orbital periods, with blue (0%) to maroon (100%).

A.1 Upper Scorpius

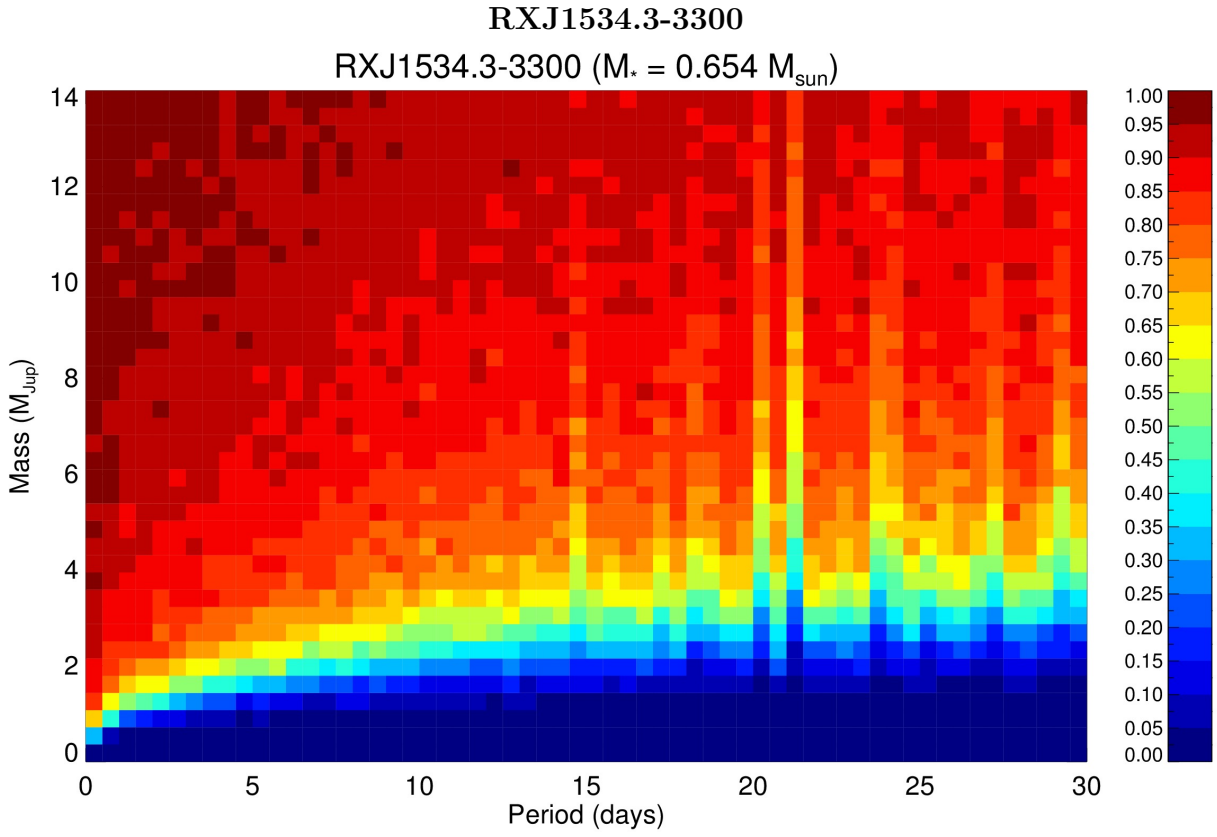

Figure 125 The detection limits are plotted for simulated planets from 0-14 M_{Jup} in 0-30 day orbital periods, with blue (0%) to maroon (100%).

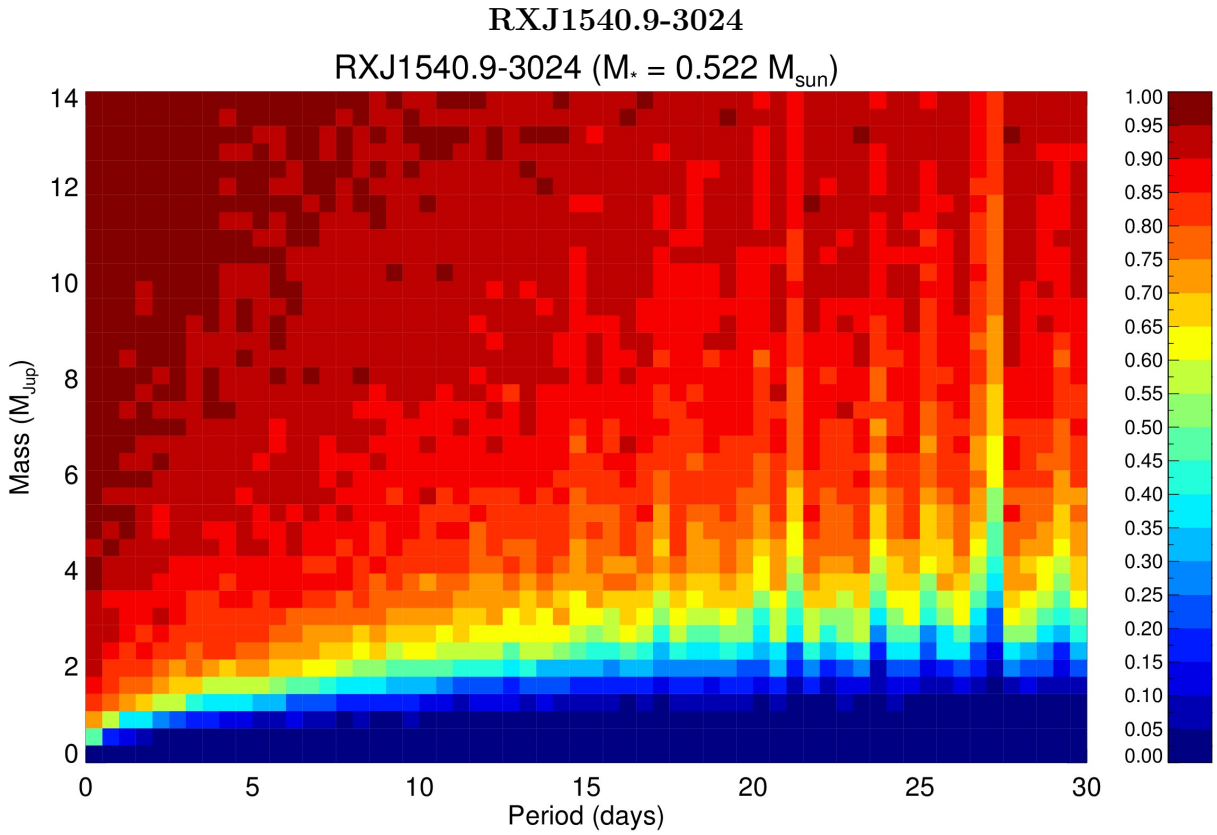

Figure 126 The detection limits are plotted for simulated planets from 0-14 M_{Jup} in 0-30 day orbital periods, with blue (0%) to maroon (100%).

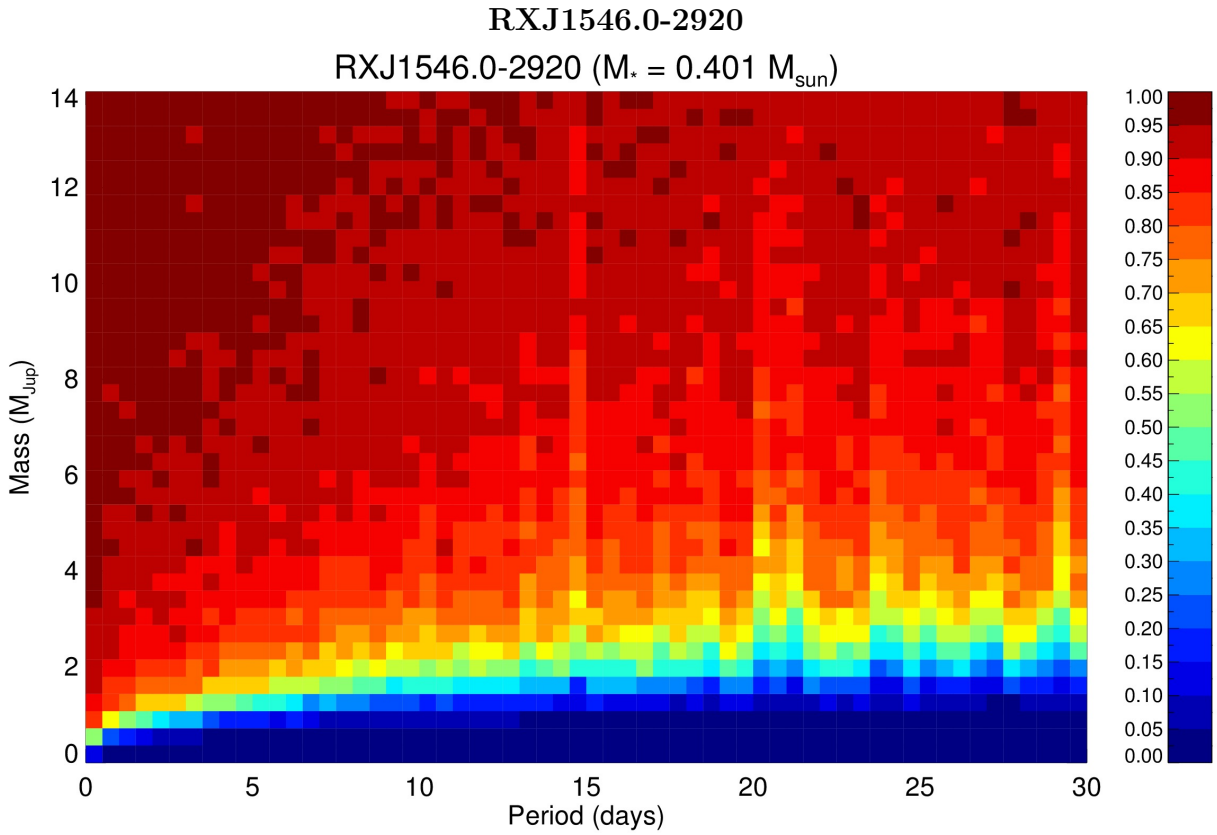

Figure 127 The detection limits are plotted for simulated planets from 0-14 M_{Jup} in 0-30 day orbital periods, with blue (0%) to maroon (100%).

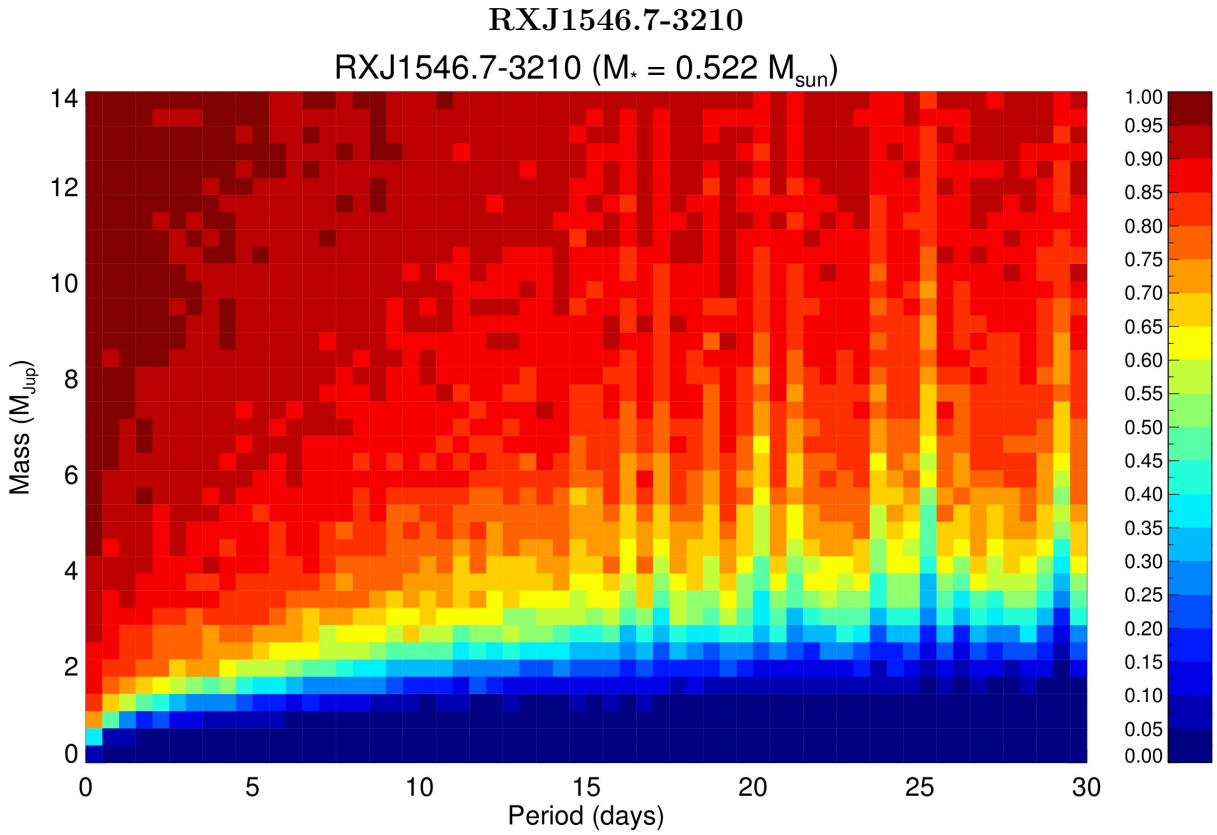

Figure 128 The detection limits are plotted for simulated planets from 0-14 M_{Jup} in 0-30 day orbital periods, with blue (0%) to maroon (100%).

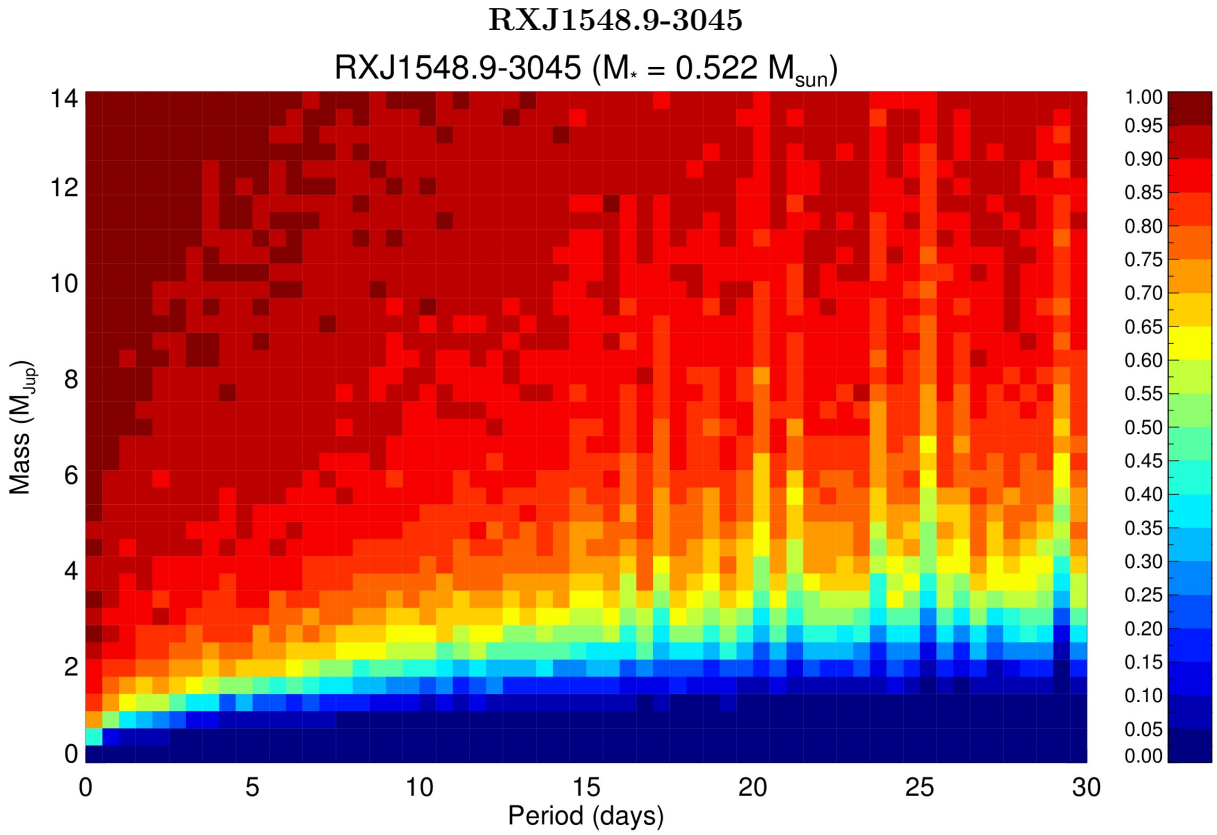

Figure 129 The detection limits are plotted for simulated planets from 0-14 M_{Jup} in 0-30 day orbital periods, with blue (0%) to maroon (100%).

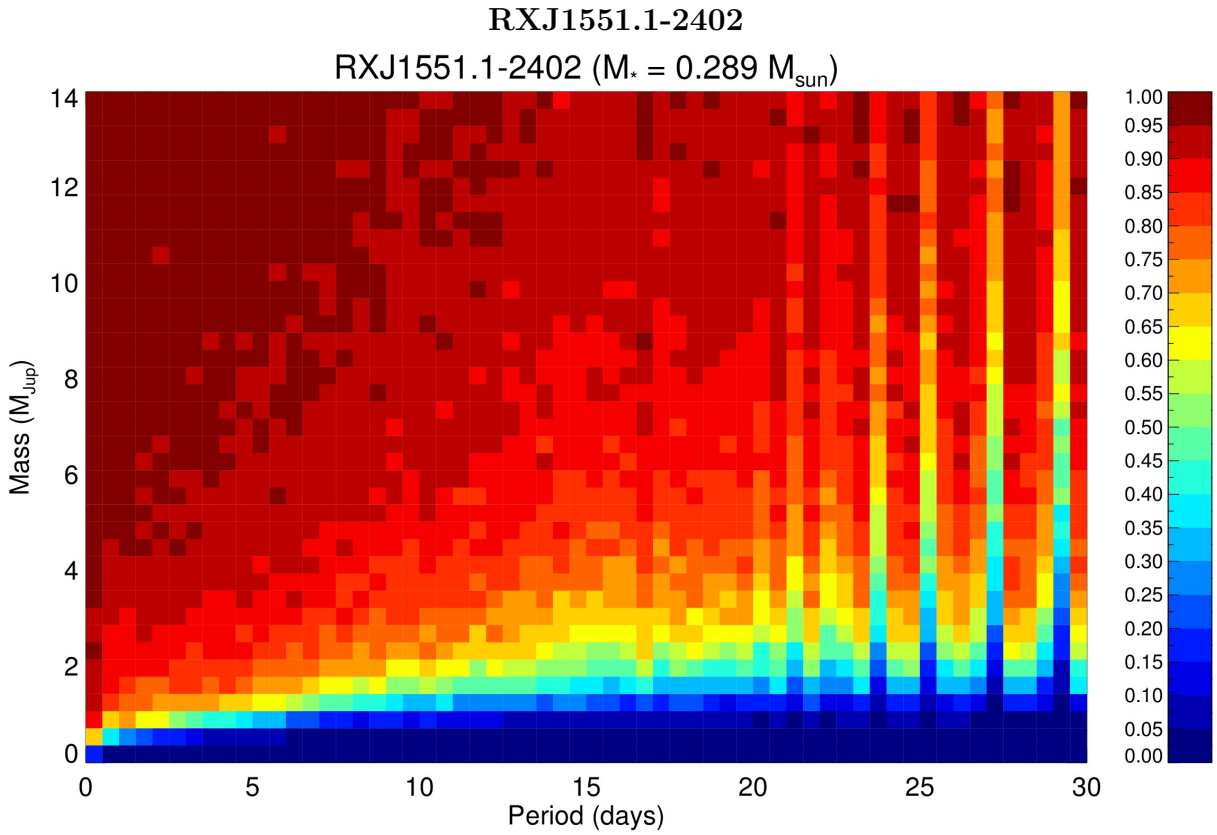

Figure 130 The detection limits are plotted for simulated planets from 0-14 M_{Jup} in 0-30 day orbital periods, with blue (0%) to maroon (100%).

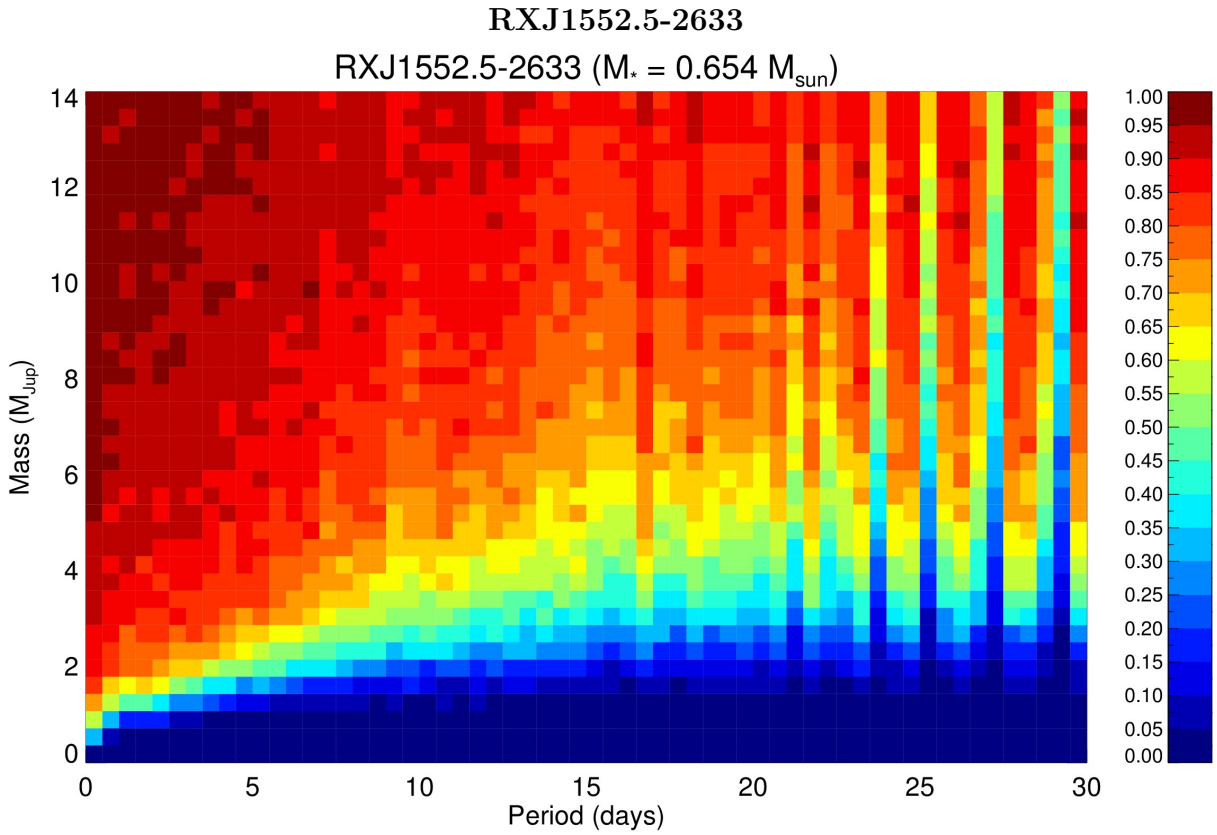

Figure 131 The detection limits are plotted for simulated planets from 0-14 M_{Jup} in 0-30 day orbital periods, with blue (0%) to maroon (100%).

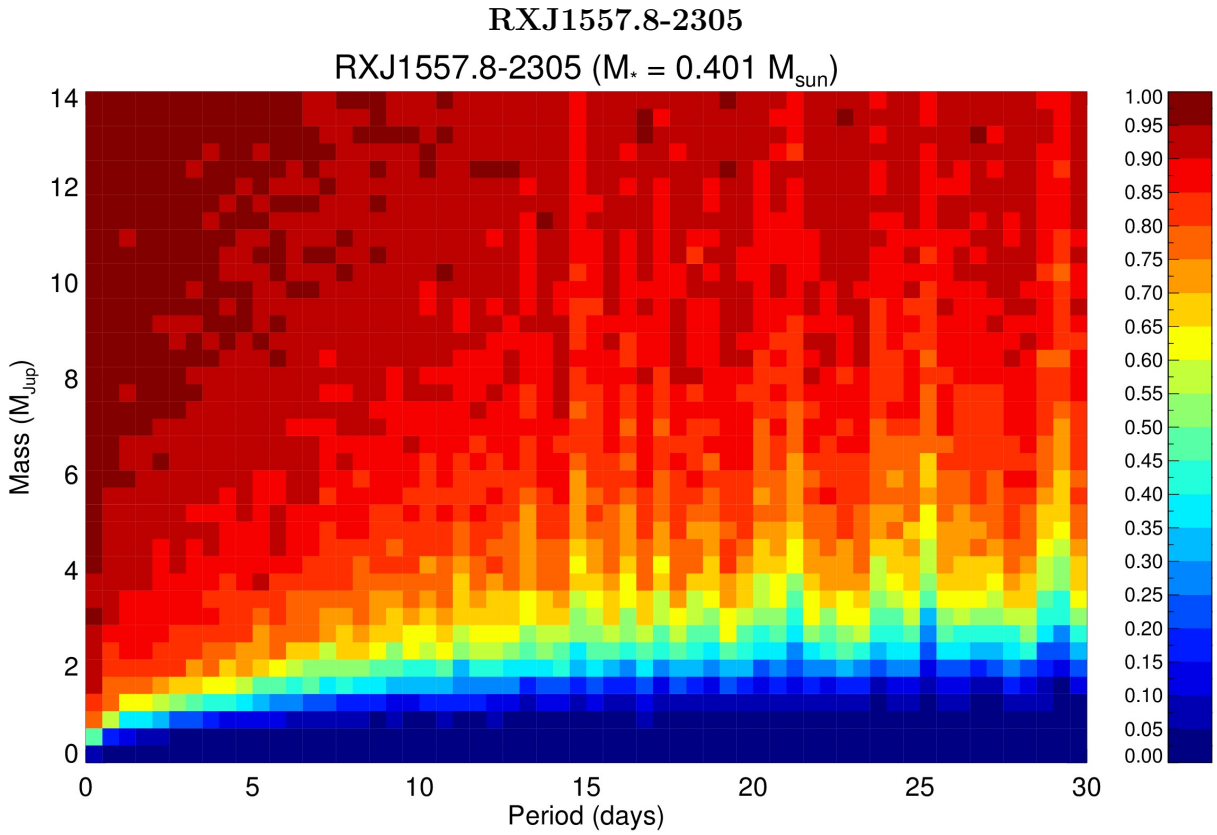

Figure 132 The detection limits are plotted for simulated planets from 0-14 M_{Jup} in 0-30 day orbital periods, with blue (0%) to maroon (100%).

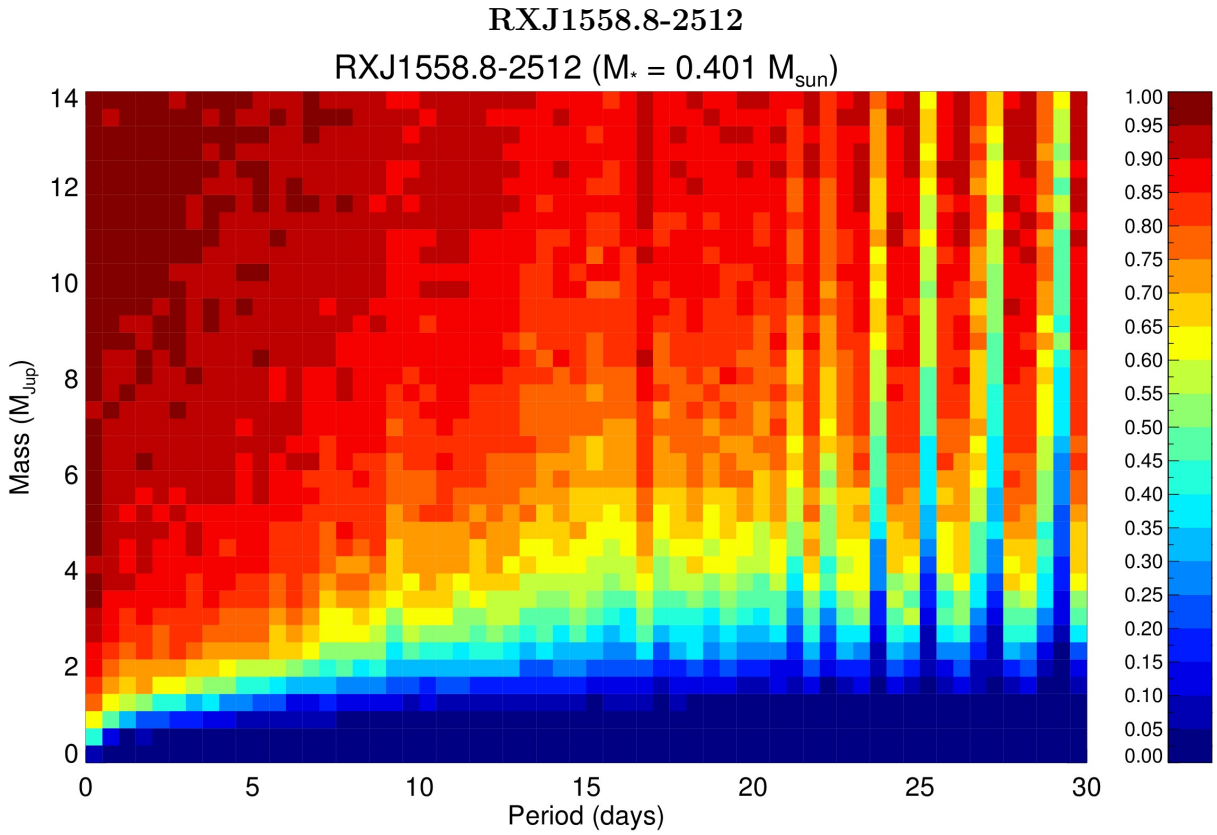

Figure 133 The detection limits are plotted for simulated planets from 0-14 M_{Jup} in 0-30 day orbital periods, with blue (0%) to maroon (100%).

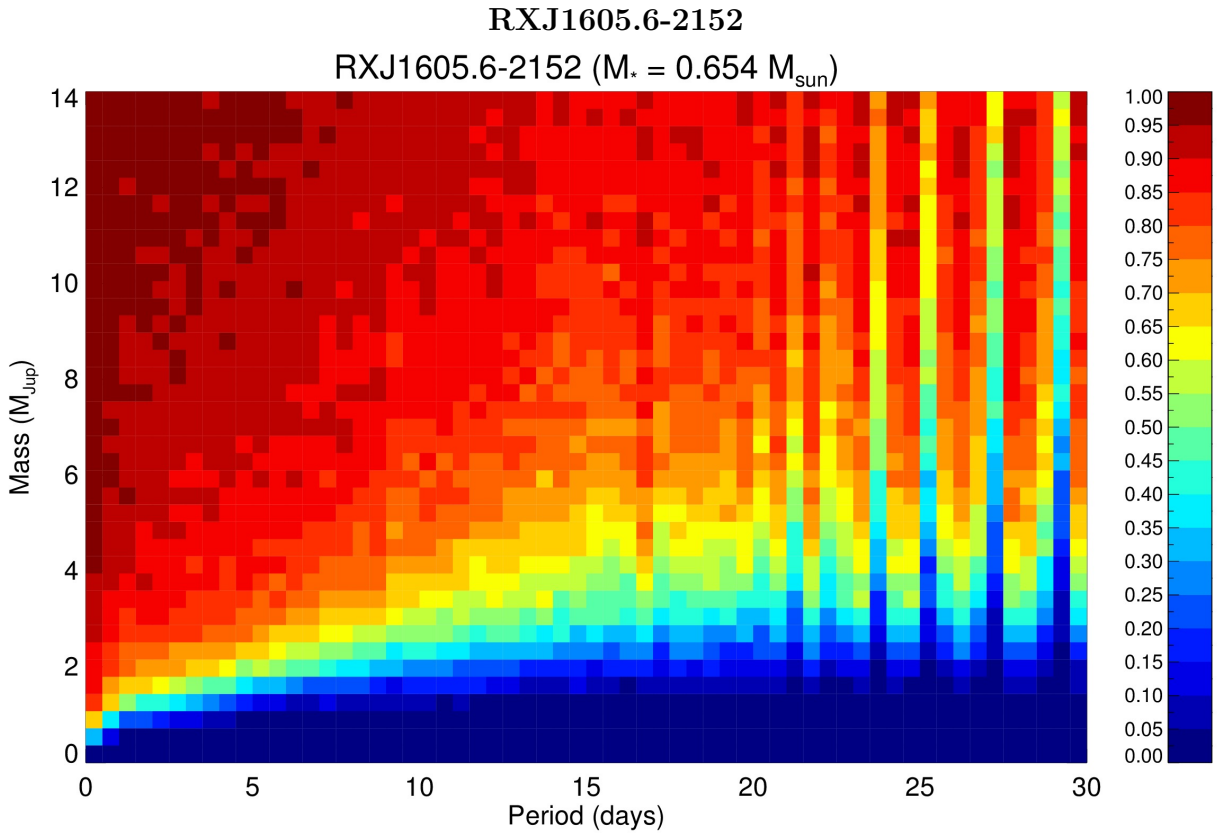

Figure 134 The detection limits are plotted for simulated planets from 0-14 M_{Jup} in 0-30 day orbital periods, with blue (0%) to maroon (100%).

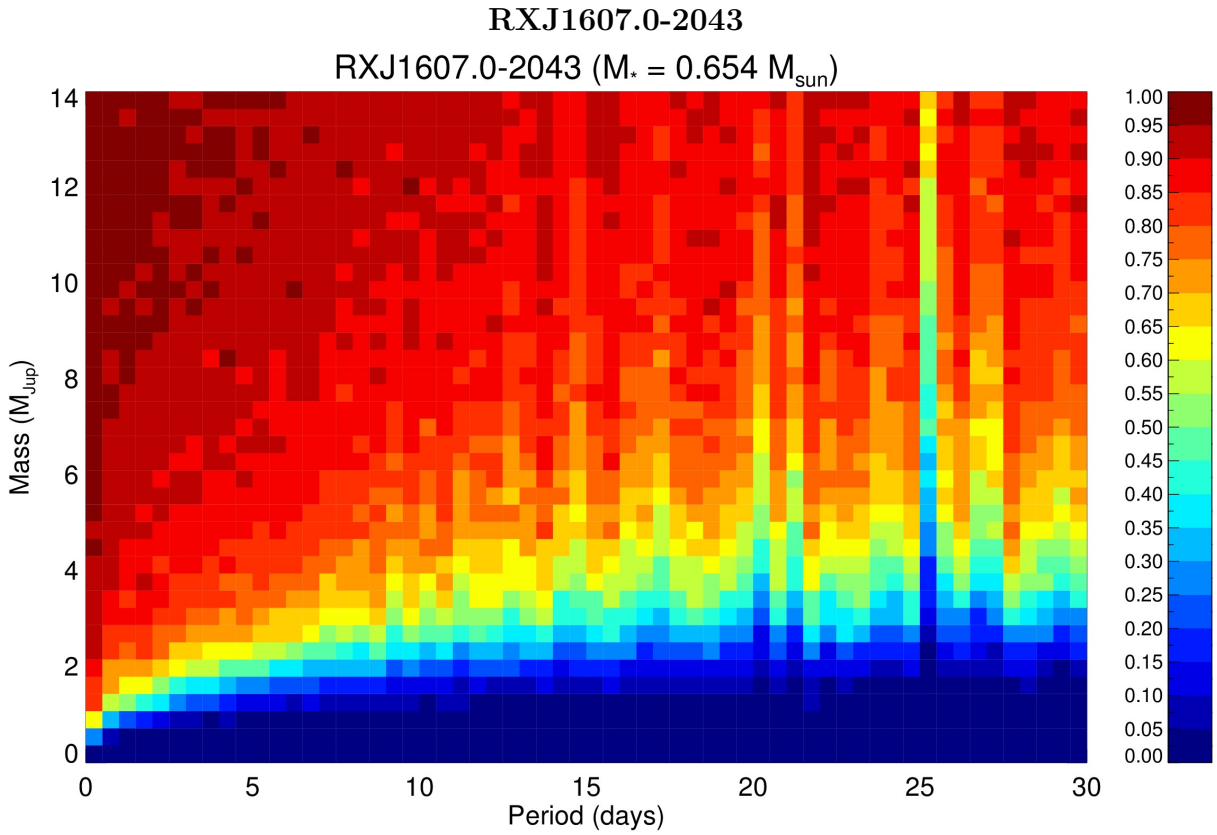

Figure 135 The detection limits are plotted for simulated planets from 0-14 M_{Jup} in 0-30 day orbital periods, with blue (0%) to maroon (100%).

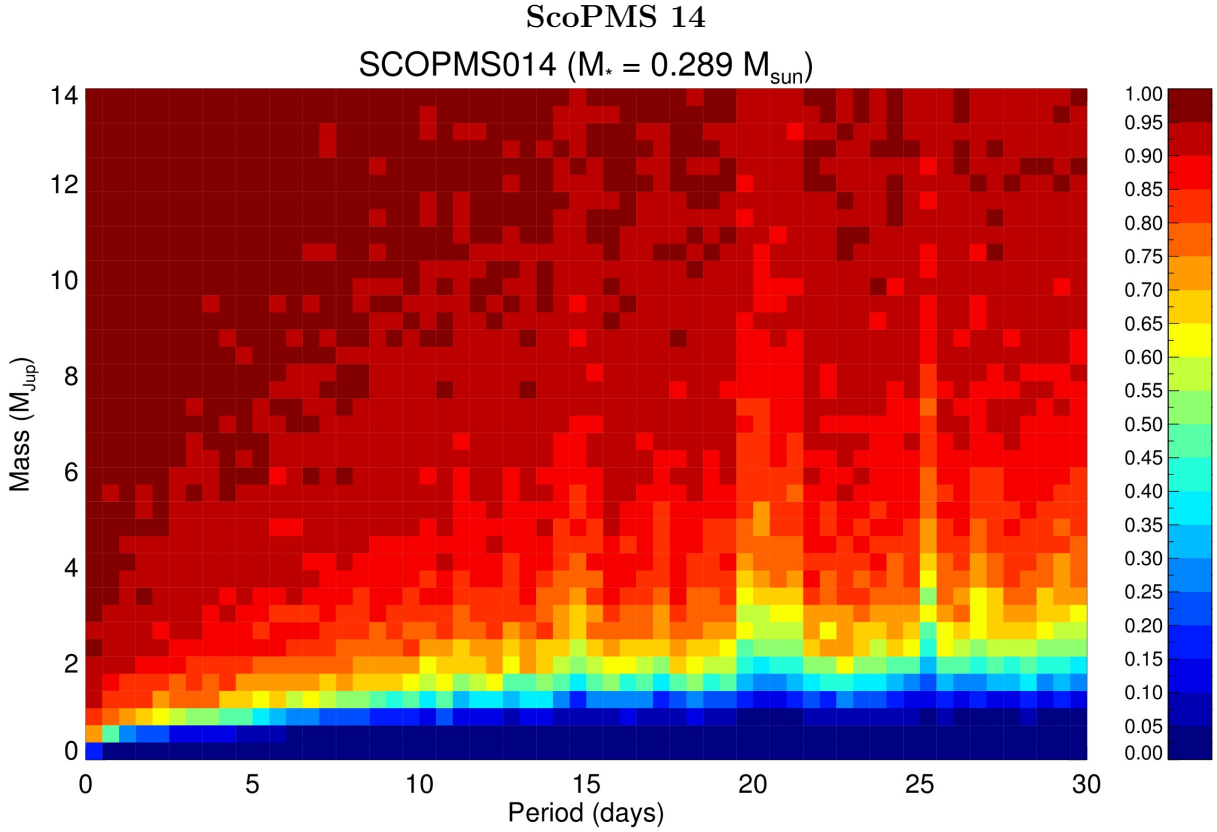

Figure 136 The detection limits are plotted for simulated planets from 0-14 M_{Jup} in 0-30 day orbital periods, with blue (0%) to maroon (100%).

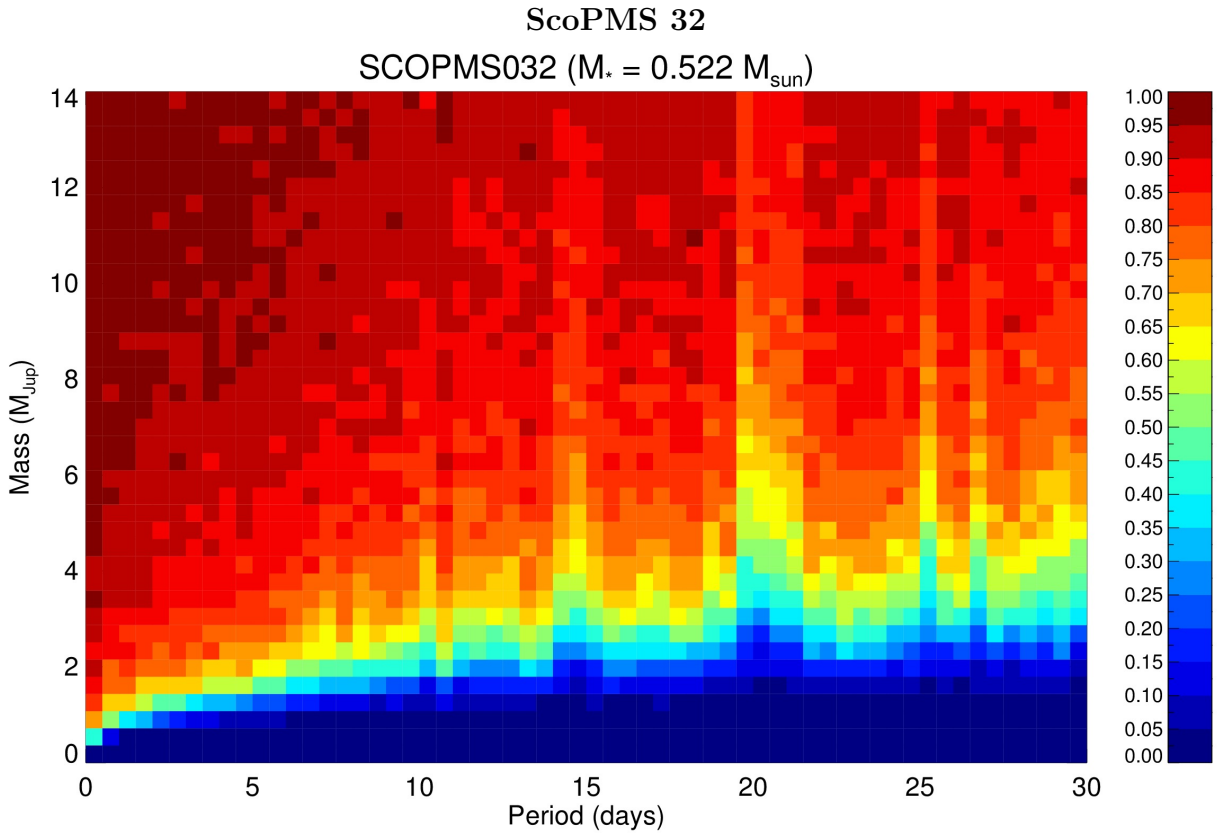

Figure 137 The detection limits are plotted for simulated planets from 0-14 M_{Jup} in 0-30 day orbital periods, with blue (0%) to maroon (100%).

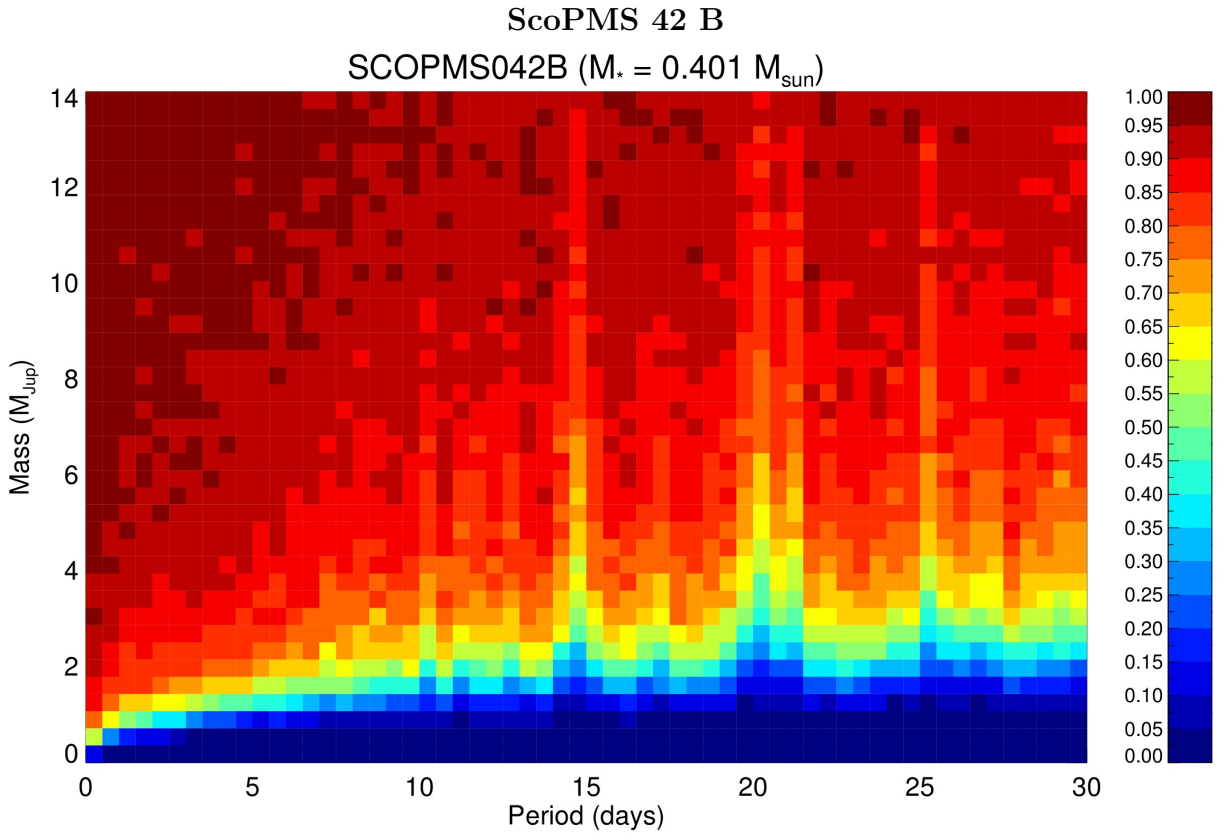

Figure 138 The detection limits are plotted for simulated planets from 0-14 M_{Jup} in 0-30 day orbital periods, with blue (0%) to maroon (100%).

A.2 Radial Velocity Standards – Keck NIRSPEC

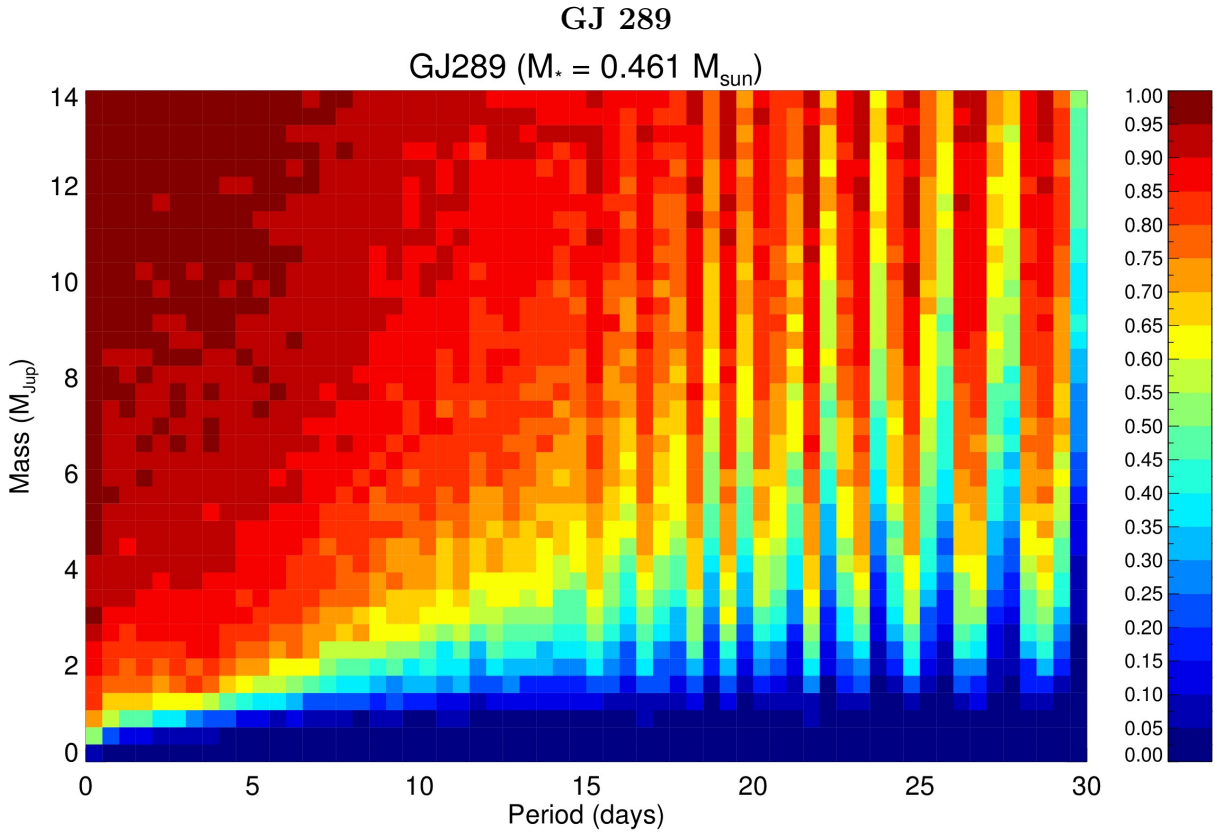

Figure 139 The detection limits are plotted for simulated planets from 0-14 M_{Jup} in 0-30 day orbital periods, with blue (0%) to maroon (100%).

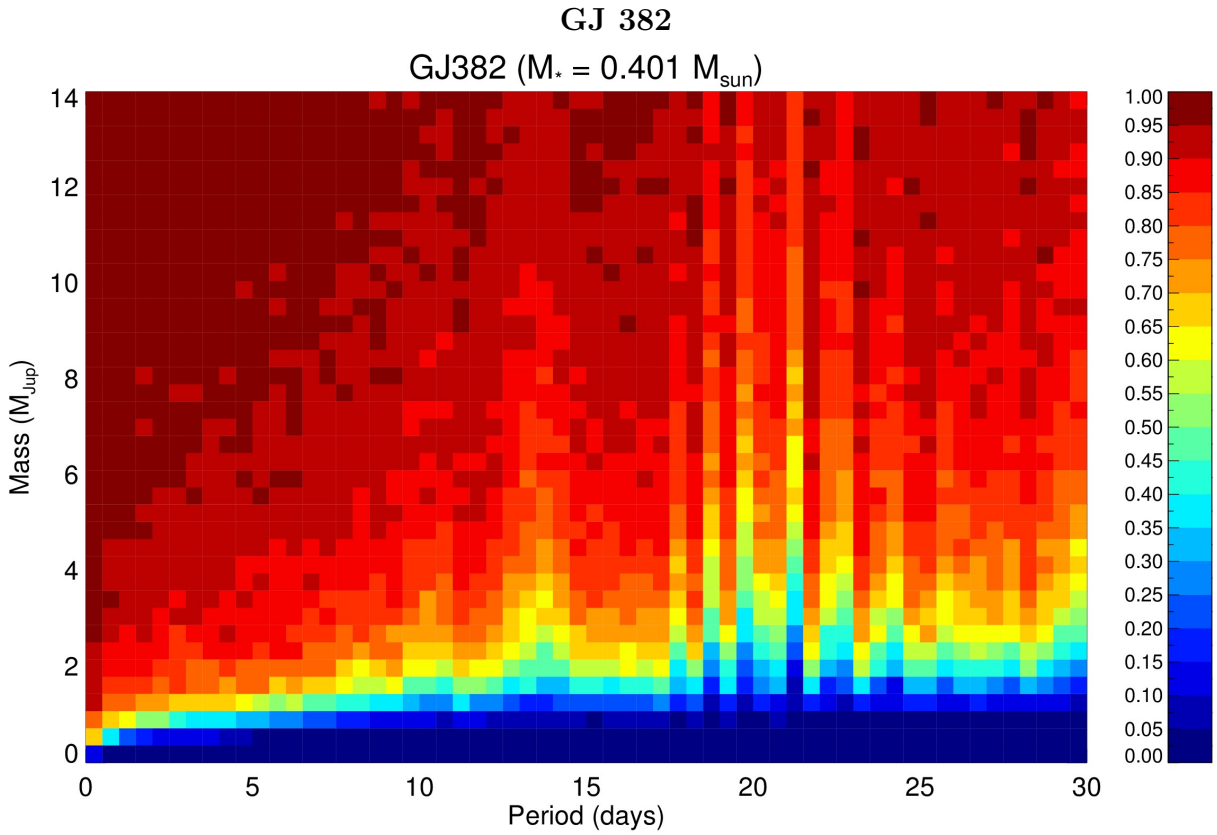

Figure 140 The detection limits are plotted for simulated planets from 0-14 M_{Jup} in 0-30 day orbital periods, with blue (0%) to maroon (100%).

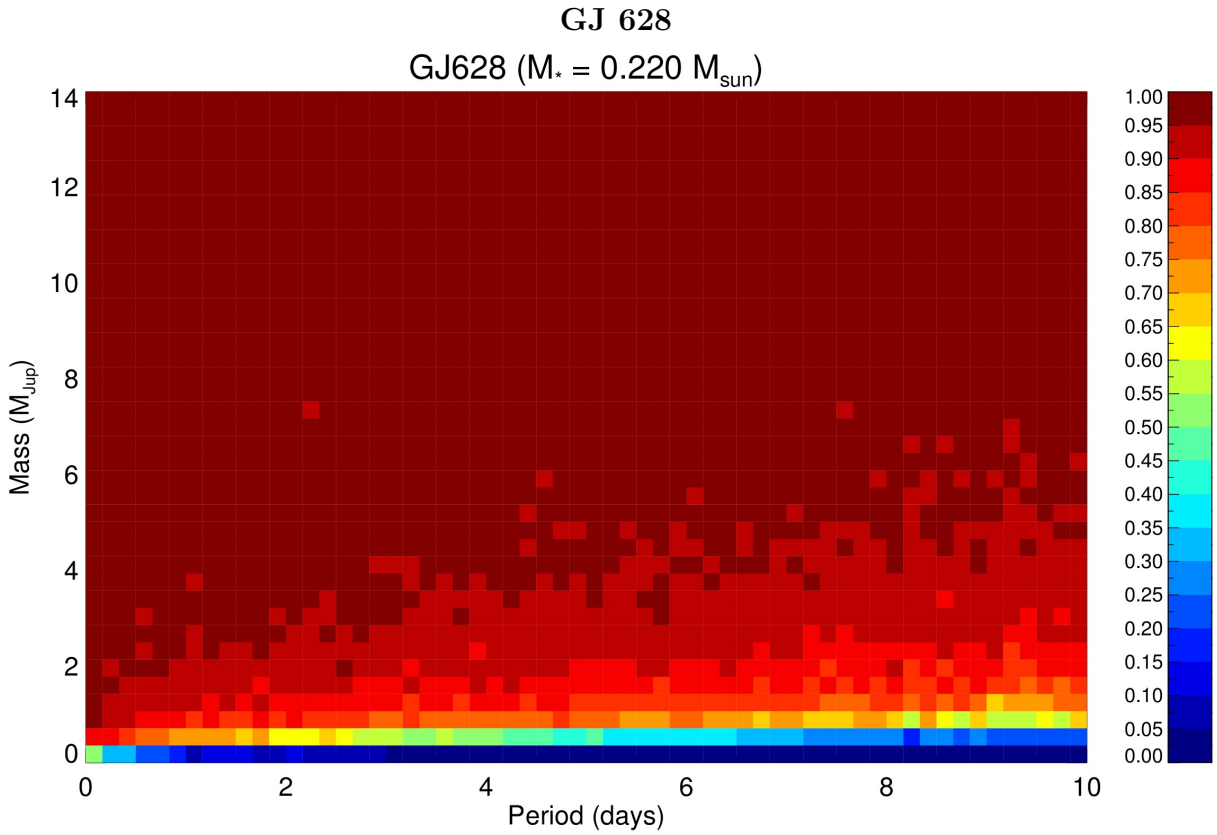

Figure 141 The detection limits are plotted for simulated planets from 0-14 M_{Jup} in 0-30 day orbital periods, with blue (0%) to maroon (100%).

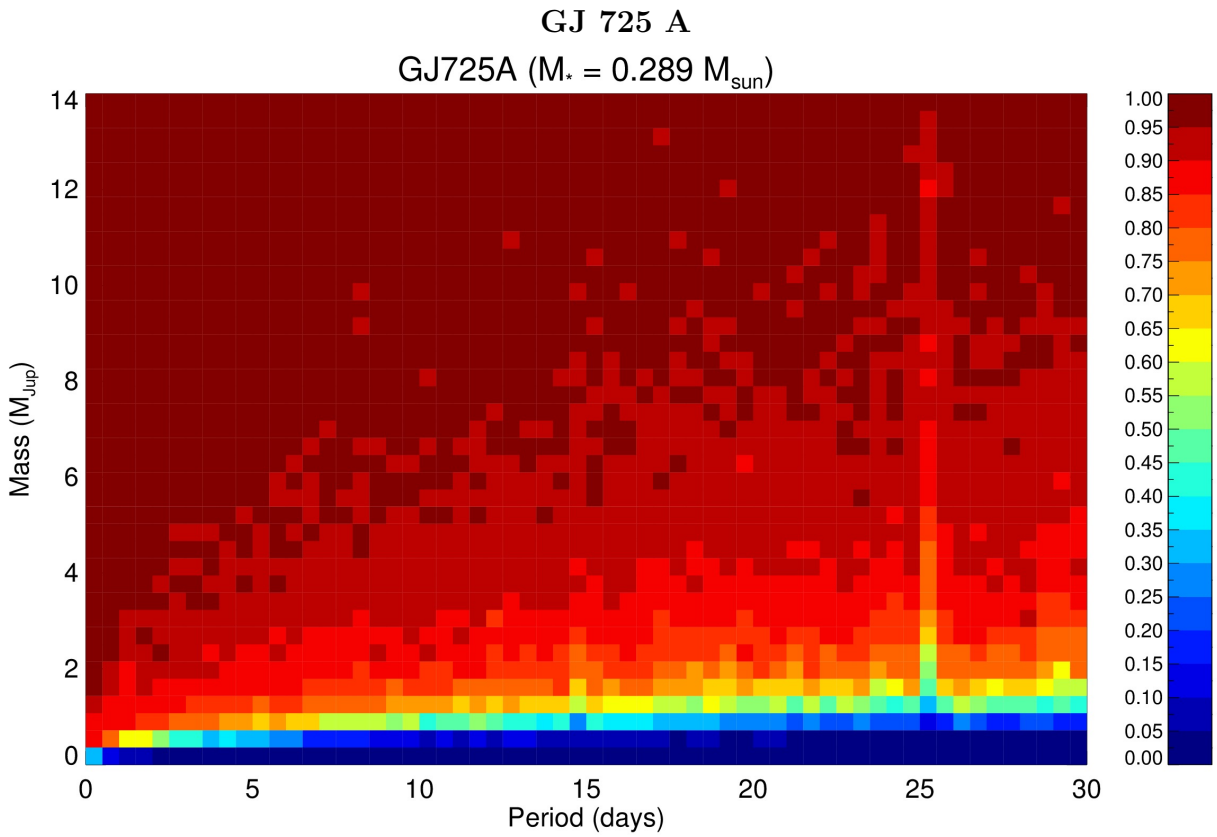

Figure 142 The detection limits are plotted for simulated planets from 0-14 M_{Jup} in 0-30 day orbital periods, with blue (0%) to maroon (100%).

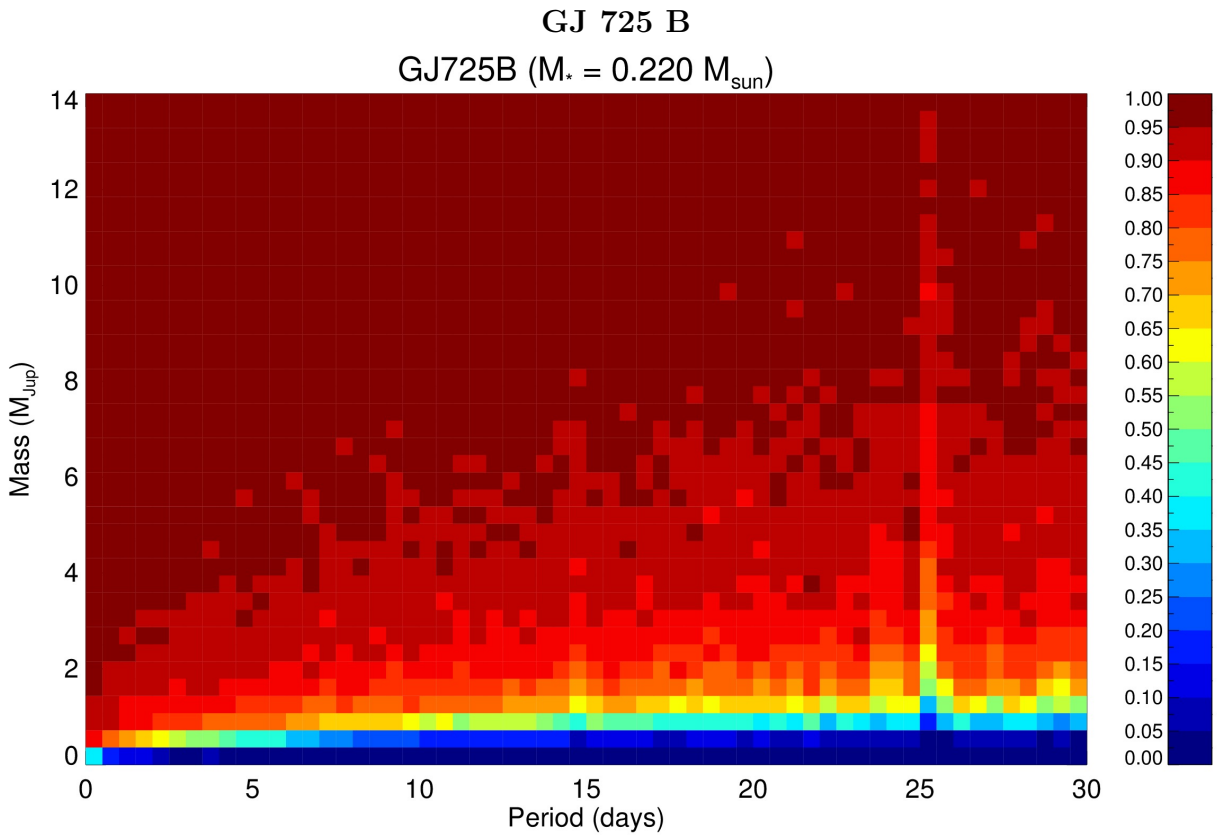

Figure 143 The detection limits are plotted for simulated planets from 0-14 M_{Jup} in 0-30 day orbital periods, with blue (0%) to maroon (100%).

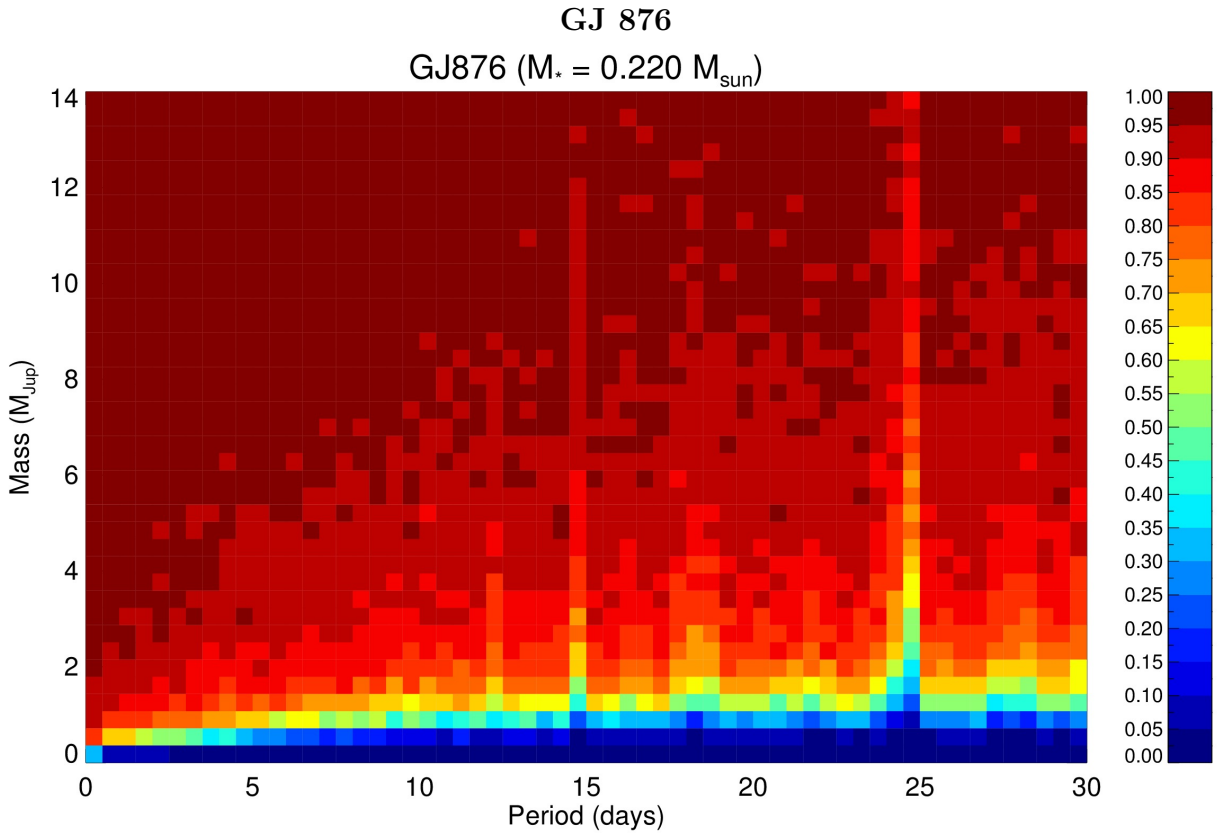

Figure 144 The detection limits are plotted for simulated planets from 0-14 M_{Jup} in 0-30 day orbital periods, with blue (0%) to maroon (100%).

REFERENCES

Absil, O. et al. 2008, A&A, 487, 1041

Adams, F. C., & Laughlin, G. 2003, Icarus, 163, 290

Adams, N. R., Walter, F. M., & Wolk, S. J. 1998, AJ, 116, 237

Albrecht, S., Winn, J. N., Butler, R. P., Crane, J. D., Shectman, S. A., Thompson, I. B., Hirano, T., & Wittenmyer, R. A. 2012, ApJ, 744, 189

Alcalá, J. M. et al. 2014, A&A, 561

Alonso, A., Arribas, S., & Martinez-Roger, C. 1995, A&A, 297, 197

Andersen, J. M., & Korhonen, H. 2015, MNRAS, 448, 3053

Andrae, R., Schulze-Hartung, T., & Melchior, P. 2010, ArXiv e-prints

Andrews, S. M., Rosenfeld, K. A., Kraus, A. L., & Wilner, D. J. 2013, ApJ, 771, 129

Anglada-Escudé, G. et al. 2012, ApJ, 751, L16

Anglada-Escudé, G., & Dawson, R. I. 2010, ArXiv e-prints

Ansdell, M. et al. 2018, MNRAS, 473, 1231

Aufdenberg, J. P. et al. 2006, ApJ, 651, 617

Bailey, J., Butler, R. P., Tinney, C. G., Jones, H. R. A., O'Toole, S., Carter, B. D., & Marcy, G. W. 2009, ApJ, 690, 743

Bailey, III, J. I., White, R. J., Blake, C. H., Charbonneau, D., Barman, T. S., Tanner, A. M., & Torres, G. 2012, ApJ, 749, 16

Baize, P. 1950, Journal des Observateurs, 33, 1

Baize, P., & Petit, M. 1989, A&AS, 77, 497

Baraffe, I., Chabrier, G., Allard, F., & Hauschildt, P. H. 1998, A&A, 337, 403

Baraffe, I., Homeier, D., Allard, F., & Chabrier, G. 2015, A&A, 577, A42

Barbieri, M., Marzari, F., & Scholl, H. 2002, A&A, 396, 219

Basri, G., & Brown, M. E. 2006, Annual Review of Earth and Planetary Sciences, 34, 193

Batten, A. H., Fletcher, J. M., & MacCarthy, D. G. 1989, Publications of the Dominion Astrophysical Observatory Victoria, 17, 1

Bean, J. L., Seifahrt, A., Hartman, H., Nilsson, H., Wiedemann, G., Reiners, A., Dreizler, S., & Henry, T. J. 2010, ApJ, 713, 410

Beaugé, C., & Nesvorný, D. 2012, ApJ, 751, 119

Bell, C. P. M., Mamajek, E. E., & Naylor, T. 2015, MNRAS, 454, 593

Benedict, G. F. et al. 1999, AJ, 118, 1086

——. 2002, ApJ, 581, L115

——. 2006, AJ, 132, 2206

Berger, D. H. et al. 2006, ApJ, 644, 475

Bergin, E. et al. 2004, ApJ, 614, L133

Bertout, C., & Genova, F. 2006, A&A, 460, 499

Bessel, M. S. 1990, A&AS, 83, 357

Bessell, M. S. 1991, AJ, 101, 662

Bessell, M. S., Castelli, F., & Plez, B. 1998, A&A, 333, 231

Biller, B. A., Kasper, M., Close, L. M., Brandner, W., & Kellner, S. 2006, ApJ, 641, L141

Biller, B. A. et al. 2013, ApJ, 777, 160

Boley, A. C., Granados Contreras, A. P., & Gladman, B. 2016, ApJ, 817, L17

Bonfils, X. et al. 2013, A&A, 549, A109

——. 2007, A&A, 474, 293

Borucki, W. J., & for the Kepler Team. 2010, ArXiv e-prints

Borucki, W. J., & Koch, D. G. 2011, in EPSC-DPS Joint Meeting 2011, 663

Bouvier, J., Covino, E., Kovo, O., Martin, E. L., Matthews, J. M., Terranegra, L., & Beck, S. C. 1995, A&A, 299, 89

Boyajian, T. S. et al. 2012, ApJ, 757, 112

Bradshaw, S. J., & Hartigan, P. 2014, ApJ, 795

Brandner, W. et al. 2000, AJ, 120, 950

Breckinridge, J. B., & Kron, G. E. 1964, PASP, 76, 139

Briceño, C., & Tokovinin, A. 2017, AJ, 154, 195

Briceno, C., Calvet, N., Gomez, M., Hartmann, L. W., Kenyon, S. J., & Whitney, B. A. 1993, PASP, 105, 686

Bryan, M. L. et al. 2016, ApJ, 821, 89

Bulger, J., Patience, J., Ward-Duong, K., Pinte, C., Bouy, H., Ménard, F., & Monin, J.-L. 2014, A&A, 570, A29

Burgasser, A. J. et al. 2000, ApJ, 531, L57

Butler, R. P., Johnson, J. A., Marcy, G. W., Wright, J. T., Vogt, S. S., & Fischer, D. A. 2006, PASP, 118, 1685

Butler, R. P., Marcy, G. W., Williams, E., McCarthy, C., Dosanjh, P., & Vogt, S. S. 1996, PASP, 108, 500

Calvet, N. et al. 2005, ApJ, 630, L185

Campbell, B., Yang, S., Irwin, A. W., & Walker, G. A. H. 1991, in Lecture Notes in Physics, Berlin Springer Verlag, Vol. 390, Bioastronomy: The Search for Extraterrestial Life — The Exploration Broadens, ed. J. Heidmann & M. J. Klein, 19–20

Carney, B. W., Latham, D. W., Stefanik, R. P., Laird, J. B., & Morse, J. A. 2003, AJ, 125, 293

Carpenter, J. M. 2001, AJ, 121, 2851

Carpenter, J. M., Mamajek, E. E., Hillenbrand, L. A., & Meyer, M. R. 2006, ApJ, 651, L49

Chatterjee, S., Ford, E. B., Matsumura, S., & Rasio, F. A. 2008, ApJ, 686, 580

Ciardi, D. R. et al. 2015, ApJ, 809, 42

Claret, A., Hauschildt, P. H., & Witte, S. 2012, A&A, 546, A14

Cohen, M. 1980, AJ, 85, 29

Cohen, M., Wheaton, W. A., & Megeath, S. T. 2003, AJ, 126, 1090

Cossou, C., Raymond, S. N., & Pierens, A. 2013, A&A, 553, L2

Costa, E., Méndez, R. A., Jao, W.-C., Henry, T. J., Subasavage, J. P., Brown, M. A., Ianna, P. A., & Bartlett, J. 2005, AJ, 130, 337

Costa, E., Méndez, R. A., Jao, W.-C., Henry, T. J., Subasavage, J. P., & Ianna, P. A. 2006, AJ, 132, 1234

Couteau, P. 1960, Bulletin Astronomique, 23, 127

Covino, E., Alcala, J. M., Allain, S., Bouvier, J., Terranegra, L., & Krautter, J. 1997, A&A, 328, 187

Crockett, C. J., Mahmud, N. I., Prato, L., Johns-Krull, C. M., Jaffe, D. T., Hartigan, P. M., & Beichman, C. A. 2012, ApJ, 761, 164

Cutri, R. M. et al. 2003, 2MASS All Sky Catalog of point sources.

Daemgen, S., Bonavita, M., Jayawardhana, R., Lafrenière, D., & Janson, M. 2015, ApJ, 799, 155

D'Alessio, P. et al. 2005, ApJ, 621, 461

David, T. J., Hillenbrand, L. A., Cody, A. M., Carpenter, J. M., & Howard, A. W. 2016, ApJ, 816, 21

de Zeeuw, P. T., Hoogerwerf, R., de Bruijne, J. H. J., Brown, A. G. A., & Blaauw, A. 1999, AJ, 117, 354

Deacon, N. R., & Hambly, N. C. 2007, A&A, 468, 163

Deacon, N. R., Hambly, N. C., Henry, T. J., Subasavage, J. P., Brown, M. A., & Jao, W.-C. 2005, AJ, 129, 409

Delfosse, X., Forveille, T., Mayor, M., Perrier, C., Naef, D., & Queloz, D. 1998, A&A, 338, L67

Delfosse, X., Forveille, T., Udry, S., Beuzit, J.-L., Mayor, M., & Perrier, C. 1999, A&A, 350, L39

Demory, B.-O. et al. 2009, A&A, 505, 205

Di Folco, E., Thévenin, F., Kervella, P., Domiciano de Souza, A., Coudé du Foresto, V.,

Ségransan, D., & Morel, P. 2004, A&A, 426, 601

Donati, J. F. et al. 2016, Nature, 534, 662

Doyle, L. R., Billingham, J., & DeVincenzi, D. L. 1998, Acta Astronautica, 42, 599

Dressing, C. D., & Charbonneau, D. 2013, ApJ, 767, 95

Drummond, J. D., Christou, J. C., & Fugate, R. Q. 1995, ApJ, 450, 380

Dubath, P., Reipurth, B., & Mayor, M. 1996, A&A, 308, 107

Ducourant, C., Teixeira, R., Galli, P. A. B., Le Campion, J. F., Krone-Martins, A., Zuckerman, B., Chauvin, G., & Song, I. 2014, A&A, 563, A121

Dumusque, X. et al. 2012, Nature, 491, 207

Dutrey, A. et al. 2008, A&A, 490, L15

Dutrey, A., Guilloteau, S., Prato, L., Simon, M., Duvert, G., Schuster, K., & Menard, F. 1998, A&A, 338, L63

Eggen, O. J. 1956, AJ, 61, 405

——. 1965, AJ, 70, 19

——. 1996, AJ, 111, 466

Eggenberger, A., Udry, S., Chauvin, G., Beuzit, J.-L., Lagrange, A.-M., Ségransan, D., & Mayor, M. 2007, A&A, 474, 273

Eisner, J. A., Hillenbrand, L. A., White, R. J., Bloom, J. S., Akeson, R. L., & Blake, C. H. 2007, ApJ, 669, 1072

Espaillat, C., Furlan, E., D'Alessio, P., Sargent, B., Nagel, E., Calvet, N., Watson, D. M., & Muzerolle, J. 2011, ApJ, 728, 49

Farrington, C. D. et al. 2010, AJ, 139, 2308

Feiden, G. A. 2016, A&A, 593, A99

Fekel, F. C. 1997, PASP, 109, 514

Ford, E. B., & Rasio, F. A. 2008, ApJ, 686, 621

Forveille, T. et al. 1999, A&A, 351, 619

——. 2009, A&A, 493, 645

Fressin, F. et al. 2013, ApJ, 766, 81

Fuhrmann, K., Pfeiffer, M., Frank, C., Reetz, J., & Gehren, T. 1997, A&A, 323, 909

Gatewood, G. 1989, AJ, 97, 1189

——. 1994, PASP, 106, 138

Gatewood, G., Stein, J., de Jonge, J. K., Persinger, T., Reiland, T., & Stephenson, B. 1992, AJ, 104, 1237

Gatewood, G. D., & Gatewood, C. V. 1978, ApJ, 225, 191

Georgakarakos, N., Eggl, S., & Dobbs-Dixon, I. 2018, ApJ, 856, 155

Glass, I. S. 1975, MNRAS, 171, 19P

Gliese, W., & Jahreiß, H. 1991, Preliminary Version of the Third Catalogue of Nearby Stars, Tech. rep.

Goldreich, P., & Tremaine, S. 1980, ApJ, 241, 425

Golimowski, D. A., Henry, T. J., Krist, J. E., Schroeder, D. J., Marcy, G. W., Fischer, D. A., & Butler, R. P. 2000, AJ, 120, 2082

Gould, A. 2003, AJ, 126, 472

Gräfe, C., Wolf, S., Roccatagliata, V., Sauter, J., & Ertel, S. 2011, A&A, 533, A89

Gray, R. O., Corbally, C. J., Garrison, R. F., McFadden, M. T., Bubar, E. J., McGahee, C. E., O'Donoghue, A. A., & Knox, E. R. 2006, AJ, 132, 161

Gray, R. O., Napier, M. G., & Winkler, L. I. 2001, AJ, 121, 2148

Greenberg, R. 2010, Astrobiology, 10, 275

Gregory, P. C. 2011, MNRAS, 415, 2523

Guillochon, J., Ramirez-Ruiz, E., & Lin, D. 2011, ApJ, 732, 74

Hale, A. 1994, AJ, 107, 306

Han, I., & Gatewood, G. 2002, PASP, 114, 224

Hansen, B. M. S., & Murray, N. 2012, ApJ, 751, 158

Hartkopf, W. I., Mason, B. D., Finch, C. T., Zacharias, N., Wycoff, G. L., & Hsu, D. 2013, AJ, 146, 76

Hartman, J. D., Bakos, G. Á., Noyes, R. W., Sipőcz, B., Kovács, G., Mazeh, T., Shporer, A., & Pál, A. 2011, AJ, 141, 166

Hauschildt, P. H., Allard, F., Ferguson, J., Baron, E., & Alexander, D. R. 1999, ApJ, 525, 871

Heintz, W. D. 1974, AJ, 79, 819

——. 1986, AJ, 92, 446

——. 1987, PASP, 99, 1084

——. 1994, AJ, 108, 2338

——. 1996, AJ, 111, 412

Henry, T. J. 2010, Royal Astronomical Society of Canada Observer's Handbook 2010.

——. 2012, Royal Astronomical Society of Canada Observer's Handbook 2012.

Henry, T. J., Franz, O. G., Wasserman, L. H., Benedict, G. F., Shelus, P. J., Ianna, P. A., Kirkpatrick, J. D., & McCarthy, Donald W., J. 1999, ApJ, 512, 864

Henry, T. J., Ianna, P. A., Kirkpatrick, J. D., & Jahreiss, H. 1997, AJ, 114

Henry, T. J., Jao, W.-C., Subasavage, J. P., Beaulieu, T. D., Ianna, P. A., Costa, E., & Méndez, R. A. 2006, AJ, 132, 2360

Henry, T. J., Kirkpatrick, J. D., & Simons, D. A. 1994, AJ, 108, 1437

Henry, T. J., & McCarthy, Jr., D. W. 1993, AJ, 106, 773

Henry, T. J., Subasavage, J. P., Brown, M. A., Beaulieu, T. D., Jao, W.-C., & Hambly, N. C. 2004, AJ, 128, 2460

Henry, T. J., Walkowicz, L. M., Barto, T. C., & Golimowski, D. A. 2002a, AJ, 123, 2002

——. 2002b, AJ, 123, 2002

Herbig, G. H. 1977, ApJ, 214, 747

Herbig, G. H., Vrba, F. J., & Rydgren, A. E. 1986, AJ, 91, 575

Hillenbrand, L. A., & White, R. J. 2004, ApJ, 604, 741

Hinkle, K. H., Cuberly, R. W., Gaughan, N. A., Heynssens, J. B., Joyce, R. R., Ridgway, S. T., Schmitt, P., & Simmons, J. E. 1998, in Proc. SPIE, Vol. 3354, Infrared Astronomical Instrumentation, ed. A. M. Fowler, 810–821

Hinkle, K. H., Joyce, R. R., Sharp, N., & Valenti, J. A. 2000, in Proc. SPIE, Vol. 4008, Optical and IR Telescope Instrumentation and Detectors, ed. M. Iye & A. F. Moorwood,

720–728

Hoffman, D. I., Harrison, T. E., & McNamara, B. J. 2009, AJ, 138, 466

Høg, E. et al. 2000, A&A, 355, L27

Horne, K. 1986, PASP, 98, 609

Houdebine, E. R. 2010, MNRAS, 407, 1657

Howard, A. W. et al. 2011, ApJ, 730, 10

——. 2012, ApJS, 201, 15

——. 2014, ApJ, 794, 51

Huang, S.-S. 1959, PASP, 71, 421

Hughes, J., Hartigan, P., Krautter, J., & Kelemen, J. 1994, AJ, 108, 1071

Ireland, M. J., & Kraus, A. L. 2008, ApJ, 678, L59

Irwin, A. W., Fletcher, J. M., Yang, S. L. S., Walker, G. A. H., & Goodenough, C. 1992, PASP, 104, 489

Irwin, A. W., Yang, S. L. S., & Walker, G. A. H. 1996, PASP, 108, 580

Itoh, Y. et al. 2005, ApJ, 620, 984

James, D. J., Melo, C., Santos, N. C., & Bouvier, J. 2006, A&A, 446, 971

Jao, W.-C., Henry, T. J., Beaulieu, T. D., & Subasavage, J. P. 2008, AJ, 136, 840

Jao, W.-C., Henry, T. J., Subasavage, J. P., Brown, M. A., Ianna, P. A., Bartlett, J. L., Costa, E., & Méndez, R. A. 2005, AJ, 129, 1954

Jayawardhana, R., Coffey, J., Scholz, A., Brandeker, A., & van Kerkwijk, M. H. 2006, ApJ, 648, 1206

Jenkins, J. S., Ramsey, L. W., Jones, H. R. A., Pavlenko, Y., Gallardo, J., Barnes, J. R., & Pinfield, D. J. 2009, ApJ, 704, 975

Johns-Krull, C. M. et al. 2016, ApJ, 826, 206

Johns-Krull, C. M., Valenti, J. A., & Koresko, C. 1999, ApJ, 516, 900

Johns-Krull, C. M., Valenti, J. A., & Saar, S. H. 2004, ApJ, 617, 1204

Johnson, H. L., MacArthur, J. W., & Mitchell, R. I. 1968, ApJ, 152, 465

Johnson, H. L., Mitchell, R. I., Iriarte, B., & Wisniewski, W. Z. 1966, Communications of the Lunar and Planetary Laboratory, 4, 99

Johnson, H. L., & Morgan, W. W. 1953, ApJ, 117, 313

Johnson, J. A. et al. 2010, PASP, 122, 149

Joy, A. H. 1945, ApJ, 102, 168

Kaeufl, H.-U. et al. 2004, in Proc. SPIE, Vol. 5492, Ground-based Instrumentation for Astronomy, ed. A. F. M. Moorwood & M. Iye, 1218–1227

Kalas, P. et al. 2008, Science, 322, 1345

Kaltenegger, L., Fridlund, M., & Kasting, J. 2002, in ESA Special Publication, Vol. 514, Earth-like Planets and Moons, ed. B. H. Foing & B. Battrick, 277–282

Kant, I. 1755, Allgemeine Naturgeschichte und Theorie des Himmels

Kasting, J. F. 1996, Ap&SS, 241, 3

Kasting, J. F., Whitmire, D. P., & Reynolds, R. T. 1993, Icarus, 101, 108

Kenyon, S. J., & Hartmann, L. 1995, ApJS, 101, 117

Kervella, P. et al. 2008, A&A, 488, 667

Kervella, P., Thévenin, F., Morel, P., Berthomieu, G., Provost, J., Bordé, P., & Ségransan, D. 2003a, in IAU Joint Discussion, Vol. 12, IAU Joint Discussion

Kervella, P., Thévenin, F., Morel, P., Bordé, P., & Di Folco, E. 2003b, A&A, 408, 681

Kidder, K. M., Holberg, J. B., & Mason, P. A. 1991, AJ, 101, 579

Kiraga, M. 2012, Acta Astronomica, 62, 67

Kirkpatrick, J. D., Henry, T. J., & McCarthy, Jr., D. W. 1991, ApJS, 77, 417

Koerner, D. W., Sargent, A. I., & Beckwith, S. V. W. 1993, Icarus, 106, 2

Köhler, R., Kunkel, M., Leinert, C., & Zinnecker, H. 2000, A&A, 356, 541

Köhler, R., Neuhäuser, R., Krämer, S., Leinert, C., Ott, T., & Eckart, A. 2008, A&A, 488, 997

Korhonen, H., Andersen, J. M., Piskunov, N., Hackman, T., Juncher, D., Järvinen, S. P., & Jørgensen, U. G. 2015, MNRAS, 448, 3038

Kraus, A. L., & Hillenbrand, L. A. 2007a, ApJ, 662, 413

——. 2007b, AJ, 134, 2340

——. 2009, ApJ, 704, 531

Kraus, A. L., Ireland, M. J., Martinache, F., & Lloyd, J. P. 2008, ApJ, 679, 762

Kraus, A. L., Shkolnik, E. L., Allers, K. N., & Liu, M. C. 2014, AJ, 147, 146

Lafrenière, D., Jayawardhana, R., van Kerkwijk, M. H., Brandeker, A., & Janson, M. 2014, ApJ, 785, 47

Lagrange, A.-M., Meunier, N., Chauvin, G., Sterzik, M., Galland, F., Lo Curto, G., Rameau, J., & Sosnowska, D. 2013, A&A, 559, A83

Landolt, A. U. 1992, AJ, 104, 372

Lannier, J. et al. 2016, A&A, 596, A83

Lee, J. W., Kim, S.-L., Kim, C.-H., Koch, R. H., Lee, C.-U., Kim, H.-I., & Park, J.-H. 2009, AJ, 137, 3181

Leggett, S. K. 1992, ApJS, 82, 351

Leinert, C., Haas, M., Allard, F., Wehrse, R., McCarthy, D. W., Jahreiss, H., & Perrier, C. 1990, A&A, 236, 399

Lépine, S., Hilton, E. J., Mann, A. W., Wilde, M., Rojas-Ayala, B., Cruz, K. L., & Gaidos, E. 2013, AJ, 145, 102

Lépine, S., & Shara, M. M. 2005, AJ, 129, 1483

Lépine, S., & Simon, M. 2009, AJ, 137, 3632

Lin, D. N. C., Bodenheimer, P., & Richardson, D. C. 1996, Nature, 380, 606

Lissauer, J. J. 1993, ARA&A, 31, 129

Livingston, W., & Wallace, L. 1991, An atlas of the solar spectrum in the infrared from 1850 to 9000 cm-1 (1.1 to 5.4 micrometer)

Lopez Martí, B., Jimenez Esteban, F., Bayo, A., Barrado, D., Solano, E., & Rodrigo, C. 2013, A&A, 551, A46

Lowell, P. 1895, Popular Astronomy, 2, 255

Luhman, K. L., Briceño, C., Stauffer, J. R., Hartmann, L., Barrado y Navascués, D., & Caldwell, N. 2003, ApJ, 590, 348

Luhman, K. L., & Steeghs, D. 2004, ApJ, 609, 917

Luhman, K. L. et al. 2006, ApJ, 649, 894

Lutz, T. E. 1971, PASP, 83, 488

Luyten, W. J. 1957, A catalogue of 9867 stars in the Southern Hemisphere with proper motions exceeding 0.“2 annually.

Mahmud, N. I., Crockett, C. J., Johns-Krull, C. M., Prato, L., Hartigan, P. M., Jaffe, D. T., & Beichman, C. A. 2011, ApJ, 736

Malin, M. C., & Edgett, K. S. 2000, Science, 288, 2330

Malo, L., Artigau, É., Doyon, R., Lafrenière, D., Albert, L., & Gagné, J. 2014, ApJ, 788

Mann, A. W. et al. 2016, AJ, 152, 61

Marchwinski, R. C., Mahadevan, S., Robertson, P., Ramsey, L., & Harder, J. 2015, ApJ, 798, 63

Marcy, G. W., Butler, R. P., Fischer, D., Vogt, S. S., Lissauer, J. J., & Rivera, E. J. 2001, ApJ, 556, 296

Marcy, G. W., Butler, R. P., Vogt, S. S., Fischer, D., & Lissauer, J. J. 1998, ApJ, 505, L147

Marilli, E. et al. 2007, A&A, 463, 1081

Marion, G. M., Fritsen, C. H., Eicken, H., & Payne, M. C. 2003, Astrobiology, 3, 785

Mason, B. D., McAlister, H. A., Hartkopf, W. I., & Shara, M. M. 1995, AJ, 109, 332

Mayor, M. et al. 2009, A&A, 507, 487

Mayor, M., & Queloz, D. 1995, Nature, 378, 355

McCarthy, K., & White, R. J. 2012, AJ, 143, 134

McCaughrean, M. J., Close, L. M., Scholz, R.-D., Lenzen, R., Biller, B., Brandner, W.,

Hartung, M., & Lodieu, N. 2004, A&A, 413, 1029

McLean, I. S. et al. 1998, in Proc. SPIE, Vol. 3354, Infrared Astronomical Instrumentation, ed. A. M. Fowler, 566–578

Melo, C. H. F. 2003, A&A, 410, 269

Mentuch, E., Brandeker, A., van Kerkwijk, M. H., Jayawardhana, R., & Hauschildt, P. H. 2008, ApJ, 689, 1127

Mermilliod, J.-C. 1986, Catalogue of Eggen's UBV data., 0 (1986)

Messina, S., Desidera, S., Lanzafame, A. C., Turatto, M., & Guinan, E. F. 2011, A&A, 532, A10

Messina, S., Desidera, S., Turatto, M., Lanzafame, A. C., & Guinan, E. F. 2010, A&A, 520

Monet, D. G. et al. 2003, AJ, 125, 984

Monnier, J. D. et al. 2007, Science, 317, 342

Montes, D., López-Santiago, J., Gálvez, M. C., Fernández-Figueroa, M. J., De Castro, E., & Cornide, M. 2001, MNRAS, 328, 45

Montes, D., Ramsey, L. W., & Welty, A. D. 1999, ApJS, 123, 283

Mould, J. R., & Hyland, A. R. 1976, ApJ, 208, 399

Moulds, V. E., Watson, C. A., Bonfils, X., Littlefair, S. P., & Simpson, E. K. 2013, MNRAS, 430, 1709

Nagasawa, M., Ida, S., & Bessho, T. 2008, ApJ, 678, 498

Neuhäuser, R. et al. 2000, A&AS, 146, 323

Nguyen, D. C., Brandeker, A., van Kerkwijk, M. H., & Jayawardhana, R. 2012, ApJ, 745,

119

Nidever, D. L., Marcy, G. W., Butler, R. P., Fischer, D. A., & Vogt, S. S. 2002, ApJS, 141, 503

O'Connor, C. E., & Hansen, B. M. S. 2018, MNRAS, 477, 175

Oja, T. 1984, A&AS, 57, 357

——. 1993, A&AS, 100, 591

Parkinson, C. D., Liang, M.-C., Hartman, H., Hansen, C. J., Tinetti, G., Meadows, V., Kirschvink, J. L., & Yung, Y. L. 2007, A&A, 463, 353

Pasquini, L., Liu, Q., & Pallavicini, R. 1994, A&A, 287, 191

Patience, J. et al. 2002, ApJ, 581, 654

Paulson, D. B., & Yelda, S. 2006, PASP, 118, 706

Pecaut, M. J., Mamajek, E. E., & Bubar, E. J. 2012, ApJ, 746, 154

Pepe, F. et al. 2011, A&A, 534, A58

Perryman, M. A. C. et al. 1997, A&A, 323, L49

Pourbaix, D. 2000, A&AS, 145, 215

Pourbaix, D. et al. 2002, A&A, 386, 280

Poveda, A., Herrera, M. A., Allen, C., Cordero, G., & Lavalley, C. 1994, Revista Mexicana de Astronoma y Astrofsica, 28, 43

Qian, S.-B., Liao, W.-P., Zhu, L.-Y., & Dai, Z.-B. 2010, ApJ, 708, L66

Queloz, D. et al. 2001, A&A, 379, 279

Quinn, S. N. et al. 2015, ApJ, 803, 49

Quintana, E. V., Adams, F. C., Lissauer, J. J., & Chambers, J. E. 2007, ApJ, 660, 807

R., G. P., J., Q., V., Y., J., H., M.C., C., E., K., T., B. C., & E., K. S. ????, Geophysical Research Letters, 28, 1671

Raghavan, D., Henry, T. J., Mason, B. D., Subasavage, J. P., Jao, W.-C., Beaulieu, T. D., & Hambly, N. C. 2006, ApJ, 646, 523

Raghavan, D. et al. 2010, ApJS, 190, 1

Rasio, F. A., & Ford, E. B. 1996, Science, 274, 954

Reid, I. N. et al. 2004, AJ, 128, 463

Reid, I. N., & Gizis, J. E. 1997, AJ, 113, 2246

Reid, I. N., Hawley, S. L., & Gizis, J. E. 1995, AJ, 110, 1838

Rice, W. K. M., Wood, K., Armitage, P. J., Whitney, B. A., & Bjorkman, J. E. 2003, MNRAS, 342, 79

Riedel, A. R. et al. 2014, AJ, 147, 85

Rivera, E. J., Laughlin, G., Butler, R. P., Vogt, S. S., Haghighipour, N., & Meschiari, S. 2010, ApJ, 719, 890

Rivera, E. J. et al. 2005, ApJ, 634, 625

Riviere-Marichalar, P. et al. 2012, A&A, 538, L3

Robertson, P., & Mahadevan, S. 2014, ApJ, 793, L24

Robertson, P., Mahadevan, S., Endl, M., & Roy, A. 2014, Science, 345, 440

Royer, F., Gerbaldi, M., Faraggiana, R., & Gómez, A. E. 2002, A&A, 381, 105

Royer, F., Zorec, J., & Gómez, A. E. 2007, A&A, 463, 671

Ruck, M. J., & Smith, G. 1995, A&A, 304, 449

Samus, N. N., Durlevich, O. V., & et al. 2004, VizieR Online Data Catalog, 2250

Santos, N. C., Benz, W., & Mayor, M. 2005, Science, 310, 251

Saylor, D., Lepine, S., Crossfield, I., & Petigura, E. A. 2018, AJ, 155, 23

Schmidt, B. E., Blankenship, D. D., Patterson, G. W., & Schenk, P. M. 2011, Nature, 479, 502

Schmidt, S. J., Cruz, K. L., Bongiorno, B. J., Liebert, J., & Reid, I. N. 2007, AJ, 133, 2258

Scholz, R.-D., McCaughrean, M. J., Lodieu, N., & Kuhlbrodt, B. 2003, A&A, 398, L29

See, V., Jardine, M., Vidotto, A. A., Petit, P., Marsden, S. C., Jeffers, S. V., & do Nascimento, J. D. 2014, A&A, 570, A99

Ségransan, D., Delfosse, X., Forveille, T., Beuzit, J.-L., Udry, S., Perrier, C., & Mayor, M. 2000, A&A, 364, 665

Ségransan, D., Kervella, P., Forveille, T., & Queloz, D. 2003, A&A, 397, L5

Selsis, F., Kasting, J. F., Levrard, B., Paillet, J., Ribas, I., & Delfosse, X. 2007, A&A, 476, 1373

Simon, M. et al. 2017, ApJ, 844, 158

Smith, A. W., & Lissauer, J. J. 2009, Icarus, 201, 381

Söderhjelm, S. 1999, A&A, 341, 121

Strand, K. A. 1969, AJ, 74, 760

Subasavage, J. P., Jao, W.-C., Henry, T. J., Bergeron, P., Dufour, P., Ianna, P. A., Costa, E., & Méndez, R. A. 2009, AJ, 137, 4547

Tarter, J. C. et al. 2007, Astrobiology, 7, 30

Tinney, C. G., Butler, R. P., Jones, H. R. A., Wittenmyer, R. A., O'Toole, S., Bailey, J., & Carter, B. D. 2011, ApJ, 727, 103

Tokovinin, A. A. 1997, A&AS, 124, 75

Torres, C. A. O., Quast, G. R., da Silva, L., de La Reza, R., Melo, C. H. F., & Sterzik, M. 2006, A&A, 460, 695

Torres, G., Henry, T. J., Franz, O. G., & Wasserman, L. H. 1999, AJ, 117, 562

Tuomi, M. 2011, A&A, 528, L5

Turner, N. H., ten Brummelaar, T. A., McAlister, H. A., Mason, B. D., Hartkopf, W. I., & Roberts, Jr., L. C. 2001, AJ, 121, 3254

Uyama, T. et al. 2017, AJ, 153, 106

Valenti, J. A., Butler, R. P., & Marcy, G. W. 1995, PASP, 107, 966

Valenti, J. A., & Fischer, D. A. 2005, VizieR Online Data Catalog, 215

van Albada, G. B. 1957, Contributions from the Bosscha Observervatory, 5

van Altena, W. F., Lee, J. T., & Hoffleit, E. D. 1995, The general catalogue of trigonometric [stellar] parallaxes

Vogt, S. S., Butler, R. P., Rivera, E. J., Haghighipour, N., Henry, G. W., & Williamson, M. H. 2010a, ApJ, 723, 954

Vogt, S. S. et al. 2010b, ApJ, 708, 1366

von Braun, K. et al. 2011, ApJ, 729, L26

Walker, A. R. 1983, South African Astronomical Observatory Circular, 7

Walter, F. M., Vrba, F. J., Mathieu, R. D., Brown, A., & Myers, P. C. 1994, AJ, 107, 692

Weidner, C., & Horne, K. 2010, A&A, 521, A76

Weis, E. W. 1993, AJ, 105, 1962

——. 1996, AJ, 112, 2300

Weise, P., Launhardt, R., Setiawan, J., & Henning, T. 2010, A&A, 517, A88

Wichmann, R., Covino, E., Alcalá, J. M., Krautter, J., Allain, S., & Hauschildt, P. H. 1999, MNRAS, 307, 909

Wiegert, P. A., & Holman, M. J. 1997, AJ, 113, 1445

Wieth-Knudsen, N. 1957, Journal des Observateurs, 40, 93

Wilson, O. C. 1966, ApJ, 144, 695

Winn, J. N., & Fabrycky, D. C. 2015, ARA&A, 53, 409

Winn, J. N., Johnson, J. A., Albrecht, S., Howard, A. W., Marcy, G. W., Crossfield, I. J., & Holman, M. J. 2009, ApJ, 703, L99

Woolf, V. M., & Wallerstein, G. 2005, MNRAS, 356, 963

Worley, C. E., & Behall, A. L. 1973, AJ, 78, 650

Wright, J. T., Marcy, G. W., Howard, A. W., Johnson, J. A., Morton, T. D., & Fischer, D. A. 2012, ApJ, 753, 160

Xiao, H. Y., Covey, K. R., Rebull, L., Charbonneau, D., Mandushev, G., O'Donovan, F., Slesnick, C., & Lloyd, J. P. 2012, ApJS, 202, 7

Yu, L. et al. 2017, MNRAS, 467, 1342

Zucker, S., & Mazeh, T. 1994, ApJ, 420, 806

Zuckerman, B., & Song, I. 2004, ARA&A, 42, 685